

BARC NEWSLETTER
FOUNDER'S DAY SPECIAL ISSUE

OCTOBER 2014



भारत सरकार
Government of India



भाभा परमाणु अनुसंधान केंद्र
Bhabha Atomic Research Centre

BARC NEWSLETTER

Founder's Day

Editorial Committee

Chairman

Dr. S.K. Apte,
Director, Bio-Science Group

Editor

Dr. K. Bhanumurthy
Head, SIRD

Associate Editors for this issue

Dr. K. Bhanumurthy, SIRD
Dr. S.C. Deokattey, SIRD

Members

Dr. S.K. Apte, Bio-Science Group
Dr. R.C. Hubli, MPD
Dr. D.N. Badodkar, DRHR
Dr. K.T. Shenoy, ChED
Dr. A.P. Tiwari, RCnD
Dr. S.M. Yusuf, SSPD
Dr. A.K. Tyagi, ChD
Mr. G. Venugopala Rao, APPD
Dr. C.P. Kaushik, WMD
Dr. G. Rami Reddy, RSD
Dr. S. Kannan, FCD
Dr. A.K. Nayak, RED
Dr. S.K. Sandur, RB&HSD
Dr. S.C. Deokattey, SIRD

From the Editor's Desk...

The Founder's day Special Issue of the BARC Newsletter published every year on Founder's Day, carries award winning work of our Scientists and Engineers. DAE Awards 2012 received in 2013 and Merit Awards for R&D work in 2013.

DAE Awards 2012 received in 2013 and Merit Awards for R&D work in 2013 are being published in this issue. This year a total of sixty papers have been published. DAE Awards constitute 65% of the total award papers spanning a wide range of areas: from Chemical Sciences, Physical Sciences to Computer Sciences, Bio Sciences and Engineering. Some of the papers are purely research-based whereas others are application-oriented.

Apart from DAE Awards, BARC Scientists and Engineers received several awards for their R&D work, which was presented at various national and international fora (Merit Awardees). Some of the R&D work received special awards instituted by the sponsoring organizations. Some included oral presentations and others were Poster presentations.

This CD contains all the sixty papers which are grouped under 1.DAE Awards and 2. Merit Awards. Individual papers can be accessed from the Contents as well as from the Author index by clicking on the hyperlinks.



Dr. K. Bhanumurthy

On behalf of the Editorial Committee

DAE AWARDS 2012		
DAE Homi Bhabha Science & Technology Award [2012]		
1	Development of Process Sensors for Nuclear Reactor Applications P. R. Patil Reactor Control Division <i>Shri P.R. Patil is the recipient of the Award</i>	1
2	Indigenous Development of Laser Spectrometers for Investigation of Important Atmospheric Reactions P. D. Naik Radiation & Photochemistry Division <i>Dr. P.D. Naik is the recipient of the Award</i>	8
3	Science and Technology of Thin Film and Photonic Multilayers: Applications in Neutrons, X-rays, Lasers to Terahertz Spectral Regimes N.K. Sahoo Atomic & Molecular Physics Division <i>Dr. N.K. Sahoo is the recipient of the Award</i>	16
4	Secure Network Access System (SNAS) Gigi Joseph Computer Division. <i>Shri Gigi Joseph is the recipient of the Award</i>	26
5	Small-Angle Neutron Scattering from Bio- and Nano-Materials V.K. Aswal Solid State Physics Division <i>Dr. V.K. Aswal is the recipient of the Award</i>	31
6	Ultrafast Charge Transfer Dynamics in Super-Sensitized Quantum Dot Solar Cell Hirendra N. Ghosh Radiation and Photochemistry Division <i>Dr. Hirendra N. Ghosh is the recipient of the "DAE-SRC Outstanding Investigator Award"</i>	37
DAE Scientific & Technical Excellence Award [2012]		
7	Computational Hydrodynamics and MHD for Strategic Systems Srinivasagopalan Madhavan and Shashank Chaturvedi Computational Analysis Division, BARC, Visakhapatnam <i>Shri Srinivasagopalan Madhavan is the recipient of the Award</i>	43
8	Computational Hydrodynamics for Critical Systems Venkata Ramana Ikkurthi and Shashank Chaturvedi Computational Analysis Division, BARC, Visakhapatnam <i>Dr. Venkata Ramana Ikkurthi is the recipient of the Award</i>	46
9	Design and Development of High Precision Instruments, Automated Systems and Special Purpose Machines Sameer Bhatt Centre for Design & Manufacture <i>Shri Sameer Bhatt is the recipient of the Award</i>	49
10	Design Improvements in Spent Fuel Chopper at Prefe-2, Tarapur A.K. Jha, F.T. Qureshi and K. Agarwal Nuclear Recycle Board. <i>Shri A.K. Jha is the recipient of the Award</i>	53
11	Development of Assisting Tools (Software) for Prediction and Analysis of Impact of Radiation Emergency Rajvir Singh and K.S. Pradeepkumar Radiation Safety Systems Division <i>Shri Rajvir Singh is the recipient of the Award</i>	56
12	Development of Four Piece Servo manipulator R.V.Sakrikar, U. Sarkar, D. D. Ray, B. Sony, D. C. Biswas and K. Jayarajan Division of Remote Handling & Robotics <i>Shri R.V. Sakrikar is the recipient of the Award</i>	60
13	Extracting Equilibrium Unbinding Free Energy of Protein-Drug Complexes from Nonequilibrium Simulations Tusar Bandyopadhyay Theoretical Chemistry Section, Chemistry Group <i>Dr. Tusar Bandyopadhyay is the recipient of the Award</i>	66
14	Investigation of Interface Magnetic Structure of Thin Films using Polarized Neutron Reflectometry Surendra Singh and Saibal Basu Solid State Physics Division <i>Dr. Surendra Singh is the recipient of the Award</i>	71
15	Laser Based Instrumentation Aseem Singh Rawat Laser & Plasma Technology Division <i>Shri Aseem Singh Rawat is the recipient of the Award</i>	74
16	Nanomaterials for Luminescence and Hyperthermia Applications R. S. Ningthoujam Chemistry Division <i>Dr. R. S. Ningthoujam is the recipient of the Award</i>	79
17	Reactions involving Weakly Bound Nuclei: Role of Projectile Breakup S. Santra Nuclear Physics Division <i>Shri S. Santra is the recipient of the Award</i>	83
18	Synthesis of Palladium thiolate/Selenolate Complexes as Catalysts for Suzuki C-C Coupling Reactions Sandip Dey Chemistry Division <i>Dr. Sandip Dey is the recipient of the Award</i>	87
19	Generation and Thermodynamic Characterization of FGM induced Isentropic Compression. Aditi Ray Theoretical Physics Division <i>Dr. Aditi Ray is the recipient of the Award</i>	91
20	R&D related to Ear, Nose and Throat at the Medical Division Nalini Bhat Medical Division <i>Dr. Nalini Bhat is the recipient of the Award</i>	95
DAE Young Engineer Award [2012]		
21	Design and Development of Compact Pulse Forming Lines Surender Kumar Sharma and Anurag Shyam Energetics & Electromagnetic Division, BARC, Visakhapatnam <i>Dr. Surender Kumar Sharma is the recipient of the Award</i>	97
22	Development of Oxidation resistant High Temperature Mo based Alloy Bhaskar Paul and R.C. Hubli Materials Processing Division. <i>Shri Bhaskar Paul is the recipient of the Award</i>	102
23	Development of Remotely Operated Hydraulic Equipment for Remote Dismantling and Decommissioning of Nuclear Facilities P.K. Mishra, Abhijit Khuperkar, Shiju Varghese, Rites Ranjon, N.L. Soni and R.J. Patel Refueling Technology Division <i>Shri P.K. Mishra is the recipient of the Award</i>	106
24	Experimental Investigation on Coolability of Simulated Corium Melts with different Cooling Strategies P.P. Kulkarni, A.K. Nayak and P.K. Vijayan Reactor Engineering Division <i>Shri P.P. Kulkarni is the recipient of the Award</i>	111
25	Process Modeling and Simulation to develop UO₂-TRISO Coated Particle for Indian High Temperature Reactors P. K. Mollick, D. Sathiyamoorthy, P. T. Rao, R. Venugopalan and J. K. Chakravarty Powder Metallurgy Division, Materials Group <i>Shri P. K. Mollick is the recipient of the Award</i>	114
26	Variable Elimination from Linear Modular Constraints K.J. Ajith Reactor Control Division <i>Shri K.J. Ajith is the recipient of the Award</i>	117
DAE Young Scientist Award [2012]		
27	Separation and Complexation studies of Trivalent Actinides and Lanthanides using Soft Donor Ligands Arunasis Bhattacharyya Radiochemistry Division Shri Arunasis Bhattacharyya is the recipient of the Award	120
28	Novel Approaches for Mitigation of Radiation Toxicity by Modulation of Immune System Deepak Sharma and S. Santosh Kumar Radiation Biology & Health Sciences Division <i>Dr. Deepak Sharma is the recipient of the Award</i>	124
29	Photocatalytic oxidation (VOCs) : a Short Review on Gas-Solid Interactions Kaustava Bhattacharyya Chemistry Division <i>Dr. Kaustava Bhattacharyya is the recipient of the Award</i>	128
DAE Young Applied Scientist & Technologist Award [2012]		
30	Design, Development and Characterization of Single and Multilayer Films Arup Biswas Atomic & Molecular Physics Division <i>Shri Arup Biswas is the recipient of the Award</i>	131
31	Retrofitting of Servo-manipulator System in HLW Vitrification Cells of WIP, Trombay S.R. Shendge, D.S. Sandhanshiv, K.M. Singh, Shivani Patankar and Suresh Babu Nuclear Recycle Group <i>Shri Shivaji R. Shendge is the recipient of the Award</i>	136
32	Shock Studies using Electric Gun and Fabry-Perot Velocimeter A. K. Saxena, T.C. Kaushik and Satish C. Gupta Applied Physics Division <i>Shri A. K. Saxena is the recipient of the Award</i>	139
DAE Group Achievement Award [2012]		
33	Development of Hot Cells and their Embedded Parts K. Jayarajan, B. Sony, V.K. Shrivastava, R. Sahu, S. Panda, A.N. Jha and M.N. Rao Division of Remote Handling and Robotics, Design, Manufacturing & Automation Group Vivek Mahadev Seismology Division A.K. Pradhan Isotope Applications Division S. Sethi, S.P. Dey, K. Karmakar and S.B. Gaikwad Laser & Plasma Technology Division V.R. Bhave and Kuldeep Sharma Sealed Sources and Logistics, BRIT Anwer Tariq RAPP Cobalt Handling Facility, BRIT <i>Shri K. Jayarajan is the recipient of the Award</i>	142
34	Bench Scale Demonstration of Uranium Recovery from Acidic Nitrate based Nuclear Waste using Dispersion Liquid Membrane In Micro Porous Polymeric Fiber Contactor S. Mukhopadhyay Chemical Engineering Division, Chemical Engineering Group <i>Dr. Sulekha Mukhopadhyay is the recipient of the Award</i>	145
35	Design and Development of Tele Distress Alarm Device 'NIRBHAYA' C.K. Pithawa, S.K. Lalwani, V. Sinha, S. Srivastava, S. Bharade, S. Khole, A.D. Kamble, P. Jyothi, L.V. Muralikrishna and S.K.Patil Electronics & Instrumentation Group <i>Shri C.K. Pithawa is the recipient of the Award</i>	148
36	Development of Machinery Protection System D. A. Roy, Prema Kumar Kavalan, Mohit Kalra, Sanjay K. Jain and Gaurav Reactor Control Division, Electronics & Instrumentation Group <i>Shri D. A. Roy is the recipient of the Award</i>	151
37	Development, Installation and Commissioning of Protein Crystallography Beam-line at Indus-2 Synchrotron Source Ashwani Kumar, Himanshu Kumar Poswal, Biplab Ghosh, Ravindra D. Makde, K. K. Pandey and Surinder M. Sharma High Pressure & Synchrotron Radiation Physics Division, Physics Group Jagannath Technical Physics Division M.V. Hosur Raja Ramanna Fellow A.K. Sinha Centre for Design and Manufacture <i>Dr. S.M. Sharma is the recipient of the Award</i>	155
38	Thermal hydraulic and Material Compatibility Studies in Molten Salts A.K. Srivastava, A. Borgohain, S. S. Jana, V.K. Gupta and N.K. Maheshwari Reactor Engineering Division, Reactor Design & Development Group S. Rangarajan Water & Steam Chemistry Division A.G. Kumbhar and S.J. Keny Radiation & Photochemistry Division <i>Dr. N.K. Maheshwari is the recipient of the Award</i>	160
DAE Special Contribution Award [2012]		
39	Catalysts for Hydrogen Mitigation by Passive Autocatalytic Recombiner Salil Varma Chemistry Division <i>Shri Salil Varma is the recipient of the Award</i>	165
MERIT AWARDS 2013		
40	On the Isotope Effects of ZrCO_x (X = H, D and T): a First-Principles Study D. Chattaraj, S.C. Parida and Smruti Dash Product Development Division C. Majumder Chemistry Division <i>This Paper received the Mettler-Toledo Best Oral Presentation Award at the 19th DAE-BRNS Symposium on Thermal Analysis, held at Mumbai from Dec. 19-21, 2013</i>	168
41	Pore Diffusion controlled Leaching Model incorporating Particle Size Distribution: a Case Study K. Anand Rao, T. Sreenivas and A.K. Suri Mineral Processing Division <i>This Paper received the Misra Award for paper presented at the IIME Mineral Processing Technology Seminar, held at Bhubaneswar, from Dec.10-12, 2013</i>	171
42	Phase transition and Thermal Stability studies of Materials used as Electroceramics, Catalyst and Superconductors B.N. Wani Chemistry Division <i>This Paper received the NETZSCH-ITAS Award at the 19th DAE-BRNS Symposium on Thermal Analysis, held at Mumbai, from Dec. 19-21, 2013</i>	180
43	Hybrid Membrane Technology for Removal of Uranium from Ground water P.K.Tewari, R.C. Bindal, D. Goswami, K.P.Bhattacharyya, A.K.Ghosh, S. Shivayyanamath S.A.Tiwari and S. Pal Desalination Division <i>This Paper received the Nina Saxena Excellence in Technology Award [Competition for Nina Saxena Excellence in Technology Award held at IIT Kharagpur on 29th July, 2013]</i>	183
44	Stimuli-responsive Cucurbituril-adorned Supramolecular Micellar Assemblies of Cetylpyridinium Chloride Jyotirmayee Mohanty Radiation & Photochemistry Division <i>This Paper received the Samanta Chandra Sekhar Award 2011, at the Annual Meeting of the Odisha Bigyan Academy</i>	187
45	Fluorescence Enhancement with Plasmonic Nanostructures Sharmistha Dutta Choudhury Radiation & Photochemistry Division <i>This Paper received the SERB Women Excellence Award 2013 [Award constitutes a research grant for three years]</i>	191
46	Estimation of Distance Error by Fuzzy Set Theory required for Strength Determination of HDR ¹⁹²Ir Brachytherapy Sources Sudhir Kumar S, D. Sharma, G. Chourasiya and D. A. R. Babu Radiological Physics & Advisory Division D. Datta Health Physics Division D.N. Sharma Health Safety and Environment Group <i>This Paper received the Best Oral Paper Award from the Association of Medical Physicists of India, at the 34th National Conference of Association of Medical Physicists of India, Kolkata, Nov. 13-16, 2013.</i>	195
47	Hydrogen Isotope Storage Behavior of ZrCo_{1-x}Ni_x Alloys Ram Avtar Jat, S.C. Parida, Renu Agarwal and A.R. Joshi Product Development Division K.L. Ramakumar Radiochemistry and Isotope Group <i>This Paper received the Best Oral Presentation Award at the 19th DAE-BRNS Symposium on Thermal Analysis, held at Mumbai from Dec. 19-21, 2013</i>	199
48	Occupational Safety and Health Issues for Construction Projects-Supply Chain in BARC Praveen Dubey, S.D. Bharambe and S. Soundararajan Radiation Safety Systems Division Kaushik Kayal Civil Engineering Division <i>This Paper received the Best Paper Presentation Award at the International Conference on Managing Supply Chain for Global Competitiveness, held at the Indian Institute for Industrial Engineering, Nagpur, Oct. 25-27, 2013.</i>	205
49	Pre-Test Analysis of Molten Salt Natural Circulation Loop Using FLiNaK Salt A. K. Srivastava, A. Borgohain, N. K. Maheshwari, P. K. Vijayan Reactor Engineering Division <i>This Paper received the Best Poster Presentation Award at the [International Conference on Molten Salts In Nuclear Technology] held at Mumbai, from Jan. 9-11, 2013.</i>	210
50	Template-free Electrolysis of Gold Nanoparticles of Controlled Size Distribution for the Determination of Lead at Ultratrace Levels. Saurav K. Guin, Jisha S. Pillai, Arvind S. Ambolikar and Suresh K. Aggarwal Fuel Chemistry Division <i>This paper received the Best Poster Presentation Award at the 64th Annual Meeting of International Society of Electrochemistry (ISE) on "Electrochemistry for a new era" held at Santiago de Querétaro, Mexico, Sep. 8-13, 2013</i>	215
51	Titanium – Stainless Steel Brazing using Ag-Based alloys A. Laik and G.K. Dey Materials Science Division A. A. Shirzadi The Open University, Milton Keynes MK7 6AA, United Kingdom <i>This paper received the Best Poster, 2nd Prize (Materials Science) at the International Conference on Electron Microscopy & XXXIV Annual Meeting of EMSI, Kolkata, 3-5 July, 2013.</i>	219
52	Development of Rare Earth based Magnetic Alloy Powders by Reduction-Diffusion Method Kinshuk Dasgupta, Deepak Sahoo, Harvinderpal Singh Rare Earths Development Section, Materials Group Alok Awasthi Materials Processing Division <i>This paper received the Best Presentation Award at the International Conference on Magnetic Materials and Applications (MagMA 2013), IIT Guwahati, Dec. 5-7, 2013</i>	225
53	Thermodynamic Study of Uranium Sorption onto Biosynthesized Melanin Amardeep Singh Saini and Jose Savio Melo Nuclear Agriculture & Biotechnology Division <i>This Paper received the Best Oral Presentation Award at the 19th DAE-BRNS Symposium on Thermal Analysis, held at Mumbai from Dec. 19-21, 2013</i>	228
54	Corrosion of Modified 9Cr-1Mo Steel and Indian RAFMS in Static Pb-17Li at 773K P. Chakraborty, R.K. Fotedar and N. Krishnamurthy Fusion Reactor Materials Section, Materials Group M. J. Naik Indian Institute of Technology, Roorkee P. K. Pradhan Materials Processing Division <i>This Paper received the Best Oral Presentation Award at the 19th DAE-BRNS Symposium on Thermal Analysis, held at Mumbai from Dec. 19-21, 2013</i>	231
55	Structure based Variation in the Antimutagenic/Antioxidant Properties of Different Naphthoquinones Sanjeev Kumar, Satyendra Gautam and Arun Sharma Food Technology Division <i>India (EMSI) on "Current Perspectives on Environmental Mutagenesis and Human Health", Mumbai, Jan. 28-30, 2013.</i>	235
56	Perturbation of Cellular Redox as a Novel Strategy to Ameliorate Radiation-induced Gastro-intestinal Syndrome Lokesh Gambhir, Rahul Checker, Deepak Sharma and S. Santosh Kumar Radiation Biology & Health Sciences Division <i>This paper received the Best Poster Award at the International Conference on Advances in Free Radicals, Redox Signalling and Translational Antioxidant Research, Lucknow, Jan. 30- Feb. 1, 2013</i>	240
57	Investigation of the Effects of -OH group Substitution on the Radiation Stability of FAP (Fluoro alkyl phosphate) based Imidazolium Ionic Liquids Apurav Guleria, Ajay K. Singh, Sisir K. Sarkar and Soumyakanti Adhikari Radiation & Photochemistry Division <i>This paper received the Best Poster Award at the National Symposium on Radiation & Photochemistry (NSRP-2013), North Eastern Hill University, Shillong, 20-22 March, 2013</i>	247
58	Structure and Properties of Water in the Hydration Shell of Halide Ions as revealed by Raman Spectroscopy Mohammed Ahmed, Ajay K Singh, Jahur A. Mondal and Sisir K. Sarkar Radiation & Photochemistry Division <i>This paper received the Best Poster Award at the National Symposium on Radiation & Photochemistry (NSRP-2013), North Eastern Hill University, Shillong, 20-22 March, 2013</i>	250
59	Novel Designing of Thermo-elastic macroporous agarose-alginate composite biomaterial Anuj Tripathi and Jose Savio Melo Nuclear Agriculture & Biotechnology Division <i>This Paper received the Best Poster Award at the 19th DAE-BRNS Symposium on Thermal Analysis, held at Mumbai from Dec. 19-21, 2013</i>	253
60	FrmE: A Cadmium Inducible Protein is Characterized as a Disulfide Isomerase having Role in Oxidative Stress Tolerance in Deinococcus radiodurans Nivedita P. Khairnar and H.S. Misra Molecular Biology Division Min-Ho Joe, Sang-Yong Lim, Dong-Ho Kim Radiation Research Division for Biotechnology, Korea Atomic Energy Research Institute, Jeongseup, Republic of Korea. <i>This paper received the Best Poster Award during XXXIII Annual Conference of Environmental Mutagen Society of India and National Conference on Current Perspectives on Environmental Mutagenesis and Human Health, Mumbai, Jan. 28-30, 2013</i>	256
Author Index		

DEVELOPMENT OF PROCESS SENSORS FOR NUCLEAR REACTOR APPLICATIONS

P.R. Patil
Reactor Control Division

Shri P.R. Patil is the recipient of the DAE Homi Bhabha Science & Technology Award for the year 2012

Abstract

The importance of process sensors in monitoring, control and protection of nuclear reactor plant is well established. The process sensors for reactor applications are special in its category because of the challenges to perform reliably in the environment of high pressure, high temperature, nuclear radiation and harsh environmental conditions. Reactor Control Division has undertaken indigenous development program of highly customized process sensors for compact Light Water Reactor to achieve self-reliance in this important field. Different types of process sensors are successfully developed and qualified under this program. The salient features of various indigenously developed process sensors are presented in this article.

Introduction

The sensors are used in process systems of nuclear reactor plant for monitoring, plant control, protection and actuation of safety systems. The reliable functioning of the process sensors in all modes of the plant is important for plant availability and safety. Reactor Control Division (RCnD) of BARC has developed customized sensors for process systems of compact Light Water Reactor (LWR) project. Indigenously developed sensors are highly customized and designed to meet the specific application requirements, high pressure, high temperature, nuclear radiation endurance, stringent qualification requirements viz. environmental qualification, shock and vibration qualification, EMI/EMC qualification. These application requirements could not be met by commercially available sensors. As an application requirement of the plant, the sensors used for measurement of process parameters of reactor systems of LWR are designed with the following important features.

- Sensors designed to achieve zero leakage, welded process connection for the sensors connected to Reactor Coolant System (RCS) and high pressure system of the plant. Provision of back up pressure boundary in case of inadvertent failure of primary pressure boundary of the sensor, to prevent leakage of the coolant.
- Sensors are designed with bi-block arrangement wherein electronic converters are physically separated from primary converters. This arrangement enables primary converter to be mounted inside the containment and the electronic converter can be located outside the containment. Thus during accident, only the primary converters will encounter the accidental ambient conditions.
- Sensors of the safety systems which are mounted inside the containment are designed to withstand ambient conditions which may exist during Loss of Coolant Accident (LOCA).
- Sensors are designed for high process pressure, high temperature and high radiation.

BARC NEWSLETTER

Founder's Day

- Designed to meet the stringent environmental qualification tests, EMI/EMC, shock and vibration qualification tests.
- Level sensors are designed with top mounting due to layout constraints, accessibility and maintenance considerations.
- Remote health-check facility provided in sensor electronic converters which enables electronic converter health check and ensuring connectivity with the control system.

Process sensors developed for compact LWR

Multipoint Ultrasonic Level Sensor

Multipoint ultrasonic level sensor is designed to measure the water level in pressurized vessel reliably under varying process conditions, from atmospheric pressure to 21 MPa pressure and temperature up to 200°C, under the presence of high gamma radiation. As the vessel is embedded in the shielded cavity, conventional differential pressure (DP) type level measurement method for pressurized vessel cannot be used. Hence top mounted multipoint ultrasonic level sensor has been developed.

The sensor measures the level reliably during normal operating conditions as well as under accident conditions like LOCA which is associated with varying process conditions and harsh environmental conditions.

The level sensor works on the principle of change in ultrasonic energy while passing through liquid or gas, due to difference in acoustic impedance of water and gas. The sensor consists of identical 23 pairs of piezoelectric crystals hermetically sealed in stainless steel (SS) housing, which sense the water level at 23 different elevations in the vessel covering a measurement range of 0 – 2500 mm with measuring accuracy of ± 5 mm at each sensing point.

Piezoelectric crystal material and its bonding to the SS housing is very important for proper functioning

of the ultrasonic sensors particularly under varying temperature conditions and high gamma radiation. Technique for bonding of piezoelectric crystals to SS housing has been developed. After bonding of piezoelectric crystals in the sensor housing, sensors are hermetically sealed by welding. Special welding techniques are developed to avoid any damage to the piezoelectric crystals and signal wires inside the sensor housing during welding. The sensor is designed as fully welded construction and provided with a special flange suitable for welding to the mounting flange on the process vessel to ensure leak free joint. The sensors are tested for hydrotest pressure of 24 MPa.

The sensor is interfaced with electronic converter with high frequency signal cable of length up to 30 metre. Electronic converter excites the transmitting piezoelectric crystals, receives the signal generated by

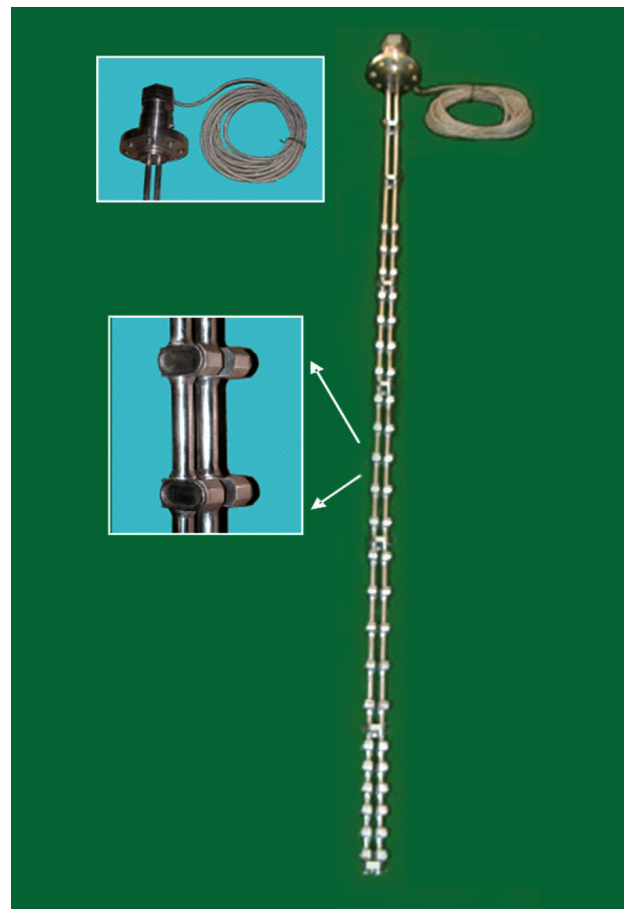


Fig.1: Multipoint Ultrasonic Level Sensor

BARC NEWSLETTER

Founder's Day



Fig.2: Electronic Converter and Discrete Level Indicator for Multi-point Ultrasonic Level Sensor

receiving crystals and generates analog output and level indication in discrete level indicator. Fig.1 shows Multipoint Ultrasonic Level Sensor and Fig.2 shows its electronic converter and Discrete Level Indicator.

The salient features of multipoint ultrasonic level sensor are as follows.

- Fully welded construction, welded process connection to ensure zero leakage.
- The level indication is not affected by changes in fluid properties due to change in process pressure and temperature; hence gives true level indication in all operation regimes of the plant including accident situation like LOCA.
- There is no drift in level indication and the sensor does not require periodic calibration or adjustments.
- The signal cables from the sensor pass through a specially designed high pressure cable seal mounted in the sensor head assembly which serves as a back up pressure boundary in case of inadvertent rupture of immersed portion of the level sensor.

LOCA qualified Absolute Pressure Sensor

Measurement of reactor coolant system pressure in all modes of reactor operation including accident conditions is important from safety consideration. As a safety requirement, pressure sensors connected to reactor coolant system are mounted inside the

containment and they must withstand the normal ambient conditions and harsh ambient conditions which exist during accident like LOCA. The signals for these pressure sensors are used for actuation of reactor safety systems. The pressure sensor should function during accident and maintain its functionality after the accident to ensure the safety of the plant.

Considering these requirements, bi-block type absolute pressure sensor with remotely mounted electronics is developed, so that the electronics can be kept out of accident zone and the pressure sensor is located inside the containment. Pressure sensor connected to remotely mounted electronics through pressure-tight screened cable up to 100 metre length.

Pressure sensor uses Bourdon tube as basic pressure sensing element. The deflection at the free end of the Bourdon tube due to the applied pressure is converted to electrical signal by customized high temperature Linear Variable Differential Transformer (LVDT). The pressure sensor is provided with back up pressure boundary to contain the process fluid in case of accidental rupture of Bourdon tube. The sensor is designed as fully welded construction with welded process connection to ensure zero leakage.

Absolute pressure sensors are developed for ranges, 0 – 25 MPa and 0 – 10 MPa with measurement accuracy of $\pm 1.0\%$ of span at reference condition. The over range pressure of the sensor is 150% of full scale. It provides 4 – 20 mA output (4 wire configuration) proportional to the measured pressure. The pressure sensor is designed to operate under LOCA, accidental ambient conditions of 180°C, 10 bar saturated steam atmosphere and Total Integrated Dose (TID) 50 MRad of gamma. Steam chamber test has been successfully carried out on the pressure sensor for LOCA qualification and performance checking under accidental (LOCA) environmental conditions. LOCA qualified Absolute Pressure Sensor is shown in Fig.3.



Fig.3: LOCA qualified Absolute Pressure Sensor

Three Channel Ultrasonic Flowmeter

The measurement of feed water flow rate to steam generators is important for plant safety and protection and hence requires triplicated measurement of feed water flow rate. Three channel ultrasonic flowmeter is developed for measurement of feed water flow rate to steam generators of nuclear reactor plant. The flowmeter has three independent channels on a single SS body. The ultrasonic flowmeter covers measurement range of 2 to 60 m³/hr with measurement accuracy of $\pm 1\%$ full scale. The measurement range can be extended up to 100 m³/hr. Design pressure and temperature of the flowmeter is 10 MPa and 90°C respectively.

The flowmeter works on principle of time of flight method and makes use of multiple reflections of the ultrasound to achieve high rangeability of around 30:1.

The performance of the flowmeter has been successfully tested in the flow calibration facility at IDEMI, Mumbai. Fig.4 shows Three Channel Ultrasonic Flow Meter.

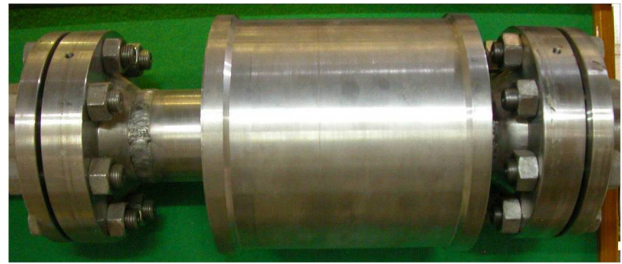


Fig.4: Three Channel Ultrasonic Flow Meter

The salient features of the three channel ultrasonic level sensor are as follows.

- Each measuring channel of the flowmeter is independent and provides four galvanically isolated analog outputs proportional to volumetric flow rate.
- Each measuring channel is provided with on-line diagnostic facility, remote health check, channel fault detection, zero calibration facility.
- Considering the compact layout and available short upstream straight length, the flowmeter is provided with specially designed in-built flow straightener.
- Measurement not affected by change in sonic velocity due to change in process temperature and pressure.

Thermocouple Assembly for reactor coolant temperature measurement

Measurement of reactor coolant inlet and outlet temperature is important for reactor control and protection. These measurements are challenging as they have to be carried out inside the reactor pressure vessel due to layout constraints. Response time of these sensors is very important as reactor coolant temperature signals are used for reactor control and protection. To achieve fast response, thermocouple assemblies are designed for direct contact with the reactor coolant. Hence, they are designed for pressure and temperature of reactor coolant system. The body of the thermocouple assembly is made of SS 321 and it has fully welded construction. The

BARC NEWSLETTER

Founder's Day

thermocouple assemblies are inserted into the reactor vessel through the guide tubes from the nozzles provided on the vessel and welded to the nozzles to ensure zero leakage. Proper support arrangement has been designed in the sensor assembly to reduce the flow induced vibrations. Thermocouple assemblies are designed to function under LOCA conditions. To ensure integrity of the sensor throughout its life, the thermocouple assemblies are subjected to various tests viz. Autoclave test, hydrostatic test at 40 MPa, Insulation Resistance test at room temperature and at high temperature (400°C), temperature cycle test, helium leak test, radiographic examination. Fig.5 shows the thermocouple assemblies for reactor coolant temperature measurement.

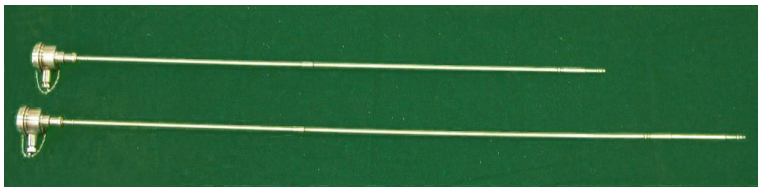


Fig.5: Thermocouple Assembly for reactor coolant temperature measurement

Capacitance type flexible level sensor

The capacitance level sensor is meant for continuous measurement of water level in the tanks of the process systems of the plant. The principle of the operation is based on the considerable difference in the dielectric constants of water and gas. Hence, the capacitance of the level sensor changes linearly with the change in water level of tank.

The capacitance level sensors are designed for pressure of 7 MPa and temperature up to 200 °C with measuring range of 0 – 900mm to 0 – 2000mm with accuracy of $\pm 1.5\%$ of span.

The level sensor is designed as flexible element to allow removal and installation of the sensor in the tanks with limited head room. The sensor has minimum bending radius of 600 mm. Capacitance Type Flexible Level Sensor is shown in Fig. 6.



Fig.6: Capacitance Type Flexible Level Sensor

The level sensors are provided with remotely mounted electronics and support a cable length of 30 metre. It provides 4 – 20 mA output (4 wire configuration) proportional to the measured level.

Ultrasonic type Presence of Gas Detector

Ultrasonic type presence of gas detector is developed to detect presence of gas in the top cavity of canned motor pump. In the canned motor pump, the pumped primary water is used for lubricating the bearings of the motor. If the lubricating water is absent in the top cavity of the pump, the pump operation should be stopped to avoid damage to the bearings. The sensor works on the principle of change in ultrasonic energy while passing through liquid or gas, due to difference in acoustic impedance of the water and air. The sensor is designed for 21 MPa pressure and temperature up to 200°C. It has fully welded construction and welded process connection. A specially designed high pressure cable seal provided in the sensor head assembly which serves as a back up pressure boundary in case of inadvertent rupture



Fig.7: Ultrasonic type Presence of Gas Detector

BARC NEWSLETTER

Founder's Day

in immersed portion of the level sensor. Ultrasonic type presence of gas detector is shown in Fig.7.

the water temperature with in built Resistance Temperature Detector (RTD).



Fig.8: Single point Ultrasonic Level Singnalizers

2.7 Single Point Ultrasonic Level Signalizers

The single point ultrasonic level signalizers are used to detect high and low water level in closed tanks. Four types of single point ultrasonic level signalizers have been developed are shown in Fig.8. These level sensors are designed with SS body, pressure of 21 MPa and temperature up to 200 °C.

2.8 Salinity Sensors

Salinity sensors are used to detect inadvertent ingress of sea water into DM water systems of plant. Salinity is the concentration of dissolved salt in a solution and is determined by measuring the conductivity of the solution by conductivity cell of known cell constant. The sensor continuously measures conductivity at process temperature and converts to conductivity at reference temperature of 25 °C by automatic temperature compensation. From the conductivity at reference temperature, salinity of the water is determined. Automatic temperature compensation is provided by sensing

Salinity sensors are developed to cover the salinity measurement range of 0.4 – 4 mg/litre, 1 – 10 mg/litre, 4 – 40 mg/litre, 10 – 100 mg/litre and 40 – 400 mg/litre. The sensors are designed for process pressure of 10 MPa and temperature 100°C. The remotely mounted electronics connected to the salinity sensor with a cable of

maximum 50 metre long. It provides analog output proportional to salinity of water and relay output on specified high salinity limit. Fig. 9 shows different types of salinity sensors.



Fig.9: Salinity Sensors

3. Qualification Requirements

The process sensors developed are subjected to the following qualification tests.

- Environmental qualification tests (High Temperature Test, Low Temperature Test, Moisture Resistance Test, High ambient pressure test, Low ambient pressure test, Water spray test, Salt spray test)
- EMI/EMC tests (as per MIL-STD 461C/E),

BARC NEWSLETTER

Founder's Day

- Shock qualification tests
- Vibration qualification tests,
- Radiation Endurance test
- Steam chamber test for checking the performance of the sensor during LOCA conditions

Conclusion

Reactor Control Division has successfully developed and qualified the process sensors for compact LWR, thus gaining self-reliance in this vital field. These sensors are indigenously developed to meet the customized application requirements of nuclear reactor plant, stringent environmental qualification requirements, EMI/EMC, shock and vibration qualification requirements. Technology for these sensors, manufacturing processes and inter stage testing methods have been developed. Testing and qualification requirements for the sensors have been

formulated. Development of technology for these sensors resulted in successful manufacturing of variety of sensors for the project with participation of indigenous industries. The technical know-how is transferred to ECIL for manufacturing of these sensors for future projects.

Acknowledgements

The author is thankful to Shri C.K. Pithawa, Director, E&I Group and Shri Y.S. Mayya, Associate Director, E&I Group, BARC for encouragement and support for sensor development program. Author is also thankful to Shri G.P. Srivastava, Ex-Director, E&I Group, Shri R.K. Patil, Ex-Associate Director, E&I Group and Shri B.B. Biswas, Ex-Head, RCnD for guidance. Author acknowledges the contributions of colleagues from BARC who have been associated with this sensor development program at various stages.

INDIGENOUS DEVELOPMENT OF LASER SPECTROMETERS FOR INVESTIGATION OF IMPORTANT ATMOSPHERIC REACTIONS

P.D. Naik

Radiation & Photochemistry Division

Dr. P.D. Naik is the recipient of the DAE Homi Bhabha Science & Technology Award for the year 2012

Abstract

The chemistry occurring in earth atmosphere, particularly in the troposphere and stratosphere, is of great concern to mankind. The most important pathway for the destruction of a chemical species in the troposphere is its reaction with OH radicals. Thus, the rate coefficient of a chemical species with OH radicals mainly determines its lifetime in troposphere. The chemical species having a longer lifetime enters the stratosphere and undergoes UV-photon induced photochemical reactions. The halogen atom generated by UV-photodissociation of halogen-containing chemical species takes part in the catalytic destruction of ozone, depleting the protective ozone layer. In our laboratory, the bimolecular rate coefficients of fluoroalcohols with OH have been measured employing laser photolysis- laser induced fluorescence technique, and estimated their tropospheric lifetimes. The formation dynamics of halogen atoms on UV- photon induced dissociation of halothane has also been investigated using indigenously developed Resonance Enhanced Multiphoton Ionization- Time-of-flight mass spectrometer setup. These studies provide information on fate and role of a chemical pollutant in atmosphere.

Introduction

Earth atmosphere can be divided into several layers depending on the properties under the consideration. With regard to temperature variation, the atmosphere can be divided into five major layers, namely, troposphere, stratosphere, mesosphere, thermosphere and exosphere. We are mainly concerned about the chemical reactions taking place in the troposphere and stratosphere, as man-made activities can influence the reaction taking place in these two layers. Moreover, the troposphere is the home place of everyday weather, and stratosphere consists of ozone layer, which absorbs harmful UV-radiation. Many chemicals are released in the troposphere due to anthropogenic and natural activities. The fate of these chemicals is decided by the

chemical/ physical process initiated by (1) solar photon of wavelength > 300 nm, (2) oxidizing species such as OH, O_3 , NO_3 , Cl etc., and (3) precipitation agents such as water droplet, rain, cloud, dew etc. present in the troposphere. Among all the above pollutant removal processes, the degradation by the OH oxidant species is the most important pathway. Hence, pollutant tropospheric lifetime is related to the rate of the above process. If this lifetime is short, few days, it contributes only to the local effect, such as smog, acid rain etc. However, if lifetime is long, it mainly contributes to the global effect such as global warming, and also diffuses into the stratosphere and takes part in stratospheric reactions. The former effect depends on pollutant's radiative forcing efficiency, which is related to absorption cross section in far-IR region,

BARC NEWSLETTER

Founder's Day

apart from its tropospheric lifetime. In stratospheric chemistry, the influence of chlorofluorocarbon (CFC) is well known. CFC being troposphericly stable and thus having long lifetime, enters the stratosphere, where on UV photon induced dissociation leads to the formation of Cl atom, a species which acts as a catalyst in ozone destruction reaction. Since 1970, about 4% per decade decline in stratospheric ozone was observed and much higher in Antarctic region during springtime [1].

The tropospheric global warming and ozone depletion in stratosphere have generated a lot of interest in atmospheric chemistry, and many research activities were initiated to assess the impact of industrially employed chemicals and new synthesized chemicals of potential applications, especially as refrigerants and fire extinguishers, on the tropospheric and stratospheric chemistry. Radiation and Photochemistry Division, BARC, has developed Laser Photolysis – Laser Induced Fluorescence (LP-LIF) for measurement of rate coefficients of chemical species with the OH radical, and Resonance Enhanced Multiphoton Ionization-Time-of-flight mass spectrometer (REMPI-TOF-MS) for understanding halogen atom formation dynamics on UV photoexcitation of halogen containing molecules. The article covers the kinetic measurement of the OH radical reaction with fluoroalcohols ($\text{CF}_3\text{CH}_2\text{OH}$, $\text{CF}_3\text{CF}_2\text{CF}_2\text{CH}_2\text{OH}$ and $\text{CHF}_2\text{CF}_2\text{CH}_2\text{OH}$) employing LP-LIF setup, and Cl and Br atom formation dynamics on 235 nm excitation of halothane employing REMPI-TOF-MS.

Tropospheric Impact: Tropospheric lifetime of fluoroalcohols with respect to OH radical reaction

Experimental setup

Partially fluorinated alcohols (HFAs) have been considered as new generation alternative of CFC for

applications such as cleaning of electronic components, refrigeration, and as carrier compounds for lubricants [2]. Due to the presence of both abstractable hydrogen atoms and OH group, the chemical reactivity of HFAs is likely to be higher than the present alternative of CFC, i.e., hydrofluorocarbons (HFCs). The major pathway of HFAs removal in troposphere is expected to be by reaction with the OH radical. We have measured the rate coefficients of fluoroalcohols ($\text{CF}_3\text{CH}_2\text{OH}$, $\text{CF}_3\text{CF}_2\text{CF}_2\text{CH}_2\text{OH}$ and $\text{CHF}_2\text{CF}_2\text{CH}_2\text{OH}$) with the OH radical, using indigenously developed LP-LIF experimental setup [3-5]. A schematic of the same is shown in Fig. 1. Hydrogen peroxide, which

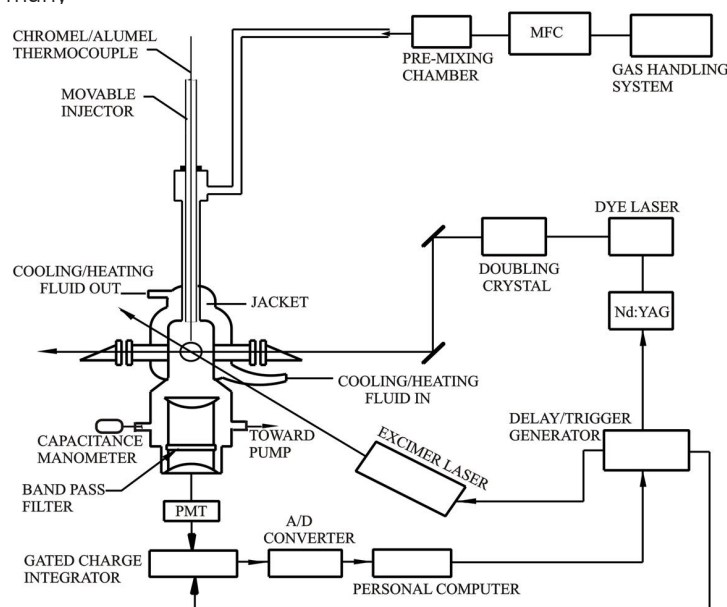


Fig. 1. : Schematic of LP-LIF setup employed for kinetic studies.

gives exclusively OH radical on 248 nm (KrF excimer laser) photolysis, was used as precursor for the OH radical. A Nd:YAG pumped frequency-doubled dye laser, tuned to ~ 308 nm, was employed as a probe laser to excite the $P_1(2)$ line in the (0,0) band of the ($A^2\Sigma$) $\leftarrow (X^2\Pi)$ transition. The reaction chamber is a double-walled Pyrex glass cell, fitted with MgF_2 windows at the Brewster angle, and experiments were carried out under flow condition. The pump and the probe laser beams, intersect at right angle at the center of the reaction cell. The reaction cell temperature was varied and maintained by circulating water through the outer

BARC NEWSLETTER

Founder's Day

jacket from a thermostatic bath. Temperature at the intersection zone of the pump and the probe laser beams was measured by introducing a Chromel-Alumel thermocouple from the top. A capacitance manometer was used to measure the total pressure in the reaction cell, and the partial pressures of the individual gases were estimated based on their flow rates. The fluorescence of OH from the intersection volume was collected by a lens (diameter = 38 mm, focal length = 50 mm), and detected by a photomultiplier tube (PMT; Hamamatsu, model R928P), kept orthogonal to both the laser beams, after passing through a band pass filter. The reaction is initiated by generating OH by photolysis of its precursor H_2O_2 by pump laser, in a flowing mixture of reactant, precursor and buffer gas. The time $t=0$ is the time at which the pump laser is fired. The temporal profile of the OH concentration was obtained by varying the delay between the pump and the probe laser pulses and measuring the LIF signal, which is integrated by a boxcar and averaged for 30 laser pulses, at each delay time. The signal is fed into an interface for A/D conversion. Both the pump and the probe laser intensities were monitored by photodiodes, and the average values of 30 laser pulses were used to normalize the averaged LIF signal intensity at each delay time.

To obtain OH decay profile at various concentrations of fluoroalcohols, the flow rates of fluoroalcohols–He mixture and pure helium were adjusted at different ratios, keeping the total flow rate of these two together constant. All the kinetic measurements were carried out at nearly constant total pressure of ~ 55 Torr. The flow velocity of the experimental mixture was kept to ~ 10 cm/s, to make sure that a fresh gaseous reaction mixture was seen by each pulse of the photolysis laser operating at 20 Hz. The number density of H_2O_2 molecule in the reaction cell was maintained to around 1×10^{14} molecules cm^{-3} . At this concentration of H_2O_2 , the concentration of OH generated is estimated to be in the range of 10^{10} – 10^{11} molecules cm^{-3} , using the laser fluence employed

for the experiments and absorption cross-section of H_2O_2 at 248 nm. The concentration of a fluoroalcohol estimated on the basis of total pressure and flow rates was cross-checked by measuring the FTIR spectrum of the mixture, collected downstream of the reaction cell.

Results and Discussion

The intensity of the fluorescence signal is proportional to the concentration of OH, and its variation with time, i.e., the pump-probe delay time, gives the concentration of OH as a function of reaction time. The experiments are carried out under pseudo first order condition, the concentration of fluoroalcohol \gg [OH]. Thus, at a given temperature and composition of the reaction mixture, the OH fluorescence intensity decay follows a first-order exponential relation,

$$S_t = S_0 e^{-k't} \quad (1)$$

Where, S_t and S_0 are the LIF intensities at time $t = 0$ and t , respectively. The pseudo-first-order rate coefficient, k' , is obtained from the linear least-square fit of the plot of $\log(\text{LIF intensity})$ vs. time, as shown in Fig. 2. The rate coefficient, k' , is related to the bimolecular rate coefficient, k_{II} , by the expression,

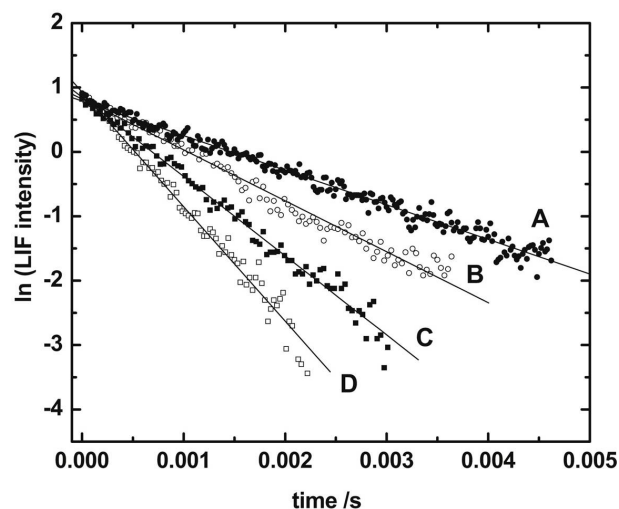


Fig. 2 : Typical profiles of OH radical decay with time, at room temperature, with increasing concentration of $\text{CHF}_2\text{CF}_2\text{CH}_2\text{OH}$.

BARC NEWSLETTER

Founder's Day

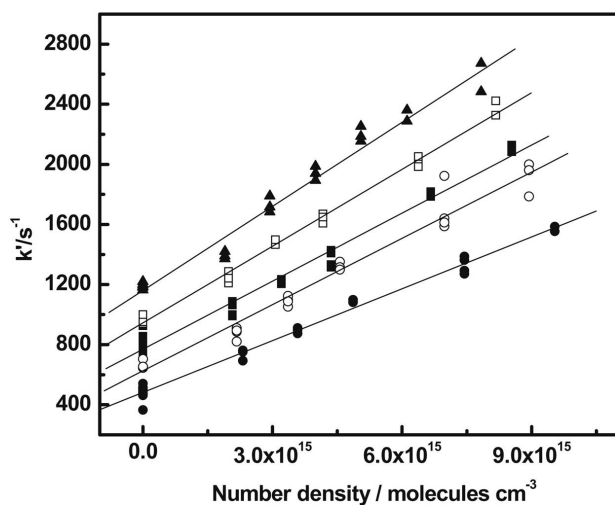


Fig. 2: Typical profiles of OH radical decay with time, at room temperature, with increasing concentration of $\text{CHF}_2\text{CF}_2\text{CH}_2\text{OH}$.

$$k' = k_{\text{II}} [\text{fluoroalcohol}] + k_0, \quad (2)$$

where $[\text{fluoroalcohol}]$ is the number density of fluoroalcohol and k_0 is the sum of all first-order rate coefficients of OH loss, except by reaction with fluoroalcohol. The ratio $[\text{fluoroalcohol}]/[\text{OH}]$ are kept in the order of 10^5 , to minimize the secondary reactions. A typical plot of k' vs. $[\text{fluoroalcohol}]$ at different temperature is shown in Fig. 3. From the plots the values of the bimolecular rate coefficient $k_{\text{II}}(T)$ at that temperature T , and k_0 , were obtained. The bimolecular rate coefficients were obtained at various temperatures, and Arrhenius plot of the same is constructed to calculate E_a/R and the A-factor.

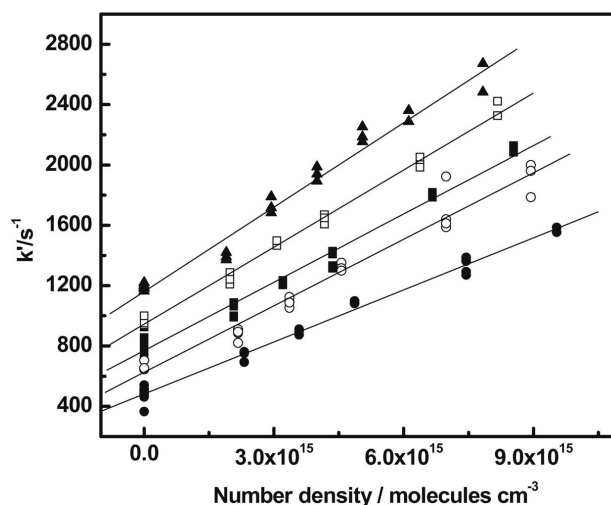


Fig. 3: Pseudo first-order decay constants (k') with the concentration of $\text{CHF}_2\text{CF}_2\text{CH}_2\text{OH}$ at different temperatures.

The kinetic parameters, k_{298} and E_a/R , for reaction of the OH radical with primary fluoroalcohols, obtained in our laboratories along with other reported work, are tabulated in Table 1. From these kinetic data, two conclusions can be drawn. (1) The reactivity of fluoroalcohols increases with the increase in its number of abstractable hydrogen atom in the fluorinated chain, and is more pronounced for the hydrogen atom on the terminal carbon atom. (2) The reactivity has negligible dependence on the number of CF_2 units in the molecule.

Atmospheric implications

We have estimated the tropospheric lifetime of the studied fluoroalcohols with respect to the OH radical reaction

Table 1: k_{298} and E_a/R for fluoroalcohols with $-\text{CH}_2\text{OH}$ end group.

Molecule	$k_{298} \times 10^{13}$ ($\text{cm}^3 \text{ molecule}^{-1} \text{ s}^{-1}$)	E_a/R	Method and Reference
$\text{CF}_3\text{CH}_2\text{OH}$	1.03 ± 0.10	760 ± 170	LP-LIF (our work [5])
$\text{CF}_2\text{HCH}_2\text{OH}$	2.52 ± 0.44		LP-RF [6]
	4.57 ± 0.38		RR-FTIR [7]
$\text{CFH}_2\text{CH}_2\text{OH}$	16.3 ± 0.9	330 ± 45	PLP-LIF [8]
	13.9 ± 0.5		RR [7]
$\text{CF}_3\text{CF}_2\text{CH}_2\text{OH}$	1.0 ± 0.1	900 ± 70	LIF [9]
$\text{CHF}_2\text{CF}_2\text{CH}_2\text{OH}$	1.67 ± 0.04	565 ± 40	LP-LIF [5]
$\text{CF}_3\text{CF}_2\text{CF}_2\text{CH}_2\text{OH}$	1.15 ± 0.10	765 ± 85	LP-LIF [5]
$\text{CF}_3\text{CHF}_2\text{CF}_2\text{CH}_2\text{OH}$	1.30 ± 0.08	880 ± 40	LP-LIF [10]

BARC NEWSLETTER

Founder's Day

Table 2: Comparison of tropospheric lifetimes of fluoroalcohols with CFC and HFC.

Molecule	Tropospheric lifetime		GWP (Time Horizons)		
	τ_{OH}	τ_{total}	20 yr	100 yr	100 yr
CF ₃ CH ₂ OH	154 day	106 day			
CF ₃ CF ₂ CF ₂ CH ₂ OH	142 day	137 day	90	25	8
CHF ₂ CF ₂ CH ₂ OH	81 day	46 day			
CFC-12		100 yr.	10340	10720	5230
HFC134 (CHF ₂ CHF ₂)		9.6 yr.	3200	1090	337

at 272 K, which is taken as the average temperature of the troposphere for chemical species lifetime estimation. Apart from the reaction with the OH radical, the other important pathway for removal of fluoroalcohols in the troposphere is uptake in the cloud droplets and subsequent rain out. The estimated tropospheric lifetimes are tabulated in Table 2, along with the reported values. The global warming potential at various time horizons for CF₃CF₂CF₂CH₂OH and CFC-12 and HFC-134 are also included in Table 2. It may be concluded that fluoroalcohols are better candidates than CFC-12 and HFC-134, in terms of their global warming implication.

Stratospheric Impact: Cl and Br formation dynamics on UV-photodissociation of halothane

Experimental

The indigenously developed resonance-enhanced multiphoton ionization (REMPI) with time-of-flight (TOF) mass spectrometer was employed for investigating photodissociation dynamics of halothane, by detecting the photoproducts, Br($4P_{3/2}$), Br*($4P_{1/2}$), Cl($3P_{3/2}$) and Cl*($3P_{1/2}$) atoms, state-selectively. The photograph of the setup is shown in Fig. 4, which is described in detail in our previous publications [11, 12]. In brief, a pulsed supersonic molecular beam was generated using a solenoid valve nozzle and conical skimmer. A time-of-flight mass spectrometer (TOF-MS), two-stage Wiley-McLaren type [13], was mounted vertically, perpendicular to the horizontal MB, with 18 mm dual microchannel plates as a detector. The halothane molecules seeded in helium were obtained by bubbling helium through



Fig. 4 : Photograph of REMPI-TOF-MS setup

a sample maintained at room temperature, and the molecular beam, formed after passing through nozzle-skimmer arrangement, was intercepted by a laser beam in the ionization region of the TOF assembly. In this experiment, a single colour laser was used for both photodissociation of the parent molecule and ionization of the photoproducts, halogen atoms. A Nd:YAG pumped dye laser was employed for generating the requisite tunable laser beam in 586-607 nm range. This fundamental dye laser output after frequency-doubling followed by mixing with the fundamental output of the Nd:YAG laser gives output in the range 230-236 nm for 2+1 REMPI of Cl and Br atoms. The laser line width was broadened ($> 1.5 \text{ cm}^{-1}$) for all the REMPI experiments by operating the Nd:YAG laser without an injection seeder, and the dye laser without a set of line width narrowing prisms in

BARC NEWSLETTER

Founder's Day

the laser cavity. The laser line width was always greater than the Doppler profile of the recoiling halogen atom fragments. The laser beam was passed through a converging lens of 200 mm focal length, and the distance between the lens and the interaction zone was adjusted to obtain the best ratio of on- and off-resonant signals.

Digital delay/pulse generator of 20 ps pulse resolution was used as master for time synchronization of all the instruments. The ion signal from MCP was fed to a boxcar gate integrator and after averaging for 30 laser pulses, passed on to an interface (SRS 245) for A/D conversion. A PC was used to control the scan of the dye laser via an RS232 interface, and collect data from SRS 245, through a GPIB interface, using a control and data acquisition program. For obtaining TOF spectrum, the MCP signal was fed to a 500 MHz digital oscilloscope (LeCroy 9350A), which was interfaced to a Pentium PC. The contributions to the signal from pump-oil related background and the multiphotonic processes were removed by subtracting the off-resonant signals from the on-resonant signals.

A double Fresnel rhomb was used for rotation of the laser beam polarization entering the chamber. TOF profiles were taken for three different experimental configurations, vertical (laser polarization || detection axis), horizontal (laser polarization \perp detection axis), and magic angle (laser polarization at 54.78° to the detection axis).

Analysis of the Experimental Data

Analysis of TOF profile

Photodissociation of halothane at ~ 234 nm generates Br and Cl, in both the ground ($^2P_{3/2}$) and the excited ($^2P_{1/2}$) spin orbit states, which were detected using (2+1)-REMPI and TOF mass spectrometer. The observed TOF profiles of Br, Br*, Cl and Cl* were analyzed, using a forward convolution method, described in detail in earlier publication [14], and the photofragment speed distribution, $P(v)$ and anisotropy parameter, β , were

obtained. The former is converted into the center-of-mass translational energy distribution, $P(E_T)$ and the average translational energy was calculated. A typical photofragment center-of-mass translational energy distribution $P(E_T)$ for Cl atom is shown in Fig. 5.

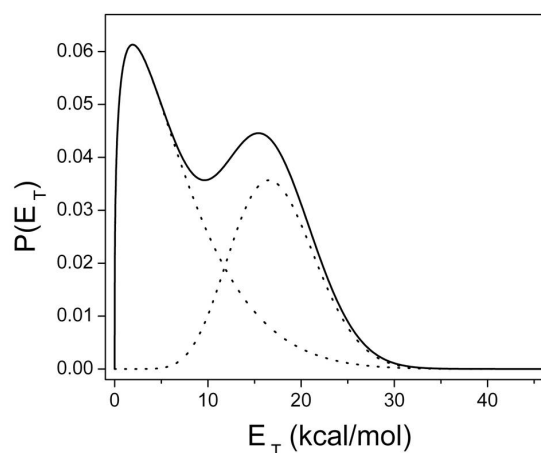


Fig. 5: Photofragment centre-of-mass translational energy distribution of chlorine atom, the dashed lines indicate the speed distributions for the fast and slow component.

Spin-orbit branching ratio

The ground $X(^2P_{3/2})$ and the spin-orbit excited $X(^2P_{1/2})$ atomic halogen photoproducts were scanned in the region of their two photon transitions, and the ion intensity due to a species X, $S(X)$, is obtained. The ratio of number density of X^* , $N(X^*)$ and X, $N(X)$ species is related to the measured ion intensity ratio by an expression,

$$\frac{N(X^*)}{N(X)} = k \frac{S(X^*)}{S(X)} \quad (3)$$

where k represents the relative ionization probability. The quantum yield values of spin orbit excited halogen atom, $\Phi(\text{Br}^*)$ and $\Phi(\text{Cl}^*)$, were calculated from the number density ratios to be 0.23 ± 0.05 and 0.22 ± 0.02 , respectively.

Discussion and Stratospheric Impact

The UV excitation of halothane at ~ 234 nm leads to the $\sigma^*(\text{C-Br}) \leftarrow n(\text{Br})$ transition. The parent molecule

BARC NEWSLETTER

Founder's Day

undergoes the C-Br bond rupture on the excited potential energy surface, which is repulsive along the C-Br bond, and produces bromine atom in both the ground $\text{Br}(^2P_{3/2})$ and the spin-orbit excited $\text{Br}^*(2P_{1/2})$ states, with the former accounting for 77% of the total bromine yield. Both Br and Br^* are produced with anisotropic distributions, characterized by the recoil anisotropy parameter β value of 0.6 ± 0.2 . This β value is lower than the expected value of 2.0 for a parallel transition. This indicates that some contribution from the perpendicular transition and non-adiabatic curve crossing may be responsible for lower β value. We measured translational energy distributions and estimated the fraction of the available energy partitioned to the relative translation (f_r) to be 0.17 for both the Br and Br^* channels, which is in reasonably good agreement with the predicted value of 0.22 by a soft impulsive model.

In addition to the C-Br bond rupture in halothane, we also observed the unexpected C-Cl bond cleavage channel on UV laser excitation, with β value of 0.3 ± 0.1 . Since only the C-Br bond is directly excited at 234 nm, the formation of chlorine atom involving the C-Cl bond rupture cannot be through the direct excitation of halothane. Based on our excited state calculations the C-Cl bond rupture is explained by intramolecular electronic energy transfer involving an avoided crossing of the $n\sigma^*(\text{C-Br})$ and the $n\sigma^*(\text{C-Cl})$ diabatic potential energy surfaces near the excitation energy of ~ 122 kcal/mol above the ground electronic state. Thus, the C-Cl bond rupture results due to the transition from the $n\sigma^*(\text{C-Br})$ to the $n\sigma^*(\text{C-Cl})$ surface. Like formation of the bromine atom, the chlorine atom also has two pathways producing Cl and Cl^* , with the former accounting for 78% of the total chlorine yield. Although, the velocity distribution of bromine atom has a single component, that of chlorine atom has two components (shown in Fig. 5), implying two different mechanisms of chlorine formation. The relative translational energies for the fast (high energy) and slow (low energy) Cl channels are 17.5 ± 2.0 and 7.5 ± 1.0 kcal/mol, respectively. The fractions of the

low and high translational energy components are determined to be 75% and 25%, respectively, for the Cl channel. Similarly, the average translational energies for the fast and slow Cl^* channels are 21.0 ± 2.0 and 9.5 ± 1.0 kcal/mol, respectively. For the Cl^* channel as well, the slow component contributes predominantly to the total yield, accounting for about 95%. The minor fast Cl atom channel originates from the impulsive C-Cl bond rupture. Hence, the experimental fT values agree well with the predicted value by the soft impulsive model. The slow chlorine atoms are most likely generated from the vibrationally excited ground electronic state of halothane after fast internal conversion from the lower adiabatic state. The measured fT values of the slow chlorine atoms are somewhat greater than the statistical values. The β values of chlorine atom channels are reduced to 0.3 ± 0.1 from that of the bromine atom channels (0.6 ± 0.2), due to the curve crossing. The branching ratio of the low kinetic energy C-Cl bond scission to the high energy C-Cl bond scission is 0.65/0.35.

The branching ratio of the C-Br bond scission to the C-Cl bond scission channel in halothane on excitation at 234 nm was estimated, using the relative ionization probability of Cl to that of Br^* as 1.24 ± 0.30 [15], and found to be $\sim 13.0/1.0$. Thus, the C-Br bond rupture is the major C-X bond dissociation channel accounting for $\sim 93\%$ of the total X (Br and Cl) yields. As per atom basis, bromine has global ozone depletion potential 60 times higher than chlorine; hence impact on stratosphere will be quite significant if any transfer of halothane from troposphere to stratosphere takes place.

Conclusion

The author is involved in indigenously development of several state-of-the-art experimental facilities for chemical physics research, and setups described in this article are two of them. The facilities are employed to deduce the microscopic aspects of chemical reactions relevant to atmospheric chemistry. The

BARC NEWSLETTER

Founder's Day

facilities developed have potential applications in environmental studies, ultrasensitive remote analytical techniques for nuclear waste, explosive detection, etc.

Acknowledgments

Author sincerely acknowledges with thanks the significant contributions made by his colleagues in Chemical Dynamics Section, Radiation & Photochemistry Division, BARC. He would also like to thank Dr. D.K. Palit, Dr. B.N. Jagatap, Dr. S.K. Sarkar and Dr. T. Mukherjee for their support and encouragement throughout the course of this work.

References

1. NOAA, Scientific Assessment of Ozone Depletion, 1998 and 2010
2. Hurley, M.D., Misner, J.A., Ball, J.C., Wallington, T.J., Ellis, D.A., Martin, J.W., Mabury, S.A., Sulbaek Andersen, M.P., Atmospheric chemistry of $\text{CF}_3\text{CH}_2\text{CH}_2\text{OH}$: Kinetics, mechanisms and products of Cl atom and OH radical initiated oxidation in the presence and absence of NO_x , *J. Phys. Chem. A*, 109 (2005) 9816-9826.
3. Naik, P.D., Kumar, A., Upadhyaya, H.P., Bajaj, P.N. and Sarkar, S.K. Laser Induced Fluorescence Spectroscopy, Lasers in Chemistry, Vol. 1, Ed. M. Lackner, Wiley-VCH Verlag GmbH (2008), p 463
4. Naik, P.D., Upadhyaya, H. P., Kumar, A., Sapre, A. V. and Mittal, J. P. Dynamics of Acetic Acid Dissociation at 193.3 nm: Selectivity in OH Reaction Channel, *Chem. Phys. Letters*, 340 (2001) 116-122
5. Indulkar, Y.N., SenGupta, S., Waghmode, S.B., Awadhesh Kumar, Dhanya, S., Naik, P.D., Kinetic study of gas phase reactions of OH with $\text{CF}_3\text{CH}_2\text{OH}$, $\text{CF}_3\text{CF}_2\text{CF}_2\text{CH}_2\text{OH}$ and $\text{CHF}_2\text{CF}_2\text{CH}_2\text{OH}$ using LP-LIF method, *Atmospheric Environment* 45 (2011) 6973-6979.
6. Kovács, G., Szász-Vadász, T., Papadimitriou, V.C., Dobe, S., Berces, T., Marta, F., Absolute rate coefficients for the reactions of OH radicals with $\text{CH}_3\text{CH}_2\text{OH}$, $\text{CF}_2\text{HCH}_2\text{OH}$ and $\text{CF}_3\text{CH}_2\text{OH}$, *Reaction Kinetics and Catalysis Letters* 87 (2006) 129-138.
7. Sellevåg, S.R., Nielsen, C.J., Søvde, O.A., Myhre, G., Sundet, J.K., Stordal, F., Isaksen, I.S.A., Atmospheric gas-phase degradation and global warming potentials of 2-fluoroethanol, 2,2-difluoroethanol, and 2,2,2-trifluoroethanol, *Atmospheric Environment* 38 (2004) 6725-6735.
8. Rajakumar, B., Burkholder, J.B., Portmann, R.W., Ravishankara, A.R., Rate coefficients for the $\text{OH} + \text{CFH}_2\text{CH}_2\text{OH}$ reaction between 238 and 355K, *Phys. Chem. Chem. Phys.* 7 (2005) 2498-2505.
9. Tokuhashi, K., Nagai, H., Takahashi, A., Kaise, M., Kondo, S., Sekiya, A., Takahashi, M., Gotoh, Y., Suga, A., Measurement of the OH reaction rate coefficients for $\text{CF}_3\text{CH}_2\text{OH}$, $\text{CF}_3\text{CF}_2\text{CH}_2\text{OH}$, and $\text{CF}_3\text{CH}(\text{OH})\text{CF}_3$, *J. Phys. Chem. A*, 103 (1999) 2664-2672.
10. Chen, L., Tokuhashi, K., Kutsuna, S., Sekiya, A., Yonei, Y., Yamamoto, A., Kinetic study of gas phase reactions of $\text{CF}_3\text{CHFCH}_2\text{CH}_2\text{OH}$ with OH radicals at 230-430 K, *Chem. Phys. Letters*, 382 (2003) 277-282.
11. Naik, P.D., Upadhyaya, H. P., Kumar, A., Bajaj, P.N., Sinha, A.K., Bhatt, S. and Gupta, M.D.P., Development of resonance-enhanced multiphoton ionization system, BARC Report No.: BARC/2009/E/011.
12. Upadhyaya, H.P., Saha, A., Kumar, A., Bandyopadhyay, T., Naik, P.D. and Bajaj, P.N. Photodissociation Dynamics of Phosphorus Trichloride (PCl_3) at 235 nm Using Resonance Enhanced Multiphoton Ionization (REMPI) with Time-of-Flight (TOF) Mass Spectrometry, *J. Phys. Chem. A*, 114 (2010) 5271-5278.
13. Wiley, W.C., McLaren, I.H., Time-of-Flight Mass Spectrometer with Improved Resolution, *Rev. Sci. Instrum.* 26 (1955) 1150-1157.
14. Saha, A., Kawade, M., Upadhyaya, H. P., Awadhesh Kumar, Naik, P.D., Photoexcitation of 2-bromo-2-chloro-1,1,1-trifluoroethane (halothane) to repulsive surface $\sigma^*(\text{C-Br})$ at 234 nm: Dynamics of C-Br and C-Cl bond rupture, *Chem. Phys.* 416 (2013) 1-10.
15. Park, M.S., Jung, Y.J., Lee, S.H., Kim, D.C., Jung, K.-H., The role of 3P^0+ in the photodissociation of BrCl at 235 nm, *Chem. Phys. Letters* 322 (2000) 429-438.

SCIENCE AND TECHNOLOGY OF THIN FILM AND PHOTONIC MULTILAYERS: APPLICATIONS IN NEUTRONS, X-RAYS, LASERS TO TERAHERTZ SPECTRAL REGIMES

N.K. Sahoo

Atomic and Molecular Physics Division

Dr. N.K. Sahoo is the recipient of the DAE Homi Bhabha Science & Technology Award for the year 2012

Abstract

Thin film multilayers as 1D photonic crystal has been serving the science world both technologically as well as with fundamental research interest. It's the tailored photonic band gap that is made use of in the efficient reflection, antireflection and polarization of electromagnetic radiations from terahertz, infrared, optical, X-rays to neutron wavelength regime. The physical basis of these multilayers is to essentially create an appropriate refractive index (or polarizability) contrast between the layers in order to manipulate the amplitude, phase and polarizations of these electromagnetic radiations to serve the ultimate interests. However, each wavelength and energy regime has specific complex issues in designing and developing these multilayers. Moreover, with the emerging novel electromagnetic sources, the challenges are being compounded regularly to appropriately overcome the materials, numerical design, development and characterization issues. The present article is a small attempt to present a glimpse of the multilayer R&D issues and possible solution in the present science and technology context.

Introduction

Presently, the word "thin film" no longer needs a formal introduction or explanation. Thin film technology, simultaneously, is one of the oldest arts as well as one of the ever expanding science and technology [1]. The field have shown remarkable progresses, especially over the past few decades, depicting unparalleled potentials from scientific to commercial domains. It has been projected to be one of the major processing techniques to fabricate electronic, optical, optoelectronic, photonic, spintronics, magnetic data storage devices, sensors, fuel cells, solar cells, communication devices, etc [2]. Departmentally, thin films and multilayer devices have been dominating the high-end scientific and technology researches in various atomic energy programs pertaining to the material sciences, astrophysical sciences, space-telescope technology, solar cell researches, laser

spectroscopy, reactor core-viewing optical periscopes and wide range of sensor technologies. The very basis of interplaying and transporting of electromagnetic radiations emanated from conventional discharges, lasers, synchrotrons, neutron sources critically depend on the single and multilayer thin film coatings which control the propagation and manipulation of these radiations from hard X-ray to far infrared wavelengths extending to terahertz regimes [3]. Several laser spectroscopic researches, analytical spectro-chemical techniques and optical communication programs primarily rely on dense wavelength division multiplexing (DWDM) of electromagnetic pulse or CW radiations utilizing multilayer thin film devices matching to the various customized experimental needs.

Conceptually, periodic thin film multilayers belong to the family of 1D photonic crystal, in which there is periodic variation in the dielectric constant or

BARC NEWSLETTER

Founder's Day

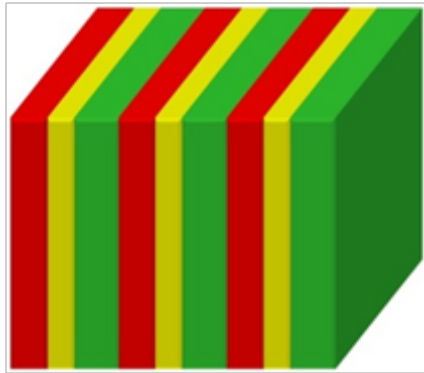


Fig.1(a): Example of 1D-Photonic Crystals

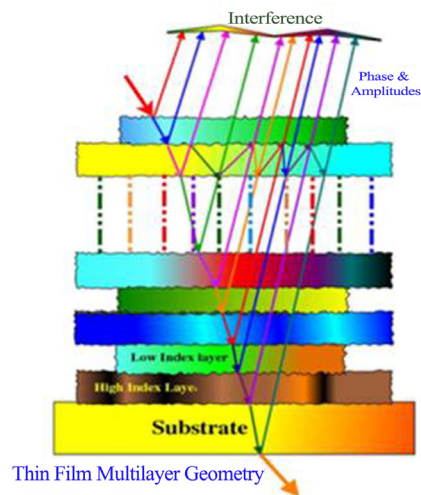


Fig.1(b): Example of 1D-Photonic Crystals

polarizability and hence in the refractive index [4]. In general, photonic crystal (PCs) families are periodically distributed material structures in one (1D), two (2D), or three spatial directions (3D) that exhibit stop bands or photonic band gaps (PBGs) as shown in layer geometries in Figs.-1(a) & (b).

In this regard, 1D photonic crystal geometry as multilayers or super-lattices is the most practicable as well as demanding option to fabricate devices for scientific, commercial and technological applications. Historically, although multilayer films received intensive study over an century, it was when Yablonovitch and John in 1987 joined the tools of classical electromagnetism and solid-state physics, that the concepts of omnidirectional photonic band gaps in 1D to 3D was introduced [5]. This generalization, which inspired the name "photonic crystal," led to many subsequent developments in their fabrication, theory, and application; from integrated optics to negative refraction to optical fibres that guide light in ambient. As can be seen in the Fig. 2, a multilayer of alternative layered thin film materials as 1-dimensional photonic crystal is the array of 1D lattice points in the reciprocal space. The very basis of this formulation is to create a contrast in the dielectric or optical properties between the successive layers for predictive manipulation of the propagation of electromagnetic radiations that can be extended to 3D geometries as shown in Fig. 3.

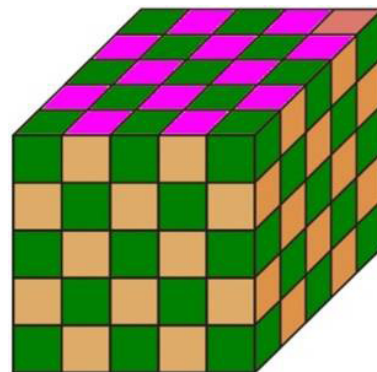


Fig.3: A 3D-Photonic Crystal

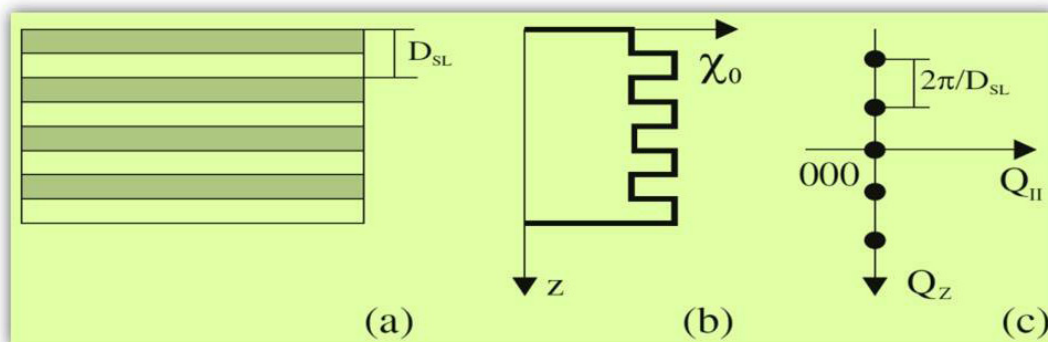


Fig.2: Presentation of a multilayer depicting (a) layer structures in real space, (b) corresponding variation of polarizability between the layers and (c) ultimately its depiction as 1D lattice in reciprocal space

BARC NEWSLETTER

Founder's Day

Multilayers for Lasers, X-Rays and Neutrons

Multilayer Coatings, as mirrors, anti-reflectors, filters and polarizers, play vital roles in the extended spectral range of electromagnetic radiations starting from Neutron, X-ray, UV-Vis- IR to Terahertz frequency and wavelength regimes [6]. In spite of distinct differences amongst these radiations there are striking similarities in designing guiding thin film based components commonly used to transport these radiations and beams. One of the essential as well as most demanding requirements in guiding these beams has been the high efficient reflection or anti-reflection components or subsystems that often decide the quality of the high-end experiments, instrumentations or performance. The design and development such mirror system become more complex when issues of polarization and high peak flux pulse nature of the radiation are to be tackled. It is interesting to note that irrespective of the diversity

amongst the radiations, numerical design formulations used for multilayer interference laser mirrors can be conveniently adapted for neutron and X-ray mirrors only with the appropriate re-formalism of the refractive index and extinction coefficient variables. Historically, there have been very interesting evolutions in the field of multilayer science and technology, especially related to the numerical design and computations. In mid-sixties, Seeley and Smith [7] developed an interesting method of adapting results obtained in the synthesis of lumped electrical circuits for use in multilayer thin-film optical filters. The concept and the analogy of using the lumped electrical network circuit in designing optical multilayer dielectric edge filter or the wavelength multiplexer are depicted in Fig. 4. Such formulations can also be extended to more complex designs like omnidirectional reflecting multilayers [8, 9]. But presently more complex numerical methods are available [10, 11].

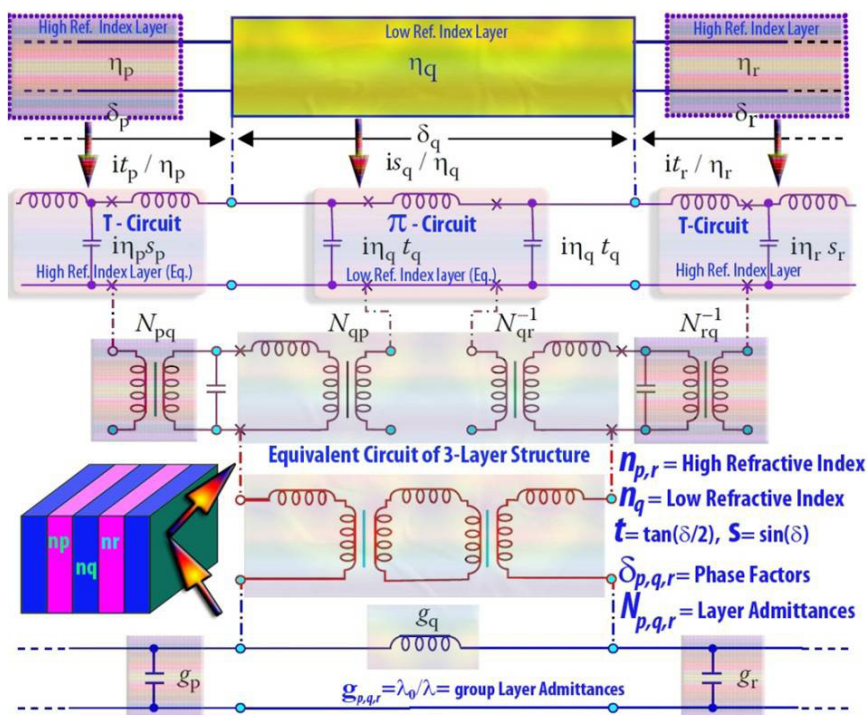


Fig. 4 : Analogy of a dielectric multilayer with the equivalent circuit of a lumped electric filter in computing the reflectance, transmittance as well as absorptance. The conversion used in the computation is shown here by diagrammatic form. In this formulation High-index layers are first replaced by a T circuit and low-index ones by a π circuit. This figure shows the step-by-step process by which a multilayer thin-film filter can be converted into a lumped electric filter in such a way that the elements of the electric filter can be identified with the optical thickness of the films, the indices of the films being specified with absolute independence.

Refractive Index: the prime factor in formulating any Optics and Photonics

The propagation of electromagnetic radiation is generally presented according to an optical formalism in which the properties of a medium are described by a fundamental parameter termed as refractive index. Knowledge of the refractive index is sufficient to predict what will happen to all such electromagnetic radiations at an interface; that is to establish the Snell's laws and to calculate the Fresnel coefficients for reflection and transmission. The laws of propagation of radiation, and in particular the refractive index, depend on the fundamental phenomena involved in the interaction of radiation with matter. The main process of interaction in the visible region

BARC NEWSLETTER

Founder's Day

of the electromagnetic spectrum is the polarization of the molecules in case of an insulator/dielectric and plasmonic in metals. At higher energies as with X-rays, it is generally sufficient to take into account the interactions with the atoms and at the highest X-ray energies only the electrons need be considered in the interaction process. Neutrons interact with the nuclei of the materials, and also have another interaction with the electrons for those atoms which carry a magnetic moment. Since the neutron or X-ray refractive indices of most condensed phases are only slightly less than that of air or vacuum, total external reflection is more commonly observed instead of the total internal reflection experienced with light of optical regime. The critical angle for total reflection is such that the reflectivity of neutrons or X-ray of a given wavelength from a bulk interface is unity at lower glancing angles (ignoring absorption effects) and falls sharply at larger angles. A critical comparison of the above explanations is presented in the Fig. 5.

Similarities in Multilayers for Lasers, X-Rays and Neutrons

The propagation of neutron de Broglie waves in a potential field is analogous to the propagation of light waves in a medium with a continuously variable refractive index. The potential can be gravitational, magnetic, or nuclear. For example, slow neutrons follow a parabolic path under the effect of gravity as in classical mechanics. Neutrons in a constant magnetic field experience a torque and undergo precession. In a non-uniform magnetic field they experience a force that depends on the relative orientation of the spin and field vectors.

The similarity of the mathematical descriptions for neutron wave and light propagation gives rise to phenomena that are analogous to those of classical optics. In fact, virtually all the well-known classical optical phenomena that are characteristic of light and

Parameter	Light	X-Ray	Neutron
Refractive Index	$\hat{n} = (n) + (-ik)$	$n(r) = 1 - \delta(r) + i\beta(r)$	
Electro Magnetic	$\hat{n}_L = \sqrt{\epsilon_r \mu_r}$	$n_x(r) = 1 - \frac{n_a r_e \lambda^2}{2\pi} (f_1^0 - i f_2^0) + \text{Magnetic}$	$n_{\pm N}(r) = \sqrt{1 - \frac{V_{nuc}(r) \mp \mu B_{eff}}{E}}$
Real Part	$n = \frac{1}{\sqrt{2}} \sqrt{(\epsilon_r^2 + \epsilon_r'^2)^{1/2} + \epsilon_r'}$	$\delta = \frac{\lambda^2}{2\pi} r_e \rho_e = \frac{\lambda^2}{2\pi} r_e n_a f_1^0(\omega)$	$\delta = \frac{\lambda^2}{2\pi} b \cdot \rho_n$
Imaginary part	$k = \frac{1}{\sqrt{2}} \sqrt{(\epsilon_r^2 + \epsilon_r'^2)^{1/2} - \epsilon_r'}$	$\beta = \frac{\lambda}{4\pi} \cdot \mu_x = \frac{\lambda^2}{2\pi} r_e n_a f_2^0(\omega)$	$\beta = \frac{\lambda}{4\pi} \cdot \mu_n$
Critical Angle	$\theta_c = \text{Sin}^{-1} \left(\sqrt{\frac{\epsilon_2 \mu_2}{\epsilon_1 \mu_1}} \right)$	$\theta_c = \sqrt{2\delta} = \sqrt{\frac{n_a r_e \lambda^2 f_1^0(\lambda)}{\pi}}$	$\theta_{c\pm} = \sqrt{2\delta} = \sqrt{\frac{\lambda^2 \cdot b \cdot (\rho_n)}{2\pi}}$
Definition of the Parameters	n = Real part k = Imaginary part ϵ_r = Dielectric Constant μ_r = Magnetic Permeability	δ = Real part, β = Imaginary part, r_e = Electron Radius, ρ_e = Electron Density, μ = magnetic, f_1 = Atomic scattering factor (Real), f_2 = atomic scattering factor (Im), n_a = No. of atoms	δ = Real part, β = Imaginary part, r_e = Electron Radius, ρ_e = Electron Density, μ_n = Nuclear magnetic moment, V_{nuc} = Nuclear potential, $-\mu \cdot B_{eff} = V_{mag}$ = Magnetic potential, b = Scattering Length Density (SLD), Note: neutron magnetic moment μ is negative, i.e. "spin up" has positive V_{mag} and the vice versa

Fig.5: Formulation of complex refractive index in the optical, X-ray and neutron wavelength regime depicting the dependance of real and imaginary part on the medium as well as on the material parameters.

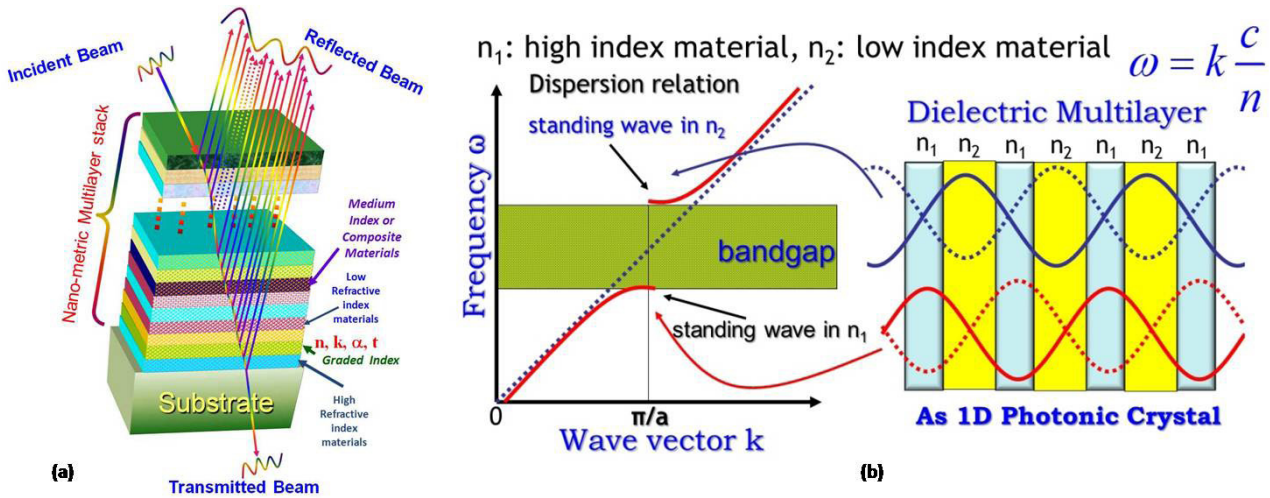


Fig.6: (a) A typical design example of a multilayer geometry in which multiple combination of thin film materials with appropriate thickness, refractive index, polarizabilities, absorption coefficients can be used in satisfying the objectives, and (b) Origin of the photonic band gap in a 1D photonic crystal or a periodic multilayer structure with all-dielectric or metal-dielectric or metal-metal layer geometries.

X-rays have also been demonstrated with neutrons. In geometric optics, there are not only the refraction and reflection of neutrons by materials, but also special properties in magnetic media. In wave optics, there is Bragg diffraction from crystalline materials, and so on, as for X-rays, but there are also other phenomena completely analogous to classical optics. Essentially the mirror or the high reflecting property of the multilayers designed and formulated for all these electromagnetic radiations is closely associated with the achievement of 1D photonic band gap in an appropriate thin film multilayer geometry. As a specific example, a generalized multilayer formulation with an objective of 1D photonic band gap for the laser applications is presented in the Fig. 6.

Mirrors and Super Mirrors for ultra-fast lasers

Current laser technology characteristically has an inverse relationship between pulse duration and bandwidth, requiring any optical component used in short pulse applications to provide the desired response over a large bandwidth. Due to

this increased bandwidth, the time domain shape of the ultra-short laser pulse of femto-second (10^{-15} sec) or less is adversely affected by material dispersion. In general, the longer wavelengths of laser light will travel faster than the shorter wavelengths resulting in an unusable signal. More specifically, the dispersion causes phase velocity of the pulse to increase in relation to the group velocity (hence the term Group-Delay-Dispersion GDD). The GDD of the laser amplifying medium, along with other components of the system, must be compensated for, to achieve or maintain the desired pulse shape. Chirped mirrors, a rather recent development in the area of non-linear optics, have provided a solution for these phenomena which utilizes the multilayer formulations of the super mirror designs [12]. Chirped mirrors are now the essential elements in ultrafast optics in order to compensate for positive Group Velocity Dispersion (GVD) suffered by a short

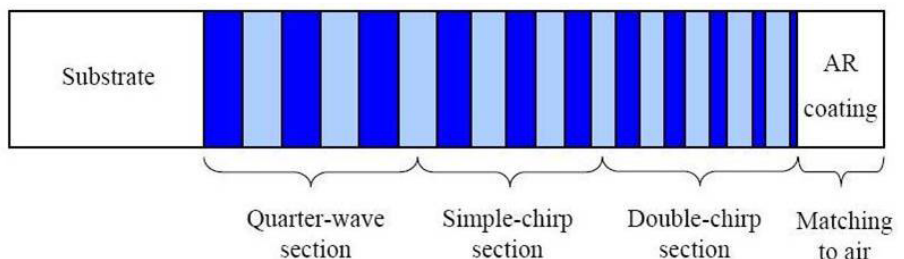


Fig. 7 : Double Chirped Mirror (DCM) design at AR coating the front for the dispersion control in femtosecond lasers

BARC NEWSLETTER

Founder's Day

laser light pulse, which travels through a dispersive medium. Design and deposition of a chirped mirror are more complicated than that of an ordinary multilayer dielectric reflector, because one has to fit not only an amplitude target, but also a phase target. The Fig. 7 presents the layer design for a Double chirped mirror (DCM). An impedance-matching section and an AR-coating on top of the mirror avoid the oscillation in the group delay.

Mirrors and Super Mirrors for X-rays

Compton showed that X-ray reflection was governed by the same laws as reflection of light but with different refractive indices depending on the number of electrons per unit volume. The advances in X-ray optics during the last 25 years were facilitated by the availability of bright synchrotron radiation sources, the invention of multilayer x-ray mirrors with high reflectance, and the development of high resolution zone plates. In this context, it is important to note that the multilayer coated mirrors can reflect X-ray beams efficiently at grazing angles up to 10 times larger than the critical angle of a single layer (Fig.8).

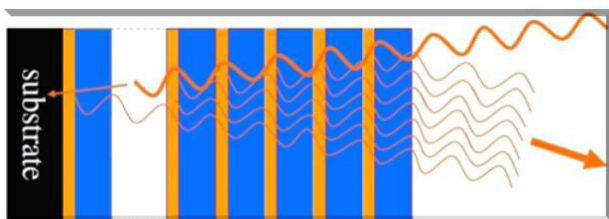


Fig.8: A typical design example of a X-ray multilayer highlighting critical issues with respect to the design as well as development.

The efficiency is also better even at normal incidence, especially for soft X-rays with $\lambda > 25 \text{ \AA}$ in a spectral or angular region around the Bragg angle. These properties make them useful as beam deflectors, spectral filters, collimators or focussing elements. They are efficient polarizers for incidence angles around 45° . The imaging performance of mirrors is considerably better at normal incidence than at grazing incidence angles, and optical systems with multilayer mirrors can be used for high resolution imaging as well. Soft

x-ray telescopes for imaging of the solar corona have obtained images with about one order of magnitude better resolution than grazing incidence telescopes; the actual resolution (about 0.5 arc sec) is presently not limited by the quality of the optics but by the detectors, the pointing stability of the spacecraft, and the available photon flux. Pictures from the multilayer mirror telescopes on the SOHO and TRACE spacecraft are available on the Internet at <http://umbra.nascom.nasa.gov/eit/> and <http://vestige.lmsal.com/TRACE/>.

Mirrors & Super Mirrors for Neutrons

In 1946 Fermi and Zinn first demonstrated the mirror reflection of neutrons (Fermi and Zinn, 1946). Again this follows the same fundamental equations as optical reflectivity but with different refractive indices. Neutrons are scattered by nuclei and the neutron refractive index depends not only on the number of nuclei but also on how strongly they scatter. A quantity known as the "scattering length" that indicates a nucleus' ability to scatter neutrons may be defined [13]. A neutron refractive index of any material is a function of the scattering length density (SLD) of its constituent nuclei and the neutron wavelength. As with light, total reflection may occur here when neutrons pass from a medium of higher refractive index to one of lower refractive index. Since the neutron refractive indices of most condensed phases are only slightly less than that of air or vacuum, total external reflection is more commonly observed instead of the total internal reflection experienced with light.

The critical angle for total reflection is such that the reflectivity of neutrons of a given wavelength from a bulk interface is unity at lower glancing angles (ignoring absorption effects) and falls sharply at larger angles. Fermi and Zinn had observed the total reflection of thermal neutrons below the critical angle. Since the neutron refractive index, unlike X-rays, is related to its composition and to the scattering lengths of its constituent atoms, it does not follow any systematics as shown in Fig. 9.

BARC NEWSLETTER

Founder's Day

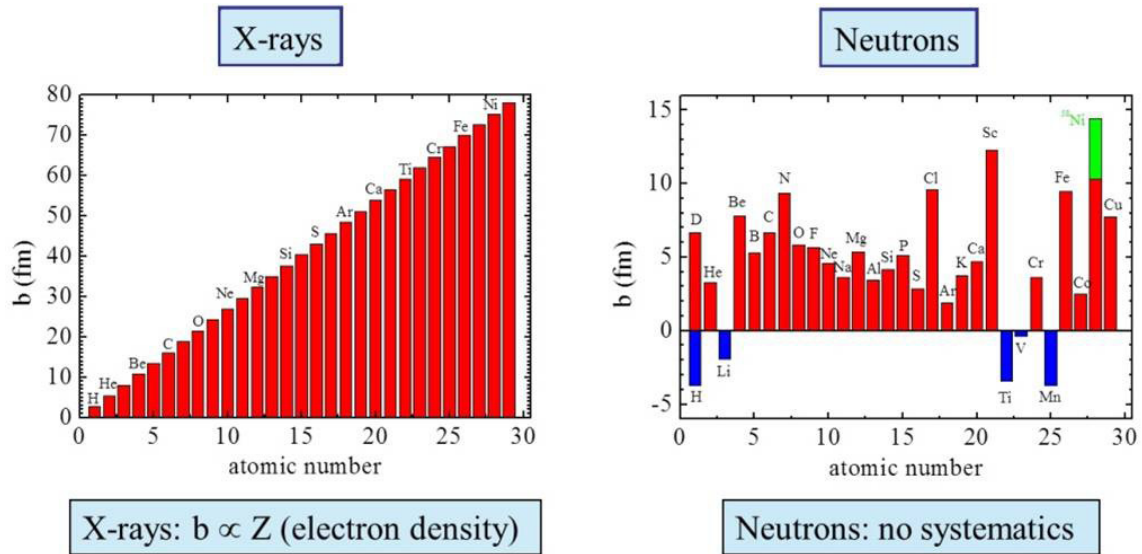
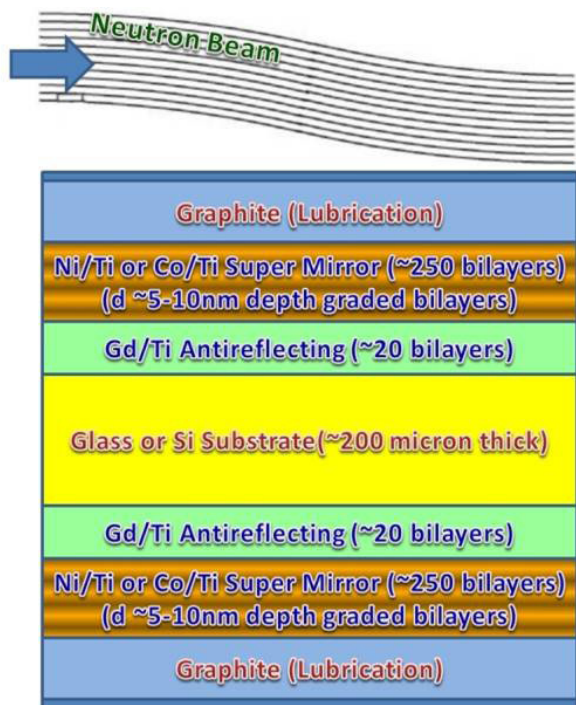


Fig.9: Depicting how the the critical parameter of the refractive index which is termed as scattering length density (SLD) vary in case of X-rays and neutron with respect to the atomic number. As it can beseen there is a systematic in case of X-rays and no systematics for the neutrons.



Schematic of Neutron Waveguide with Super Mirror Coatings

Total Number of Layer : $540 \times 2 = 1080$ Layers

Fig.10: schematic of multilayer depth graded neutron super mirror polarizer with 1080 layers, coated both sides of a substrate

Initially, neutron guides were fabricated from glass plates coated on their inside with a thin layer of

natural Ni or enriched Ni. In such guides neutrons are transported by total reflection on the inner guide walls, with typical neutron reflection losses of 1% per bounce. Starting about ten years ago, neutron guides equipped with 'Super-Mirror' coatings were developed. A typical neutron supermirror used for guiding thermal neutrons consists of typically ~250 bilayers (500 Layers) of Ni/Ti or Co/Ti of varying thickness followed by ~20 anti-reflecting bilayers of Gd/Ti. So the layer geometry and sequence is quite complex as shown in Fig. 10. Experimentally, such mirrors are realized by sophisticated magnetron sputtering process with precise process control formulations [14]. In this case the substrate is the glass with a typical thickness of 200 micron. The total layer thickness of mirror is 7.2 micron and the glass substrate needs to have such super mirror coatings both the side for the desired waveguide applications as depicted above. With the magnetron sputtering system now readily available, a typical Super Mirror deposition process takes 15-20 hours (one side). Such magnetron sputtering system usually has the provision to load 5-15 such substrates (with standard substrate dimensions 141 mm x 254 mm) while carrying out the multilayer coatings as shown in Fig. 11.



Fig.11: An indigenously developed magnetron sputtering system for super mirror developments at A&MPD

Mirrors for Terahertz Regime (T-rays)

The terahertz (THz or 10^{12} Hz) is the part of the electromagnetic spectrum (wavelengths typically ranging from $100 \mu\text{m}$ to $1000 \mu\text{m}$), where most molecules have rotational and vibrational absorption modes and therefore is a rich area for molecular spectroscopy, chemical and biological analysis [15]. The frequency range is also termed the far-infrared but the terahertz term was originally used for the region between photonic devices and electronic transit-time devices where few practical sources of radiation were previously available, termed the THz gap (roughly 200 GHz to 10 THz - or $30 \mu\text{m}$ to 1.5 mm wavelength) (Fig. 12). In the last 5 years this situation has changed significantly and there are many THz sources available with differing power, bandwidth and operating temperatures. The frequency range is particularly interesting for medical and security imaging and spectroscopy as the radiation is non-ionising and hence is far safer than X-ray or gamma camera techniques. However, with terahertz wavelengths ranging from 100 to $1000 \mu\text{m}$, the diffraction limit for this long wavelength light means that it is difficult to measure small volume samples. The development of electromagnetic, artificial-lattice structured materials

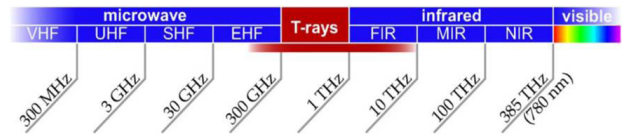


Fig.12: Terahertz regime

(photonic crystals), termed as metamaterials, has led to the realization of phenomena that cannot be obtained with natural materials

In the terahertz regime, unlike optical region, interactions of both electric and magnetic components of EM radiation with matter need to be considered. Concepts of Metamaterials or Negative Refractive Index Materials [16] arise primarily due to the following mathematical formulation depicting the relationship of refractive index with electric and magnetic permeability factors as follows:

$$n^2 = [\epsilon_r \mu_r] \Rightarrow n = \pm \sqrt{\epsilon_r \mu_r} \quad \dots(1)$$

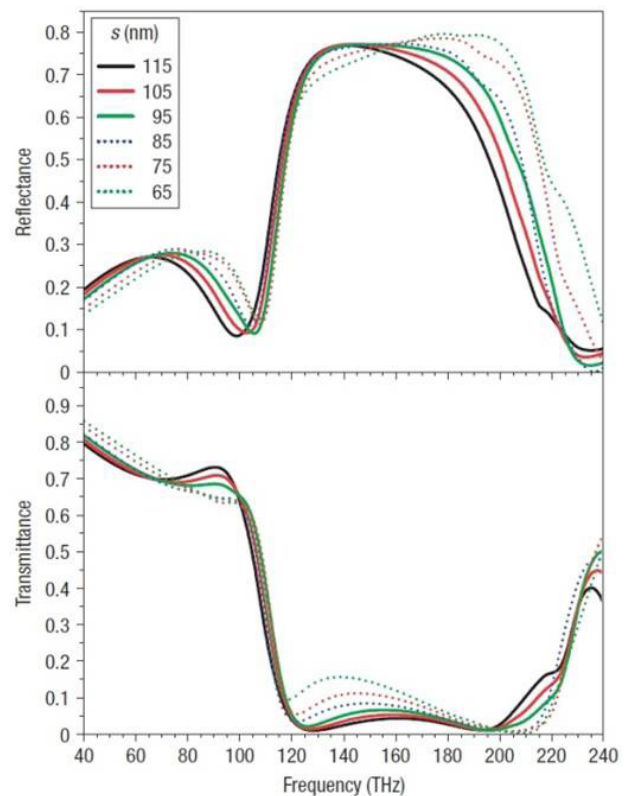


Fig.13(a): Reflectance and Transmittance characteristics of structured multilayer for the geometry depicted in Fig. 13(b)

BARC NEWSLETTER

Founder's Day

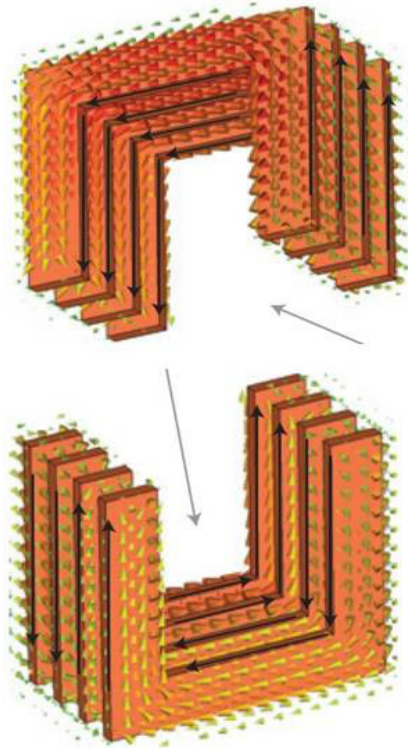


Fig.13(b): A representative structured multilayer using metamaterials meant for terahertz regime accounting electric and magnetic fields in the multilayer split ring resonator geometry.

Where, ϵ_r is the relative electrical permittivity, defined as $\epsilon_r = \epsilon / \epsilon_0$ and μ_r is the relative magnetic permeability, defined as $\mu_r = \mu / \mu_0$. Usually, for conventional materials + sign is taken. But for metamaterials, both ϵ_r and μ_r are simultaneously negative. This only possible by designing a structured multilayer in which the material property and geometry both carry the similar importance. A typical design of a reflecting multilayer using this formulation of metamaterial multilayer is depicted in Figs. 13(a) & (b).

Conclusion

The science and technology of multilayers for transporting as well as manipulating electromagnetic radiations has ever expanding domain both with respect to the design formulations and practical realizations. The wavelength domain starting from terahertz, infrared, visible, X-ray to neutron have

their specific complex issues and considerations with respect to design concepts, geometries and material choices. In spite of distinct differences amongst these radiations there are striking similarities in designing guiding multilayer thin film based components commonly used to transport these radiations and beams. It is also interesting to note that irrespective of the different radiation-matter interaction processes, numerical design formulations used for multilayer interference laser mirrors can be conveniently adapted for neutron and x-ray mirrors only with the appropriate re-formalism of the refractive index and extinction coefficient variables. Further, the super-mirror design initially visualized for the neutron beams to extend the angular-range of the reflected mirror coating utilizing a graded geometric layered structure has also drawn significant attention for X-ray and ultrafast laser mirror related technologies. However, with increasing demand on quality, precision, efficiency, dimension and long term stability on the multilayer mirrors there are serious issues related to selection of new thin film materials, processes, process-monitoring and characterization techniques. In the Department a strong scientific and technology base has been established to carry out the R&D and develop such state-of-the-art multilayer devices with challenging as well as customized needs of the nuclear energy programs.

Acknowledgement

The author would acknowledge the scientific and technical expertise and contributions of various scientists working in the Atomic and Molecular Physics Division (A&MPD) and also various R&D scientists and engineers of other Divisions in the Department collaborating with the multilayer thin film R&D programs of the Division.

References

1. Macleod H A 1996 Recent trends in optical thin films Review of Laser Engineering 24 3–10
2. Ronald R. Willey, "Practical design and production

BARC NEWSLETTER

Founder's Day

- of optical thin films", Willey Optical, CRC Press, Marcel Dekker Inc., Charlevoix, Michigan, 2002
3. H.S. Nalwa, Handbook of Advanced Electronic and Photonic Materials and Devices, Vols 1–10 (Academic Press, San Diego, 2001) (now Elsevier).
 4. Furman S A and Tikhonravov A V 1992 Basics of Optics of Multilayer Systems (Gif-sur-Yvette: Editions Frontières)
 5. Yablonovitch E 1993 Photonic band-gap structures Journal of the Optical Society of America, B 10 283–297
 6. H. A. Macleod, Thin-Film Optical Filters (Macmillan/McGraw-Hill, New York, 1986)
 7. Seeley J S and Smith S D, "High performance blocking filters for the region 1μ to 20μ ", Applied Optics 5, 81–85, (1966)
 8. Fink Y, Winn J N, Fan S, Chen C, Michel J, Joannopolous J D, and Thomas E L 1998, "A dielectric omnidirectional reflector", Science 282 1679–1682
 9. J.-Q. Xi, ManasOjha, J. L. Plawsky, and W. N. Gill, Jong Kyu Kim and E. F. Schubert, Internal high-reflectivity omni-directional reflectors, Appl. Phys. Letts. 87, 031111, (2005)
 10. N.K. Sahoo and K.V.S.R. Apparao, "Modified Complex Method for constrained design and optimization of optical multilayer thin film devices", Applied Physics A, 59, 317 (1994)
 11. N.K. Sahoo, S. Thakur, M. Senthilkumar and N.C. Das, "Determination and analysis of non-linear index profiles in electron beam deposited MgOAl₂O₃ZrO₂ ternary composite thin film optical coatings", Applied Physics A, 80, (2005), 829
 12. Jablonski M, Takushima Y, and Kikuchi K, "The realization of all-pass filters for third-order dispersion compensation in ultrafast optical fiber transmission systems", Journal of Lightwave Technology 19, (2001) 1194–1205
 13. Z. Zhong, W. Zhan-Shan, Z. Jing-Tao, W. Feng-Li, W. Yong-Rong, Q. Shu-Ji, C. Ling-Yan, "Design and fabrication of Ni/Ti Multilayer for neutron supermirror", Chin. Phys. Lett. 23, 2678, (2006)
 14. R. Maruyama, D. Yamazaki, T. Ebisawa, M. Hino, K. Soyama, Physica B, 385, 1256, (2006)
 15. Hu Tao, A. C. Strikwerda, K. Fan, W. J. Padilla, X. Zhang, and R. D. Averitt, "Reconfigurable Terahertz Metamaterials", PRL 103, 147401 (2009)
 16. N.R. Han, Z.C. Chen, C.S. Lim, B. Ng, and M.H. Hong, "Broadband multi-layer terahertz metamaterials fabrication and characterization on flexible substrates" Optics Express, 19, (2011), 6990-6998

SECURE NETWORK ACCESS SYSTEM (SNAS)

Gigi Joseph
Computer Division

Shri Gigi Joseph is the recipient of the DAE Homi Bhabha Science & Technology Award for the year 2012

Abstract

Cyber-security has emerged as an important issue because of the sophisticated cyber attacks on information assets and industrial assets which lead to serious threats to power plant control and critical information of our organization. It is a well known fact that cyber security related products sourced from other countries may have built-in trap doors. Hence development of indigenous security solutions are very important. In April 2012, SNAS was launched as a commercial product at national level by Dr. Srikumar Banerjee in the presence of Dr. Rajagopala Chidambaram in Delhi. ECIL is providing marketing and support of SNAS. This article details some of the major highlights of SNAS.

Introduction

Secure Network Access System (SNAS) is an indigenously developed integrated host-aware network security appliance. It secures any enterprise network by intelligently sensing security threats and responding to them automatically. With next generation portable devices, network access has become trouble-free. Users can be simultaneously connected to multiple networks. But this renders the concept of perimeter firewall based network security useless. In such a scenario, firewalls need to be aware of the endpoint status and health to counter the threats to organizational networks.

SNAS combines the features of a perimeter firewall with those of an endpoint security solution to provide a bird's eye view of the entire network as well as detailed information about each entity connected to it. SNAS is a highly scalable system which can be easily configured to suit the requirements of any small, medium or large enterprise with varying security concerns. It identifies the "who, what and where" of the devices connected in the network. SNAS can identify everything on your network – the devices, their operating systems, applications running on them and their network activities.



Fig.1: SNAS Appliance BOX

BARC NEWSLETTER

Founder's Day

SNAS Subsystems

SNAS has got many subsystems which themselves can also be implemented as independent systems.

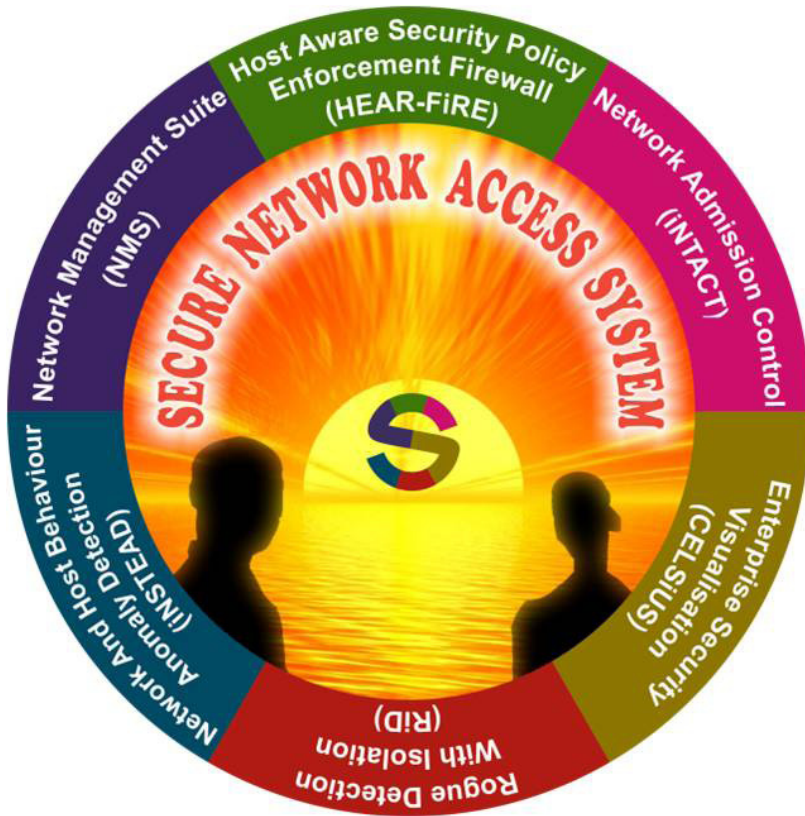


Fig.2: SNAS Subsystems

NeTwork Admission ConTrol (iNTACT)

SNAS offers a comprehensive solution for proactive network security by determining the policy compliance of the connected end-systems. End-systems are allowed to access network services only if they are in compliance with the security policy defined for them. The identification and subsequent authentication of the end-systems can be based on a multitude of factors. Among others, these include IP, MAC, location, generated network traffic, running operating system, open application ports, disk-partition serial

number, installed and running software and services. If the security state of the end-system is such that it casts negative impact on other devices then SNAS can isolate it from the internal network also. This way NeTwork Admission ConTrol (iNTACT) module of SNAS ensures that the end-systems remain unharmed by compromised systems.

Host AwaRE security Policy Enforcement FIREwall (HEAR-FiRE)

If an end-system complies with the security policy, the firewall rules are dynamically manipulated so that it can only access the network services that it is authorized to. Once an end system has securely gained access to the network, continuous monitoring, threat analysis and policy enforcement are provided through intelligent integration with other SNAS components. This capability makes SNAS a Host AwaRE security Policy Enforcement FIREwall (HEAR-FiRE). The acronym HEAR-FiRE stands for the capability of SNAS to listen to the state of

hosts, check their security compliance and configure the firewall rules accordingly.

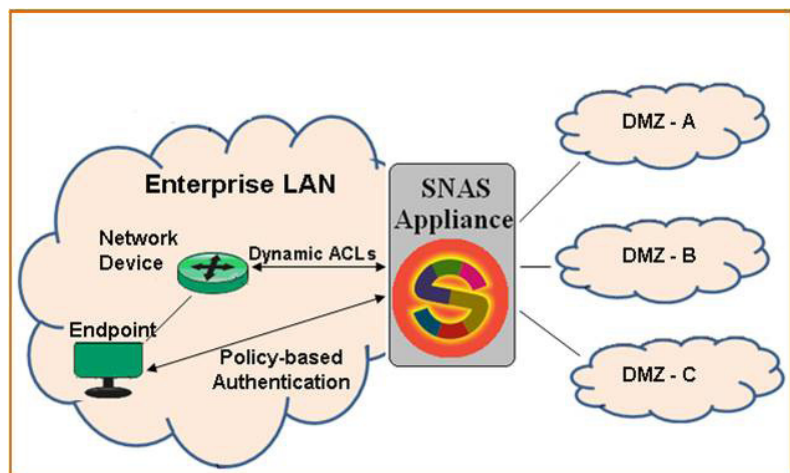


Fig.3: SNAS End Point Policy Enforcement Architecture

BARC NEWSLETTER

Founder's Day

Complete SEcUrity viSualisation (CELSiUS)

SNAS provides a Complete SEcUrity viSualisation (CELSiUS) of all the entities present in the network. It measures the security state of the end-systems in the network using various parameters. The SNAS dashboard enables administrators to monitor the status of the network. It provides them with an interface to know what processes and services are running, whether they are trusted or not, what software have been installed, when they have been installed, what network application ports are open on the devices, which devices have connected to those application ports and the traffic that is being generated by the systems.

This functionality is a major advancement to that provided by traditional Intrusion Detection and Prevention System (IDS/ IPS). The approach used by SNAS is capable of detecting and mitigating even those attacks whose packets do not reach the SNAS appliance. SNAS can identify any malicious behavior of end points in terms of network traffic, applications and threat propagation. Endpoints causing Denial of service (DOS) attack are detected and isolated from the network in near real-time. SNAS approach of integrated network admission control and anomaly detection provides a dynamic intrusion response and proactive prevention against zero-day attacks



Fig.4: SNAS dashboard

Network and hoST Anomaly DEtection (iNSTEAD)

Network and hoST Anomaly DEtection (iNSTEAD) ensures that whatever happens in the network is trusted and any non-trusted behaviour is isolated.

SNAS Network Management Suite (NMS)

SNAS Network Management Suite (NMS) provides a mechanism to monitor and manage the various network devices and end-systems present in the

BARC NEWSLETTER

Founder's Day

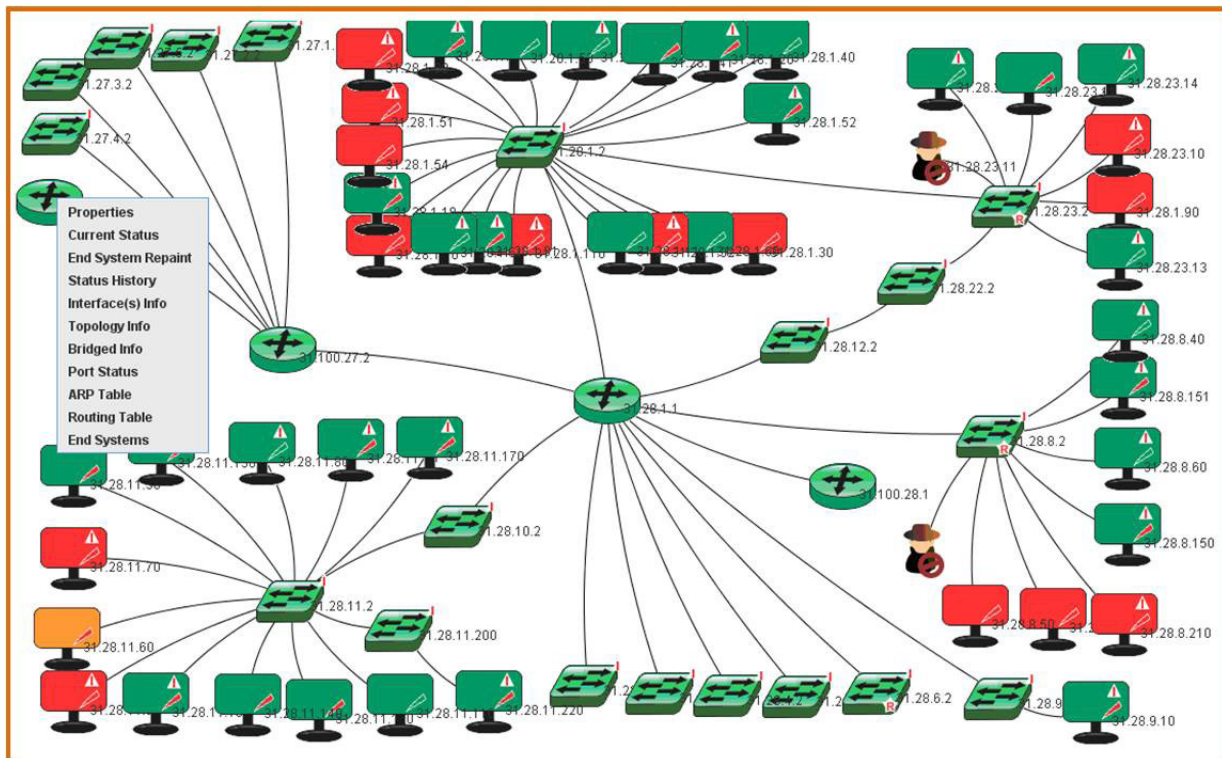


Fig.5: SNAS Security Visualization and NMS dashboard

network. It provides the details about the device, their configuration, current status, their link with other devices and status of those links. It also helps administrators in managing IP address allocation, device movement and generating periodic reports for the purpose of network auditing.

Rogue Detection with Isolation (RiD)

The Rogue Detection with Isolation (RiD) module of SNAS ensures that as soon as any unknown device enters the network, it can be identified and isolated in near real-time. This module is able to scan a sufficiently large network and detect and isolate unknown systems in less than a minute. True to its name, this module rids administrators from the menace caused by unknown entities.

Backdoor Detection

Users connected to internal networks can connect to external networks simultaneously using wireless

devices e.g. USB dongles, smart-phones etc. This can not only compromise the confidentiality of information present on that system, but it can also be used as a point to attack the enterprise's internal network. SNAS can detect endpoints which are connected directly to outside networks. They pose a threat to organizational security as they bypass all network security systems and act as a bridge between outside world and internal secure networks. Such end-points can be easily detected by SNAS and blocked from using the internal network while they are connected to external networks.

USB Storage Management

USB based storage devices are prominently used for data transfer between different machines. But they also act as hub for the spread of viruses and worms and pose a threat to network security. SNAS can track the movement and usage of USB-storage devices within the network. It can ensure that only authorized USB-based storage devices are used on an end-system.

BARC NEWSLETTER

Founder's Day

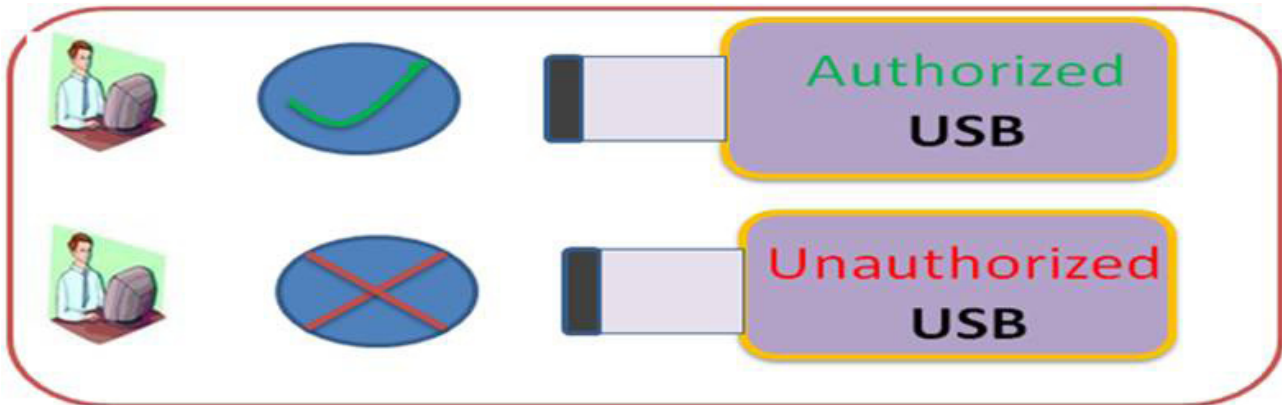


Fig.6: SNAS USB Module

This will help in ensuring that there is no unintended data loss from PCs through removable media. Also, once a pen-drive is registered, the user can get full details about when and where his/her pen-drive has been used.

Network Bridging Sensor

When multiple isolated networks are extended to user's end, there is a definite chance of network bridging. SNAS detects any bridging immediately and disconnects the devices to keep your networks isolated.

Trust Monitor

SNAS monitors and mitigates the impact of untrusted programs and services on the network. SNAS builds a profile of trusted applications and services running on

the endpoints. Patterns of newly found processes can be monitored and easily analyzed to handle threats.

Conclusions

SNAS can be deployed in enterprise networks to replace the existing firewalls between intranet segments (LAN) and various demilitarized zones and WAN. SNAS will ensure that the devices in the user segment comply with security policy and all internal network attacks are identified and mitigated. The SNAS security suite provides a comprehensive solution for mitigation of internal and external attacks. As on today, SNAS is the only Indian integrated network security solution present in the country. The SNAS is being accepted as an Intranet security solution at national level and installation of SNAS in various organizations including strategic ones is in progress.

SMALL-ANGLE NEUTRON SCATTERING FROM BIO- AND NANO-MATERIALS

V.K. Aswal

Solid State Physics Division

Dr. V.K. Aswal is the recipient of the DAE Homi Bhabha Science & Technology Award for the year 2012

Abstract

Bio- and nano-materials possess a specific shape and charge, which regulate and control their functionality and stability. The particles in aqueous solution are known to interact through different interaction forces. Different phases in any of these systems are preceded and followed by structural changes among them, which can be induced simply by varying temperature or neutralizing the charge on the particle by salt or breaking the water structure by urea. We have used small-angle neutron scattering (SANS) technique for studying the evolution of structure and interaction in different phases of biological and nanomaterial systems.

Introduction

Small-angle neutron scattering (SANS) is a powerful technique in the study of biological and nanostructured systems as for most of these systems their 3D structure have a length scale in the range 1 - 100 nm [1]. The major advantage of the method lies in its ability to provide structural information about partially or completely disordered systems. SANS allows to study the structure of native particles in near physiological environments and to analyze structural changes in response to variations in external conditions. Both structure as well as interaction in these systems can be determined by SANS [2]. The applications cover extensive studies of different types of biomolecules (e.g. proteins, lipids, nucleic acids, macromolecular complexes and polyelectrolytes) and nanomaterials (e.g. nanoparticles, fullerenes, dendrimers and composites) as well as their conjugates. The contrast variation SANS either by deuterating the particle or solvent is widely used in such multi-constituents systems. This article presents some of our recent results.

Evolution of Structure and Interaction in Protein Solutions

Proteins are macromolecules made of amino acids perform structural, transport, catalytic, sensory and many other important biological functions. In solutions, they are known to exhibit rich phase behavior. It is believed that many of these phases of protein solutions can be explained by the interaction combining short-range attraction along with the long-range repulsion [3]. The tuning of these two interaction components can lead to different phase transitions including liquid-liquid phase transition (LLPT). In LLPT, the protein solution gets divided into two phases one rich in protein while the other protein deficient. The liquid-liquid phase is one of the important phases that can enhance solid phase such as crystallization. The LLPT in aqueous salt solutions of lysozyme protein has been studied by SANS (Fig. 1a). Measurements were carried out on fixed protein concentration with varying salt concentration approaching LLPT [4]. The data are fitted considering protein interaction by two Yukawa (2Y) potential which combines short-

BARC NEWSLETTER

Founder's Day

range attraction and long-range repulsion. We showed that LLPT arises because of enhancement of non-DLVO short-range attraction without any conformational structural change of the protein. This attractive interaction is believed to be arising from entropy driven dehydration induced by the hydrated salt ions. The salt concentration required for LLPT as well as corresponding short-range attraction decrease significantly with increase in protein concentration (Fig. 1b).

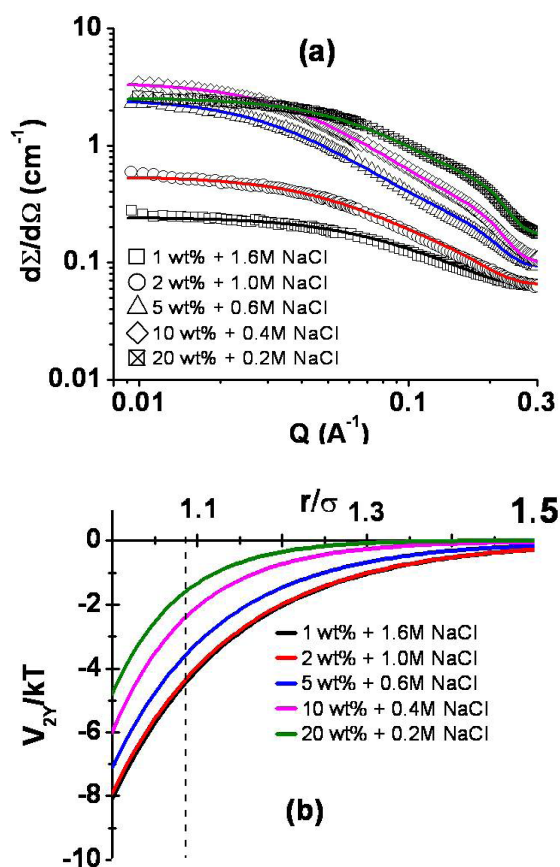


Fig. 1: The correlation of (a) SANS data and (b) total potential for different protein concentrations in presence of salt on approaching LLPT.

Proteins function depends absolutely on its three-dimensional folded structure. Proteins can undergo unfolding/refolding transitions in presence of denaturants such as urea, surfactant and pressure. Protein unfolding process involves the disruption of H-bonds, disulphide bonds, salt bridges and hydrophobic interactions, leading to its successive

alteration of quaternary, tertiary, and secondary structure [5]. We have used SANS to study protein unfolding and refolding if any in protein bovine serum albumin (BSA) due to perturbation in its native structure as induced by different protein denaturing agents [6]. BSA protein unfolds for urea concentrations greater than 4 M and is observed to be independent of protein concentration. The addition of surfactant unfolds the protein by the formation of micelle-like clusters of surfactants along the unfolded polypeptide chains of the protein and depends on the ratio of surfactant to protein concentration. We used the dilution method to show the refolding of unfolded protein in presence of urea and surfactant. BSA does not show any protein unfolding up to the pressure of 450 MPa. The presence of urea and surfactant (for concentrations prior to inducing their own unfolding)

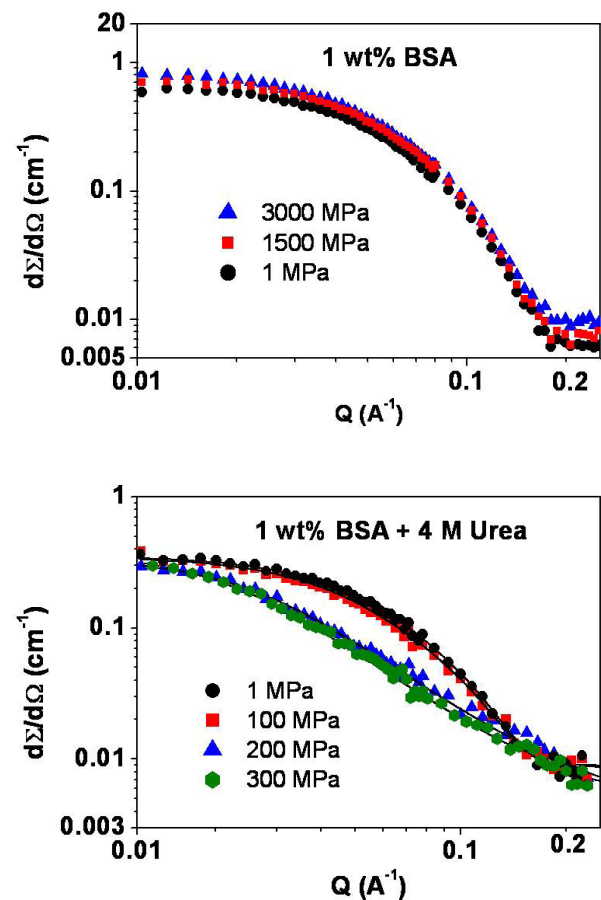


Fig. 2: SANS data (a) 1 wt% BSA and (b) 1 wt% BSA + 4 M Urea as a function of pressure

has been used to examine pressure-induced unfolding of the protein at lower pressure. The protein unfolds at 200 MPa pressure in presence of urea, however no unfolding is observed with surfactant (Fig. 2). The protein unfolding is shown to be reversible in all these denaturing methods.

Synthesis and Characterization of Nanoparticles

Recently an economical, environmentally benign and fast synthesis methodology for gold nanoparticles using block copolymer has been developed [7]. In this synthesis, block copolymer plays the dual role of reducing agent as well as stabilizing agent. The formation of gold nanoparticles comprises three main steps, reduction of AuCl_4^- by the block copolymers in the solution and formation of gold clusters, adsorption of block copolymers on gold clusters and reduction of AuCl_4^- ions on the surfaces of these gold clusters for the growth of gold particles in steps and finally its stabilization by block copolymers. The control over these three different steps decides the output of the synthesis of gold nanoparticles. We have looked into the role of different components and optimization of concentrations to enhance the yield of the synthesis. This method usually has a very limited yield which does not simply increase with the increase in the gold salt concentration. We showed that the yield

can be enhanced by increasing the block copolymer concentration but is limited to the factor by which the concentration is increased [8]. On the other hand, the presence of an additional reductant (trisodium citrate) in 1:1 molar ratio with gold salt enhances the yield by manyfold (Fig. 3 a). In this case (with additional reductant), the stable and high-yield nanoparticles having size about 14 nm can be synthesized at very low block copolymer concentrations. These nanoparticles thus can be efficiently used for their application such as for adsorption of proteins (Fig. 3 b).

Nanoparticle dispersions are known to show rich phase behavior and find numerous applications. Many of these phases can be explained by DLVO theory governed by the competition of short-range van der Waals attraction and a long-range electrostatic repulsion among the particles [9]. However, there are numerous cases where DLVO theory fails and non-DLVO contributions (e.g. hydration and depletion interactions etc.) are required to explain the system behavior. The depletion force arises in a system consisting of two significantly different sizes of structures (e.g. nanoparticles, micelles, polymers) due to the exclusion of a non-adsorbed smaller structure from the gap region between larger structures. The resulting concentration difference produces an osmotic pressure imbalance between the gap

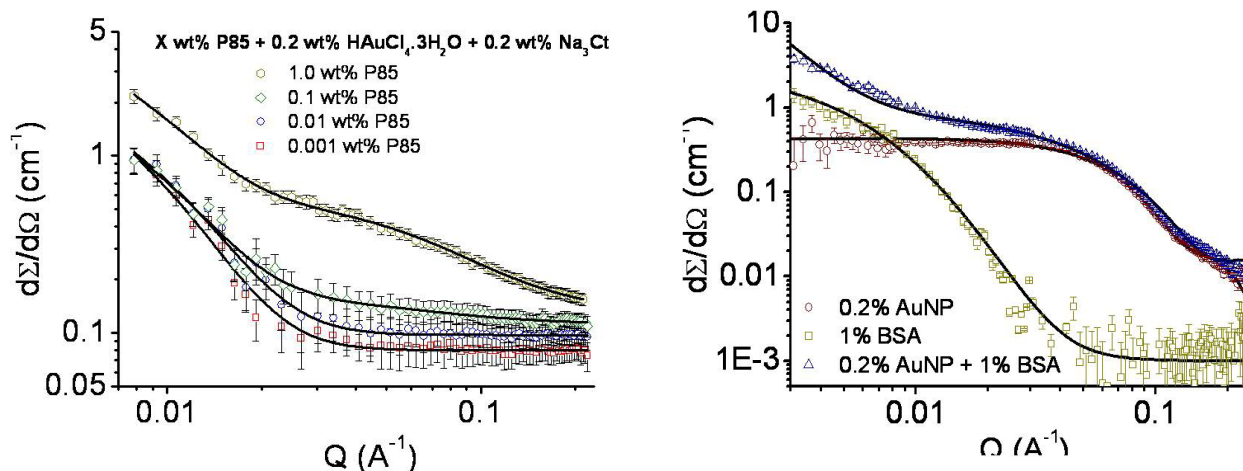


Fig. 3: SANS data of varying P85 concentration for 0.2 wt% $\text{HAuCl}_4 \cdot 3\text{H}_2\text{O}$ with 0.2 wt% Na_3Ct at 15 oC. SANS data of gold nanoparticles and BSA and their conjugates. The gold nanoparticles in all these studies are prepared using 0.01 wt% P85 + 0.2 wt% $\text{HAuCl}_4 \cdot 3\text{H}_2\text{O}$ + 0.2 wt% Na_3Ct system. The pH for BSA in all the samples is kept at 7.

and bulk, resulting in a net attractive force. The depletion interaction has been mostly considered as short-range attraction and found applicable to the systems which are sterically stabilized as hard sphere potential as repulsive part. SANS has been carried out to examine block copolymer induced depletion interaction of charged silica nanoparticles in aqueous solution (Fig. 4a) [10]. The measurements were performed on anionic Ludox silica nanoparticles in the presence of 0.1 M NaCl and varying concentration of polyethylene oxide-polypropylene oxide-polyethylene oxide (PEO-PPO-PEO) P85 [(EO)26(PO)39(EO)26]

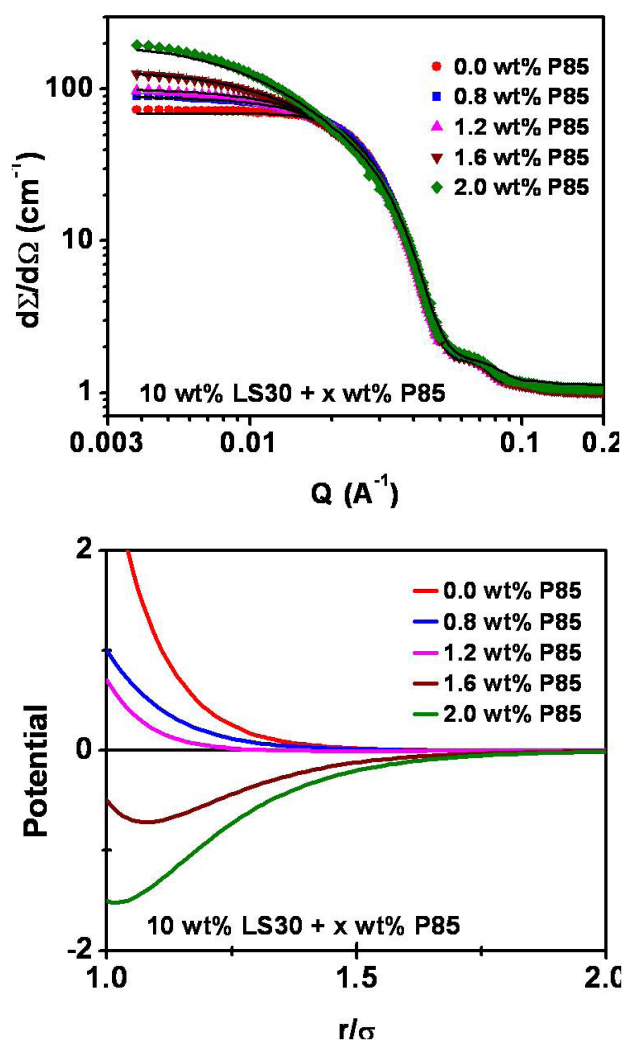


Fig. 4. SANS data of 10 wt% LS30 silica nanoparticles with varying concentration of P85 block copolymer at 20 °C. Inset highlights the variation in low Q data. (b) total interaction potential for 10 wt% LS30 silica nanoparticles with varying concentration of P85 block copolymer.

block copolymer. The depletion interaction is found to be long-range attraction whose magnitude and range increase with block copolymer concentration (Fig. 4 b). The depletion interaction is further enhanced by tuning the self-assembly of block copolymer through the variation of temperature. The increase of depletion interaction ultimately leads to clustering of nanoparticles and is confirmed by the presence of a Bragg peak in the SANS data. The positioning of Bragg peak suggests simple cubic type packing of particles within the clusters. The scattering from the clusters in the low Q region is governed by the Porod scattering indicating clusters are quite large (order of micron). The depletion interaction is also found to be strongly dependent on the size of the nanoparticles.

Interaction and Resultant Structure of Nanoparticle and Protein Complexes

The nanoparticles, being small, can interact with cellular machinery in biological applications. For example, nanoparticle-protein systems are extensively utilized in drug delivery, catalysis, biological imaging, biosensors and bio fuel cell [11]. Silica nanoparticles are one of the most commonly used model inorganic nanoparticles, which are non-toxic and biocompatible. The globular proteins (e.g. BSA and lysozyme) are known to be highly stable and easily soluble in water. We have examined the differences in the interaction and structural evolution of colloidal silica nanoparticles for their interaction over a wide range of concentration of lysozyme and BSA proteins at physiological conditions [12]. It is found that despite of having different nature (opposite charge) both the proteins can render to the same kind of aggregation of silica nanoparticles. However, the concentration regions over which the aggregation is observed are widely different for the two proteins. The lysozyme with very small amount (e.g. 0.01 wt. %) leads to the aggregation of silica nanoparticles. On the other hand, silica nanoparticles coexist with BSA as independent entities at low protein concentrations and turn to aggregates at high protein concentrations (> 1 wt.

BARC NEWSLETTER

Founder's Day

%). In the case of lysozyme, the charge neutralization by protein on the nanoparticles gives rise to the protein-mediated aggregation of nanoparticles. The nanoparticle aggregates coexist with unaggregated nanoparticles at low protein concentrations whereas with free protein at higher protein concentrations. For BSA, the non-adsorbing nature of protein produces the depletion force that causes the aggregation of nanoparticles at higher protein concentrations. The nanoparticle aggregation is found to be governed by the short-range attraction for lysozyme and long-range attraction for BSA (Fig. 5). The aggregates are characterized by diffusion limited aggregate type of mass fractal morphology.

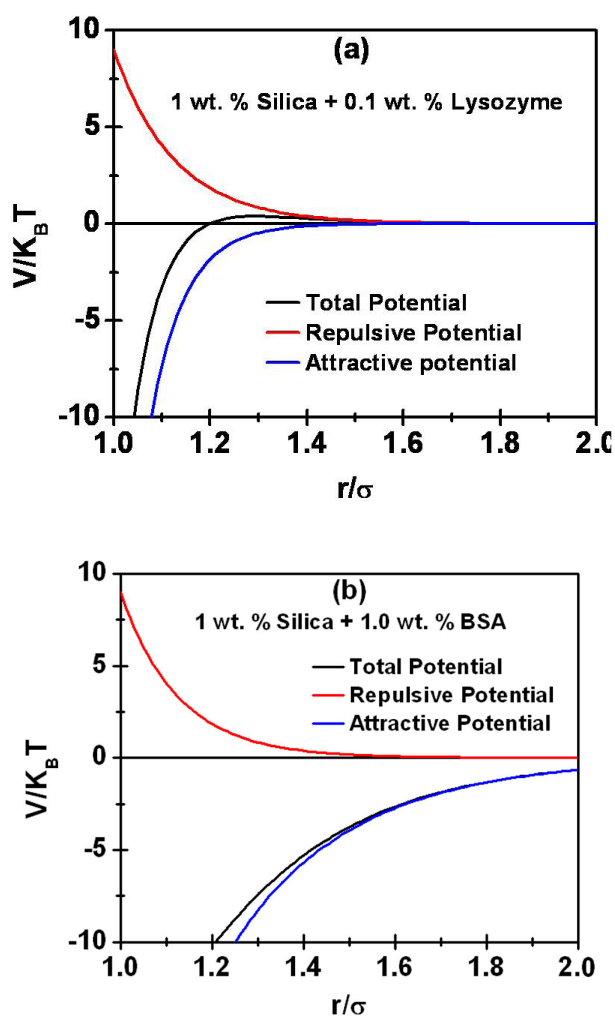


Fig. 5. The calculated interaction potentials from SANS data responsible for aggregation of silica nanoparticles in presence of (a) lysozyme and (b) BSA proteins.

SANS has also been used to study resultant structures formed from lysozyme protein adsorption on different sized silica nanoparticles [13]. The studies were carried out on the nanoparticle systems having sizes much larger than the protein size. The protein adsorption on nanoparticle shows an exponential behavior with adsorption coefficient and saturation values increasing with the size of the nanoparticle. The adsorption of protein leads to the aggregation of nanoparticles which are characterized by the fractal structure. The nanoparticle aggregates coexist with un-aggregated particles at low protein concentrations whereas at high protein concentrations the excess free proteins are found with the nanoparticle aggregates. It is also found that the native protein structure is disturbed on their adsorption on nanoparticles.

In summary, SANS is an ideal technique for investigating the phase behavior of bio- and nanomaterials. We have extensively used this technique in protein and nanoparticle solutions as well as their complexes. Our results show that the phase behavior in these systems is governed by the delicate interplay of short-range/long-range repulsive and attractive interactions followed by formation of structures from nano to micron length scales.

Acknowledgement

I thank Dr. S.L. Chaplot, Director, Physics Group and Dr. R. Mukhopadhyay, Head, SSPD, BARC for their encouragement and support. I am also thankful to my colleagues and collaborators associated in this work.

References

1. D. Svergun and M.H.J. Koch, *Rep. Prog. Phys.* 66, 1735 (2003)
2. S. Chodankar and V.K. Aswal, *Phys. Rev. E* 72, 041931 (2005)
3. A. Stradner, H. Sedgwick, F. Cardinaux, W.C.K. Poon, S.U. Egelhaaf, and P. Schurtenberger, *Nature* 32, 492 (2004)

BARC NEWSLETTER

Founder's Day

4. A. J. Chinchalikar, V. K. Aswal, J. Kohlbrecher and A. G. Wagh, Phys. Rev. E 87, 062708 (2013)
5. S. Chodankar, V.K. Aswal, P.A. Hassan and A.G. Wagh, Physica B 398, 112 (2007).
6. V. K. Aswal, S. Chodankar, J. Kohlbrecher, R. Vavrin and A. G. Wagh, Phys. Rev. E 80, 011924 (2009)
7. D Ray, V. K. Aswal and D. Srivastava, Nanosci. Nanotechnol. 10, 6356 (2010).
8. D. Ray, V. K. Aswal and J. Kohlbrecher, Langmuir 27, 4048 (2011)
9. A.J. Chinchalikar, V.K. Aswal, J. Kohlbrecher and A.G. Wagh, Chem. Phys. Lett. 542, 74 (2012).
10. S. Kumar, M.-J. Lee, V. K. Aswal and S.-M. Choi, Phys. Rev. E 87, 042315 (2013)
11. D. Ray and V. K. Aswal, J. Nanopart. Res. 14, 778 (2012)
12. I. Yadav, S. Kumar, V. K. Aswal and J. Kohlbrecher, Phys. Rev. E 89, 032304 (2014)
13. S. Kumar, V.K. Aswal and J. Kohlbrecher, Langmuir 27, 10167 (2011)

ULTRAFAST CHARGE TRANSFER DYNAMICS IN SUPER-SENSITIZED QUANTUM DOT SOLAR CELL

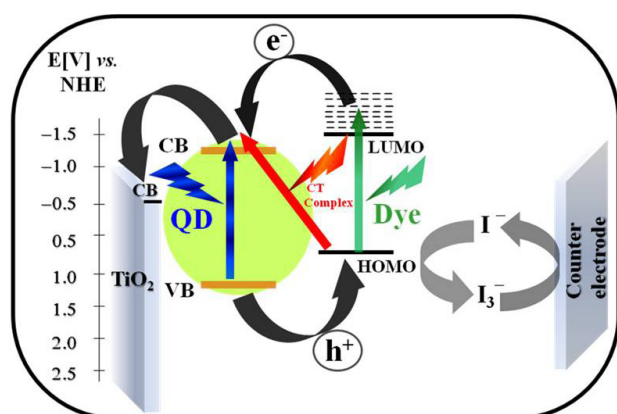
Harendra N. Ghosh

Radiation and Photochemistry Division

Dr. Harendra N. Ghosh is the recipient of the DAE-SRC Outstanding Investigator Award for the year 2012

Abstract

Working principle and charge transfer dynamics in ultrafast has been demonstrated in quantum dot (QD) /dye composite materials where dye and composite form strong charge transfer (CT) complex in the ground state. Charge separation processes found to take place in three in three different pathways: by transferring photo-excited hole of QD to dye, electron injection from photo-excited dye to QD and direct electron transfer from HOMO of dye to conduction band of QD. Charge transfer dynamics was monitored by direct detection of dye cation radical and electron in the QD in the transient absorption spectra. Electron injection and electron transfer process are found to be pulse width limited (< 100 fs) however hole transfer time measured to be sub-picosecond. Charge recombination dynamics has been found to be very slow. Photovoltaic response of CdS/DBF super sensitized TiO_2 quantum dot solar cell found to be improved drastically due to spatial charge separation (electron in CdS QD and hole in DBF).



Scheme 1: Schematic Diagram of Super-sensitized Quantum Dot Solar Cell.

Augmentation of current conversion efficiency in dye sensitized solar cell (DSSC) is one of the most challenging tasks. So far the record conversion efficiency of above 13% in DSSC has been reported by Graetzel and co-workers using specially synthesized Zn-porphyrin and

cobalt (II/III)- based redox electrolyte, which is believed to be lower for commercial application. In this regard design and development of quantum dot sensitized solar cell (QDSSC) has been started world-wide for the next generation solar module. It is believed that single photon can generate more than one electron-hole pair multiple exciton generation (MEG) in quantum dot which in turn can drastically increase the efficiency of the devices. It has been verified that efficiency of quantum dot solar module can be enhanced significantly by dissociating or separating the multi-exciton before ultrafast exciton-exciton annihilation. However, so far the highest conversion efficiency in QDSC has been reported by Kamat and co-workers to be ~ 5.2 %. By introducing inorganic-organic heterojunction and hybrid passivation the efficiency could be increased up to ~ 7 %, which is still much lower than conventional dye-sensitized solar cells (DSSCs). In QD materials majority of exciton recombines before it dissociates

BARC NEWSLETTER

Founder's Day

as a result efficiency realized in QDSC is much lower than expected. By using suitable molecular adsorbate (electron or hole acceptors) exciton dissociation in QD materials can be reality. In addition to that it has been realized that limited absorption of solar radiation of QDs and slow hole transfer rate are the main reasons for overall low efficiency of QDSC. These problems can be tackled by introducing super sensitizer in QDSC, where quantum dot and molecular adsorbate can exchange charge carriers on photo-excitation. In super sensitization in addition to photosensitizing the quantum dot material, molecular adsorbate also can act as hole transporting materials for photosensitized quantum dot, as a result grand charge separation takes place in QD-molecular composite material.

In this article we intend to demonstrate charge transfer mechanism and grand charge separation of super-sensitized solar cell materials. For this purpose we have chosen CdS QD and di-bromo fluoresce (DBF) dye molecule where both CdS QD and DBF individually can sensitize TiO₂ nanoparticles. Redox energy levels of CdS QD and DBF molecule imply that conduction band (CB) of CdS lies below LUMO level which allows photo-excited DBF to inject electron in to the CB of CdS QD and HOMO level of DBF lies above the valence band (VB) of CdS QD allowing photo-excited hole transfer to DBF molecule. Interestingly CdS QD and DBF forms strong charge transfer (CT) complex where on photo-excitation direct electron transfer from DBF to CdS QD is feasible. We have carried out steady state and time-resolved emission measurements to confirm hole and electron transfer processes following different path ways in the above system. Femtosecond transient absorption spectroscopy and Fluorescence Up-conversion techniques have been employed to monitor the charge (both electron and hole) transfer dynamics in ultrafast time scale and to demonstrate grand charge separation in CdS QD/DBF composite system.

Oleic-capped CdS QDs were synthesized by following the previously reported method of high-temperature

reaction of precursors in hot noncoordinating solvent ODE. Fig. 1 shows the high resolution TEM images of CdS QD particle and particle size were determined to be 2.5 nm.

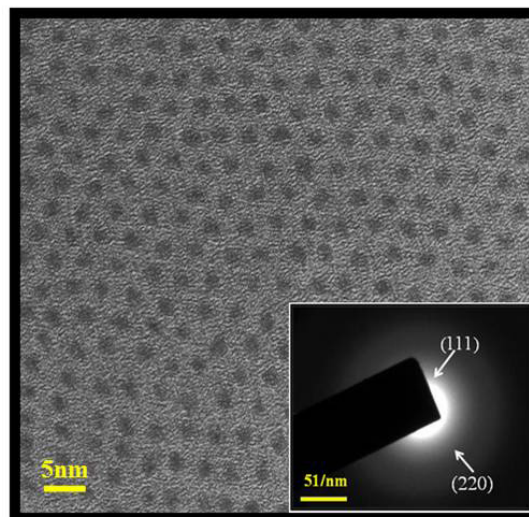


Fig. 1: The HRTEM image of synthesized CdS QD. Particle size was measured to be 2.5 nm (scale bar 5 nm). Inset: The SAED pattern of CdS QD (scale bar 5 nm⁻¹).

To understand charge transfer interaction in the excited state it is very important monitor ground state interaction between dye and QD materials. Fig. 2 shows the optical absorption spectra of DBF sensitized CdS QD. Pure DBF molecule shows weak optical absorption up to 550 nm with a peak at 465 in addition to an absorption band below 280 nm as depicted in Fig. 2a. Fig. 2b depicts the optical absorption spectrum of 0.49

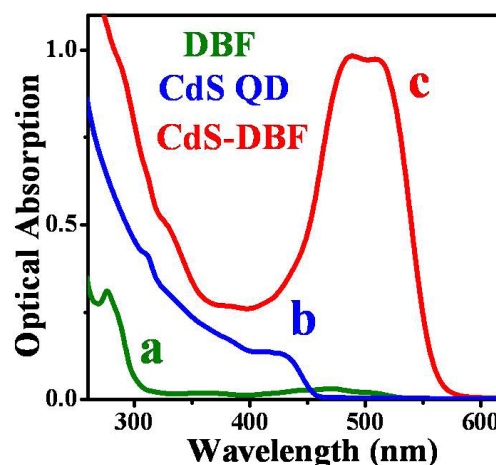


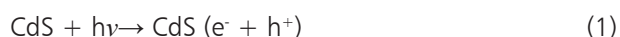
Fig. 2: Optical absorption spectra of (a) DBF dye (0.3 mM) (b) CdS QD (0.49 μ M), (c) DBF-CdS complex

BARC NEWSLETTER

Founder's Day

μM CdS QD in chloroform which shows an exciton at 433 nm and corresponding band gap can be calculated to be ~ 2.69 eV. Now on addition of CdS quantum dot (QD) in DBF solution the optical absorption band become broader and shifted to the red region of the spectrum (Fig. 2c). The color of the solution becomes deep red (while the color of free DBF and CdS is light orange and yellow respectively) indicating formation of strong charge transfer (CT) complex between CdS QD and DBF. High extinction co-efficient of the CdS-DBF complex suggest that the composite materials form strong CT complex where partial charge transfer takes place in the ground state. This observation clearly suggests that CdS-DBF composite material is a potential material for super-sensitizer, which can absorb more solar radiation as compared to that of the individual CdS QD and DBF molecule.

To understand charge transfer dynamics steady state and time-resolved emission studies for both CdS QD and DBF molecule separately and also in the composite system by selective excitation. Figure 3a shows steady state luminescence spectra of CdS QD in chloroform after exciting the sample at 375 nm, which consist an emission peak at 450 nm with high quantum yield ($\phi_f=0.24$). Fig. 3b shows the emission spectra of CdS QD in presence of 0.3mM DBF. It is clearly seen that CdS emission is completely quenched in presence of DBF. As we have already mention that the valence band (1.35V vs NHE) of CdS lies below the HOMO (0.8 V vs NHE) of DBF (Scheme 2), so photo-excited hole can be captured by DBF which is thermodynamically viable. Hole transfer reaction can be expressed by the equations below:



To find the hole transfer dynamics time-resolved emission studies has been carried out of free CdS QDs and also in presence of DBF and shown in Fig. 3 inset (upper panel). The emission decay traces of CdS

QD and CdS/DBF composite have been monitored at 450 nm after exciting the samples at 406nm. The emission decay traces can be fitted multiexponentially with time constants of $\tau_1 = 0.58$ ns (39%), $\tau_2 = 23.8$ ns (32%), $\tau_3 = 5.2$ ns (29%) with $\tau_{\text{avg}} = 9.4$ ns for CdS QD and of $\tau_1 = 0.12$ ns (61%), $\tau_2 = 0.94$ ns (22%), $\tau_3 = 3.4$ ns (17%) with $\tau_{\text{avg}} = 0.9$ ns for CdS/DBF system. The average lifetime of CdS/DBF system is ten times shorter as compared to that of CdS QD, which confirms hole transfer process in the composite materials as suggested in equation 2. Presumably the observed decrease in lifetime arises due to hole transfer (HT) from CdS QD to DBF molecule, then the HT rate constant can be determined through the following expression

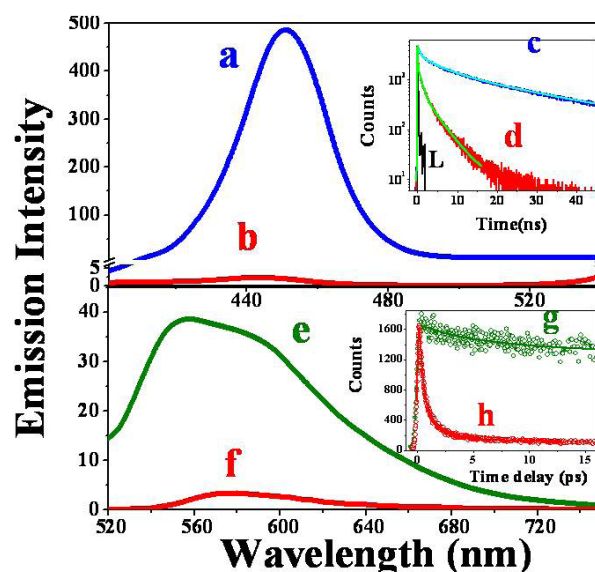


Fig. 3: Upper panel: Photoluminescence (PL) spectra of CdS QD (a) in absence and (b) in presence of DBF in chloroform solution after exciting at 375nm. Inset: Emission decay traces of (c) CdS QD and (d) CdS-DBF composite after exciting at 406 nm and monitoring at 450 nm. Lower panel: Photoluminescence (PL) spectra of DBF (e) in absence and (f) in presence of CdS QD after exciting at 500nm. Inset: Fluorescence upconversion traces of (g) DBF and (h) CdS-DBF composite after exciting at 435 nm and monitoring at 560 nm. $[\text{CdS}] = 0.49\mu\text{M}$ and $[\text{DBF}] = 0.3\text{mM}$.

$$k_{\text{HT}} = 1/\tau_{\text{CdS+DBF}} - 1/\tau_{\text{CdS}} \quad (3)$$

Using the average lifetime values of 9.4 ns (CdS) and 0.9 ns (CdS-DBF) the hole transfer rate constant can be determined to be $1.1 \times 10^9 \text{ sec}^{-1}$.

BARC NEWSLETTER

Founder's Day

Now from Scheme 2 it is clear that photo-excited DBF molecule can inject electron into the conduction band of CdS QD. To monitor this electron transfer process from photo-excited DBF to CdS QD we have carried out emission spectroscopy in the present investigation after exciting DBF molecule. Electron injection dynamics from photo-excited xanthenes dyes (DBF is a xanthenes dye) to the conduction band of TiO₂ have been demonstrated by us. Since xanthenes dye molecules are highly luminescent, it is easy to demonstrate electron transfer process by monitoring the luminescence quenching measurements. Fig. 3 lower panel depicts the emission spectra of DBF and DBF-CdS composite after exciting the samples at 500 nm. Fig. 3e shows the emission spectra of DBF which has emission peak at 557 nm with a hump at 584 nm. However in presence of CdS the emission intensity drastically reduces as shown in Fig. 3f. Again as we have already mentioned that LUMO (-1.5 V) of DBF lies above the conduction band (-1.3 V vs NHE) of CdS QD (Scheme 2), so photo-excited DBF can inject electron into the conduction band of CdS. The emission quenching can be attributed to electron injection from photoexcited DBF to CdS, and can be expressed by the equations below:



Now to monitor electron injection dynamics we have carried out fluorescence upconversion measurements for free DBF and also in presence of CdS QD after exciting the samples at 435 nm laser pulse and monitoring at 560 nm and shown in Figure 3 inset (lower panel). We would like to make a point that exciting pure CdS at 435 and monitoring at 560 nm, no emission signal was observed. It is clear from emission decay trace of pure DBF (Fig. 3g) that emission lifetime of DBF is too long to measured in fluorescence up-conversion technique. So to measure the emission lifetime of DBF we performed nanosecond life time measurements (TCSPC) and determined to be 1.6 ns. Fig. 3h depicts

the emission kinetics of DBF in presence of CdS QD which can be fitted bi-exponentially with time constants of $\tau_1 = 618$ fs (85%) and $\tau_2 = 1.8$ ps (15%) with average life time $\tau_{\text{avg}} = 800$ fs. If we presume that the observed decrease in lifetime arises due to electron injection from photoexcited DBF to CdS QD, then we can determine the electron injection time constant by the following expression.

$$k_{\text{inj}} = 1/\tau_{\text{DBF}+\text{CdS}} - 1/\tau_{\text{DBF}} \quad (6)$$

By following the above expression electron injection rate can be determined to be $1.2 \times 10^{12} \text{ sec}^{-1}$. With the help of time-resolved emission technique we have demonstrated both electron injection from photo-excited DBF to CdS QD and also hole transfer from photo-excited CdS QD to DBF molecule.

To substantiate charge (both electron and hole) transfer dynamics in early time scale with accuracy femtosecond transient absorption spectroscopic measurements has been carried out by exciting CdS QD, DBF and DBF-CdS QD/composite system at 400 nm laser light. Fig. 4 shows the transient absorption spectra of photoexcited CdS/DBF QD composite materials in different time delay, which comprises a bleach below 550 nm and two broad absorption bands at 550-750 nm and 750-900 nm respectively. The broad

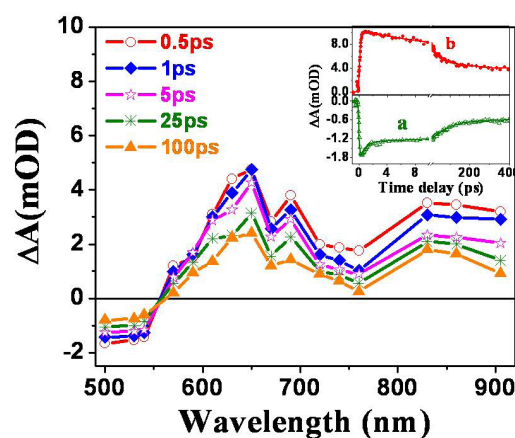


Fig. 4: Transient absorption spectra of CdS-DBF composite materials in chloroform at different time delay after excitation at 400 nm laser light. Inset: Kinetic decay trace at (a) 500 nm (b) 650 nm.

BARC NEWSLETTER

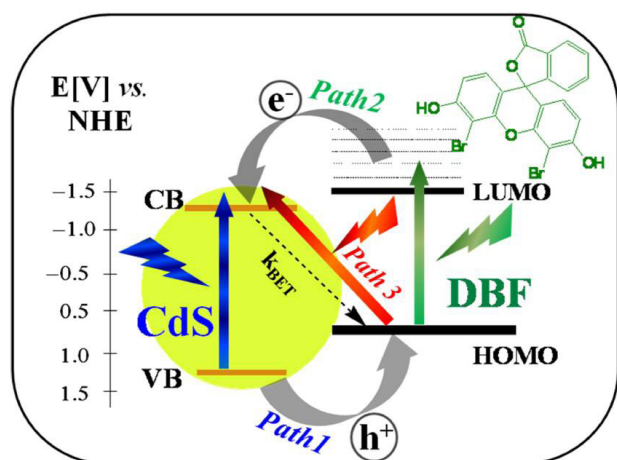
Founder's Day

spectral absorption in the 750-900 nm regions can be attributed to the electrons in the conduction band in CdS QD. The transient absorption band at 550-750 nm can be attributed to DBF cation radical. The band having maximum at 650 nm is assigned to DBF cation radical (DBF.+). We have already demonstrated that at 400 nm photo-excitation both electron injection and hole transfer process can occur in DBF/CdS composite materials. Now to understand the charge transfer and charge recombination dynamics we have monitored the kinetics at 500 nm (bleach wavelength) and 650 nm (DBF cation radical) and shown in Figure 4 inset. It is clearly seen that charge recombination dynamics is extremely slow where electrons and holes are spatially separated.

From steady state and time-resolved emission and absorption studies suggest that generation of electron in the conduction band in CdS and formation of DBF cation radical might be taking place through more than one process. Recent investigation on quantum dot solar cell suggests removal of charges (holes and electrons) from photo-excited quantum dots can be key factor to improve the conversion efficiency. In CdS-DBF composite materials it is clear from Scheme 2 that DBF can extract the photo-excited hole from CdS QD (path 1, Scheme 3). In addition to that photo-excited DBF can inject electron to the conduction band

of CdS (path 2, Scheme 2) suggesting CdS-DBF is a typical type II system of QD-molecular system. Over and above the formation of type II system, from steady state optical absorption measurements (Fig. 1) it is clear that CdS QD and DBF form strong CT complex with very high molecular extinction co-efficient, which has absorption band in the red region of the solar radiation as compared to both CdS QD and DBF molecule, as a result the absorption cross-section of CdS-DBF composite system towards solar radiation increase dramatically. Excitation of CT CdS-DBF complex electron from HOMO of DBF can move directly to the conduction band of CdS (path 3, Scheme 2) which ensure much higher charge separation as compared to both hole transfer from CdS to DBF and also electron injection from photoexcited DBF to the CB of CdS. We have demonstrated that blue part, green part and red part of the solar radiation will be absorbed by CdS QD, DBF and CdS-DBF CT complex respectively as shown in Scheme 2.

Steady state and time-resolved spectroscopic analysis suggest that CdS-DBF composite can be used as a great super sensitizer in quantum dot solar cell. The photo-electrochemical performance of mesoscopic TiO₂ films modified with CdS, DBF, and CdS/DBF was monitored under similar illumination condition of AM 1.5 irradiation (100mWcm⁻²) using a redox couple, where Pt-coated FTO is used as counter electrode. The electrolyte composition: 0.6 M 1,2 dimethyl 3-propyl imidazolium, iodide, 0.1 M LiI, 0.05 M I₂, and 0.5 M, 4-tert-butylpyridine in acetonitrile is used. It is noteworthy that Fig. 5 purely shows a comparison of solar cells based on CdS QD, DBF dye and CdS/DBF composite and actual photocurrent action spectra can be improved further by optimized fabrication of QDSC. It is interestingly to see that maximum IPCE observed for TiO₂/CdS/DBF electrode which is much higher as compared to both TiO₂/CdS electrode and TiO₂/DBF electrode, confirming efficient hole transfer from CdS QD to DBF molecule and also super sensitization through CdS-DBF charge transfer complex.



Scheme 2: Charge transfer processes (hole transfer, electron injection and charge recombination reactions) involving CdS QD and DBF dye in chloroform. Molecular structure of DBF is shown in the scheme.

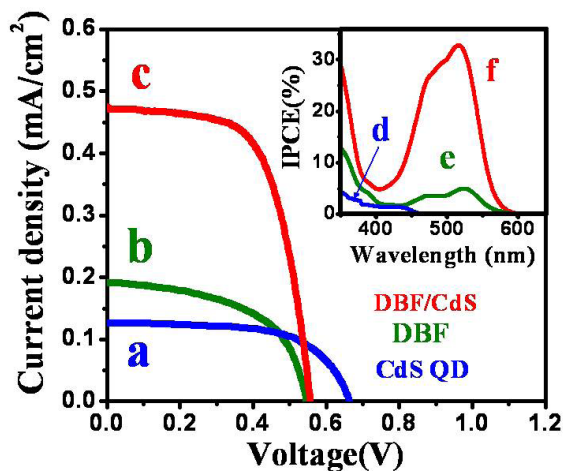


Fig. 5: Photovoltaic performance of DBF-CdS super-sensitizer: Incident photon-to current conversion efficiencies vs. wavelength for (a) CdS QD, (b) DBF molecule, and (c) CdS-DBF composite. Inset Current density (J) as a function of Voltage (V) (d) CdS QD, (e) DBF molecule, and (f) CdS-DBF composite.

This synergy between the CdS and the dye in facilitating higher photocurrent generation indicates an additional role of the dye in shuttling holes across the CdS/dye electrolyte interface. With this proposition, it becomes quite impressive to see dramatic improvement of photovoltaic response for the CdS-DBF composite on TiO₂ photo anode, which represents the high efficacy of super-sensitization in stabilizing interfacial charge separation of QDSC. This is a direct correlation of transient absorption and luminescence data and photoaction spectra which describes higher charge separation through super-sensitization. CdS-DBF composite not only effectively removes the hole from quantum dot it can also absorb more solar radiation due to formation of charge transfer complex which has very high molar extinction coefficient. Considering the fact that QDSC photoaction is exclusive outcome of kinetic competitions of electron injection, hole transfer, back electron transfer and dye-regeneration processes, this super-sensitization scheme can bring significant improvement in QDSC without much changing the device fabrication.

In conclusion ultrafast hole and electron transfer dynamics in CdS QD/di-bromo fluorescein (DBF) composite are explored and verified as a super-

sensitizer in QDSC. Optical absorption studies indicate CdS QD and DBF form strong charge transfer complex in the ground state. Steady state and time-resolved absorption and emission studies confirmed that on photo-excitation charge separation in CdS-DBF composite take place in three different pathways. As a result grand charge separation takes place in CdS-DBF composite, which confirms the usefulness as a super-sensitizer in QDSC. Ultrafast transient absorption and Femtosecond up-conversion studies indicates that path 2 and path 3 are pulse width limited (< 100 fs) however path 1 time measured to be 800 fs. Charge recombination dynamics found to very slow due to spatial charge separation in the composite. Understanding the charge transfer dynamics at molecular level in ultrafast time scale has helped in achieving superior $J-V$ and IPCE response of CdS/DBF super sensitized TiO₂ quantum dot solar cell. This observation confirms the reality of multiple exciton dissociation and finally higher photo-conversion efficiency in quantum dot solar cell.

Acknowledgement

The author acknowledges Dr. D. K. Palit and Dr. B. N. Jagatap for their encouragement.

References

1. P. Maity, T. Debnath, and H. N. Ghosh *J. Phys. Chem. Lett.* 2013, 4, 4020–4025.
2. P. Singhal, and H. N. Ghosh *J. Phys. Chem. C*, 2014, 118, ASAP. DOI:10.1021/jp408727a
3. P. Singhal, and H. N. Ghosh, *Phys. Chem. Chem. Phys.*, 2014, 16, 16824-16831.
4. T. Debnath, P. Maity and H. N. Ghosh *Chem. Eur. J.* 2014, 20, ASAP. DOI:10.1002/chem.201403267
5. T. Debnath, P. Maity, S. Maiti, and H. N. Ghosh *J. Phys. Chem. Lett.* 2014, 5, ASAP. ID jz-2014-012719.
6. P. Maity, T. Debnath, U. Chopra and H. N. Ghosh *J. Phys. Chem. C*. 2014, (Revised) Manuscript ID: jp-2014-05291z.

COMPUTATIONAL HYDRODYNAMICS AND MHD FOR STRATEGIC SYSTEMS

Srinivasagopalan Madhavan and Shashank Chaturvedi
Computational Analysis Division

Shri Srinivasagopalan Madhavan is the recipient of the DAE Scientific & Technical Excellence Award for the year 2012

Abstract

A two-dimensional lagrangian hydrocode has been developed and that was extensively used in understanding and optimizing experimental systems of DAE's interest. Our 2-D MHD code that has been used in three ways. The first is design and optimization of CAD's experiments on a multistage electromagnetic coilgun that accelerates metallic projectiles to high velocities. Secondly, the MHD code has been used for understanding and optimizing Electromagnetic Forming systems being developed at BARC. Thirdly, this MHD code has been used for scoping studies of an electromagnetic shell acceleration system in Z-pinch geometry. The code allows for various Equations of State, Dynamic strength and Fracture models, and can handle a variety of solids and fluids. These codes are in regular use as a validated design tool for supporting BARC's development of various systems and test facilities.

Keywords: Hydrocode, Elastic-Plastic analysis, MHD, Coilgun

Introduction

This report focuses on induction coilgun system and application of our 2D-MHD^{1,2,3} code for electromagnetic coilgun experimental system⁴.

Induction coilguns have been used to accelerate metallic projectiles to velocities of a few hundred meter ^{4,5} .

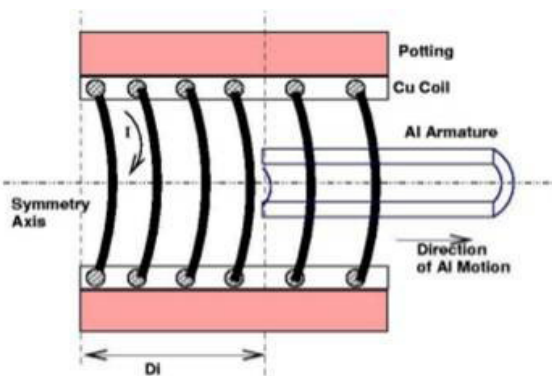


Fig. 1. Schematic of coilgun system in R-Z axisymmetric plane

Fig. 1 shows a schematic of one design of an induction coilgun system. The discharge of a charged capacitor through the coil sets up time-varying flux linkage with the projectile. This induces time-varying eddy currents that vary through the projectile length and also as a function of depth through the projectile thickness. The interaction of these eddy currents with the magnetic field produces axial and radial electromagnetic forces. The axial force accelerates the projectile out of the coil, while the radial force leads to pinching. The eddy currents causes non-uniform joule heating of the projectile, in turn affecting the spatio-temporal variation of its electrical resistivity. For this system, we have performed two-dimensional simulations as explained below.

Salient features of our 2D Computational Model

Main features of the computational model are :

- Explicit finite-difference Lagrangian Magneto-Hydrocode where mass in a cell remains constant.

BARC NEWSLETTER

Founder's Day

- Solves finite-difference⁶ approximations of mass, momentum and energy conservation equations.
- Self-consistent calculation of dynamically evolving coil current from capacitor bank discharge.
- Temperature dependent resistivity model included to account for joule heating effects.
- Handles multiple materials, solids as well as fluids.
- Contains Node-coupler⁶, to prevent ``hourglass'' formation in the mesh.
- Being lagrangian formulation the code preserves material interfaces.
- Restart option from specified dump times.
- Supports Plane, Cylindrical and Spherical geometries
- Provision for problem specific addition / deletion of cells.
- Timestep criteria:
 - o CFL based on sound speed.
 - o Based on characteristic time for evolution of internal energy, velocity, etc.
- Equation of State: The EOS computes the pressure for a given combination of density and internal energy. Mostly we use EOS table generated by CAD.
- Plastic yielding model: Von-Mises yield condition.
- Dynamic Strength models: The following models are available:
 - o Steinberg-Guinan⁷.
 - o Revised Johnson-Cook⁸.
- Includes Fracture models namely, Johnson-cooks⁹ and Bao-Wierzbickis¹⁰

Results

Coil Stability at high current

Simulations performed to identify the upper limit of the current that coil can withstand. For current up to 60 kA, it was found that coil should be potted with a material whose yield strength not less than 50 MPa to avoid coil failure. Simulations results (Fig. 2) showing the location where potting material has crossed elastic limit (yielding) whose initial yield strengths were 16 and 30 MPa.

Optimized projectile design

We have optimized the projectile shape and size. The optimized projectile be 25 mm long and has an uniform outer diameter (24 mm). Up to an axial extent 11 mm, the inner diameter is 16 mm and for the rest of the length, the inner diameter of the projectile was 20 mm. Calculated simulation results along with experimental results for various cases is listed in Table.1

Case #	Applied Volt (kV)	Peak Current of the Coil (kA)		Projectile axial Velocity under Electromagnetic force	
		Simulation	Experimental	Simulation (m/s)	Experimental (m/s)
1	2.5	28	30	66	69
2	3.5	39	41	114	112
3	4.0	45	48	141	142
4	4.5	50	52	177	169
5	5.0	55	58	197	183

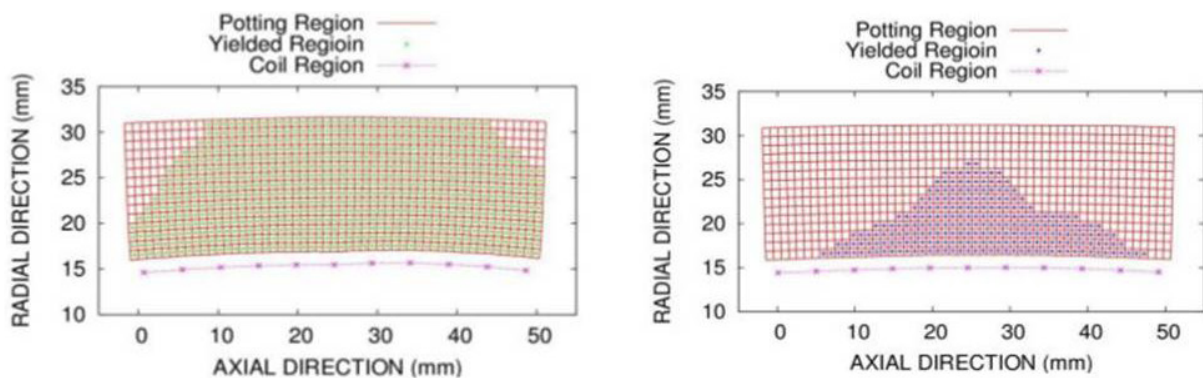


Fig. 2. Final shape of the potting shown as grids. The region crossing the yield limit is shown as green (LHS $Y_0=16$ MPa) and blue (RHS $Y_0=30$ Mpa).

BARC NEWSLETTER

Founder's Day

Projectile stability

Projectile with 2 mm thickness resulted with heavy deformation and fracture. This has been analyzed with our composite 2D-MHD axisymmetric RZ code and XY-Plane geometry codes in sequence. Firstly axisymmetric RZ code has been used to record the time and space varying electromagnetic forces on the projectile. Subsequently this was feed to 2D-XY Plane geometry code to evolve the projectile radial deformation. Since this mode includes fracture phenomena, the dynamical radial inward deformation of the projectile is obtained along with the evolution of damage parameter to define the projectile integrity. This could be one of the causes projectile failure upon radial pinch. A comparison of projectile shape is presented in Fig. 3.

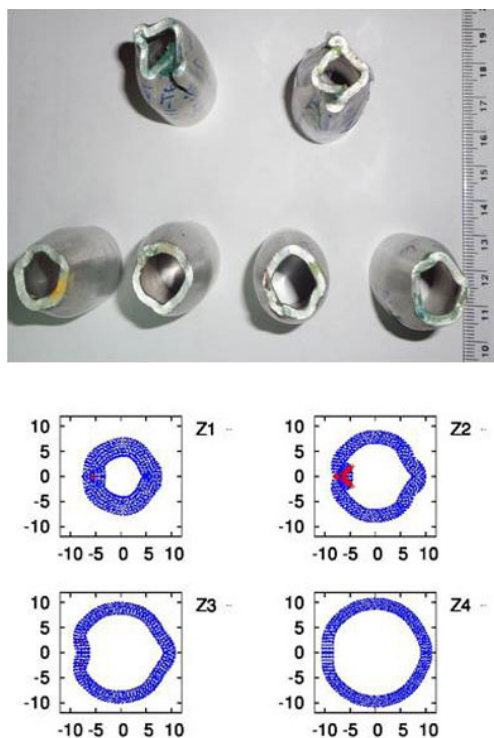


Fig. 3: LHS shows experimentally observed projectile shapes. RHS shows 2D simulations showing the radial pinch along with an indication of fracture in red marks.

Conclusions

A two-dimensional (2-D) hydrocode has been developed in-house and has been extensively used for simulation of coilgun electromagnetic system involving electromagnetic coupling between coil and

projectile. The code includes elastic-plastic temporal deformation of the coil and the projectile. The code has been validated with in-house experiments. Stability of the coil and projectile was examined using our computational tool. Projectile design for CAD's coilgun experimental system has been optimized.

References

1. S. Madhavan, C.D. Sijoy, S. Pahari and S. Chaturvedi, "Numerical simulations of an electromagnetic coilgun for impact and fracture studies," AIP Conf. Proc. Vol 1349, pp 467-468, 2011.
2. S. Madhavan, C. D. Sijoy, S. Pahari and S. Chaturvedi, "Limits imposed by solenoid damage on the maximum velocity achieved by an electromagnetic coilgun: A computational study", AIP Conf. Proc. 1447, pp 495-496, 2012 doi : 10.1063/1.4710095.
3. S. Madhavan, C.D. Sijoy, S. Pahari, S. Chaturvedi and IPF Team, "Significance of projectile resistivity, deformation and fracture in modelling coilgun performance", *IEEE Trans. Plasma Sci.* Vol 42(2) pp 323-329, 2014 doi : 10.1109/TPS.2013.2294718
4. S. Pahari, N. Shiv, S.P. Illa, S. Madhavan, C.D. Sijoy, S. Chaturvedi, "Development of an Electromagnetic Acceleration Facility for Impact and Fracture Studies at High Strain Rates", AIP Conf. Proc. Vol 1349, pp 483-484, 2011.
5. H. Mark, *IEEE Trans. Magn.* Vol. 25, pp 9, 1989
6. Wilkins, M.L. Computer simulation of dynamic phenomena. Berlin: Springer-Verlag (1999)
7. G. Johnson, W. Cook, "A Constitutive model and date for metals subjected to large strains, high strain rates and high temperature", Proc. 7th Int. Symp. on Ballistics, pp 541, 1983,
8. Steinberg, D.J., Cochran, S.G., Guinan, M.W., A constitutive model for metals applicable at high-strain rate, *Journal of Applied Physics*, Vol. 51(3), pp. 1498-1504, 1980.
9. G. Johnson, W. Cook, "Fracture characteristics of three metals subjected to various strains, strain rates, temperatures and pressure" *Engg Fracture Mech.*, Vol 21, pp 31-48, 1985
10. Y. Bao and T. Wierzbicki, *Int. J. Mech. Sci.*, Vol 46, p 81, 2004

COMPUTATIONAL HYDRODYNAMICS FOR CRITICAL SYSTEMS

Venkata Ramana Ikkurthi and Shashank Chaturvedi
Computational Analysis Division

Dr. Venkata Ramane is the recipient of the DAE Scientific & Technical Excellence Award for the year 2012

Abstract

We have indigenously developed a set of sophisticated computer code for modeling ultra high-pressure shock and detonation waves and the dynamic behavior of materials under various loading conditions. These involve a fully-parallelized, three-dimensional (3-D) hydrocode called DEPAS-3D. The code allows for various Equations of State, Dynamic strength and Fracture models, and can handle a variety of solids and fluids. These codes are in regular use as a validated design tool for supporting BARC's development of various strategic systems and test facilities. Apart from helping in system optimization, these codes provide detailed insight into the underlying physical phenomena. These codes have also been used in Multiscale modelling program to validate fracture model parameters obtained from Atomistic Simulations.

Keywords: Hydrocode, Elastic-Plastic analysis, Detonation interaction, Shock waves, Parallelization

3-D Hydrocode: Features

A three-dimensional (3-D) hydrocode called DEPAS-3D¹, has been developed in-house, broadly following the algorithm of Ref. [2]. Main features of the code are the follows:

- Explicit finite-difference Lagrangian Hydrocode where mass in a cell remains constant. Solves finite-difference² approximations of mass, momentum and energy conservation equations.

$$\frac{\partial \rho}{\partial t} + \nabla \cdot (\rho \mathbf{u}) = 0$$

$$\frac{\partial (\rho \mathbf{u})}{\partial t} + \nabla \cdot (\rho \mathbf{u} \mathbf{u}) + \nabla P = 0$$

$$\frac{\partial (\rho E)}{\partial t} + \nabla \cdot (\rho \mathbf{u} E) + P(\nabla \cdot \mathbf{u}) = 0$$

- Handles multiple materials, solids as well as fluids.

- Node-coupler², to prevent ``hourglass'' formation in the mesh.
- Material interfaces are preserved, since this is a Lagrangian code.
- Restart option from specified dump times.
- Cartesian and Pseudo-polar grids.
- Artificial viscosity to handle shocks and grid distortions.
- Cell Erosion / Chopping of cells.
- Timestep criteria:
 - o CFL based on sound speed.
 - o Based on burn fraction for explosives.
 - o Based on characteristic time for evolution of internal energy, velocity, etc.
- Equation of State: The EOS computes the pressure for a given combination of density and internal energy. Two broad types of EOS models are available:

BARC NEWSLETTER

Founder's Day

- o Tabulated EOS for several materials, generated by CAD.
- o A variety of analytical EOS:
 - ◇ Stiffened gas EOS.
 - ◇ Gruneisen EOS.
 - ◇ Six-parameter EOS for metals³.
 - ◇ Jones-Wilkins-Lee (JWL) EOS for explosives⁴.
- Wave propagation models for reactive shocks:
 - o Ignition and Growth reactive model⁴.
 - o Programmed burn model.
- Supports various initiation patterns.
- Plastic yielding model: Von-Mises yield condition.
- Dynamic Strength models: The following models are available:
 - o Steinberg-Guinan⁵.
 - o Zerilli-Armstrong⁶.
 - o Revised Johnson-Cook⁷.
- Fracture models³:
 - o Void-Growth.
 - o Cochran-Banner.
 - o Nucleation and Growth (NAG).
 - o Plastic-strain threshold based model.

Results

Parallelization performance

The code has been parallelized using the Message Passing Interface (MPI)⁸. This involves two major steps. The first is to partition the job between processors with load balancing. The second is to ensure data passage between different processors. The parallelized 3-D hydrocode is being run on a 5 TFLOP cluster. The parallelized code is being used for simulation of a variety of problems related to shock waves and high-velocity impact. Performance of a parallelized code on a cluster is expressed by 'Speedup' and 'Efficiency'. Speedup (S) involving 'n' number of processors is defined by $s = \frac{T_1}{T_n}$ where T_1 is the execution time of the code in a single processor and T_n is the execution time of the code on n processors.

Parallelization performance for a shock-wave problem involving strong exothermic reactions and shock-wave interactions is studied in detail. Figure (1) shows the speed-up obtained. Effect of mesh resolution has been studied. As the grid resolution is increased, the saturation point shifts to higher no. of processors. The effect of node coupler and cell-erosion has also been studied. If the node coupler is turned off, a better speed-up is obtained. The effect of cell-erosion, i.e., deletion of cells from calculation, contributes to reduction of speed-up, as additional message passing is done after each erosion takes place.

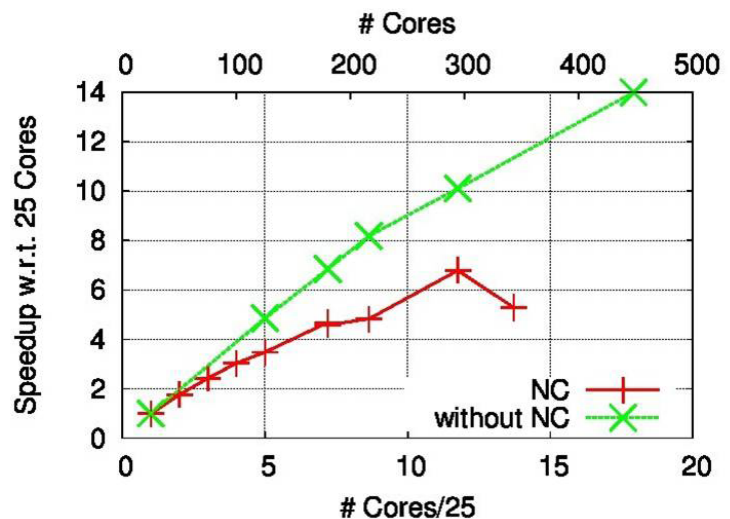


Fig. 1: Speedup obtained with parallelization along three-coordinate axes for fine mesh. Green and red curves correspond to cases without and with the use of a node coupler

Other applications

- Simulation of interaction of multiple shock waves in various geometries.
- Simulation of flyer acceleration due to impact and explosive loading.
- Simulation and design analysis of various critical systems of BARC.
- Multiscale simulations to check validity of Fracture model parameters obtained from Molecular Dynamic Simulations.

BARC NEWSLETTER

Founder's Day

Conclusions

A three-dimensional (3-D) hydrocode called DEPAS-3D has been developed in-house and has been extensively used for simulation of 3-D problems involving shock wave propagation, reactive exothermic flows and shock-wave interaction problems in solids as well as fluids. It has been parallelized using MPI. The performance of parallelization depends on the mesh resolution. Inclusion of node-coupler and cell-erosion facilities reduces the parallelization performance. The code has been used for simulation and design analysis of various critical systems and experiments in BARC and other Government Laboratories.

References

1. Ikkurthi V.R.; Majalee A; Chaturvedi S. Parallelization and load balancing issues in a 3-D hydrocode, in Proc. DAE Meeting on Parallel Computing and its Application in Science and Engineering (PASE), BARC, Mumbai (2003) 893.
2. Wilkins, M.L. Computer simulation of dynamic phenomena. Berlin: Springer-Verlag (1999).
3. Ikkurthi VR, Chaturvedi S, 2004, Use of different damage models for simulating impact-driven spallation in metal plates, *International Journal of Impact Engineering*, 30(3), 275-301 and references therein.
4. Mader, C., Numerical Modeling of Detonations, University of California Press, 1979.
5. Steinberg, D.J., Cochran, S.G., Guinan, M.W., A constitutive model for metals applicable at high-strain rate, *Journal of Applied Physics*, Vol. 51(3), 1980, pp. 1498-1504.
6. Zerilli, F.J., Armstrong, R.W., Dislocation-mechanics-based constitutive relations for material dynamics calculations, *Journal of Applied Physics*, Vol. 61(5), 1987, pp. 1816-1825.
7. Rule, W.K., Jones, S.E., A revised form for the Johnson-Cook strength model, *International Journal of Impact Engineering*, Vol. 21(8), 1998, pp. 609-624.
8. Snir M; Otto S; Huss-Lederman S; Walker D; Dongarra J. MPI: The Complete Reference. Cambridge: MIT Press (1995).

DESIGN AND DEVELOPMENT OF HIGH PRECISION INSTRUMENTS, AUTOMATED SYSTEMS AND SPECIAL PURPOSE MACHINES

Sameer Bhatt
Centre for Design and Manufacture

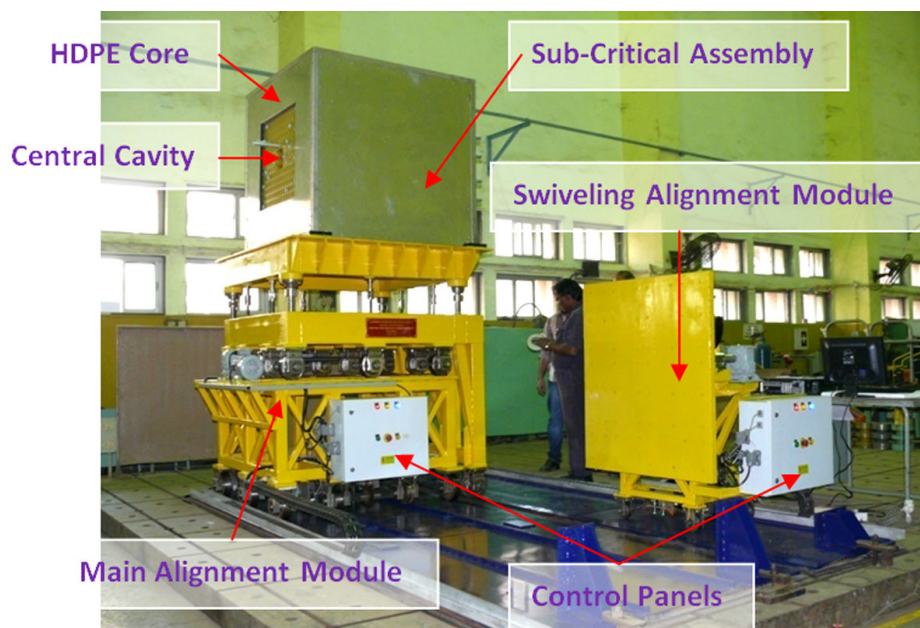
Shri Sameer Bhatt is the recipient of the DAE Scientific & Technical Excellence Award for the year 2012

Sub-Critical Facility & Alignment System

Sub-Critical Facility named as "Beryllium Reflected HDPE Moderated Multiplying Assembly" is designed & developed to conduct experiments under sub-critical regime. Sub-critical assembly is a zero power reactor which consists of HDPE core (Moderator) consisting of natural uranium as a fuel. The fuel rods are arranged in a 13x13 matrix. HDPE core is made up of a number of HDPE plates which are interlocked to each other. HDPE core is surrounded by BeO bricks (Reflector) housed in Al. boxes. Borated polythene and cadmium sheets (Absorber) are placed all around the beryllium

bricks housing. The whole assembly is on the top of alignment system. The alignment system consists of three subassemblies 1) Long travel alignment sub assembly 2) Cross travel alignment sub-assembly 3) 'Z' motion & plane alignment sub-assembly.

Criticality in design is to satisfy the load bearing capacity of the floor of the PURNIMA building which is 5 Tons/m² while the total load of the system is 8.5 tons and size of the sub-critical facility is 1.2m x 1.2m. The second challenge is to accommodate the fully automated system in a constrained space of PURNIMA hall with all the alignment and safety features. Unique



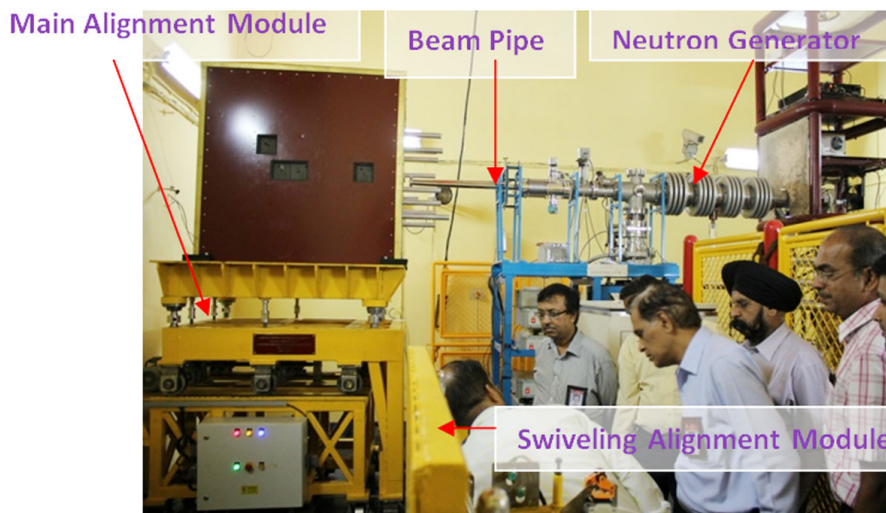
General Assembly of the Alignment Modules with Controls

BARC NEWSLETTER

Founder's Day

solution to tackle load bearing capacity was found out using composites of MS sheets and neoprene sheets to facilitate uniform distribution of the total weight of the system. This load is distributed over the area of 1.9 m² which is the total area of distributed load transferred to the floor through the composites, thus satisfying the load bearing capacity of the floor and also diffusing concentrated loads.

The sub-critical facility needs to be aligned laterally as well as along the neutron beam emanating from neutron generator when in use or to be off-positioned at a distance of 4 meters, when not in use. To facilitate positioning fully automated long travel, cross travel alignments are provided with remote operation, whilst plane alignment & height adjustment are manual. The total design load capacity of the system is 6 Tons.



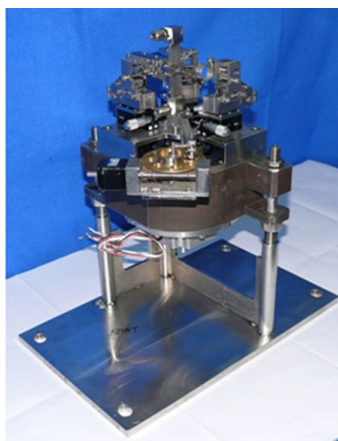
Trolleys as Installed in Constrained Space at PURNIMA

SLM Dye Laser Monochromator

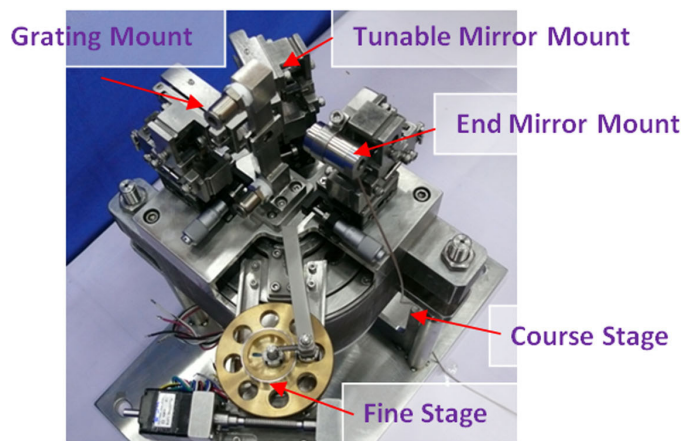
SLM Tunable Dye Laser Monochromator for L&PTD is designed and developed for U-233 clean-up programme. The requirement of this job is to rotate tunable mirror which is a part of optical cavity in the micro arc sec range while the other optical elements of

the cavity i.e. grating and end mirror are fixed as per optical layout.

Criticality in design lies in high rotational resolution of 0.04 arc-sec, compact, large range, universal mountable, optical mounts with same degree of accuracy.



SLM Dye Laser Monochromator



Optical Cavity Arrangement

BARC NEWSLETTER

Founder's Day

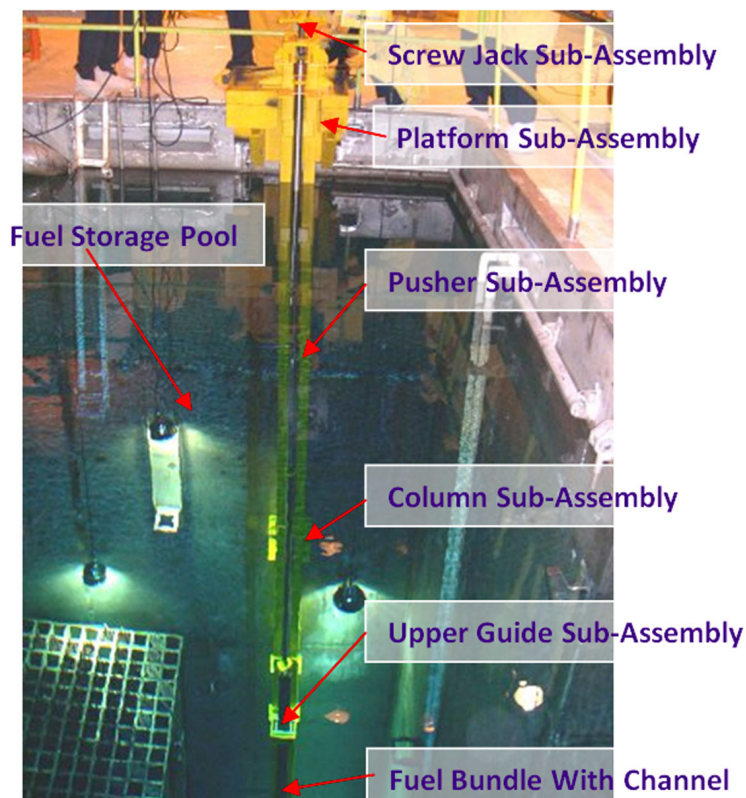
Very high rotational accuracy of the tunable mirror mount is achieved by differential drive mechanism and the eccentric cam follower system which gives resolution of 0.04 arc-sec. The rotational accuracy of 0.04 arc-secs was successfully achieved and validated in tunable SLM dye lasers in grazing incidence grating (GIG) configuration. Mode hop free tuning over the wavelength range from 556.4-568.5 nm was achieved. Minimum frequency change designed for coarse and fine tuning was 39 GHz and 3 MHz, respectively, which was experimentally validated. The total range of movement is $\pm 13^\circ$. The associated optical mounts for grating, tunable mirror and end mirror were also developed to align them in four D.O.F. motion as per optical layout in a 0.1 arc-sec range.

De-canning tool for TAPS 1&2 fuel bundle

De-canning tool was designed and developed for separation of old stuck zircalloy channels from the new

fuel bundle. Channel got stuck at the mid way of the locating surface of the bottom tie plate of fuel bundle, thus cannot be used. Criticality in design is handling of irradiated channels and foolproof de-canning without damaging the channel and fuel bundle. Channel is a 4029 mm long square box section tube, which forms an outer cover of the fuel bundle assembly. Inner size of the channel is 110.5 mm square and has a wall thickness of 1.5mm. The methodology of decanning lies on the design that the channel is rested on a plate with 148.5 mm diameter hole through which fuel bundle can pass but the channel cannot. If the fuel bundle is pushed relative to this plate, over which channel rest, the fuel bundle will pass but the channel cannot and thus de-canned. TAPS 1&2 fuel storage pool was used.

The tool consists of a working platform which is the main load bearing sub-assembly and is held firmly against the curb of the fuel storage pool. Using



De-canning Operation under Progress at TAPS

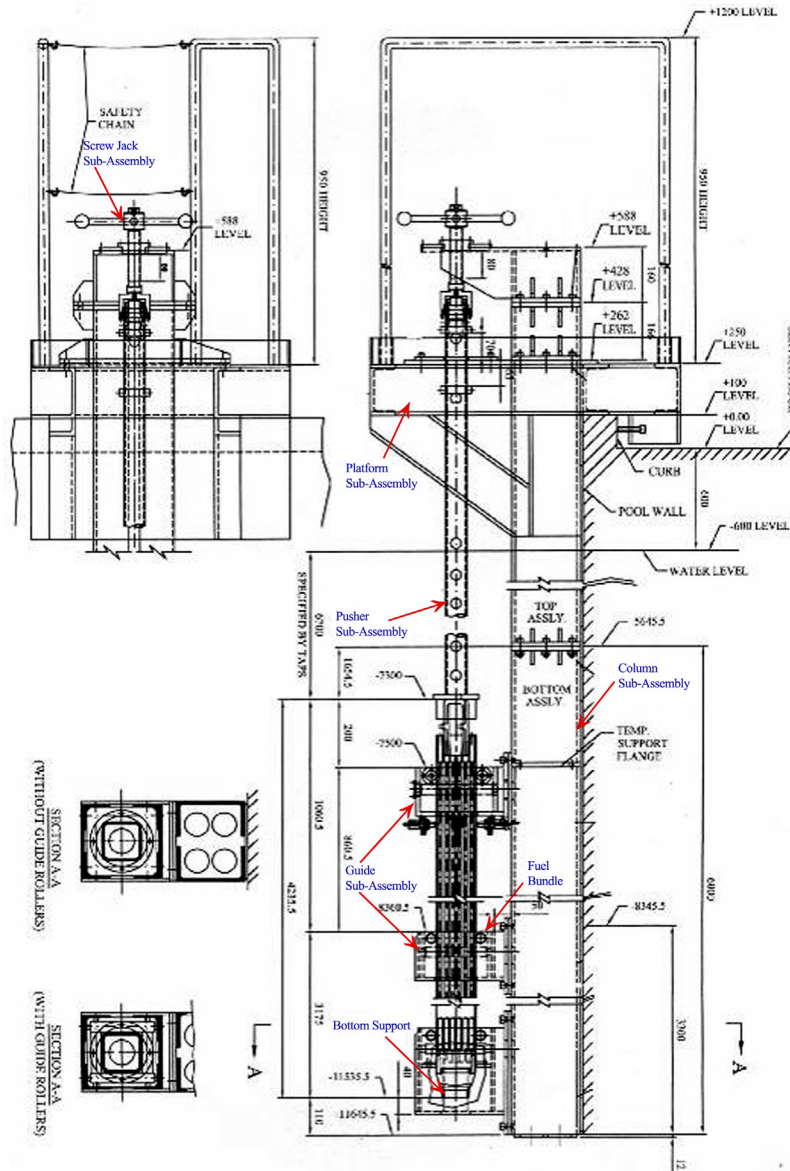
BARC NEWSLETTER

Founder's Day

this platform intermediate support columns were assembled to make its length of 10 meters.

Upper roller guide assembly and lower roller guide assembly on the columns guides the fuel bundle assembly in position and made it rest over plate

having 148.5 mm diameter hole. By means of pusher and screw jack fuel bundle is pushed to remove the channel from the fuel bundle. Using this "De-canning Tool" four nos. of irradiated stuck channels were successfully released from 4 nos. of fresh fuel bundles of TAPS 1&2 in TAPS fuel pool.



General Assembly of De-canning Tool

DESIGN IMPROVEMENTS IN SPENT FUEL CHOPPER AT PREFRE-2, TARAPUR

Shri A.K. Jha, Shri F.T. Qureshi & Shri K. Agarwal
Nuclear Recycle Board

Shri A.K. Jha is the recipient of the DAE Scientific & Technical Excellence Award for the year 2012

Abstract

Spent Fuel Chopper (SFC) is the most vital equipment for a reprocessing plant as it provides feed to the plant. The innovative concept of chopping by 'Gang Chopping Method' rather than well established 'Progressive Chopping Method' was adopted for the first time for high plant throughput. The teething problems surfaced during initial trials & first year of operation were solved by providing improved design of failed components such as Component Transfer Assembly (CTA), Shear Cover & Remote Handling Tools. This paper describes in brief about the design improvements of these components.

Background

Spent Fuel Chopping is the pivotal activity for reprocessing of spent nuclear fuel as it provides feed to the plant. The chopping of spent fuel is done by a shearing machine called "Spent Fuel Chopper". The shearing machines installed at PREFRE-1, Tarapur & KARP, Kalpakkam are based on progressive cutting, where fuel bundle is cut in steps. This process is time consuming & hence a new chopping system based on 'Gang Chopping Concept' was developed & installed at PREFRE-2, Tarapur where one full fuel bundle is chopped in one stroke, thereby reduces time of chopping & increases the plant throughput. During the course of its initial operation, this newly developed chopping system posed many challenging areas of its improvement coupled with achieving the target of meeting name plate capacity of the plant from 2011-12 onwards.

Problem Identification

A focused detailed review on performance of the machine revealed that there were three major problems areas which need to be solved in a time bound & cost effective manner without affecting plant

operation to achieve improved performance, easy maintenance, reduced man-rem exposure and higher plant availability. These areas were

- Interruption to fuel pushing inside Component Transfer Assembly (CTA) tube
- Erratic movement of CTA tube during forward & return stroke
- Interruption to CTA tube movement
- Limited visibility of shear zone
- Difficulty in maneuvering during maintenance inside shear zone
- Multiple handling of SFC components inside dissolver cell

Design Improvements:

Each of above problem area was studied in detail and feasible solutions were found by improving the existing design of related SFC components. These design modifications were verified by way of mock up trials before implementing the same in hot cell environment. The major components /areas which needed design improvements were Component Transfer Assembly, Shear Housing Cover and Remote Handling Tools.

BARC NEWSLETTER

Founder's Day

(a) Component Transfer Assembly

The Component Transfer Assembly (CTA) has a pneumatically operated tube, which reciprocates between moving and fixed blades to receive one fuel bundle at a time from the fuel feed magazine. The CTA assembly is locked with the body of SFC during machine operation. The frequent problems of dismantled fuel bundle getting stuck up during pushing and jamming of CTA tube between the blades were affecting the plant productivity. Also bundle often failed to follow the CTA tube retraction path resulted in obstruction for successive bundle pushing in the shear zone, which affected the productivity. Apart from these, "a SFC deadlock situation" arose when CTA fails to retract after receiving the spent fuel bundle from the fuel feed magazine as:

- (i) CTA could not be dismantled as it was required to be rotated for unlocking,
- (ii) Shear module along with shear blades could not be disassembled as CTA tube loaded with fuel bundle was lying between the blades.
- (iii) Fuel bundle could not be retrieved from CTA tube.

On analysis, it was observed that original CTA tube (refer Fig. 1(a)) was circular in shape with a slot for placing bundle stopper. Internal diameter of CTA tube was 86 mm, just 4 mm more than the diameter of spent fuel bundle. CTA tube ID bottom level was same as that of Fuel Feed Magazine (FFM) level. Also there was close tolerance between front bush & CTA tube.

To overcome this problem, the design of CTA tube was modified (refer Fig. 1(b)). A semi-circular tube with increased & eccentric ID was introduced in place of original CTA tube. The modified CTA design addressed the problem of jamming by providing moderate fits in the components subjected to relative motions without affecting the functional requirement. The level of tube ID was elevated by 1 mm w.r.to FFC ID level to ensure positive pushing. In order to fit this assembly within close tolerances inside radioactive cell, a full scale mock set up was made & several iterations were done to suit the cell environment. This modification on CTA has helped in reducing down-time of spent fuel chopper drastically. Also, this modification has helped to overcome "SFC deadlock situation" where no design

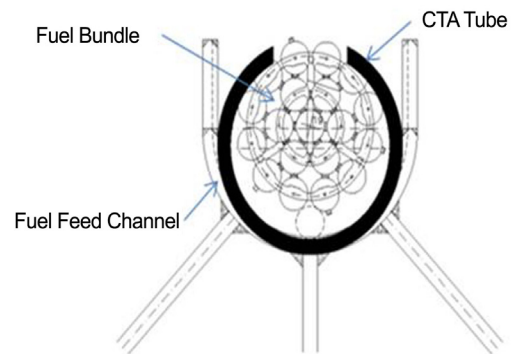


Fig. 1a: Old Component Transfer Assembly

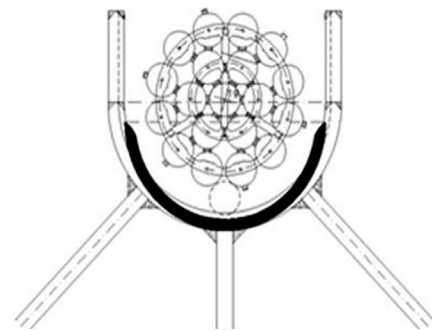


Fig. 1b: Modified Component Transfer Assembly

provision exists on 'failing CTA to retract after receiving the spent fuel bundle from the fuel feed magazine'. With this introduction of new CTA tube, the feasibility of chopping of slightly flared irradiated fuel bundles with one or two pins dismantled is possible.

(b) Shear Housing Cover

The shearing of spent fuel bundles is carried out in a contained environment to eliminate dose & contamination rise inside dissolver cell. The cutting operation is monitored through CCTV camera installed inside dissolver cell. The original shear cover was having limited visibility & was made an integral part of the housing with a hinged connection (refer Fig. 2(a)). The shear zone was not fully available for viewing and maintenance even after opening of the shear cover. Frequent disassembly of shear cover for dislodging trapped cut pieces between blades and for any maintenance inside shear zone was limiting the machine availability for continuous plant operations.

A modified shear cover (refer Fig. 2(b)) with improved visibility, to aid in maintenance and improved remote handling features was designed, demonstrated &

BARC NEWSLETTER

Founder's Day

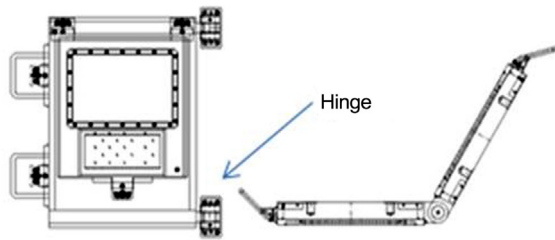


Fig. 2a: Old Shear Cover

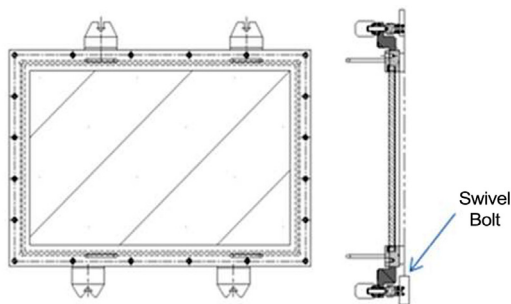


Fig. 2b: Modified Shear Cover

installed with the machine. The new design has polycarbonate sheet over its entire area which provides improved visibility of complete shear zone. The cover is attached to the shear housing by swivel bolts at four locations and can be disassembled completely from the machine by loosening these swivel bolts & thereby provides entire shear zone for carrying out any maintenance/maneuvering.

(c) Remote Handling Tools:

The remote handling tools were modified to facilitate remote handling of various components of SFC such as CTA, shear cover, shear module, pneumatic cylinders, main & side doors, chain magazine housing, wedges etc. and to sustain plant operations. Initially multiple remote handling operations inside dissolver cell were needed during maintenance of any of these SFC components, which was time consuming & limiting the machine availability to provide continuous feed to the plant. In order to increase machine availability, design of these remote handling tools were modified & made an integral part of the machine components to avoid multiple handling. Modified designs were verified by way of mock up trials prior to implementing in actual plant. These modifications are highly useful, operator friendly and have reduced man-Rem exposure

drastically. The modifications carried out on chain magazine housing & CTA have eliminated dependency on master slave manipulators for its remote disassembly/assembly with the machine (refer Fig. 3(a) & (b)).

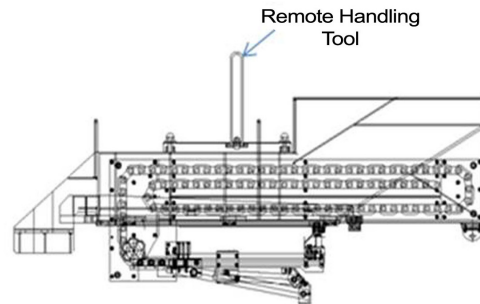


Fig. 3a: Chain Magazine Housing with Remote Handling Tool

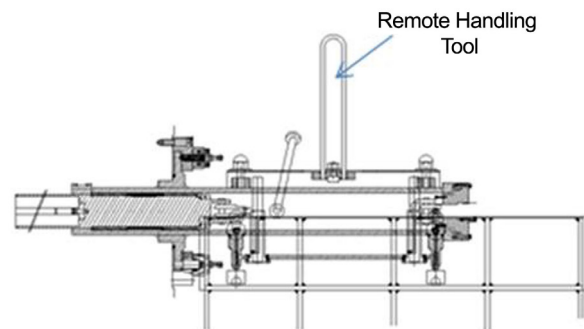


Fig. 3b: CTA with Remote Handling Tool

Conclusions

Design improvements in SFC have increased throughput of the plant by way of increased availability of the machine. In the last two years, the performance of the plant has surpassed the targets due to improved performance of the SFC.

Acknowledgement

The authors gratefully acknowledge the contribution of Shri S. Basu, Chief Executive, NRB, Shri S. Pradhan, Chief Superintendent, TNRP, Tarapur, Shri K. Dubey, Plant Superintendent, TRP, Tarapur & Shri Abhishant, SO/F, NRPSED, NRB for detailing & successful implementation of design modifications.

Reference

1. Internal Report No: BARC/RSD/SKG/2014/01

DEVELOPMENT OF ASSISTING TOOLS (SOFTWARE) FOR PREDICTION AND ANALYSIS OF IMPACT OF RADIATION EMERGENCY

Rajvir Singh and Pradeepkumar K.S.
Radiation Safety Systems Division

Shri Rajvir Singh is the recipient of the DAE Scientific &
Technical Excellence Award for the year 2012

Abstract

Though the probability of occurrence of a Radiation Emergency is extremely small at a nuclear facility or radiation facility, it can lead to release of radioactivity into public domain warranting the intervention by the authorities. It is essential to assess the radiological impact following such emergencies for planning the appropriate emergency response to mitigate the consequences. In case of large area contamination following any severe nuclear accident, fast and accurate assessment of radiological impact is essential to enable quick decision making on the implementation of the optimum countermeasures. Surveying the affected area and generating contour maps showing spatial distribution of the contamination can facilitate immediate emergency response as well as long-term management of affected area. An "Online Early Warning System for BARC, Trombay" and "Radiological Impact Prediction and Assessment Software (RIPAS)" on GIS support has been developed for impact assessment following nuclear and radiological emergencies.

Introduction

A large number of nuclear power and research reactors are in operation worldwide and there is a continuous increase in the nuclear and radiation related applications in the public domain. Nuclear power plants (NPPs) are designed, constructed, commissioned and operated in conformity with relevant nuclear safety requirements. These requirements ensure an adequate margin of safety so that NPPs can be operated without undue radiological risks to the plant personnel and members of the public. Though all the sources transported and used are under regulatory control, the possibility of the accident cannot be totally ruled out. The degree of hazard may vary by many orders of magnitude depending upon the scenario and can lead to stochastic effects and severe deterministic effects. It

is necessary to develop emergency response plans¹, as a measure of abundant caution to deal with effective management of any eventuality with a potential to result in undue radiological risk to the public.

In case of a Radiation Emergency, Authorities have to implement the protective measures timely to mitigate the radiological consequences of the radiation on Environment, Health and Property. Considering the requirement of Radiological Impact Assessment² for radiation emergency preparedness, 'Online Early Warning System' with a display in Emergency Preparedness and Response Center (EPARC), BARC and 'Radiological Impact Prediction and Assessment Software (RIPAS)' have been developed to assist the decision makers in making decisions about protective measures during emergency.

BARC NEWSLETTER

Founder's Day

Contouring Algorithm for Analysis of Irregularly Spaced (scattered) Data

The Radiometric data collected by various mobile monitoring methodologies³ are voluminous and are irregularly spaced over the monitored area. A two-stage irregularly spaced data analysis technique^{4,5} was developed to generate the continuous radiological and contour maps to aid in the decision making process.

In the case of radioactivity, the values are not exact due to its statistical nature and will always lie within few standard deviations of mean value. The mesh point value ($Z_{m,p}$) at each mesh point (node) of an imposed $m \times n$ regular grid (Fig. 1) estimated from N distinct irregularly spaced sampled data points $P_i=(x_i,y_i)$ with sampling values z_i by Distance Weighted Moving Average Technique (DWMAT) also always lie within the maximum and minimum value of given data points favouring its choice for radiometric data analysis.

In the first step, $Z_{m,p}$ at each mesh point (node) is estimated using DWMAT. A weighting factor (w) of general nature, incorporating the feature of data distribution within radius of influence (R) has been considered and is given in Equation 1.

$$w(d_i^2) = \frac{\exp\left(-\frac{d_i^2}{d_{avg}^2}\right)}{d_i^2} \quad (1)$$

where $w(d_i^2)$ is the weighting factor and d_{avg} is the average distance of the all selected data points around the mesh point within R and d_i is the distance of selected data point from the mesh point.

A maximum of 12 sectors of 30° each around each mesh point have been considered to minimize the anisotropy. The nearest data point within the R of each sector is selected for estimation of mesh point value as given in Equation 2 below.

$$Z_{m,p} = \frac{\sum_{i=1}^S w(d_i^2).z_i}{\sum_{i=1}^S w(d_i^2)} \quad (2)$$

where S is the number of sectors.

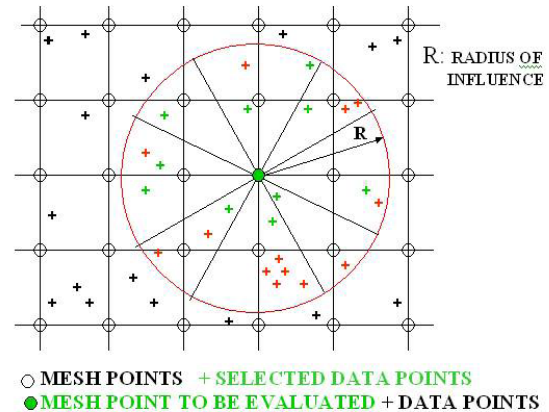


Fig. 1: Evaluation Methodology

Thus the estimated mesh point (node) value will always lie within the maximum and minimum value of the given data point within R of each sector around mesh point. The maximum numbers of data points selected to estimate the mesh point value will be equal or less than S which need a finer mesh size ($m \times n$) with more S for large and dense (clustered) data sets to increase the chances of consideration of every data point. The choice for minimum R is such that at least few data points fall within it and having no restriction on upper size of R . The selected R decides the distance up to which a data point has an influence on the mesh point (node). The size of mesh ($m \times n$), number of sectors (S) and the radius of influence (R) are dependent on the data pattern and its range.

Utilizing these mesh point values estimated by DWMAT, Bicubic Splines, a two dimensional interpolation of Cubic Splines, are evaluated for all the cells, one for each cell, of the imposed grid in the second step automatically. The Bicubic Spline of respective cell of the grid is a continuous surface having 16 terms of x and y coordinates as variables

BARC NEWSLETTER

Founder's Day

and is expressed as $a_1x^3y^3 + a_2x^3y^2 + a_3x^3y + a_4x^3 + a_5x^2y^3 + a_6x^2y^2 + a_7x^2y + a_8x^2 + a_9xy^3 + a_{10}xy^2 + a_{11}xy + a_{12}x + a_{13}y^3 + a_{14}y^2 + a_{15}y + a_{16}$ where $a_1 \dots a_{16}$ are constants to be evaluated using the mesh point values obtained by DWMAT. The Bicubic Spline of respective cell of the grid is used for contouring and mapping purposes. Although the mesh point values will always lie within the maximum and minimum of the data point, the generated surface using the Bicubic Spline may overshoot from maximum or undershoot from minimum depending on the gradient and distribution of the data. This radiological map is continuous in value, slope and curvature over whole surveyed/monitored area. With control over the w , mesh size ($m \times n$), S and R , better results can be achieved for a given data set range and pattern at the cost of computation.

Online Early Warning System (OEWS)

OEWS has been developed and installed in EPARC for online display of radiological status of BARC, Trombay Site. The input for software is the readings of installed radiation monitors and wind speed and wind direction. The software processes online the readings of installed radiation monitors and displays as the colored maps and contours along with wind speed and wind direction (Fig.2).

Radiological Impact Prediction and Analysis Software (RIPAS)

The RIPAS has been developed to predict (Fig. 3a, Fig. 3b) the radiological impact and analyze the

surveyed data (Fig. 3c, Fig. 3d) to assist the decision makers in implementing the protective measures timely and accurately. The distance weighted moving average technique and bicubic spline interpolation technique have been implemented in the software. As per the philosophy of protective measures implementation, predictive model can be used to prevent severe deterministic effects and field measurements should be used to minimize the stochastic effects. The software has the provision for prediction as per the Gaussian Plume Dispersion Model and analysis of the irregularly spaced surveyed data. It has online and offline feature for meteorological data (wind speed, wind direction, stability class (A, B, C, D, E, F), met station elevation and plain and rough terrain. The release, release height, release point and area of interest for Radiological Impact Prediction are the required input parameters. The entire area covered by the aerial or ground survey is mapped with varying color gradients corresponding to the level of contamination or dose rate in the area. The mapping feature facilitates demarcation of contaminated land and the 'hot spots', strengthening the decision support for effective implementation of countermeasures. The user can use the default parameters or can manually provide the input of radius of influence, weighting factor and grid size. The main features of the RIPAS are:

- (i) It predict the radiological impact for given met data and source term alongwith the affected area,
- (ii) It analyze the surveyed data,
- (iii) Its output is colored map with area information even on GIS

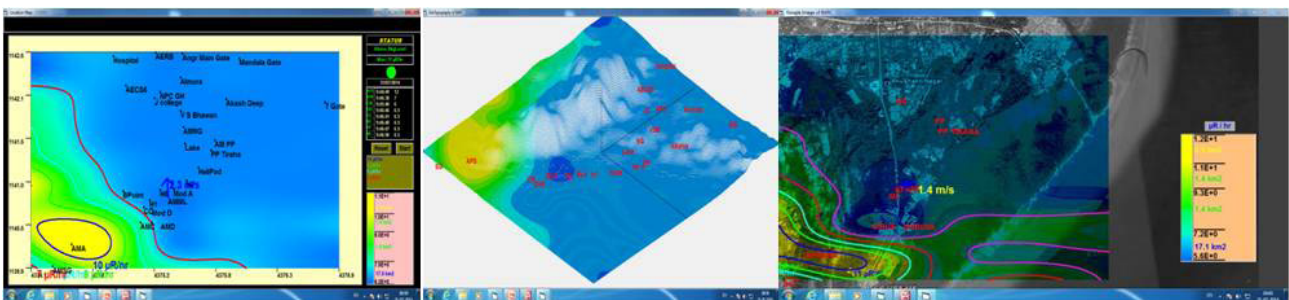


Fig.2: Online Display of OEWS in EPARC

BARC NEWSLETTER

Founder's Day

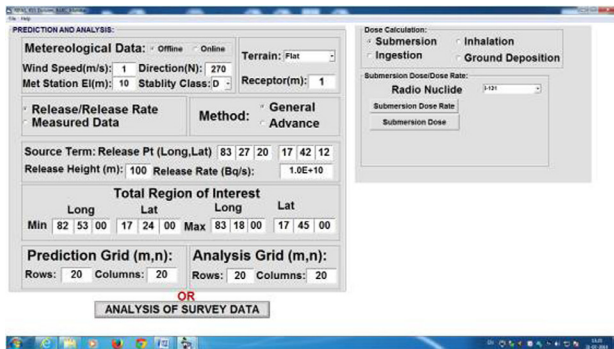


Fig.3a: Input for RIPAS

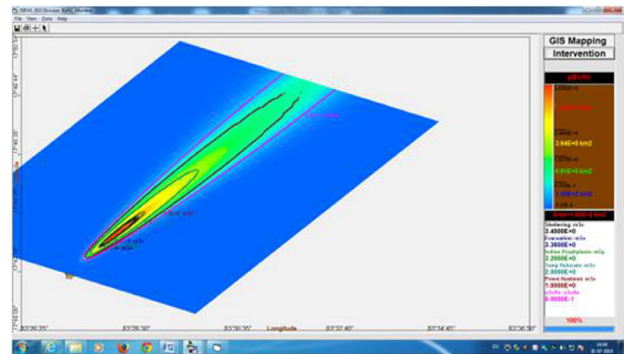


Fig.3b: Prediction of Radiological Impact

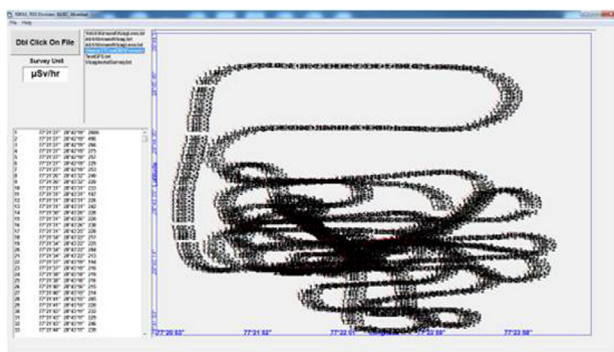


Fig.3c: AGSS surveyed data (cps) of Hindon (survey conducted at varying altitude)

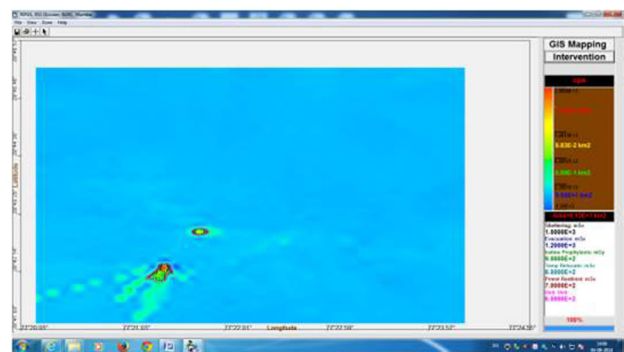


Fig.3d: Mapping and Countering generated from Survey Data

- (iv) It draws contours with or without colored map
- (v) Mouse Event for Source Term Position.

Conclusion

Radiological emergency in public domain cannot be totally ruled out due to potential orphan sources, radiological accidents or malicious acts using radioactive materials. The developed software will help the decision makers to implement the protective measures timely following nuclear or radiological emergency.

Acknowledgements

We are grateful to Dr. D.N. Sharma, Director, Health, Safety and Environment Group, BARC for his constant encouragement and guidance. The support rendered by our colleagues from Emergency Response Systems & Methods Section, RSSD, BARC and various government agencies is gratefully acknowledged.

Reference

1. Method for Developing Arrangements for Response to a Nuclear or Radiological Emergency, Updating IAEA-TECDOC-953, PUBLICATION DATE: OCTOBER 2003.
2. Dubois, G., Pebesma, E., and Bossew, P., "Automatic mapping in emergency: a geostatistical perspective", International Journal of Emergency Management, 4(3):455-467 (2007).
3. International Atomic Energy Agency (IAEA), July 2003, Guidelines for radioelement mapping using gamma ray spectrometry data, IAEA-TECDOC-1363
4. Briggs, I. C., "Machine contouring using minimum curvature", Geophysics, 39, 39-48 (1974).
5. Rajvir Singh, Probal Chaudhury, K. S. Pradeepkumar and D.N. Sharma, Radiological Mapping for Impact Prediction and Response during Emergency, 12th International Congress of the International Radiation Protection Association, Buenos Aires, Argentina, (2008).

DEVELOPMENT OF FOUR PIECE SERVO MANIPULATOR

R.V.Sakrikar, U. Sarkar, D. D.Ray, B. Sony, D. C. Biswas and K. Jayarajan
Division of Remote Handling and Robotics

Shri R.V. Sakrikar is the recipient of the DAE Scientific & Technical Excellence Award for the year 2012

Abstract

Traditionally, the Master Slave Manipulator (MSM), installed through the standard wall-sleeve, is used as dexterous, remote handling tool inside the hotcells for carrying out various operations. The next generations of manipulators are the electrically powered servo manipulators, which are installed fully inside the hotcells, usually on a movable platform or gantry, thus providing larger flexibility and reach. However large numbers of hotcells in the nuclear industry are designed for the use of wall mounted manipulators. The need for extending the superior features of a servo-manipulator to the wall mounted MSMs led to the conceptualization and development of the Four Piece Servo Manipulator (FPSM). The FPSM, which can be installed in the hotcell through a standard wall sleeve, is a bilateral master-slave servo-manipulator with force feedback. The FPSM control system is based on a tightly coupled distributed digital micro-processing technique. The paper describes the overall design and implementation of FPSM.

Introduction

Remote handling plays a vital role in all nuclear installations. In such facilities, the operators can handle the material only behind thick shields, using remote handling tools. The remote handling tools are expected to carry out varied tasks inside the Hot-cells. Master Slave Manipulators (MSMs) are the most dexterous and widely used general-purpose remote handling tools in the nuclear industry. A typical MSM has a Slave arm located in the active area of the hotcell and a Master arm, which controls the Slave arm, in the operating area of the hotcell. The motions imparted by the operator to the master arm are replicated by the slave arm to carry out the desired tasks. In MSM, the two arms are connected mechanically, across a wall-mounted through-tube [1].

The designs of the various MSM models, varying in their reach and payloads, have been standardized and

deployed in the hotcells, in the department, in large numbers.

The generation of MSM, was followed by Servo Manipulators [2], where the Master and the Slave arms are linked together electrically by an appropriate control system. Mounting of the slave arm on a movable transporter, like a gantry or mobile platform, inside the hotcell, results in higher flexibility and reach. In a mechanical manipulator, the efforts for performing a task have to be provided by the human operator, whereas in servo manipulators they are provided by an external power source, making them more operator-friendly.

The endeavor to provide the obvious advantages of the servo manipulator technology to the conventional hotcells users led to the conceptualization, design and development of the unique design of the Four-Piece Servo Manipulator (FPSM), which can be installed

BARC NEWSLETTER

Founder's Day

through the standard wall sleeves provided in the hotcells.

The Design

Mechanical Design

The FPSM has four distinct parts or subassemblies: the Master arm, the Slave arm, the Through-tube and the Motor-drive-unit. Fig. 1 shows the schematics of the FPSM along with its four distinct subassemblies. The FPSM is an adaptation of the existing Three Piece Manipulator (TPM). The Slave Arm and the Through Tube of FPSM are identical to those of the TPM. The Master Arm of TPM is replaced by the Motor Drive Unit, which is interfaced to the Through Tube. This design improves the availability of the system as the Motor Drive Unit can be replaced by the standard Master Arm in case of faults in the Motor Drive Unit or the control system.

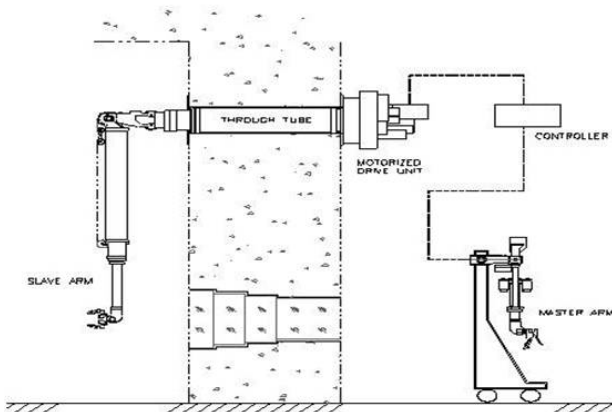


Fig. 1: FPSM Schematic

The Slave arm

The FPSM slave arm is designed to handle a payload of 20 kg in any position. The slave arm has six degrees of freedom and gripper. It has five articulated joints (X and Y canting, Azimuth rotation and Wrist Rotation and Elevation), a double co-axial telescopic joint and gripper. All the joints are powered by the motors contained in the motor drive unit. Each joint is provided

with the position sensors necessary for their operation. The various slave arm motions are illustrated in Fig. 2.

Fig. 3 shows the actual slave arm of the FPSM and the Table 1 shows the range of motion of the FPSM Slave Arm.

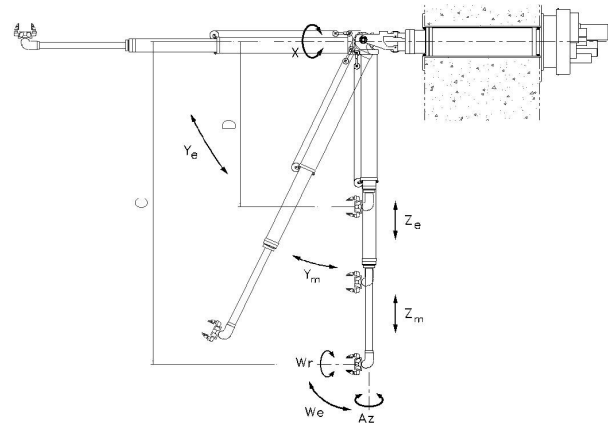


Fig. 2: FPSM Slave Arm Movements



Fig. 3: FPSM Slave Arm

Table 1: Range of motions of FPSM Slave Arm

Description	Value
X Motion (X)	-60° to +60°
Y Motion (Ym), (Ye)	-20° to +25°, -20° to +90°
Z Manual Motion (Zm)	970 mm
Z Electrical Motion (Ze)	900mm
Azimuth Rotation (Az)	-170° to +170°
Wrist Rotation(Wr)	-170° to +170°
Wrist Elevation(We)	-24° to +116°
Gripper opening	80 mm

BARC NEWSLETTER

Founder's Day

The Master Arm

The Master arm (Fig. 4) is iso-kinematic, scaled down version of the Slave arm, with handgrip and HMI keypads. It can be mounted on a trolley to offer flexibility in terms of its stationing in the operating area of the hotcell cold. The smaller size of the master arm facilitates its positioning close to the hotcell window resulting in improved operator visibility inside the hotcell. The master arm is provided with position sensors on all joints and force feedback actuators on the major axes (X, Y and Z) and handgrip. The sensors on the master arm generate the appropriate position command for the slave arm joints, resulting in Master Slave Follower operation. The master arm is fitted with two keypads providing facilities for operational parameter setting and operation of indexing motions and joint locks.

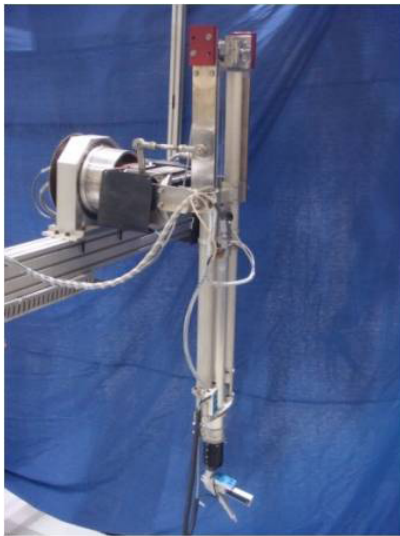


Fig. 4: FPSM Master Arm

The Through tube

The Through-Tube of FPSM contains a set of parallel shafts for transmitting motion from the motor drive unit to the slave arm. The through-tube shafts have slotted couplings at its either ends for engaging them with shafts in the slave arm and the motor drive unit. The coupling arrangement is such that the assembly and disassembly of Slave arm and Through-tube

can be carried out remotely. Sealing and shielding can be provided in the through-tube, as per the site requirements.

The Motor Drive Unit

The motor drive unit contains eight sets of servomotors, gearboxes and position sensors. Motor drive unit is designed in such a way that it is accommodated within the standard clearances available around the manipulator sleeve on the Hot-cell wall. The balancing counter weights for major axes motions are provided on the motor unit. The motor unit is coupled with the Through-tube with an adapter. Apart from its use in traditional hotcell architecture, the slave arm with the motor unit can also be mounted on a transporter, installed inside a hotcell, thereby exploiting all the flexibilities of a typical servo manipulator. Fig. 5 shows the motor drive unit mounted on a Through-tube assembly.



Fig. 5: Motor Drive unit mounted on Through-tube

Control System Design

The FPSM has a multi axis, bilateral, tightly coupled, digital distributed control system [3], [4]. It provides a master follower configuration with the position control loop from master to slave. Force feedback loops provide force reflection to the major axes (X, Y, Z) and gripper of the master arm.

BARC NEWSLETTER

Founder's Day

The main components of the FPSM control system are the actuators, motor drives, joint controllers, HMIs and the master control computer. The control schematic is as shown in Fig. 6.

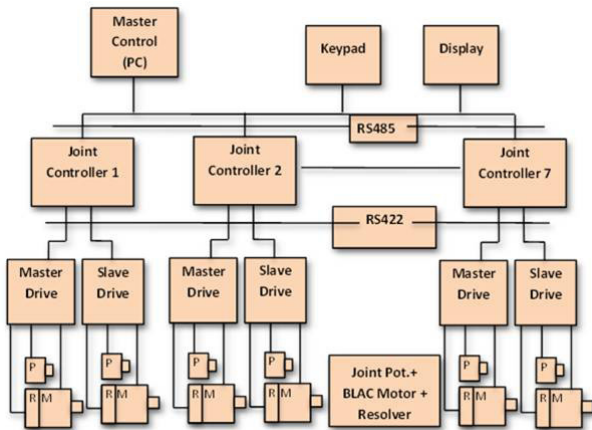


Fig. 6: FPSM Control Schematic

Actuators and Sensors

The FPSM uses wash-down duty Brushless AC servomotors, with inbuilt resolver and failsafe brake, as actuators on both the Master and the Slave arm. The motors operational characteristics suitable for accurate position control and also have linear torque-current relationship, essential for generating accurate force feedback to the operator. The resolver is used to sense the rotor position for the electronic commutation and providing positional feedback for the control loop.

A multi-turn potentiometer, mounted on each joint, provides absolute joint position for initializing the Resolver readings at power up. All the joints are provided with failsafe brakes for locking of the joints on power failure and system faults. The operator can also lock the joints in desired positions, whenever required. The load gripper can be locked individually for operator convenience during load handling.

Control Hardware

The manipulator joint controls are based on indigenously developed BLAC servomotor drives. The

hardware for all master and the slave drives is identical, with different master and slave firmware. The joint configuration of the drive is carried out using the onboard DIP switch settings. The control architecture is designed for high speed data transfer between the master and the slave drives for satisfactory operation of the manipulator. The manipulator can operate up to a distance of 100 m between the control panel and the slave arm.

The Servo-drive (Fig. 7) is fabricated in two parts. The main base board contains the power electronics and servo controller components with necessary isolations. The piggyback board, which interfaces with the base board, contains the master micro-controller executing the control loop, Resolver to Digital (R/D) conversion circuit, brake control and the position sensing circuitry.



Fig. 7: The BLAC Servo Motor Drive

Operator Interface

The master control program, deployed on an Industrial Computer, provides facilities for initialization of the manipulator parameters, display of joint status, alarm logging, and fault conditions. The GUI (Fig. 8) of the Master controller provides access control for the manipulator operation and continuously displays its operational status.

The two keypad based HMIs, on the master arm (Fig. 9), provide facilities for the operation of Joint brakes, slave gripper locking, force reflection ratio (FRR) selection, slave arm torque limit selection and Indexing motion.

BARC NEWSLETTER

Founder's Day

The status of the parameters selected is indicated by the associated LEDs on the HMI.

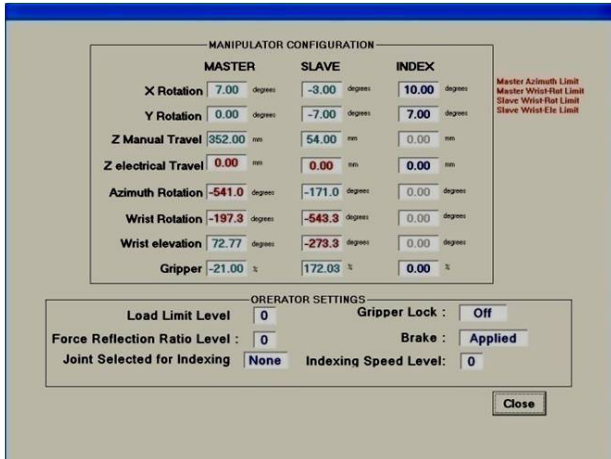


Fig. 8: FPSM Supervisory controller GUI



Fig. 9: HMI Interfaces on Master Arm

Operation Modes

The following operator selectable modes are provided through the control software:

a) Master Slave Follower mode

In this mode the slave arm, which is in the remote area, follows the movement of the master arm and the handgrip to execute the necessary tasks. The primary role of the control system, in this mode, is the continuous Master to Slave position tracking for all the joints.

b) Force Feedback mode

In this mode, the slave motor current is used for the calculation of joint load. This is applied on the corresponding master joint, which is operated in the torque control mode after necessary scaling and filtering. The direction of the master motor torque is always opposite to the torque generated by the corresponding slave motor. The resulting joint-torques contributes to the reproduction of the Slave environment force at the Master handgrip.

The Master-slave follower mode and the Force Feedback Mode can work together to operate the manipulator in bilateral mode.

The control system has additional provision for setting up of soft limits, beyond which the slave arm motions are not allowed and a stall torque is reflected on the master arm.

c) Indexed Motion mode

In this mode, the operator can independently move the selected major slave joint, without moving the corresponding master joint, using the keypad interface. This can be used to move the manipulator, along with the load, to the desired location, thereby reducing the operator efforts. This mode can also used to pre-position the Slave arm at an optimal position, as per the operational requirements, before commencing with the Master Slave mode thereby extending the reach of the operator.

Performance Evaluation

Master to Slave Positional tracking is a basic criterion for performance evaluation of a master slave manipulator. The main criteria for the evaluation are the faithfulness of the system and operational effort required for load handling. With the servo manipulator the operator effort can be easily controlled by the FRR settings. The evaluation of the Master to Slave tracking

BARC NEWSLETTER

Founder's Day

ability hence becomes the most vital parameter. Since the configurations of both the arms are same, only the rotating angle of corresponding axes needs to be compared for testing the tracking performance. Fig. 10 shows a single axis tracking performance as a representative result.

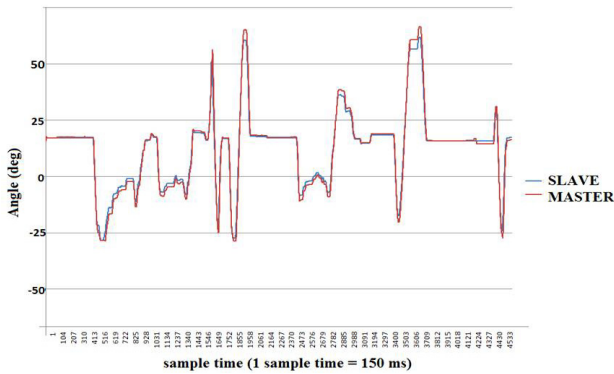


Fig. 10: Master to Slave Position Tracking

It is observed that the Positional tracking is in general satisfactory. Although, there are errors in tracking, in the range of 2-3 degrees at the motor shaft end, the actual tracking error at the end effector will be significantly less due to the mechanical reductions between the motor and the joint output. Also, due to presence of man in the loop, these errors get corrected easily and hence are not significant [5].

Due to similar kinematic configuration of Master and Slave, testing of a single axis torque tracking is sufficient to test force reflection. Fig. 11 shows the result of torque tracking with a FRR of 0.25. Smoothing

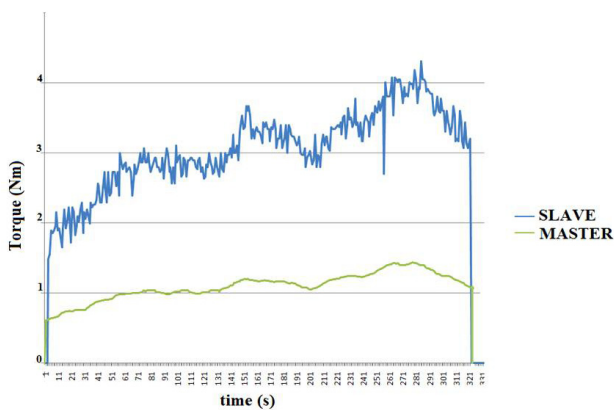


Fig. 11: Slave Torque and Reflected Master Torque

is carried out on the Slave torque feedback to filter out the noise, to avoid spurious reflection of slave torques on the master arm.

Conclusion

FPSM is a unique design, which can be installed through the standard wall-sleeves of existing hotcell, thereby providing a viable alternative to the conventional MSMs. The FPSM provides advantages such as reduced operator efforts and increased availability along with facilities for sealing and shielding as per site requirements. The manipulator is modular and hence requires less space for installation and is easier to maintain.

References

1. K. Jayarajan, and Manjit Singh, "Master-Slave Manipulators: Technology and Recent Developments", *BARC News Letter*, Issue No. 269, June 2006, pp. 2-12.
2. D.P. Kuban and H.L. Martin, "An Advanced Remotely Maintainable Force Reflecting Servo Manipulator Concept," Proc. 1984 National Topical Meeting on Robotics and Remote Handling in Hostile Environments, pp. 407-415.
3. Jouve & D. Bui, "High Performance Servo Drive Design for Distributed Motion Control," Proc. June19-21, 2001 PCIM' conference, Nurnberg, pp.1-6.
4. H.L. Martin, W.R. Hamel, S.M. Killough and R.F. Spille, "Control and Electronic Subsystems for the Advanced Servo Manipulator," Proc. 1984 National Topical Meeting on Robotics and Remote Handling in Hostile Environments, pp. 417-424
5. R. Kress, J. Jansen, M. Noakes and J. Herndon, "The Evolution of teleoperated manipulators at ORNL," Proc. of ANS 79th Topical Meeting on Robotics and Remote Systems, pp 623-631

EXTRACTING EQUILIBRIUM UNBINDING FREE ENERGY OF PROTEIN-DRUG COMPLEXES FROM NONEQUILIBRIUM SIMULATIONS

Tusar Bandyopadhyay

Theoretical Chemistry Section, Chemistry Group

Dr. Tusar Bandyopadhyay is the recipient of the DAE Scientific & Technical Excellence Award for the year 2012

Abstract

The use of protein-ligand binding free-energy landscapes rationalizes a wide range of aspects of protein behaviour in response to the ligand approach by providing a clear illustration of the different states accessible to these molecules, as well as of their populations and interaction pathways. To achieve this goal by computational methods is, however, very challenging as it requires an extensive sampling of their conformational spaces. Additionally, at an equilibrium condition, (un)binding events of ligands happen on the milliseconds or longer time scale, and is therefore not amenable to study through conventional MD (CMD) simulation techniques. Various nonequilibrium simulation protocols have been articulated to overcome this challenge with their associated utility and pitfalls. Here we will focus on two such protocols, namely, the steered molecular dynamics (SMD) and the popular metadynamics (MtD) method in relation to unbinding free energy of acetylcholinesterase (AChE) bound oxime drugs along the gorge pathway. Unfortunately however, both these methods suffer from inherent nonequilibrium features. To circumvent this we arrive at a simulation recipe, combining the strengths of equilibrium and nonequilibrium simulation techniques, that can readily decipher routes, milestones and subtlety towards the (un)binding pathway of ligand at finite temperature.

Introduction

The active site (located deep inside a 20 Å gorge) of the nerve enzyme, acetylcholinesterase that plays a pivotal role in terminating nerve impulses is also a vulnerable target of the lethal organophosphorus (OP) compounds (read chemical warfare and nerve gases). Potent reactivators of the intoxicated enzyme are nucleophiles, such as bispyridinium oximes. Despite intensive effort on designing newer oxime reactivators that will act as a wide spectrum drug against a variety of OP poisoning agents, there is little success. In fact, oxime drug administration strategy differs from one country to the other. There is no comprehensive study either on the oxime binding free energetics along the gorge pathway, enumerating metastable

intermediates, if any. The rational modulation of kinetics during lead optimization thus remains unexplored. Pharmacy at cyberspace through molecular dynamics (MD) simulation of protein-drug complexes can become quite handy to achieve this goal. However, given the "mammoth" size of the protein, extracting equilibrium energetics from standard MD techniques is beyond the scope of the most modern computers. Here we summarize some of our laboratory endeavour in search of a viable alternative towards understating the full, complete and optimal (un)binding pathways of oximes using a variety of nonequilibrium MD techniques. The reported techniques have prospective implication as they can be easily incorporated in a standard pharmaceutical work-flow for newer drug design.

BARC NEWSLETTER

Founder's Day

Steered MD

In order to perform SMD simulations, a harmonic spring is attached to the centre of mass (COM) of the drug molecule and was pulled with a constant velocity. In SMD, one utilizes nonequilibrium work theorem such as the remarkable Jarzynski equality that defies the common perception held through the second law of thermodynamics and interconnects the measured work along the nonequilibrium trajectory with the free energy differences. However, the free energies thus obtained suffer from one serious issue: the convergence properties of exponential averages of the work, inherent in the Jarzynski formalism is extremely slow. The issue of convergence, at least in principle, can be imagined to be improved upon by including reverse (pushing) trajectories in the forward (pulling) path ensemble. Bidirectional SMD protocol relies directly on the Crooks fluctuation theorem,¹ which can be formally stated as: given two systems 'a' and 'b', the equilibrium free energy difference, ΔF between the two states can be extracted from nonequilibrium work measurement through,

$$\frac{P_F(+\beta W)}{P_R(-\beta W)} = \exp[\beta(W - \Delta F)] \quad (1)$$

Here W is the external work done on the system forcing it to undergo $a \rightarrow b$ transition. P_F and P_R are the probability distribution of releasing the work W into the system during the forward (F) $a \rightarrow b$ and reverse (R) $b \rightarrow a$ transitions, respectively in a finite time. Eq. (1) calculates only the free energy differences between the end states, "a" and "b", but not along the pathway, $a \rightarrow b$, that can be measured through the SMD control parameter, $\lambda (=vt)$. To this effect, Eq. (1) can be modified with the adoption of weighted histogram analysis method (WHAM) that connects different thermodynamic microstates in between and one can arrive at an estimator,²

$$\exp(-\beta\Delta F(\lambda)) = \left\langle \frac{n_F \exp(-\beta W_F(\lambda))}{n_F + n_R \exp(-\beta W_F(\lambda_b) + \beta\Delta F)} \right\rangle_F + \left\langle \frac{n_R \exp(\beta W_R(\lambda_a) - \beta W_R(\lambda))}{n_F + n_R \exp(\beta W_R(\lambda_a) + \beta\Delta F)} \right\rangle_R, \quad (2)$$

where $W_{F(R)}(\lambda)$ refers to work done to move the system from $\lambda_{a(b)}$ to λ . ΔF is the free energy difference between the end states, and also a function of λ , $\Delta F(\lambda)$ [also known as potential of mean force (PMF)] that has to be obtained by solving Bennett acceptance ratio relation iteratively and self-consistently. Fig. 1 demonstrates the construction of PMF as a function of control parameter, λ using the above recipe.

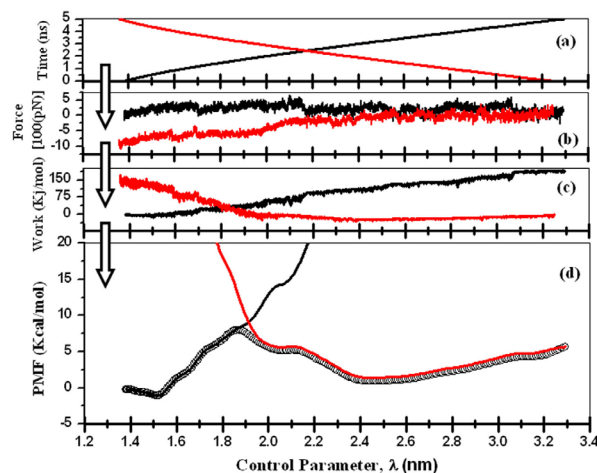


Fig. 1: In panels (a), (b), and (c) trajectories, $\lambda(t)$, force exerted on the system and work performed, respectively are presented. Data presented in black are for forward SMD and red are for reverse SMD simulations. The position of the control parameter along the pulling axis is measured relative to the COM of the enzyme. The PMF reconstructed from work profiles for repeated unbinding/binding steering of drug molecule is presented in panel (d) using Eq. (2) (symbol). Red (binding transitions) and black (unbinding transitions) solid lines in panel (d) represent PMF values that one would obtain for unidirectional pulling.

Note that the (un)binding free energy can be defined both along the path of the control spring variable, λ and as well as along the path of fluctuating molecular position, ξ . In this regard, for unidirectional biasing, viz. the Jarzynski equality and with the help of WHAM prescription can be recast into,³

$$\exp[-\beta G(\xi)] = \frac{\sum_i \langle \delta(\xi - \xi_i) \exp(-\beta W_i) \rangle / \langle \exp(-\beta W_i) \rangle}{\sum_i \exp[-\beta u(\xi, t)] / \langle \exp(-\beta W_i) \rangle}, \quad (3)$$

BARC NEWSLETTER

Founder's Day

where $G(\xi)$ is the free energy as a function of ξ and t is bin sizes over time. The resulting free energy estimator for bidirectional simulation is given by,²

$$\exp[-\beta G(\xi)] = \exp[\beta \Delta F(\lambda)] \times \frac{\sum_t \left[\left\langle \frac{n_F \delta(\xi - \xi_t) \exp\{-\beta W_t(\lambda)\}}{n_F + n_R \exp\{-\beta(W_t(\lambda) - \Delta F)\}} \right\rangle_F + \left\langle \frac{n_R \delta(\xi - \xi_t) \exp\{\beta[W_t(\lambda) - W(\lambda)]\}}{n_F + n_R \exp\{\beta(W_t(\lambda) + \Delta F)\}} \right\rangle_F \right]}{\sum_t \exp[-\beta\{u(\xi, t) - \Delta F(\lambda)\}]}, \quad (4)$$

where $\Delta F(\lambda)$ can be obtained from Eq. (2).

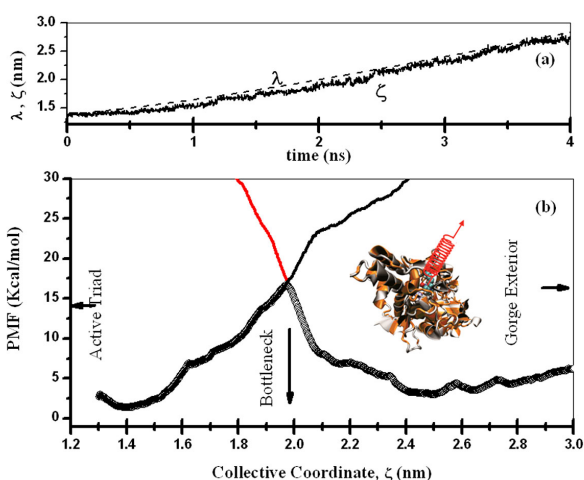


Fig. 2. (a) Time evolution of the instantaneous values of control parameter (λ) and the collective variable (ξ) differs in a typical oxime unbinding transition, and so also is the (b) reconstructed PMF as a function of ξ is different from that presented in Fig. 1. In panel (b); red and black lines are the results for unidirectional biasing. Inset in panel (b) depicts the idea behind SMD.

Fig. 2 represents results from bidirectional PMF estimators, Eq. 4, along the real molecular pathway showing peaks (barrier) and valleys (basins) for oxime (ortho-7) translocation from the exterior to the active triad through the bottleneck.⁴ Clearly the bidirectional SMD simulation is a powerful method (when compared with unidirectional estimator) to reconstruct the potential of mean force (PMF) along the translocation pathway such that the desired quantity represents an unperturbed system. This is because the rare trajectories that one misses to count for in the forward simulation can be frequently encountered during the reverse steps and vice versa. However, although the bidirectional estimator appears to be the most modern and promising, its usage is biased by the initial choice of pulling direction.

Metadynamics Simulation

To accelerate the (un)binding, in the MtD method one relies on the progressive build-up of a memory-based biasing potential energy term or "hills", V_{MtD} that penalizes the system revisiting the same region of the space and is aimed at reconstructing the multidimensional free energy landscape of a given process. Because of its inherent nonequilibrium characteristics, this method is devoid of true equilibrium thermodynamic information unless the "slow" build-up limit is adopted. MtD is however, an elegant method for conformational searching along a chosen set of collective variables (CV) (such as COM separation), $S(x)$, which itself is a function of atomic coordinates, x . The MtD approach thus consists of three steps: (i) choice of the most relevant CVs describing the dynamics of the system: (ii) MtD simulation using the physical potential energy, V_{phys} (force field) enhanced by a time dependent biasing term, which at time t reads as

$$V_{MtD}(S(x), t) = \sum_{t'=\tau_G, 2\tau_G, 3\tau_G, \dots, t} H \exp\left(-\frac{|S(x) - S(x(t'))|^2}{2w^2}\right), \quad (5)$$

where H and w are the height and width of the Gaussian bias that are added with a frequency, $1/\tau_G$: (iii) appropriate choice of MtD parameters H , w and τ_G . The MtD bias is directly related to the potential of mean force (PMF):

$$F_{MtD}(S(x), t) = -V_{MtD}(S(x), t), \quad (6)$$

in the region $\sum_{(s)}$ explored by the CV up to time t .

BARC NEWSLETTER

Founder's Day

The MtD is however, not the true dynamics of the process. The reliability of approximation in Eq. (6) depends heavily on the details of buildup process: over sampling, convergence, and accuracy of MtD run thus remains an issue. However, the MtD method (unlike SMD) can be used to generate the (un)binding pathway with absolute certainty, free from the prior assumptions on final states.

Improving the Accuracy: Combining Nonequilibrium MtD with Equilibrium Umbrella Sampling (US)

To circumvent the inherent nonequilibrium feature of the MtD method and to obtain a true equilibrium free energy pathway, we have refined the MtD discovered PMF with the help of US correction.⁵ The US corrective step is a rigorous and powerful means to determine a formally correct PMF profile along an arbitrary (un)binding pathway as obtained through the MtD approach. In effect, the resulting MtD/US correction combination provides a physically insightful and extremely efficient route of enhancing the equilibrium sampling phase when compared with the conventional US. The combined MtD/US correction approach consists of four steps: (i) perform MtD run along the chosen CV space; (ii) choose a subset of N_{US} configurational degrees of freedom, $s(x)$ from the multidimensional CV space, $s(x)$, along which the US sampling will be applied; (iii) extract the N_{US} -dimensional biasing potential energy surface, $U_{US}(s)$ by averaging over the values along the rest of the CVs from the $V_{\text{tot}}[s(x)]$; (iv) perform equilibrium MD simulation using V_{phys} increased by the time independent biasing potential $U_{US}(s)$. Ergodicity is satisfied The last US step allows, since the metastabilities along the (un)binding pathway are removed by the biasing potential $U_{US}(s)$ and the diffusive dynamics in the chosen CV space can be sampled with ease with a reasonable computational effort. During the equilibrium US run, the ergodicity is measured through the probability density,

$$\rho_{US}(s) = \frac{e^{-\frac{1}{k_B T}\{F(s)+U_{US}[s(x)]\}}}{\int ds e^{-\frac{1}{k_B T}\{F(s)+U_{US}[s(x)]\}}} \quad (7)$$

Following a histogram sorting of the chosen CV, s_i ($i=1 \dots N_{US}$), Eq. (7) can be recast into

$$\rho_{US}(s_i) \approx \frac{1}{h} \int_{s_i-h/2}^{s_i+h/2} ds \rho_{US}(s) \quad (8)$$

where h is the bin width. Finally the US corrected PMF is given by

$$F(s_i) = -V_{MD}[s_i(x), t] - k_B T \ln \rho_{US}(s_i(x)) \quad (9)$$

When compared with Eq. (6), the last term in Eq. (9) represent a corrective measure to the MtD protocol that depends heavily on the chosen MtD parameters.

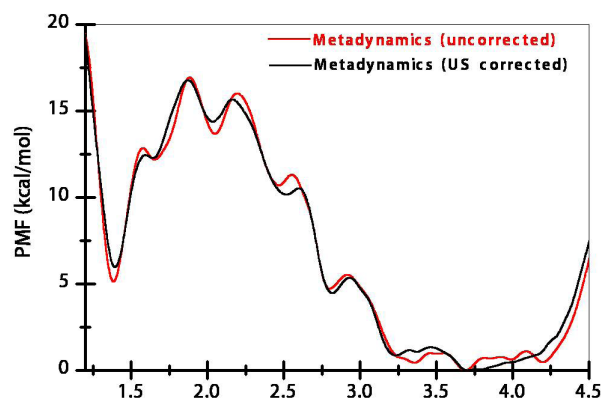


Fig. 3: PMF of obidoxime unbinding transitions from AChE gorge obtained through metadynamics and its US corrective run, as indicated.

BARC NEWSLETTER

Founder's Day

Fig. 3 shows the MtD and its US corrected values for PMF during unbinding transition of obidoxime: an US sampling phase of 310ns was chosen and the values of the COM separation CV was recorded at 1ps interval, totalling 31×10^4 samples at the end of the correction run. To evaluate Eq. (8) we choose bin size of 0.001nm.

Conclusion

Ever since the need of molecular level understanding of the protein-ligand interactions are known, an increasing repertoire of functions have been associated with the measurement of equilibrium interaction PMF leading to the discovery of various nonequilibrium MD techniques and their physico-mathematical connection to the equilibrium properties. However, each of these nonequilibrium techniques has their own inherent assumptions. Thus the equilibrium properties extracted from them remains questionable. Here we have focused on two such techniques and have discussed their strength and weakness. Finally we have arrived at a recipe where we have combined the advantages of MtD configurational searching with the equilibrium umbrella sampling. This lead to a quick and accurate determination of equilibrium PMF, which is otherwise is a formidable task to be accomplished in today's parallel computation architecture.

Acknowledgement

The author sincerely acknowledges the support from ANUPAM parallel computational facility, BARC.

References

1. Crooks G E (1999) Entropy production fluctuation theorem and the nonequilibrium work relation for free energy differences. *Phys Rev E* 60: 2721-2726.
2. Minh DDL, Adib AB (2008) Optimized Free Energies from Bidirectional Single-Molecule Force Spectroscopy. *Phys Rev Lett* 100: 180602.
3. Hummer G, Szabo A (2005) Free Energy Surfaces from Single-Molecule Force Spectroscopy. *Acc Chem Res* 38: 504-513.
4. Sinha V, Ganguly B, Bandyopadhyay T (2012) Energetics of Ortho-7 (oxime drug) translocation through the active-site gorge of tabun conjugated acetylcholinesterase. *PLOS One* 7: e40188 (14 pages).
5. Pathak AK, Bandyopadhyay T (2014) Unbinding free energy of acetylcholinesterase bound oxime drugs along the gorge pathway from metadynamics-umbrella sampling investigation. *Prot. Str. Fn. Bioinform.* DOI: 10.1002/prot.24533 (in press).

INVESTIGATION OF INTERFACE MAGNETIC STRUCTURE OF THIN FILMS USING POLARIZED NEUTRON REFLECTOMETRY

Surendra Singh and Saibal Basu
Solid State Physics Division

Dr. Surendra Singh is the recipient of the DAE Scientific & Technical Excellence Award for the year 2012

Abstract

A rapidly increasing number of research and applications in science and engineering rely on thin films, multilayers down to the sub nanometer scale. In order to understand the physical, magnetic properties of such nanostructures, a thorough and detailed structural and magnetic characterization is required. Polarized neutron reflectivity (PNR) is a nondestructive and unique technique to study magnetization depth profile of thin films with in a sub nanometer resolution. We have developed a polarized neutron reflectometer at Dhruva reactor, Mumbai. Here we present structural, magnetic and morphological properties of some of the technologically important multilayers using PNR.

Nanostructured architectures with reduced dimensionality and/or enlarged interfacial areas have been used as model systems to investigate the effect of interface on physical properties of thin films and multilayers. The availability of various heterostructures formed by depositing materials with distinct phases and properties (e.g. magnetic/semiconductor, magnetic/ferroelectric, magnetic/superconducting systems) offers new opportunities to study competing interactions at interfaces because these interactions produce a delicate balance between states with very different properties, such as ferroelectric (FE), ferromagnetic (FM), and superconducting states, and thus provide enabling ingredients for new physics and functionalities. However to understand the physical, magnetic properties of interfaces in nanostructures, a thorough and detailed structural and magnetic characterization is required. X-ray reflectivity (XRR) and polarized neutron reflectivity (PNR) are two nondestructive techniques that provide quantitative measures of the chemical and magnetic depth profiles of films with less than nanometer resolution [1-5].

Specular reflectivity (angle of incidence = angle of reflection) involves measurement of the radiation (x-ray/neutron) reflected from a sample as a function of wave vector transfer $Q [= 4\pi\sin\theta/\lambda]$, perpendicular to the sample surface, where λ is x-ray or neutron wavelength and θ is angle of incidence. Specular reflectivity is quantitatively related to the Fourier transform of the scattering length density (SLD) depth profile $\rho(z)$ [1, 4], averaged over the sample area.

For XRR, $\rho_x(z)$ is proportional to electron density [1, 4]. In case of PNR, $\rho(z)$ consists of nuclear and magnetic SLDs such that $\rho^\pm(z) = \rho_n(z) \pm CM(z)$, where $C = 2.91 \times 10^{-9} \text{ \AA}^2 \text{ cm}^3/\text{emu}$, and $M(z)$ is the magnetization (in emu/cm³) depth profile [1]. The sign +(-) is determined by the condition whether the neutron beam polarization is parallel (antiparallel) to the applied field and are represented by reflectivity, $R^\pm(Q)$. $\rho_n(z)$ and $M(z)$ can be inferred from $R^\pm(Q)$ often with less than nanometer resolution.

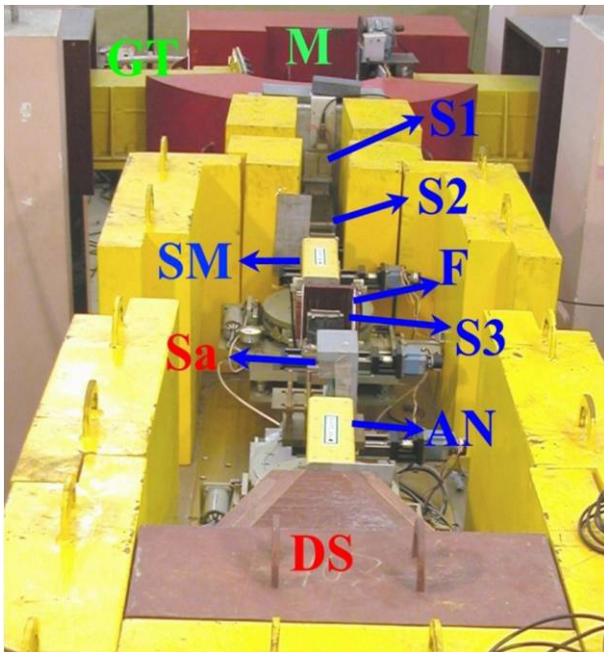
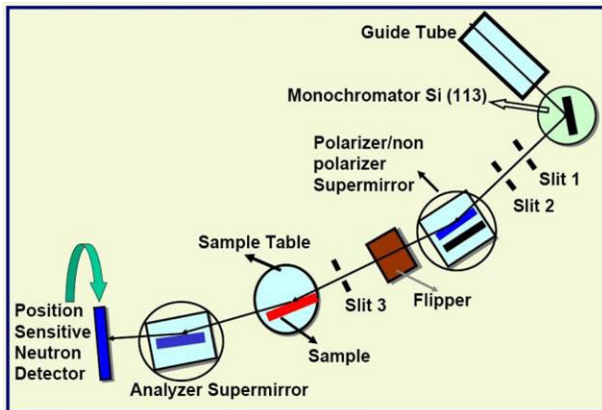


Fig. 1: schematic (top) and photograph (bottom) of PNR instrument at Dhruva and different components, shown by symbols: GT is the guide tube, M is the Si single crystal monochromator ([113] reflection), S1 and S2 are two cadmium slits comprising the collimator, SM is the super mirror polarizer/non-polarizer assembly, F is a D.C. Flipper, S3 is 3rd Cd slit, Sa is the sample on high precision rotation stage and DS is the detector inside the shield.

We have developed a Polarized neutron reflectometer at Dhruva reactor, Mumbai [5]. Fig 1 shows the schematic (top) and photograph (bottom) of the instrument. The instrument uses a linear position sensitive detector, which helps to simultaneously measure the specular and off-specular neutron reflectivity over a range of wave vector transfer. Here we present some of the recent studies using PNR technique.

Asymmetric magnetization profile at Ge/Fe/Ge interfaces

Interfaces between ferromagnetic (FM) metals and semiconductors have attracted much interest because of their potential applications in electronic and "spintronic" devices. Growth of transition metal on semiconductor generally results in intermixing/interdiffusion at the interfaces, which decreases the magnetization of FM/semiconductor structures. We have investigated interface magnetization in Fe/Ge multilayer systems [6-8]. Here we present XRR and PNR study on a Si(substrate)/Ge/Fe/Ge trilayer system. We could quantify physical and magnetic roughness as well as morphology at the interfaces of the sample.

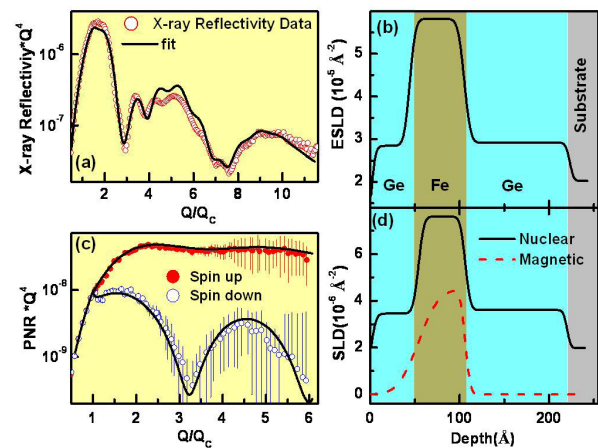


Fig. 2: (a) XRR data. (b) Electron scattering length density (ESLD) depth profile extracted from XRR. (c) PNR data. (d) Nuclear and magnetic SLD obtained from PNR data.

Fig. 2(a) shows specular XRR from the sample. Fig. 2(b) shows the electron scattering length density depth profile which gave best fit to XRR data, clearly suggesting a well-defined 3 layer structure of the film with an interface roughness of $\sim 9\text{\AA}$. Fig. 2(c) shows the specular PNR measurement for two polarization states of neutron beam. Fig. 2 (d) shows the nuclear and magnetization depth profile of the sample which gave best fit to PNR data and demonstrates the existence of different magnetic and physical density profile at interfaces in the sample. The magnetic density profile was also asymmetric compared to the physical profile at the interfaces. This was attributed to different level of inter-diffusion at interfaces as suggested by off-specular XRR.

BARC NEWSLETTER

Founder's Day

Correlation of magneto transport properties with interface structure and morphology

Fe/Au multilayer is one of the systems studied extensively, which include; prediction and experimental evidence of electron channeling, theoretical prediction of enhanced magnetic moment of Fe at interfaces and layer thickness dependent magnetic properties of Fe/Au systems [9]. However these studies lack in investigation of interface structure and magnetism and their correlation with transport properties in Fe/Au multilayers. Using specular XRR, PNR and off-specular XRR in combination with SQUID and transport measurements we established correlation between MR and physical parameters of the systems, obtained from XRR and PNR. These are fractal dimension at the interfaces, normalized magnetic moment profile at the interfaces and in-plane correlation length in these samples [10]. Two series of multilayers were deposited

on Si substrate by sputtering: one series with varying Fe layer thickness, $t_{\text{Fe}} = 30\text{-}100 \text{ \AA}$, and another with varying Au layer thickness $t_{\text{Au}} = 50\text{-}150 \text{ \AA}$.

Fig. 3(a) and (b) show the XRR and PNR data from two multilayers. This gave detailed depth dependent structure and magnetic properties of the multilayer samples. Fig. 3 (c) shows the off-specular XRR data from these multilayers, which helped to characterize the morphology of the interfaces in the multilayers. Thus the change in MR was correlated with magnetic and morphological properties of Fe/Au and Au/Fe interfaces in Fe/Au multilayer samples. We observed that large MR is associated to interfaces with larger magnetization, large in-plane correlation length (ξ) and higher Hurst (h) parameter. The variation of MR with these parameters are shown in Fig. 4.

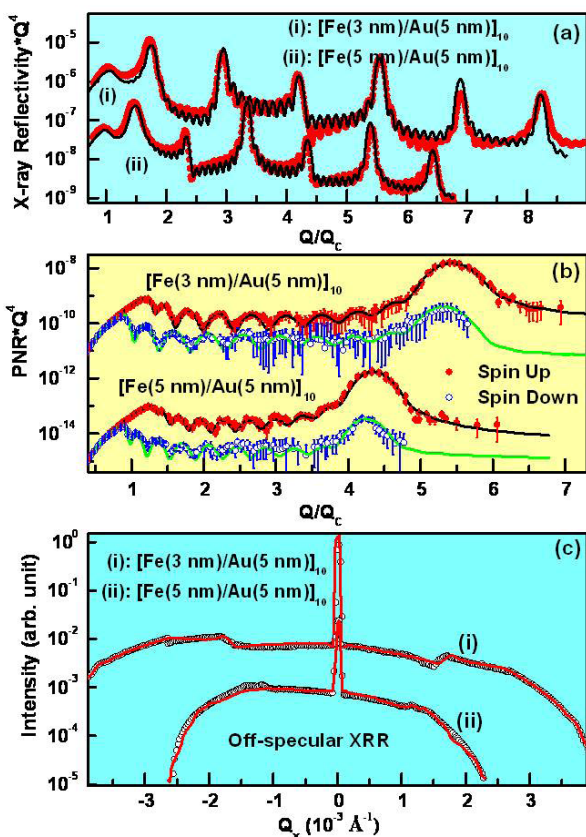


Fig. 3: Specular XRR (a) and PNR data (b) from Fe/Au multilayers with different thickness. (c) off-specular XRR from these multilayers.

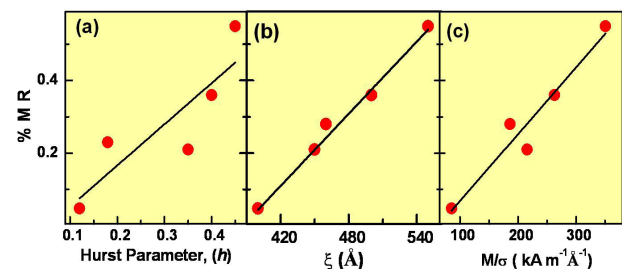


Fig. 4: Variation of magnetoresistance with (a) Hurst parameter(h), (b) in-plane correlation length (ξ) and (c) magnetization/ roughness.

References

1. M. R. Fitzsimmons and C. Majkrzak, "Modern Techniques for Characterizing Magnetic Materials" (Springer, New York, 2005), Chap. 3, pp. 107–155.
2. S. K. Sinha et al., *Phys. Rev. B* 38, 2297 (1988).
3. S. Singh et al., *Phys Rev. B* 81, 235413 (2010).
4. S. Singh et al., *Phys Rev. B* 79, 195435 (2009).
5. S. Basu and S. Singh, *J. Neut. Res.*, 44 109 (2006).
6. S. Singh et al., *Appl. Surf. Sci.* 240, 251 (2005).
7. S. Singh et al., *J. Appl. Phys.*, 101, 33913 (2007).
8. S. Singh et al., *J. Appl. Phys.*, 107, 123903 (2010).
9. D. T. Dekadjevi et al., *Phys. Rev. Lett.* 86, 5787 (2001).
10. S. Singh et al., *Thin Solid Films* 550 326 (2014).

LASER BASED INSTRUMENTATION

Aseem Singh Rawat

Laser & Plasma Technology Division

Shri Aseem Singh Rawat is the recipient of the DAE Scientific & Technical Excellence Award for the year 2012

Abstract

Laser is an excellent tool for measurement application. It offers the advantage of non-contact, non-destructive and fast measurement. Also it is more suitable for remote measurement in toxic and hazardous environment. Laser based Instrumentation deals with the design & development of instruments that use laser for sensing the physical parameter or variable. They have Industrial as well as scientific applications. In this article, Laser based instruments for diameter measurement, Surface Roughness measurement, Projectile Velocity measurement and Flow visualisation are discussed which are developed in-house.

Introduction

Laser based Instrumentation is a branch of instrumentation in which the instrument has laser as an integral part of its Sensor. Use of laser makes these instruments non-contact, non-destructive and fast in nature. Laser based instruments are replacing many conventional measuring instruments in industrial and scientific areas, at the same time also finding new applications. Optical methods are more useful generally for remote measurement in hazardous and toxic environment where human intervention is very difficult.

Laser is a light beam with the special property of Coherence. Due to this special property, Laser exhibit

characteristics like high degree of collimation, high intensity, sharp focus, monochromaticity etc. One or more of these characteristics is/are utilized to develop a Laser based Instrument.

A laser based instrument consists of following important components:

- Optoelectronic components like laser, photo detector
- Optical components like lens, mirror and other such components
- Opto-mechanical components for precisely mounting optical & opto-electronic components
- Electronic components for processing of photo detector output, computation of result and user interface through keyboard & display.

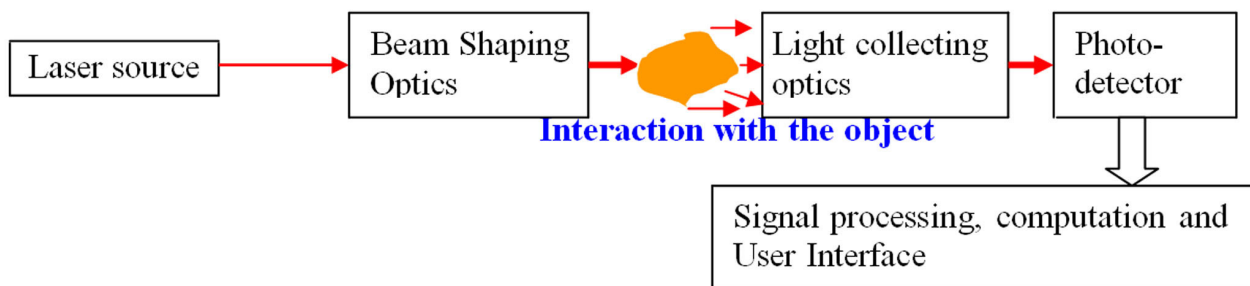


Fig 1: Generalized block diagram of a Laser-based instrument

BARC NEWSLETTER

Founder's Day

Among the large number of laser based instruments, following of them have been developed in-house:

Laser based Diameter measuring instrument – “Lascan Dia-Gauge”

Here a fine beam of visible light from diode Laser scans a measuring (vertical) plane using a rotating mirror mounted on the shaft of a DC motor and collimating lens (plano convex), with the point of reflection being the focal point of the collimating lens (Fig 2a). The beam after reflection from mirror and emerging from collimating lens during scan time, becomes parallel to the optical axis of the lens.

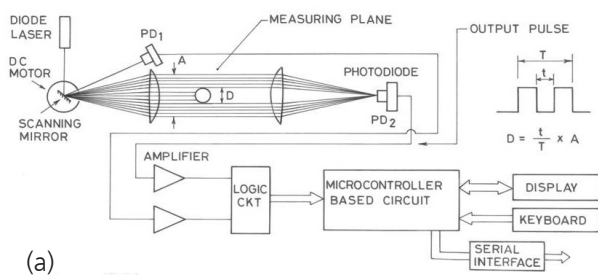


Fig. 2: a. Schematic of Laser based diameter measurement, b. Photograph of Lascan Dia-Gauge

An object kept in the measuring plane, perpendicular to the scanning beam (in fig 2 seen as perpendicular to the plane of paper), obstructs the scanning beam for the time proportional to its dimension¹. The scanning beam is then focused by a receiving optics on a photodiode to generate a shadow pulse of object. The shadow pulse width ‘t’ and the total scan time ‘T’

are measured using high speed counter. As shown in the fig 2a , the ratio of the two time when multiplied by the aperture ‘A’ of the lens gives the diameter ‘D’ of the object . A microcontroller-based circuit has been developed to calculate the diameter and interface with user through display and keyboard. Data is also transmitted through serial interface to PC for logging. Thus the instrument becomes stand-alone. Here as the beam becomes parallel after collimating lens thus the separation between the two lens can be increased as per requirement (up to 1 meter or so). The instrument can measure diameters in the range of 1 mm to 25 mm with an accuracy of 5 micron. It has application in Nuclear Industry, automobile and wire drawing industry. The technology of this instrument has been so far transferred to five private industries.

Laser based surface roughness measurement- Laser Surfcheck

One of the several optical techniques² for roughness measurement is based on measurement of specular reflectance. Optical RMS roughness, σ_o , of a surface is related with specular reflectance for range of incidence angles (near grazing) by the formula³ :

$$I_x/I_o = \exp [- (4\pi\sigma_o/\lambda)^2 \cos^2\alpha] \quad (1)$$

Where,

I_x = specularly reflected intensity from relatively smooth surface

I_o = specularly reflected intensity from perfectly smooth surface or incident intensity for near grazing angle of incidence to smooth surfaces

σ_o = optical RMS roughness

λ = wavelength of the incident beam

α = incident angle

By measuring I_x and I_o and using above formula, σ_o , can be calculated and thus from this value the corresponding value of average Roughness (Ra) can be determined using calibration curve generated from available experimental data.

BARC NEWSLETTER

Founder's Day

A Laser based instrument for roughness measurement using diode laser –“Laser Surf-check” (Fig 3.b) has been developed which measures incident as well as specularly reflected light as shown in fig 3a. Then using the above formula and a look-up table, σ_o and R_a are calculated by the microcontroller based circuit. This technique is useful for surfaces whose roughness is very less than the wavelength λ , of the incident beam. Thus if a diode Laser at 670 nm is used then surfaces of R_a in the range $0.05 \mu\text{m}$ to $0.25 \mu\text{m}$ can be measured.

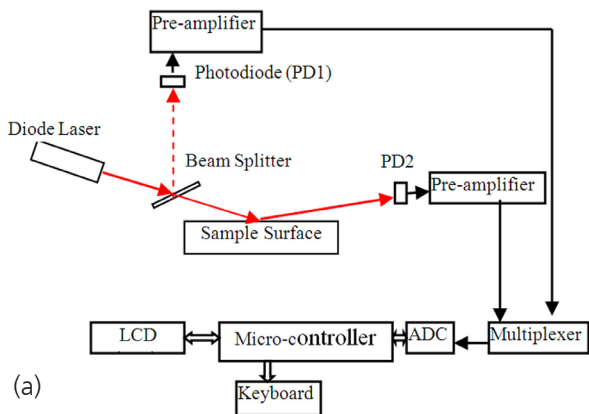


Fig. 3: a. Schematic Diagram of Laser based roughness measuring instrument, b. Photograph of Laser Surf-check

Being non-invasive in nature, it is very useful for roughness measurement of soft surfaces. The fast measurement capability makes it ideal for routine comparison of similar surfaces. Laser surf-check has LCD display and keypad for user interface. It has been supplied to Material Processing Division (MPD), BARC for measurement of surface finish of metallic mirrors.

Laser based projectile velocity measurement- Projectile Velocity Meter

Laser based projectile velocity measurement is based on time of flight principle. A horizontally moving projectile interrupts two optical screens (parallel to each other) separated by a fixed known distance D , (fig 5a) and the time between two interruptions is measured electronically to calculate the speed. An optical screen (sheet) is created using the collimated vertical Laser line that is obtained from a Diode Laser (635 nm, 15 mW) with uniform intensity line generating optics and a spherical lens for collimation (fig 4). The size of optical screen takes care of little variation in the path of the projectile. The collimated line is then focused at the receiving unit using focusing optics on a photodiode. The output of the photodiode represents the total intensity of the collimated line. When any projectile passes perpendicular to the optical screen, it reduces the intensity of the Laser line falling on the photodiode by the amount proportional to its dimension.

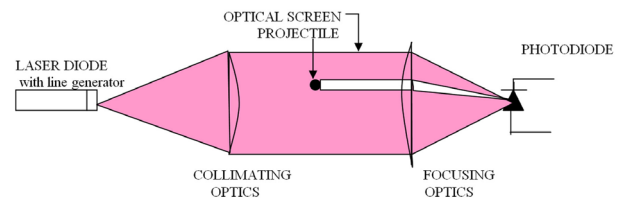


Fig. 4 Optical Screen Generation

The sensitive photodiode-amplifier circuit is designed to generate shadow pulse for this change in the intensity level. Shadow pulse generated at optical screen-1 is the start pulse and at optical screen-2 is the stop pulse for an electronic counter (Fig. 5a) operating at 10 MHz. Distance (D) between two optical screens is known (200 mm). The count value, representing time of flight, is read by micro-controller, which calculates the speed for known separation using following eqn.

$$S = D / (C * T) \quad (2)$$

BARC NEWSLETTER

Founder's Day

Where,

S -> Speed, D -> Distance between two optical screen,

C -> No. Of Counts

T -> counter clock period

Laser velocity meter instrument (Fig. 5b) has been developed based on above principle.

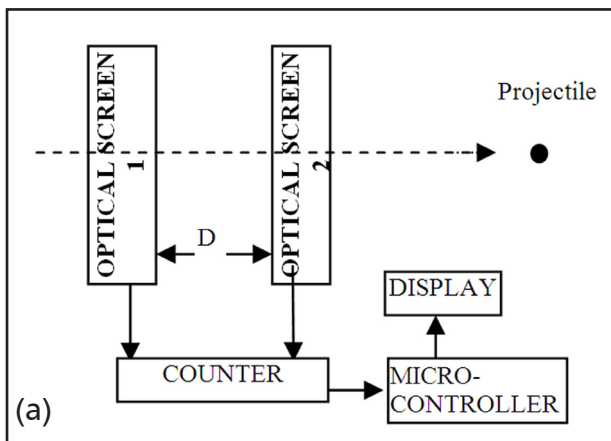


Fig. 5: a. Block Diagram, b. Photograph, of the Laser velocity meter

The ruggedness in its design is brought due to tolerance in optical design and the use of Laser line to create optical screen. It can measure velocity of projectile in the range 0.01 m/s to 5000 m/s with an accuracy better than 2.5%. This instrument has been supplied to DMRL, DRDO, Hyderabad for measurement of Projectile fired from a Gas gun for material study experiments.

Particle Image Velocimetry (PIV)

Schematic representation of the PIV set up is shown in Figure 6a. A light sheet produced from the pulsed Nd:YAG laser beam at 532 nm of 6-8 ns width using cylindrical lens is used to illuminate the seeding particles in the fluid along the direction of flow and the positions of particles in that plane are recorded using a CCD camera, kept at right angle to the plane of sheet. After some predetermined delay, another laser pulse illuminates the same plane, creating a second particle image. Two consecutive images generated corresponding to two laser light sheets are captured in the separate frames of a double-shutter digital camera for fast flowing fluids and cross-correlation is used to determine flow velocities at different points in the imaged plane.

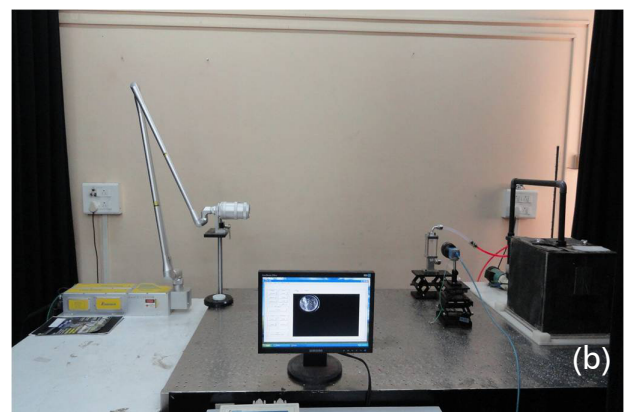
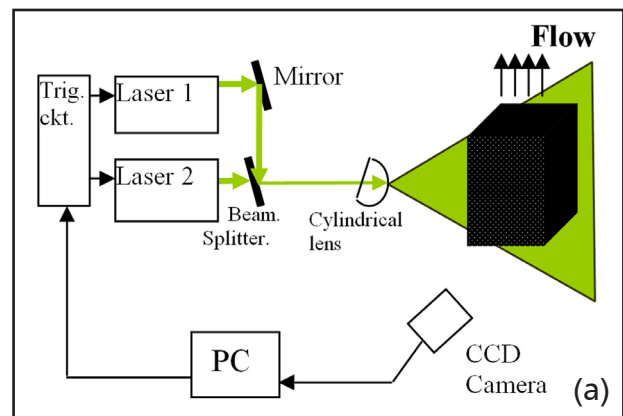


Fig.6: a. A Schematic Block Diagram of typical PIV Set-up b. Photograph of PIV set-up

BARC NEWSLETTER

Founder's Day

The triggering of laser pulses is synchronized with the camera operation by the PC to capture the two images. These particles are added to the flow and are known as seeding particles. A PIV set-up developed is shown in Fig 6b.

Flow of water in Dye cell of Dye laser and flow of water in a tank have been measured in the range of 1m/s to 20 m/s using this PIV set-up. Presently work is in progress to measure particle flow in gaseous medium.

Conclusion

The above described methods are but a few of large number of applications of laser-based instruments. Laser based Instrumentation is an upcoming field and it has wide range of metrology applications. The

developments in diode laser technology has benefited the laser based instrumentation as it becomes possible to makes compact, portable and low cost instruments using diode laser.

References

1. Industrial Lasers and their Applications James T. Luxon, David E. Parker, Prentice Hall Inc. Publication
2. Vorburger T.V., Teague E.C., *Precision Engg.* 3 (1981) 61-83
3. Whitley J.Q., Kusy R.P., Mayhew M.J., Buckthal J.E., "Surface roughness of stainless steel and electroformed nickel standard using a HeNe laser", *Optics and Laser Technology* Vol 19 No. 4 (1987) 189-196
4. Building Electro-optical Systems Philips C.D. Hobbs John Wiley & Sons Publication

BARC NEWSLETTER

Founder's Day

NANOMATERIALS FOR LUMINESCENCE AND HYPERThERMIA APPLICATIONS

R.S. Ningthoujam
Chemistry Division

Dr. R.S. Ningthoujam is the recipient of the DAE Scientific & Technical
Excellence Award for the year 2012

Abstract

SnO₂, ZnO, YPO₄, YVO₄ and CaMoO₄ nanoparticles show the luminescence in violet-blue to green region. When rare-earth ions (RE³⁺) are doped into the above hosts, an improvement of luminescence is observed due to energy transfer from host/sensitizer to RE³⁺. In hexagonal phase of YPO₄:(Eu³⁺, Ce³⁺/Bi³⁺), water molecules remain within the pores extending along the c-axis and such water molecules are stable up to 800 °C and do not freeze at -50°C. Switching on and off of luminescence are performed through redox reaction in La/GdPO₄:(Tb³⁺, Ce³⁺). Again, functionalized Fe₃O₃ superparamagnetic ferrofluids prepared by chemical route show the heating behaviour up to the hyperthermia temperature (42 °C) under AC magnetic field. 1 mg of oleic acid (OA) coated Fe₃O₃ nanoparticles shows high cytotoxicity (70%) in cancer cells (1 million) under AC magnetic field.

Introduction

Nanomaterials are those materials in which at least one side of the constituent particles lies in between 1-100 nm (1 nm = 10⁻⁹ m = 0.1 Å). Since size is so small, surface to volume atomic ratio in a particle is high and thus, it possesses excess energy as compared to bulk and naked eye cannot see extremely small particles. Here, bulk means material, which has large particle size (D > 500 nm). This can be confirmed by Mössbauer, electron microscopy, atomic force microscopy (AFM), scanning transmission electron microscopy (STEM) and calorimetric studies. With decrease in particle size, the followings are observed: quantum size effect on optical properties of semiconductors, ferromagnetic to superparamagnetic transition in magnetic material, increase of electrical resistivity or metallic to disorder/semiconducting, change in the optical and acoustic phonons, extreme hardness or change in mechanical strength, change in thermal conductivity, increase in active sites in catalysis, etc. [1]. This suggests the

change in intrinsic properties of materials with decrease of particle size or reduced dimensions as compared to bulk. Materials will be of metals, alloys, oxides, sulfides, nitrides, carbides and borides, etc. However, the materials useful in society will be great important. In such situation, we have to choose materials so that it has high impact to society. Usefulness of nanomaterials in basic sciences (biology, chemistry, physics, materials science and engineering) and their applications brought nanoscience and nanotechnology. Manipulation and engineering of such small particles will help in generation of fuel, display devices, tissue engineering, bio-separation, health care sector, cancer therapy, diagnosis and advanced nuclear reactors, etc. in economic ways. In my opinion, nanotechnology has merits and demerits in our society depending on ways of uses though this brought the revolution in sciences. However, we have to think security, safety and future consequences of this revolution. In fact, nanomaterials should be used under a frame work governed by ethics and law in order to maintain sustainable environment.

BARC NEWSLETTER

Founder's Day

In this article, I present a few examples of nanomaterials, which are useful in luminescence devices and hyperthermia based cancer therapy and nanomaterials are prepared in the laboratory of Chemistry Division, BARC.

Luminescence Devices

Over the last decade, the semiconducting nanomaterials such as SnO_2 , TiO_2 , $\text{SnO}_2\text{-TiO}_2$, ZnO , A_2O_3 ($\text{A} = \text{Y, Gd, La}$), AVO_4 , APO_4 , CaMoO_4 and their compounds with rare earth ions ($\text{RE}^{3+} = \text{Eu}^{3+}, \text{Dy}^{3+}, \text{Tb}^{3+}, \text{Sm}^{3+}$) were prepared by chemical routes [2, 3]. These particles can produce emission in UV, visible and NIR regions (Fig. 1). Improvement in luminescence was found by the following: (a) energy transfer from host to RE^{3+} , (b) core-shell model, (b) dispersion in another dielectric medium, (c) removal of quencher, (d) heating, (f) co-doping with Li^+ , Bi^{3+} or sensitizer, which either enhance absorption cross-section or

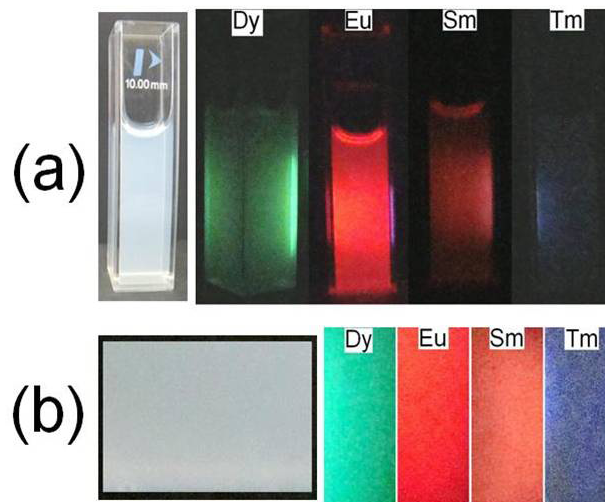


Fig. 1: Photographs of $\text{GdVO}_4:\text{RE}$ after UV excitation: (a) dispersed particles and (b) films [2].

overlapping of the emission band of the sensitizer or host with absorption band of activators. Quantum size effect in optical study of ZnO and PbSe was

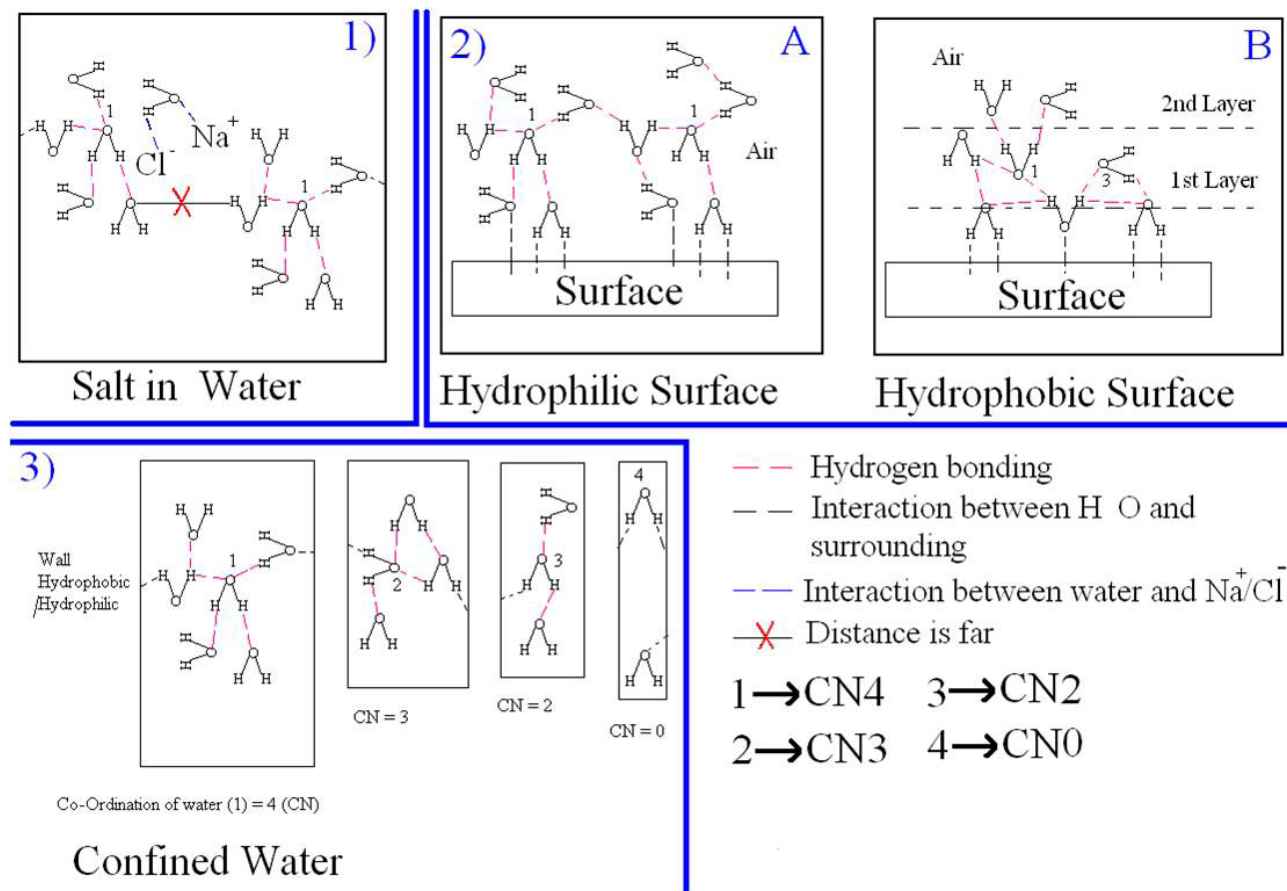


Fig. 2: Types of hydrogen bonding when (1) salt is added to water, (2) water is contacted with hydrophilic (A) and hydrophobic (B) surfaces, (3) water is in different confined regions.

BARC NEWSLETTER

Founder's Day

observed. It suggests the red shift in absorption/emission peak with increase of particle size. Switching on and off of luminescence was performed in Ce^{3+} co-doped $LaPO_4:Tb^{3+}$ and $GdPO_4:Tb^{3+}$ through redox reactions [3].

For the first time, the free water on the surface of particles and confined water in the pores or interstitial water in the hexagonal structure of orthophosphate ($REPO_4$) were confirmed using NMR technique [4]. There are different types of hydrogen bonding present in water depending on container/interface/region (Fig. 2). This finding will be useful in production of water molecules from 10 to 10^{10} in a particle under

controlled NIR/microwave excitation. Also, this concept will be useful in biological system, therapy, micro-chips, etc. in which limited water molecules are needed. Luminescence quenching in such hexagonal $REPO_4$ phase was observed and this is due to content of confined water, which is near to metal ion ($Y^{3+}/Bi^{3+}/Eu^{3+}$) and far from PO_4 group. This confined water is not frozen even at -50 °C due to less number of H-bonding. In such system, the water molecules are stable up to 800 °C [5, 6]. The $REPO_4$ compounds are available in rocks. This finding will give an alternative evidence for possibility of water present in rocks available in many planets, where temperature level goes up to 800 °C.

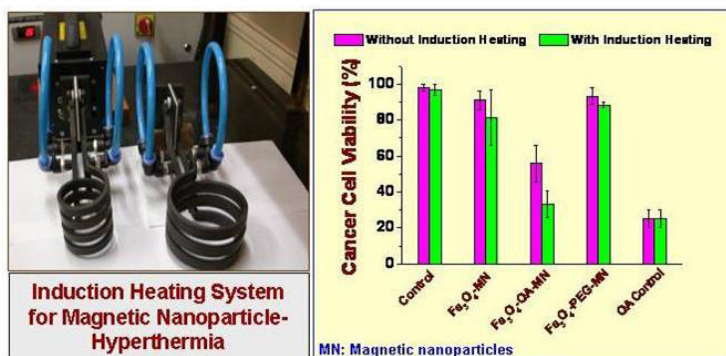


Fig. 3: Induction coil in which cancer cells can be inserted (left) and cell viability (right). 1 mg of each sample is added to 106 cells [7].

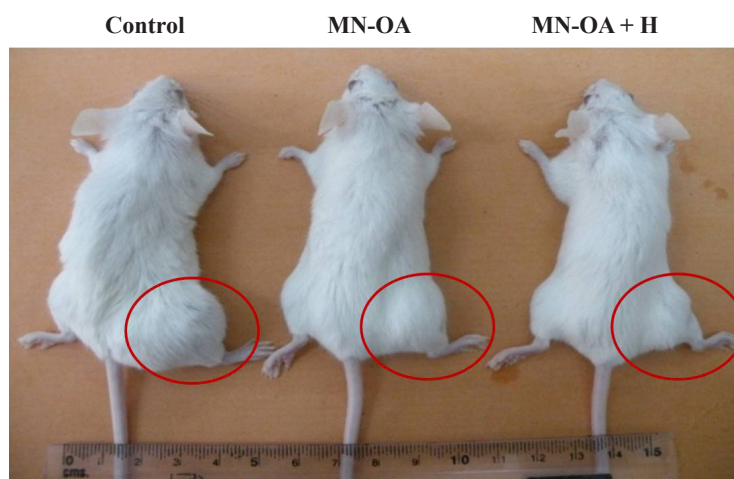


Fig. 4: Tumor growth showed significant regression in mice after MN-OA and hyperthermia treatment. Control indicates the treatment without MN-OA and without hyperthermia. MN-OA indicates the treatment after injection of MN-OA. MN-OA + H indicates the treatment after injection of MN-OA and heating through induction.

Hyperthermia based Cancer Therapy

Magnetic nanoparticles (MN) of Fe_3O_4 , $CoFe_2O_4$, $NiFe_2O_4$, Co-Fe-B, FePd, Co and Ni were prepared by chemical routes. These were tested for heating behaviour under AC magnetic field (265 kHz frequency, 80-400 Oe field). Fe_3O_4 coated with polyethylene glycol (PEG) were incorporated into thermally sensitive liposome. 6-carboxy fluorescein (CF) was used as indicator. The enhanced release of CF in presence of magnetic nanoparticles at 42 °C was found. Fe_3O_4 MN coated with PEG and oleic acid were tested in a human breast cancer cell line (MCF7) [1,7]. Killing of cancer cells was found up to 70% within 10 minutes for oleic acid (OA) coated MN (Fig. 3). Bi-functional properties of MN-Luminescence (Fe_3O_4 - YPO_4 :Eu) having very high specific absorption rate ($SAR = 100\%$) and red emitter at 615 and 695 nm, which is in range of biological window were tested in mouse fibrosarcoma (Wehi 164) tumor cells by Prussian blue staining. The intra-cellular uptake of MN was observed. In order to perform site selective of cancer cells (including metastability), some new approaches are under process. Now, in vivo study in mice

BARC NEWSLETTER

Founder's Day

study shows significant decrease of tumour size within 8 days in the presence AC magnetic field when MN were incorporated in mice (Fig. 4). This study will be useful in clinical trials.

Note

This work is in collaboration with Dr. R.K. Vatsa, Chemistry Division, Dr. B.N. Pandey and Neena V. Jadhav, RBHSD.

Acknowledgement

I thank Dr. B. N. Jagatap, Director, Chemistry Group and Dr. V. K. Jain, Head, Chemistry Division, BARC for their encouragement and support during the research work.

References

1. R.S. Ningthoujam, R.K. Vatsa, A. Kumar, B.N. Pandey, "Functionalized Magnetic Nanoparticles: Concepts, Synthesis and Application in Cancer Hyperthermia", *Functionalized Materials*. 2012, Editors: S. Banerjee and A.K. Tyagi, Elsevier Publications, pages 229-260.
2. N.S. Singh, R. S. Ningthoujam, Ganngam Phaomei, S.D. Singh, A. Vinu, R. K. Vatsa, "Re-dispersion and film formation of GdVO₄:Ln³⁺ (Ln³⁺ = Dy³⁺, Eu³⁺, Sm³⁺, Tm³⁺) nanoparticles: particle size and luminescence studies", *Dalton Transactions* 41 (2012) 4404.
3. R.S. Ningthoujam, "Enhancement of luminescence by rare earth ions doping in semiconductor host", *Synthesis, characterization and applications of multifunctional materials*. 2012, Editors: S. B. Rai, and Y. Dwivedi, Nova Science Publishers Inc, USA, Chapter 7, pages 145-182.
4. R.S. Ningthoujam, "Finding confined water in hexagonal phase of Bi_{0.05}Eu_{0.05}Y_{0.90}PO₄.xH₂O and its impact for identifying the location of luminescence quencher", *Pramana J. Phys.* 80 (2013) 1055.
5. M.N. Luwang, R. S. Ningthoujam, S. K. Srivastava, Jaganath, R. K. Vatsa, "Effect of Ce³⁺ co-doping and annealing on phase transformation and luminescence of Eu³⁺ doped YPO₄ nanorods: D₂O solvent effect", *J. Am. Chem. Soc.* 132 (2010) 2759.
6. M. N. Luwang, R. S. Ningthoujam, S. K. Srivastava, R. K. Vatsa, "Disappearance and recovery of luminescence in Bi³⁺, Eu³⁺ co-doped YPO₄ nanoparticles due to the presence of water molecules up to 800 °C", *J. Am. Chem. Soc.* 133 (2011) 2998.
7. R. Ghosh. L. Pradhan, Y.P. Devi, S.S. Meena, R. Tewari, A. Kumar, S. Sharma, N. S. Gajbhiye, R. K. Vatsa, B. N. Pandey, R. S. Ningthoujam, "Induction heating studies of Fe₃O₄ magnetic nanoparticles capped with oleic acid and polyethylene glycol for hyperthermia", *J. Mater. Chem.* 21 (2011) 13388.

REACTIONS INVOLVING WEAKLY BOUND NUCLEI: ROLE OF PROJECTILE BREAKUP

S. Santra
Nuclear Physics Division

Shri S. Santra is the recipient of the DAE Scientific & Technical
Excellence Award for the year 2012

Abstract

A large number of nuclear reactions involving weakly bound projectiles have been studied to investigate the special features in complete fusion, elastic scattering and alpha particle production compared to those involving strongly bound projectiles. These features are found to be mainly due to a large probability of breakup of the projectiles in the Coulomb as well as nuclear field of the target nuclei.

Introduction

The study of nuclear reaction mechanisms involving weakly bound stable heavy ions (e.g., ${}^6\text{Li}$, ${}^9\text{Be}$) has been very interesting due to the observation of many nonconventional behaviors compared to those involving strongly bound projectiles (e.g., ${}^4\text{He}$, ${}^{12}\text{C}$, ${}^{16}\text{O}$, ${}^{19}\text{F}$, etc). A suppression in complete fusion cross section at above Coulomb barrier energies, a drastic change in the energy dependence of the optical potential, and a large production of α particles are some of the important features associated with the above reactions. These observations are known to be largely due to the effect of projectile breakup on other channels.

Projectile dissociation [e.g., ${}^6\text{Li} \rightarrow \alpha + d$ or ${}^7\text{Li} \rightarrow \alpha + t$] while passing through the field of a target nucleus is a topic of great interest because of its application to the determination of radiative capture cross section of astrophysical interest. Understanding the reaction mechanisms of loosely bound projectiles and the effect of their breakup on various channels is also very important, especially in the context of the increasing number of the radioactive ion beam facilities and the quest for super heavy elements by the fusion

of nuclei near the drip line. With this aim we have performed a series of measurements on fusion, elastic scattering, breakup and inclusive alpha production cross sections and many theoretical calculations based on coupled channels equations. Results of some of the investigations with interesting observations are as in the following.

Complete fusion in ${}^6\text{Li}$ and ${}^9\text{Be}$ induced reactions

The effect of the breakup of weakly bound (stable or radioactive) nuclei on the fusion process is a subject of current experimental and theoretical interest¹. Although sub-barrier fusion involving strongly bound stable nuclei is well understood, there are contradictory results and predictions about the enhancement or suppression of the fusion cross section, over predictions of the single fusion barrier, around the Coulomb barrier, when one of the collision partners is a weakly bound nuclide. There are theoretical calculations that predict either suppression of the complete fusion (CF) cross sections due to breakup of loosely bound nucleus or enhancement of the same due to coupling of the relative motion of the colliding nuclei to the breakup channel.

BARC NEWSLETTER

Founder's Day

To understand the effect of projectile breakup on fusion reactions, we made a systematic study on several reactions by measuring the complete fusion cross sections for ${}^6,7\text{Li}+{}^{144,152}\text{Sm}$, ${}^9\text{Be}+{}^{89}\text{Y}$ and ${}^9\text{Be}+{}^{124}\text{Sn}$ reactions at energies around the Coulomb barrier^{2,3}. In Fig.1, the CF cross sections normalized to πR_B^2 are plotted as a function of beam energy normalized to Coulomb barrier. It shows that the CF cross section for ${}^6\text{Li}+{}^{144}\text{Sm}$ (filled circles) at above barrier energies gets suppressed by $\sim 32\%$ compared to (i) the coupled-channels (CC) calculations (dashed line) as well as (ii) the cross sections for reactions involving tightly bound projectiles, ${}^{20}\text{Ne}+{}^{133}\text{Cs}$ (filled triangles) and ${}^{12}\text{C}+{}^{141}\text{Pr}$ (filled squares), forming similar compound nuclei. It is interesting to find that the solid line, which is obtained by multiplying the cross sections of CC calculations by a factor of '0.68', is pretty close to the measured CF cross sections data. It means that the CF cross sections for ${}^6\text{Li}+{}^{144}\text{Sm}$ reaction are suppressed by $\sim 32\%$ and this is probably because of the loss of incident flux due to projectile breakup prior to the fusion of the projectile with the target. A large cross section of incomplete fusion (ICF) measured for the present reaction supports the above explanation based on projectile breakup².

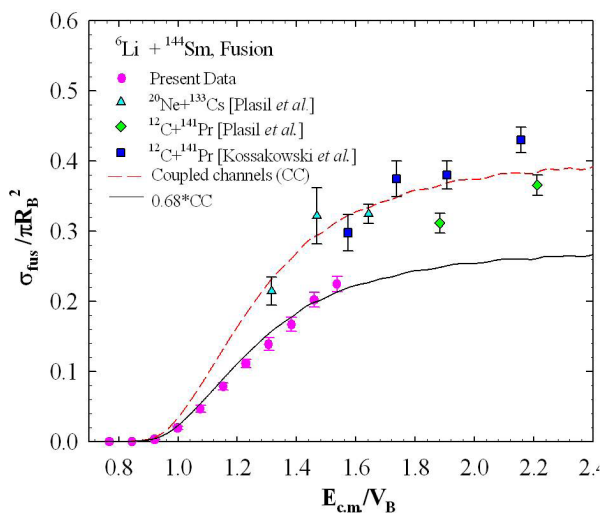


Fig.1: Reduced cross sections ($\sigma_{\text{fus}}/\pi R_B^2$) as a function of $E_{\text{c.m.}}/V_B$ for the present system (filled circles) along with two other reactions ${}^{12}\text{C} + {}^{141}\text{Pr}$ (filled diamonds, filled squares) and ${}^{20}\text{Ne} + {}^{133}\text{Cs}$ (filled triangles). Dashed line is the result of CC calculations. Solid line is obtained by multiplying the CC results by a factor of 0.68.

Studies made for several other reactions (i.e., ${}^6\text{Li}+{}^{152}\text{Sm}$, ${}^7\text{Li}+{}^{144,152}\text{Sm}$, ${}^9\text{Be}+{}^{89}\text{Y}$ and ${}^9\text{Be}+{}^{124}\text{Sn}$) where we have again observed the suppression in CF cross section at energies above the Coulomb barrier compared to those for reactions involving tightly bound projectiles and also to the theoretical estimates. A systematic study on the suppression of CF cross sections has been made as shown in Fig.2. It was observed that CF suppression for reactions involving a particular projectile is independent of the target. It was also observed that the suppression increases with the decrease in projectile breakup threshold. That means the suppression is highest for ${}^6\text{Li}$ whose breakup threshold is the lowest and the reverse is true for ${}^{11}\text{B}$.

Effect on elastic scattering

When we get a set of optical potentials that fit the measured elastic scattering at different beam energies, an anomalous behavior in the energy dependence of the nuclear potential is observed around the Coulomb barrier energies known as "threshold anomaly". The non-negligible probability of inelastic excitations and few nucleon exchange among the projectile and target nuclei is the reason behind this observation

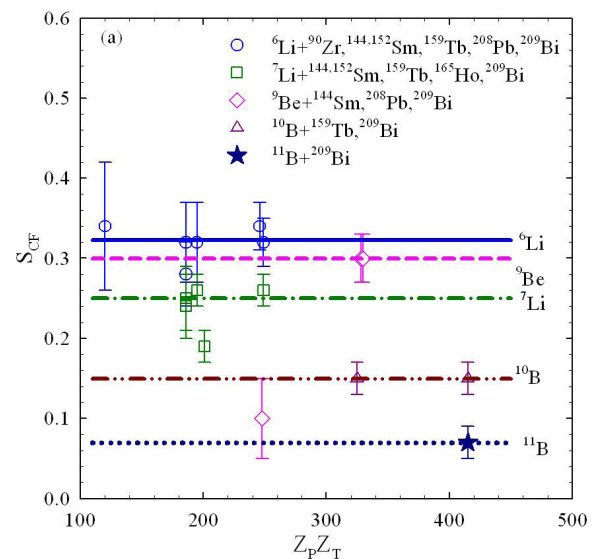


Fig.2: CF suppression factor as a function of the product of atomic numbers of projectile and target. Symbols corresponding to different reactions are explained in the legend given inside the figure itself.

BARC NEWSLETTER

Founder's Day

that modifies the cross sections of not only fusion but also the elastic scattering. Although this behavior is observed for most of the reactions involving strongly bound stable projectiles, for example⁴, $^{12}\text{C} + ^{208}\text{Pb}, ^{209}\text{Bi}$, it is not true for the reactions involving weakly bound projectiles with large breakup probability. However, contradictory results exist in literature involving same weakly bound projectiles, implying that a clear understanding of the effect of breakup on the energy dependence of the optical model (OM) potential is still elusive. Systematic studies of more reactions involving weakly bound projectiles are necessary to unfold these effects. It would also be interesting to see whether a simultaneous description of all the channels as well as the energy dependence of the OM potential is possible for a particular system (e.g., $^6\text{Li} + ^{209}\text{Bi}$) through the same coupled-channels calculations with a large amount of experimental data for inelastic, transfer, and fusion channels as constraints.

With the above motivation, elastic, inelastic, transfer and breakup cross sections were measured for $^6\text{Li} + ^{209}\text{Bi}$ system. From optical model analysis the energy dependences of the optical model potentials were obtained which were found to be different from those involving strongly-bound projectiles. CC calculations are made to understand this using the potentials and coupling parameters that simultaneously explain the measured elastic, inelastic, transfer and breakup cross sections. It was found that the presence of projectile breakup channels modifies the interaction potential which makes the shape of the energy dependent optical potentials so different⁵.

To find the relative contribution of the breakup channels to the total reaction cross section particularly at sub-Coulomb energies, the ratios of cross sections for breakup, CF, target inelastic, and transfer channels to σ_{react} are plotted as a function of energy in Fig. 3. At sub-barrier energies, it was interesting to observe that with decreasing energy, the calculated non-capture breakup cross section (solid line) and ICF (stars) increases, in contrast to the behavior of CF (triangles

down), the inelastic (dash-dot line), and transfer (dashed line) cross sections. The transfer cross section represents the sum of the cross sections calculated for ($^6\text{Li}, ^7\text{Li}$), ($^6\text{Li}, ^5\text{Li}$), and ($^6\text{Li}, ^5\text{He}$) channels. The above observation implies that when all the other channels start closing at sub-barrier energies, the breakup channel does not close, possibly due to the small breakup threshold energy of ^6Li , and the breakup can be caused by even Coulomb excitation. Thus it explains why the imaginary part of the optical potential does not vanish even much below the Coulomb barrier.

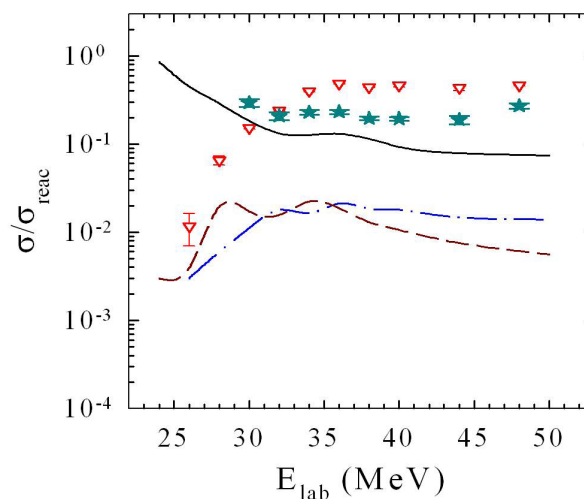


Fig.3. The ratios of cross sections for CF (triangles down) data, ICF (stars), calculated exclusive $\alpha + d$ breakup (solid line), target inelastic (dash-dot line), and transfer (dashed line) channels to total reaction cross section (σ_{react}) to show their relative contributions at different energies.

Inclusive alpha production

The observation of a large cross section for inclusive α ($\sigma^{\text{incl}}(\alpha)$) produced by breakup and different transfer channels for reactions involving weakly bound projectiles with cluster structure ' $\alpha + x$ ' is well established. It has been observed that the production of α in a reaction is much higher compared to that of the valence cluster x . It is a challenging task to understand the reaction mechanisms responsible for such a large cross section of inclusive α . Attempts have been made to understand the origin of such a large α cross section but it is far from fully understood.

BARC NEWSLETTER

Founder's Day

Inclusive α cross sections are measured for the ${}^6\text{Li}+{}^{209}\text{Bi}$ reaction at bombarding energies $E_{\text{lab}} = 24\text{--}50$ MeV. The cross section was observed to be a substantial fraction of the total reaction cross section over the entire energy range, and it exhausts almost whole of the reaction cross section at sub-barrier energies. An investigation on the origin of large inclusive α reveals that most of the α particles, as shown in Fig.4, are

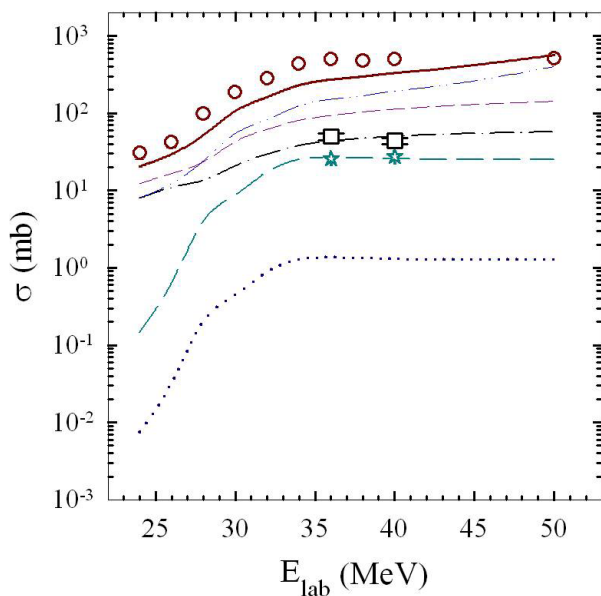


Fig.4. Inclusive breakup α (circles) and α contributions from transfer and breakup channels. Squares and stars represent data on exclusive “ $d + \alpha$ ” (sequential) breakup and “ $p + \alpha$ ” breakup, respectively. (See text for details)

produced by non-capture breakup (${}^6\text{Li} \rightarrow \alpha + d$, dashed line) and ICF via deuteron capture (dash-dot-dot line). The combined cross sections (solid line) of non-capture breakup, d capture, and transfer reactions (dotted line) successfully explain the origin of most of the experimental $\sigma^{\text{incl}}\alpha$ over the measured energy range⁵. A comparison of the $\sigma^{\text{incl}}\alpha$ versus reduced energies for several targets involving ${}^6\text{Li}$ as projectile shows that the cross sections are independent of target. Interestingly, the difference between reaction and CF cross sections “ $\sigma_{\text{react}} - \sigma_{\text{CF}}$ ” for several reactions also shows the same behavior.

References

- 1 L.F.Canto et al., *Phys.Rep.* 424(2006)1; N.Keeley et al., *Prog. Part. Nucl. Phys.* 59(2007)579.
- 2 P. K. Rath, S. Santra et al., *Phys. Rev. C* 79, 051601(2009) ; *Nuclear Physics A* 874 (2012) 14 ; *Phys. Rev. C* 88 (2013) 044617.
- 3 C. S. Palshetkar, S. Santra et al., *Phys Rev. C* 82 (2010) 044608.
- 4 S. Santra et al., *Phys. Rev. C* 64 (2001) 024602; *Phys. Rev. C* 60 (1999) 034611.
- 5 S. Santra et al., *Phys. Lett. B* 677 (2009) 139; *Phys. Rev. C* 83 (2011) 03461.

SYNTHESIS OF PALLADIUM THIOLATE/SELENOLATE COMPLEXES AS CATALYSTS FOR SUZUKI C–C COUPLING REACTIONS

Sandip Dey
Chemistry Division

Shri Sandip Dey is the recipient of the DAE Scientific & Technical Excellence Award for the year 2012

Abstract

The new hybrid ligands dimethylaminoalkyl dichalcogenide and 4,4'-dipyridyldiselenide were developed and explored the complex chemistry of platinum group metals. A variety of complexes of the type $[PdX(E^nN)]_n$ ($X = Cl, OAc$; $E = S, Se$; $E^nN = ECH_2CH_2NMe_2, ECH_2CH_2CH_2NMe_2$), $[PdCl(4-SeC_5H_4N)(PR_3)_2]$ and $[PdCl(4-SeC_5H_4N)(PR_3)]_n$ were synthesized. The complex $[PdCl(4-SeC_5H_4N)(PR_3)]_n$ exists in bi- and tri-nuclear forms. These complexes were characterized by multinuclear NMR spectroscopy in solution and single crystal X-ray diffraction analyses in solid state. The catalytic activity of palladium complexes in Suzuki C–C cross coupling reactions has been investigated.

Introduction

The palladium catalyzed C–C cross-coupling reaction has become the most powerful and versatile tool for the synthesis of pharmaceuticals, agrochemicals and advanced materials both on laboratory and industrial scale^{1,2}. The importance of this general class of reactions was recognized by the awarding of the Nobel Prize in Chemistry in 2010 to Richard Heck, Ei-ichi Negishi and Akira Suzuki. Catalyst design has remained of paramount importance for understanding various catalytic processes as well as for improving the activity of catalyst system. The excellent Pd catalyst systems developed initially with Group 5 compounds such as bulky or electron rich phosphine ligands and later with nitrogen-containing ligands or N-heterocyclic carbenes, oxime and imine. Most of these types of catalysts are very air, moisture sensitive and difficult to prepare and to recover. Although compounds containing sulfur was neglected as potential homogeneous catalysts due to

the extended belief of sulfur to be a catalyst poison, palladium complexes derived from chalcogen ligands (S, Se, Te) have recently emerged as highly effective catalysts and are air and moisture stable. Palladium complexes containing S, Se and Te in palladacycles, carbenes, Schiff bases and ether type ligands have been developed as highly effective phosphine-free palladium catalysts in Suzuki and Heck reactions³⁻⁵. The palladium chalcogenolate complexes owing to the stronger Pd–ER linkage may offer an attractive potential in C–C coupling reactions. However their utility as a catalyst in C–C coupling reactions remained rather unexplored due to their tendency to polymerize leading to insolubility/ sparingly solubility in organic solvents.

We have designed and developed the hybrid and hemilabile N,N-dimethylalkyldichalcogenide⁶ and 4,4'-dipyridyldiselenide⁷ ligands which can not only yield low nuclearity complexes and but also enhance complex stability and solubility. Hemilabile ligands

BARC NEWSLETTER

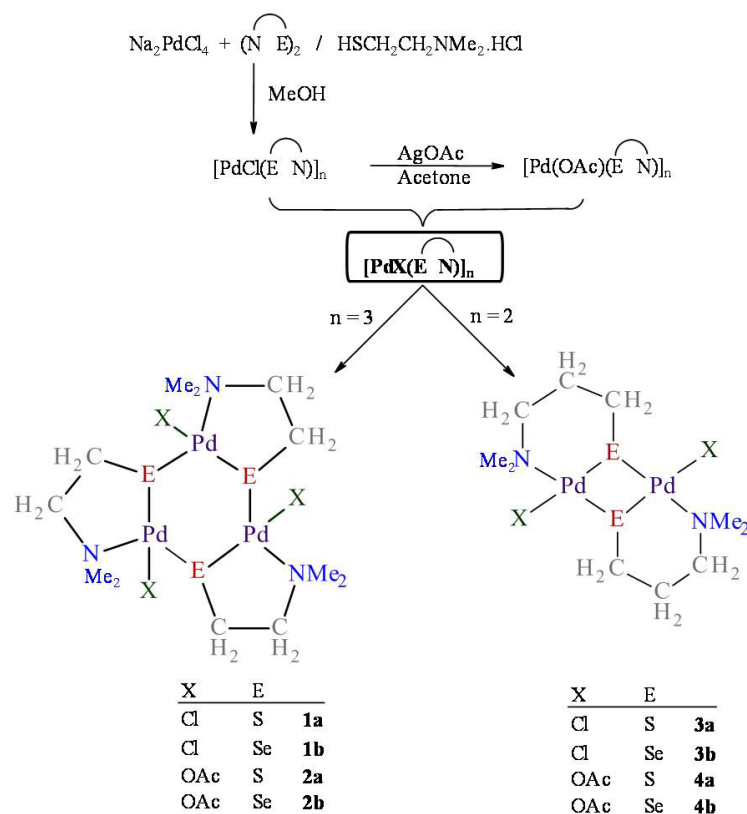
Founder's Day

have an advantage as they can protect one or more coordination sites that are formed during catalytic reaction and are also capable of stabilizing the active catalytic species/ reactive intermediates. Employing these ligands the chemistry of palladium and platinum complexes was explored. The catalytic activity of several palladium complexes were evaluated in various coupling reactions such as Suzuki^{7,8}, Carbonylative Suzuki⁹ and Sonogashira¹⁰ reactions. A few recent results are briefly discussed here.

Discussion

1. (i) Syntheses of dimethylaminoalkylchalcogenolate complexes of palladium(II)

Reactions of the ligands $(E^{\wedge}N)_2$ with Na_2PdCl_4 yielded sparingly soluble products $[PdCl(E^{\wedge}N)]_n$ ($E = S$ or Se ; $n/ E^{\wedge}N = 3/ECH_2CH_2NMe_2$ (**1**) and $2/ECH_2CH_2CH_2NMe_2$ (**3**)). Treatment of $[PdCl(E^{\wedge}N)]_n$ with silver acetate in acetone-methanol mixture at room temperature



Scheme 1: Syntheses of palladium chalcogenolate complexes.

afforded corresponding acetato-complexes, $[Pd(OAc)(E^{\wedge}N)]_n$ (**2** and **4**) (Scheme 1). Complex **4** can also be prepared by a redistribution reaction between $[Pd(OAc)_2]_3$ and $[Pd(ECH_2CH_2CH_2NMe_2)_6]$. The 1H NMR spectra of **2** displayed a resonance at ~ 2.0 ppm attributable to acetato group. The $^{13}C\{^1H\}$ NMR spectra of **2** exhibited a signal at $\delta \sim 177.3$ ppm due to carbonyl carbon. The mass spectra of **2** did not show molecular ion peaks, but fragmentation ion peaks with isotopic pattern consistent with Pd_3 species suggesting trimeric nature of **2**. The TG analysis showed that these complexes are stable up to 200 °C.

The molecular structures of dimeric $[PdX(ECH_2CH_2CH_2NMe_2)]_2$ and trimeric $[PdX(ECH_2CH_2NMe_2)]_3$ ($X = Cl$ or OAc) were established by single crystal X-ray diffraction analysis. In all these structures both the ligands 2-dimethylaminoethyl chalcogenolate and 3-dimethylaminopropyl chalcogenolate act as chelating-bridging mode. The chloride and acetate ligands are bonded as monodentate terminal groups to palladium center.

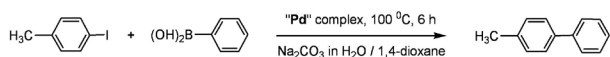
(ii) Catalysis reactions

The coupling reaction of 4-iodotoluene and phenyl boronic acid was studied in the presence of all the palladium complexes as catalysts (0.1 mol%) (Table 1). The yields of biaryls under the same reaction conditions varied between 63–98% depending on the nature of catalyst. It is evident from Table 1 that the binuclear palladium complexes (**3** and **4**) are more active than the trinuclear derivatives (**1** and **2**). Within the series the acetato complexes (**2** or **4**) are superior than the corresponding chloro compounds (**1** or **3**). The activity of the sulfur derivatives within the series was marginally higher than the corresponding selenolate complexes.

BARC NEWSLETTER

Founder's Day

Table 1: Suzuki-Miyaura cross-coupling of aryl halide with arylboronic acid.



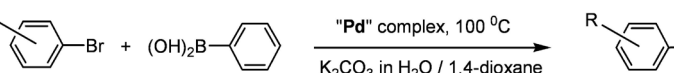
Entry	'Pd' catalyst	Yield (%)
1.	[PdCl(SCH ₂ CH ₂ NMe ₂) ₃ (1a)]	87
2.	[PdCl(SeCH ₂ CH ₂ NMe ₂) ₃ (1b)]	63
3.	[PdCl(SCH ₂ CH ₂ CH ₂ NMe ₂) ₂ (3a)]	96
4.	[PdCl(SeCH ₂ CH ₂ CH ₂ NMe ₂) ₂ (3b)]	93
5.	[Pd(OAc)(SCH ₂ CH ₂ NMe ₂) ₃ (2a)]	92
6.	[Pd(OAc)(SeCH ₂ CH ₂ NMe ₂) ₃ (2b)]	71
7.	[Pd(OAc)(SCH ₂ CH ₂ CH ₂ NMe ₂) ₂ (4a)]	98
8.	[Pd(OAc)(SeCH ₂ CH ₂ CH ₂ NMe ₂) ₂ (4b)]	92

is attributed to a trinuclear species while the other to the dimer (Scheme 2). Both di- and trimeric forms could be separated and structurally characterized. The crystal structure of [PdCl(SeC₅H₄N)(PPh₃)₂] (**7b_v**) is a centrosymmetric dimer with a *sym-trans* configuration. The two palladium atoms are held together by two bridging selenolate groups. The two pyridyl groups of the bridging selenolate adopt an *anti* configuration. The complex [PdCl(4-SeC₅H₄N)(PEt₃)₃] (**7a**) represent an example of neutral nearly triangular shaped molecule. The pyridyl ring is almost perpendicular to the metal square plane.

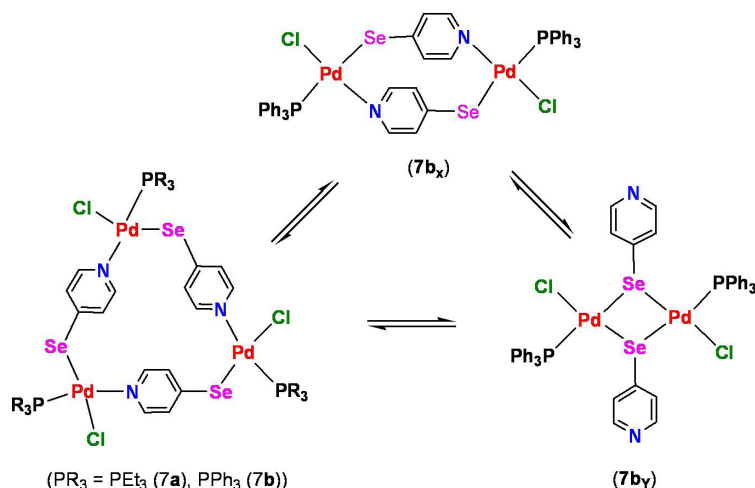
2. (i) Syntheses of 4-pyridylselenolate complexes of palladium(II)

4-Pyridylselenolate ligand has been employed to design various motifs ranging from mononuclear to trinuclear Pd complexes with the general formula *trans*-[PdX(4-SeC₅H₄N)(PPh₃)₂] (X = Cl (**5**) or SeC₅H₄N (**6**)) and *cis*-[Pd(4-SeC₅H₄N)₂(dppe)]. Reactions of [Pd₂Cl₂(μ-Cl)₂(PR₃)₂] with two equivalents of Na-4-SeC₅H₄N gave complexes of composition [PdCl(4-SeC₅H₄N)(PR₃)_n] (R = Et (**7a**), Ph (**7b**)) which were isolated as trimer/dimer containing bridging selenolate ligands. The ³¹P and ⁷⁷Se NMR spectra of **7a** show single resonances in solution but **7b** exhibit two such resonances. One

Table 2: Suzuki-Miyaura cross-coupling of aryl bromide with phenylboronic acid.



S. No.	R	Complex	mol% Pd	Time (hrs)	Yield (%)	TON
1.	4-CH ₃	5	0.1	8	27	270
2.	4-CH ₃	5	0.1	20	39	390
3.	4-CH ₃	5	0.3	8	40	133
4.	4-CH ₃	5	0.5	8	80	160
5.	4-CH ₃	7b	0.1	8	28	280
6.	4-NO ₂	5	0.1	8	91	910
7.	4-NO ₂	7b	0.1	8	97	970
8.	4-NO ₂	7b	0.01	8	62	6200
9.	2-CHO	5	0.01	6	82	8200
10.	2-CHO	7b	0.01	6	84	8400
11.	4-COCH ₃	5	0.01	12	14	1400
12.	4-COCH ₃	7b	0.01	12	29	2900



Scheme 2: Dimers and trimers of complexes [PdCl(4-SeC₅H₄N)(PR₃)_n] (**7**)

(ii) Catalysis reactions

Both **5** and **7b** were examined as catalysts in Suzuki cross-coupling reactions of arylbromide and arylboronic acid to yield biaryls (Table 2). Catalysts are tolerant to various functional groups, such as CHO, NO₂, COCH₃, etc. Cross-coupling yielded products almost quantitatively when electron deficient arylbromides were used (Table 2, entries 6-7). High yields were also obtained (> 82%) when the catalyst concentration was

BARC NEWSLETTER

Founder's Day

lowered by ten times in the case of electron-deficient arylbromides (Table 2, entries 9-10). The catalytic activity of monomeric complex **5** and trimeric-dimeric complex **7b** are comparable as both gave similar yields of biaryls under similar reaction conditions. As it is commonly believed that catalytically active species are generally monomeric which indirectly also supports the trimer-dimer-monomer equilibrium of **7b** prior to catalyst initiation.

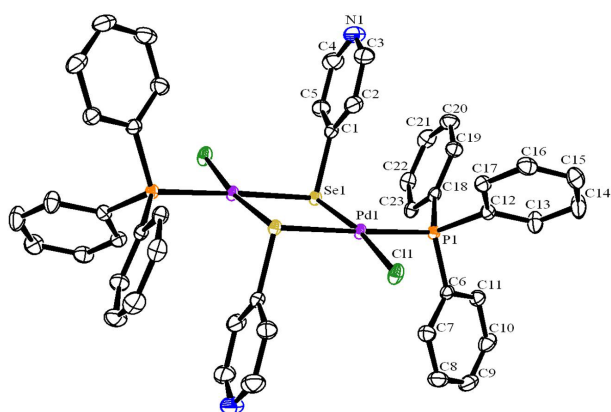


Fig. 1: Molecular structure of $[PdCl(4-SeC_3H_4N)(PPh_3)]_2$ (**7b**.)

Conclusions

The hybrid and hemilabile ligands dimethylaminoalkyl dichalcogenide and 4,4'-dipyridyldiselenide have been designed and developed. Using these ligands the chemistry of palladium and platinum complexes was explored. The nuclearity of complexes $[PdX(E^N)]_n$ is influenced by the chain length of the ligand. The non-chelating ligand 4-pyridylselenolate has a promising potential in constructing multinuclear complexes. The palladium complexes have been shown to serve as catalyst in Suzuki C–C coupling reactions. Catalytic activity of $[PdX(E^N)]_n$ follow the trend: $OAc > Cl$; $S > Se$; binuclear $>$ trinuclear.

Acknowledgements

Dilip Paluru, K. V. Vivekananda, A. Wadawale, N. Bhuvanesh and V. K. Jain are acknowledged for collaborations.

References

1. Negishi, E. Handbook of organopalladium chemistry for organic synthesis, Ed. John Wiley & Sons, Inc., 2002.
2. Wu, X.-F.; Neumann, H.; Beller, M. *Chem. Rev.* 2013, 113, 1-35.
3. Yao, Q.; Kinney, E.P.; Zheng, C. *Org. Lett.* 2004, 6, 2997-2999.
4. Kumar, S.; Rao, G.K.; Kumar, A.; Singh, M.P.; Singh, A.K. *Dalton Trans.* 2013, 42, 16939–16948.
5. Yuan, D.; Huynh, H.V. *Organometallics* 2010, 29, 6020–6027.
6. Dey, S.; Jain, V.K.; Chaudhury, S.; Knoedler, A.; Lissner, F.; Kaim, W. *J. Chem. Soc., Dalton Trans.* 2001, 723-728.
7. Vivekananda, K.V.; Dey, S.; Wadawale, A.; Bhuvanesh, N.; Jain, V.K. *Dalton Trans.* 2013, 42, 14158–14167.
8. Paluru, D.K.; Dey, S.; Wadawale, A.; Jain, V.K. *J. Organomet. Chem.* 2013, 728, 52-56.
9. Paluru, D.K.; Dey, S.; Chaudhuri, K.R.; Khedkar, M.V.; Bhanage, B.M.; Jain, V.K. *Tetrahedron Lett.* 2014, 55, 2953-2956.
10. Khairnar, B.J.; Dey, S.; Jain, V.K.; Bhanage, B.M. *Tetrahedron Lett.* 2014, 55, 716–719.

GENERATION AND THERMODYNAMIC CHARACTERIZATION OF FGM INDUCED ISENTROPIC COMPRESSION

Aditi Ray

Theoretical Physics Division

Dr. Aditi Ray is the recipient of the DAE Scientific & Technical Excellence Award for the year 2012

Abstract

The feasibility of achieving isentropic compression using functionally graded materials (FGM) has been explored in both gas gun and explosive driven systems. Qualitative analyses of temporal profiles of pressure pulse generated with various density distributions within FGM impactors showed that quadratic density variation is most suitable for this purpose. The signatures of isentropic compression are established from basic thermodynamic aspects like target temperature rise and deviation of entropy from theoretical isentrope. Optimum density profile within FGM flyer that leads to minimum entropy change found to follow quadratic variation. Further, it is shown that efficiency of spherical implosive system can be enhanced by use of FGM flyers with optimum density interval.

Introduction

High energy density (HED) physics deals with behavior of matter under extreme thermodynamic conditions of pressure and temperature. Several fields of research involve high energy density; e.g., astrophysics, geophysics, inertial confinement fusion (ICF), explosive and impact loading of materials, Z -pinch devices, etc¹. With the advent of modern laser based technologies, ICF has driven much of the development of HED physics at laboratory level, National Ignition Facility (NIF) of USA being one example of it. Realizing HED by any approach involves dynamic compression experiments where energy is deposited in a small region at extremely fast rate leading to hydrodynamic motion and propagation of shock waves. Though static compression techniques like diamond anvil cell can lead to Mbar pressures, but disadvantage associated with long time duration makes them unsuitable.

Dynamic compression is realized either in strong shock loading or isentropic compression experiments (ICE). Difference between the two is that there is an abrupt increase of material temperature by shock (ns timescale), which is in contrast to relatively low temperature rise for isentropic methods, that occur over longer (μ s) timescales. It is known that, maximum achievable compression in strong shock is limited due to irreversible heating and subsequent melting or vaporization. On contrary, there is no theoretical limit on maximum attainable compression by the latter. Thus, isentropic method offers a practical way for comprehensive determination of material response in a broad range of phase diagram that cannot be achieved by strong shock techniques.

Shock pressures are generated by impact of high velocity flyer plates accelerated in a powder gun, single/ two-stage gas gun or by burning high explosives (HE)².

BARC NEWSLETTER

Founder's Day

There are several approaches to generate ICE each with the aim of increasing peak pressure and its rise time. In laser systems, it is realized by suitably tailoring the pulse shape³. Other approaches include: multiple shock, shock reverberation and shaped current pulses for magnetic compression⁴.

Recent advances in fabrication of FGM have opened a new front in generating smooth, continuous isentropes in gas gun devices^{6,7}. FGMs are composite materials with composition varying along thickness in such a way that certain material property is allowed to vary continuously or step-wise from one side to the other. The idea of varying density along the thickness is to generate a smooth variation of shock impedance, which is the product of density and shock speed. We have carried out detailed study on generation and thermodynamic characterization of isentropic compression wave by FGM^{7,8}. The present article provides a brief description of our achievements towards generating ramp pressure waves and brings out new insight in this area.

Isentropic loading in gas gun system

Simulation of typical hydrodynamic experiments performed by impact loading of normal and FGM flyers accelerated by gas gun, as displayed in Fig. 1, shows longer rise time of pressure pulse obtained by FGM. Isentropic compression is characterized from the temporal profiles of pressure pulse applied at target by different functional forms of density variation along FGM thickness. Quantitative analysis supported by physical reasoning enables us to arrive at

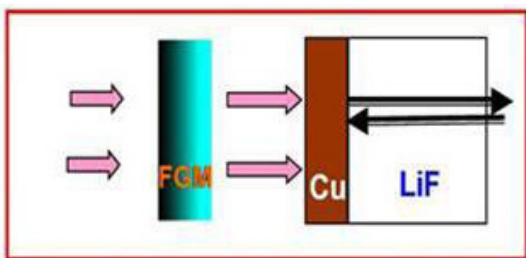


Fig.1: Schematics of impact loading exp., either in gas gun or HE burn

the conclusion that quadratic variation is best density profile for FGM layers for generating ideal ramp compression⁷. Simulation results for pressure profile with 1 km/sec impact of Al, linear (L) and quadratic (Q) FGM flyers on to Cu target are illustrated in Fig. 2. In case of LFGM, peak pressure as well as its rise time is more, but the pulse shape does not have characteristics of ideal isentrope. The pulse shape is reminiscent of linear ramp wave with QFGM. Profile of target-window interface velocity, measured through VISAR techniques, followed similar ramping pulse⁷.

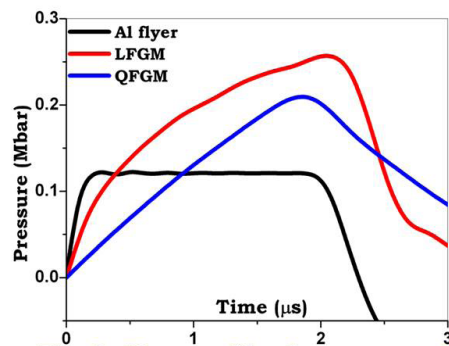


Fig.2: Time profile of pressure pulse applied to a target by normal, linear and quadratic FGM flyers

Isentropic loading by HE driven FGM plates:

Since flyers can be accelerated to higher velocities by explosive burn, the possibility of generating isentropic wave in HE driven FGM plate impact has also been explored. Our study revealed the first observation that with moderate flying HE driven QFGM produces smooth ramp pressure pulse leading to an ideal isentrope, as displayed in Fig. 3. Pressure pulse in

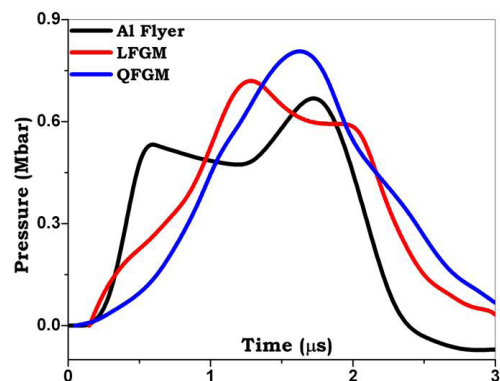


Fig.3: Pressure profile for HE driven normal and graded density flyer impact

BARC NEWSLETTER

Founder's Day

contact geometry shows up an undesirable initial spike due to shock jump⁷. Moreover, peak pressure realized in HE driven system is much greater than what can be achieved by gas gun system with identical FGM flyer.

Thermodynamic characterization of FGM induced isentropes: Signatures of isentropic compression have been identified from basic thermodynamic aspects of target temperature rise and entropy increase from an ideal isentrope. Theoretical evaluation of EOS temperatures along Hugoniot and FGM induced isentropes show that for significant compression the temperature rise by shock pressure is much larger than that generated by any kind of FGM flyer⁸. Nevertheless, target heating due to all types of FGMs are nearly same. Fig. 4 compares target temperature for Hugoniot pressure and isentropic pressures of Fig. 3, delivered by HE driven QFGM.

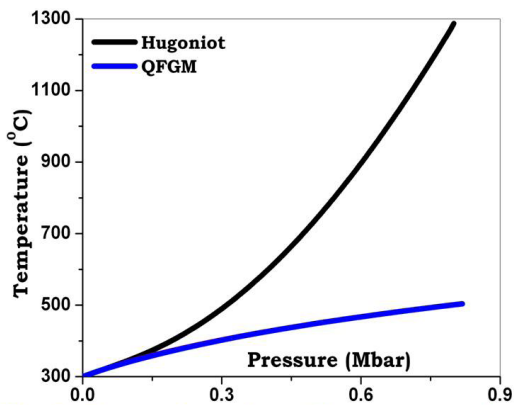


Fig.4: Temperature rise with pressure along Hugoniot and HE driven FGM flyer impact

Increase in entropy on any arbitrary (P-V) state from an ideal isentrope is the measure of irreversible energy loss due to shock heating. Thus lower this entropy deviation, better it is for ICE. Fig. 5 displays the entropy increase as a function of pressure along Hugoniot and isentropes obtained with linear and quadratic FGMs in gas gun acceleration. It is clear that entropy change by FGM loading is nearly two orders of magnitude smaller than that of Hugoniot⁸. It is also obvious that, QFGM is most suitable as it leads to least entropy change for a specific peak pressure.

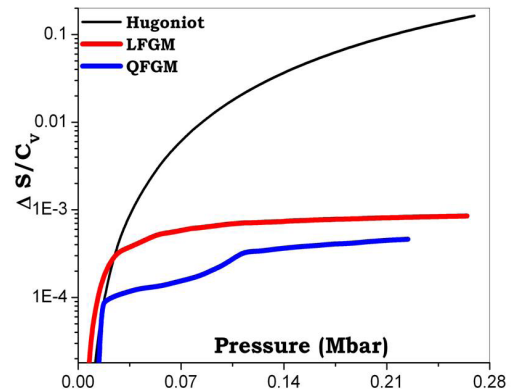


Fig.5: Entropy production vs pressure for Hugoniot and FGM induced isentropes

Further, optimum density profile of a 14-layer FGM flyer that produces minimum entropy at target with pre-decided peak pressure has been obtained by finding densities of individual layer through optimization technique. Interestingly, profile fits very well with quadratic function as shown in Fig. 6

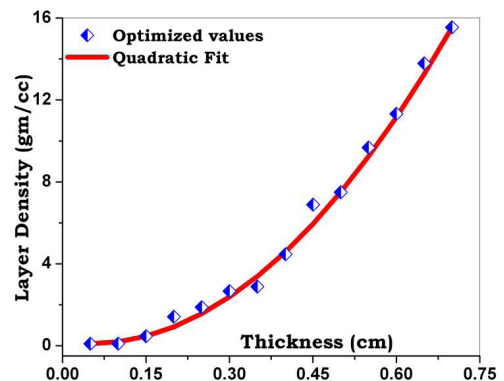


Fig.6: Optimized density profile of FGM for least entropy production

Effect of FGM flyer in spherical geometry: Due to converging detonation waves produced by explosive burn, it is possible to achieve higher velocities and pressures in spherical geometry than planer case. Our simulation of spherical implosion system, as depicted in Fig. 7, shows that use of FGM flyer enhances impact velocity, W at target to some extent for LFGM and to a great extent with QFGM, as compared to normal flyer⁷. Table-1 compares the maximum attainable impact velocities for Fe flyer and those found by optimizing densities of front and rear layers of FGM flyers with given configuration.

BARC NEWSLETTER

Founder's Day

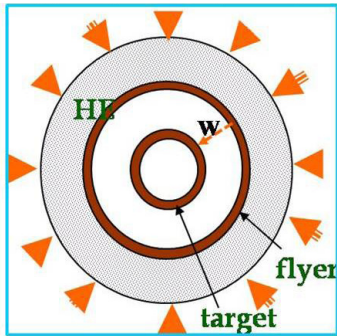


Fig.7: Typical spherical implosion system

Table 1: Optimized density intervals for LFGM and QFGM corresponding to maximum impact velocity

Imp. Type	ρ_{min} gm/cc	ρ_{max} gm/cc	W km/s
Fe	-	7.85	6.13
LFGM	0.94	10.43	8.58
QFGM	0.94	6.02	8.90

Conclusions

Results of detailed hydrodynamics simulations of dynamic compression experiments for generating isentropic pressures are presented. The main conclusions emerging from the studies are: shape of pressure pulse can be suitably tailored by appropriate density variation within FGM and quadratic FGM is best choice for ICE since it produces linear ramp pulse with least temperature rise and entropy production in the target.

Acknowledgements

Author is indebted to Dr. Vinod Kumar and Dr. N. K. Gupta for constant encouragement and technical support provided during this work.

References

1. R.P. Drake, High-Energy-Density Physics: Fundamentals, Inertial Fusion, and Experimental Astrophysics, Springer-Verlag (2006)
2. W. J. Nellis, *Rep. Prog. Phys.* 69, 1479 (2006).
3. K.T. Lorenz, M.J. Edwards, A.F. Jankowski, S.M. Pollaine, R.F. Smith, B.A. Remington, *High Ener. Dens. Phys.* 2, 113 (2006).
4. D.B. Hayes, C.A. Hall, J.R. Asay, M.D. Knudson, *J. Appl. Phys.* 96, 5520 (2004).
5. N. Holmes, *Sci. and Tech. Rev. LLNL*, Livermore, (2000).
6. J.H. Nguyen, D. Orlikowski, Frederick H. Streitz, John A. Moriarty, and Neil C. Holmes, *J. Appl. Phys.* 100, 023508 (2006).
7. A. Ray and S.V.G. Menon, *J. Appl. Phys.* 105, 064501 (2009)
8. A. Ray and S.V.G. Menon, *J. Appl. Phys.* 110, 024905 (2011)

BARC NEWSLETTER

Founder's Day

R&D RELATED TO EAR, NOSE AND THROAT AT THE MEDICAL DIVISION

Nalini Bhat

Department of ENT, Medical Division

Dr. Nalini Bhat is the recipient of the DAE Scientific & Technical Excellence Award for the year 2012

Abstract

As an ENT specialist Dr. Bhat handles cases related to ear, nose, throat and cancers of the head and neck region in her practice. Besides routine and emergency clinical and operative work she is also a teacher for post- graduate training in ENT (accredited by Diplomate of National Board) and guides her students in their thesis work. Her main areas of interest are hearing loss and its rehabilitation, endoscopic sinus surgery and speech disorders. She has upgraded her department to offer state of the art facilities in these sub-specialities of ENT. She has started the neonatal screening for hearing loss programme and the cochlear implant programme at her department. The department also has a computerized, modern speech laboratory and a multidisciplinary thyroid clinic. She has started sialendoscopy facilities. This is the current recommendation to handle benign salivary gland disease and is being offered by very few centres across the country. She is also currently researching the role of genetic mutations in people with severe congenital deafness.

As part of her R&D, Dr. Bhat studied the various presentations of tuberculosis of head and neck that she had come across in her practice. The retrospective study included 117 patients of primary head and neck TB. Clinical presentations of different areas affected and the diagnostic modalities used in various settings are discussed in the paper. Cervical lymphadenopathy was the commonest presentation followed by laryngeal tuberculosis. Other areas such as retropharyngeal, cervical spine, oropharynx etc were solitary cases. FNAC is a very easy and reliable method to diagnose TB. However newer diagnostic tests should be used in suspected cases if FNAC is negative. The study stresses the need to rule out lung or other systemic TB, in cases of head and neck TB. It also recommends culture and drug sensitivity, at least in cases of previous or subsequent TB, to reduce the problem of multidrug resistance TB. The subjective level of satisfaction in patients of presbycusis using monoaural hearing

aids from Feb 2008 to Sept 2009 was studied, and the various attributes affecting hearing aid use among patients. The study reported a significantly high level of satisfaction among hearing aid users (74%). Almost half the subjects reported no problems with their hearing aids. Subjects with mild hearing impairment were less satisfied with their hearing aids than the others. Most people under used their hearing aids even when they were satisfied. Subjects with severe hearing loss used their hearing aids for longer duration daily. Thus Mono-aural hearing aid fitting was found to be a satisfactory and a cost effective option of rehabilitating people with age related hearing loss, especially in developing countries like ours. This book is a useful guide for all ENT surgeons who are performing endoscopic sinus surgery or are keen to learn the same. The chapter outlines the diagnosis of sinusitis based on clinical guidelines, nasal smears and imaging modalities. Each of these has been discussed

BARC NEWSLETTER

Founder's Day

in detail and flow charts have been presented to assist the reader in step-wise management of different situations in sinusitis. Also a pre-operative checklist, pre-anaesthesia preparation and surgical planning have been discussed. A consent form specifically for ENT surgeries has been presented and recommended. The chapter stresses on the need for a thorough pre-operative preparation and has suggested a step-wise approach so as to significantly improve the chances of success in sinus surgery. She has also published a number of unusual case reports that she has come across in her practice with a view to increase awareness regarding incidence, presentation, diagnosis and treatment of these unusual cases. This is a report of an interesting case of anaplastic thyroid carcinoma, (a rare, extremely aggressive tumour) in a colloid goiter of long standing, in a 80 year old lady who went on to develop lung metastasis and a paraneoplastic syndrome in spite of good regional control. Epithelial-myoeplithelial carcinoma (EMC) arising from the minor salivary gland of the hard palate is very rare. Besides the rarity of the case, diagnostic difficulties are discussed. FNAC and histomorphology though suggestive were not diagnostic. Immunohistochemistry was used to clinch the diagnosis. Post treatment outcomes were extremely good. Lipomas though common benign tumours, are uncommon in the oral cavity and account for only 1-5 % of all the oral benign neoplasms. This case of lipoma of tongue was presented in view of its rarity. A 71 year old man presented with a history of a slowly enlarging, painless mass on right side of tongue since 1 month. A presumptive diagnosis of lipoma was based on the clinical and MRI findings. The tumour

was excised enbloc, transorally. Histopathologic examination of the tumour confirmed that it was a lipoma.

References

1. Bhat Nalini, Subramaniam Vinayak: Tuberculosis in ENT practice –its diagnosis and presentation. *American Journal of Otolaryngology and Head and Neck surgery*. Vol 27, pg 39-45. Jan 2006.
2. Bhat, Nalini: Hearing aids- Statistical Analysis and satisfaction survey in patients with presbycusis .” Poster presentation at the Annual Conference of the Indian Society of Otology in Feb 2010. (Recd. The First Prize).
3. Prabodh karnik, Nalini Bhat, Shalaka Shewale, Roshini Nambiar: Pre-operative Considerations in Endoscopic Sinus surgery. *Functional Endoscopic Sinus Surgery. ECAB Clinical Update: Otorhinolaryngology*. pg 20-40. Publishers – Elsevier, 2012.
4. Nalini Bhat: Anaplastic thyroid carcinoma with paraneoplastic Syndrome – a case report. *Journal of Post graduate Medical Education, Training and Research*, Vol 2, no 4, July-Aug 2007.pg 55-57.
5. Susan Cherian, R.K. kulkarni, Bhat Nalini: Epithelial- myoeplithelial carcinoma of Hard Palate- a case report. *Acta Cytologica*, Vol 54 Sep-Oct 2010. No. 5, pg 835-839.
6. Shewale S.S., Bhat, N.R., Hansrajani, V., Vaidya, S.I.,: Lipoma of tongue. *Gujrat J Otorhinolaryngology and Head & Neck Surgery*, Vol. 8 No. 3, December 2011, 48-49.

DESIGN AND DEVELOPMENT OF COMPACT PULSE FORMING LINES

Surender Kumar Sharma & Anurag Shyam
E&ED

Dr. Surender Kumar Sharma is the recipient of the
DAE Young Engineer Award for the year 2012

Abstract

Pulse forming line (PFL) is an important subsystem of pulsed power system for shaping and delivering fast pulses to the load. PFLs with higher dielectric constant ceramics materials and alternative engineering topologies are designed and developed to reduce its size. A novel technique is also proposed using the transmission line characteristics of the PFL to generate fast repetitive double pulse (~ 100 ns) with very short (~ 30 ns) inter pulse repetition interval.

Keywords: Pulsed Power, PFL, Ceramic, Helical

Introduction

Pulsed power is a technology to accumulate energy over a longer duration of time and then releasing it in a shorter duration, thus increasing the instantaneous power levels (Fig 1).

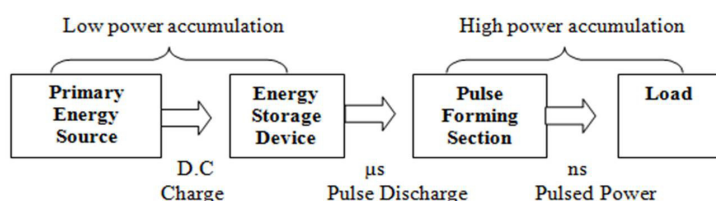


Fig 1. : Block diagram of pulsed power system [1]

This technology can be found useful for industrial, medical and environmental applications. Nowadays, the pulsed power field is driven by size, weight, and volume constraints and certain applications require technology that can be deployed in smaller volume.

Compact Pulsed Power

Compact pulsed power technologies are characterized by concentration of energy both in time and size to

generate pulses of high intensity. The development of compact pulsed power technologies requires combined efforts at three levels: efficient and robust devices at component levels, novel circuits and architecture at the system level, and effective technique to deliver fast pulses at the application levels. The pulse conditioning system is an important part of pulsed power system, its general functions are the storage, switching, and scaling [2].

Compact Pulse Forming Line

Transmission line based PFL can be made by using commercially available coaxial cables or by putting two/three concentric cylinders with suitable dielectric filled between them. The design of PFL includes optimization of inner and outer radius of the coaxial cylinder of length, dielectric material (ϵ_r), to get required pulse duration (τ) and source impedance (Z_0).

BARC NEWSLETTER

Founder's Day

Development of Solid dielectric PFL using ceramic material

The length of the PFL is, $L \sim 1/\epsilon^{1/2}$. The higher ϵ can lead to shorter length of the PFL. The ceramic material has large dielectric constant (> 100) and is ideal for energy storage in PFL. Barium Titanate ceramic was not widely used in pulsed power systems because of its piezoelectric properties. A composite dielectric PFL is designed and developed using barium titanate and neoprene rubber [3]. Rubber is an elastic material, when local stresses are developed in barium titanate during the high voltage discharges the rubber will expand and contract to absorb the stress.

Fabrication of barium titanate – rubber PFL

A coaxial PFL was made using two SS 304 cylinders of length ($l = 350\text{mm}$) (Fig 2). The inner and outer diameter, and the thickness was 120 mm, 240 mm and 2 mm respectively.



Fig. 2: Barium Titanate Rubber PFL

The volume between the two cylinders was filled with composite mixture of barium titanate and neoprene rubber. The composite mixture was prepared by mixing barium titanate of 1-3 micron size with neoprene rubber in the ratio of 1:10. Other additives are added for the curing of the rubber and mixed in rolling mill

for an hour, and then it is filled between the cylinder by heating the mixture and then gradually cooling it to room temperature. The parameters measured of the composite dielectric PFL are inductance (48 nH), capacitance (2.4 nF) and impedance (4.5 Ω).

Measurement of dielectric constant of the composite dielectric

A disc of composite dielectric was cut to measure its dielectric constant. The diameter (d) and the thickness (t) of the composite dielectric material disc are 90 mm and 10 mm. The dielectric constant (ϵ_r) of the composite dielectric material of capacitance (C) and area of disc ($A = \pi d^2$) is, $\epsilon_r = \epsilon_r \frac{C \cdot t}{\epsilon_0 \cdot A}$. The capacitance was measured to be 475 pF. The dielectric constant of the composite dielectric was calculated to be 85.

Testing of barium titanate – rubber PFL

The PFL was pulse charged with pulse transformer and discharged through sparkgap across 5 Ω resistive load. The pulse transformer charge the composite dielectric PFL to 120 kV, the sparkgap switch after the PFL breaks and the PFL discharge into the 5 Ω resistive load. A high voltage pulse of 70 kV, 21 ns pulse was measured across the load (Fig 3). The compactness in length of the PFL was achieved by mixing of barium titanate in neoprene rubber, which reduces the length of the PFL by a factor of 3.8 as compared to neoprene rubber ($\epsilon_r = 6, \mu_r = 1$) dielectric material PFL.

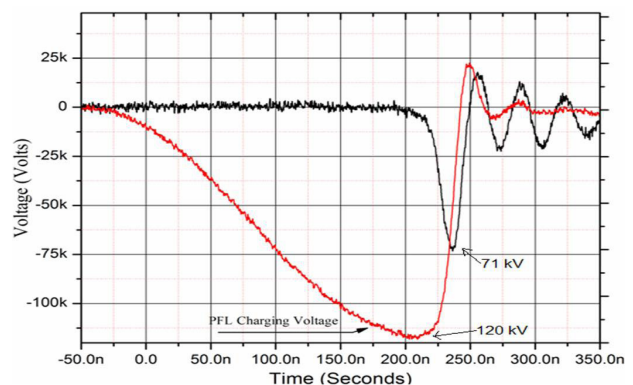


Fig. 3: PFL charging and load voltage

BARC NEWSLETTER

Founder's Day

Investigation of non linear effect of electric field on composite dielectric

The ceramic materials behave non-linearly with different applied electric field [4]. The composite dielectric PFL was charged at different voltage and discharged across the load. The duration of pulse width ($T = 2 \frac{\sqrt{\epsilon_r \mu_r}}{c} l$) across the load depends on dielectric constant and the length of the PFL. The pulse width was measured experimentally with applied electric field (Fig 4). The length of the PFL was fixed and we found no variation in the value of dielectric constant of the composite dielectric up to the electric field strength of 20 kV/cm.

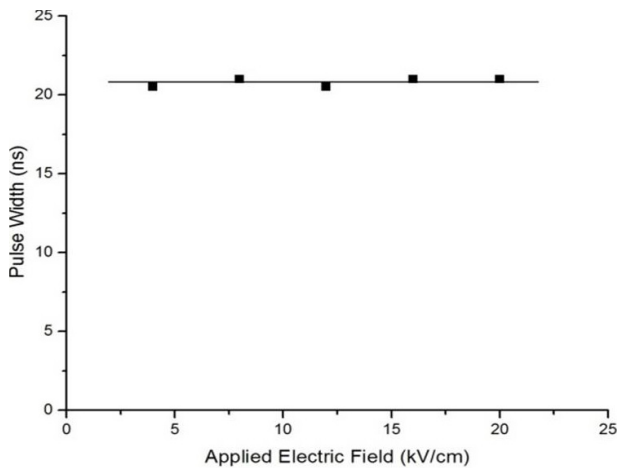


Fig 4. Pulse width measured at different applied electric field

Development of water helical PFL

Deionised water is used as liquid dielectric medium in PFL because of its high dielectric constant and high dielectric strength [5]. The length of the coaxial PFL increases for the generation of longer duration pulses. The pulse width can also be increased by using helical inner conductor as it has higher inductance and also increases the transit time [6].

Fabrication of water helical PFL

Water helical PFL was designed and developed (Fig 5). The helical PFL inner conductor was made up of 13 turns of SS-304 strip (Width, thickness = 39.5 mm, 0.5 mm) rolled on the delrin cylinder (Diameter =

168 mm). The outer cylinder was made up of SS-304 (Diameter, thickness = 237 mm, 2mm). The length of the PFL was 800 mm. The impedance of the helical PFL is 22 Ω . The volume between the inner strip and outer cylinder was filled with deionised water circulated through a pump and deionizer unit.

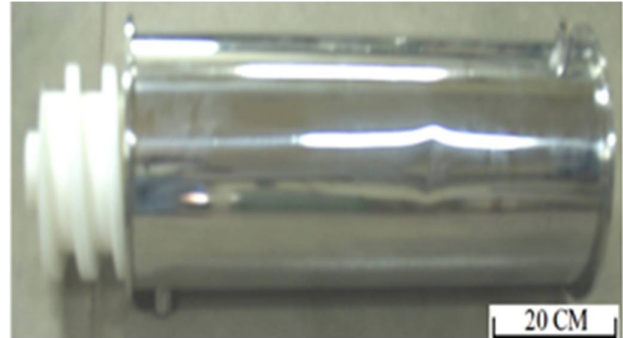


Fig 5. Water helical PFL

Testing of water helical PFL

The performance of helical PFL is tested by pulse charging it to 200 kV and discharging it across the matched resistive load (22 Ω). The voltage pulse was measured across the helical PFL and the load (Fig 6). The helical PFL produces 100 kV, 260 ns pulse across the matched load. So, the pulse width of 260 ns is generated with 800 mm length of the helical PFL, as compared to coaxial PFL, which generates 50 ns pulse with 800 mm length of the PFL.

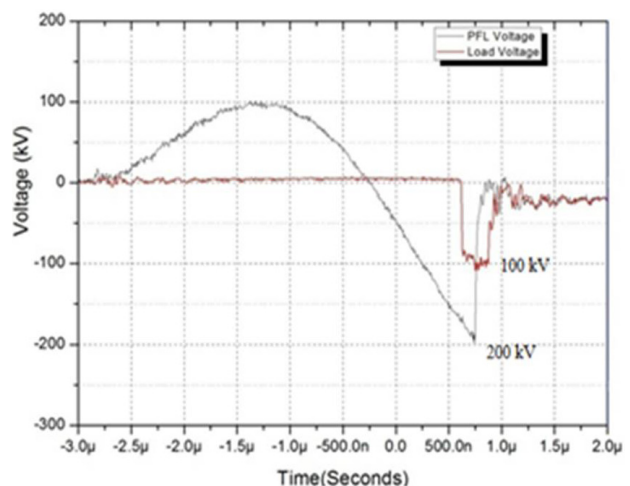


Fig 6: PFL charging voltage and load voltage

BARC NEWSLETTER

Founder's Day

Effect of reduction in water temperature on the pulse width

The deionised water inside the helical PFL was circulated through a water chilling unit and its temperature was reduced from 25 °C to 5 °C, the pulse width was experimentally measured across the matched load at different temperature (Table 1). The increase in pulse width was due to increase in the relative permittivity of the water with the reduction in temperature of water. The relative permittivity of the water increases with the reduction in the temperature of the water [5]. The dependence of relative permittivity of water on the temperature is given by (i)

$$\epsilon_r = 78.54 (1 - 4.579 \times 10^{-3} T_1) + 1.17 \times 10^{-5} T_1^2 - 2.8 \times 10^{-8} T_1^3 \quad (i)$$

Where $T_1 = T_0 - 25$, T_0 is Temperature in (°C)

Table 1: Pulse width measured at different temperature

Water Temperature	Pulse width (FWHM)
25 °C	260 ± 1 ns
20 °C	265 ± 1 ns
15 °C	270 ± 1 ns
10 °C	275 ± 1 ns
5 °C	280 ± 1 ns

The increase in relative permittivity with decreasing temperature is due to decrease in thermal agitation of molecular dipole of water. The relative permittivity of water was experimentally measured at different temperature (Fig 7).

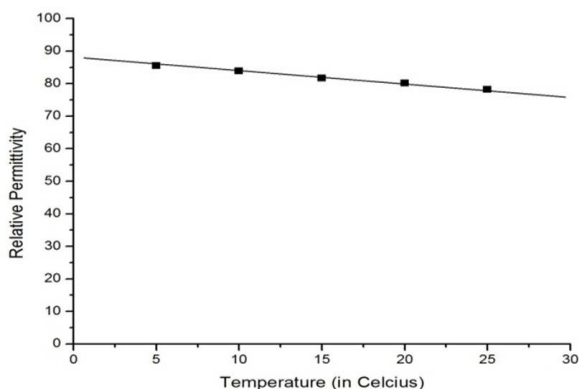


Fig. 7: Experimentally relative permittivity measured at different temperature

The pulse width generated across the load increases up to 6 % with the reduction in the temperature of the water from 25°C to 5°C. So the length of the PFL can further be reduced with the cold water circulation and the size of the PFL can be reduced.

Fast repetitive double pulse generation using compact PFL

The repetition rate of the pulsed power system is determined by various factors such as the capacitance or inductance of electrical circuit, power supply, load characteristic and switch etc [7]. Transmission line characteristics of the helical PFL was investigated to generate fast repetitive double pulse with extremely short inter pulse repetition interval [8]. Fast repetitive double pulse could be used to study double pulse laser ablation [9]. The two turns at the input side of the helical PFL are covered with 3 mm of ethylene propylene rubber tape ($\epsilon_r \sim 3$) on the SS strip (Fig 8).

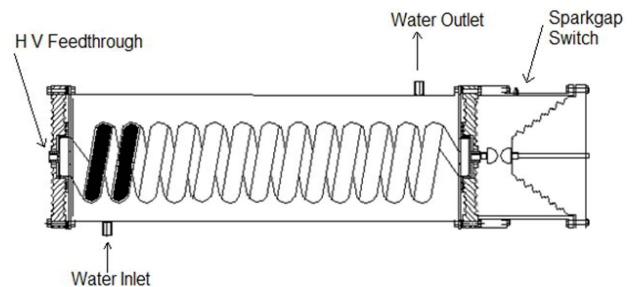


Fig. 8: Inner conductor of helical PFL

The testing was done by pulse charging the helical PFL to 200 kV and discharging it into the matched

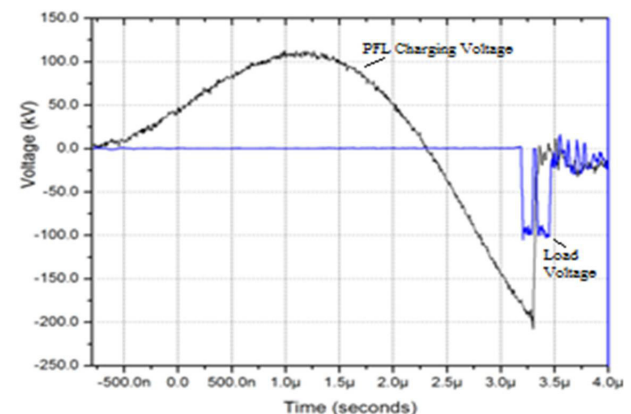


Fig. 9: Voltage measured across PFL & load

BARC NEWSLETTER

Founder's Day

22Ω resistive load, while discharging it generates two fast pulses of 100 kV, 100 ns with 30 ns inter pulse repetition interval across the load (Fig 9).

When high voltage was applied to the inner conductor of the helical PFL and pulsed charged to 200 kV, the water capacitor was fully charged where there was no ethylene propylene rubber on the SS strip inner conductor. At the input side of the PFL maximum potential appears across the ethylene propylene rubber, and the water capacitor was charged to lesser extent due to its higher relative permittivity compared to that of ethylene propylene rubber. The self breakdown sparkgap switch closes at 200 kV and the PFL discharges into the load. While discharging the forward voltage wave travels towards the source and voltage appears across the load. The voltage across the load appears till it discharges up to the initial 2 turns. Then there was less voltage across the water capacitor above the ethylene propylene rubber, so no voltage appears across the load. When the wave is reflected from the input end due to the high impedance of pulse transformer it again appears across the load after the end of the 2 turns. So, the two pulses of 100 kV, 100 ns pulse width and interval of 30 ns between the pulses appears across the load.

Conclusion

The compactness of the PFL depends on the length of the conductor (l), dielectric constant (ϵ_r) and temperature of the medium. Compact PFLs were developed using high dielectric constant composite dielectric material and an alternative topology using helical inner conductor for pulse compression. A novel technique is also developed using the transmission line characteristics of the helical PFL for generation of very fast repetitive pulse with very short inter pulse repetition interval.

References

1. I.R. Smith, B.M. Novac, "An Introduction to the Physics and Technology of Pulsed Power", Taylor and Francis Publisher (2010)
2. Nunnally W.C., "Critical component requirements for compact pulse power system architectures", *IEEE Trans. on Plasma Sci*, 33,1262-1267 (2005)
3. S.K. Sharma, P. Deb, R. Shukla, T. Prabakaran & A. Shyam, "Compact pulse forming line using barium titanate ceramic material", *Rev. of Sci. Instrum*, 82, 115102 (2011)
4. C.R. Wilson, M.M. Turner and P.W. Smith, "Electromagnetic shock-wave generation in a lumped element delay line containing nonlinear ferroelectric capacitors" *IEEE Trans. Electron Devices* 38, 767 (1991)
5. A.I. Gerasimov, "Water as insulator in pulsed facilities", *Instruments and Experimental Techniques*, Vol 48. No. 2, pp 141 – 167 (2005)
6. S.K. Sharma, P. Deb, A. Sharma, R. Shukla, T. Prabakaran, B. Adhikary & A. Shyam, "Compact helical pulse forming line for longer duration rectangular pulse generation", *Rev. of Sci. Instrum.*, 066103 (2012)
7. Schneider L., Reed K., Harjes H., Pena G., Martinez L., Harden M., presented at 12th IEEE International Pulsed Power Conference, Vol 1, 523 - 527 (1999)
8. S.K. Sharma, P. Deb, Archana Sharma & A. Shyam, "Fast double pulse system using the transmission line characteristics of the PFL", *Rev. of Sci. Instrum*, 83,115108 (2012)
9. S.K. Sharma, P. Deb, R. Kumar, Archana Sharma and A. Shyam, "Compact pulsed power driver for double pulse effect studies in nanosecond laser ablation", *IEEE Trans. Plasma Sci.* 41 (10), 2609 (2013)

BARC NEWSLETTER

Founder's Day

DEVELOPMENT OF OXIDATION RESISTANT HIGH TEMPERATURE MO BASED ALLOY

Bhaskar Paul and R.C. Hubli
Materials Processing Division

Shri Bhaskar Paul is the recipient of the
DAE Young Engineer Award for the year 2012

Abstract

Refractory metal intermetallic composites (RMICs) are being pursued as high temperature material beyond nickel based alloys. The results on in-situ synthesis of Mo based RMIC and its characterization have been presented in the present article. Silicothermic co-reduction and reaction hot pressing techniques were explored to prepare Mo-16Cr-4Si (wt.%) alloy. The multiphase alloy was consisted of Mo_3Si and discontinuous (Mo, Cr) (ss) phase with volume percentage of 28%. The synthesized alloys were characterized with respect to composition, phases, microstructure, hardness and their oxidation behaviour. The composite shows an excellent balance of low temperature mechanical properties with promising environmental resistance at temperatures above 1000 °C.

Introduction

Design of high temperature structural material having favorable properties such as high temperature oxidation resistance, strength, creep resistance on the one hand and room temperature fracture toughness on the other is a challenging task in materials science. Maximum operating temperature capability of superalloys has risen significantly, but eventually it faces melting point limitation of major alloying element e.g. Co, Ni. The next choice is the refractory metals and alloys, because of their high melting points and high temperature strength. Amongst the various refractory metal alloys, molybdenum based alloys are considered as most attractive and promising due to their superior high temperature properties such as excellent creep and tensile strength at elevated temperature, adequate compatibility with molten metals such as Pb, Pb-Bi eutectic etc. and exceptionally high melting temperature. The major barrier to the use of molybdenum based alloys for high-temperature applications is their catastrophic

behaviour under oxidizing environments. In contrast, molybdenum silicides have excellent high-temperature oxidation resistance with high melting point. However silicides in monolithic form have inadequate damage tolerance and extremely low fracture toughness and the suitability for the practical applications of these materials as structural components, thus are hindered by these drawbacks. It has been reported in some literature that the fracture toughness of silicides can be improved by incorporating a ductile Mo phase i.e., ductile phase toughening or refractory metal-intermetallic composites (RMICs). It is known from the binary phase diagram of Mo-Si system that below 9.0 wt.% of Si, the microstructure consists of Mo and Mo_3Si . The oxidation resistance of Mo_3Si has been found to be enhanced by the addition of Cr due to the formation of thermally stable impervious oxide layer of Cr_2O_3 . The multiphase approach has led to the study of the systems such as Mo-Cr-Si provide a high level of freedom in selecting compositions of the constituent phases in order to obtain a more favorable balance of high temperature strength, creep, good oxidation

BARC NEWSLETTER

Founder's Day

resistance and at the same time damage tolerance ability particularly at lower temperatures.

The primary objective of this study to investigate the effectiveness of the Mo-Cr-Si alloy system as an oxidation resistant alloy.

Preparation of the alloys

The Mo-16Cr-4Si was prepared by two methods:

Hot pressing

Elemental powders of Mo, Cr and Si with a purity of 99.9% and an average particle size of 5, 8 and 6 microns, respectively, were thoroughly mixed, in the desired composition ratios of Mo-16Cr-4Si (wt.%) alloy using a turbo-mixer unit. The mixed powder was uniaxially pressed under 200MPa into pellets with dimensions of $\Phi 25\text{mm} \times 20\text{ mm}$. Green densities of the samples were measured using the geometrical dimensions. The compacts were placed into a graphite die and then hot-pressed under vacuum at 1600°C for 3 to 5 h by applying a pressure of 10MPa. The hot pressed alloy pellets were grinded from all sides to remove the graphite (C) layer using standard metallographic grinding techniques. Sintered densities were determined through the immersion method based on the Archimedeian principle using alcohol as the liquid medium. The polished sintered samples were etched using a mixed solution of 5 ml HNO_3 , 10 ml HF, 15 ml H_2SO_4 and 50 ml H_2O , and the microstructure of the specimens were observed under SEM. X-ray diffraction pattern was recorded for characterizing the phases evolved after hot pressing.

Co-Reduction method

An alternative self sustaining synthesis route for synthesis of high temperature material is "Co-reduction

synthesis route" In this process, metal oxides are co-reduced simultaneously by a reductant which could be anyone or a combination of Al, Si, Ca, B, Mg etc. and the reactions which when triggered goes to completion because of their own exothermic heat. This process has many distinct advantages over other melting processes such as relatively high proportion of metallic products, low processing cost, fast process rate, high energy and time efficiency, may or may not require external heating from high-temperature furnace, flexibility of batch size etc.

In the present study, attempts have been made to prepare Mo-16Cr-4Si (wt.%) alloy by co-reduction smelting technique using Si as reductant.

Characterizations and Property evaluation:

Microstructural characterization

Fig-1a and Fig-1b show the microstructures of the co-reduced and hot pressed Mo-16Cr-4Si alloy, showing two different contrast regions, namely white and black. The quantitative microanalyses in these regions were carried out by EDS for evaluating the compositional variation. From the composition of the two phases, it is seen that the first phase (phase-A) appearing light (white) is made up of a solid solution phase, basically of Mo and Cr, containing small amount of Si. The second phase (phase-B, appearing dark) is made up of $(\text{Mo, Cr})_3\text{Si}$ intermetallic phase, which has been confirmed by the XRD analysis.

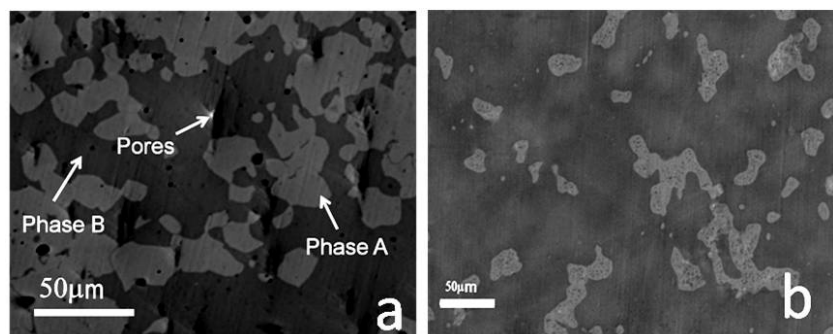


Fig.1: BSE image of Mo-16Cr-4Si prepared by (a) hot pressing (b) silicothermic co-reduction

BARC NEWSLETTER

Founder's Day

Oxidation Studies

Specimens were cut from the prepared alloy button followed by polishing and ultrasonically cleaning in acetone. For isothermal oxidation studies, polished sintered samples of approximate size of $10 \times 5 \times 5$ mm were introduced into the furnace in an alumina crucible when the furnace temperature reached the set value. For isothermal experiments, samples were oxidized for different time intervals up to 50 h. Each sample was carefully weighed before and after exposure to determine the weight changes during the oxidation. Phases present on the surface of the oxidized samples were characterized by XRD. The morphology and nature of oxide layer were investigated by observing the surface in SEM.

Fig. 2a shows the data of weight change per unit area with time, obtained during isothermal oxidation at different temperatures. Initially the rate of mass loss is high, because of the volatilization of MoO_3 at all the isothermal conditions. Later on, the oxidation rates decrease substantially due to the formation of the protective mixed SiO_2 and Cr_2O_3 layer over the alloy surface. Formation of the cristobalite phase of SiO_2 (matched with JCPDS 820403) and Cr_2O_3 (matched with JCPDS 841616) have been confirmed by XRD analysis of surface oxide layer of the alloy after 50 h, shown in the inset of Fig. 2b.

Fig. 2b shows the SEM images of the oxidized surfaces of the alloy after oxidation at 1000°C for 5 and 50 h. The morphologies of the oxide scales are particulate

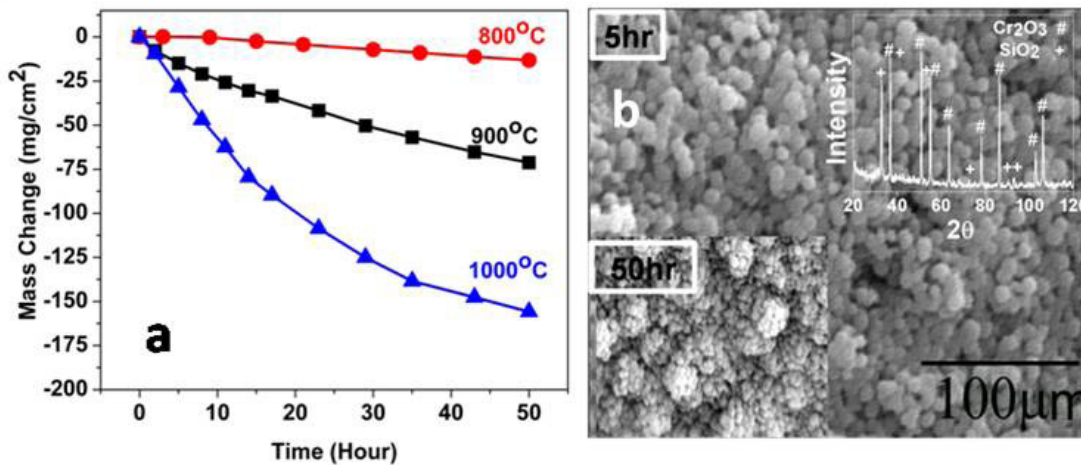


Fig-2 (a) weight change per unit area with time at different temperatures (b) SEM images of the oxidized surfaces of the alloy after oxidation at 1000°C for 5 and 50 h. Inset shows the XRD of the oxidized surfaces of the alloy after oxidation at 1000°C for 50h.

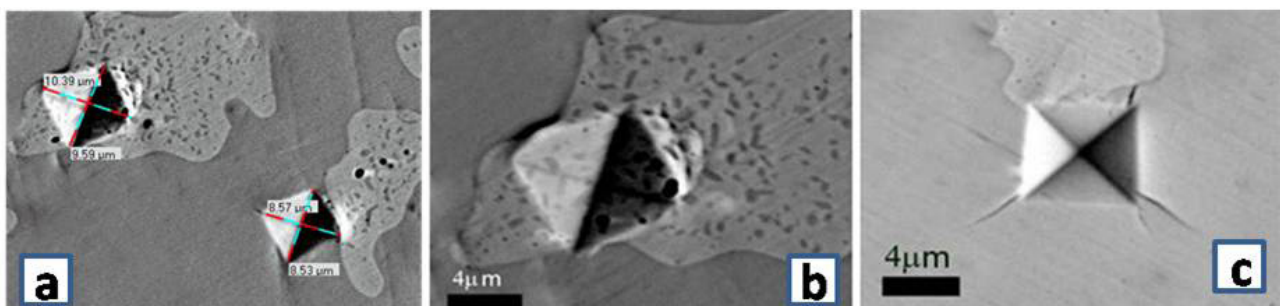


Fig-3: (a) Vickers indentation profiles at 3 N load (b) Vickers indentation profiles at 3 N load at phase A showing pile up (c) the crack arresting capability of phase A

BARC NEWSLETTER

Founder's Day

in nature. The oxidized surfaces are free of cracks; however, the porosities are detected until the initial 5h. With increase in time, the coagulation/agglomeration of oxide particles tries to close the pores, and makes the oxide layer more protective.

Mechanical Testing

The room temperature flexure strength and the fracture toughness of the alloy determined using standard equations were found to be 615 ± 15 MPa and 10.7 ± 0.5 MPa.m^{1/2}, respectively. The average values of hardness are 6800 ± 15 MPa and 11300 ± 10 MPa for phase A and B, respectively. The profiles of a 3 N Vickers indentation along the corners and the faces at both phases are shown in Fig-3a. No pile-up is observed around indentation at phase B while a clear ≥ 500 nm high pile-up is present along the faces of indentation at phase A (Fig-3b). The pile up is due to the plastic flow of the material, showing the evidence of ductility of phase A. The fracture toughness increases due to the crack arresting capability of phase A, which is clearly seen in Fig-3c. Crack intercepts by the primary Mo phase, hinder the catastrophic fracture through the formation of unbroken ductile-particle ligaments in the crack wake. The fracture toughness of the system could be enhanced by the presence of the ductile phase; it is either by crack blunting, branching, deflection or combinations of these. Crack deflection

or branching alters the mode of loading (I to mode II) so crack propagation is hindered resulting in increase in fracture toughness. Due to the crack hindrance (Fig. 3) and plastic deformation (Fig. 3) of the Mo-phase, together with crack deflection and interfacial de-bonding the toughness of the alloy is enhanced.

Conclusion

On the basis of the present experimental results the following conclusions can be drawn:

1. The technical feasibility of preparation of Mo based oxidation resistant alloy of nominal composition Mo-16Cr-4Si (wt.%) was demonstrated through systematic investigation by direct silicothemy and hot pressing.
2. The alloy is included by a ductile refractory solid solution phase of Mo and Cr containing 0.9-1.9 wt% Si and an intermetallic matrix of (Mo,Cr)₃Si.
3. The multiphase alloy is consisted of Mo₃Si and discontinuous (Mo, Cr) (ss) phase with volume percentage of 28%.
4. Due to the crack hindrance and plastic deformation of the Mo-phase, together with crack deflection and interfacial de-bonding the toughness of the alloy is enhanced.
5. The alloy exhibited better oxidation resistant as compared to single phase Mo alloy.

DEVELOPMENT OF REMOTELY OPERATED HYDRAULIC EQUIPMENT FOR REMOTE DISMANTLING AND DECOMMISSIONING OF NUCLEAR FACILITIES

P.K. Mishra, Abhijit Khuperkar, Shiju Varghese, Rites Ranjon, N.L. Soni and R.J. Patel
Refuelling Technology Division

Shri P.K. Mishra is the recipient of the
DAE Young Engineer Award for the year 2012

Abstract

Decommissioning of heavily contaminated components, equipment and concrete structures made up of high strength materials in ageing nuclear facilities require heavy duty remotely operated tools. Remotely controlled hydraulic operated heavy duty end effectors compatible with existing Remotely Operated Hydraulic Trolley Alongwith 6 DOF Manipulator (ROHYTAM) were developed for demolition of thick RCC structure, cutting of contaminated pipe & electrical cable and reducing the Person Sievert. A hydraulic operated Diamond Wire Sawing (DWS) Technique and system was also developed to cut block of desired shape and size from thick RCC wall in a controlled manner. The remote demolition using these end effectors and DWS technology was demonstrated on the 750 mm thick RCC wall mock-up. This paper discusses about this technology and experiences gained.

Keywords: hydraulic, end effectors, concrete, decommissioning, diamond wire sawing

Introduction

Department of Atomic Energy has several nuclear facilities for nuclear research, fuel fabrication, reprocessing and power generation. These nuclear facilities are getting aged and require decommissioning at the end of their useful life. During decommissioning large, heavy, complicated and heavily contaminated concrete/metallic structures have to be dismantled. It requires heavy duty remotely operated tools and equipment to carry out various operations like breaking, splitting, drilling in thick RCC structure, cutting of contaminated pipes, structural sections and thick electrical cables etc. Sometimes large RCC structures are to be decommissioned without affecting the integrity of nearby structures.

A Remotely Operated Hydraulic Trolley Along with 6 DOF Manipulator (ROHYTAM)^[1] was earlier developed to handle various nuclear emergencies like remote handling of accidentally fallen irradiated fuel bundle of PHWRs, manual override operation of direction control valves of PHWRs fuelling machines in case of stuck-up situations, nut splitting for decommissioning of unserviceable heat exchangers etc. It can be operated remotely using wireless video feedback from closed circuit camera mounted on it. It is a self-contained hydraulic driven unit having its own battery bank, power-pack and accessories. It has a payload capacity of 50 Kg at gripper and 500 kg at fore arm. Being a self-propelled vehicle, ROHYTAM was best suited as a carrier for remotely operated tools/end effectors for decommissioning activities inside nuclear facilities^[2].

BARC NEWSLETTER

Founder's Day

This paper discusses about the development of such remotely operated hydraulic systems, tools & techniques for decommissioning purposes.

Remotely Operated Decommissioning End Effectors

Various oil hydraulic operated hand held tools like drill, breaker, splitter, cut-off saw, metal cutter, combination tool etc. were commercially available for concrete and metallic structure decommissioning. These tools had either manual lever or switch for operation. Such tools were procured and automated by replacing their manual switches by solenoid valves so that they can be operated remotely. Special attachments for mounting these tools at the end of the ROHYTAM fore arm were designed and fabricated. These tools/end effectors were integrated with its hydraulic and control system. All these tools operate at 12 – 15 MPa pressure & 30 lpm flow. Since, ROHYTAM has limited flow capability; separate power pack was utilized to power up these tools.



Fig. 1: Drilling end effector

The remotely operated drilling end effector (Fig. 1) can drill 50 mm dia. through hole in 1.2 m thick RCC wall and can break the reinforcement bars present there in. The remotely operated breaking/chipping end effector (Fig. 2) can break/chip off concrete either from horizontal or vertical surfaces.



Fig. 2: Breaking/chipping end effector

A cutting end effector (Fig. 3) was in-house developed to cut contaminated pipes (50 OD x 3 mm thick), 400 mm² armoured electrical cables, angles of 25x25x3 mm size, channels or beams of 25 mm width and depth, etc.

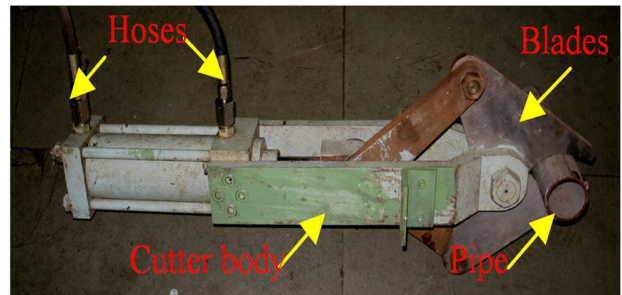


Fig. 3: In-house developed cutting end effector

The concrete splitting end effector (Fig. 4) can split 1 m thick concrete during decommissioning. A novel pressure cycling technique (Fig. 5) to generate tremendous pulsating force for applying fatigue loading on 1 m thick concrete structure for splitting it in desired plane was also been developed.

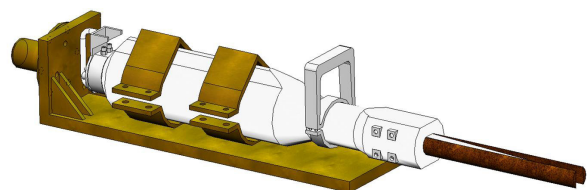


Fig. 4: Splitting end effector

BARC NEWSLETTER

Founder's Day

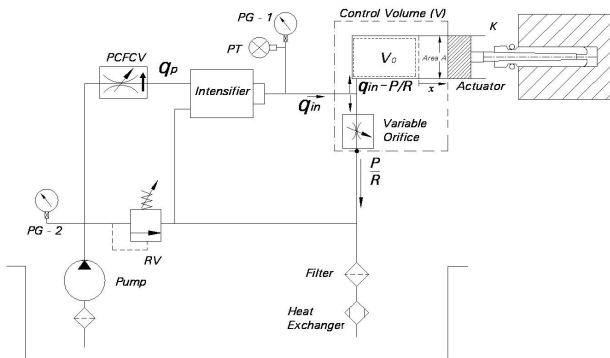


Fig. 5: Scheme of pressure cycling technique

A miniature high pressure (60 MPa) hydraulic cylinder for tools (Fig. 6) and hydraulic operated core drilling system were developed to create larger size openings in the concrete walls for various purposes.



Fig. 6: In-house developed 60MPa miniature cylinder for tools

Technique for Removing Heavy Concrete Blocks for Decommissioning

A hydraulic driven Diamond Wire Sawing (DWS) technique was developed for removing heavy concrete blocks during decommissioning. In this technique,

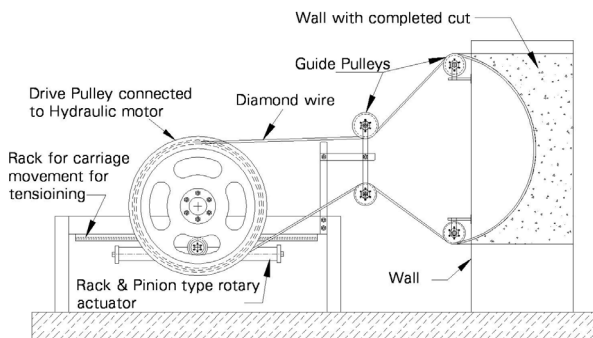


Fig. 7: Scheme of concrete sawing using diamond wire sawing machine

continuous loop of tensioned diamond wire (commercially available, 10 – 11 mm in dia.), joined at ends, runs over concrete structure guided by series of drive & guide pulleys (Fig. 7).

A hydraulic motor driven machine having a main drive pulley and a rack & pinion rotary actuator based tensioning mechanism has been developed. A 30 kW oil hydraulic power pack (Fig. 8) with load sensing hydraulic control was also developed for this purpose. Commercial electroplated diamond wire (Fig. 9) and guide pulleys were procured.



Fig. 8: 30 kW oil hydraulic power pack.



Fig. 9: Electroplated diamond wire used during wire sawing demonstration

Demonstration of Remotely Operated Hydraulic Equipment for Remote Dismantling and Decommissioning

Initially all tools were manually operated to have a feel of the required time and effort. After integrating all

BARC NEWSLETTER

Founder's Day

these remotely operated end effectors on ROHYTAM, a demonstration was carried out on a 750 mm thick RCC mock up wall. More than two dozen through holes with position accuracy of ± 5 mm were drilled, cracks were developed along the plane of the holes and concrete breaking/chipping was carried out using respective end effectors mounted on ROHYTAM to make safe opening of 750 mm x 750 mm. During the demonstration, ROHYTAM was controlled from the distant located control room using wireless control (Fig. 10 & 11). Cutting end effector was utilized for size reduction of armoured 400 mm² electrical cables for disposal purpose at 11 kV Hill substation and 11 kV control panel at Hall-3. Nut splitting was also demonstrated.

DWS technique was also demonstrated on same 750 mm thick RCC wall to make an opening of 500 mm x 200 mm. Initially four through holes were drilled in the RCC wall using drilling end effector. A diamond wire loop was made after passing the diamond wire through two holes and wrapped on the drive pulley of machine. Experiment was done to first saw bottom side using tap water as a coolant (Fig. 12). Similarly other three sides were cut. Motor operating pressure was 5 MPa and flow 50 lpm. Wire speed was 25 m/sec approx. Total wire cutting process took approx. 3 hours to make the opening (Fig. 13). All reinforcement bars in the RCC wall were easily cut by the wire saw.

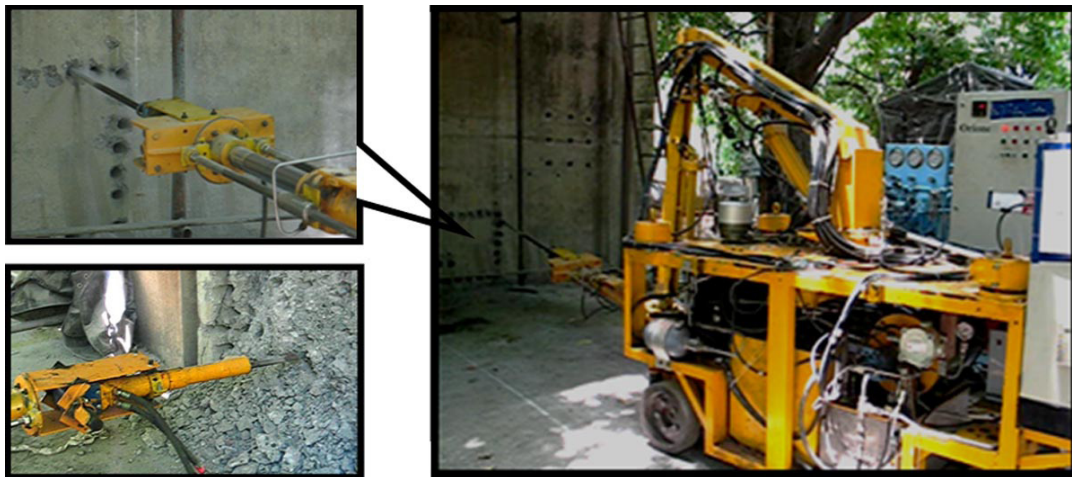


Fig. 10: ROHYTAM drilling breaking with mounted drilling and breaking end effector

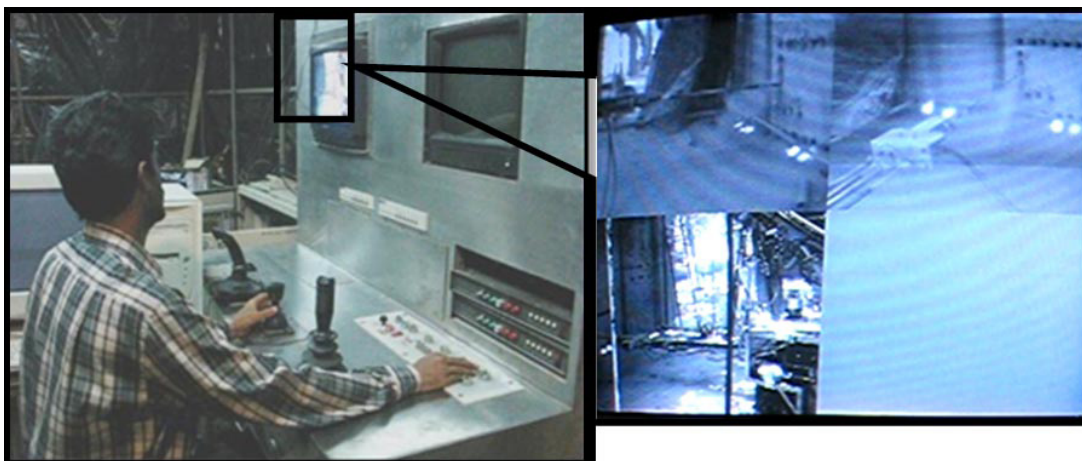


Fig. 11: ROHYTAM control room with video feedback during remote drilling

BARC NEWSLETTER

Founder's Day



Fig. 12: Diamond wire sawing machine in action



Fig. 13: Concrete block removed from the wall & opening after removal of the block

Results and Discussion

Manual and remote operations were carryout using these tools. The execution time comparison is given in table – 1.

During DWS demonstration very little noise and no weakening of surrounding structures occur. The operator needs to approach the radioactive structure only for installation of the setup and wire looping. Rest of the operation can be done remotely and hence, minimizing the radiation exposure. It is very useful for sawing heavily contaminated large, extremely thick

Table-1: Comparison of time taken for various activities by manual and end effectors

Activity	Approx. time for manual operation	Time end effectors on ROHYTAM
Drilling of 50 dia hole in 750 mm thick wall	2 hours per hole (using 2 persons)	18 minutes per hole
Chipping of concrete on horizontal flat surface	8 hours per m ³	4 hours per m ³
Chipping of concrete on vertical wall	Not feasible	Feasible @ 6 hr/ m ³ concrete
Armored Cable (400 mm ²) cutting in 1000 pieces	15 minutes per cut approx.	15 seconds per cut

& heavily reinforced concrete and metallic structures of awkward shapes especially in constricted areas of nuclear plants and facilities. Cooling by water generates secondary waste. Use of liquid nitrogen for cooling will eliminate the problem. Vibration generated during conventional drilling can be avoided by using diamond core drilling technique.

Conclusion

A wireless controlled remotely operated hydraulic decommissioning unit (ROHYTAM) with various decommissioning end effectors was developed, demonstrated and proven. The unit is able to do the job with minimum effort, time and negligible radiation exposure.

Diamond wire sawing technology has been developed, demonstrated and proven to make an opening in available 750 mm thick mock-up wall. It is found efficient to size reduce large and thick concrete structures as well as embedded sections in concrete structures with a minimal noise, vibration and heat generation. Because of short duration needed only for setting up this system, there can be significant reduction in operator fatigue and Person Sievert in decommissioning of structures like reactor walls, cell walls of reprocessing plants etc. in radiation environments.

This is an initiative with further scope of improvements to adapt to the specific requirements of the plants.

References

1. "Fluid power technology for Remote handling and demolition in Nuclear facilities", A. Khuperkar, et al., BARC newsletter (Founder's Day Special Issue), October 2010, p.p. 185-189.
2. "Development of hydraulic operated decommissioning technology for decommissioning of nuclear facilities", P. K. Mishra, et al., International conference on Peaceful Uses of Atomic Energy, 2009, thematic paper: RS-23, p.p. 146-155.

EXPERIMENTAL INVESTIGATION ON COOLABILITY OF SIMULATED CORIUM MELTS WITH DIFFERENT COOLING STRATEGIES

P.P. Kulkarni, A.K. Nayak, P.K. Vijayan
Reactor Engineering Division

Shri P.P. Kulkarni is the recipient of the
DAE Young Engineer Award for the year 2012

Abstract

Severe accident research helps us in understanding the realistic accidental phenomena for the assessment of associated risk. The societal impact of radiological leakage to the environment has demanded further robustness in the defense of nuclear safety. Thus, to ensure the cooling and stabilization of corium within reactor containment in case of severe accident scenarios, future reactors have been envisaged with core catcher. In this regard, corium coolability still remains an unresolved issue in spite of several efforts being taken towards its understanding. Several strategies have been contemplated for quenching and stabilization of core melt. However, the effectiveness of these schemes is yet to be determined properly, for which, lot of experiments are needed. In the present paper we have described results of different experiments carried out wherein a single simulant material with about same mass was cooled with different techniques starting from the same initial temperature. The result showed that, while top flooding and indirect cooling took several hours to cool, bottom flooding took a few minutes to cool the melt which makes it the most effective technique.

Introduction

Following a severe accident in a nuclear reactor, stabilization and termination of molten pool/debris is necessary to ensure safety of the public. In this regard, ex-vessel corium coolability still remains an unresolved issue in spite of several efforts being taken towards its understanding¹. Extensive research has been carried out in the field of corium coolability phenomenon, but the outcome is far from establishing a certainty of complete coolability of melt under all possible scenarios. The typical core melt stabilization techniques used by various reactors are: flooding from top, indirect cooling and flooding from bottom.

Top flooding is the simplest of these techniques where the core melt is simply flooded with ample

amount of water from top of the melt. In indirect cooling techniques, the core melt is often collected in an external vessel containing sacrificial material or contained inside the RPV and the vessel is then cooled externally by water. In bottom flooding technique, the melt is first spread on large surface containing sacrificial material and then flooded by water from below using injection nozzles. Literature survey reveals that, the previous experimental investigations are very scattered. Some of these tests have been conducted on laboratory scale and some on engineering scale. Besides, they involve different simulant materials and have been conducted at different initial temperatures which make it very difficult to judge effectiveness of a particular technique and advantage over the other. In the present work, experiments were carried out on engineering scale to test the performance

BARC NEWSLETTER

Founder's Day

of different techniques starting from same initial temperature.

Experiments conducted

In all, three tests were conducted with conditions listed as above. In all the three tests, about 40 kg of molten sodium borosilicate glass at 1200 °C was used as a simulant material corresponding to height of about 300 mm. In actual reactors, when corium falls on the concrete and ablates substantial part of it, the resulting mixture comprises metal oxides and silicates which form glass type mixture. Hence, glass was chosen as simulant material. The test setups used for the above tests are given in Fig. 1a to c. For top and bottom flooding condition, similar test sections was used which consists of 300 NB Sch 160 CS pipes of 500 mm height. For indirect cooling experiment, 300 NB Sch 120 SS 304 pipe of 460 mm height was used. These test sections were well instrumented using several thermocouples to record temperatures at different locations inside the melt.



(a) Melt coolability under top flooding



(b) Melt coolability by indirect cooling



(c) Melt coolability under bottom flooding

Fig 1. Test setups used for melt coolability experiments

In top flooding experiment, molten glass was poured in the test section and subsequently, water was poured onto it from top with a fixed rate. It was expected that, a molten glass like material, when flooded with water up to half a meter water column, would fracture as a result of thermal gradient because of fast quenching.

For melt coolability with indirect cooling, a slightly different test section was used which consists of a horizontal cylindrical test section submerged in the water pool similar to calandria of the PHWR. Molten glass was poured in the test section which was surrounded by pool of water and heat was transferred to water through the vessel wall only.

In bottom flooding experiment, a sand bed was placed at the bottom. On the top of the bed, a plate having six nozzles of different heights was placed. Molten glass was poured in the test section on the plate and after pouring, water was fed from bottom at 1.2 bar head, through the nozzles which injected water inside the melt at different heights of 20, 50 and 100 mm from bottom.

Experimental results:

In top flooding experiment, as soon as water was poured, there was a momentary steam eruption which stopped immediately. Subsequently, water started accumulating on the top of the melt shown by steady rise in level. It took several hours to cool the melt (Fig 2a) and a solid glass with a small amount of fractured debris on top was observed at the end of experiment. A tough crust formed below the debris limited the heat transfer to the melt resulting in poor heat removal.

In indirect cooling experiment, it was observed that there is a strong temperature gradient inside the melt along the radial height. The melt at the top was at 600 °C even after several hours of pouring whereas the temperature near vessel surface was at saturation (Fig 2b). The heat transfer to the surrounding water was very poor and in fact, the water in the pool did not boil at all. It also took several hours to cool the melt.

BARC NEWSLETTER

Founder's Day

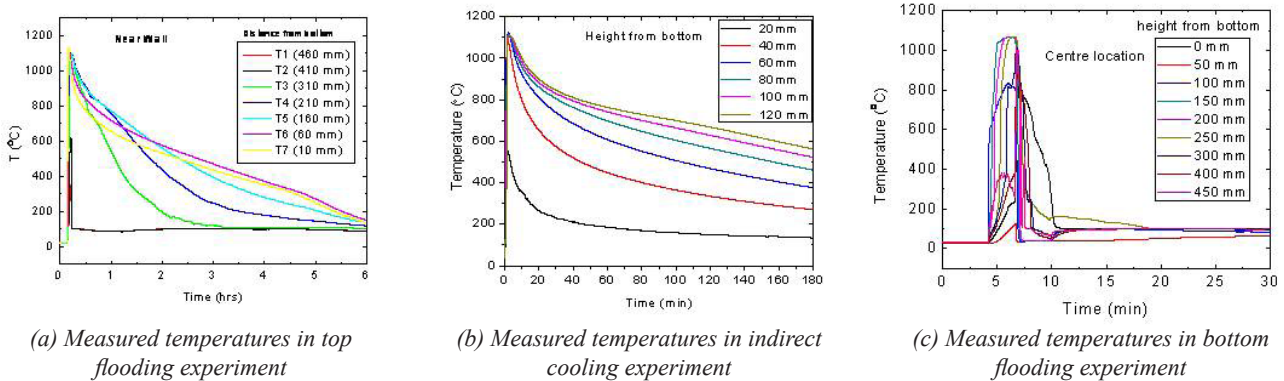


Fig. 2: Experimental results

In bottom flooding experiment, it was observed that, as soon as water supply was started, there was large eruption of steam from the outlet and thermocouples showed complete quenching within few minutes (Fig 2c). As a result of steam generation and the back pressure of water inflow, the melt is converted into porous debris. The water flowed easily through the debris cooling it instantly.

Conclusions

- Under top flooding condition, it took several hours to cool the melt under adiabatic conditions and water ingression occurred only upto 10 mm depth, below which a stable solid crust was formed which limited the heat transfer, which highlights that, top flooding is insufficient to quench the molten pool in case of severe accidents.
- In indirect cooling also, it took long time to cool the melt as a crust of glass formed between melt pool and vessel which acted as an insulation and resulted into poor heat removal.

- With bottom flooding, the steam formation below the melt and water backpressure induce porosity inside the otherwise impervious melt, which leads to quenching of melt in very short period of time. It took a few minutes to cool the melt to room temperature which otherwise took several hours in previous experiments
- The above series of experiments highlighted that, bottom flooding is a better way to achieve complete coolability of molten corium. With these experiments, we have validated the bottom flooding concept with properly engineered injection nozzles which is presently envisaged in the AHWR core catcher.

References

1. Sehgal. B. R. "Stabilization and termination of severe accidents in LWRs", *Nuclear Engineering and Design*, 236, (2006): 1941–52.

PROCESS MODELING AND SIMULATION TO DEVELOP UO_2 -TRISO COATED PARTICLE FOR INDIAN HIGH TEMPERATURE REACTORS

P.K. Mollick, D. Sathiyamoorthy, P.T. Rao, R. Venugopalan and J.K. Chakravartty
Materials Group

Shri P.K. Mollick is the recipient of the
DAE Young Engineer Award for the year 2012

Abstract

This work reports process modeling and its simulation to fabricate TRISO (TRistructural-ISotropic) coated Uranium Oxide particle. The development of TRISO coating on spherical fuel microspheres of $500\ \mu\text{m}$ size was carried out in a hot spouted bed reactor by chemical vapor deposition. A particle growth model is proposed and simulated to fix process parameters for TRISO coating in a single campaign. The coating thickness of each layer is controlled using indigenously developed pressure fluctuation technique. Results shows the potential of present process to arrive at uniform TRISO coated particles with specified coating thickness and corresponding coating densities.

Introduction

TRISO (TRistructural-ISotropic) coated particle is proposed to be used in the upcoming Indian High Temperature Reactors (IHTRs) as the fuel component. Compact High Temperature Reactor (CHTR) is one of them which is mainly aimed to produce hydrogen from water and electricity for remote areas using process heat at reactor operating temperature close to $1000\ ^\circ\text{C}$.¹

TRISO coated particle is a four layered coated particle. A schematic of the TRISO coated particle fuel is shown in Fig.1. The fuel kernel size is $500\ \mu\text{m}$ over which successive layers of low density Buffer Pyrolytic Carbon (B.PyC), high density Inner Pyrolytic Carbon (I.PyC), Silicon Carbide (SiC) and a repeat of high density Outer Pyrolytic Carbon (O.PyC) are uniformly deposited by Chemical Vapor Deposition (CVD) process in a spouted bed reactor²⁻⁴. A schematic of the spouted bed is shown in Fig. 2.

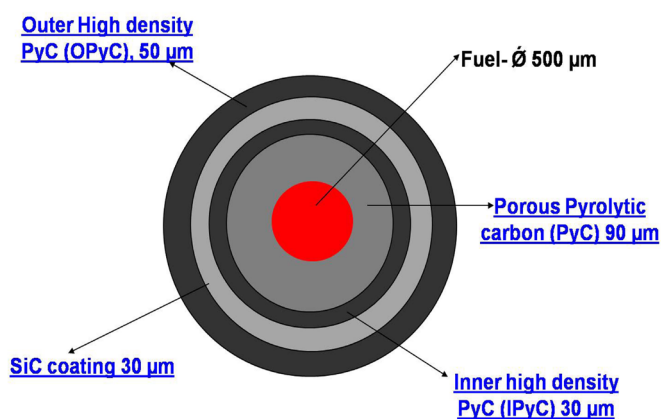


Fig. 1: Schematic of TRISO coated particle

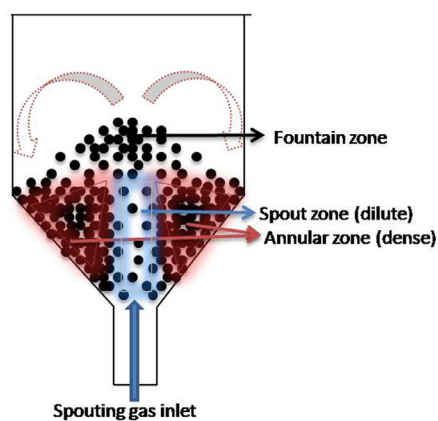


Fig. 2 Schematic of Spouted bed

BARC NEWSLETTER

Founder's Day

Process Development, Modeling and Simulation

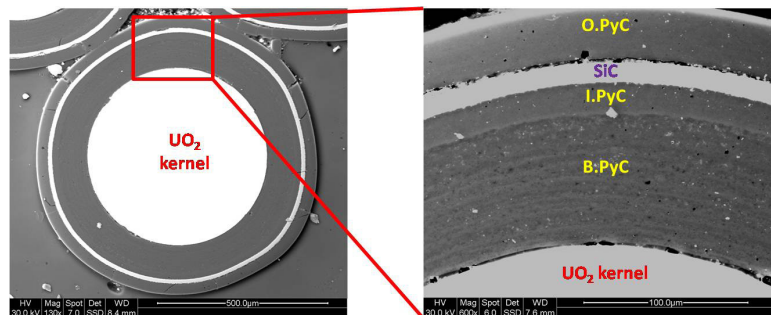
A kinetic model was proposed for the CVD to occur in spouted bed reactor and subsequently simulated to find optimum operating conditions.³ The hydrodynamics of the reactor was studied in cold condition in order to find minimum spouting velocities required for various process conditions and was correlated with the pressure fluctuation which occurs in various operating conditions.⁴ Hydrodynamic correlations were further used at high temperature after suitable calibrations. The pressure fluctuation technique which was indigenously developed was used to identify various spouting regimes and thereby the status of the coating process at operating condition during single batch TRISO coating process.

A particle growth model was developed considering the change in particle size and overall particle density with coating time. A typical model prediction is presented in Fig. 3 which also shows change in bed height and corresponding bed volume during the four layers of coating. According to the dynamic change in particles and bed properties the operating parameters were set based on the results obtained from

kinetic model simulation as well as hydrodynamics correlations (calibrated at operating temperature) for single batch TRISO coating process.

Experimental

Experiment was carried out in a spouted bed CVD furnace on natural urania microspheres (average size falls between 500 to 600 μm). According to the simulated process parameters, operating parameters were set through LABVIEW programming to control all precursor and carrier gases flow through the reactor inlet nozzle. Status of the coating process was monitored in terms of pressure fluctuation data which was recorded simultaneously during the coating process.



(a) Single urania coated TRISO particle (b) Individual layer in TRISO coated particle
Fig. 4: Cross section of UO₂-TRISO coated fuel particle

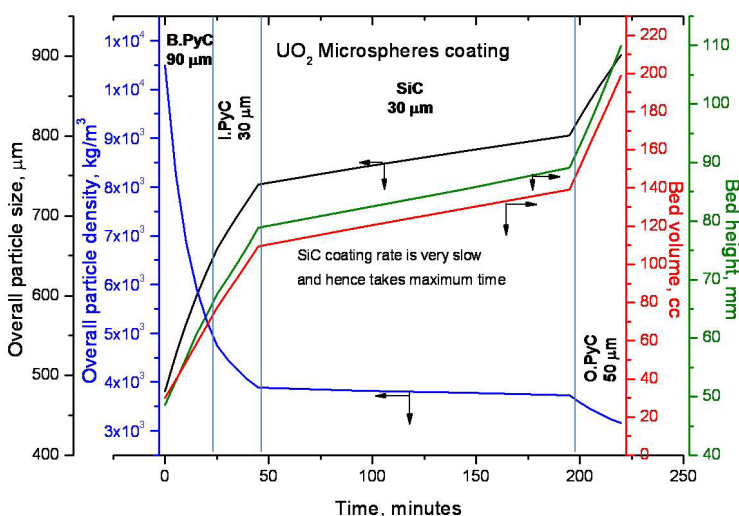


Fig. 3: Profile showing changes in particle and bed properties during TRISO coating

Results and discussion

SEM micrograph of cross section of the TRISO coated fuel particles is shown in Fig. 4. It is seen that all coated layers are uniform which results in completely spherical particles. The coating thickness of the individual layers is seen to agree well with the model predictions as shown in Table 1. It is also confirmed that the overall particle density falls in accordance with the model predictions.

BARC NEWSLETTER

Founder's Day

Table 1: Comparison of experimental and model predicted coating thickness

Coated Layer	Thickness in mm (Internationally practiced)	Coating thickness we intended, mm (according to model simulation)	Coating thickness we achieved, mm	Deviation, %
BPyC	90	90	81.2	9.8
IPyC	30	20	21.1	5.5
SiC	30	15	15.3	2.0
OPyC	50	30	28.2	5.8

Conclusions

Demonstration of the above process modeling and its simulation shows success of UO₂-TRISO coating process and the capability of the spouted bed reactor to produce uniform coated layers. Hence the proposed model and the simulated operating parameters will be useful for mass production of the TRISO coated particle with any specified coating thickness and density.

References

1. Dulera I. V., Sinha R. K., "High Temperature Reactors", *J. Nucl. Mater.*, 383 (2008) 183–188.
2. Mathur K. B., Epstein N., Spouted Bed; Academic Press: New York, 1974.
3. Mollick P. K., Sathiyamoorthy D., Rao P. T., Rao V. G., "Modeling of Chemical Vapor Deposition of Pyrolytic Carbon in a Gas Spouted Bed Reactor", *Ind. Eng. Chem. Res.*, 50 (23), (2011), 13313-13321.
4. Mollick P. K., Sathiyamoorthy D., "Assesment of Stability of Spouted Bed Using Pressure Fluctuation Analysis", *Ind. Eng. Chem. Res.*, 51 (37), (2012), 12117-12125.

VARIABLE ELIMINATION FROM LINEAR MODULAR CONSTRAINTS

Ajith K.J.
Reactor Control Division

Shri Ajith K.J. is the recipient of the
DAE Young Engineer Award for the year 2012

Abstract

Application of formal verification and analysis tools is recommended in the development of hardware and software systems used in safety-critical applications. Formal verification tools for such systems generate constraints (formulae) that are solved by solving algorithms. Variable elimination (existential quantifier elimination) from these constraints facilitates the simplification of the constraints. This is crucial in improving the scalability of the verification tools to target systems of increased complexity. This paper presents efficient techniques for variable elimination from a class of such constraints called linear modular constraints, and an application of these techniques in the formal verification of FPGA based hardware designs.

Introduction

Ensuring the correctness of hardware and software systems used in safety-critical applications is extremely important, as bugs in such systems can have disastrous consequences. Hence, application of formal verification and analysis tools that use rigorous mathematical reasoning for functional verification is recommended in the development of systems used in safety-critical applications. However, in spite of the technological advancements made over years, there is an increasing gap between the sizes of the systems being designed and sizes of systems amenable to automatic formal verification. Moreover, many of the commercial formal verification tools have prohibitive prices and have restrictions on transfer of technology. This motivates development of *efficient* and *indigenous* formal verification techniques that can target systems of increased complexity.

Formal verification tools for hardware and software systems generate constraints (formulae) that are

solved by solving algorithms. Variable elimination (existential quantifier elimination) involves elimination of variables from these constraints in order to compute another set of simplified constraints that depend only on variables relevant for the formal specification being verified. This facilitates significant simplification of the constraints, and thereby improves the scalability of the verification tools.

Linear modular constraints are a class of constraints extremely important in the context of formal verification and analysis tasks. Let p be a positive integer constant, x_1, \dots, x_n be p -bit non-negative integer variables, and a_0, \dots, a_n be integer constants in $\{0, \dots, 2^p-1\}$. A linear term over x_1, \dots, x_n is a term of the form $a_1x_1 + \dots + a_nx_n + a_0$. A linear modular equality (LME) is a formula of the form $t_1 = t_2 \pmod{2^p}$, where t_1 and t_2 are linear terms over x_1, \dots, x_n . Similarly, a linear modular disequality (LMD) is a formula of the form $t_1 \neq t_2 \pmod{2^p}$, and a linear modular inequality (LMI) is a formula of the form $t_1 \leq t_2 \pmod{2^p}$. We use linear modular constraint (LMC) to denote an LME, LMD or

BARC NEWSLETTER

Founder's Day

LMI. Conventionally 2^p is called the modulus of the LMC.

The most dominant technique used in practice for eliminating variables from LMCs is conversion to bit-level constraints¹, followed by bit-level variable elimination. Since LMCs can be expressed as formulae in integer arithmetic, variable elimination techniques for integer arithmetic such as OmegaTest¹ can also be used to eliminate variables from LMCs. However these techniques scale poorly as the modulus of the LMCs increases. In this paper, we present efficient techniques for variable elimination from LMCs that significantly outperform variable elimination techniques based on bit-level reasoning and integer arithmetic.

Algorithms for Variable Elimination from Linear Modular Constraints

In this section, we present an efficient algorithm for variable elimination from conjunctions of LMCs called **Project**³. Later on, we present an algorithm **QE_LMDD** – an extension of **Project** for variable elimination from Boolean combinations of LMCs.

Project uses a layered approach to eliminate variables from a conjunction of LMCs. Sound but incomplete, cheaper layers are invoked first, and expensive but complete layers are called only when required. The first layer of **Project** (Layer1) involves simplification of the given conjunction of LMCs using the LMEs present in the conjunction. For example, consider the problem of eliminating the variable x from the conjunction of LMCs $(6x+y = 4)$ and $(2x+z \neq 0)$ with modulus 8. Note that $(6x+y = 4)$ can be equivalently expressed $(2x = 5y+4)$ in modulo 8 using modular arithmetic operations¹. The variable x can be eliminated from the conjunction by replacing the occurrences of $2x$ in the conjunction by $5y+4$. Simplifications as above using LMEs present in the conjunction forms the crux of Layer1.

The second layer of **Project** (Layer2) makes use of an efficient combinatorial heuristic to identify unconstraining LMIs and LMDs that can be dropped from the conjunction of LMCs without changing the set of satisfying solutions of the conjunction. For example, consider the problem of eliminating the variable x from the conjunction of LMCs $(2x = 5y+4)$ and $(x+y \leq 3)$ with modulus 8. Note that x, y are 3-bit variables here. It can be observed that $(2x = 5y+4)$ is independent of the most significant bit of x , denoted as $x[2]$. It can be observed that every solution of $(2x = 5y+4)$ can be engineered to become a solution of the conjunction of $(2x = 5y+4)$ and $(x+y \leq 3)$ by choosing $x[2]$ appropriately. This means that $(x+y \leq 3)$ is irrelevant (unconstraining) as far as the elimination of the variable x from the conjunction of $(2x = 5y+4)$ and $(x+y \leq 3)$ is concerned. Layer2 drops such unconstraining LMDs and LMIs from the conjunction of LMCs, and thereby simplifies the problem instance.

The cases that are not computed by the application of the above computationally cheap layers are handled by expensive but more complete techniques. The third layer of **Project** (Layer3) involves a variant of the classical Fourier-Motzkin² variable elimination algorithm for reals adapted to work for LMCs. The final layer (Layer4) involves model enumeration that eliminates the variable by enumeration of all possible values in the domain of the variable.

The algorithm **QE_LMDD** extends **Project** for variable elimination from Boolean combinations of LMCs using a data-structure called Linear Modular Decision Diagram (LMDD)². LMDDs are decision diagrams with nodes labelled with LMEs or LMIs. Given a Boolean combination of LMCs represented as an LMDD, **QE_LMDD** traverses the LMDD in a top-down manner converting the problem of variable elimination from Boolean combination of LMCs into a set of simpler sub-problems each of which involves variable elimination from a conjunction of LMCs.

BARC NEWSLETTER

Founder's Day

Applications

The primary motivation for the development of our techniques comes from a formal verification tool for FPGA based hardware designs, Vhdl Bounded Model Checker (VBMC)³, developed in Reactor Control Division, BARC. VBMC accepts a hardware design in VHDL, functional property in PSL, and verification bound (number of cycles of operation) as inputs. It either proves that the design satisfies the functional property for the given verification bound or generates a counterexample providing the reason of violation. Suppose we wish to use VBMC for proving that a given VHDL design satisfies a formal specification for N cycles of operation. VBMC performs this by deriving the transition relation of the VHDL design (relation between the present and next states of the design), unrolling the transition relation N times, conjoining the unrolled relation with the negation of the property, and then checking for the satisfiability of the resulting constraint using a constraint solver. However, unrolling the transition relation a large number of times can give a constraint with a large number of variables, which can crucially affect the performance of the constraint solver.

VBMC alleviates this problem by computing a simplified (abstract) transition relation that relates only a chosen subset of variables in the VHDL design relevant to the property being checked. As the transition relations of real-life VHDL designs largely belongs to the theory of LMCs, VBMC makes use of **QE_LMDD** for abstract transition relation computation. We have

experimentally found that using **QE_LMDD** for abstract transition relation generation significantly outperforms the use of bit-level or integer arithmetic based techniques.

Conclusions

The application of formal verification and analysis tools in the development of hardware and software systems is extremely important, particularly when they are used in safety-critical applications. Our experiments demonstrate that efficient variable elimination techniques are crucial in enhancing the scalability of such formal verification and analysis tools to target systems of real-life complexity.

References

1. Ajith John and Supratik Chakraborty. "A Quantifier Elimination Algorithm for Linear Modular Equations and Disequations", Proceedings of 23rd International Conference on Computer Aided Verification (CAV), 2011
2. Ajith John and Supratik Chakraborty. "Extending Quantifier Elimination to Linear Inequalities on Bit-Vectors", Proceedings of 19th International Conference on Tools and Algorithms for the Construction and Analysis of Systems (TACAS), 2013
3. Ajith K. J., A. K. Bhattacharjee, M. Sharma, G. Ganesh, B. B. Biswas. " Design and Application of a Formal Verification Tool for VHDL Designs", *BARC Newsletter* ISSN: 0976-2108, 2012

SEPARATION AND COMPLEXATION STUDIES OF TRIVALENT ACTINIDES AND LANTHANIDES USING SOFT DONOR LIGANDS

Arunasis Bhattacharyya
Radiochemistry Division

Shri Arunasis Bhattacharyya is the recipient of the
DAE Young Scientist Award for the year 2012

Abstract

Mutual separation of trivalent actinides (An^{3+}) and lanthanides (Ln^{3+}) is an important and challenging task in the back end of the nuclear fuel cycle due to their very similar ionic potential values. Soft (S, N) donor ligands show selectivity towards An^{3+} over Ln^{3+} due to the higher spatial distribution of the '5f' orbitals of An^{3+} ions. Our studies address the separation of these two classes of 'f' block metal ions using a combination of 'S' and 'N' based ligands leading to spectacular enhancement in the selectivity for the An^{3+} ions. The An^{3+}/Ln^{3+} complexation studies and DFT calculations on their complexes were carried out to explain their separation behaviour with these soft donor ligands.

Introduction

Ln^{3+} and An^{3+} ions possess similar chemical behaviour thereby making their mutual separation a challenging task. Their separation is, however, essential prior to the transmutation of the minor actinides (Am, Cm and Np) due to very high neutron absorption cross section of some of the lanthanide isotopes present in the nuclear waste [1]. It is, therefore, required to design a suitable method for the separation of trivalent actinides from the lanthanides. Higher spatial distribution of the '5f' orbitals of the An^{3+} ions as compared to the '4f' orbitals of the Ln^{3+} ions results in stronger covalent interactions with the soft donor ligands in case of former leading to selectivity for An^{3+} over Ln^{3+} .

Solvent extraction / liquid membrane studies

A number of literature reports are available on the Ln/An separation studies with various 'S' and 'N' donor ligands. Very high separation factor (D_{Am}/D_{Eu}) was reported using a 'S' donor ligands, bis(2,4,4-

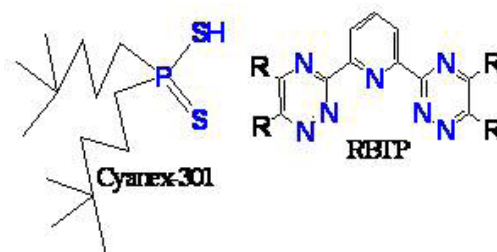


Fig. 1: Structural formulae of Cyanex-301 and tetra-alkylBTP ligands studied for Ln/An separations

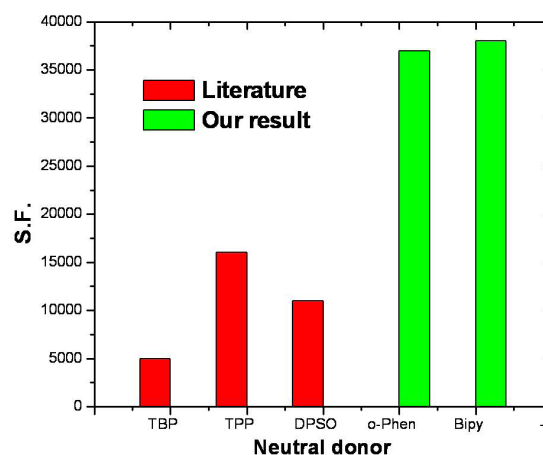


Fig. 2: Separation factor (D_{Am}/D_{Eu}) values using Cyanex-301 along with various neutral donor ligands

BARC NEWSLETTER

Founder's Day

trimethylpentyl) dithio-phosphinic acid (Cyanex-301 (Fig.1)) [2]. Neutral 'O' donor auxiliary ligand (synergist), viz. tri-n-butyl phosphate (TBP), triphenyl phosphate (TPP), carbamoyl methylene phosphine oxide (CMPO) etc. have been used along with Cyanex-301 [3]. In these cases, however, selectivity decreases as the extractability of the synergistic mixture increases. Cyanex-301 is, however, inefficient at low pH ($\text{pH} < 3$). We have used an 'N' donor ligand (2,2'-bipyridine / 1,10-phenanthroline) along with Cyanex-301, which showed very high selectivities even at lower pH ($\text{pH} < 3$) [4].

Liquid membrane separation studies yielded highly encouraging results and hollow fiber supported liquid membrane (HFSLM) studies carried out at litre scale of synthetic feeds spiked with radiotracers indicated (Fig. 3) that Am^{3+} could be separated from a bulk of lanthanides even at pH 2.5 within 10 minutes with a decontamination factor > 100 [5].

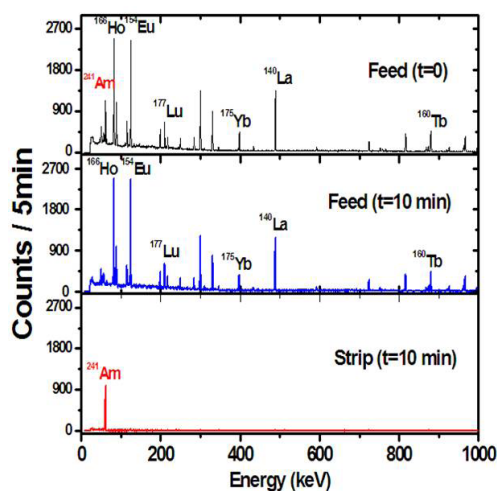


Fig. 3: Quantitative and selective transport of Am^{3+} from a bulk of Ln^{3+} in 10 min using HFSLM of Cyanex-301

Computational studies

Density functional theoretical studies were carried out in order to explain such a high selectivity of Cyanex-301 for Am^{3+} over the Ln^{3+} ions [6]. The results indicate significantly higher covalence in the 'Am-S' bonds as compared to that in the 'Eu-S' bonds resulting in

shorter bond length in case of former in spite of larger ionic radius of Am^{3+} as compared to that of Eu^{3+} . Optimized geometries of nitrate and Me_2PS_2^- (lower homologue of Cyanex-301) complexes of Am^{3+} and Eu^{3+} are shown in Fig. 4.

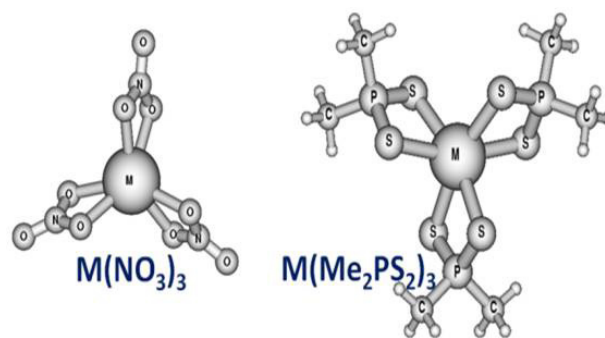


Fig. 4: DFT optimized structures of Am^{3+} and Eu^{3+} complexes with NO_3^- and Me_2PS_2^- (lower homologue of Cyanex-301)

In spite of using neutral donor synergists, Cyanex-301 is inefficient to extract at $\text{pH} < 2$. Various ter and tetradentate 'N' donor ligands, viz. bis-(1,2,4-triazinyl) pyridine (RBTP) and bis-(1,2,4-triazinyl) bipyridine (RBTBP) derivatives, which have been reported to be promising for the Ln/An separation [7] were, therefore, synthesized and evaluated at a higher acidity ($\sim 1\text{M HNO}_3$).

Complexation Studies

Complexation studies of An^{3+} and Ln^{3+} ions are essential in order to understand the separation behaviour. RBTP (tetraalkylBTP) derivatives are promising ligands for Ln/An separations. Solution phase complexation of An^{3+} and Ln^{3+} were studied using UV-Vis absorption spectrophotometry, time resolved laser induced fluorescence spectroscopy (TRLFS), electro spray ionization mass spectrometry (ESI-MS) studies [8]. The results showed the formation of higher stoichiometric complexes with higher stability constants in case of Am^{3+} with all the RBTP (R= H, methyl and ethyl) derivatives studied as compared to that of the Ln^{3+} ions indicating stronger complexation in case of Am^{3+} . The change in the Am^{3+} absorption spectra due to the formation of its RBTP complexes is shown in Fig. 5.

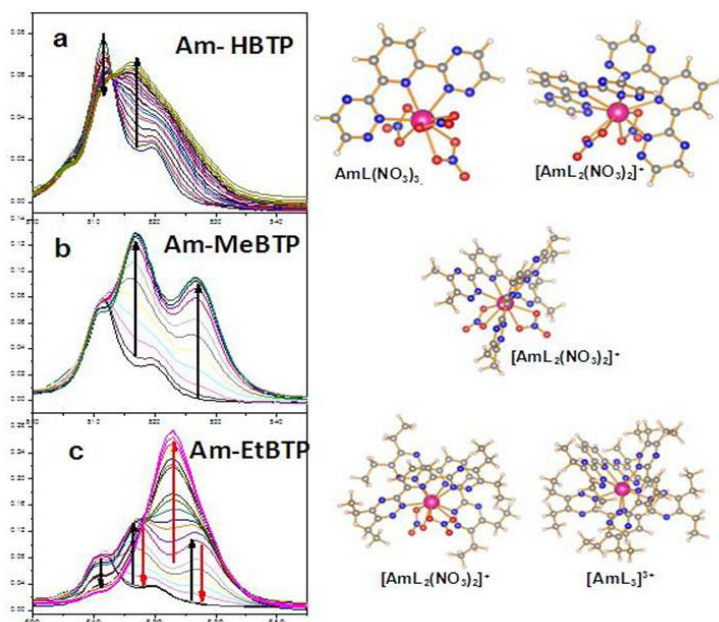


Fig. 5: Formation of Am^{3+} complexes with RBTP derivatives: UV-Vis spectrophotometry and DFT studies

DFT studies were carried out to find out the optimized geometries of the Am^{3+} and Eu^{3+} complexes considering the stoichiometries obtained from the solution phase experimental studies. Optimized geometries of different Am^{3+} complexes of RBTP are shown in Fig. 5. 'Am-N' bond distances were found to be invariably shorter as compared to the 'Eu-N' bond distances in spite of the larger ionic radius of Am^{3+} . This, clearly,

indicated stronger covalence in the 'Am-N' bond in the Am^{3+} complexes as compared to the 'Eu-N' bond in the Eu^{3+} complexes rationalizing the experimental observations. In order to have clear understanding of the structures of RBTP complexes, single crystals of Eu^{3+} complexes of the three RBTP derivatives were synthesized from acetonitrile medium. The structures, as shown in Fig. 6, indicates the formation of a dimeric complex in case of HBTP and mono-meric complex in case of EtBTP. MeBTP, on the other hand, forms both mono and di-meric complexes. Dimeric complex is, therefore, less favoured as the alkyl chain length increases. For the similar complexes (either mono or dimeric), the bond distances between Eu^{3+} and the 'N' atom of the central pyridine ring (Nc) of the RBTP increases with increasing the alkyl chain length of RBTP due to the increasing steric hindrance.

Conclusions

Cyanex-301, along with 'N' donor neutral synergists, shows enormously high selectivity for Am^{3+} over Eu^{3+} . Ln/An separation was demonstrated in liter scale with

Cyanex-301 and neutral 'N' and 'O' donor ligands using HFSLM based technique with a D.F. value >100 . The selectivity of Cyanex-301 towards Am^{3+} over Eu^{3+} was attributed to higher covalence in 'Am-S' bond as indicated by the shorter 'Am-S' bonds as compared to the 'Eu-S' bonds from the DFT based calculations. Solution phase complexation studies of Am^{3+} and Ln^{3+} ions with RBTP derivatives show stronger complexation in case of Am^{3+} , which results in selectivity of this class of ligands for Am^{3+} over the Ln^{3+} ions.

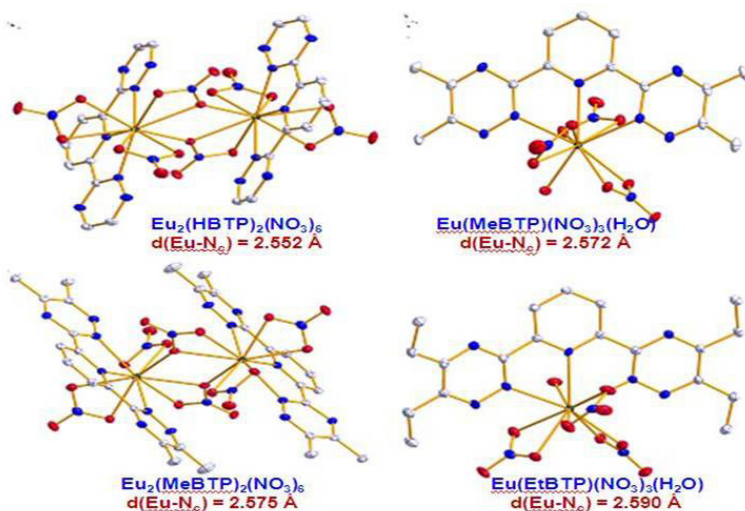


Fig. 6: Solid state crystal structures of Eu^{3+} complexes of RBTP derivatives

BARC NEWSLETTER

Founder's Day

Acknowledgements

I would like to thank Dr. P.K. Mohapatra and all the co-authors of our published papers. The encouragement and support from Dr. A. Goswami, Head, Radiochemistry Division is greatly acknowledged also thanks Prof. K.R. Czerwinski, UNLV, USA for hosting and Indo-US Science & Technology Forum for financial support to carry out part of the work in USA.

References

1. B. Christiansen, C. Apostolidis, R. Carlos, O. Courson, J.P. Glatz, R. Malmbeck, G. Pagliosa, K. Romer, D. Serrano-Purroy, *Radiochim. Acta* 2004, 92, 475
2. Y. Zhu, J. Chen, R. Jiao, *Solv. Extr. Ion Exch.* 1996, 14, 61
3. C. Hill, C. Madic, P. Baron, M. Ozawa, Y. Tanaka, *J. Alloys and Compounds*, 1998, 159, 271–273
4. A. Bhattacharyya, P. K. Mohapatra, and V. K. Manchanda, *Solv. Extr. Ion Exch.*, 2006, 24, 1-17
5. A. Bhattacharyya, P.K. Mohapatra, V.K. Manchanda; *J. Memb. Sci.*, 2008, 312, 1-5
6. A. Bhattacharyya, T.K. Ghanty, P.K. Mohapatra, V.K. Manchanda, *Inorg. Chem.* 2011, 50 (9), 3913-3921
7. Z. Kolarik, U. Müllich, F. Gassner, *Solv. Extr. Ion Exch.* 1999, 17, 23
8. A. Bhattacharyya, E. Kim, P. Weck, P. M. Forster and K. R. Czerwinski, *Inorg. Chem.*, 2013, 52, 761-776

NOVEL APPROACHES FOR MITIGATION OF RADIATION TOXICITY BY MODULATION OF IMMUNE SYSTEM

Deepak Sharma and S. Santosh Kumar
Radiation Biology & Health Sciences Division

Dr. Deepak Sharma is the recipient of the
DAE Young Scientist Award for the year 2012

Abstract

Radiation induced toxicity to normal tissues is a major concern during planned or accidental exposure. Immune system and hematopoietic stem cells are overtly sensitive to radiation. However, growth factors and cytokines produced by immune cells during inflammation can prevent radiation toxicity to normal cells and tissues. We hypothesized that modulation of immune response could be an effective modality for prevention and treatment of radiation toxicity in normal tissues. We have used cellular redox modifiers for controlling the expression of transcription factors and genes involved in detoxification of radiation derived free radicals and also regeneration of immune system in vivo.

Introduction

The white blood cells (leukocytes) of an individual with functionally competent normal immune system can safeguard against most of the infectious agents and internal parasites. The immune system uses homeostatic mechanisms to adapt to the continuously changing requirements imposed by pathogens. These homeostatic mechanisms include production of different subsets of leukocytes like neutrophils, macrophages, T cells, B cells and natural killer cells, their maintenance and survival in the periphery and finally periodic removal of the excess leukocytes. The leukocytes are produced from hematopoietic stem progenitor cells (HSC) in the bone marrow. The lymphocytes (T cells and B cells) are maintained in a large diversity of naïve cells which give rise to the effector cells following antigen exposure. Once the infection is cleared, the excess of activated lymphocytes rapidly die and a limited number of memory cells survive for many years.

Dysregulated immune response can lead to chronic inflammatory conditions leading to diseases like autoimmunity, allergy, obesity and cancer. On the contrary, a diminished immune response can result in increased susceptibility of the individuals to infectious agents like bacteria, virus and fungal pathogens. In order to kill the pathogens, the immune cells produce a variety of reactive oxygen species in response to pathogens. At the same time, they are also highly sensitive to both endogenous and exogenous oxidative stress.

Low levels of ionizing radiation are present in the environment and are not known to cause any significant health hazards. However, exposure to higher doses (in excess of safety limits) of ionizing radiation can occur during radiotherapy of cancer, medical imaging or accidental exposures in nuclear industry or nuclear warfare. Ionizing radiation causes significant apoptosis and mitotic arrest in the hematopoietic stem progenitor cells in the bone marrow. Higher

BARC NEWSLETTER

Founder's Day

doses of radiation (>2Gy) induce excessive oxidative stress leading to massive death of mature leukocytes in the generative as well as secondary lymphoid organs and peripheral blood which results in lymphopenia. Under these conditions, the immune system is severely compromised and death may occur due to increased infections. We are involved in development of new and effective countermeasures to reduce, prevent or lower the risk of normal tissue radiation-toxicity. Therefore, we have studied the cellular and molecular mechanisms involved in homeostasis of lymphocytes following exposure to ionizing radiation. We have also examined the role of cellular redox status in maintaining a normal immune system using various anti-oxidants and pro-oxidants. Based on our understanding of the role of cellular redox in immune system, we have developed novel approaches which can be used for prevention of radiation induced immune-suppression and also for mitigation of toxic effects of ionizing radiation. The present article highlights summary of our findings with potential for translational medicine.

Molecular and cellular mechanism of lymphocytes homeostasis following exposure to radiation

T cells are the lymphocytes that play a central role in cell mediated immunity against pathogens. A large variety of T cells are continuously produced and trained in the thymus. These newly produced naïve T cells enter the blood and compete with the existing pool of the T cells for their survival. Following exposure to radiation a massive cell death ensues in the T cells resulting in lymphopenia. The remaining T cells sense the lymphopenia and undergo homeostatic proliferation to fill this empty lymphoid space¹.

We showed that homeostatic proliferation of CD4+ helper T cells takes place in specific anatomical locations in the body including spleen and lymph nodes and not in the peritoneum of irradiated lymphopenic mice¹. Pharmacological inhibitors of the cellular signaling molecules PI3kinase, extracellular regulated kinase (ERK), protein kinase c (PKC) and mammalian

target of rapamycin (mTOR) inhibited mitogen induced proliferation and cytokine production by T cells. However, homeostatic proliferation of helper T cells was not affected by these inhibitors². The transcription factor NF-κB was activated during both mitogen induced proliferation as well as homeostatic proliferation¹. Higher activation of NF-κB was related to lower cells death in lymphocytes exposed to radiation in vitro³. Gamma tocotrienol, which is found in palm oil, enhanced the homeostatic proliferation of T cells indicating its potential application for enhancing the recovery from radiation induced lymphopenia⁴.

Immunostimulatory and radioprotective effects of an antioxidant chlorophyllin and a pro-oxidant 1,4-naphthoquinone

Chlorophyllin is a water soluble mixture of sodium-copper salts of green plant pigment chlorophyll and is the constituent of over the counter drug derifil. It has been shown to possess a variety of health benefits including antimutagenic, chemopreventive, anticarcinogenic and suppression of body odor. We found that chlorophyllin acts as an antioxidant in cells as well as animals. Administration of chlorophyllin to mice modulated the lymphocyte homeostasis and immune system in vivo. It enhanced the number of lymphocytes in the spleen and peritoneum and also increased the innate immune responses mediated by phagocytes and adaptive immune responses mediated by T cells and B cells in immunized mice. Chlorophyllin upregulated anti-apoptotic genes in the lymphocytes and also prevented radiation induced apoptosis. Thus the immune-stimulatory effects of chlorophyllin were mediated by increasing the survival and homing of lymphocytes⁵. Our recent data has shown that administration of chlorophyllin significantly protected the mice against whole body irradiation induced death (Fig. 1A). Chlorophyllin administration enhanced the abundance of hematopoietic stem progenitor cells in the bone marrow and also increased the recovery of immune system in mice exposed to sub-lethal doses of radiation (Fig. 1B). We have also introduced

BARC NEWSLETTER

Founder's Day

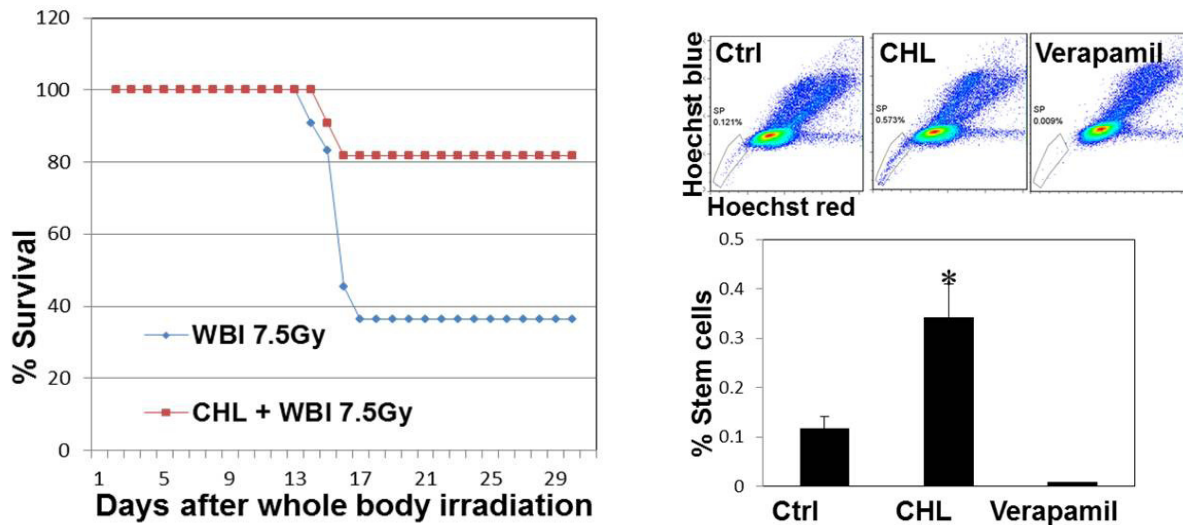


Fig.1. Chlorophyllin administration prevents whole body irradiation (7.5Gy) induced death of mice (A) and enhances the abundance of hematopoietic stem cells in the bone marrow (B). Verapamil was used as negative control for Hoechst side population assay.

a modified method for multi-color flow cytometry which could save upto 80% cost of antibody without compromising on the sensitivity or specificity of the assay for quantification of lymphocytes, epithelial cells, tumor cells and stem cells^{6,7}.

Cellular redox is determined by the delicate balance between anti-oxidants and pro-oxidants. We for the first time showed that 1,4-naphthoquinone, a pro-oxidant, disrupted the cellular redox by decreasing

cellular glutathione levels. It ameliorated radiation-induced apoptosis through activation of the calcium-ERK1/2-Nrf2 pathway. Most importantly, administration of NQ to mice significantly protected them against radiation induced mortality⁸.

Conclusion and future prospects

Our data suggests that homeostatic mechanisms in immune system that regulate lymphocyte production,

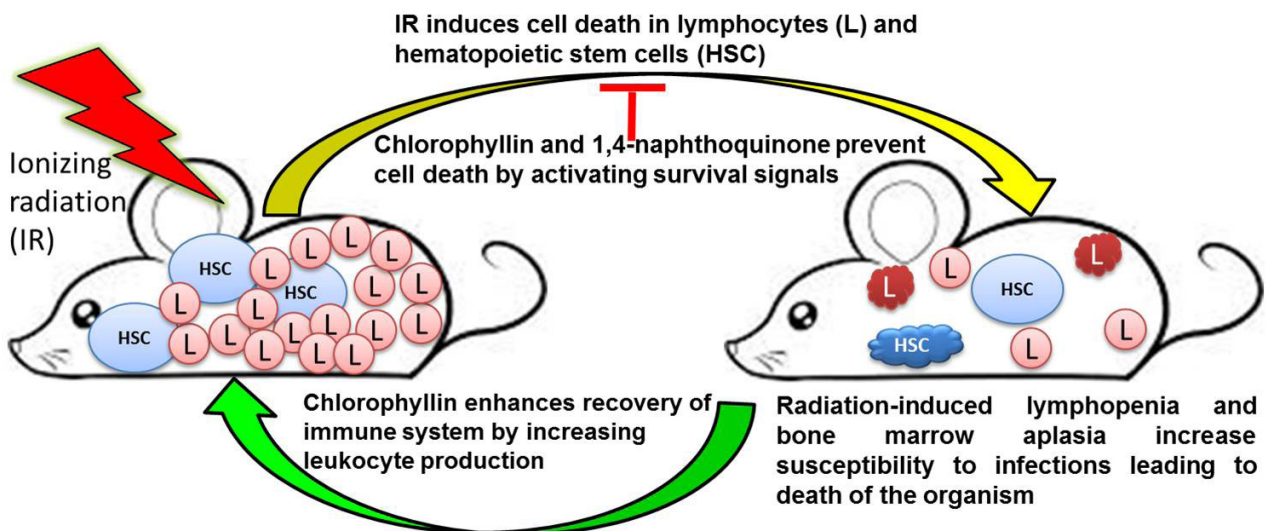


Fig. 2: The antioxidant chlorophyllin and the pro-oxidant 1,4-naphthoquinone prevent radiation induced cell death in lymphocytes. Chlorophyllin enhances recovery from radiation induced lymphopenia.

BARC NEWSLETTER

Founder's Day

survival, proliferation and death are sensitive to subtle redox changes. The changes in cellular redox by anti-oxidants or pro-oxidants can be harnessed for either augmentation of immune responses in weak immune-compromised patients or for suppression of chronic inflammatory disorders. Most importantly, with careful studies, either anti-oxidants or pro-oxidants can be used for prevention and mitigation of radiation toxicity (Fig. 2). Pre-clinical studies are in progress to evaluate the radioprotective efficacy of chlorophyllin for translation to humans.

References

1. "Spatial distribution, kinetics, signaling and cytokine production during homeostasis driven proliferation of CD4+ T cells.", Sharma D, Kumar SS, Checker R, Raghu R, Khanam S, Krishnan S, Sainis KB, *Molecular Immunology* 46(11-12), (2009):2403-12,
2. "Differential modulation of mitogen driven proliferation and homeostasis driven proliferation of T cells by rapamycin, Ly294002 and chlorophyllin", Sharma D, Kumar SS, Raghu R, Khanam S, Sainis KB, *Mol Immunol* 44(11), (2007):2831-40
3. "Differential Activation of NF-kappaB and Nitric Oxide in Lymphocytes Regulates In vitro and In vivo Radiosensitivity", Sharma D, Sandur SK, Rashmi R, Maurya DK, Suryavanshi S, Checker R, Krishnan S and Sainis KB, *Mutation Research*, 703, (2010): 149-157.
4. "Role of Immunoregulatory Transcription Factors in Differential Immunomodulatory Effects of Tocotrienols." Wilankar C, Sharma D, Checker R, Khan NM, Patwardhan RS, Patil A, Sandur SK and Devasagayam TPA, *Free Radical Biology & Medicine* 51(1), (2011):129-43.
5. "Antiapoptotic and immunomodulatory effects of chlorophyllin", Sharma D, Kumar SS, Sainis KB, *Mol Immunol.* 44(4), (2007):347-59.
6. "Benchmarks: Effective flow cytometric phenotyping of cells using minimal amounts of antibody", Sharma D, Eichelberg MR, Haag JD, Meilahn AL, Muelbl MJ, Schell K, Smits BMG and Gould MN, *Biotechniques* 53(1), (2012):57-60.
7. "Quantification of epithelial cell differentiation in mammary glands and carcinomas from DMBA and MNU-exposed rats", Sharma D, Smits BMG, Eichelberg MR, Meilahn AR, Muelbl MJ, Haag JD and Gould MN, *Plos One* 6(10), (2011): e26145.
8. "Prooxidants Ameliorate Radiation Induced Apoptosis Through Activation of Calcium-ERK1/2-Nrf2 Pathway ", Khan NM, Sandur SK, Checker R, Sharma D, Poduval TB and Sainis KB, *Free Radical Biology & Medicine* 51(1), (2011):115-28.

PHOTOCATALYTIC OXIDATION (VOC's) : A SHORT REVIEW ON GAS-SOLID INTERACTIONS

Kaustava Bhattacharyya
Chemistry Division

Dr. Kaustava Bhattacharyya is the recipient of the
DAE Young Engineer Award for the year 2012

Abstract

The photo-oxidation of the different VOC's (Volatile Organic Carbon) materials were studied using different V-doped TiO₂ and V-doped -TiO₂ dispersed over the mesoporous material MCM-41. The catalytic efficiency was monitored using UV and visible irradiation. The photocatalytic efficiency was incremented double on dispersing the photocatalysts on the mesoporous materials. The photocatalysts so synthesised were thoroughly characterized and their photocatalytic efficiencies were compared in the light of different structural parameters affecting their photooxidation properties. The detailed mechanism for the gas phase oxidation reactions were proposed using *in situ* FT-IR.

Introduction

Photo-process (oxidation/reduction) of hydrocarbons and CO₂ by heterogeneously catalyzed systems represents an extensive family of key processes. Occurrence of such process follows a number of different sequential phenomena such as intrapore diffusion of the reactants in gas-phase, adsorption, surface reactions, products desorption and diffusion. Nanosized materials are known to exhibit different properties relative to their bulk complements predominantly in surface-promoted processes like catalysis for diverse reasons. Change in the electron density as a function of particle size causes a disparity in chemical properties, results in different binding modes of the adsorbate molecules than that which is observed in corresponding bulk materials. Different structural parameters like oxidation state, particle size, band gap etc. play different and significant roles to alter the photocatalytic activity of the catalyst. Equivalently different surface intermediates are being produced depending on alteration of the surface,

source of irradiation and reaction conditions leading to modification in the efficiency and the final product of the photocatalyst. Some typical results for the V doped TiO₂ nano-TiO₂ and doped nano-TiO₂ dispersed in mesoporous materials, will be discussed in details. The *in situ* FT-IR was used extensively to understand the intermediates. The present short review is that of the photocatalytic oxidation work along with the mechanism and structure activity co-relation.

Experimental

A simple method of sol-gel process was employed for the preparation of the nano titania and V-doped titania, which required stoichiometric amount of ammonium metavanadate [2] as precursor of vanadium (Aldrich, 97%) initially dissolved in nano pure water at ambient conditions. To the above solution, Ti(IV) isopropoxide solution in isopropanol (IPA) was added drop wise in a controlled manner over a period of 1 h, with vigorous stirring until the formation of a uniform gel. The gel was kept for nucleation for 12 h in the dark, and then

dried in an oven at 100 °C for 4 h. The resulting solid mass was crushed and calcined at 500 °C for 4 h. The best V-doped TiO₂ photocatalyst was dispersed in MCM-41 (a mesoporous material synthesized in house) for differential loading percentages by incipient wet impregnation technique to find a better photocatalyst [3]. The materials were thoroughly characterised using techniques like XRD, HRTEM, TEM, XPS, DR-UV-Vis, Raman, FT- IR etc. techniques. The catalysts so obtained were evaluated as VOC (like ethylene, methane, propylene) oxidation reactions in the presence of UV light and visible light. Further the reaction mechanism for the gas phase reaction was studied using *in situ* FT-IR technique [4, 5].

Result and Discussion

Single phasic anatase titania with up to 10 mol % vanadium doping, having a particle size of about 12 nm, was synthesized by a sol-gel route and its photocatalytic behavior evaluated for the photo-oxidation of ethane using sunlight-type excitation. Vanadium doping led to a red shift in the UV-visible absorbance spectra compared to pristine titania, thus enhancing the absorption in the visible region. Synthesized nanotitania and vanadia-doped titania exhibit enhanced photocatalytic activity compared to the commercial bulk anatase TiO₂, with maximum activity obtained for the 5 mol % vanadium-doped titania sample, which was attributed to an optimum concentration of V⁴⁺ and V⁵⁺ species. The higher concentration of V in TiO₂ tends to stabilize V in the 5+ state predominantly, which is detrimental to the photocatalytic activity. The present study thus suggests that a mere change in the band gap by V doping in the TiO₂ lattice sites is not enough to further enhance the photocatalytic activity of the TiO₂ photocatalysts, but a favorable ratio of V⁴⁺/V⁵⁺ is also essential for this purpose. This is reflected in Fig. 1 [1]. *In situ* FTIR studies were undertaken to elucidate the mechanistic pathway for ethylene oxidation on these two catalyst surfaces. The ethylene decomposition occurs via formation of ethoxy groups, transformed

to acetaldehyde or enolates, subsequently to acetates/formates, and then to CO₂. The enolates were more stabilized on the TiO₂ surface, leading to formation of formates along with the acetates. On vanadium-doped TiO₂, acetaldehyde was more stabilized than its enol tautomer, leading to the formation of labile acetic acid and acetates. The formation of the labile acetic acid, adsorbed acetates, and the adsorbed acetate -M salts led to easier oxidation of them to provide higher yield of CO₂[2]. The higher positive charge density over Ti in Ti_{0.95}V_{0.05}O₂ with respect to nano TiO₂ makes the acetate (stronger nucleophile) a more stable intermediate on it Fig. 2A represents the above mechanism.

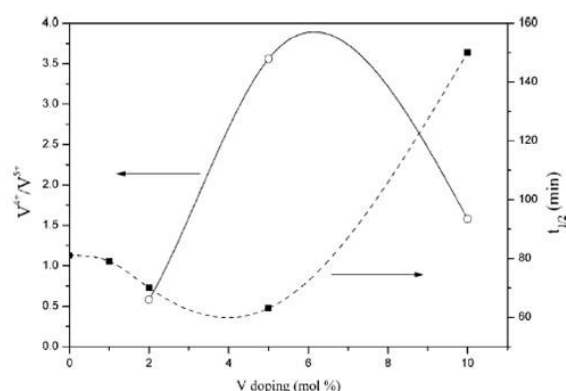


Fig. 1: Comparison of ratio of V⁴⁺/V⁵⁺ states ratio and that of the t_{1/2}.

Nanoparticles of Ti_{0.95}V_{0.05}O₂ were found to be impregnated in the hexagonal channels of the MCM-41 host, with a distribution of some particles on the surface, thus leading to an effective variation in the particle size as a function of loading host MCM-41 matrix.

This better catalytic activity is explained in light of the structure–activity correlation, and this can be attributed to an electronic interaction between the host and guest molecules, as established from X-ray photoelectron spectroscopy [4].

To understand the mechanistic aspect of the photooxidation of ethylene on the vanadium-

BARC NEWSLETTER

Founder's Day

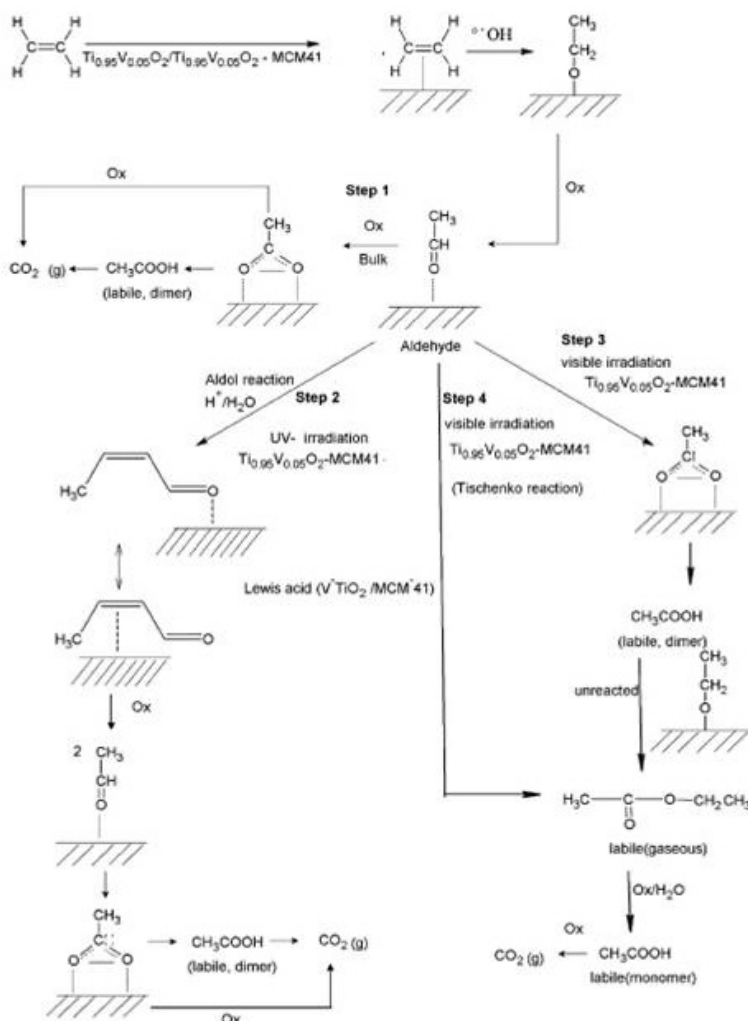


Fig. 2: Scheme showing the different intermediates formed on the V-doped TiO_2 surface, $\text{Ti}_{0.95}\text{V}_{0.05}\text{O}_2$ on MCM-41 with UV and visible irradiation.

doped titania dispersed in the MCM-41 matrix. The intermediate species produced on bare $\text{Ti}_{0.95}\text{V}_{0.05}\text{O}_2$ are different from that produced on the $\text{Ti}_{0.95}\text{V}_{0.05}\text{O}_2/\text{MCM-41}$ surface. Moreover, different intermediates were produced during ethylene oxidation under UV and visible irradiation, thus leading to different rates. In the case of $\text{Ti}_{0.95}\text{V}_{0.05}\text{O}_2/\text{MCM-41}$ catalyst with UV irradiation, the adsorbed acetaldehyde thus formed undergoes aldol condensation over the Lewis acid sites to lead to the formation of crotonaldehyde, which is subsequently oxidized to acetate and consequently to CO_2 . It was observed that during visible irradiation

labile ethyl acetate is produced either by the Tischenko reaction or by the reaction between the labile acetic acid and the unreacted ethoxy groups. The ethyl acetate produces acetic acid monomer, which is oxidized to CO_2 . Furthermore, in this work the effects of particle size on the intermediate species were also studied [4].

Conclusion

The photocatalytic oxidation of ethylene by V-doped TiO_2 reveals that not only the band gap but also the oxidation state of the dopant plays a very important part in the photocatalytic rate. The other factors like surface area, particle size along with the different intermediates formed on the surface dictates the reaction rate.

Acknowledgement

The author thanks Dr. A. K. Tripathi, Dr. A.K. Tyagi, Dr. S. Varma and Dr. S. Bharadwaj for their valuable contributions.

References

1. K. Bhattacharyya, S. Varma, A. K. Tripathi, S. R. Bharadwaj, and A. K. Tyagi *J. Phys. Chem. C*, 2008, 112 (48), 19102-19112
2. K. Bhattacharyya, S. Varma, A. K. Tripathi, S. R. Bharadwaj, and A. K. Tyagi *J. Phys. Chem. B*, 2009, 113 (17), 5917-5928.
3. K. Bhattacharyya, S. Varma, A. K. Tripathi, A. K. Tyagi, *J. Mat. Res.*, 2010, 25, 125
4. Kaustava Bhattacharyya, Salil Varma, Arvind Kumar Tripathi, Ajayan Vinu, and Avesh Kumar Tyagi *Chem. Eur. J.* 2011, 17, 12310 – 12325.

DESIGN, DEVELOPMENT AND CHARACTERIZATION OF SINGLE AND MULTILAYER FILMS

Arup Biswas

Atomic & Molecular Physics Division

Shri Arup Biswas is the recipient of the DAE Young Applied Scientist & Technologist Award for the year 2012

Introduction

It is well known that in order to get a specific spectral response of a wave after reflection or transmission, thin film multilayer device is unavoidable. Two materials having maximum contrast of refractive index and minimum absorption coefficient are deposited alternatively in pre decided fashion on optically smooth substrate for getting desired spectral response. In visible optics it can be used as high-reflecting mirrors, low/high/band-pass filters, anti reflecting surface, notch filters etc. In x-ray and neutron optics it can be used as mirrors, monochromators, polarizer/analyzer, filters, focusing devices etc. In this communication some of the devices which are in-house designed, developed and characterized are discussed.

Development of Soft X-ray Multilayer

Refractive index of any material in the X-ray region is < 1 and so for grazing angle of incidence beyond a certain critical angle the reflectivity falls off exponentially according to Fresnel's Law. Hence, in order to reflect X-rays at higher angle, the multilayer mirrors which are basically artificial Bragg crystals made up of alternate thin layers of low index (high Z, viz. W, Mo, Pt etc.) and high index (low Z, viz. Si, C etc.) materials are used. On the other hand due to the unavailability of suitable natural crystal or grating, in the soft X-ray band of 10–150Å, thin film multilayers become essential components in the optical devices as mirrors and monochromators. During design of

the X-ray multilayer structure, both materials (high Z and low Z) are required to be selected carefully to avoid absorption of X-ray inside the multilayer which depends on wavelength of X-ray. For example, W/Si and W/C can be used as potential material for multilayer mirror in less than 100Å region.

In order to develop the soft x-ray multilayer mirror an Ion Beam Sputtering (IBS) system has been developed in-house¹. Subsequent to installation and commissioning of the system single layer (W, Si, C), bi-layer (W/Si, W/C) and trilayer (W/Si/W and W/C/W) films are deposited at different deposition conditions and have been characterized by spectroscopic ellipsometry and specular and non-specular X-ray reflectivity measurements. From the results of all these measurements the optimized deposition condition for depositing W/Si and W/C multilayer have been selected¹⁻². The variation of density and roughness of the films have also explained by simulation using Monte Carlo code "TRIM"³.

At optimized process parameter obtained as above 5, 7, 9, 13, 17 and 25 layers W/Si multilayers have been deposited having 20Å of W and 28Å of Si in each bi-layer. These mirrors are designed such that it will have maximum reflectivity at 30° grazing angle of incidence for 45Å wavelength of light. The GIXR spectra of all multilayer samples have been shown in Fig. 1, which shows the presence of first Bragg peak at 0.92° for all the samples, which is close to the theoretical value, showing good thickness uniformity achieved in the

BARC NEWSLETTER

Founder's Day

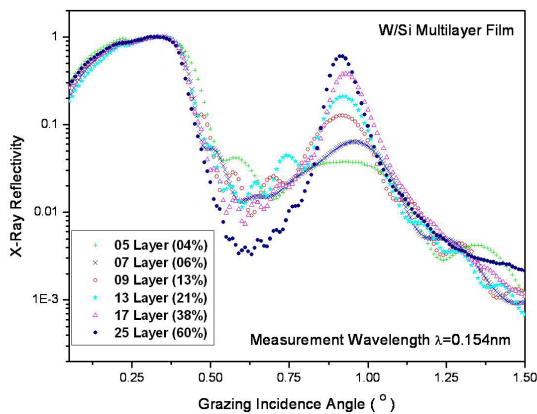


Fig. 1: GIXR spectra of 5, 7, 9, 13, 17, 25 layer W/Si multilayer film deposited by IBS technique

IBS system². Similarly 11, 15, 21 layer W/C multilayer samples have been deposited by Ion Beam Sputtering technique, on c-Si substrates. In the GIXR spectra the first Bragg peak for all the samples has been observed to appear at 0.75° grazing angle of incidence. It is also observed that the value of reflectivity increases from 24% to 45% as the number of layers increase from 11 to 21. Another 25-layer W/C sample, designed to give peak reflectivity at 26° for 44Å soft x-ray, has also been

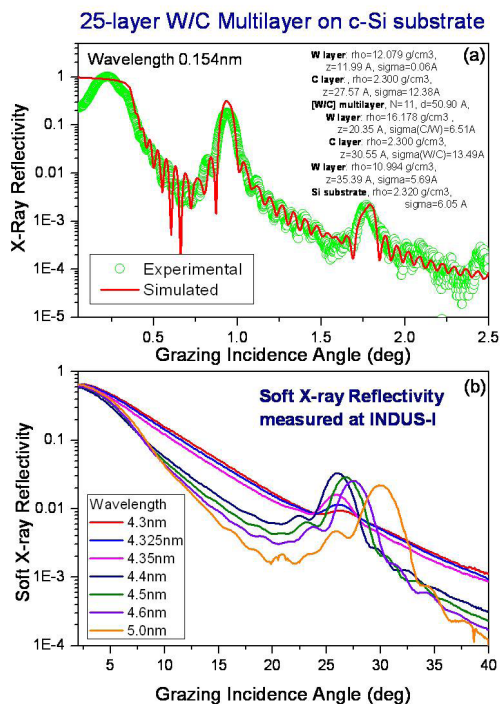


Fig. 2: (a) GIXR spectra of 25 layer W/C film along with best fitted spectra and result. (b) Soft x-ray reflectivity measured spectra of the same sample.

deposited, the first Bragg peak for this sample is found to appear at 0.93° grazing angle of incidence in GIXR measurement as shown in the Fig. 2(a) along with best fitted result. Some of the W/Si and W/C multilayer have been characterized at the reflectivity beamline of INDUS-I synchrotron source. The 25-layer W/Si mirror, which is designed for 45Å wavelength at 30° grazing angle of incidence, shows peak reflectivity at 33° grazing angle at 45Å. Similarly 21-layer W/C multilayer sample has also been characterized by measuring soft X-ray reflectivity in the range 0 to 35° grazing angle of incidence and with several probe wavelengths between 40-50Å. The measured reflectivity spectra, as shown in Fig. 2(b), depicts reasonably good reflectivity of the samples at the Bragg reflection peak in this wavelength regime⁴.

Development of Neutron Multilayer

Since refractive index of neutrons is also less than 1 for most of the materials, neutrons, also suffer total external reflection below critical angle and the reflectivity of the materials in this region is ~ 1 . A multilayer device prepared by depositing two alternate materials having strong contrast of neutron scattering length density creates high reflectivity Bragg peaks even beyond the critical angle or critical value. Due to their strong contrast in scattering length densities, Ni and Ti pairs are generally preferred in fabrication of such multilayer devices to be used as optical components in neutron delivery system. A supermirror, on the other hand, is a non-periodic multilayer device of hundreds of alternate layers of two materials having contrast of neutron scattering length density like Ni and Ti, where the thickness of a bi-layer or the value of the multilayer gradually increases from the substrate to the top of the device. A supermirror can thus be conceived as a stack of several multilayers having their individual Bragg peaks whose positions vary continuously and the closely spaced superimposed Bragg peaks pushes the critical angle of total external reflection by a large extent compared to a single layer film⁵. The performance of the supermirror is generally described

BARC NEWSLETTER

Founder's Day

by its 'm-value' which is actually the ratio of critical angle of total external reflection of the supermirror to the critical angle of natural Ni, viz, ($m = \frac{\theta_c^{SM}}{\theta_c^{Ni}}$)⁵. A computer code has been developed in house for the design of the structure of the neutron supermirrors based on Hayter and Mook formalism⁶.

In order to develop Ni/Ti based thin film multilayers as neutron reflectors an indigenously-built r.f. magnetron sputtering system has been used. Initially the deposition conditions for Ni and Ti films have been optimized for highest density and lowest surface roughness by depositing several single layer Ni and Ti films on c-Si substrates at different deposition conditions. At the optimized condition 11-layer, 21-layer, 31-layer and 51-layer Ni/Ti periodic multilayer thin film of different bilayer thickness have been deposited. GIXR measurements on the samples (Fig.3), shows that that unlike the single layer samples, the top layer roughness of the multilayers does not depend on the total thickness of the multilayers and the interface width of layers strongly depends on the bilayer thickness of the multilayers. It is proposed that similar power law for growth of roughness in single layers can be applied for multilayer interface width as a function of bilayer thickness⁷.

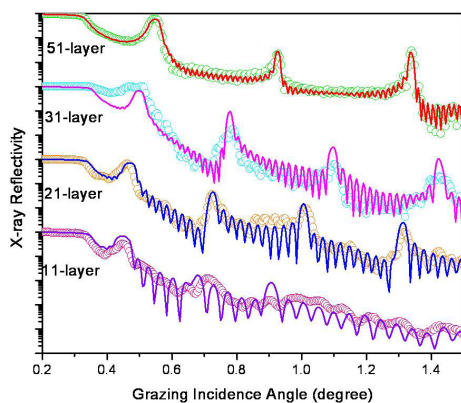


Fig 3: GIXR spectra of Ni/Ti multilayer films prepared by RF sputtering technique along with best fitted spectra

Subsequently, using the in-house developed code and indigenous sputtering system, two supermirrors of $m=1.75$ and $m=2.0$ having 62-layer and 98-layer Ni/Ti stack have been designed, deposited and have

been characterized by measuring neutron reflectivity at DHRUVA reactor at BARC, Trombay using 2.5\AA neutron wavelength. As shown in Fig. 4 the $m=1.75$ supermirror has shown more than 92% reflectivity while the $m=2.0$ supermirror has shown more than 71% of reflectivity which agree quite well with the theoretically generated reflectivity spectra of the samples.

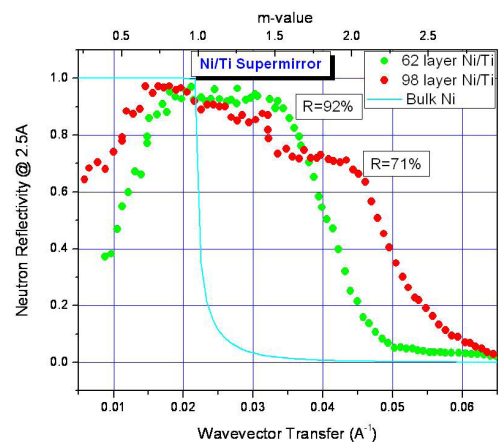


Fig 4: Neutron reflectivity of $m=1.75$ and $m=2.0$ Ni/Ti supermirror prepared by RF sputtering technique

Characterization by Spectroscopic Ellipsometer

In visible region normally multilayer devices are designed in such a way that every layer is a $\lambda/4$ plate for the designed wavelength and a combination of high index and low index material viz., $\text{TiO}_2/\text{SiO}_2$, $\text{HfO}_2/\text{SiO}_2$, $\text{Gd}_2\text{O}_3/\text{SiO}_2$ are chosen to achieve the target spectral characteristics. Electron beam evaporation or RF/Pulsed DC sputtering techniques are generally used to deposit these multilayer devices. Ex-situ analysis of these multilayer structures is a difficult task due to the presence of a large number of interdependent parameters and Spectroscopic Ellipsometry is a very important tool in this respect, where important information regarding the thickness and optical constants of the layers can be derived quite accurately by fitting the experimental results with theoretical spectra generated using a suitable model sample structure. Apart from the proper choice of sample

BARC NEWSLETTER

Founder's Day

structure, selection of proper dispersion relation of the material is also important in the ellipsometric analysis⁸. Fig. 5(a) shows an example of spectroscopic ellipsometric analysis of a 11-layer TiO₂/SiO₂ Fabry-Perot mirror deposited by electron beam (EB) evaporation technique and pulse-DC (PDC) sputtering technique which shows that the refractive index of TiO₂ and SiO₂ are more for PDC deposited sample compared to the EB deposited sample. The same samples have also been characterized by grazing incidence x-ray reflectivity (GIXR) technique (Fig.5(b)) which shows that densities of TiO₂ and SiO₂ films deposited by PDC technique are more than the densities obtained

by EB technique. This ellipsometric analysis feedback helps in the development of a 21-layer non-quarterwave high-pass edge filter required for the application pertaining to radio photoluminescence dosimeter⁹. Multilayer coatings are also done to increase the efficiency of photo-thermal conversion in solar collector. A new approach is to deposit graded index layer on a reflecting metal surface in which the refractive index and extinction coefficient continuously decrease from the substrate to the surface. Such a tandem absorber provides high absorbance and low emittance in the solar spectrum and can be used as solar selective absorber in solar collectors. By analyzing

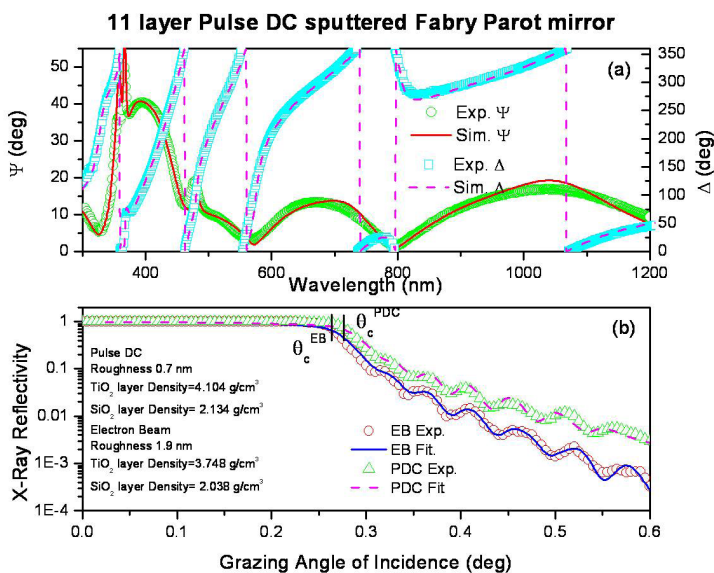


Fig. 5: (a) Spectroscopic Ellipsometric (b) GIXR spectra of 11-layer TiO₂/SiO₂ PDC sputtered Fabry Perot mirror along with best fitted spectra.

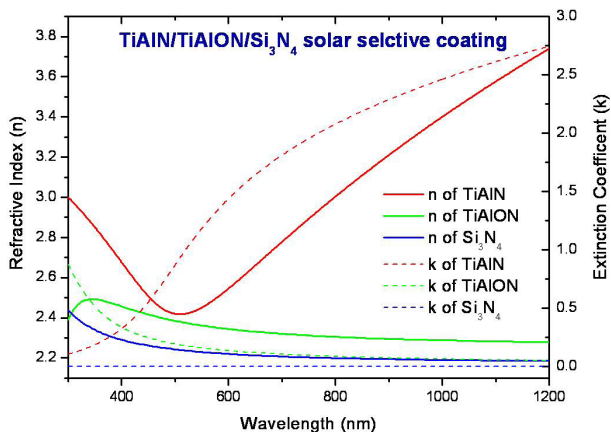


Fig 6: The n and k of different layers of TiAlN/TiAlON/Si₃N₄ solar selective coating measured by Spectroscopic Ellipsometry

the spectroscopic ellipsometric data the depth profiling of refractive index and absorption coefficient of the tandem can be carried out which provides very important information for improving the performance of this type of multilayer devices¹⁰⁻¹⁴. In Fig.6, the refractive index (n) and absorption coefficient (k) of a TiAlN/TiAlON/Si₃N₄ multilayer, as obtained from ellipsometric measurement is shown^{10,11}. It is observed that from surface layer (Si₃N₄) to the bottom layer (TiAlN), n and k decrease resulting in high absorbance (0.95) and a low emittance (0.07) of the device¹⁰.

Summary

Over the last several years, Atomic & Molecular Physics Division, BARC has developed state-of-art expertise to design, grow and characterize thin film multilayer devices for optical applications. The multilayer devices can be designed and developed for a wide range of electromagnetic spectra and for particle beam like neutron. Optical multilayers are generally grown by E-beam evaporation technique and characterized by Spectroscopic Ellipsometry technique, while soft X-ray multilayers which are thin layers of very low roughness metallic and non-metallic films are generally grown by indigenously developed Ion beam sputtering technique and characterized by specular

BARC NEWSLETTER

Founder's Day

and non-specular grazing incidence X-ray reflectivity (GIXR) measurements. Multilayer neutron mirrors and supermirrors are, on the other hand, prepared by indigenously developed magnetron sputtering systems and characterized by GIXR technique. Both soft X-ray and neutron mirrors are also characterized by INDUS-1 synchrotron soft X-ray source and DHRUVA nuclear reactor respectively.

References

1. Biswas, A; Poswal, A.K; Tokas, R.B; Bhattacharyya, D; *Appl. Surf. Sci.* 254 (2008) 3347.
2. Biswas, A; Bhattacharyya, D; *J. App. Phys.* 109 (2011) 084311.
3. Biswas, A; Bhattacharyya, D; *Nuc. Inst. Meth. in Phys. Res. B* 268 (2010) 1594.
4. Biswas, A; Bhattacharyya, D; AIP Conf. Proc. 1451 (2012) 79.
5. Mezei, F *Comm. Phys.* 1 (1976) 81.
6. Hayter, J.B; Mook, H.A *J. Appl. Cryst.* 22 (1989) 35.
7. Maidul Haque S; Biswas, A; Bhattacharya, Debarati; Tokas, R.B; Bhattacharyya, D; and Sahoo, N.K *J. Appl. Phys.* 114 (2013) 103508.
8. Bhattacharyya, D; Biswas A, *J. Appl. Phys.* 97 (2005) 053501.
9. Sagdeo, P.R.; Shinde, D.D; Misal, J.S; Kamble, N.M.; Tokas, R.B; Biswas, A; Poswal, A.K; Thakur, S; Bhattacharyya, D; Sahoo, N.K; Sabharwal, S.C; *J. Phys. D: Appl. Phys.*, 43 (2010) 045302.
10. Barshilia, Harish C; Selvakumar, N; Rajam, K. S; Sridhara Rao, D. V; Muraleedharan, K; Biswas A, *Appl. Phys. Lett.* 89 (2006) 191909
11. Biswas, A; Bhattacharyya, D; Barshilia, Harish C; Selvakumar, N; Rajam, K.S; *Appl. Surf. Sci.* 254 (2008) 1694.
12. Barshilia, Harish C; Selvakumar, N; Rajam, K.S; Biswas, A *J Appl. Phys.* 103 (2008) 023507.
13. Barshilia, Harish C; Selvakumar, N; Rajam, K.S; Biswas, A *Sol. Energy Mater. Sol. Cells*, 94 (2010) 1412.
14. Selvakumar, N; Manikandanath, N.T; Biswas, A; Barshilia, Harish C *Solar Energy Materials & Solar Cells* 102 (2012) 86.

RETROFITTING OF SERVO-MANIPULATOR SYSTEM IN HLW VITRIFICATION CELLS OF WIP, TROMBAY

Shendge S.R., Sandhanshive D.S., Singh K.M., Shivani Patankar, Suresh Babu
Nuclear Recycle Group

Shri S.R. Shendge is the recipient of the DAE Young Applied Scientist & Technologist Award for the year 2012

Abstract

Manipulators play a vital role for remote operations in radiochemical plants and help in achieving the most essential requirement of ALARA principle during operation and maintenance of such plants. The earlier Servo-Manipulator (SM) system, installed at Waste Immobilization Plant (WIP), Trombay had metallic tapes, ropes and pulleys for motion transfer and was prone to frequent maintenance problems due to failure of wires and tapes. Hence, a higher payload capacity SM having gears and links for motion transfer was developed and rigorously tested to prove its cell worthiness. This system was then installed in vitrification bay of high level WIP, Trombay in the year 2012. Since then the SM is working satisfactorily till date. This paper describes the details of this SM system.

Details of Servo-Manipulator System

The master and slave arms of SM system are electrically linked, the slave arm is installed on the existing boom of SM carriage inside the hot cell. This facilitates movement of the slave arm throughout four shielded hot cells to carry out any remote operations. The master arm is installed in the SM workstation having CCTV monitoring system for these hot cells (Fig. 1).



Fig. 1: Operating with the Master arm in SM workstation

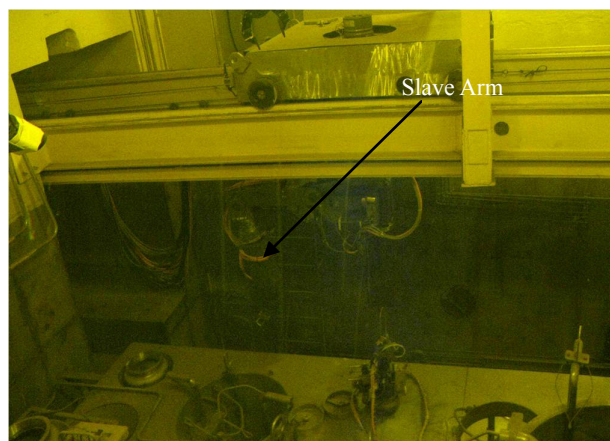


Fig. 2: The Slave arm in hot cell

Both these arms are anthropomorphic and have elbow up construction with six degrees of freedom (DOF) & an end effector (i.e. gripper). The DOFs are shoulder rotation, upper & lower arm pitch motions, azimuth rotations and pitch & roll motions of wrist joint. The pay load capacity of the slave arm is 25 Kg at the gripper (in all positions and all orientations). A Force Feed Back (FFB) system provides the additional safety during the remote operations which prevents

BARC NEWSLETTER

Founder's Day

mechanical failure of the components.

The control architecture is based on a high end centralized Digital Signal Processing (DSP) system & individual drives & controller for all the 13 axes of the system (Fig. 3). The system can provide variable FFB from 0 to 8 kg to reduce operator's fatigue. The slave arm can be operated through PC, Pendant switch or by using the master arm while viewing the task environment through CCTVs.

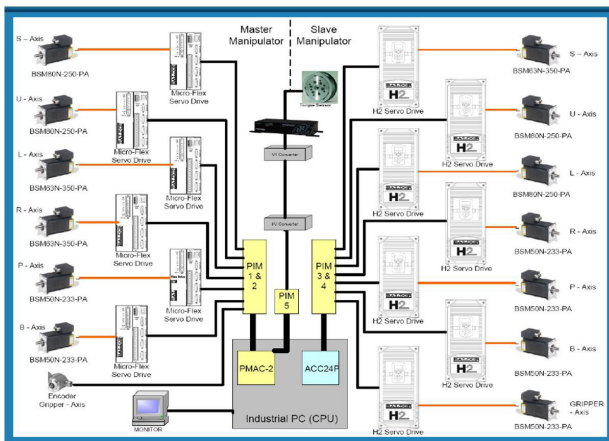


Fig. 3: System Architecture

The SM controller performs the following functions:

1. Positional tracking of the slave arm joints with respect to the master arm joints and control of slave arm dynamics i.e. Master-Slave operation mode (Fig. 4).

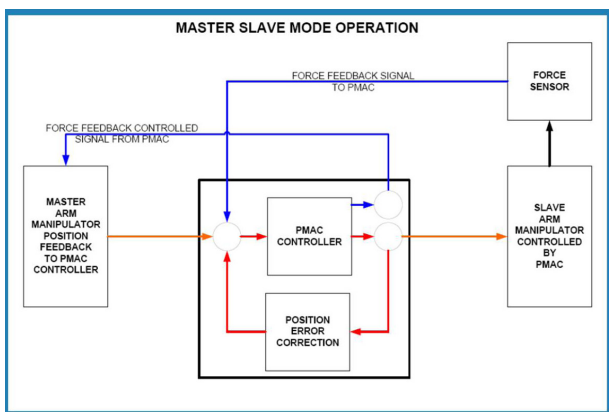


Fig. 4: Master-Slave operation mode

2. Variable Force Feed Back reflection.
3. Status monitoring and self diagnostic reporting.
4. Electronic counterbalancing calculation.
5. Indexing of individual axis.
6. Braking of individual axis.
7. Warning against various errors/unsafe conditions and suggests corrective actions.
8. Variable gripping force.

Testing of SM system

A seven stage detailed testing procedure was formulated in consultation with the experts from DRHR for the testing of the SM to prove its cell worthiness and also to scrutinize the parameters like friction, inertia, back lash, load, rigidity, accuracy etc (Fig. 5 & 6).



Fig. 5: Testing of SM system



Fig. 6: The Slave arm during testing

BARC NEWSLETTER

Founder's Day

Advanced Features of the SM System

- Advanced DC servo motors and gear boxes to reduce inertia, back lash and improved accuracy.
- Variable FFB to the operator.
- Fine speed control of individual motors and precise positioning of slave by commands through PC.
- Linear movement of end effector in X, Y or Z direction through PC.
- Enhanced flexibility of operation: Master canting mode, Slave canting mode, Master-slave mode and maintenance mode.
- Radiation resistant electrical cables.
- Enhanced safety: Soft switches, overload tripping etc.
- Easy maintenance: Modular assemblies for quick replacement, easily accessible joints.

- The control system has the capability of performing repetitive operations of the slave arm, as a robot, through programming.

Summary

The new SM system has various modes of operation and advanced features which improves flexibility during operation, safety of mechanical and electrical components and reduces maintenance related issues of the system. Further, as though the SM design has improved with respect to mechanical maintenance issues and add on advanced features, but in doing so the SM system has become bulky in size and there is a scope to improve the same in next version of the manipulator.

SHOCK STUDIES USING ELECTRIC GUN AND FABRY-PEROT VELOCIMETER

A.K. Saxena, T.C. Kaushik and Satish C. Gupta
Applied Physics Division

Shri A.K. Saxena is the recipient of the DAE Young
Applied Scientist & Technologist Award for the year 2012

Abstract

To study material behavior under shock loading an 8 kJ electric gun system has been developed with capabilities to drive small diameter (6 mm) aluminum flyers up to 4.5 km/s and polyimide flyers up to 6.2 km/s. Main diagnostic of this setup is a Fabry-Perot velocimeter, that has been developed to measure projectile as well as target-window interface velocities with an accuracy of 0.2 km/s. Impact experiments have been carried out on various metals like tantalum, tin, aluminum and iron up to shock pressures of 70 GPa. In thin iron samples a shock induced phase transition at 13.6 GPa, and reverse transition in release path at 10.8 GPa has been recorded.

Introduction

Understanding the behavior of solids at high pressures has been a topic of interest for research community related to fields like astrophysics, inertial confinement fusion, impulse technology and strategic applications. High impulse pressures are commonly generated by impact of a high velocity planar projectile to a target material. Various experimental techniques like explosives, gas gun, rail gun, magnetically accelerated flyer plates, and electric gun are used to accelerate projectiles to high velocities. Most of these techniques, except electric gun require special experimental facilities, complex technology and intensive operational procedures. Furthermore electric gun setup can be designed for small scale laboratory operations^{1,2} with capabilities to accelerate small projectiles to high velocities. These devices have been reported to generate pressures up to 0.78 TPa³ and can be used in research on precious or hazardous materials as only small quantity are needed. The principle of electric gun is to use the energy initially stored in a fast capacitor bank to explode a thin metallic bridge foil sandwiched

in between two dielectric sheets supported at one side by a heavy tamper and an appropriate size barrel on the other (Fig.1). Due to fast explosion, foil material expands and punches out a section of the dielectric sheet (flyer) positioned adjacent to it and drives it up in the barrel to suitably high velocities. The target under study is placed at the other end of barrel, which is subjected to shock loading on flyer impact.

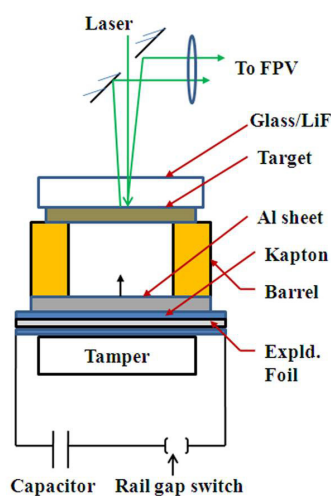


Fig.1: Schematic of electric gun setup for shock studies.

BARC NEWSLETTER

Founder's Day

Study of equation of state (EOS) of materials at such high pressures requires the knowledge of projectile as well as the particle velocity in target material. Optical interferometric techniques are commonly implemented for these measurements and are based on determining the Doppler shift in the light reflected from the moving surface. Fabry-Perot velocimeter (FPV) is one such potential technique in which time evolution of fringe diameters are recorded on a streak camera and used to calculate the velocity profile of moving surface.

To experimentally investigate the response of materials from 10 to 100 GPa pressure, low energy portable electric gun setups have been developed in our laboratory along with a Fabry Perot velocimeter. The details these techniques and shock studies carried out on different metals are given in following sections.

Experimental setup

Three portable electric gun systems have been developed in our laboratory for various applications. The ELG-2 (1.6 kJ) setup is dedicated for studies related to energetic materials, ELG-8 (8kJ) is utilized for shock studies on different metal targets and ELG-16 (16 kJ) is under characterization for studies related to materials relevant for nuclear systems. Shock studies reported here are carried out on ELG-8 setup and details of this system may be found in Ref-1. The photograph of this system is shown in Fig. 2; it consists of an energy storage capacitor of rating 10 μ F/ 40 kV, triggered rail-gap switch, parallel plate transmission lines and

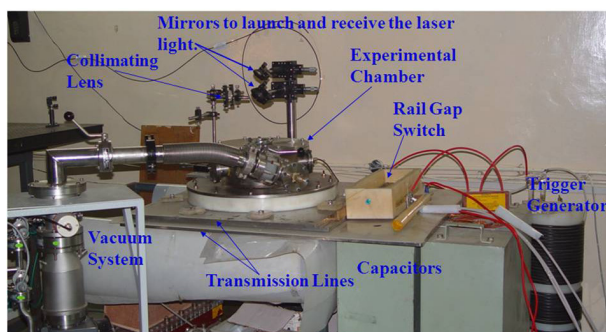


Fig.2: Photograph of experimental setup.

a cylindrical experimental chamber for connecting exploding foil sandwiches. This electric gun setup has been optimized to achieve a pre-defined velocity from 1.5 km/s to 4.5 km/s on 6 mm diameter aluminum-polyimide composite flyers and up to 6.3 km/s on polyimide flyers.

The major diagnostic of this set up is a Fabry-Perot velocimeter⁴ which is designed to record velocities in the range of 0.5 to 10 km/s with an estimated resolution of 0.2 km/s. This velocimeter has also been optimized to measure velocities of two surfaces on a single record⁵ for precise EOS measurements.

Experimental Results:

Experiments were carried out on different metal targets like aluminum, tin, tantalum and iron. Some results have already been reported in earlier published work^{1, 5} where implementation of single FPV for simultaneous measurement of two surface velocities have also been discussed and here we present our recent results on iron and tantalum. The iron is one of the important material found in earth core, and is reported to have a reversible shock transformation from a body-centered-cubic (α) to hexagonal-closed-packed (ϵ) structure above 13 GPa. We carried out a series of experiments on thin iron foils (100 μ m) under shock loading from 20 GPa to 55 GPa and measured the target/ window interface velocity profiles. Pressure profiles deduced

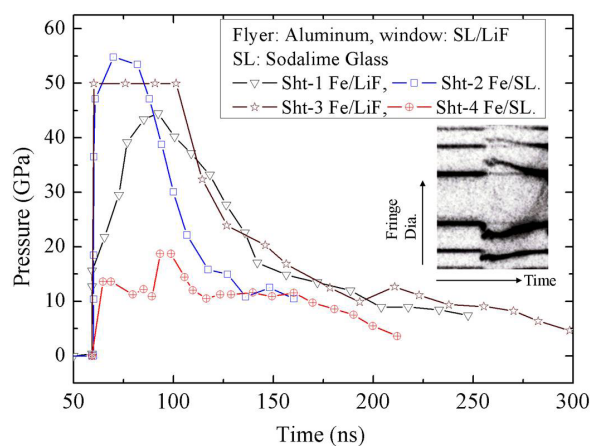


Fig.3: Shock studies on iron.

BARC NEWSLETTER

Founder's Day

from Fabry-Perot records using equation of state of target, window and flyer materials are shown in Fig.3. Due to change in density involved in phase transition, single shock is split in two waves. A kink near 15 GPa has been observed when the sample was subjected to a peak pressure of 44 GPa, indicating a polymorphic transition. At lower pressures near to 20 GPa, a clear two wave structure with a detailed release profile was recorded. The streak record showing the movement of Fabry-Perot fringe diameters is also shown in inset of Fig.3. Deuced pressure profiles shows a transition in iron from bcc to hcp phase at 13.6 GPa under shock and a reverse phase transition in the release path at 10.8 GPa, which is well in agreement with the reported values. Shock experiments were also carried out on Tantalum up to 70 GPa and is shown in Fig. 4, here due to limited time resolution of streak camera flat pressure region could not be determined accurately and rarefaction appears to be just following the shock.

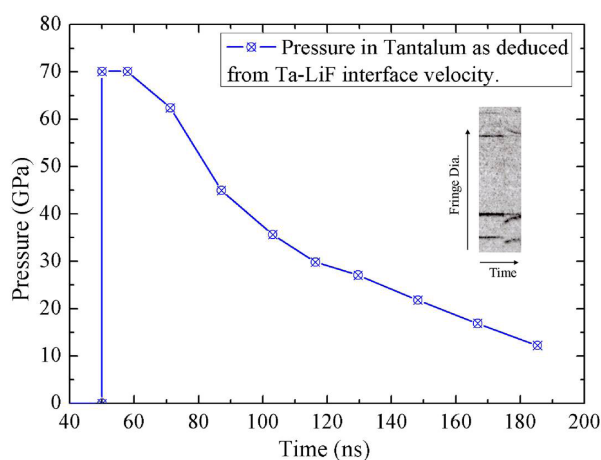


Fig.4: Pressure profile in tantalum.

Conclusions

Electric gun setups along with Fabry-Perot velocimeter have been developed in our laboratory for shock studies up to 70 GPa on different metals. A detailed pressure profile showing the polymorphic phase transition in iron from bcc to hcp at 13.6 GPa under shock and reverse transition in release path at 10.8 GPa has been recorded. Tantalum has been subjected up to a peak pressure of 70 GPa. Work is in progress to achieve still higher pressures, and to carry out systematic shock studies.

References

1. A.K. Saxena, T.C. Kaushik, and Satish C. Gupta, *Rev. Sci. Instrum.*, 81, (2010): 033508.
2. Guiji Wang, Jia He, Jianheng Zhao, Fuli Tan, Chengwei Sun, Jianjun Mo, Xin Xong and Gang Wu, *Rev. Sci. Instrum.*, 82, (2011): 095105.
3. K.E. Froeschner, R.S. Lee, H.H. Chau and R.C. Weingart, *Shock Waves in Condensed Matter - 1983*, eds. J.R. Asay, R.A. Graham, and G.K. Straub, Elsevier, Amsterdam, (1984): 85.
4. A.K. Saxena, T.C. Kaushik, A.M. Rawool, L.V. Kulkarni and S.C. Gupta, BARC Report, BARC/2007/E013, (2007).
5. A.K. Saxena, T.C. Kaushik, A.M. Rawool and Satish C. Gupta, *J. of Phys: Conf. Series.* 377, (2012): 012049.

BARC NEWSLETTER

Founder's Day

DEVELOPMENT OF HOT CELLS AND THEIR EMBEDDED PARTS

K. Jayarajan, B. Sony, V.K. Shrivastava, R. Sahu, S. Panda, A.N. Jha, M.N. Rao

Division of Remote Handling and Robotics

Vivek Mahadev

Seismology Division

A.K. Pradhan

Isotope Application Division

S. Sethi, S.P. Dey, K. Karmakar, S.B. Gaikwad

Laser and Plasma Technology Division

V.R. Bhave, Kuldeep Sharma

Sealed Sources and Logistics, BRIT

Anwer Tariq

RAPP Cobalt Handling Facility, BRIT

Shri K. Jayarajan is the recipient of the DAE Group Achievement Award for the year 2012

Abstract

Hotcell facilities are used for handling radioactive materials for various applications, like waste management, radioisotope production and post-irradiation examination. We have been involved in the development of hot cells, water pools and associated equipments. Hot cell embedded parts like personal access doors, external transfer drawers, inter-cell transfer drawer, wall sleeves, plugs and hot cell liners play a major role in the operation of the plant and safety of the operators. The article describes our recent experience in development of these components.

Introduction

In nuclear industry, shielded nuclear radiation containment chambers are referred as hot cells. They protect operators and the environment from the harmful effects of radiation. Hot cell walls are made from lead-bricks or from concrete. Thickness of the concrete wall vary from 1 m to 2 m depending upon the shielding requirements.

The walls and the floor of hot cells are embedded with a variety of equipments or components. Embedded parts (EPs), such as wall liners, wall sleeves and rails are static. However, EPs like access door,

inter-cell transfer drawer and external transfer drawer contain heavy moving parts. These EPs maintains shielding integrity during normal and accidental conditions. Safety inter locks are provided on dynamic EPs to avoid accidental exposure of radiation to operator.

CCTV cameras or radiation shielding windows are used for viewing the hot cell. Objects in the hot cells are usually handled using general-purpose remote handling tools like Master Slave Manipulators, Power Manipulators and In-cell Cranes. Viewing systems and remote handling tools are not in the scope of the article.

BARC NEWSLETTER

Founder's Day

Recently, we have been involved in development of hot cells and associated embedded parts for the following facilities.

- Augmentation of Cobalt Handling Facility, Kota (ACHF)
- Augmentation of Hotcell and Associated Facilities for Radiation Technology Applications, Trombay (AHCAFRTA)
- Integrated Facility for Radiation Technology, Vashi (IFRT) and
- Uranium Clean-Up Facility, Trombay (UCUF).

In ACHF hot cells, the adjuster rods are processed to recover cobalt-60 pencils and pellets for making sealed sources. Fig.1 shows irradiated adjuster rod sub-assemblies of power reactors placed in the RAPPCOF Water Pool.

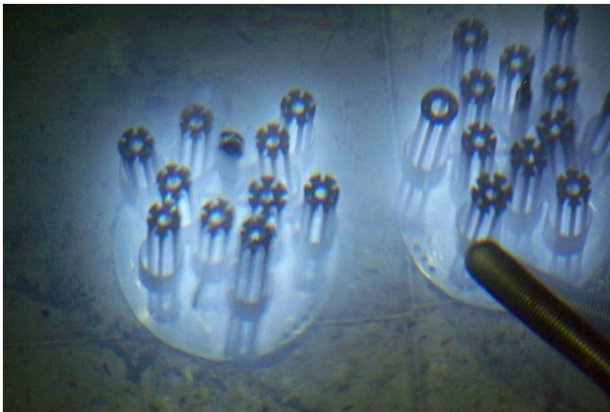


Fig. 1: Irradiated Adjuster Rod Sub-assemblies at RAPPCOF Water Pool

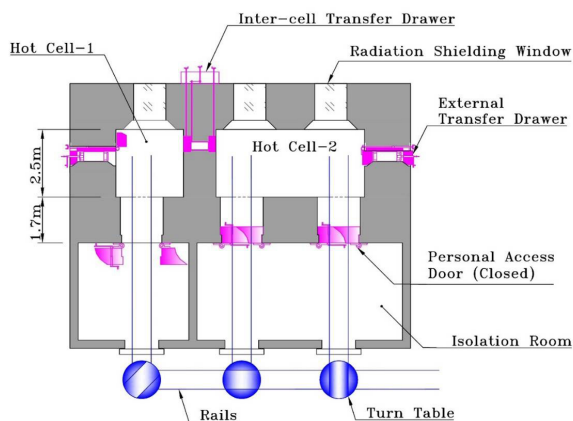


Fig. 2: Major EPs of a Typical Hot Cell (Top View)

Fig. 2 shows the plan view of a typical hot cell facility indicating commonly used EPs. The hot cells (red zone) are connected to the high bay area (green zone) through isolation rooms (amber zone) as per radiation zoning principle.

Fig. 3 shows the sectional end view of one of the hot cells.

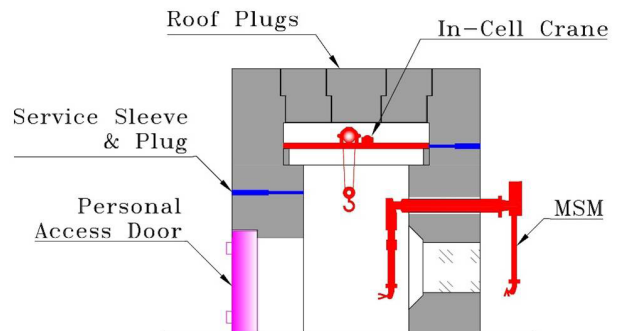


Fig. 3 EPS and Remote Handling Tools of a Hot Cell (Side view)

Common Embedded Parts

Personal Access Door

Personal access doors are used for personnel entry into the hot cell and for transferring radioactive materials between the cold area and the hot cell in shielded flasks. Access doors are of two types: hinged or sliding.



Fig. 4: Personal Access Door of ACHF, Kota at Fabricator's Shop

BARC NEWSLETTER

Founder's Day

They may be motorised or manual. Mild steel doors are designed to provide radiation-shielding equivalent that of the concrete cell wall. Fig.4 shows the door designed by us for ACHF, Kota. The mild steel door weighing about 45 tons has a door flap thickness of 600 mm.

External Transfer Drawer

The external transfer drawer embedded in the concrete wall is used for transferring materials into the hot cell from outside and vice versa. It has two shielded doors, a transfer drawer and mechanisms for operating the doors and the transfer drawer. The doors are mechanically interlocked to avoid simultaneous opening of both doors.

Inter-cell Transfer Drawer

The inter-cell transfer drawer, embedded in the common wall of adjacent hot cells, is used for transferring materials from one hot cell to the other. It consists of an outer casing, two shielded doors, a transfer drawer and remote mechanisms for operating the doors and the drawer. The doors are mechanically interlocked to avoid simultaneous opening of both doors.

Service Sleeves and Plugs

For transmission of electric power, electric signal, pneumatic supply, etc. across the hot cell walls, service sleeves and plugs are provided on the walls. The plugs are housed in the sleeves, which are embedded in the wall. Their shapes are designed to avoid direct radiation streaming.

Rails and Turntables

Active components are transferred between the water pool and the hot cells in heavy shielded flask placed

on a trolley. Rails are laid on the floors of hotcell and outside for transferring the trolley. Turntables are provided at the junctions of the rails. The rails in the hot cell are lined with stainless steel plates.

Hot Cell Liner

Walls and floor of the hot cells are lined with stainless steel plates for easy decontamination. The stainless steel plates are welded to the grid embedded in to the wall or floor.

Water Pool Liner

Leak tightness is one of the major requirements of any storage pool in a nuclear installation. As the first barrier of leakage, the walls and the floors of the pools are lined with stainless steel plates. The liner is designed to withstand internal as well as external hydrostatic pressure. Stringent quality control is implemented to ensure leak tightness.

Lead Bricks

In place of concrete, mild steel encased lead bricks can be used to construct the walls of a hot cell. Although expensive, it will significantly reduce the thickness of hot cell walls. To avoid radiation streaming, the bricks are made with interlocking edges. Such lead bricks are used in two wall of the alpha- beta- gamma shielded hot cell of UCUF.

Conclusion

Embedded parts of hot cells play a major role in the operation of the plant and safety of the operators. EPs of our design are installed in the hot cells of AHCF, ACHFRTA, IFRT and UCUF. ACHF is operational at RAPP COF, Kota. It has been producing and supplying Industrial Irradiator Sources and Tele-therapy Sources of cobalt-60.

BENCH SCALE DEMONSTRATION OF URANIUM RECOVERY FROM ACIDIC NITRATE BASED NUCLEAR WASTE USING DISPERSION LIQUID MEMBRANE IN MICRO POROUS POLYMERIC FIBER CONTACTOR

S. Mukhopadhyay

Chemical Engineering Division

Dr. Sulekha Mukhopadhyay is the recipient of the DAE Group Achievement Award for the year 2012

Abstract

Chemical Engineering Division has developed a process for recovery of uranium from acidic nitrate waste stream of uranium purification plant and demonstrated the process in bench scale. The developed process is based on application of dispersion liquid membrane composed of TBP in Dodecane as organic extractant and Sodium Bicarbonate as strippant in a cluster of micro porous polymeric fiber contactors of effective contact area 8.1 m² at 60 LPH throughput. In the demonstration run, 200 liters of filtered waste acidic raffinate solution from uranium refining plant was treated in the bench scale set up bringing down the source stream concentration of uranium below 30 ppm in continuous countercurrent mode. With recycle of the stripping solution after adjusting for pH in a semi batch mode in the same set up, the uranium concentration upto 5.6 gpl was obtained in the product stream, which can be directly taken up for recovery of uranium by precipitation. These studies have successfully demonstrated and established quantitative recovery of Uranium from acidic raffinate steam of uranium metal purification plant, leading to easy disposal of raffinate. The demonstration runs were jointly conducted with UED.

Introduction

The uranium refining plants generate acidic raffinate waste stream in nitrate form, which is either neutralized and sold as low value byproduct or diluted and dispersed depending on the level of concentration of nitrates and uranium. Uranium recovery from such lean streams is of immense importance in view of generation of clean waste streams, which are easily disposable. Conventional techniques like solvent extraction, ion exchange etc are not economical for such streams due to issues of large organic solvent

requirement, poor selectivity and process inefficiency due to equilibrium limitations. In order to address such issues, a process has developed by ChED based on application of Dispersion type Liquid Membrane (DLM) in micro porous polymeric fiber contactors, which provide high specific interfacial area of mass transfer through micro bore polymeric lumens with micro-porous wall. The DLM technique has the advantage of simultaneous extraction and stripping across thin organic membrane. This provides high driving force throughout the separation enabling complete polishing of lean streams with relatively low requirement of

BARC NEWSLETTER

Founder's Day

organic solvent compared to conventional solvent extraction process in conventional contactors.

Experiments and Demonstration runs

Uranium Metal Plant of BARC generates acidic raffinate waste stream containing 700 to 1000 ppm of uranium in 1 to 2 M nitric acid medium with traces of impurities like iron, aluminum, magnesium, nickel, manganese, boron, etc. This stream was taken up for recovery of uranium value with 30% TBP in Dodecane as organic solvent and 1M Sodium Bicarbonate solution as stripping agent. Initially lab scale studies were conducted using smaller micro porous polymeric fiber modules (effective contact area 1.4 m²) at 12 LPH flow rate. These studies showed the dispersion liquid membrane in micro porous polymeric fiber to



Fig. 1: Single hollow fiber contactor set up operating in recirculation mode; Flow rate: 12LPH; Feed: U raffinate; dispersion: aq/org 1:1, aq (1 M NaHCO₃), org (30 % v/v TBP in Dodecane)



Fig. 2: Experimental set up of 3 small HF contactors in series operating in once through mode; Flow rate: 12LPH; Feed: U raffinate; dispersion: aq/org 1:1, aq (1 M NaHCO₃), org (30 % v/v TBP in Dodecane)

be quite efficient, stable and promising for complete recovery of uranium from plant raffinate in continuous countercurrent mode.

Based on the lab scale experimental studies and predictions of developed mathematical model for the dispersion liquid membrane in micro porous polymeric fiber system, bench scale experimental facility by employing larger membrane contactors (effective contact area 8.1 m²) was set up and trials were carried out at a throughput of 60 LPH. A flux of 2.5 x 10⁻¹⁰ moles/cm²/s was obtained for uranium which is about 3-4 times of supported liquid membrane in micro porous polymeric fiber module and about 10-50 times of solvent extraction in conventional contactor. Based on the above encouraging findings, bench scale

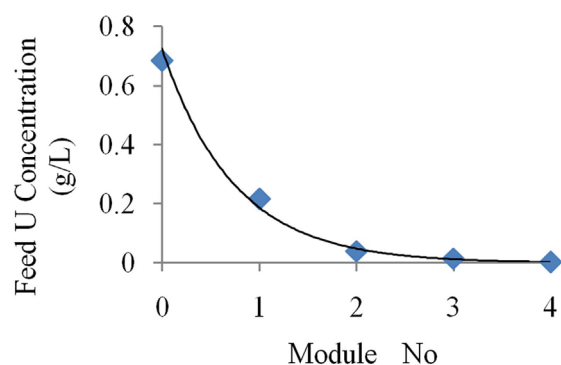


Fig. 3: Conc of U in raffinate at module exits
Feed: U raffinate; dispersion: aq/org 1:1, aq (1 M NaHCO₃), org (30 % v/v TBP in Dodecane); flow rate: 60LPH; 4 big modules

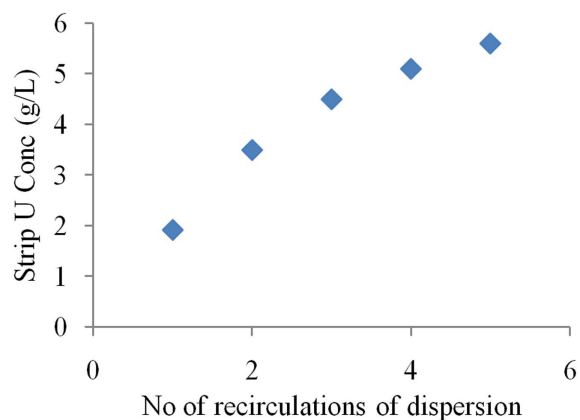


Fig. 4: Conc of U in product after alkali make up and recycles
Feed: U raffinate; dispersion: aq/org 1:1, aq (1 M NaHCO₃), org (30 % v/v TBP in Dodecane); flow rate: 60LPH; 4 big modules strip re-circulation.

BARC NEWSLETTER

Founder's Day

demonstration using four big micro porous polymeric fiber modules in series has been successfully conducted jointly with Uranium Extraction Division. About 200 liters of filtered waste acidic raffinate solution from Uranium Metal Plant was treated at 60 LPH flow rate in the bench scale set up, bringing down the source stream concentration of uranium below 30 ppm from about 900 ppm. The phase flow ratio of Feed: Organic: Strip was 1:0.5:0.5. With adjustment of pH and recycle of the stripping solution in a semi batch mode in the same set up, the uranium concentration upto 5.6 gpl was obtained in the product stream

(0.7M alkaline), which can be directly taken up for recovery of uranium by precipitation. A flow sheet for recovery of uranium from lean acidic nitrate wastes has been developed and successfully demonstrated in bench scale.

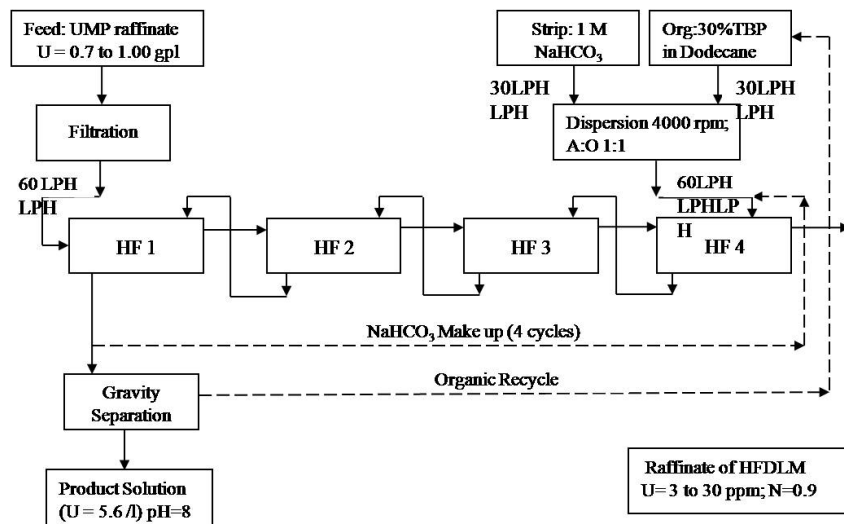
Conclusion

These studies have successfully demonstrated and established quantitative recovery of uranium from acidic raffinate of uranium metal purification plant, leading to easy disposal of raffinate.



Fig. 5: Bench scale set up: Four large HF modules in series Feed: U raffinate; dispersion: aq/org 1:1, aq (1 M NaHCO₃), org (30 % v/v TBP in Dodecane); flow rate: 60LPH

Flow sheet for recovery of U from Uranium plant raffinate using HFDLM technique:



DESIGN AND DEVELOPMENT OF TELE DISTRESS ALARM DEVICE 'NIRBHAYA'

Pithawa C.K., Lalwani S.K., Sinha V., Srivastava S., Bharade S., Khole S.,
Kamble A.D., Jyothi P., Muralikrishna L.V and Patil S.K.
Bhabha Atomic Research Centre

Shri C.K. Pithawa is the recipient of the DAE Group Achievement Award for the year 2012

Abstract

'Nirbhaya' is a small, low cost electronic distress alarm device which can be used in case of any distress like fear of attack or medical emergency to get immediate help. When activated, this single-button, single-press operation device can send SMS alerts, through user's cell phone, to near and dear ones including police. The SMS alert containing a pre-formatted user defined message, GPS coordinates of the device & Google maps link is sent to user defined telephone numbers. After activation, the device continues to send the message and latest GPS location every minute to the same phone numbers. The device operates on rechargeable battery and pairs with user's cell phone via Bluetooth. The technology of this device has been transferred to ECIL for its mass production.

Introduction

In recent times, there have been increasing attacks on women and on elderly persons living alone. Children need to travel long distances for their schooling and many are kidnapped. Persons working during odd hours and traveling alone are also prone to attacks. To provide timely help to such persons in case of attack, medical emergency, accident or kidnapping, an electronic device has been developed which alerts relatives, friends, police and doctor just by pressing a single button on the device. Nowadays, almost every one carries a mobile phone. But in case of attack or medical emergency, the person may not be able to use the phone. It may be snatched by attacker or kidnapper. In case of medical emergency, it may not be possible to use the phone due to physical disability. Hence, for this purpose, a Tele Distress Alarm Device named 'Nirbhaya' was designed and developed. It is a small

device which can be carried in purse or pocket. It is a single button single press operation device which sends SMS alerts via user's cell phone to five user defined mobile numbers along with its GPS location.

Description

Fig. 1 shows the block diagram of the device. Main components used are a microcontroller, Bluetooth interface, GPS receiver, battery charging circuits, single

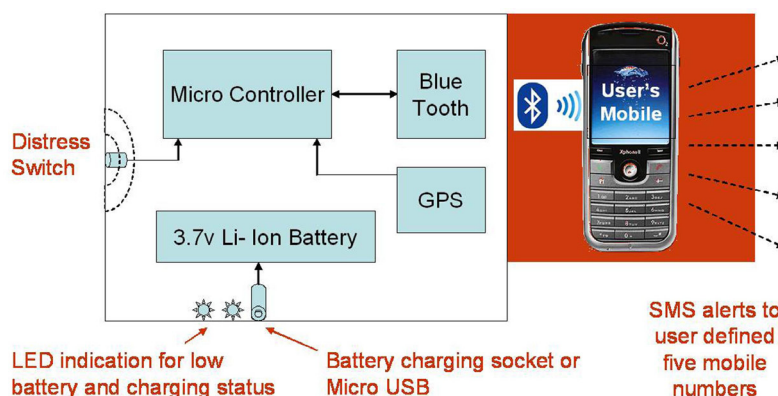


Fig. 1: Block diagram of Tele Distress Alarm Device 'Nirbhaya'

BARC NEWSLETTER

Founder's Day

cell Li-Ion battery and a push-button (distress) switch. Bluetooth is used to pair the device with the user's mobile for sending the information to the mobile application running in the background when the distress switch is pressed. The distress switch needs to be pressed once only in case of distress. When the switch is pressed, the device gets activated and starts sending SMS alerts to the five phone numbers via the application running in the user's cell phone. The SMS contains personal information, GPS coordinates (latitude, longitude) of the device, date, time and Google maps link to the GPS location.

A typical SMS alert can be "I am Shubham, F/25, Blood Gr. B+Ve. Please HELP. My PRESENT location is: Latitude:19.011552N, Longitude:072.920624E, Date:19/05/2014, Time (IST):15:18:00 For location on Google Maps click on <https://maps.google.com/?q=19.011552+072.920624>". Once activated, the device continues to send the message and its latest GPS location every minute to the same phone numbers. Thus if the person is being kidnapped, the latest location will be available. In case Bluetooth link is broken after device activation, due to snatching of the device or the cell phone by the attacker, the mobile application continues to send the SMS with last GPS coordinates.

The device is rugged and cannot be switched off. The battery cannot be removed easily. The switch is located

in such a way that it cannot be pressed accidentally. With 700mAh rechargeable Li-Ion battery, it has standby time of more than 5 days and active time of more than 12 hours. It can be charged using standard cell phone charger. Battery low and charging status indicators have been provided on the device. Fig. 2 shows the photograph of the device along with the SMS alert received by the receiving mobile.

Device Configuration Software

Before the device can be put to use, it needs to be enabled and configured once. This involves storing personal information in the device (name, age, sex, blood group) and five phone numbers, to which the alarm SMS will be send in case of distress. In order to avoid unauthorized change of this information, the process of storing or changing the stored information is password protected. Device configuration can be

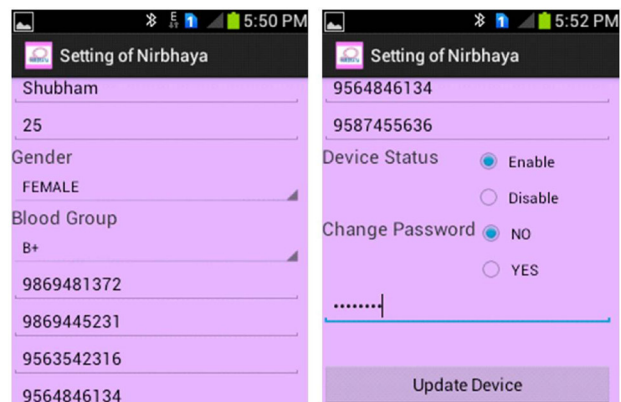


Fig. 3: Device configuration using mobile



Fig. 2: Photograph of 'Nirbhaya' device and the SMS alert received by receiving mobile

carried out using either a mobile or a PC. An Android OS based mobile application has been developed for configuring the device using a mobile phone. Similarly a Windows based application program has been developed for configuring the device using a Personal Computer. Fig. 3 and Fig. 4 show the screen print of the GUI for device configuration using mobile phone and PC respectively.

BARC NEWSLETTER

Founder's Day

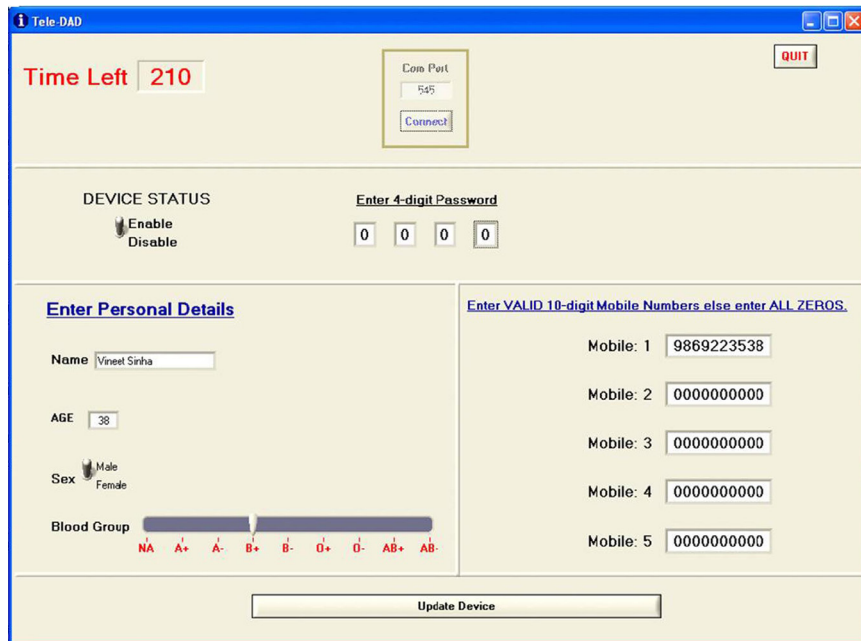


Fig. 4: Device configuration using PC

Mobile Application Software

Application software has been developed for mobiles using Android or Symbian OS. This application needs to be loaded and kept running in the background in the user's mobile phone for operation of the device. Whenever the distress switch is pressed, this program receives SMS alert contents from the device and sends the SMS to five numbers provided by the device. In case the Bluetooth link is broken with the device, this application keeps sending the SMS alerts every minute with the last GPS location of the device.

Applications

The 'Nirbhaya' device has been developed for societal applications and is a means for sending SMS alerts for help to friends and relatives when needed. It will be of immense use in case of personal attacks, accidents, medical emergency and kidnapping. The device is useful for women, children, elderly persons, security

personnel working in isolated areas and persons working during odd hours.

Future Scope

This device requires a mobile phone for sending the SMS alerts. An enhanced version of the device is under development which has on board GSM modem for sending the SMS thereby dispensing with the need of user's mobile phone. Other improvements could be changing the shape of the device to a wearable form e.g. wrist band, necklace or pendant.

Conclusion

A Tele Distress Alarm Device named 'Nirbhaya' has been designed and developed for societal applications. It is a small, low cost device which can be used for sending SMS alerts to five user defined mobile numbers in case of any distress like fear of attack, medical emergency etc. The technology of the device has been transferred to ECIL, Hyderabad where it is under mass production.

DEVELOPMENT OF MACHINERY PROTECTION SYSTEM

D.A. Roy, Prema Kumar Kavalan, Mohit Kalra, Sanjay K. Jain and Gaurav
Reactor Control Division

Shri D.A. Roy is the recipient of the DAE Group Achievement
Award for the year 2012

Abstract

A DSP based Machinery Protection System (MPS) has been designed and developed jointly by BARC and ECIL. The system is designed to protect the rotating machines from catastrophic failures due to excessive vibration. The system provides continuous, online monitoring of vibration and related signals. The system is manufactured by ECIL and two units of MPS have been installed and commissioned in NTPC power plants for protection of Turbo Generator Machinery.

Introduction

Health of large rotating machinery gets reflected in the vibration and other dynamic signals collected from the rotating equipment and supporting structures. Using this data, it is possible to detect impending trouble in the machine so that preventive action can be taken in time and catastrophic failures can be avoided. An on-line vibration monitoring and protection system thus plays an important role in ensuring safety and economics of the plant.

With the aim to address the need for such an on-line system having state-of-art features, indigenous

development of a Digital Signal Processor (DSP) based Machinery Protection System (MPS) was initiated by RCnD, BARC as a joint effort along with ECIL, Hyderabad under an MOU between BARC and ECIL.

The main components of the system (Fig-1) are the front-end instrumentation consisting of transducers (for vibration, speed and related parameters) and signal conditioning, DSP based data acquisition and protection module and back-end PC-based monitoring and configuration station. The main objective of the system is to monitor vibration and other dynamic signals to detect any deviation from normal levels and to provide alarm and trip signals in case the deviations are beyond certain set limits.

The Machinery Protection System (MPS) acquires a number of dynamic input signals (like vibration, displacement, eccentricity etc.) and speed input signals from field and on detecting signal levels beyond certain limits it provides alert signal to operator and generates contact outputs to shutdown (trip) the machine. The system can be configured to measure the following parameters:

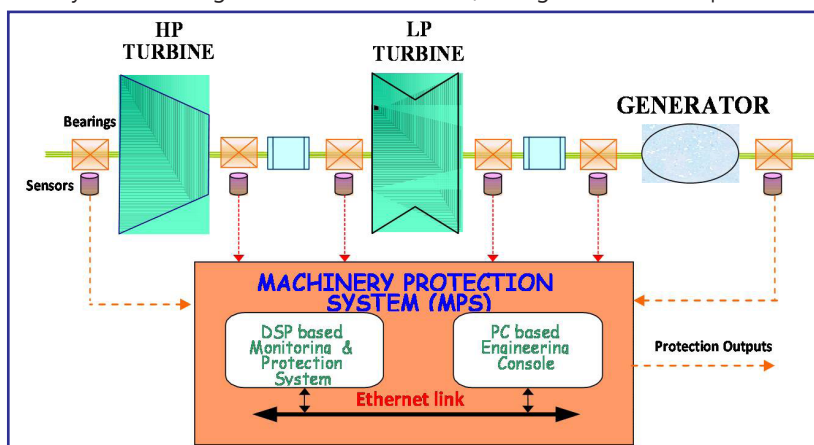


Fig.-1: Machinery Protection System (MPS)

BARC NEWSLETTER

Founder's Day

1. Absolute Vibration
2. Relative Shaft Vibration
3. Absolute Shaft Vibration
4. Shaft Position
5. Shaft Eccentricity
6. Absolute Expansion
7. Relative expansion

Protection is achieved by generating contact output to trip (shutdown) the machine when any of the above measured parameter exceeds the set limit. It sends relevant information on Ethernet for display to operator on a PC based Engineering Console. The Engineering Console also provides facility to configure various input parameters and their trip settings.

System Architecture

The Machinery Protection System (MPS) consists of an Embedded system and a PC-based Engineering Console (EC), which are connected through Ethernet. The embedded system is of modular construction and is user configurable through the Engineering Console. The system acquires various dynamic signals like vibration signal, displacement signals etc. and if any of these signals crosses the ALARM (alert) limit, it generates a alarm contact output and if the measured value crosses the TRIP (danger) limit then it generates a trip contact output which is used to protect/shutdown the machinery.

Apart from the protection function the embedded system also sends the acquired data to the Engineering Console for monitoring, analysis and display. The engineering console is used to configure the embedded system, to analyze the data received from embedded system and also to display the data in different formats.

Embedded System

The Embedded System consists of various hardware modules performing signal conditioning, data

acquisition, signal processing and protection functions. These modules are designed and fabricated as standard 6U cards and installed in a 19" bin. The Embedded System consists of following hardware modules which are assembled as shown in Fig-2.

- Machinery Protection Module (MPM)
- Input Output Module (IOM)
- Relay Output Module (ROM)



Fig. 2: Embedded system with Engineering Console

Machinery Protection Module (MPM) The MPM acquires analog signals, processes the acquired inputs using a DSP and if any parameter exceeds the set alarm or trip limits, it generates signal for alarm or trip. This module consists of DSP, Microcontroller, Memory, communication controller and other peripherals. It can process 4 Dynamic (Vibration) channels and 2 Speed Channels. It performs digital filtering using DSP as well as signal processing functions like integration and rectification and provides signal parameters like peak, RMS. It performs online diagnostics on hardware and software and generates messages in case of fault. It interfaces with the Input Output Module through backplane mechanism.

The MPM sends the processed data and messages to the Engineering Console through Ethernet and receives configuration data from the Engineering Console during system configuration. The module can be used as standalone protection unit for small systems.

Input Output Module (IOM) forms the input output interface of MPS. The inputs and outputs of the MPS

BARC NEWSLETTER

Founder's Day

are terminated on the screw terminals provided on the facia of IOM. This module provides signal conditioning for various sensors. This module also provides the power supplies to various transducers. It can cater to 4 dynamic channels and two speed channels. There is provision for online testing of the channels. It interfaces to the MPM and generates alert and trip signals for ROM. The MPM and IOM modules are shown in Fig. 3.



Fig. 3: MPM and IOM boards of MPS

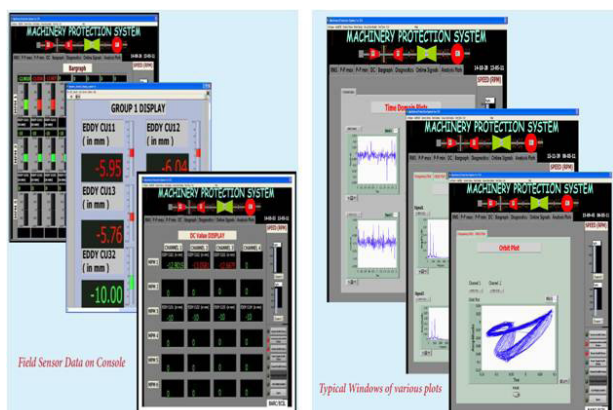


Fig. 4: Various GUI screens of MPS on EC.

Relay Output Module (ROM) provides relay outputs for alert and trip (danger) conditions. This board consists of 16 relays and one pair of contacts of each relay is available on the screw terminal mounted on the facia of the board. The relays in ROM are

driven by the open collector signals generated in IOM and available in the back plane. These relay outputs can be dynamically configured from the Engineering Console.

The design and development of the above hardware modules as per required standard and development of complex embedded software residing in MPM was entirely carried out in-house.

Engineering Console

A PC based Engineering Console (EC) is used for configuring the MPS and it also acts as a display station for MPS. It displays the data received from MPS in different formats like tabular, bar graph, trend etc. It also displays the alert/trip, diagnostic and various system states in message and LED display format. It also shows long term trend display of RMS parameters of signals, real-time frequency spectrum, waterfall and orbit plots (see Fig. 4)

System Acceptance Testing and Manufacture

After completion of the design and development of the system, it was subjected to extensive testing at TSI lab of ECIL. After successful completion of acceptance testing, the system was taken up for manufacture by ECIL as a product. ECIL has received an order for supply of the system to 4 units of NTPC power station at Kahalgaon.

Installation and Commissioning of MPS at NTPC

MPS was installed and commissioned at two units (210 MWe each) of Kahalgaon Super Thermal Power Station by a joint team of BARC and ECIL engineers. Two MPS systems configured as Turbo Supervisory Instrument (TSI) and Vibration Monitoring System (VMS) were installed for each unit. The systems provide online monitoring and machine protection for the turbo-generator set

BARC NEWSLETTER

Founder's Day

of the power plant. The TSI system monitors following parameters

- Axial Shift
- Turbine Speed
- Differential Expansion
- Case Expansion
- Eccentricity
- CVSM valve Position

The VMS provides monitoring and analysis of vibration at various bearing locations. Fig. 5 shows the MPS systems installed at NTPC, Kahalgaon.



Fig. 5: MPS systems installed at NTPC, Kahalgaon.

Conclusion

With the above development, an indigenous, state-of-art and user-configurable system is available to meet the requirements of machinery protection in various plants. The system is being manufactured and marketed by ECIL who also provide long

term maintenance support. This indigenous development is aimed at reducing the dependence on imported systems.

Acknowledgement

The authors express thanks to Shri Y.S. Mayya, Head, RCnD and Shri C.K. Pithawa, Director, E&I Group, BARC for their encouragement and support for this development. The authors are also thankful to Shri R.V. Reddy, DGM, CAD, ECIL and his team for their wholehearted support during development, integration, testing and deployment of the system.



References

1. Jain, Sanjay K, et al, Design Manual of Machinery Protection System, Rev 0, Mumbai, Jan 2009.
2. Jain, Sanjay K, et al, "Machinery Protection System", *BARC Newsletter*, Jan-Feb 2013 issue.

BARC NEWSLETTER

Founder's Day



DEVELOPMENT, INSTALLATION AND COMMISSIONING OF PROTEIN CRYSTALLOGRAPHY BEAM-LINE AT INDUS-2 SYNCHROTRON SOURCE

Ashwani Kumar, Himanshu Kumar Poswal, Biplab Ghosh, Ravindra D. Makde,
K.K. Pandey and Surinder M. Sharma

High Pressure & Synchrotron Radiation Physics Division

Jagannath

Technical Physics Division

M.V. Hosur

Raja Ramanna Fellow, ACTREC

A. K. Sinha

Centre for Design and Manufacture

Dr. S.M. Sharma is the recipient of the DAE Group
Achievement Award for the year 2012

Introduction

A living organism has thousands of different proteins, and each one folds into a specific 3D structure to perform its specific cellular function. Determining 3D structure of proteins is crucial for understanding its cellular function at an atomic detail that eventually may help us to understand and control the diseases. Most prominent way to determine 3D structure is the X-ray diffraction of protein in crystalline forms. However, the protein crystals are weakly diffracting in nature. It is primarily due to presence of low Z atoms like carbon, nitrogen and oxygen and high content of disordered solvent. In addition, it is due to less number of repeating units in a diffracting crystal, often impaired by imperfection in crystal lattice. Determination of structures of novel proteins require the phases to be determined experimentally along with the diffracted intensities. The phases are obtained from anomalous and/or dispersive signals derived from the diffracted intensity data, collected at the specific X-ray energies. These methods of exploiting tunability of the X-ray beam for maximizing anomalous and dispersive signals are popularly known as Single-wavelength

Anomalous Diffraction (SAD) and Multi-wavelength Anomalous Diffraction (MAD) experiments. The Protein Crystallography (PX) beam-line aims to exploit two main features of synchrotron source: high brilliance of beam which is good for weakly diffracting crystals and energy tunability that is essential for solving phases. The beam-line efficiently transports X-rays from the synchrotron ring to the sample position through a series of optical elements, designed and installed at calculated positions, for providing the best possible match to the sample requirements. PX beam-line on Indus-2 synchrotron is likely to cater to the needs of about 50 independent research groups in India working in the area of structural biology.

Source

The PX beam-line installed at 1.5 T bending magnet source and is located at port no. 21 (10° port) of Indus-2 synchrotron. The beam-line "Front-End" (FE) which ends at 14 m from the source consists of a 2.2 mrad (H) beam defining copper-mask, various pneumatic gate valves, water cooled shutters which include safety-shutter and fast-closing-shutter. The FE

BARC NEWSLETTER

Founder's Day

employs fast-closing-shutter and delay line for UHV protection of the storage ring. The 250 μm thick beryllium window at the end of FE separates the storage ring vacuum from the beam-line. It also acts as high pass filter removing all the photons having energy below ~ 5 keV, reducing heat load on the downstream optical components.

Optics

The beam-line is 36 m long starting from the source to the sample position. It comprises of several components namely, water cooled slits, Collimating Mirror (CM), Beam Position Monitors (BPM), Double Crystal Monochromator (DCM), focusing Torroidal Mirror (TM) and an experimental station as depicted schematically in Fig. 1. Some of the actual components of PX beam-line are shown in Fig. 2 (a) & (b). Most of the components of the beam-line, such as water-cooled primary slit, water-cooled compact slits, mirror chambers along with hexapods, beam pipes, support tables and Beam Position Monitors (BPM) were designed and developed indigenously. A water cooled primary slit is placed just after the FE to select the central cone of the X-ray beam for the collimating mirror, with optimal dimension. The BPM placed after the primary slit measures the X-ray beam

profile and position. X-ray beam shines at 3 mrad incidence angle on a Rhodium coated collimating mirror surface reflecting it downward. The collimation of the beam improves flux and energy resolution. Due to heat load both the mirrors and first crystal of DCM are cooled with water. The BPM installed immediately after the CM used for the alignment of the mirror in X-rays. DCM monochromatizes the X-ray beam by using a pair of Si crystals in (+,-) configuration which ensures constant exit beam height. In PX beam-line, the DCM is installed at 18.5 m from the source and consists of two pairs of crystals viz. Si(111) and Si(220) which can be exchanged in vacuum as per user requirement for resolution. The maximum energy resolution ($\Delta E/E$) with Si (111) crystal is $\sim 1.33 \times 10^{-4}$, while Si (220) provides $\sim 5.12 \times 10^{-5}$. The monochromatic beam can be resized by using the water cooled compact slit. BPM-3 helps in monochromator alignment. The monochromatic beam is focused on the sample at experimental station by using the TM, which is placed at 24 m from the source and focuses the X-ray beam in both vertical as well as in sagittal planes. BPM-4 is used for alignment of TM. The manipulation of both the mirrors in X-ray beam is done using hexapods that provide all possible translations and rotations in 3D space with ~ 10 micron translation and ~ 0.1

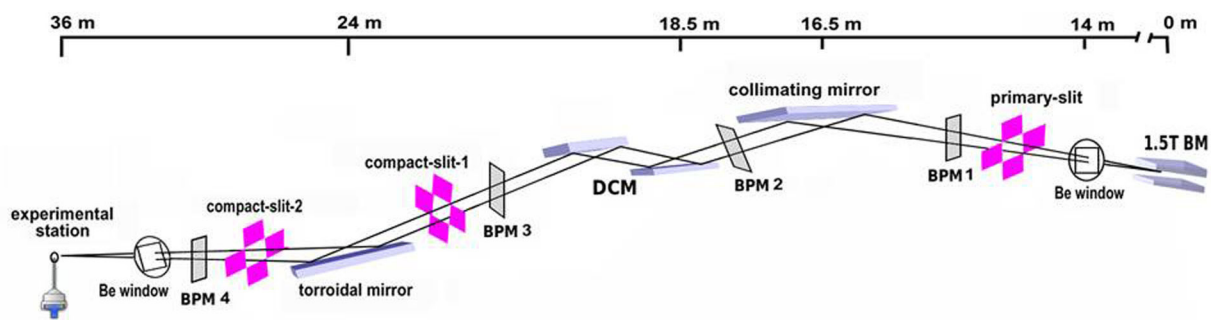


Fig. 1: Schematic of PX beam-line.

Table-1: PX beam-line characteristics

Energy range	5 - 20 keV
Energy resolution ($\Delta E/E$)	1.4×10^{-4} with a flat Si (111) DCM
Spot size	0.5 mm (H) x 0.5 mm (V)
Photon flux (measured at 80mA at 2.5 GeV)	6.4×10^9 photons/sec at sample
Beam divergence (horizontal) at sample	< 4 mrad

BARC NEWSLETTER

Founder's Day

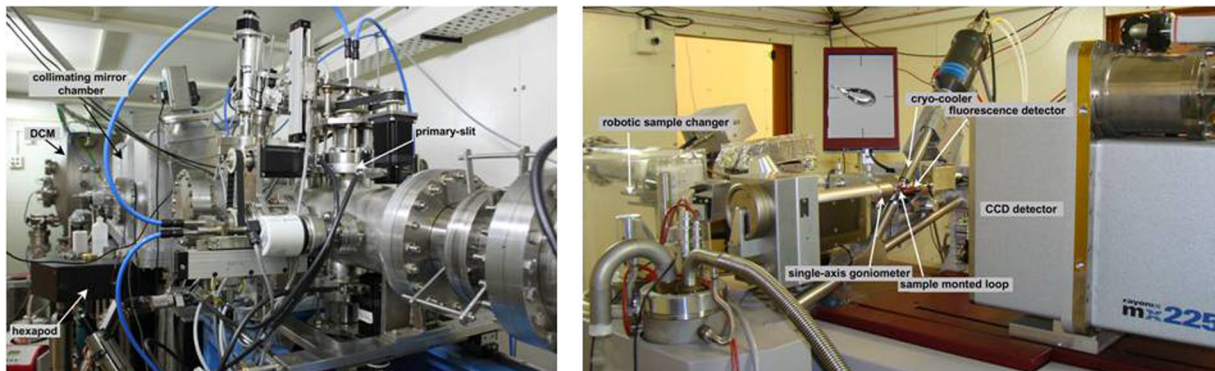


Fig. 2: (a) Actual photograph of PX beam-line at Indus-2 synchrotron showing its various; (b) The experimental station at the PX beam-line

mrad angular accuracy. Lead shielded hutches and interlocked doors are provided for user safety.

Experimental station

The PX beam-line is equipped with a state of the art experimental station to handle delicate and temperature sensitive protein crystals. The experimental station shown in Fig. 2 (b), comprises of a cooled CCD detector with detection area of $225 \times 225 \text{ mm}^2$ and pixel size of 72 micron, for fast (~ 1 sec) data acquisition. To avoid radiation damage in the protein samples, an LN₂ cryo-streamer (100K) has been coupled with the experimental station. Automatic sample loading/unloading is also possible by the attached robotic sample changer. A fluorescence detector has been integrated with the station for recording fluorescence from heavy atoms in crystals for enabling anomalous diffraction experiments.

Beam line alignment and optimization

Beam-line alignment and spot optimization are crucial for maximizing flux at sample position. A total of four wire-cum-fluorescence BPM are used for the alignment of optical components. The indigenously developed BPMs have two components: 1) a tungsten wire to measure photo current ($\sim \text{nA}$) and 2) a phosphor coated water cooled copper plate for beam viewing which can also act as a beam stopper. The intensity profile of the X-ray beam is calculated from

the measured photo current with the stepper motor position (in the vertical direction) as shown in Fig.3. The X-ray beam is visualized (Fig. 3 inset) through the fluorescence from the phosphor coated plate using a CCTV camera. Thus the combination, wire current and fluorescence, provide both qualitative and quantitative information of the X-ray beam. Alignment of the mirrors, both CM and TM, are done using their downstream BPM. Both the mirrors are dynamically bent for matching source and focal point. The bending curvature and incident angle of TM are used to achieve optimal focus size at sample. Also TM is placed in 2:1 configuration, which minimizes the chromatic aberrations (sagittal and tangential). Typical beam-line characteristics are shown in Table-1.

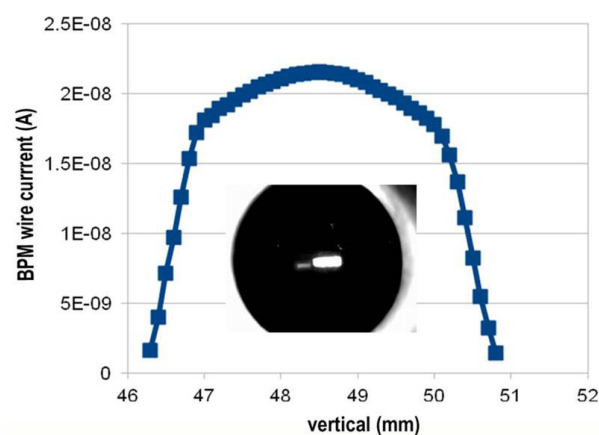


Fig 3: The measured beam profile for 4 mm vertical opening of the primary slit. Inset shows the white beam as visible from the BPM phosphor plate using CCTV camera

BARC NEWSLETTER

Founder's Day

The combination of Be window which act as low pass filter and the Rh coated mirrors that act as high pass filter ensure the beam-line working range from 5 keV to 20 keV. This range covers most of the heavy element absorption edge. The measured spot size at sample position is 0.5 mm (V) X 0.5 mm (H) which is close to the calculated spot size of 0.4 mm (V) X 0.4 mm (H) and the brilliance is $\sim 4.4 \times 10^{10}$ photons s^{-1} mm^{-2} $mrad^{-2}$ at 80 mA (2.5 GeV).

Beam-line validation and data collection on lysozyme

X-ray diffraction data were collected on lysozyme protein (Fig. 4) and few organic crystals at 12.0 keV energy. A total of 90 oscillation frames were collected, each with 1 degree oscillation and an exposure time of 60 sec when ring current was at 60 mA at 2.5 GeV. The lysozyme crystal diffracted to ~ 1.8 angstrom resolution with $I/\sigma = 24.8$ and $R_{merge} = 0.052$. The diffraction data collection statistics are shown in Table-2. Subsequently fine tuning and spot optimization reduced the data collection time to 10 sec per frame with improved statistics.

Structure determination of a novel protein using single-wavelength anomalous diffraction

We solved a novel protein structure using single-wavelength anomalous diffraction (SAD) experiment at the Selenium K-edge (Fig. 5). The protein (monomeric mass ~ 37 kDa) is a Xaa-Pro dipeptidase from *Deinococcus radiodurans* (GenBank accession, NP_294970) and consists of 349 residues. The six native sulphur-methionine residues of the protein were replaced by selenium-methionine using biochemical techniques and subsequently the protein was used to grow single crystals. The crystals (size ~ 200 microns) were diffracted at the PX beam-line at 12.666 keV energy. The data were processed using XDS and scaled using AIMLESS (CCP4) programs. The protein structure was solved by SAD phasing method using ShelX suite. The $\langle d''/\sigma F \rangle$ value of > 1.3 suggested

a significant anomalous signals in the dataset. The selenium atoms (six number) and their occupancies were determined using ShelXD with CCall $> 45\%$. The initial map was significantly improved by density modification using ShelXE suite. The map clearly distinguished between the correct and the wrong enantiomer. The residues were auto-built into density modified map using ARP/aWRP Classic software. The structure was refined using PHENIX-refinement with intermittent manual building using COOT suites. The structure was refined to Rwork/Rfree value of 20/22 % with good stereochemistry.

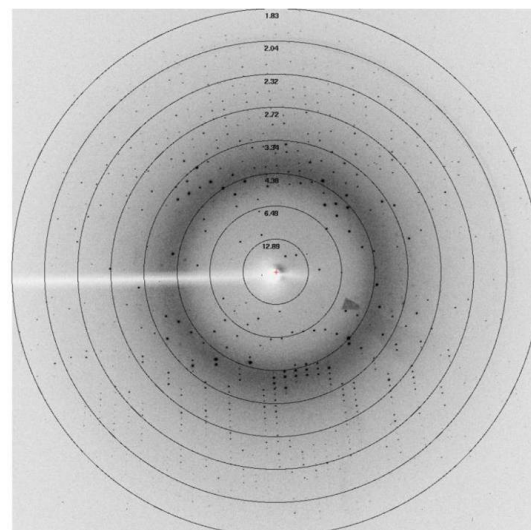


Fig. 4: First diffraction image form lysozyme crystal at PX beam-line

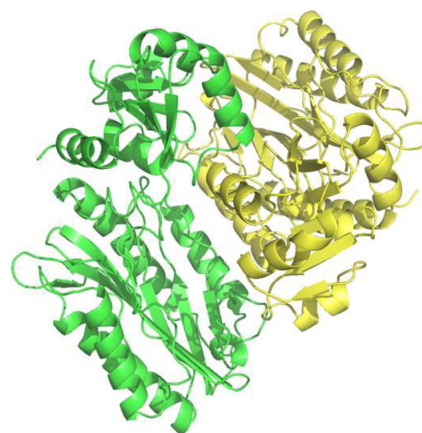


Fig.5: A ribbon representation of the 3D structure of Xaa-Pro dipeptidase protein from *Deinococcus radiodurans*

BARC NEWSLETTER

Founder's Day

Table-2: Data processing statistics for lysozyme protein crystal

	Overall	Inner Shell	Outer Shell
Low resolution limit	22.10	22.10	1.93
High resolution limit	1.83	5.80	1.83
Rmerge	0.051	0.036	0.124
Total observations	81043	2531	11743
Unique observations	11286	422	1596
Mean(I)/sd(I)	25.7	34.0	13.9
Completeness	99.3	98.3	98.6
Multiplicity	7.2	6.0	7.4
Average mosaicity	0.01		
Unit cell	a=b=79.69, c=38.52; $\alpha=\beta=\gamma=90.0$		
Unit cell (PDB reported) 1BVX	a=b=79.20, c=38.04; $\alpha=\beta=\gamma=90.0$		
Space group	P4 ₃ 2 ₁ 2		
Maximum resolution:	Beyond 1.83 Å		

Acknowledgments

The front-end of PX beam-line was installed by Indus Synchrotron Utilization Division of RRCAT, Indore. Group also acknowledges the unlimited support extended by Dr. P.D. Gupta, Director, RRCAT during installation and commissioning. The team is also grateful to Dr. R.K. Sinha, Chairman AEC for constant

encouragement and to Dr. R. Chidambaram for discussions and advice.

Reference

1. Conceptual Design Report for the High-Throughput Macromolecular Crystallography Beam-line at the Indus-2; Ashwani kumar and Jagannath; BARC (External) Report 2007.

THERMAL HYDRAULIC AND MATERIAL COMPATIBILITY STUDIES IN MOLTEN SALTS

A.K. Srivastava, A. Borgohain, S. S. Jana, V.K. Gupta and N.K. Maheshwari

RED

S. Rangarajan

WSCD

A.G. Kumbhar and S.J. Keny

RPCD

Dr. N.K. Maheshwari is the recipient of the DAE Group Achievement Award for the year 2012

Abstract

Molten salt is increasingly getting more attention as fuel, blanket and coolant for High Temperature Reactors (HTR) as well as a coolant and storage medium for solar power tower systems. This article deals with the activities performed on molten salt coolant technologies for high temperature reactor and solar power tower applications. With the objectives to study the thermal-hydraulic behavior of different molten salts and compatibility of different structural material with molten salts, two different experimental facilities namely Molten Salt Natural Circulation Loop (MSNCL) and Molten Salt Corrosion Test Facility (MOSCOT), have been designed, fabricated, installed and successfully operated.

Introduction

BARC is developing a High Temperature Reactor (HTR), capable of supplying process heat at 1000°C to facilitate hydrogen production by splitting water. BARC is also developing a potential technology to make solar power dispatchable, such that solar heat can be used to generate electricity at will. In both the cases it has been proposed to use molten salts as a coolant since it has low melting point and high boiling point, enabling us to operate the system at low pressure. Molten fluoride salts and molten nitrate salts are proposed as candidate coolants for HTR and solar power tower systems respectively. Some of the challenges related to the use of above salts include understanding its thermal-hydraulic behavior, development and testing of related high temperature instruments and study of its compatibility with different structural materials

[1,2,3]. In this regard the heat transfer and pressure drop characteristics of molten fluoride salt as well as molten nitrate salt has been theoretically studied already [4,5]. A comparative study of the steady state and transient behavior of natural circulation loop with various heat transfer media has also been performed [6]. Nevertheless theoretical studies are not sufficient enough to qualify these salts for HTR and solar power applications. Development of suitable test facilities and detailed experimentation in these setups will create a complete database on the characteristics of molten salts under various operating conditions. This will also help in validating in-house and commercially available codes with molten salts. In view of this, two different experimental facilities- Molten Salt Natural Circulation Loop (MSNCL) for thermal hydraulic studies of molten salts and Molten Salt Corrosion Test Facility (MOSCOT) for material compatibility study in such environment

BARC NEWSLETTER

Founder's Day

have been setup in BARC. Pre-test analyses of MSNCL have also been carried out using one dimensional in-house developed code LeBENC, acronym of Lead Bismuth Eutectic Natural Circulation [7].

Description of the Test Facilities

Molten Salt Natural Circulation Loop (MSNCL)

Considering the importance of natural circulation in high temperature systems and taking into account the scarcity of experimental data, a Molten Salt Natural Circulation Loop (MSNCL) has been setup. Fig. 1 and Fig. 2 show the isometric view and photograph of the MSNCL respectively. Initially, molten nitrate salt; i.e. a mixture of NaNO_3 and KNO_3 in 60:40 ratio; has been taken for the experimental studies. MSNCL comprises of five parts viz. heater section, cooler, melt tank, expansion tank and main loop piping. All components and piping of the loop are made of Inconel 625 material. It has been designed in such a way that the effect of different orientations of heater and cooler on the mass flow rate can be studied. An expansion tank has been provided at the top of

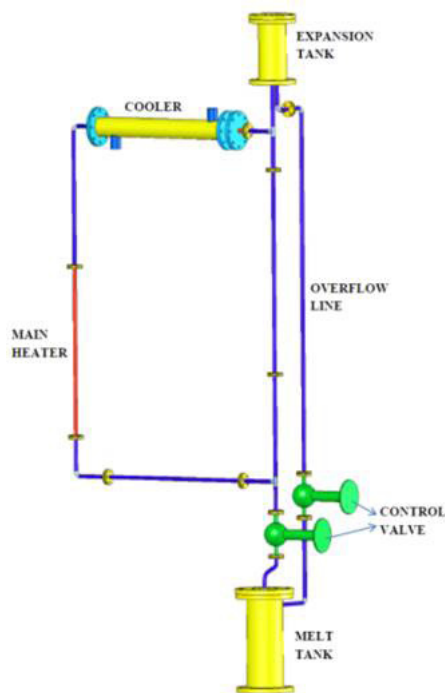


Fig. 1: Isometric view of MSNCL

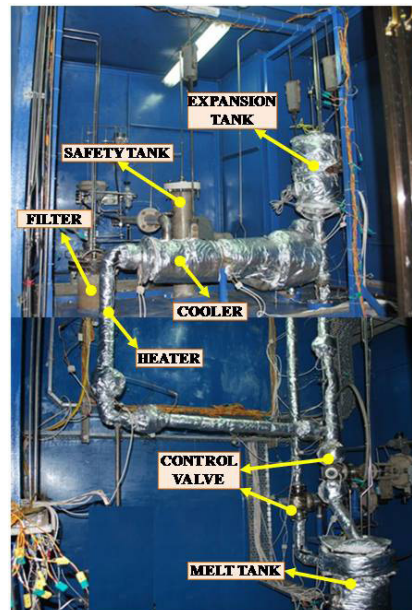


Fig. 2: Photograph of MSNCL

the loop to accommodate the volumetric expansion of the salt. Instruments for measuring temperature, pressure and level have been installed in the loop. A central control system has been provided to control the process parameters.

Molten Salt Corrosion Test Facility (MOSCOT)

Molten Salt Corrosion Test Facility (MOSCOT) consists of two cylindrical vessels called melt tank and main vessel. Figure 3 and Fig. 4 show the schematic and photograph of the MOSCOT facility respectively. Both the vessels have been fabricated with Inconel-625 material. The inner surface of the vessels was coated with nickel to reduce corrosion. The test facility has been designed for in-situ measurement of static and dynamic corrosion in molten salt environment. Eutectic mixture of lithium fluoride, sodium fluoride and potassium fluoride (FLiNaK) has been used as a working fluid for the study. To carry out in-situ corrosion measurements, electrochemical technique has been used for which a Potentiostat-Galvanostat (PG-Stat) has been installed in the facility. The resulting data and its interpretation provide estimation of corrosion rate of the material in the given molten salt environment. In order to maintain the chemistry of the molten salt,

BARC NEWSLETTER

Founder's Day

high purity argon gas has been provided as a cover gas in both the vessels, which has been purged to atmosphere through a water scrubber.

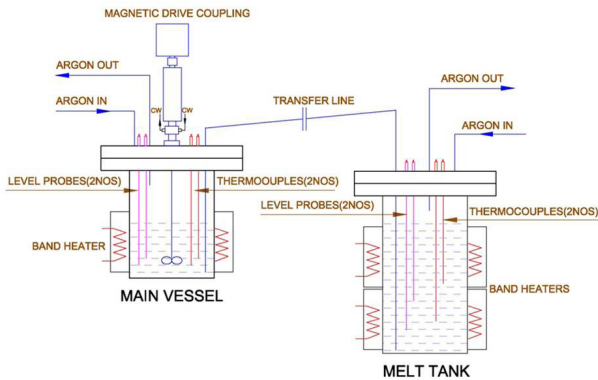


Fig. 3: Schematic of MOSCOT facility



Fig. 4: Photograph of MOSCOT facility

Results

Thermal hydraulic studies in MSNCL

Various steady state and transient experiments such as loss of heat sink transient, step power increase have been performed in the loop for Vertical Heater and Horizontal Cooler (VHHC) orientation. An in-house developed one dimensional code LeBENC was already validated with water and lead-bismuth eutectic [6,8]. Further it is

validated with the experimental results of molten nitrate salt. The results for the same are as follows:

Steady state analysis

In the steady state natural circulation experiment, the loop was allowed to reach steady state conditions at different powers. By observing the trend of molten salt temperature at different location, the steady state conditions can be judged. For steady state natural circulation, Vijayan [9] showed that the flow in a single phase uniform or non-uniform diameter natural circulation loops can be expressed as,

$$Re_{ss} = c \left(\frac{Gr_m}{N_G} \right)^r \quad (1)$$

Where, constants 'c' and 'r' depends upon the nature of flow i.e. laminar or turbulent. Parameter N_G depends upon the geometry of the loop. The detailed derivation of Eq. 1 can be found in Vijayan [9]. The same correlation is compared with experimental data in Fig 5. It is found that the experimental results uniformly lag with correlation values due to the heat losses in the loop.

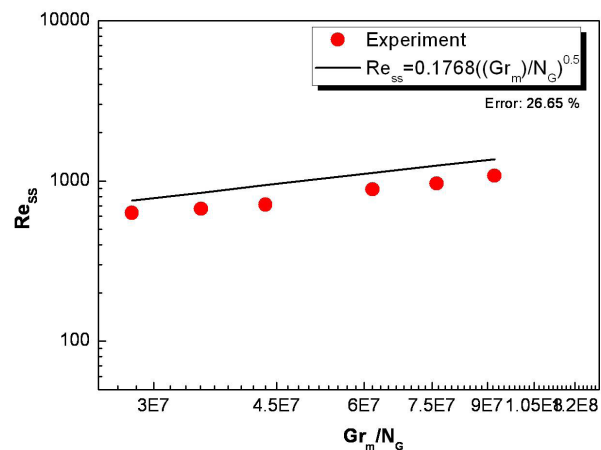


Fig. 5: Comparison of experimental Data with steady state correlation given by Vijayan et. al.

Transient Studies

Various transients' viz. loss of heat sink, heater trip, startup of natural circulation and step change in power

BARC NEWSLETTER

Founder's Day

has been performed in MSNCL. A typical temperature profile of cooler inlet and cooler outlet in loss of heat sink transient is shown in Fig. 6. Results obtained from LeBENC are compared with experimental data and found in good agreement.

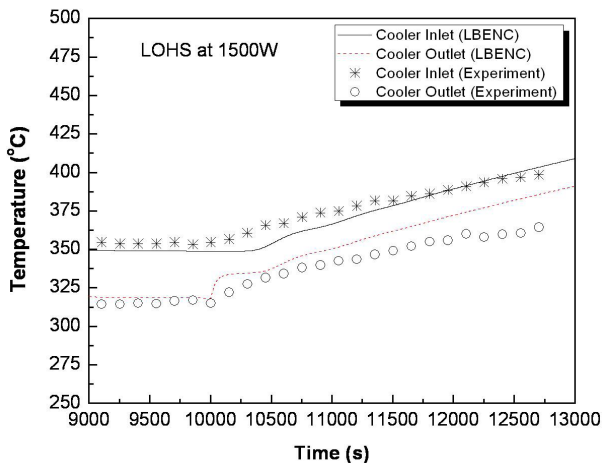


Fig. 6: Cooler Inlet and outlet temperature variation in LOHS transient and its comparison with LBENC

Corrosion studies in MOSCOT facility

In situ corrosion tests were performed on four different Ni-alloys viz. Inconel 625, Inconel 617, Inconel 600 and Incoloy 800 at five different temperatures 550 °C, 600 °C, 650 °C, 700 °C and 750°C using electrochemical polarization (Taffel plot) technique. Corrosion current (ICorr) obtained from the intersection of cathodic and anodic Taffel lines was used for the estimation of corrosion rate. A typical impedance spectra and Taffel curve of Inconel 600 are shown in Fig. 7 and Fig. 8

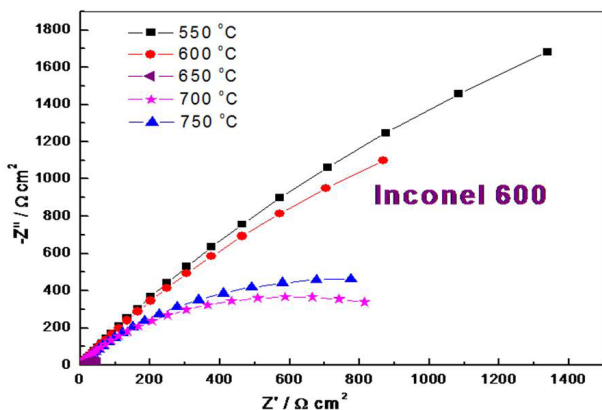


Fig. 7: Impedance spectra of Inconel 600 at different temperature

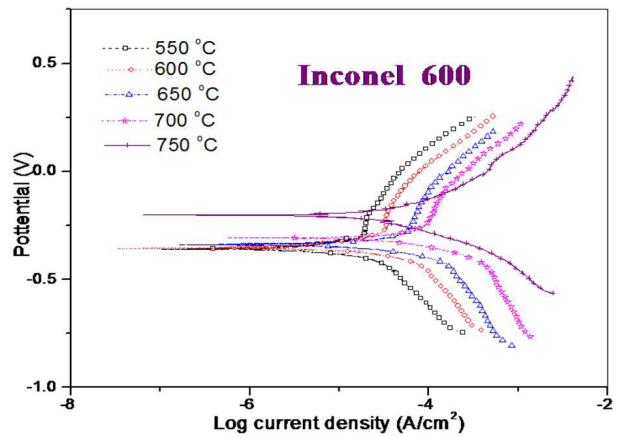


Fig. 8: Taffel curve of Inconel 600

respectively. Corrosion rates (mills per year) of all the selected materials at different temperatures obtained from the experiments have been listed in table.1. The results show that the corrosion rate is temperature dependent and at highest experimental temperature Inconel 600 has lowest corrosion rate.

Table 1: Corrosion rate (mpy) of different materials in molten fluoride salt environment at different temperatures

Material \ Temp (°C)	Inconel 600	Inconel 617	Inconel 625	Incoloy 800
550	6.2	10.0	-	17.4
600	12.2	18.2	6.1	30.1
650	25.9	22.7	5.0	31.2
700	25.4	33.9	71.3	45.4
750	15.8	97.9	127.6	33.2

Concluding Remarks

The present Molten salt test facilities have facilitated thermal hydraulic and material related studies at high temperatures and development/testing of instruments like level sensor, control valves etc. Steady state and transient behavior of molten nitrate salt in natural circulation flow condition have been studied in MSNCL. On the other hand, material compatibility studies using electrochemical technique under fluoride salt environment have been performed in MOSCOT facility. Both the facilities are being used to generate

BARC NEWSLETTER

Founder's Day

extensive experimental data which are relevant to high temperature coolant system design and solar application. The experimental data obtained from MSNCL is being used for the validation of in-house developed computer codes and CFD codes essential for the design of high temperature reactor systems.

References

1. Cooke J.W., Development of the Variable Gap Technique for Measuring the Thermal Conductivity of Fluoride Salt Mixture, ORNL-4831, Oak Ridge National Laboratory.
2. Grele M.D., Gedoen L., Forced convection Heat transfer characteristics of Molten FLiNaK flowing in an Inconel X system, NACA RM E53L18, National Advisory Committee for Aeronautics (1954).
3. Ambrosek J., Anderson M., Sridharan K., Allen T., Current Status of Knowledge of Fluoride Salt (FLiNaK) Heat Transfer, Nuclear Technology, 165 (2009) 166.
4. Srivastava A. K., Vaidya A. M., Maheshwari N. K., Vijayan P. K., Heat Transfer and Pressure Drop Characteristics of Molten Fluoride Salt in Circular Pipe, *Journal of Applied Thermal Engineering*, Volume 61, Issue 2, 3 November 2013, Page 198-205, (2013).
5. Srivastava A.K., Vaidya A.M., Maheshwari V, Vijayan P.K., Heat Transfer and Pressure Drop Characteristics of Molten Nitrate Salt In Circular Pipe, Thirty Ninth National Conference on Fluid Mechanics and Fluid Power December 13-15 (2012) SVNIT Surat, Gujarat, India.
6. Jaiswal B.K., Srivastava A.K., Borgohain A, Maheshwari N.K., Vijayan P.K., A Comparative Study of the Steady State and Transient Behavior of Natural Circulation Loop with Various Heat Transfer Media, 38th National Conference on Fluid Mechanics and Fluid Power December 15-17 (2011) MANIT, Bhopal.
7. Srivastava A. K., Borgohain A., Maheshwari N. K., Vijayan P. K., Pre-Test Analysis of Molten Salt Natural Circulation Loop Using FLiNaK Salt, International Conference on Molten Salts In Nuclear Technology, January 9-11 (2013) BARC, Mumbai.
8. Borgohain A., Jaiswal B.K., Maheshwari N.K., Vijayan P.K., Saha D., Sinha R.K., Natural circulation studies in a lead bismuth eutectic loop, *Progress in Nuclear Energy* 53 (2011) 308-319.
9. Vijayan P.K., Experimental and numerical investigations on the nature of the unstable oscillatory flow in a single-phase natural circulation loop, XVII National and VI ISHMT/ASME Heat and Mass Transfer Conference, IGCAR, Kalpakkam, Jan 5-7 HMT-2004-C100, pp 600-606.

Nomenclature

Re_{ss}	Steady state Reynolds number
Gr_m	Modified Grashof number,
D	Diameter, m
ρ	Density of working fluid, kg / m^3
β	Volumetric coefficient of expansion, $1 / K$
g	Acceleration due to gravity, m / s^2
ΔT_r	Reference temperature difference, $(QH / A\mu C_p)$, K
Q	Total heat input rate, W
H	Loop height, m
A	Flow area, m^2
C_p	Specific heat, $J / kg.K$
μ	Dynamic viscosity, $Pa.s$

CATALYSTS FOR HYDROGEN MITIGATION BY PASSIVE AUTOCATALYTIC RECOMBINER

Salil Varma
Chemistry Division

Shri Salil Varma is the recipient of the DAE Special
Contribution Award for the year 2012

Abstract

Hydrogen released in nuclear reactor containment from clad/fuel – steam interaction under severe accident scenario poses a threat to containment and hence can lead to release of radioactivity. Regulating of hydrogen concentration by catalytic recombination is a viable solution to this problem. Various supported platinum, Platinum-ruthenium and platinum-palladium catalysts, with stainless steel or cordierite support have been developed for this purpose. The catalysts prepared have been characterised for the loading of noble metal, phase purity, surface morphology and surface composition. The catalysts have been evaluated for recombination of varying concentrations of hydrogen with oxygen in ambient and moist air. The performances of these catalysts in presence of various poisons like moisture, CO₂, CO and hydrocarbons provide data about use of these catalysts under the actual scenario. While, SS wiregauze supported catalysts are found to perform better in presence of humidity and condensed moisture and within limited CO concentrations, the cordierite based catalysts exhibit poor performance in presence of condensed moisture and have enhanced resistance to carbon monoxide.

Introduction

Under loss of coolant accident condition (LOCA) large amount of hydrogen accumulated in nuclear reactor after failure of emergency core cooling system (ECCS). Once this hydrogen surpasses the flammability limit in air (4%) it could create adverse impact on environment as there can be chances of radioactivity to fallout [1]. Three mile Iceland (US), Fukushima (Japan) have been suffered from endanger of hydrogen explosion. To avoid this kind of situation lots of efforts have been put by concern nuclear organizations over worldwide. Several alternatives have been proposed for dealing with this issue viz. pre and post inerting, deliberate ignition system, dilute venting, and passive autocatalytic recombiner. Passive Autocatalytic Recombiner (PAR) is one of the most suitable candidates to deal with this situation. Because

it has an inherent advantages over others that it can be auto initiated, cannot depend on external power supply, it can be placed at any location in containment and it can be operate by remote handling also [2]. Various types of catalysts such as Pt/Al₂O₃, Pt/SnO₂, Pt/Polyester, etc. have been reported have been reported so far for meeting the specification of PAR [3]. Herein, our group developed various wiregauze and cordierite ceramic supported Pt, Pt-Pd, Pt-Ru catalysts. Catalytic activity study compared for various H₂ concentrations in air and for various probable poisons like CO₂, CH₄, CO, relative humidity and condensed water.

Experimental

Here, for this purpose SS wiregauze and cordierite plates with dimensions of 5 cm X 16 cm were exploited as support. Using suitable precursors of noble metal

BARC NEWSLETTER

Founder's Day

and reducing agent wiregauze and cordierite based catalysts has been prepared. Electroless deposition route has been attempted for the synthesis of Pt, Pt-Pd, Pt-Ru/wiregauze based catalysts whereas chemical reduction route has been employed for the synthesis of Pt, Pt-Pd/Cordierite based catalyst. All prepared samples has been characterized for their noble metal content by NAA, phase purity using XRD, Surface area by BET, Surface morphology by using FEG-SEM, elemental distribution by EDS and surface composition by XPS.

Result and Discussion

Fig.1 shows the SEM images for wiregauze and cordierite supports before after deposition of noble metals. SEM images reveal the difference in morphology and in particle size for all the samples. Fig. 1a) and 1b) shows the SEM images of wiregauze and cordierite support before coating. Fig.1c) shows the SEM image of Pt-Pd/Wg sample. Particles observed with dimension of ~ 0.1 to 0.5 micron. Fig. 1d) shows the SEM image of Pt-Pd/Cord sample. The observed particle size is in the range of 3.5 to 5 nm.

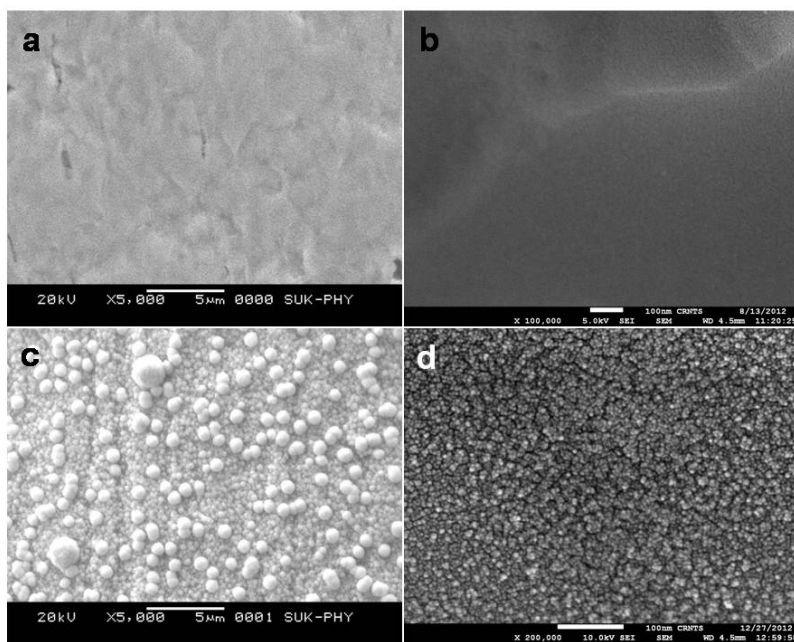


Fig.1: SEM images of (a) Blank wiregauze, (b) blank cordierite, (c) Pt-Pd wiregauze and (d) Pt-Pd cordierite

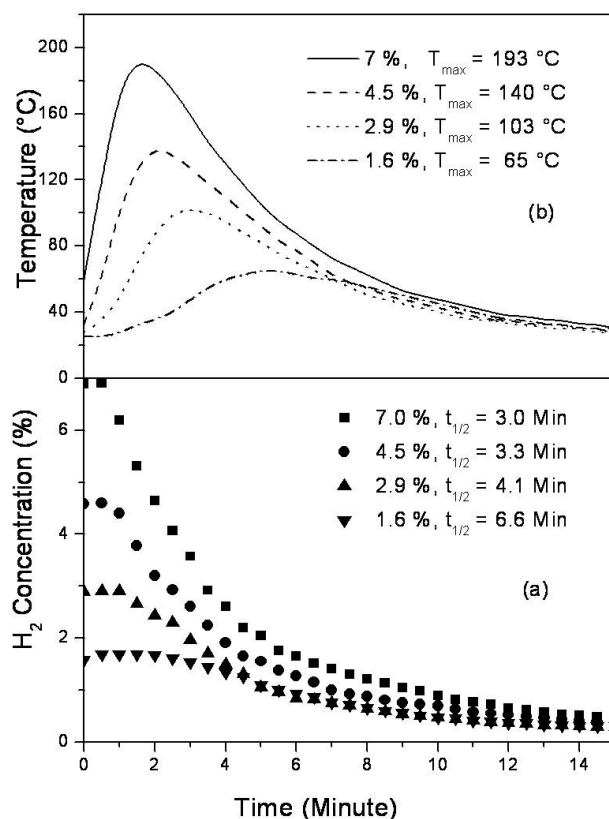


Fig. 2: Catalytic activity details for Pt-Pd/Cord catalyst in terms of change in (a) H₂ concentration & (b) Temperature rise.

Fig.2 (a) & (b) shows the variation in t_{1/2} and T_{max} for Pt-Pd/cord catalysts with different hydrogen concentration. It has been observed that with increase in hydrogen concentration, time required for completion of half of the reaction (t_{1/2}) has been decreased and maximum temperature rise on the catalyst surface (T_{max}) has increased. Maximum temperature (T_{max}) rise observed for various hydrogen concentrations is in the range of 65 to 193 °C.

Table 1 shows the comparable study of catalytic activities for wiregauze and cordierite based catalysts. Here it depicts that Pt and Pt-Pd/Wg based catalysts shows better catalytic activity in presence of condensed moisture whereas Pt, Pt-Pd/Cordierite based catalysts performs better in presence of carbon monoxide.

BARC NEWSLETTER

Founder's Day

Table1. Catalytic activity details of all catalysts in presence and absence of poisons

S. No.	Catalysts	NM Wt. gain (%)	$t_{1/2}$ (min)	T_{max} (°C)	$t_{1/2}$ (min)					$t_{1/2}$ after flushing (min)
					CH ₄ (0.5%)	CO ₂ (0.5%)	CO	Rel. Humidity (100 %)	Condensed Water	
1.	Pt/Wg	0.83	2.0	207	2.0	1.8	5.0a	3.8	-	2.1
2.	PtPd/Wg	0.83	1.8	233	1.9	2.1	2.3b	2.6	-	2.1
3.	PtRu/Wg	0.90	2.0	268	2.2	2.3	3.7c	2.5	5.6	2.1
4.	Pt/Cord	0.20	3.3	148	3.4	3.5	4.7d	3.6	24.3	3.4
5.	Pt+Pd/Cord	0.20	3.3	140	3.5	3.8	3.9e	3.4	9.5	3.3

a, b = 50 ppm of CO, c) 400 ppm of CO d) = 2000 ppm of CO and e) 1000 ppm of CO

In case of CO poisoning better performance of Pt-Ru/Wg based catalysts found compared to Pt-Pd/Wg but not as good as cordierite based catalysts.

Conclusion

Wiregauze and cordierite supported Pt, Pt-Ru and Pt-Pd catalysts successfully prepared by electroless deposition and chemical reduction route method. It has been observed that Pt, Pt-Pd/Wg supported catalysts performs better in presence of condensed water whereas Pt, Pt-Pd/Cordierite catalysts shows better catalytic activity in presence of carbon monoxide.

Acknowledgement

Authors thanks Sh. Kiran Sanap (CSIR SRF), Dr. S. Waghmode (University of Pune) and Dr. S. R. Bharadwaj (Chemistry Division, BARC) for their valuable contribution.

References

1. T.N. Srinivasan, T.S. Gopi Rethinaraj, *Energy Policy*, 52, 2013, 726–736.
2. IAEA-TECDOC-1196, International Atomic Energy Agency 2001.
3. K.K. Sanap, S. Varma, D. Dalavi, P.S. Patil, S.B. Waghmode, S.R. Bharadwaj, *International Journal of Hydrogen Energy*, 36, 2011, 10455-10467.

ON THE ISOTOPE EFFECTS OF $ZrCoX_3$ (X = H, D AND T): A FIRST-PRINCIPLES STUDY

D. Chattaraj, S.C. Parida and Smruti Dash

Product Development Division

and

C. Majumder

Chemistry Division

This Paper received the Mettler-Toledo Best Oral Presentation Award at the 19th DAE-BRNS Symposium on Thermal Analysis, held at Mumbai from Dec. 19-21, 2013

Abstract

The ZrCo-X (X= H, D and T) system gained considerable attention because of its use in fusion reactor program for the storage of hydrogen isotopes. The isotopic effects on $ZrCoX_3$ (X= H, D and T) were computed using the density functional theory (DFT). The variation of vibrational and thermodynamic properties of $ZrCoX_3$ with temperature also revealed isotopic effects. The calculated formation energies of $ZrCoX_3$, including the ZPE, were -146.66, -158.25 and -164.10 kJ/(mole of $ZrCoX_3$) for X = H, D and T, respectively. The heat capacities of $ZrCoX_3$ were found to be higher than that of ZrCo alloy.

Introduction

Tritium will be used as fuel in fusion reactors. This radioactive isotope of hydrogen is required to be stored safely in a suitable material. Metal hydrides are the unique choice for this purpose. Development and delivery of such systems for tritium storage are of requirement in the International Thermonuclear Experimental Reactors (ITER) project. Conventionally, uranium is used for the storage of hydrogen isotopes because of its favourable properties. However, the uranium hydride is highly pyrophoric in nature and uranium is also a radioactive material. An alternate material, the intermetallic ZrCo has been found to be suitable for the safe storage, supply and recovery of hydrogen isotopes in the ITER [1].

Li *et al.* [2] reported the structural, vibrational and thermodynamic properties of ZrCo using first principles method. As the electronic properties are unable to distinguish the $ZrCoH_3$ and its different isotopic

analogues, a systematic study of the hydrides based on phonon calculations is required. This study is focused on the ab-initio calculations of the thermodynamic properties of the ZrCo and $ZrCoX_3$ (X= H, D and T) using DFT and frozen phonon approach.

Computational details

All calculations have been performed using the plane wave-pseudopotential method under the framework of DFT as implemented in the Vienna ab-initio simulation package (VASP). The ionic optimization is carried out using the conjugate gradient scheme and the forces on each ion are minimized upto 5meV/Å. A 6x6x6 Monkhorst-Pack k-point mesh has been used for the Brillouin zone sampling.

The phonon frequencies of ZrCo and $ZrCoX_3$ (X=H, D and T) were calculated by the PHONON program using the forces based on the VASP package. A 3x3x3 supercell of ZrCo containing total 54 atoms

BARC NEWSLETTER

Founder's Day

and a 3x1x2 supercell of $ZrCoX_3$ (X=H, D and T) containing 120 atoms have been used for the phonon calculations. A small displacement of 0.02 Å has been given to the atoms present in the supercell of ZrCo and $ZrCoX_3$ (X=H, D and T). The temperature dependent thermodynamic functions of $ZrCoH_3$, $ZrCoD_3$ and $ZrCoT_3$ have been calculated from the phonon frequencies.

Results and discussion

Structural properties

The crystal structure of ZrCo is CsCl-type cubic (bcc) with a lattice parameter of 3.196 Å. The hydride of ZrCo, i.e.; $ZrCoH_3$ favors a simple orthorhombic $ZrNiH_3$ -type crystal structure with the room temperature lattice parameters listed in Table 1. To obtain the ground state structural parameters, the atomic and electronic structure of the ZrCo and $ZrCoH_3$ were optimized by varying the lattice parameters (summarized in Table 1). The lattice parameters are found to be within $\pm 1\%$ accuracy from the experimental data.

Thermodynamic properties

The temperature-dependent thermodynamic functions of a crystal, such as the internal energy (E), entropy (S), Helmholtz free energy (F) and constant volume heat capacity (C_v) are calculated from their phonon density of states as a function of frequencies using the standard equations cited in literature [5]. The variation of F, E, S and C_v are shown in Fig. 1(a-d) upto 600 K, which is below the decomposition temperature of $ZrCoX_3$ (X= H, D, and T).

The calculated zero point energies (ZPE) are 5.01, 43.65, 32.05 and 26.21 kJ/mol for the ZrCo, $ZrCoH_3$, $ZrCoD_3$ and $ZrCoT_3$, respectively. The enthalpy of formation of ZrCo (at 0 K) changes from -55.94 kJ/mol to -50.93 kJ/mol after including the ZPE. The enthalpy of formation (ΔfH) at 0 K for $ZrCoH_3$ is -190.31 kJ/mol without considering ZPE. After including the ZPE correction, the heat of formation of $ZrCoH_3$ changes from -190.31 to -146.66 kJ/mol. Similarly, ZPE corrected ΔfH at 0 K for $ZrCoD_3$ and $ZrCoT_3$ are -158.25 and -164.10 kJ/mol, respectively. It is interesting to note that, although $ZrCoH_3$ and its isotopic analogues $ZrCoD_3$ and $ZrCoT_3$ have the same crystal and electronic structure, $ZrCoT_3$ and $ZrCoD_3$ are more stable than $ZrCoH_3$. Fig. 1(a) shows that the free energy (F) for all three hydrides decreases gradually with increase in temperature. In contrast, the internal energy E and entropy S increases with increase in temperature as shown in Fig. 1(b) and 1(c).

We have also calculated the heat capacities of $ZrCoX_3$ (X = H, D, and T). The temperature dependence of heat capacity (C_v) of $ZrCoX_3$ (X= H, D, T) is shown in Fig. 1(d). It is seen that at low temperature, upto 300 K, the heat capacities of $ZrCoX_3$ (X = H, D, and T) increase rapidly with increase in temperature and thereafter increases slowly up to 600 K, and attain the saturation values which is known as Dulong-Petit classical limit. From the fig. 1(d) it is seen that upto 100 K, the variation of C_v versus T curve follows the same trend for all $ZrCoX_3$ compounds, but above 100 K it shows different trend: $C_v(ZrCoT_3) > C_v(ZrCoD_3) > C_v(ZrCoH_3)$. The heat capacities of hydrides are higher compare to its precursor alloy ZrCo. It is due to the contribution of high frequency optical modes of X2

Table 1: Crystal structure of ZrCo and $ZrCoH_3$.

System	Crystal system	Space group	Calc. lattice parameters (at 0 K)	Expt. (at 298 K) [Ref.]
ZrCo	bcc	Pm-3m	a (Å) = 3.181	3.196 [3]
			V0 (Å ³) = 32.19	32.65
$ZrCoH_3$	orthorhombic	Cmcm	a (Å) 3.531	3.527 [4]
			b (Å) 10.395	10.463
			c (Å) 4.311	4.343
			V0 (Å ³) 79.11	80.13

BARC NEWSLETTER

Founder's Day

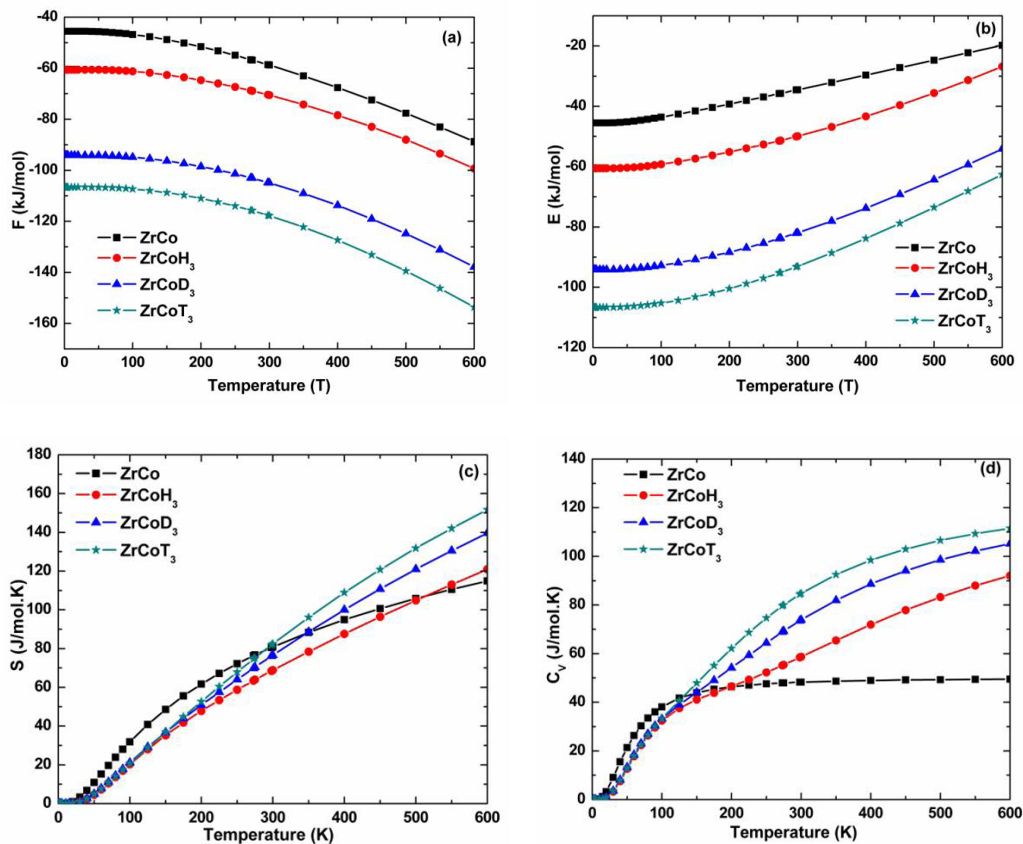


Fig. 1: The calculated thermodynamics functions for ZrCo and ZrCoX₃ (X= H, D and T)

(X= H, D and T) to the C_v of hydrides. In addition, the heat capacity plot shows a broad hump around 100 K for all three compounds. At low temperature, below 100 K, the acoustic modes, in which the Zr, Co and H atoms are vibrating 'in-phase', dominate the heat capacity contribution. At higher temperature, above 100 K, the optical modes of vibration, in which the light H atoms vibrate against the heavy and almost stationary Zr and Co atoms, dominates the heat capacity. Hence, around 100 K, this transition from predominant acoustic vibration to optical vibration cause a change in heat capacity function leading to a broad hump.

Conclusion

The first principles calculations of crystal structures and thermodynamic properties of ZrCo and ZrCoX₃ (X= H, D, T) have been reported in this work. The thermodynamic functions were determined within the

harmonic approximation from the phonon frequencies. The isotopic effect of ZrCoX₃ was also reflected in the thermodynamic properties. The ZPE corrected enthalpies of formation (ΔfH at 0 K) were determined for ZrCoX₃ (X= H, D, T). It has been suggested that ZrCoT₃ and ZrCoD₃ are more stable than ZrCoH₃.

References

1. S. Konishi, T. Nagasaki, N. Yokokawa, Y. Naruse, *Fusion Eng. Des* 10 (1989) 355-358.
2. G. Li, H. Zhou, T. Gao, *J. Nucl. Mater.* 424 (2012) 220-223.
3. I.R. Harris, D. Hussain, K.G. Barraclough, *Scr. Mater.* 4 (1970) 305-307.
4. A.V. Irodova, V.A. Somenkov, S.S. Shil'shtein, L.N. Padurets, A.A. Chertkov, *Kristallografiya* 23 (1978) 1044-1045.
5. C. Lee, X. Gonze, *Phys. Rev. B* 51 (1995) 8610-8613.

PORE DIFFUSION CONTROLLED LEACHING MODEL INCORPORATING PARTICLE SIZE DISTRIBUTION: A CASE STUDY

K. Anand Rao and T. Sreenivas

Mineral Processing Division, BARC Hyderabad

and

A.K. Suri

Bhabha Atomic Research Centre

This Paper received the Misra Award for paper presented at the IIME Mineral Processing Technology Seminar, held at Bhubaneswar, from Dec.10-12, 2013

Abstract

High rock permeability and liberation of uranium minerals in coarser sizes render leaching kinetics of medium to high grade ($>0.2\%$ U_3O_8) uranium ores to be best described either by homogeneous or topochemical reaction models. But in case of low-grade uranium ores with very fine dissemination of uranium minerals, the rate controlling step is observed to be the process of diffusion of dissolved ions in liquid within pores of rock particles. In the present study, the experimental leaching data generated on a low grade uranium ore from Tummalapalle in Andhra Pradesh, India is described by a pore diffusion model integrating particle size distribution.

The Tummalapalle ore contains 0.01% pitchblende as uranium mineral in intimate association with pyrite. The gangue minerals are 83% carbonates, 11.3% quartz, 0.47% pyrite. The diffusion of leachant phases like CO_3^{2-} and O^{2-} inside the ore particles and the counter current diffusion of the reaction product uranyl carbonate anions is assumed to be the rate controlling step. The Effective diffusivity (D_{eff}) in turn is a function of porosity and tortuosity of the ground ore particles. Experiments included variation of partial pressure of oxygen from 4.5 kg/cm² to 6.5 kg/cm², stirring speed between 573 rpm to 900 rpm, reaction temperature in the range 125°C to 165°C and average particle size from 25.8 μ to 34.76 μ . Gates-Gaudin-Schumann size distribution was incorporated into the kinetic model developed and the effective diffusivity was computed for different combinations of experimental conditions. The effective diffusivity was found to be in the range 0.61 cm²/s to 5.67 cm²/s. It is observed to be increasing with increase in partial pressure of oxygen, increase in stirring speed, increase in temperature and decrease in average particle size. Arrhenius plot of $\log(D_{eff})$ Vs $1/T$ yielded activation energy of 3.27 kcal/mole, which qualifies the assumption of diffusion controlled mechanism. The calculated and experimental conversions of uranium with time were found to be in good agreement.

Keywords: Pore diffusion model; Particle size distribution; Tummalapalle uranium ore; Alkaline leaching; Diffusivity

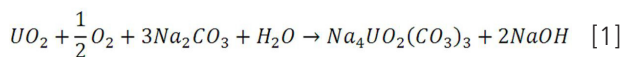
BARC NEWSLETTER

Founder's Day

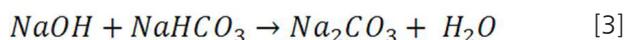
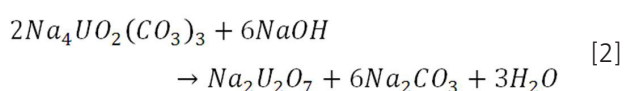
Introduction

The demand for uranium is on steady increase in India in recent past due to setting-up of new nuclear power plants in various parts of the country. These requirements are planned to be met with a mix of indigenous resources and imports (Anon 2012). An outcome of this scenario is the expansion programmes of the existing mills at Jaduguda and Turamdih in Singhbhum and setting-up of the third uranium mill at Tummalapalle in Andhra Pradesh based on alkaline leaching technology. A kinetic model is developed to describe the leaching behaviour of uranium from the Tummalapalle ore. Results of this study are presented in the paper.

Alkaline leaching of uranium ores involve oxidation of uranium present in uraninite / pitchblende followed by its dissolution in carbonate solution. The macroscopic chemical reaction, combining both the above steps, is given by Eq.(1) (Merrit, 1970).



The hydroxyl ion precipitates uranium back as $Na_2U_2O_7$ according to Eq.(2), if not neutralized by sodium bicarbonate. The neutralization reaction is



The above chemical reactions during extraction of uranium into fluid phase from ground ore particles are controlled by various factors (1) degree of liberation of uranium in the ore, grain size of uranium, porosity of gangue as well as uranium minerals (2) type of leachant (3) type of oxidant and (4) system properties like temperature, pressure, stirring speed and type of stirrer, leachant vessel. If uranium minerals are fully liberated, the popular shrinking core model mechanisms (1) mass transport through the boundary layer fluid film surrounding each particle or (2) internal surface chemical reaction are applicable. If the product

layer is porous, (3) core-shell (topochemical reaction model) diffusion, is applicable. Usually, the uranium minerals in the ground ore are fully / partially liberated by grinding. In high grade ores, even if uranium is partially liberated, the above mechanisms of shrinking core model generally fit the kinetic data. This is due to high rock permeability to the leachants (Barlett, 1971; Du Preez et al, 1981). But for low grade and finely disseminated uranium ores like Tummalapalle ore in Andhra Pradesh, no single mechanism of shrinking core model was found to be applicable. Earlier attempts to fit a shrinking core kinetic model to the leaching data obtained on this ore resulted in a mixed controlled model, initially chemical reaction and later shell diffusion controlled (Anand Rao, 2010). This could be due to low rock permeability of the rock. Low permeability is evident from the low average specific surface area ($0.42 \text{ m}^2/\text{g}$ given in Table 1) and low pore volume ($0.002 \text{ cm}^3/\text{g}$ given in Table 1). Transport of dissolved metal in liquid within pores of rock particles is likely to be rate controlling step in overall extraction process, especially for low grade ores (Roach et al, 1978). Counter current diffusion of uranyl anion out of the particle with CO_3^{2-} and O^{2-} ions of the fluid phase diffusing into the particle is involved. The diffusivity in turn is a function of porosity and tortuosity of the ground ore particles. Hence, a pore diffusion rate controlling extraction kinetic model is presented herein for the case of low grade uranium ore from Tummalapalle, Andhra Pradesh, India.

Experimental

Materials

The low grade uranium ore from Tummalapalle, India is phosphatic silicious dolomitic limestone containing about 80% carbonates, 12% quartz, 1.2% pyrite as the main gangue minerals and 0.01% pitchblende in intimate association with pyrite. Due to high acid consuming gangue, the alkaline reagent, mixture of Na_2CO_3 and $NaHCO_3$ dissolved in water, was used as leachant. Oxygen gas under pressure was used as oxidant.

BARC NEWSLETTER

Founder's Day

A five litre capacity cylindrical shape autoclave made of stainless steel is used for carrying out kinetic tests of leaching. It is equipped with gas induction type hollow shaft fitted with 50 mm diameter single stage turbine type impeller, oxygen inlet pipe one end connected to oxygen cylinder through pressure reducing valve, cooling water coil, pressure sensor, rupture disk and a solenoid valve which releases pressure whenever exceeds the set point. Top lid of the vessel is coupled to motor drive with a magnetic seal and provided with a thermo well for thermocouple. Electrical heater along with insulation is wrapped outside the cylindrical vessel. Heater is connected to temperature indicator and controller to maintain constant temperature. Cooling water tank with pump is provided with auto mechanism of starting the pump whenever there is a rise in temperature due to exothermicity of the reactions inside the vessel.

Method

The Tummalapalle uranium ore was crushed to -1/4" size in a laboratory jaw crusher and then ground using ball mill for three different time periods to prepare different sized feed samples. The specific surface area determined by BET method using CO₂ adsorption and the porosity determined by Mercury Porosimeter of the ore sample (-1/4") are given in Table 1.

Table 1: Characteristics of Tummalapalle ore

Surface area (m ² /g)	0.42
Pore volume (cm ³ /g)	0.002
Pore dia.(μ)= $\frac{6 \text{ PoreVolume}(c.c. / g)}{\text{Surface area}(m^2 / g)}$	0.03

In each leaching experiment, dry ground ore (1 kg) and predetermined amount of tap water were placed in the autoclave. Autoclave lid was then closed; agitator started at low speed and heated up to 80° C, at which instance the reactor was pressurized to arbitrarily chosen pressure of about 3 kg/cm² using oxygen. The contents were then continued to be heated using electrical heater, which was set to the

desired temperature (>1000C). Incidental increase in pressure of the reactor was observed, while heating so. Required amounts of alkali reagents dissolved in small amount of water were loaded into the autoclave using positive displacement pump. The pressure of the reactor was increased to the desired total pressure using oxygen, the agitator motor was set to the desired stirring speed and the clock time noted as starting time of leaching experiment. Leaching continued for 6 hr. Slurry samples at time intervals of 1 hr, 2 hr, 4 hr and 6 hr were drawn, solids filtered out and the leach liquors were analysed for their U₃O₈ content by spectrophotometry. Solid samples at the end of 6 hr were also analysed for their U₃O₈ content. The average of back calculated feed values of U₃O₈ computed in all the experiments was used in calculating experimental conversion (α_{exp}) with time in each leaching test.

The constant parameters and levels of the variable parameters of present study, given in Table 2, were fixed around the optimum values observed in previous studies (Suri et al, 2010) on Tummalapalle ore.

Table 2 Constant and variable parameters of Tummalapalle ore leaching

Constant Parameter	Value
Pulp density	50% (by wt.)
Na ₂ CO ₃	50 kg/ton of ore
NaHCO ₃	50 kg/ton of ore
Variable Parameter	Levels
Partial pressure of oxygen, P _{O₂} in kg/cm ² (absolute)	4.5, 5.5*, 6.5
Stirring speed, s in rpm	573, 764*, 900
Particle Size, d in μ	25.8*, 32.36, 34.76
Temperature, T in K	398*, 413, 438

* The constant values used when the effect of other parameters was investigated

Pore diffusion rate controlled extraction model

The fraction of uranium extracted, α , from a single spherical particle of radius R_i in time t, is given by following Eq.(4) according to pore diffusion model (Jost, 1960; Perry, 1950).

BARC NEWSLETTER

Founder's Day

$$\alpha(t, R_i) = 1 - \frac{6}{\pi^2} \sum_{K=1}^{\infty} \left(\frac{1}{K^2} e^{-k^2 \pi^2 D_{eff} t / R_i^2} \right) \quad (4)$$

where $K = 1, 2, \dots$ and D_{eff} = Effective diffusivity which can be described by Eq.(5).

$$D_{eff} = \frac{D_{AB} \varepsilon}{\tau_D} \quad (5)$$

where, ε = porosity and the τ_D = tortuosity factor of the ground ore particle and D_{AB} = Diffusivity of solute A in solvent B.

Incorporating particle size distribution into the pore diffusion model

Murhammer et al (1986) showed that the error obtained by assuming uniform particle size distribution (= average of minimum and maximum size) was less than 5%, only if the ratio of maximum to minimum particle size is less than 5 (Murhammer et al, 1986). Gbor et al (2004) showed that if coefficient of variation of particle size distribution following gamma function is more than 0.3, shrinking core model without considering particle size distribution would lead to substantial errors. Hence, the size distribution of ground ore particles is considered. Gates-Gaudin-Schumann (GGs) relation, the most common representation of particle size distribution, is given by Eqs.(6) and (7) (Kelly and Spottiswood, 1982).

$$y(R_i) = \left(\frac{R_i}{R_{max}} \right)^m \quad (6)$$

where $y(R_i)$ is cumulative weight fraction finer than size R_i and R_{max} is size of largest particle. The fraction of material, $\Delta y(R_i)$, in size range between R_i and $R_i - \Delta R_i$ is obtained by differentiation of the above equation

$$\Delta y(R_i) = \frac{m R_i^{m-1}}{R_{max}^m} \Delta R_i \quad (7)$$

Sum of weight fractions of discrete size intervals between the smallest and largest size should be constrained to 1.

$$\sum_{R_i=R_{min}}^{R_{max}} \Delta y(R_i) = 1 \quad (8)$$

The cumulative fraction extracted after an extraction time period t is obtained by summation of products of fraction extracted in each size R_i according to Eq.(4) and the fraction of material in small interval size R_i and $R_i - \Delta R_i$ according to Eq.(7),

$$\alpha(t) = \sum_{R_i=R_{min}}^{R_{max}} \left(1 - \frac{6}{\pi^2} \sum_{K=1}^{\infty} \left(\frac{1}{K^2} e^{-k^2 \pi^2 D_{eff} t / R_i^2} \right) \right) \Delta y(R_i) \quad (9)$$

Fitting experimental data

The fractional conversion (α_{exp}) was calculated using the average back calculated feed assay, 737 ppm U_3O_8 , obtained from residue assay and leach liquor assay in each experiment and the leach liquor concentration measured at different time intervals in all the experiments.

$$\alpha_{exp} = \frac{CV}{Wf}$$

where, C = Concentration of U_3O_8 in the leach liquor at time t , g/L

V = Volume of leach liquor = 0.9 L

W = weight of feed = 1000 g

f = average % U_3O_8 in the feed = 0.0737

Sieve analysis data of three feed samples are fitted by GGS distribution function according to Eq.(6) as shown in Fig.1. The plots of all the three products yielded a linear relation with high degree of correlation. From the slope and intercept values of straight lines obtained in Fig.1, the values of m and R_{max} corresponding to three different sized feed samples are tabulated in Table 3.

BARC NEWSLETTER

Founder's Day

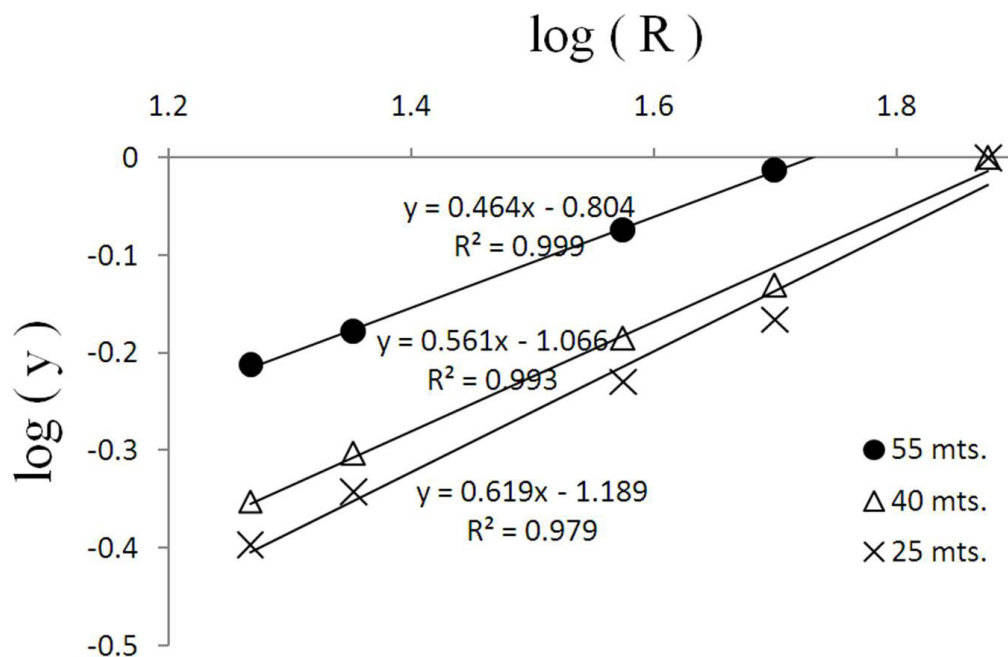


Fig. 1: Gates Gaudin Schumann plots of three feeds of Tummalapalle ore generated with different time periods of grinding

Table 3: Particle size distribution parameters of Tummalapalle ore samples used in leaching experiments

R_{av} (μ)	Gates Gaudin Schumann distribution parameters	
	m	Rmax (μ)
12.4	0.46	54
16.2	0.56	79
17.4	0.62	83

Eq.(9) can be solved for the only unknown D_{eff} for each set of leaching conditions. In order to fit the experimental data to this model equation, a computer program is written to find the effective diffusion coefficient, D_{eff} , in each experiment. Using m and R_{max} values of the feed sample used in each experiment, the value of $\Delta y(R_i)$ is computed according to Eq.(7) for each R_i , using 600 values of $R_i = R_{max}/600$ to R_{max} with step size of $R_{max}/600$, and stored. The step size used was found to be lower enough to meet the constraint stated as Eq.(8). For a value of t , for which α_{exp} is available, sum of the terms of infinite series in Eq.(9) is approximated to a finite series sum such that values of K ranged from 1 to k where k is the least value of K whose term in the sum is less than 0.0005 of the cumulative sum of all previous terms. The omitted terms in the finite series make a

negligible contribution to the sum. For each value of t , the cumulative conversion, $\alpha(t)$ was computed by summing the product of $\alpha(t, R_i)$ and $\Delta y(R_i)$ over all the values of R_i (no. of R_i values being 600 as indicated above). Value of D_{eff} is calculated to minimize the error given by

$$Error = \sum_1^{N_m} (\alpha_{exp} - \alpha_{cal})^2 \quad (11)$$

where α_{exp} is the experimental value of fractional conversion, α_{cal} is the calculated value of fraction reacted using Eq.(9), and N_m is the total number of data, which is 4 in the present case, as α_{exp} in each kinetic experiment is available for four time periods of leaching.

BARC NEWSLETTER

Founder's Day

Table 4: Results of kinetic leaching experiments on Tummalapalle ore along with calculated Diffusivity (D_{eff} cm²/min) and conversion of U_3O_8

Expt. No.	Partial Pressure of O_2 , P_{O_2}	P_{H_2O} at temp. T	Total pressure, P_{total}	Stirring speed, s	Average particle radius, R_{av}	Temp., T	$D_{eff} \times 10^{11}$ (calculated)	Time, t	Conversion of U_3O_8 , α_{exp}	Conversion of U_3O_8 , α_{cal}
	(kg/cm ²)	(kg/cm ²)	(kg/cm ²)	rpm	μ	K	(cm ² /s)	(hr)	fraction	fraction
1	4.5	2.3	5.8	764	12.4	398	0.607	1	0.5	0.47
								2	0.53	0.53
								4	0.59	0.61
								6	0.61	0.65
2*	5.5	2.3	6.8	764	12.4	398	2.43	1	0.63	0.61
								2	0.71	0.68
								4	0.74	0.76
								6	0.74	0.8
3	6.5	2.3	7.8	764	12.4	398	2.43	1	0.65	0.6
								2	0.67	0.68
								4	0.75	0.76
								6	0.79	0.8
4	5.5	2.3	6.8	573	12.4	398	2.025	1	0.61	0.59
								2	0.69	0.66
								4	0.71	0.74
								6	0.73	0.78
5	5.5	2.3	6.8	900	12.4	398	2.835	1	0.67	0.62
								2	0.73	0.7
								4	0.74	0.77
								6	0.75	0.81
6	5.5	3.6	8.1	764	12.4	413	2.835	1	0.69	0.62
								2	0.74	0.7
								4	0.73	0.77
								6	0.75	0.81
7	5.5	7.0	11.5	764	12.4	438	5.67	1	0.78	0.7
								2	0.76	0.77
								4	0.81	0.84
								6	0.82	0.88
8	5.5	2.3	6.8	764	17.4	398	0.957	1	0.43	0.36
								2	0.47	0.43
								4	0.48	0.51
								6	0.54	0.56
9	5.5	2.3	6.8	764	16.2	398	1.435	1	0.47	0.4
								2	0.55	0.48
								4	0.51	0.56
								6	0.55	0.61

*Base experiment, conducted at the constant values of each variable, when other parameters are changed

BARC NEWSLETTER

Founder's Day

Results and Discussion

The values of D_{eff} computed using Eq.(11) and corresponding values of α_{cal} along with the set of experimental conditions of each experiment are given in Table 4. The predicted and experimental conversion values of U3O8 given in Table 4 are plotted as a parity plot in Fig.2.

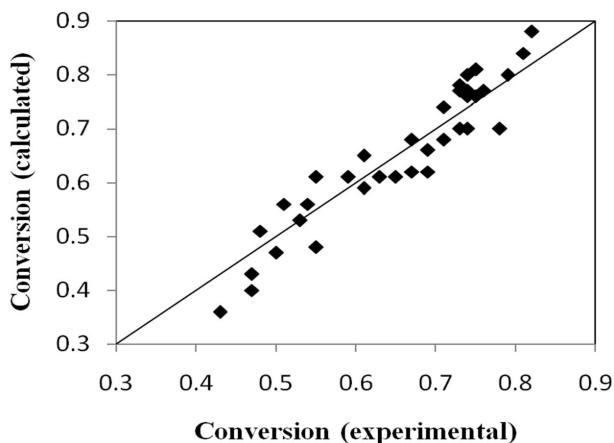


Fig.2: Parity plot of calculated and experimental conversion of uranium in leaching of Tummalapalle uranium ore

Effect of partial pressure of oxygen

The effective diffusivity is found to be increasing from 0.61×10^{-11} cm²/s to 2.43×10^{-11} cm²/s when partial pressure of oxygen increased from 4.5 kg/cm² to 6.5 kg/cm². This could be due to increase in solubility of oxygen with the increase in partial pressure of oxygen leading to increased concentration gradient between the bulk of the solution and the mineral surface.

Effect of stirring speed

Effective diffusivity is found to be increasing from 2.03×10^{-11} to 2.84×10^{-11} cm²/s with increase in stirring speed from 573 to 900 rpm which could be due to increased rate of diffusion at higher agitation speeds.

Effect of temperature

Effective diffusivity is found to be increasing with increase in temperature. Arrhenius plot of $\log(D_{eff})$ Vs $1/T$, given in Fig.3, has yielded activation energy (E_a) of 3.27 kcal/mole. Less than 5 kcal/mole of Arrhenius activation energy cross validates the assumption of diffusion controlled mechanism (Laidler, 1965).

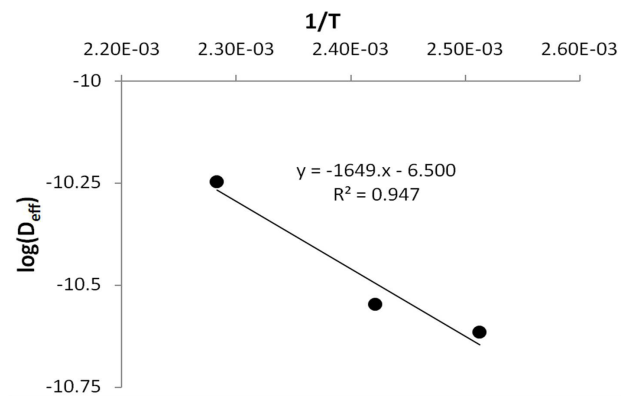


Fig.3: Arrhenius plot of Diffusivity for leaching of Tummalapalle uranium ore

Effect of particle size

The effective diffusivity is found to be decreasing with increase in particle size. The algebraic function is however incorporated in the leaching model given in Eq.(9).

Conclusion

Pore diffusion model coupling particle size distribution has been applied to the data generated on carbonate leaching of Tummalapalle uranium ore. The effective diffusivities of the solutes during leaching under different process conditions of leaching were estimated. The variables studied included partial pressure of oxygen (4.5 to 6.5 kg/cm²), stirring speed (573 to 900 rpm), different particle size distributions with maximum particle radius from 54 to 83 μ and

BARC NEWSLETTER

Founder's Day

temperature 398 to 438 K. The effective diffusion coefficient in leaching of Tummalapalle uranium ore was found to be in the range 0.6×10^{-11} cm²/s to 5.67×10^{-11} cm²/s.

Acknowledgements

The authors thank the staff of Mineralogy Petrology group of Atomic Minerals Directorate for Exploration and Research, Hyderabad for ore microscopy studies. They also acknowledge services of Chemical Lab, Mineral Processing Division, Bhabha Atomic Research for timely chemical analyses. Authors wish to thank Dr. J.K. Chakravarty, Director, Materials Group, Bhabha Atomic Research Centre for his encouragement during the investigations.

Nomenclature

C	concentration of uranium in leach liquor at time t , g/L
D_{eff}	effective diffusion coefficient for diffusion in a porous solid, cm ² /s
D_{AB}	ordinary diffusion coefficient for molecular diffusion in a fluid phase, cm ² /s
E_a	Arrhenius activation energy, kcal/mole
ϵ	porosity of the particle - volume fraction of pore space
f	feed assay U_3O_8 , percent
K	integer index, integer
m	particle size parameter of the Gates Gaudin Schuhmann function
R_i	radius of i th uranium ore particle, μ
R_{min}	radius of smallest uranium ore particle, μ
R_{max}	radius of largest uranium ore particle, μ
T	reaction temperature, °K
t	reaction time, h
s	stirring speed, rpm
τD	tortuosity factor for diffusion in pores (usually ≈ 2)
$y(R_i)$	cumulative weight fraction of ore particles finer than radius R_i , fraction

$\Delta y(R_i)$ fraction of particles in size range between R_i and $R_i + \Delta R_i$, fraction

V volume of leach liquor, L

W weight of feed, g

Greek Letters

$\alpha(t, R_i)$ fractional conversion of uranium ore particle of radius R_i at time t , fraction

α_{cal} calculated value of fraction of uranium reacted, fraction

α_{exp} experimental value of fraction of uranium reacted, fraction

References

1. Anand Rao, K., Sreenivas, T., Venkitakrishnan, R.R., Serajuddin, Md., Karthikayini, P., Padmanabhan, N.P.H., 2010. A kinetic model for alkaline leaching of uranium from dolomitic limestone ore. Proceedings of International Seminar on Mineral Processing Technology (MPT 2010), Jamshedpur, Vol I, 657 -665.
2. Anon, 2012. Uranium 2011: Resources, Production and Demand, A Joint Report by the Organization for economic co-operation and Development (OECD) Nuclear Energy Agency and the International Atomic Energy Agency, ISBN 978-92-64-17803-8, (OECD 2012NEA No. 7059), 253.
3. Barlett, R.W., 1971. Conversion and extraction efficiencies for ground particles in heterogeneous process reactors, *Metallurgical Transactions* 2, 2999-3006.
4. Du Preez, J.G.H., Morris, D.C. and Van Vuuren, C.P.J., 1981. The chemistry of uranium, part XXVII. Kinetics of the dissolution of uranium dioxide powder in a solution containing sodium carbonate, sodium bicarbonate and potassium cyanide. *Hydrometallurgy* 6, 197-201.
5. Gbor, P.K., Jia, C.Q., 2004. Critical evaluation of coupling particle size distribution with the

BARC NEWSLETTER

Founder's Day

- shrinking core model, *Chemical Engineering Science* 59, 1979-1987.
6. Jost, W., 1960. Diffusion in solids, liquids, gases, Academic Press Inc., New York, 46.
 7. Kelly, E.G., Spottiswood, D.J., 1982. Introduction to Mineral Processing, John Wiley, 26.
 8. Laidler, K.J., (1965), Chemical Kinetics, Second ed., McGraw-Hill Book Co., New York.
 9. Merrit, C. Robert., 1970. The Extractive Metallurgy of Uranium, Colorado School of Mines Research Institute, Golden Colorado, United States Atomic Energy Commission, Colorado.
 10. Murhammer, D., Davis, D., Levenspiel, O., 1986, Shrinking core model/reaction control for a wide size distribution of solids, *Chemical Engineering Journal* 32, 87-91.
 11. Perry J.H., (1950), Chemical Engineers Handbook, 3rd edition, 1230 (1950).
 12. Roach, G.I., D., Prosser, A.P., 1978. Prediction of rates of chemical processes for treatment of low-grade materials: theory and tests for mass transfer controlled reactions, Institution of Mining and Metallurgy, C129-C137.
 13. Suri, A.K., Padmanabhan, N.P.H., Sreenivas, T., Anand Rao, K., Singh, A.K., Shenoy, K.T., Mishra, T., Ghosh, S.K., 2010. Process development studies for low-grade uranium deposit in alkaline host rocks of Tummalapalle, Proceedings of IAEA Technical Meeting on low-grade uranium deposits at Vienna.

PHASE TRANSITION AND THERMAL STABILITY STUDIES OF MATERIALS USED AS ELECTROCERAMICS, CATALYST AND SUPERCONDUCTORS

B.N.Wani
Chemistry Division

This Paper received the NETZSCH-ITAS Award at the 19th DAE-BRNS Symposium on Thermal Analysis, held at Mumbai, from Dec. 19-21, 2013

Abstract

Phase transition and thermal stability of material play a vital role in deciding its application in different fields. An extensive knowledge in thermophysical properties can be achieved using different thermoanalytical tools like Thermogravimetry (TG), Differential Thermal Analysis (DTA), Differential Scanning Calorimetry (DSC), Temperature Programmed Oxidation/Reduction/Desorption (TPDRO), Thermodilatometry, High Temperature X-ray Diffraction etc. All the above techniques were explored to study different materials related to electroceramics, fluorides, various mixed oxide catalysts and superconducting materials. Recently above techniques were further explored to study feasibility of various cell components of solid oxide fuel cells.

Introduction

Phase Transitions

Phase transitions in materials occur due to symmetry changes in the material as a result of changing external conditions, viz., temperature, pressure, etc. They are one of the most important factors that influence properties of materials. The 'purpose' of the transformations is to achieve thermodynamic equilibrium in the system under the new external conditions. All stages of phase transformations are subjected to thermal effects, which is the necessity to redistribute internal energy in the material that undergoes the transformation. We have studied phase transitions in various systems as listed in Fig.1.

One such interesting system was CsH_2PO_4 which was investigated for its reversible first order phase transition property using TG/DSC and high temperature optical microscopy way back in 1980. Superionic phase

transition leading to an abrupt increases in proton conductivity from 10^{-6} to $10^{-2} \text{ S cm}^{-1}$ was observed around this transition. The noted phase transition at 234°C before loss of water molecule starts, makes it suitable candidate as proton conducting electrolyte only under humid condition at $230\text{-}300^\circ\text{C}$. This data can be of relevance for usage of this material as

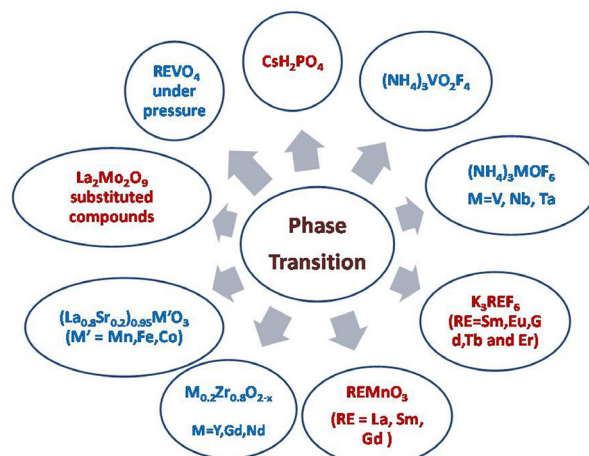


Fig. 1: Phase transition study in various systems

BARC NEWSLETTER

Founder's Day

electrolyte in Intermediate Temperature Solid Oxide Fuel Cells.

Electroceramic

In last two decades solid electroceramic materials have been explored as gas sensors, cell component materials in solid oxide fuel cells. List of materials studied in our group have been listed in Fig. 2. In this study various thermoanalytical techniques like thermodilatometry, High temperature XRD, and conductivity measurements were done using impedance spectroscopy and four probe techniques.

One of the interesting system evaluated, was vanadium and strontium substituted lanthanum molybdate. All the substituted compounds exhibit α (LT phase) \rightarrow β (HT phase) transition. The ionic conductivity of β - $\text{La}_2\text{Mo}_2\text{O}_9$, $\sigma_{1073\text{K}} = 0.06$ S/cm-1 higher than that of YSZ, $\sigma_{1073\text{K}} = 0.04$ S/cm-1. Substitution could not suppress the phase transition completely. The $\alpha \rightarrow \beta$ phase transition causes an abrupt increase in ionic conductivity. In β - phase, the maximum conductivity was noticed in Sr substituted $\text{La}_2\text{Mo}_2\text{O}_9$ due to increase in oxygen vacancy.

The main limitations for practical applications of non-substituted $\text{La}_2\text{Mo}_2\text{O}_9$ as solid electrolyte is the phase

transition. The phase transition produces a drastic drop in the conductivity below 560 °C and possibly mechanical failure due to the high thermal expansion of the unit cell volume between the high and low temperature polymorphs.

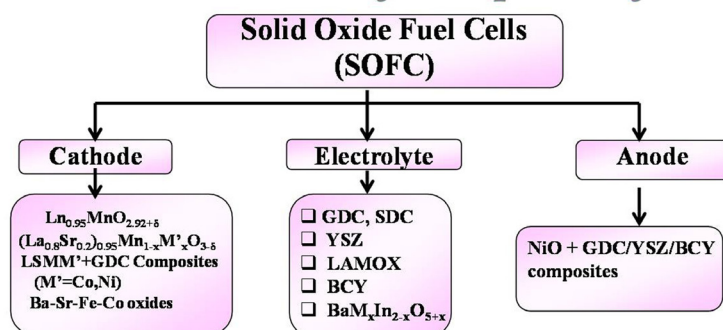
Superconducting oxides

To study the solid state nuclear magnetic resonance of superconducting oxides like Y-123, Y-124 and Sr_2CuO_3 , fluorine was incorporated in to the oxides using solid gas reaction mechanism. To confirm the fluorine incorporation in to these materials, Differential thermal analysis was the sole technique. Superconducting oxide $\text{Sr}_2\text{CuO}_2\text{F}_2$ was prepared by fluorinating Sr_2CuO_3 using NH_4HF_2 as fluorinating agent. As the concentration of NH_4HF_2 increases more and more fluorine was incorporated into Sr_2CuO_3 to form $\text{Sr}_2\text{CuO}_2\text{F}_2$. This fact could be established only by using DTA (Table 1). All the endothermic peaks were reversible and it was due to melting points of product identified.

Catalysis

Mixed oxide based catalysts were explored for pollution abutments like CO oxidation reaction, dye degradation and few organic reactions. The higher catalytic activity for CO oxidation reaction for manganese substituted LaVO_4 and its reproducibility during redox cycles was due to the lowering of the reduction temperature and improved resistance to sintering as shown by temperature programmed reduction/oxidation (TPDRO) techniques. Based on all factors i.e. thermal stability over successive redox cycles, light off temperature and conversion at reaction temperature range of 350 - 400°C, two compositions $\text{LaMn}_{0.5}\text{VO}_{4-d}$, $\text{LaFe}_{0.4}\text{VO}_{4-d}$ and $\text{Fe}_{0.5}\text{La}_{0.5}\text{VO}_4$ of substituted LaVO_4 systems stand out as excellent catalysts.

Electroceramic Materials for components of SOFC



SYNTHESIS \rightarrow (Ceramic, sol-gel, gel-combustion)
CHARACTERIZATION \rightarrow (XRD, SEM)
ELECTRICAL CONDUCTIVITY \rightarrow (4-probe, A.C impedance)
THERMAL EXPANSION STUDIES \rightarrow (Dilatometry)
REDUCTION BEHAVIOR \rightarrow (TPR, TG, DTA)

Fig. 2: Various electroceramic systems explored for cell components of SOFC.

BARC NEWSLETTER

Founder's Day

Table 1: Summary of DTA results of fluorinated Sr_2CuO_3 samples

$Sr_2CuO_3:NH_4HF_2$	DTA endotherm ($^{\circ}C$)	Residue identified
1:0	1168	Sr_2CuO_3
1:1	1078, 1141, 1168, 1414	Sr_2CuO_3 , $SrCuO_2$, SrF_2
1:2	1085, 1436	$SrCuO_2$, SrF_2
1:3	1016, 1057, 1437	$SrCuO_2$, $SrCu_2O_3$, SrF_2
1:6	1091, 1139, 1490	CuO , SrF_2

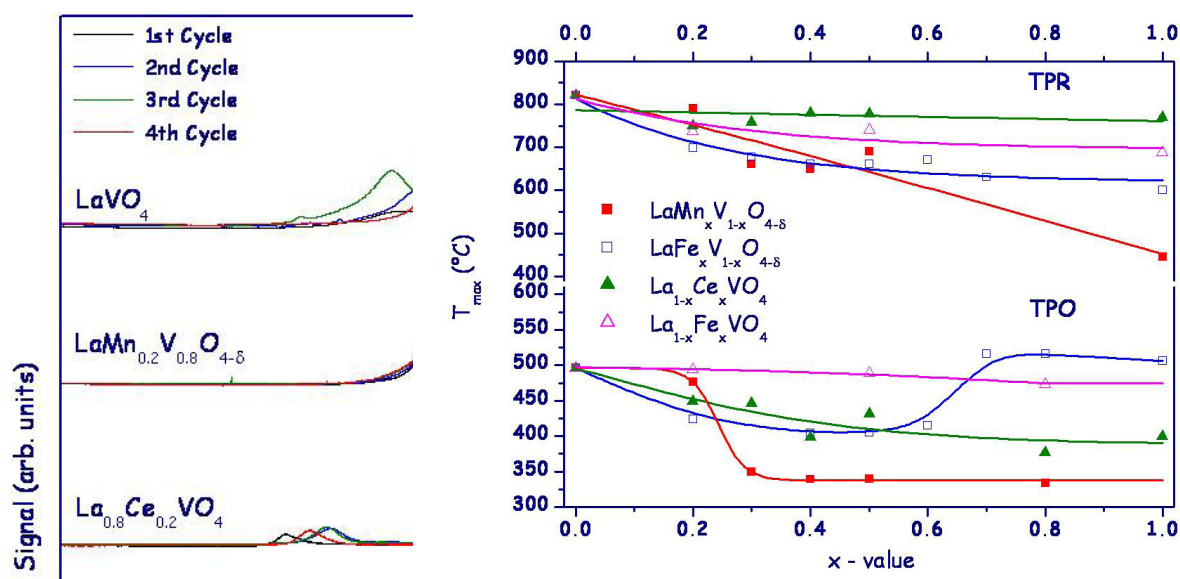


Fig. 3: Successive redox cycles and light off temperatures obtained from TPDRO.

Conclusions

One can get vital information by exploring different thermal analysis techniques for practical applications of mixed oxides based catalyst, electroceramics and superconducting oxides.

Acknowledgement

I would like to acknowledge all present and previous co-authors and collaborators who have contributed to my research work.

BARC NEWSLETTER

Founder's Day



HYBRID MEMBRANE TECHNOLOGY FOR REMOVAL OF URANIUM FROM GROUND WATER

P.K. Tewari, R.C. Bindal, D. Goswami, K.P. Bhattacharyya, A.K. Ghosh,
S. Shivayyanamath, S.A. Tiwari and S. Pal
Desalination Division

This Paper received the Nina Saxena Excellence in Technology Award [Competition for Nina Saxena Excellence in Technology Award held at IIT Kharagpur on 29th July, 2013]

Abstract

Other than the problem of arsenic, fluoride, iron, salinity, heavy metals etc. the elements like uranium is also chemically toxic and there is few reported case where high uranium level in water was found like in some places of the State of Punjab. It was found in rural areas of Punjab that most of the uranium contaminated water also contains multiple contaminants mainly higher salinity and microorganisms. Hence to get the drinking quality water, it is necessary to remove all the contaminants beyond permissible limit. Desalination Division (BARC) has developed an innovative hybrid membrane based removal technique at the point-of-use to avoid the intake of uranium through drinking water pathway and also removes colloidal matters, microorganisms and salinity to a permissible limit. The water purification system comprises of microfiltration (MF) followed by ultrafiltration (UF) and hyperfiltration module. This hybrid membrane technology include tailor-made membrane making technology consists of 5-10micron MF to remove suspended solids, indigenously developed 0.01micron UF to remove bacteria & viruses and 0.001 micron hyperfiltration to remove uranium and excess salinity. Field testing was carried out to study the effectiveness of this hybrid membrane unit in removing uranium contamination from the ground water in six districts of the State of Punjab. From a peak of round 700ppb uranium concentration in the feed water samples, it is brought down to less than 10 ppb which is much below the permissible level of uranium in drinking water (60 ppb) prescribed by Atomic Energy Regulatory Board (AERB).

Introduction

Water resources all over the world are threatened not only by over exploitation and poor management of the natural resources but also by ecological degradation. This can also be attributed to the anthropogenic activities such as discharge of untreated waste, dumping of industrial effluents, leaching from the waste dump sites, run-offs from agricultural fields etc. Ultimately, contamination of drinking water source causes problem to human health and leads to water borne diseases. Toxicity of uranium in water mainly depends upon the solubility and chemical behavior

of its compounds. For example, a study in Southern Finland concluded that the uranium concentration in well waters in the range of 5.6 – 3410 $\mu\text{g/L}$ (ppb) does not have any adverse health effect on exposed populations due to the predominance of two calcium complex species $\text{Ca}_2\text{UO}_2(\text{CO}_3)_3$ and $\text{CaUO}_2(\text{CO}_3)_2$ - which are nontoxic in nature. Uranium is a natural element present in water since the inception of the earth. Elevated concentration of uranium in water samples has been reported in several countries throughout the world. In India, there is few reported high uranium level in water like in some places of the State of Punjab (Fig. 1). Being a low specific activity element, generally

BARC NEWSLETTER

Founder's Day

the chemical toxicity of uranium is overriding the radiological one for soluble compounds. It is a well-known nephrotoxic element and causes occurrence of higher protein β -microglobulin in urine and damage the kidney. Hence it is necessary to bring down the elevated concentration of uranium to the permissible level (60 ppb) prescribed by Atomic Energy Regulatory Board (AERB) for drinking purposes.

Water treatment processes such as coagulation / filtration at high pH, lime softening, ion exchange, activated charcoal adsorption, bone charcoal adsorption, zero valent iron etc. are used for uranium removal in several countries. Laboratory studies for removal of uranium were reported with ferric sulphate and aluminium sulphate coagulation in the pH range of 4 – 10. The uranium removal efficiency is 70 and 90% at pH 6 and 10 respectively with ferric sulphate and the removal efficiency is 90-95% at pH 10 with 50 – 85% at pH 6 with aluminium

sulphate. However, coagulation method is highly dependent on coagulant dose or pH or both. Lime softening method removes 85-90% at pH 10.6 or more. But some other metal hydroxide precipitates out sometime. Ion exchange method removes very effectively (99%) but uranium must remain in ionic form and the removal efficiency varies greatly on the type of the resin, loading capacity, bed volumes, concentration of other interfering ions in water etc. All the aforementioned treatment methods are used in many countries with optimized parameters for maximum removal of uranium. However, each technique is dependent on pH, dissolved solid content, speciation of the contaminant, selectivity of the medium etc. These added extra chemicals to the treated water which needed further treatment to get drinking quality water. Hence, the present innovation is based on the filtration using hybrid membrane technology comprises of microfiltration (MF) followed by ultrafiltration (UF) and hyperfiltration membrane.

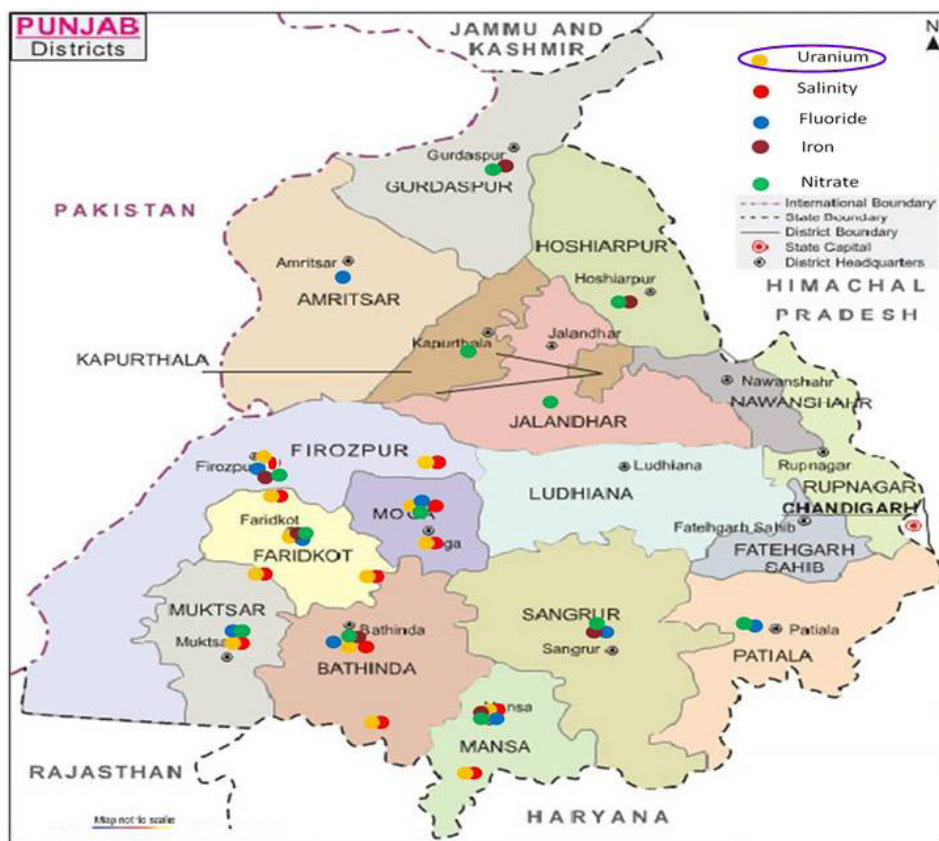


Fig. 1: Places in Punjab where high level of uranium are found in drinking water sources

BARC NEWSLETTER

Founder's Day

Uranium removal from surface water using indigenously developed hybrid membrane technology

We have developed an innovative hybrid membrane based removal technique at the point-of-use to avoid the intake of uranium through drinking water pathway. From the detailed source water analysis (from rural area of Punjab) it was found that the ground water is contaminated with other impurities too apart from uranium beyond the permissible limit by WHO or IS10500 for drinking water. As the pressure driven membrane processes cover entire range of separation from suspended matters to soluble ions, the hybrid membrane technology is the better option for this application. Hybrid membrane technology includes MF (5-10 μ m) to remove suspended materials, indigenously developed UF (0.01 μ m) to remove colloidal matters with microorganisms and hyperfiltration (<0.001 μ m) to remove uranium and other dissolved contaminants. A water purifier manufactured by one of the licensee based on our innovative hybrid membrane technology is shown in Fig. 2. The technology has following features.

- Removal technique at the point-of-use to avoid the intake of uranium through drinking water pathways
- As the variation of contaminants are many, hybrid membrane systems give the total solution (our unit comprises of MF,UF and hyperfiltration membranes)
- The concentrate or reject stream management can be done through indigenously developed uranium selective resin if required.
- It is sustainable, economical, reliable and user friendly technology.

Field testing of the in-house developed hybrid membrane system

Uranium decontamination from drinking water in Punjab has been field tested using in-house developed microfiltration-ultrafiltration-hyperfiltration hybrid membrane system. Water samples from six districts of the state of Punjab viz. Ferozpur, Faridkot, Muktsar, Bhatinda, Mansa and Moga were collected and tested. After measuring the total uranium concentration in water samples, the raw water was

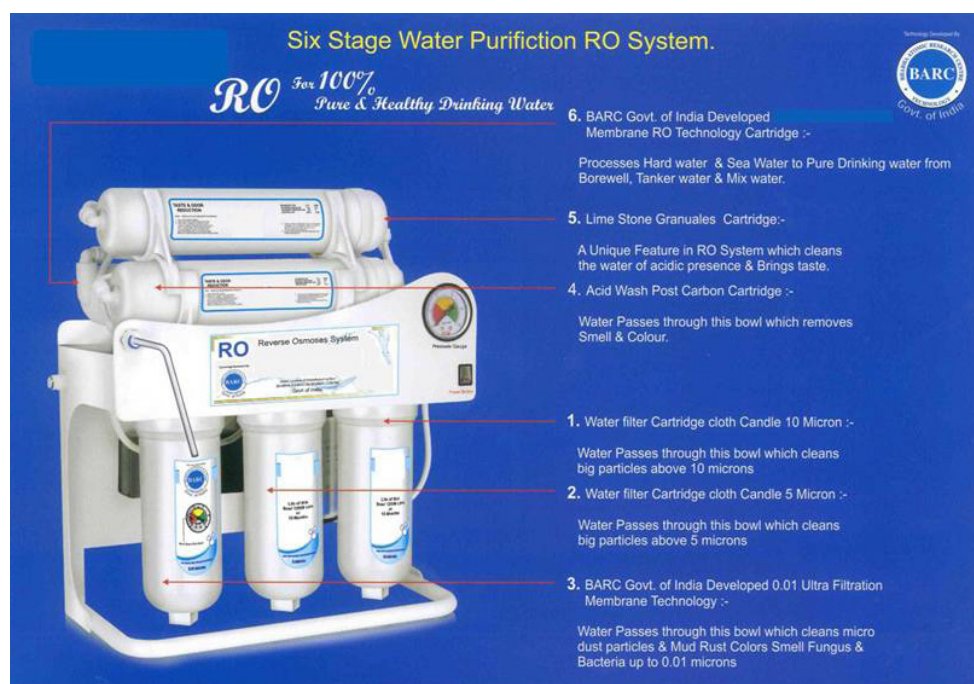


Fig. 2: Picture of a water purifier based on innovative hybrid membrane technology

BARC NEWSLETTER

Founder's Day

passed through the hybrid membrane based water purification system. The filtered and reject water were analysed for uranium concentration with other water quality parameters. From a peak of around 700 ppb uranium concentrations in the feed water samples, it was brought down to less than 10 ppb which is well below the permissible limit of various water standards including world health organization (WHO) and Atomic Energy Regulatory Board (AERB). The summary of the feasibility study on use of BARC developed hybrid membrane technology based water

purification system is shown in Table 1. Based on this experience, treatment of 50m³/hr. uranium containing contaminated water has been proposed (mass flow diagram is shown in Fig. 3).

Conclusions

Uranium decontamination from drinking water in presence of multiple contaminants has been demonstrated using in-house developed hybrid membrane technology consisting of microfiltration, ultrafiltration and hyperfiltration membranes. The technology is affordable and robust for the wells used for domestic and drinking purpose generally in rural areas of India. As we have full-fledged advanced membrane development and application facility, the innovative technology development has been tailor-made for the rural areas of Punjab or elsewhere having uranium contamination issues in ground water. It is sustainable with a win-win situation for the user and supplier serving a societal cause.

Table 1: Summary of the feasibility study

Parameters	Unit	Range	Mean
U concentration in water samples	ppb	3.7 – 685	184
TDS levels in water samples	ppm	174 - 4040	1346
U concentration in purifier filtered water	ppb	0.2 – 6.0	2.2
TDS in purifier filtered water	ppm	12 - 159	68

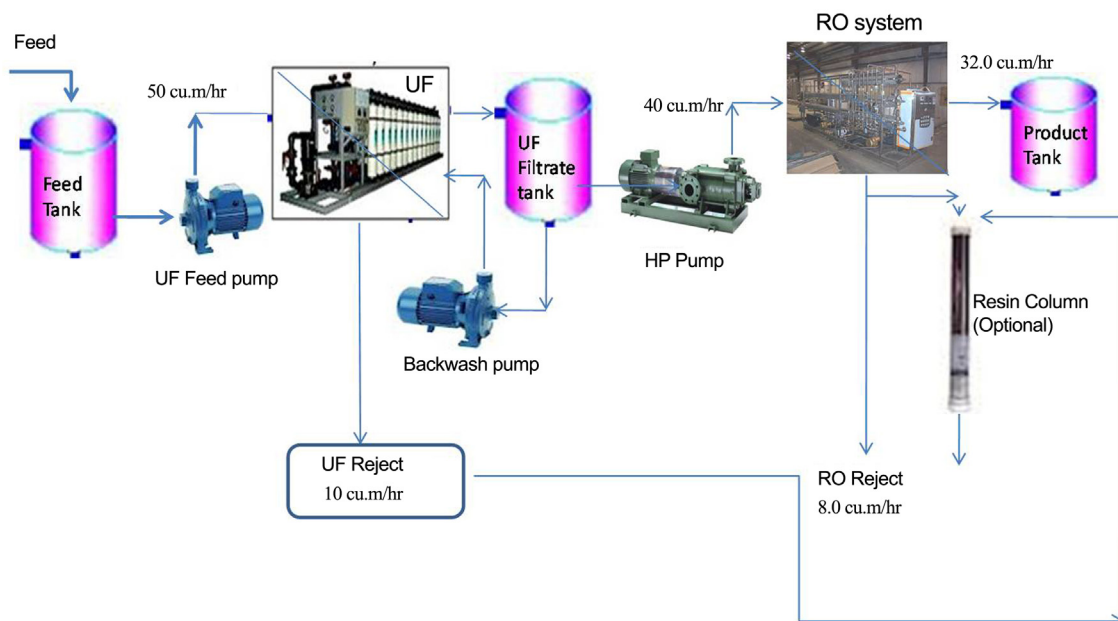


Fig.3 Mass flow diagram for treatment of 50m³/hr. uranium containing contaminated water

STIMULI-RESPONSIVE CUCURBITURIL-ADORNED SUPRMOLECULAR MICELLAR ASSEMBLIES OF CETYLPYRIDINIUM CHLORIDE

Jyotirmayee Mohanty

Radiation & Photochemistry Division

This Paper received the Samanta Chandra Sekhar Award 2011,
at the Annual Meeting of the Odisha Bigyan Academy

Abstract

The molecular recognition behavior of versatile macrocyclic receptors, cucurbiturils (CBs) have been investigated in relation to their host-guest interaction with amphiphilic molecules, especially cationic surfactants having widespread technological importance. Construction of novel cucurbituril (CB)-adorned supramolecular micellar assemblies of a cationic surfactant, cetylpyridinium chloride (CPC), through noncovalent host-guest interactions has been demonstrated. The distinct cation receptor features and cavity dimensions of the CB5 and CB7 homologues assert that the macrocyclic hosts remain complexed with the CPC monomers and take part in the micelle formation with a shift in *cmc*, a unique observation in contrast to that of classical host, β -cyclodextrin, and has been characterized by photochemical, surface tension, conductivity, DOSY NMR and SANS measurements. The reversible response of these soft supramolecular micellar structures to thermal-stimuli, which project their utility for *on-demand* smart drug-delivery vehicles, has also been established.

Key Words: Host-guest interaction, cucurbiturils, surfactant, supramolecular-micellar assemblies, stimuli-responsive

Introduction

Supramolecular encapsulation of guest molecules through macrocyclic hosts presents a convenient pathway for modulation of molecular properties, as it can introduce pronounced effects on the physico-chemical properties of the included guest.¹ Host-guest interaction finds immense importance in obtaining photostability, drug delivery, catalysis, and sensor applications. Cucurbiturils (CBs), relatively new addition to the repertoire of macrocyclic hosts, are a unique class of water soluble macrocyclic receptor molecules consisting of methylene bridged glycoluril

units (Chart 1).^{1,2} Structurally, the pumpkin-shaped CBs constitute highly symmetrical hydrophobic cages of low polarity and polarizability with two identical dipolar portal ends comprised of carbonyl functional groups.^{1,2} As a macrocyclic host, CBs have attracted considerable attention in recent years owing to their excellent binding abilities for varieties of guests. Among different CBs, the homologue cucurbit[7]uril (CB7, with 7 glycoluril units) forms stable inclusion complexes with several guest molecules, like organic dyes, protonated alkyl and aryl amines and cationic dyes, via a combination of hydrophobic and ion-dipole interactions.¹⁻⁴ The lower homologue cucurbit[5]uril

(CB5), having a smaller cavity size, interacts with metal ions or forms exclusion complex with cationic organic guests through its highly polarized carbonyl portals.² In this article, the supramolecular interactions of CB5 and CB7 hosts with a cationic surfactant, cetylpyridinium chloride, have been described in relation to the modulation in the *critical micelle concentration (cmc)*, temperature-responsive tunability and their potential applications.

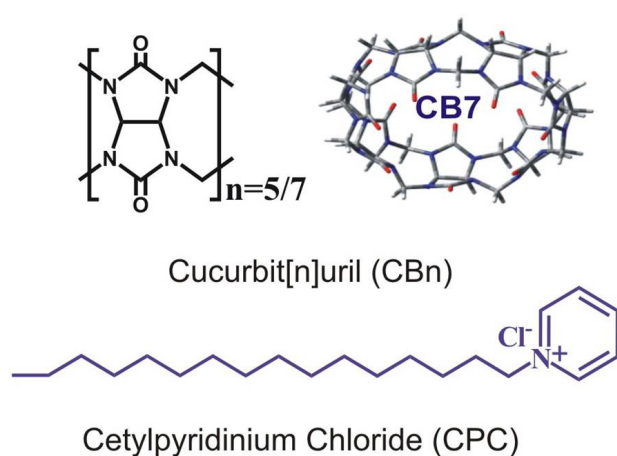


Chart 1: Chemical structures of the cucurbituril hosts and CPC surfactant.

Cucurbituril-adorned Supramolecular Micellar Assemblies

Cetylpyridinium chloride (CPC, Chart 1) belongs to a class of frequently used cationic surfactants and exhibits intriguing microstructural changes with anionic additives such as hydrotropes, electrolytes, bile salts, etc. Owing to its vast applications, we attempted to explore its intriguing assembly features in the presence of supramolecular host, CBs, to have control for an on demand uptake and release.

In the photochemical approach, we employ a fluorescent probe, Nile Red (NR), which shows characteristic changes in its spectral properties due to its preferential positioning in the interfacial region of the micelle. As shown in Fig. 1, the micellization behavior was examined in the presence of the macrocyclic host, CB7 and CB5. With increasing CB7

concentrations, the *cmc* gradually increases from its normal value of 1 mM to 1.63 mM in the presence of 2 mM CB7 (Fig.1 a-c). In contrast, the titration of NR with CPC in the presence of CB5 (1 mM), displayed a downward shift in the *cmc* (0.57mM) (Fig.1 d, e).⁵ The shift in *cmc* of CPC in the presence of CB5/CB7 was also confirmed by surface tension and conductivity measurements.

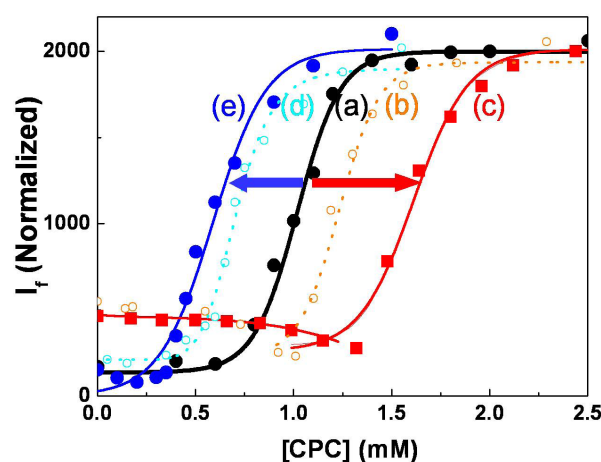


Fig. 1: Fluorescence titration curves of NR (~2 μM) with different concentrations of CPC in the absence and presence of CB hosts: absence of CBs (a); 1.5 mM CB7 (b); 2.0 mM CB7 (c); and 0.5 mM CB5 (d); 1 mM CB5 (e). $\lambda_{ex} = 550 \text{ nm}$, $\lambda_{mon} = 660 \text{ nm}$.

Considering the dimensions of the CB portals (portal diameter ~5.4 Å and ~2.4 Å for CB7 and CB5, respectively),² and CPC (width of pyridinium group <5 Å and length of hydrocarbon chain ~17 Å), it is apparent that the pyridinium group of CPC can be accommodated within the CB7 cavity. CPC cannot be accommodated inside the CB5 cavity, however, an exclusion complex based on ion-dipole interactions is possible. Earlier studies using cyclodextrin (CD)/CB7 hosts and other surfactant molecules have suggested that the reduction in the surfactant-monomer concentration is the prevailing mechanism for the upward *cmc* shift where the host-bound surfactant monomers do not participate in the micelle formation.^{6,7} However, a similar mechanism in the present case cannot explain the contrasting *cmc* shifts observed with the CB7 and CB5 hosts, which points to possible participation of the CB-bound CPC monomers in the micelle formation.

BARC NEWSLETTER

Founder's Day

The participation of the CB hosts in the micelle structure has also been confirmed by DOSY NMR measurements. If the cucurbiturils remain attached to the CPC as inclusion or exclusion (in the vicinity of the CPC head group) complexes, the diffusion coefficients of both the CPC protons as well as the CB7 protons would get affected on micellization. The average diffusion coefficient of the $-CH$ protons of CPC in the presence of CB5 or CB7, decreases with increasing CPC concentrations. While the diffusion coefficient of CB5 protons remain unchanged, CB7 protons show a gradual decrease even beyond the cmc (Fig. 2), indicating that the CB7-CPC unit is incorporated within the micellar assembly. However, similar studies with β -cyclodextrin (β CD) displayed such changes after an initial slight decrease, which was expected for its involvement with the monomers.⁵

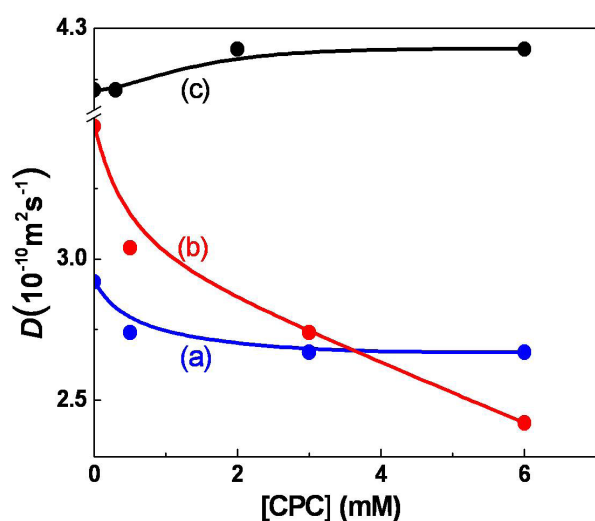


Fig.2: Plot of the diffusion coefficient values for the β -CD (a), CB7 (b) and the CB5 (c) protons with CPC concentration.

Small-angle neutron scattering (SANS) measurements on the CB7-CPC system revealed that the micellar structure of CPC is prolate ellipsoidal with axes 34.3 Å (a) and 18.5 Å (b). However, in the presence of CB7, there is slight elongation along the major axis from 34.3 to 35.9 Å with a

significant decrease in the surface charge on the micelle (0.17 to 0.10). This is very much in line with the existence of CB7 beaded CPC micelle. On the other hand, in the CB5-CPC system, though the SANS data indicated a significant reduction in the surface charge, the micellar dimensions remained unchanged, suggesting an externally embedded CB5 on the CPC micelle. Based on the above results, the positioning of the CB7/CB5 hosts in the CPC micelle can be visualized as in Fig. 3. In the case of CB5, the macrocycle remains in the periphery of the micellar structure, whereas in the case of CB7, the CB7-CPC complex is incorporated within the micellar structure leading to the formation of mixed micelles. The incorporation of CB7 at the neck of the pyridinium head group provides optimum interaction for the negatively polarized CB portals with the cationic charge of the pyridinium head group. In addition a part of the alkyl chain is included in the cavity of the macrocycle due to favorable hydrophobic interactions. The partial encapsulation of alkyl chain of CPC within the CB7 host can reduce the hydrophobicity of the alkyl chain and can lead to an increase in the *cmc*.⁵

Stimuli-responsive Tuning

The advantages of the contrasting supra-molecular *cmc* shift established in CPC on using CB7 or CB5 has been explored further to demonstrate a supramolecularly tunable *cmc*, which has implications in drug transport, binding and release strategy, etc. The effect of increasing CB7 concentration or solution temperature on the *cmc* of CPC in a solution containing 1 mM

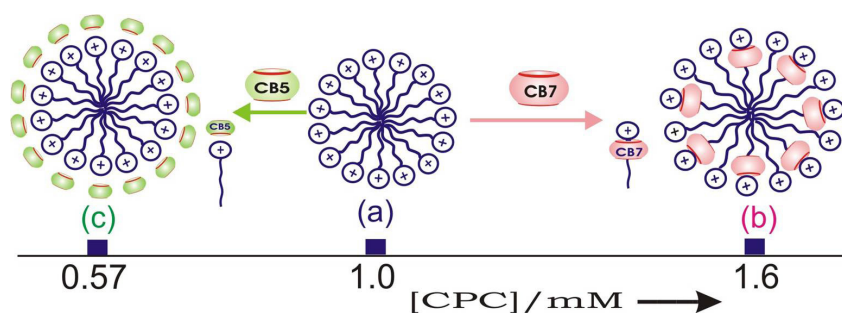


Fig.3: Schematic representation of the distinct cucurbituril adorned micellar assemblies formed by CPC (a), in presence of CB7 (b), and CB5 (c).

BARC NEWSLETTER

Founder's Day

CB5 has been investigated. The fluorescence titration curves progressively shifted with the addition of CB7 or increasing temperature and the corresponding *cmc* values demonstrated a tunable range from 0.57 to 1.6 mM (Fig. 4).⁵ The addition of CB7 or increase in temperature at the above discussed conditions disrupts the CB5-CPC micellar structure, which establishes a facile host/temperature-induced release mechanism having direct relevance in drug delivery applications.

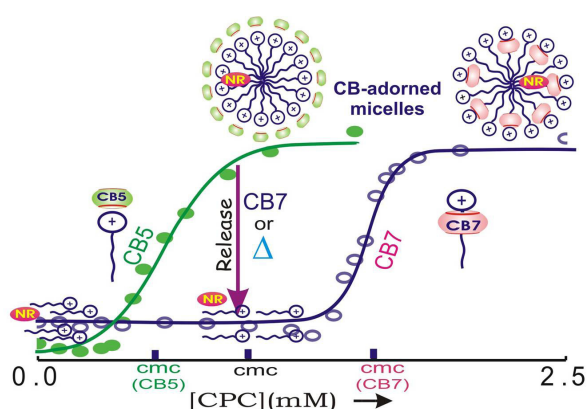


Fig. 4: Micellization curve for the CB5 or CB7 adorned CPC surfactant and the proposed release mechanism for the CB5 assembly.

Conclusion

The established cucurbituril-adorned, thermo-responsive on/off supramolecular micellar assemblies of the cationic surfactant, CPC, is schematically shown in figure 4. While the supramolecular additive, CB5, exhibits an early micellization of CPC at ~ 0.57 mM, the CB7 host delays the same to about 1.6 mM of CPC. Response of these systems to external stimuli, such as, temperature or the combination of CB5/CB7,

demonstrates a continuous tunable range for the micellization of CPC. The supramolecular modulation of the surfactant aggregates, envisioned in the present work is very potent and promising for pharmacological applications and for designing tunable artificial molecular devices or nanoreactors.

Acknowledgements

I acknowledge all my collaborators and co-authors of our published works. I also thank the colleagues in RPCD and CG, BARC for their constant encouragement and support.

References

1. Bhasikuttan, A. C., Pal, H., Mohanty, J. *Chem. Commun.* (Feature Article), 47, (2011): 9959-9971.
2. Lee, J. W., Samal, S., Selvapalam, N., Kim, H.-J., Kim, K. *Acc. Chem. Res.* 36, (2003): 621-630.
3. Mohanty, J., Nau, W. M. *Angew. Chem. Int. Ed.* 44, (2005): 3750-3754.
4. Mohanty, J., Bhasikuttan, A. C., Dutta Choudhury, S., Pal, H. *J. Phys. Chem. B (Letts.)*, 112, (2008): 10782-10785.
5. Dutta Choudhury, S.; Barooah, N.; Aswal, V. K.; Pal, H.; Bhasikuttan, A. C.; Mohanty, J. *Soft Matter*, 10, (2014): 3485-3493.
6. Martini, A.; Artico, R.; Civaroli, P.; Muggetti, L.; Ponti, R. D. *Inter. J. Pharmaceutics*, 127, (1996): 239-244.
7. Mehta, S. K.; Bhasina, K. K.; Dham, S.; Singla, M. *L. J. Colloid Interface Sci.*, 321, (2008): 442-451.

FLUORESCENCE ENHANCEMENT WITH PLASMONIC NANOSTRUCTURES

Sharmistha Dutta Choudhury
Radiation & Photochemistry Division

This Paper received the SERB Women Excellence Award 2013
[Award constitutes a research grant for three years]

Abstract

The interactions of fluorophores with plasmonic nanostructures lead to several favorable effects such as increased brightness, better photostabilities and reduced excited-state lifetimes that can be exploited to improve fluorescence technology. This article describes the development of novel silver-gold nanocomposite structures for metal-enhanced fluorescence and silver nanostructures for efficient fluorescence correlation spectroscopy, with reduced detection volumes and increased signal intensities.

Keywords: Metal-Enhanced Fluorescence, Silver-Gold Nanocomposites, Surface-Plasmon, Fluorescence Correlation Spectroscopy, Single Molecule Fluorescence

Introduction

Fluorescence detection is a versatile and widely used research tool due to its high sensitivity, ease of detection and rapid response. Today fluorescence spectroscopy and microscopy require minimal sample volumes and extremely low concentration of fluorophores for single molecule detection. The coupling of fluorescence with surface-plasmon oscillations in metal nanostructures provides us the opportunity to create new kinds of ultrabright fluorescent probes or develop alternative methodologies that can improve the capabilities of modern fluorescence technology.¹

A fluorophore that is placed at a certain optimal distance from metal nanoparticles, can exhibit increased fluorescence intensities, decreased fluorescence lifetimes and improved photostabilities. This interesting phenomenon, known as metal-enhanced fluorescence (MEF), arises due to two effects. First, is the creation of an intense excitation

field around the metal nanoparticle that provides increased excitation rates for a fluorophore that is placed in its vicinity. Secondly and more importantly, the near-field coupling of fluorescence with the localized surface-plasmon oscillations in the metal nanoparticle, increases the radiative decay rate of the fluorophore. The coupled plasmon-fluorophore system eventually radiates into the far-field with increased emission intensity.¹ Since fluorophore-plasmon interactions depend on the properties of metal nanostructures, it is essential to construct robust and reproducible metallic nano substrates with controlled geometry and tunable optical features, in an easy and cost effective manner, to realize the full potential of MEF. We have demonstrated the facile fabrication of silver-gold nanocomposite (Ag-Au-NC) substrates by galvanic replacement reaction of silver by gold. Our studies indicate that these substrates are not only easy to prepare but also provide excellent fluorescence enhancements for widely used fluorescent dyes.^{2,3} Another important area where plasmonic

BARC NEWSLETTER

Founder's Day

nanostructures can play a major role is fluorescence correlation spectroscopy (FCS).⁵ With typical diffraction limited observation volumes obtained with conventional confocal microscopy systems, it is possible to perform FCS measurements only at low fluorophore concentrations (pico- to nanomolar). We have shown that simple silver nanostructures (AgNS), can be used to increase the upper concentration limit for FCS measurements and also provide increased fluorescence intensities for better detection efficiency.⁵

Fluorescence enhancement using silver-gold nanocomposite substrates

The galvanic replacement reaction of silver with gold is an elegant approach for preparing novel metal nanostructures, that is driven by the difference in the reduction potentials of $\text{AuCl}_4^-/\text{Au}$ and Ag^+/Ag .⁶ Immersion of silver coated glass slides into the HAuCl_4 solution causes spontaneous oxidation of elemental silver and the deposition of nanoscale Au particles on the surface of the sacrificial silver substrate, leading to formation of the nanocomposite substrate, Ag-Au-NC. The fabricated substrates with surface deposited gold nanoparticles provide a robust surface, while at the same time the residual silver provides favorable metal-fluorophore interactions for better fluorescence enhancement. Fig. 1 shows a schematic of the substrate fabrication and the large intensity enhancement observed for the fluorophore, ATTO655, immobilized on Ag-Au-NC substrate. Most interestingly, the intensity enhancement is accompanied by decrease in the fluorescence lifetime of ATTO655, which is a clear signature of fluorophore-plasmon coupling effect.^{2,3} Scanning confocal microscopy images (Fig. 1) show much brighter fluorescence spots on the nanocomposite surface compared to a control glass slide.

These bright spots correspond to emission from single fluorescent molecules and indicate that the emission intensities are actually enhanced on a molecule by molecule basis. Statistical analysis reveals a large distribution in the intensities of individual ATTO655 molecules on Ag-Au-NC in comparison to glass. This is attributed to differences in metal-fluorophore interactions at different sites on the fabricated substrate. Single molecule studies, therefore, help in gaining additional information on the heterogeneity of the Ag-Au-NC substrate, which is masked in ensemble fluorescence measurements. Very high intensities (~ 80 fold enhancement) can be achieved for single molecules that are suitably located in the "hot spots" of the plasmonic substrate.²

These results are expected to have a large implication for biological studies. For example, MEF can improve the fluorescence intensities and hence the detection of fluorophore labeled biomolecules. By proper choice and design of the nano metallic substrate it is possible to obtain intensity enhancements for the intrinsically weak fluorescence from biomolecules that emit in the UV region, like proteins or DNA.¹ Thus, fluorophore-plasmon coupling provides the opportunity for label-free studies of biomolecules.

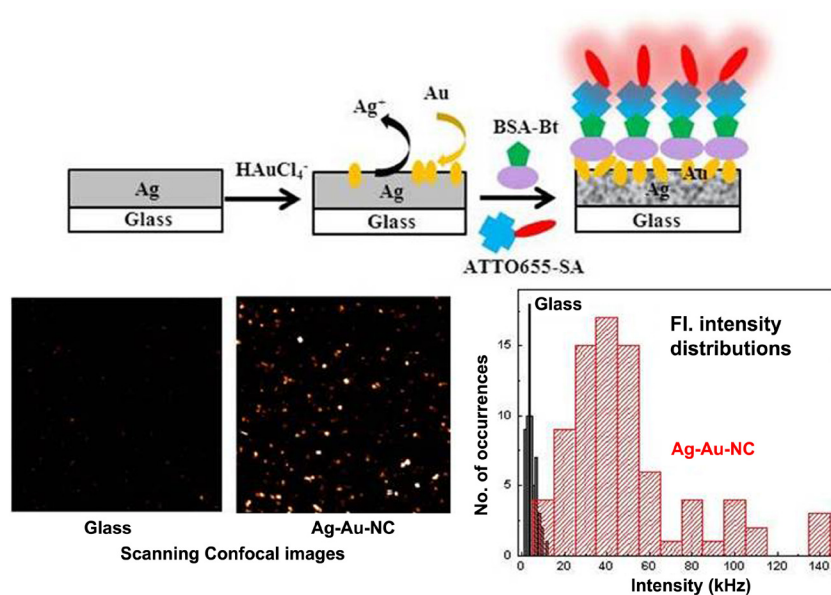


Fig. 1: Metal-enhanced fluorescence with Ag-Au-NC substrates.

BARC NEWSLETTER

Founder's Day

Further, since MEF is accompanied by reduction in the fluorescence lifetimes, the photostability of the probe molecule can be significantly increased. This leads to dramatic improvements especially for single molecule fluorescence studies of biological molecules, for high-throughput bioassays and medical diagnostics. The metal proximity-induced fluorescence enhancement can also be used to design novel experiments for selective biomolecular binding and recognition.

Fluorescence correlation spectroscopy with silver nanostructures: reduced detection volumes and increased intensities

Fluorescence correlation spectroscopy (FCS) is a widely used technique to investigate the interactions and dynamics of molecules, below micromolar concentrations. We have shown that silver nanostructure (AgNS) substrates that are conveniently prepared in the laboratory (by wet chemical synthesis or thermal vapour deposition) without any elaborate nanofabrication, can extend the applicability of FCS to higher concentrations by reducing the effective detection volume.⁵ In addition to reduced detection volumes, the plasmonic nanostructures also allow tuning of the fluorescence properties of molecules. Compared to open volume, fluorescence bursts with very high signal intensities are observed on the AgNS substrate. This interesting behaviour is attributed to fluorophore-plasmon coupling effects. Moreover, the introduction of plasmonic nanostructures has the distinct advantage of making FCS studies feasible at high concentrations without any modification of the conventional optical set-up. Figure 2 shows a schematic of the FCS set-up in open volume and on AgNS substrates. The autocorrelation functions, obtained for the fluorescence intensity fluctuations due to diffusion of the fluorescent probe molecule,

ATTO655, show several notable features, particularly an increase in the amplitude and a decrease in the correlation time, on AgNS compared to the open volume. Most interestingly, at 9 μM fluorophore concentration, no time correlation can be observed in the open volume whereas a distinct correlation is observed on AgNS (Figure 2). These results suggest that there is a reduction in the effective fluorescence detection volume on the AgNS substrates. From a statistical analysis of several independent measurements at different positions on the AgNS, the effective detection volume is estimated to be reduced by about a factor of 18 ± 10 on the AgNS substrate in comparison to open volume.⁵ We propose that two effects are responsible for the reduction in the detection volumes in the present substrates. First, is the physical confinement of the molecules within the nanospaces between the silver nanoparticles and second is the modification of the near-fields in the vicinity of the plasmonic nanoparticles. Since the plasmon coupled near-field effect exists within a small region (upto ~ 200 nm) around the metal nanoparticles, a very small and bright fluorescence volume is created in the immediate vicinity of these particles. This effect also increases the fluorescence count rates and improves the detectability of single diffusing molecules.

This study highlights the simplicity with which plasmonic nanostructures can be incorporated on

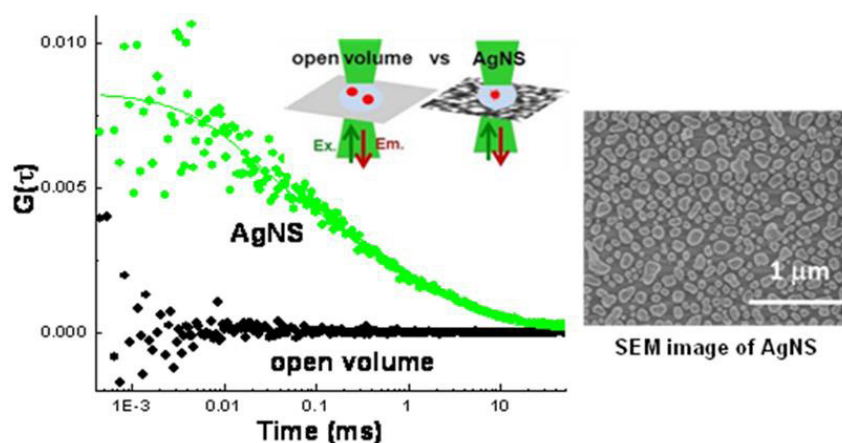


Fig. 2: Schematic of the FCS set-up on silver nanostructure (AgNS) substrates and the autocorrelation plots of 9 μM ATTO655 in open volume and AgNS.

BARC NEWSLETTER

Founder's Day

a standard confocal microscopy set-up to augment its measurement capabilities. We believe that the plasmonic AgNS substrates will be a widely used platform for performing FCS studies and addressing many biological problems that demand observation volumes below the classical diffraction limit.

Acknowledgements

I would like to thank Prof. J. R. Lakowicz, University of Maryland Baltimore, for introducing me to this interesting subject area and also the co-authors of our published papers. I thank all colleagues of RPCD and CG for their encouragement and support.

References

1. Lakowicz, J. R., Ray, K., Chowdhury, M., Szmajcinski, H., Fu, Y., Zhang, J.; Nowaczyk, K., *Analyst*, 133 (2008) 1308.
2. Dutta Choudhury, S.; Badugu, R.; Ray, K.; Lakowicz, J. R., *J. Phys. Chem. C* 116 (2012) 5042.
3. Dutta Choudhury, S.; Badugu, R.; Ray, K.; Vanam, P. S.; Lakowicz, J. R., *Proc. of SPIE* 8234 (2012) 82340B.
4. Levene, M. J.; Korlach, J.; Turner, S. W.; Foquet, M.; Craighead, H. G.; Webb, W. W., *Science* 299 (2003) 682.
5. Dutta Choudhury, S., Ray, K., Lakowicz, J. R., *J. Phys. Chem. Lett.* 3 (2012) 2915.
6. Sun, Y.; Xia, Y., *J. Am. Chem. Soc.*, 126 (2004) 3892.

ESTIMATION OF DISTANCE ERROR BY FUZZY SET THEORY REQUIRED FOR STRENGTH DETERMINATION OF HDR ^{192}Ir BRACHYTHERAPY SOURCES

Sudhir Kumar, S.D. Sharma, G. Chourasiya and D.A.R. Babu

Radiological Physics and Advisory Division

and

D. Datta

Health Physics Division

and

D.N. Sharma

Health Safety and Environment Group

This Paper received the Best Oral Paper Award from the Association of Medical Physicists of India, at the 34th National Conference of Association of Medical Physicists of India, Kolkata, Nov. 13-16, 2013

Abstract

Verification of the strength of high dose rate (HDR) ^{192}Ir brachytherapy sources on receipt from the vendor is an important component of institutional quality assurance programme. Either reference air-kerma rate (RAKR) or air-kerma strength is the recommended quantity to specify the strength of gamma emitting brachytherapy sources. The use of Farmer-type cylindrical ionization chamber of sensitive volume 0.6 cm^3 is one of the recommended methods for measuring RAKR of high dose rate (HDR) ^{192}Ir brachytherapy sources. While using the cylindrical chamber method, it is required to determine the positioning error of the ionization chamber with respect to the source which is called the distance error. An attempt has been made to apply the fuzzy set theory to estimate the subjective uncertainty associated with the distance error. A simplified approach of applying this fuzzy set theory has been proposed in the quantification of uncertainty associated with the distance error. In order to express the uncertainty in the framework of fuzzy sets, the uncertainty index was estimated and was found to be within 2.5% which further indicates that the possibility of error in measuring such distance may be of this order. This indicates that the relative distance l_i values estimated using analytical methods are within 2.5% uncertainty. This value of uncertainty in distance measurement should be incorporated in the uncertainty budget while estimating the expanded uncertainty in HDR ^{192}Ir source strength measurement.

Introduction

Verifying the strength of high dose rate HDR ^{192}Ir brachytherapy sources on receipt from the vendor is an important component of institutional quality assurance programme[1,2]. The recommended quantity to specify the strength of gamma emitting

brachytherapy sources is either reference air-kerma rate (RAKR) or air-kerma strength (AKS). Calibration of the ^{192}Ir sources used in HDR remote afterloading brachytherapy units is carried out either by using a thimble ionization chamber (in-air jig method) or by using a well-type ionization chamber. A Farmer-type cylindrical ionization chamber of nominal

BARC NEWSLETTER

Founder's Day

sensitive volume of 0.6 cm³ is frequently used for in-air calibration of HDR ¹⁹²Ir brachytherapy sources in addition to a suitable well-type ionization chamber as cylindrical ionization chambers are readily available in the hospitals[3-4].

A 370 GBq (10 Ci) ¹⁹²Ir source provides an ionization current of only about 1x10⁻¹¹ amp in a 1.0 cm³ ionization chamber at a distance of 20 cm[5]. It is true that very near to a brachytherapy source, the radiation intensity changes very rapidly due to inverse-square law. A 0.1 cm error in a 10 cm distance causes a 2% error in calibration[6]. Small errors in positioning the chamber can translate into large errors in the estimation of source strength. Increasing the separation between centers of the chamber and the source will improve the measurement accuracy. However, this will result in proportionate reduction in the current leading to larger percentage contributions by leakage current and gamma-ray scattering from the room surroundings and poor reproducibility. Getting closer of course worsens the distance error and requires a large geometric correction for the size and shape of the ionization chamber[7].

The seven distance method is recommended as a standard method to maximize the accuracy in measuring the strength of HDR brachytherapy sources by using cylindrical ionization chamber[4-6]. While using the cylindrical chamber method, it is required to determine the positioning error of the ionization chamber with respect to the source which is commonly called as the distance error. Earlier, we have developed the analytical methods to estimate the distance error[8-9]. As further research in this work, an attempt has been made to apply the fuzzy set theory to estimate the subjective uncertainty associated with the distance error.

In view of the application of fuzzy set theory in the domain of image analysis in medical dosimetry, we have proposed an approach of applying this theory in the quantification of uncertainty associated with the

distance error. Since the measured distance possesses some error during the measurement and the input components are imprecise, fuzzy set theory is an appropriate tool to estimate the uncertainty present in such an ambiguity [10].

Materials and Methods

Multiple distance measurement technique

The microSelectron-HDR unit from Nucletron was used in this work. This unit uses an old design micro-Selectron ¹⁹²Ir HDR brachytherapy source with 370 GBq (10 Ci) nominal activity to treat brachytherapy patients with high dose rate comparable to teletherapy.

To determine experimentally, the RAKR of an HDR ¹⁹²Ir brachytherapy source using a PTW 0.6 cm³ Farmer-type cylindrical ionization chamber, a multiple distance measurement technique was used. This measurement has historically been made at seven separate distances. Thus the technique has been termed the '7 distance' measurement (7 DM). While using cylindrical ionization chamber for measurement of the strength of HDR ¹⁹²Ir brachytherapy sources, it is necessary to estimate three items, viz. (i) the positioning error (\pm) of the ionization chamber with respect to the source, (ii) the contribution of scatter radiation (M_s) from the floor, walls, ceiling, and other material in the treatment room and (iii) a proportionality constant. The 7DM was suggested to determine these parameters and thereafter the strength of HDR ¹⁹²Ir brachytherapy sources[4-5]. Kumar et al. [8-9] has described in detail the procedure for measuring the RAKR of HDR ¹⁹²Ir brachytherapy sources. In this 7 DM method, the output of the source in air is measured at seven different distances each corresponding to a meter reading M_d , which is the sum of primary and scattered radiation

$$M_d = M_p + M_s \quad (1)$$

where M_p is the meter reading due to primary radiation only and M_s is the meter reading due to scattered

BARC NEWSLETTER

Founder's Day

radiation only, which is assumed to be independent of distance. As the primary radiation follows inverse square law, Equation (1) can be written as

$$M_p = (M_{d_i} - M_s) = \frac{f}{(d_i + c)^2} \text{ where } i = 0 \dots\dots 6 \quad (2)$$

where d_i is the apparent distance between source and the chamber centers, 'c' is the offset error in the distance measurement and f is a proportionality constant which is independent of distance. On solving Equation (2), one may obtain the following functional form for relative distance l_i between the successive measurement points ($i = 1, 2, \dots, 6$)

$$l_i = (d_i - d_0) = f^{1/2} \left\{ \left(\frac{1}{M_{d_i}^{1/2}} \right) - \left(\frac{1}{M_{d_0}^{1/2}} \right) \right\} + \frac{M_s f^{1/2}}{2} \left\{ \left(\frac{1}{M_{d_i}^{3/2}} \right) - \left(\frac{1}{M_{d_0}^{3/2}} \right) \right\} \quad (3)$$

where M_{d_i} is the meter reading at distance d_i from the source. Equation (3) has two unknowns (f and M_s) which were determined by bi-variate linear regression analysis by adopting the least square method. After obtaining f and M_s , the value of 'c' was determined using Equation (2). Having determined the value of f, the air-kerma rate (AKR) (Gys-1) can be calculated using the formula

$$AKR = \frac{N_K f}{(d + c)^2 \Delta t} \quad (4)$$

where, N_K , is the interpolated air-kerma calibration coefficient of the chamber for HDR ^{192}Ir brachytherapy source and Δt is the time interval of the measurement. RAKR can then be determined using the following equation

$$RAKR = AKR \left(\frac{d + c}{d_{ref}} \right)^2 \quad (5)$$

where d_{ref} is the reference distance of 1 m.

Fuzzy Set theory

Zadeh introduced the fuzzy set as a class of object with a continuum of grades of membership[10-11].

In contrast to classical crisp sets, the fuzzy approach relates to a grade of membership between 0 and 1. The membership function of a fuzzy set, A is defined in the form of a triangular or trapezoidal fuzzy number as shown in Fig. 1(a-b). The details about fuzzy set may be found elsewhere[11]. An algorithm for implementing alpha cut representation of fuzzy set theory to compute the associated uncertainty is presented below

Algorithm to compute α -cut representation of distance

1. Given a fuzzy parameter, say, constant of proportionality, f (see Equation (2)) as a triangular fuzzy number: $\langle f \rangle = \langle f_{LB}, f_{\text{most likely}}, f_{UB} \rangle = \langle 1945, 1972, 1999 \rangle$, we have the α -cut representation as $[f_{\alpha}^{LB}, f_{\alpha}^{UB}] = [1950.4, 1993.6]_{\alpha=0.2}$.
2. In a similar way, α -cut representations of all other fuzzy parameters are constructed.
3. α -cut representation being an interval number, we use the interval arithmetic operation of

$$[f]^{1/2} \times \left\{ \left[\left(\frac{1}{M_{d_i}} \right) \right]^{1/2} - \left[\left(\frac{1}{M_{d_0}} \right) \right]^{1/2} \right\} \text{ as:}$$

$$[f_{\alpha}^{LB}, f_{\alpha}^{UB}]^{1/2} \times \left\{ \left[\left(\frac{1}{M_{d_i}} \right)_{\alpha}^{UB}, \left(\frac{1}{M_{d_i}} \right)_{\alpha}^{LB} \right]^{1/2} - \left[\left(\frac{1}{M_{d_0}} \right)_{\alpha}^{UB}, \left(\frac{1}{M_{d_0}} \right)_{\alpha}^{LB} \right]^{1/2} \right\}$$

$$= [f_{\alpha}^{LB}, f_{\alpha}^{UB}]^{1/2} \times \left\{ \left[\left(\frac{1}{M_{d_i}^{1/2}} \right)_{\alpha}^{UB} - \left(\frac{1}{M_{d_0}^{1/2}} \right)_{\alpha}^{LB} \right], \left[\left(\frac{1}{M_{d_i}^{1/2}} \right)_{\alpha}^{LB} - \left(\frac{1}{M_{d_0}^{1/2}} \right)_{\alpha}^{UB} \right] \right\}$$

$$4. [A, B] = [f_{\alpha}^{LB}, f_{\alpha}^{UB}]^{1/2} \times [\eta, \lambda] =$$

$$\left\{ \begin{array}{l} \min \left[\left(f_{\alpha}^{LB} \right)^{1/2} \eta, \left(f_{\alpha}^{UB} \right)^{1/2} \eta, \left(f_{\alpha}^{LB} \right)^{1/2} \lambda, \left(f_{\alpha}^{UB} \right)^{1/2} \lambda \right], \\ \max \left[\left(f_{\alpha}^{LB} \right)^{1/2} \eta, \left(f_{\alpha}^{UB} \right)^{1/2} \eta, \left(f_{\alpha}^{LB} \right)^{1/2} \lambda, \left(f_{\alpha}^{UB} \right)^{1/2} \lambda \right] \end{array} \right\}$$

$$\text{where, } \eta = \left(\frac{1}{M_{d_i}^{1/2}} \right)_{\alpha}^{UB} - \left(\frac{1}{M_{d_0}^{1/2}} \right)_{\alpha}^{LB} \quad \lambda = \left(\frac{1}{M_{d_i}^{1/2}} \right)_{\alpha}^{LB} - \left(\frac{1}{M_{d_0}^{1/2}} \right)_{\alpha}^{UB}$$

5. α -cut representation being an interval number, we use the interval arithmetic operation of

BARC NEWSLETTER

Founder's Day

$$\frac{1}{2}[(M_s)] \times [f]^{1/2} \times \left\{ \left[\frac{1}{M_{d_i}^{3/2}} \right] - \left[\frac{1}{M_{d_i}^{3/2}} \right] \right\} \text{ as:}$$

$$[C, D] = \frac{1}{2}[(M_s)_{\alpha}^{LB}, (M_s)_{\alpha}^{UB}] \times [f_{\alpha}^{LB}, f_{\alpha}^{UB}]^{1/2} \times \left\{ \left[\frac{1}{M_{d_i}^{3/2}} \right]_{\alpha}^{UB} - \left[\frac{1}{M_{d_i}^{3/2}} \right]_{\alpha}^{LB} \right\}, \left[\frac{1}{M_{d_i}^{3/2}} \right]_{\alpha}^{LB} - \left[\frac{1}{M_{d_i}^{3/2}} \right]_{\alpha}^{UB} \right\}$$

$$6. \text{ Finally, } l_i^{\alpha} = \{[A, B] + [C, D]\} = [A + C, B + D]$$

The alpha cut value of 0.5 of a fuzzy set was used to quote the bounds of the uncertainty of the imprecise or vague information applied to any physical quantity because the uncertainty bounds of the input triangular fuzzy parameters are taken as one sigma level, i.e., $f_{LB,UB} = (f^{\text{most likely}} \pm \sigma)$ according to the principle of measurement uncertainty. Hence, l_i values were chosen for 0.5 alpha cut value [10] and compared with the analytically estimated values. Here, in this case, the bounds are positive numbers and hence in case of multiplication operation of two intervals, we have applied restricted Dong, Shah and Wang (DSW) algorithm[10].

Support of a triangular fuzzy number is defined as the range of the extremes at α -cut = 0 as shown in Fig. 1(c). From Fig. 1(c), we can write the support of a fuzzy set as $S = (R-P)$, where, R and P are the two extreme bounds. In order to express the uncertainty

in the framework of fuzzy sets, we define uncertainty index[11] as the ratio of the support to the most likely value (crisp value at membership equal to 1). Again, from Fig. 1(c), uncertainty index of the given fuzzy set is written as $U = (S/Q)$, where, Q is the most likely value. Here, in this paper, we have estimated the uncertainty index for each relative distance measured experimentally.

Results and Discussion

We have estimated the uncertainty of the relative distance, $l_i [= (d_i - d_0)]$ for experimentally measured distances such as 5, 10, 15, 20, 25 and 30 cm. The membership function for one measured distance (say 10 cm) is shown in Fig. 2. It can be interpreted from Fig. 2 that the membership function of the distance (l_i) for measurement distance is turned out to be a triangular in shape because the initial consideration of the subjective based uncertain parameters are taken into consideration as "around the measured value". Since the measurement uncertainty is always quoted at one sigma level, fuzzy set theory based approach of uncertainty quantification is also quoted at an equivalent level, and here this is alpha cut value of 0.5 of the fuzzy set. Results of α -cut = 0.5 of the fuzzy distance (l_i) along with experimental and

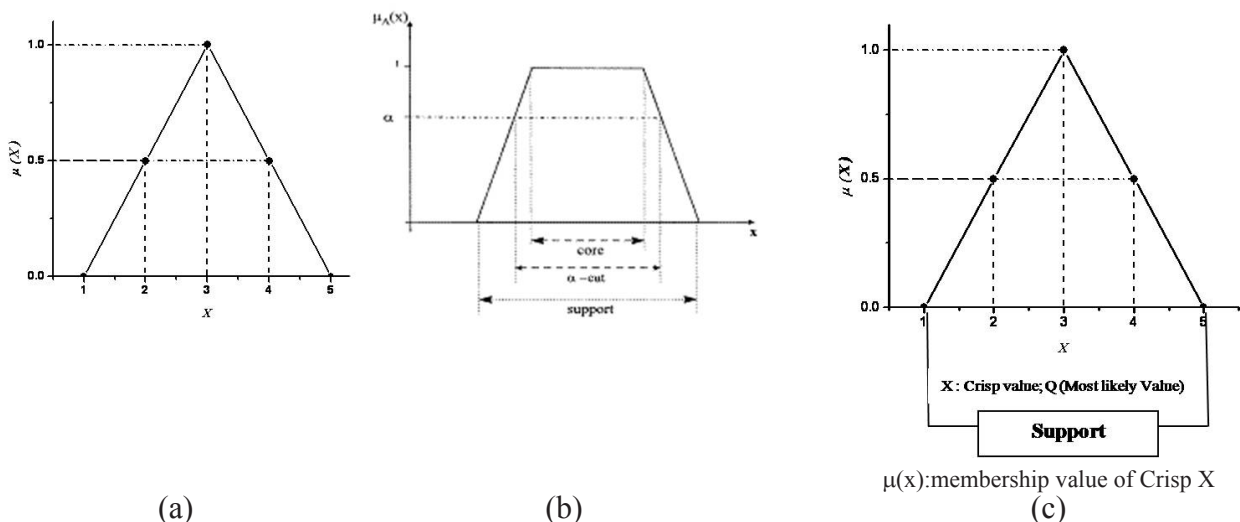


Fig.1: Pictorial representation of the membership function of a fuzzy set (a) triangular, (b) trapezoidal and (c) support of a triangular fuzzy number

BARC NEWSLETTER

Founder's Day

Table 1: Comparison of experimentally recorded, analytically calculated and fuzzy set theory computed values of $l_i [= (d_i - d_0)]$

Experimental	Analytical	Fuzzy set theory	
		$(l_i)^L$	$(l_i)^U$
5	4.999	4.968	5.031
10	9.961	9.907	9.961
15	15.009	14.931	15.091
20	20.041	19.934	20.152
25	24.977	24.840	25.119
30	30.001	29.829	30.180

analytical values of (l_i) are presented in Table 1 and it can be seen that analytical value as well as the experimentally measured relative distance lie within the bounds of the subjective uncertainty of the l_i . Support of each membership values corresponding to each experimental distance and the associated uncertainty index are further shown in Table 2. It can be seen from Table 2 that the uncertainty indices remain invariant for all the experimentally measured distances indicating that each and every triangular fuzzy membership function is normalized and convex. Maximum value of the uncertainty index is found to be within 2.5% which further indicates that the possibility of error in measuring such distance may be of this order.

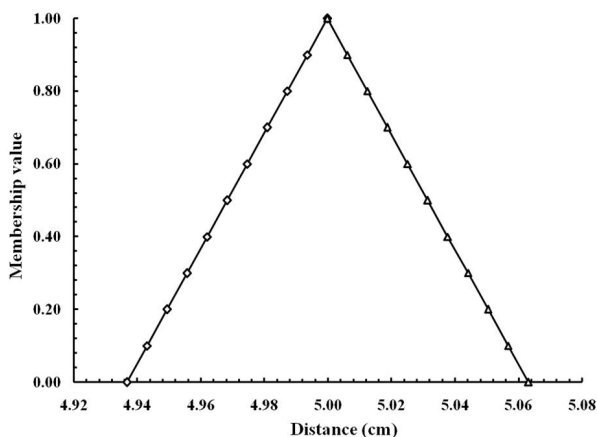


Fig.2: Membership function of relative distance of $l_i [= (d_i - d_0)]$ for 5 cm (\diamond : lower bound, Δ : upper bound), Distance (cm): l_i , Membership value: $\mu(l_i)$

Table 2: Support and uncertainty index of relative distance l_i

Experimental	Support	Uncertainty Index
5	0.126	0.025
10	0.218	0.022
15	0.321	0.021
20	0.435	0.022
25	0.559	0.022
30	0.702	0.023

Conclusions

Uncertainty of the positioning error, the so called "distance error", of the ionization chamber with respect to the source was evaluated. Fuzzy set theory was applied for this evaluation due to the subjectivity involved in the experimental facility. Uncertainty in the possible input parameters was addressed as triangular fuzzy number. Propagation of uncertainty of the input parameters is carried out on the basis of the model described in this work (see sub-section: algorithm to compute α -cut distance representation of distance) via the alpha cut of a fuzzy set. The crisp values of l_i estimated using analytical method lie within the bounds computed using fuzzy set theory. This indicates that l_i values estimated using analytical methods are within 2.5% uncertainty. This value of uncertainty in distance measurement should be incorporated in the uncertainty budget while estimating the expanded uncertainty in HDR ^{192}Ir source strength measurement.

References

1. Nath R, Anderson LL, Meli JA, Olch AJ, Stitt JA, Williamson JF. Code of practice for brachytherapy physics: Report of the AAPM Radiation Therapy Committee Task Group No. 56. *Med Phys*, 24(1997): 1557–1598.
2. Kubo HD, Glasgow GP, Pethel TD, Thomadsen BR, Williamson JF. High dose rate brachytherapy treatment delivery: Report of the AAPM Radiation Therapy Committee Task Group No. 59. *Med Phys*, 25(1998): 375 – 403.

BARC NEWSLETTER

Founder's Day

3. Marechal MH, de Almeida CE, Ferreira IH, Sibata CH. Experimental derivation of wall correction factors for ionization chambers used in high dose rate ^{192}Ir source calibration. *Med Phys*, 29(2002): 1-5.
4. International Atomic Energy Agency (IAEA). Calibration of photon and beta ray sources used in Brachytherapy, TECDOC 1274, IAEA, Vienna; 2002.
5. Goetsch S.J., Attix FH, Pearson D.W., Thomadsen BR. Calibration of ^{192}Ir high dose rate afterloading system. *Med Phys*, 18(1991): 462 – 467.
6. Goetsch S.J., Attix F.H., DeWerd L.A., Thomadsen BR. A new re-entrant ionization chamber for the calibration of Iridium-192 high dose rate sources. *Int J Radiation Oncology Bio Phys*, 24(1992): 167-170.
7. Kondo V.S., Randolph ML. Effect of finite size of ionization chambers on measurement of small photon sources. *Radiat Res*, 13(1960): 37-60.
8. Kumar S., Srinivasan P., Sharma S.D., Mayya Y.S. A simplified analytical approach to estimate the parameters required for strength determination of HDR ^{192}Ir brachytherapy sources using Farmer-type ionization chamber. *Appl Radiat Isot*, 70(2012): 282-289.
9. Kumar S., Srinivasan P., Sharma S.D., Subbaiah K.V., Mayya Y.S. Evaluation of scatter contribution and distance error by iterative methods for strength determination of HDR ^{192}Ir brachytherapy source. *Med Dosim*, 35(2010): 230-237.
10. Klir GJ, Yuan B. Fuzzy Sets and Fuzzy Logic: Theory and Applications, Prentice-Hall, Upper Saddle River, New Jersey; 1994.
11. Dubois D., Prade H. Fuzzy sets and systems: Theory and applications, Academic Press, New York; 1980.

HYDROGEN ISOTOPE STORAGE BEHAVIOR OF $ZrCo_{1-x}Ni_x$ ALLOYS

Ram Avtar Jat, S.C. Parida, Renu Agarwal and A.R. Joshi

Product Development Division

and

K.L. Ramakumar

Radiochemistry and Isotope Group

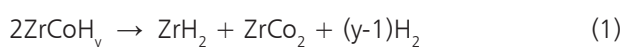
This Paper received the Best Oral Presentation Award at the 19th DAE-BRNS Symposium on Thermal Analysis, held at Mumbai from Dec. 19-21, 2013

Abstract

The $ZrCo_{1-x}Ni_x-D_2$ systems were investigated in this study by generating the deuterium desorption pressure-composition isotherms (PCIs) in the temperature range of 524-603 K using Sievert's type volumetric apparatus. A van't Hoff plot was constructed using plateau pressure data of each PCI and the thermodynamic parameters like enthalpy and entropy change for desorption of deuterium in the $ZrCo_{1-x}Ni_x-D_2$ systems were calculated. A comparison of data obtained in this study with the hydrogen PCIs data reported in an earlier study revealed that these alloys show normal hydrogen isotope effect where the equilibrium pressure of D_2 is higher than that of H_2 at all experimental temperatures.

Introduction

ZrCo is being considered as a suitable candidate material for storage, supply and recovery of hydrogen isotopes in International Thermonuclear Experimental Reactor (ITER) Storage and Delivery System (SDS) as it is non-radioactive and non-pyrophoric at room temperature and has similar tritium storage properties as uranium [1]. Beside its higher storage capacity (H/f.u. up to 3, f.u. = ZrCo), it has been reported [2] that upon repeated hydriding-dehydriding cycles, the hydrogen storage capacity of ZrCo decreases, which is attributed to the following disproportionation reaction:



This results in reduction of hydrogen storage capacity of ZrCo, which is not desirable for its use in ITER SDS. Several attempts have been made to improve the

durability against disproportionation of ZrCo by ternary alloying without substantially altering the storage behaviour. A very limited study is reported in literature on the effect of ternary alloying on hydrogen storage behavior of ZrCo based alloys [3, 4]. In an earlier study, Jat et al. [3] have thoroughly investigated the effect of Ni content on the hydrogen storage behaviour of $ZrCo_{1-x}Ni_x$ alloys and found out that Ni substitution improves the durability against disproportionation. The present study is aimed to investigate the hydrogen isotope effect on the storage behaviour of $ZrCo_{1-x}Ni_x$ alloys which will enable to predict the tritium partial pressure for these alloys.

Experimental

Alloys of compositions $ZrCo_{1-x}Ni_x$ ($x = 0.0, 0.1$ and 0.2) were prepared by arc-melting method and characterised by XRD, SEM and EDS. The details of alloys

BARC NEWSLETTER

Founder's Day

preparation and their characterization are reported in our earlier study [3]. For the preparation of the $ZrCo_{1-x}Ni_x$ deuterides, the alloy sample was initially activated by hydriding-dehydriding method described in an earlier publication [3]. The activated alloy was loaded in the reaction vessel kept at room temperature and allowed to react with a known amount of deuterium gas to form the deuteride phase. The formation of the deuteride phase was confirmed by X-ray powder diffraction method.

The pressure-composition-temperature (PCT) measurements were carried out using a conventional Sievert's type volumetric apparatus (PCT Pro-2000, SETARAM Instrumentation, France). A known amount of the activated sample was loaded in to the reaction vessel of known volume of the Sievert's apparatus and the deuteride phase was prepared as described in earlier section. This deuteride phase was heated to the desired experimental temperature under a known overpressure of deuterium in the system to generate desorption pressure-composition isotherm (PCI). Desorption equilibrium was established by evacuating

a known amount of deuterium from the reservoir and allowing the system to re-attain equilibrium. This allows to simultaneously calculate the value of deuterium concentration ($= D/f.u.$, $f.u. = ZrCo_{1-x}Ni_x$) and the corresponding equilibrium deuterium desorption pressure at the experimental temperature. Thereafter, the value of $D/f.u.$ was altered by aliquoting a known amount of deuterium from the reservoir and allowing the attainment of a new equilibrium. This process was repeated till the entire isotherm was generated. Following this procedure, PCIs for $ZrCo_{1-x}Ni_x-D_2$ systems were generated in the temperature range of 524-603 K with a step of 20 K.

Results and Discussion

The formation of $ZrCo_{1-x}Ni_x$ alloys and their deuterides are confirmed by comparing their XRD patterns with the JCPDS (Joint Committee on Powder Diffraction Standards) files. The deuterium desorption pressure-composition isotherms for $ZrCo_{1-x}Ni_x - D_2$ systems are shown in Fig.1 which can be attributed to the following de-deuteration reaction;

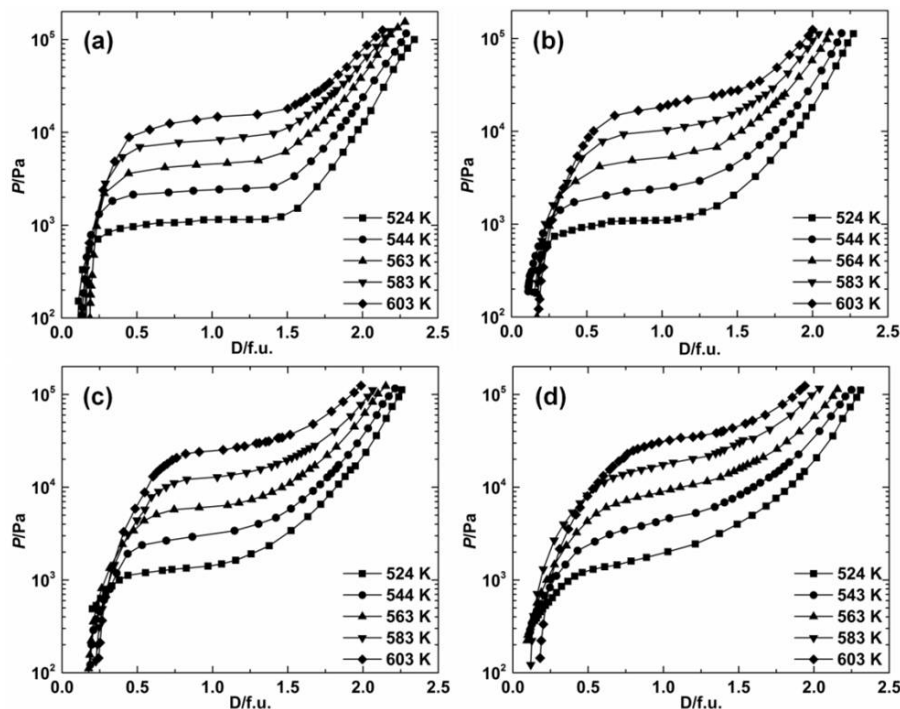
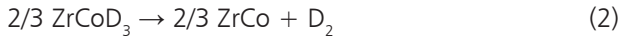


Fig.1: Deuterium desorption pressure-composition isotherms for $ZrCo_{1-x}Ni_x-D_2$ systems: (a) $x = 0$, (b) $x = 0.1$ (c) $x = 0.2$ and (d) $x = 0.3$.

BARC NEWSLETTER

Founder's Day



It is evident from all the isotherms shown in Fig.1 that in the temperature range of investigation, a single desorption plateau is observed and the plateau width found to decrease with increase in temperature. The temperature dependence of the equilibrium plateau pressure for $\text{ZrCo}_{1-x}\text{Ni}_x\text{-D}_2$ systems is best represented by the van't Hoff plot, shown in Fig.2.

From the van't Hoff plot the enthalpy and entropy change for the de-deuteration of $\text{ZrCo}_{1-x}\text{Ni}_x$ deuterides are deduced at the average experimental temperature of 563 K and listed in Table 1. It is evident from the data reported in Table 1 that the Ni-substitution substantially changes the enthalpy and entropy of de-deuteration reaction compared to ZrCo-D_2 system.

It can be seen from Fig.2 that the deuterium desorption plateau pressure increases with increasing

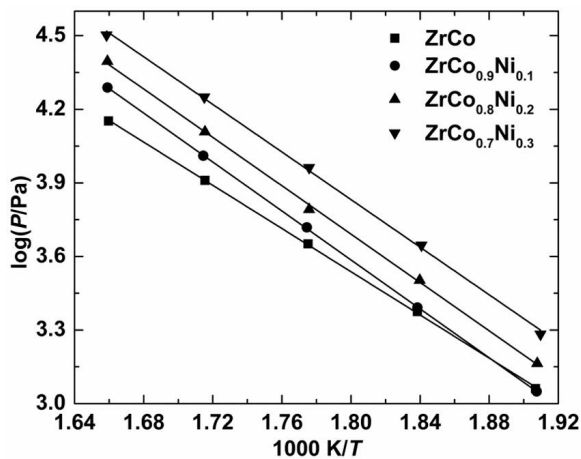


Fig.2: van't Hoff plots for $\text{ZrCo}_{1-x}\text{Ni}_x\text{-D}_2$ systems

the Ni-content in the $\text{ZrCo}_{1-x}\text{Ni}_x\text{-D}_2$ system. However, for the composition with $x = 0.1$, the desorption plateau pressure is lower than that of ZrCo-D_2 system below 530 K. Similar behavior of the crossover of van't Hoff plots is also observed in our previous study [3] for ZrCo-H_2 and $\text{ZrCo}_{0.9}\text{Ni}_{0.1}\text{-H}_2$ systems. For the practical application of these metal-hydrogen systems in ITER SDS, it is essential to know the desorption temperature for release of 100 kPa of hydrogen. From the van't Hoff relations, the desorption temperature (T_{des}) for the $\text{ZrCo}_{1-x}\text{Ni}_x\text{-D}_2$ systems are calculated and listed in Table 1. The variation of T_{des} with Ni-content is also shown in Fig.3. It is evident from this figure that the T_{des} decreases with increase in Ni-content which suggest that Ni-substituted ZrCo alloys are favorable for use in ITER SDS.

A comparison of thermodynamic parameters for $\text{ZrCo}_{1-x}\text{Ni}_x\text{-D}_2$ systems with those reported previously

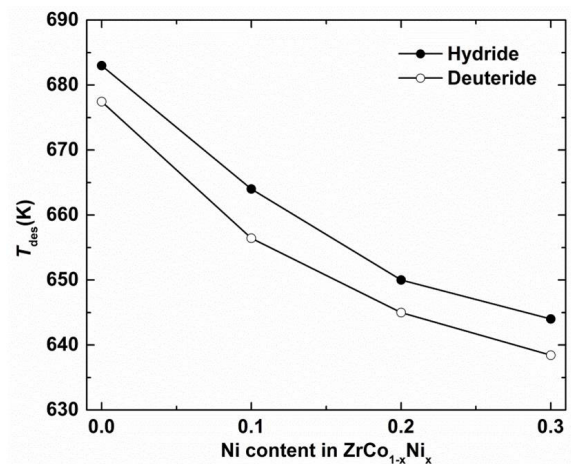


Fig.3: Variation of T_{des} (for supply of 100 kPa of hydrogen/deuterium) with Ni content in $\text{ZrCo}_{1-x}\text{Ni}_x$ alloys

Table 1: Thermodynamic functions for desorption of hydrogen/deuterium in $\text{ZrCo}_{1-x}\text{Ni}_x\text{-H}_2/\text{D}_2$ systems.

System		ZrCo	$\text{ZrCo}_{0.9}\text{Ni}_{0.1}$	$\text{ZrCo}_{0.8}\text{Ni}_{0.2}$	$\text{ZrCo}_{0.7}\text{Ni}_{0.3}$	Ref.
$\Delta_r H$ (kJ/mole H ₂)	Hydride	84 ± 3.9	95 ± 0.9	93 ± 3.3	93 ± 2.3	[3]
	Deuteride	84 ± 0.6	95 ± 0.4	94 ± 1.3	93 ± 1.6	This study
$\Delta_r S$ (J/(mole H ₂ ·K))	Hydride	122 ± 3.9	144 ± 0.8	144 ± 3.4	144 ± 2.5	[3]
	Deuteride	124 ± 1.1	145 ± 1.2	145 ± 1.2	145 ± 2.3	This study
T_{des} (K)	Hydride	683	664	650	644	[3]
	Deuteride	677	656	645	638	This study

BARC NEWSLETTER

Founder's Day

[3] for $\text{ZrCo}_{1-x}\text{Ni}_x\text{-H}_2$ systems is also made in Table 1. It can be deduced from Table 1 that the equilibrium plateau pressure for $\text{ZrCo}_{1-x}\text{Ni}_x\text{-D}_2$ systems is higher than that of $\text{ZrCo}_{1-x}\text{Ni}_x\text{-H}_2$ systems which is expected based on normal hydrogen isotope effect [4]. The hydrogen isotope effect on the equilibrium pressure of hydrogen arises from the interplay of two thermodynamic factors namely, entropy and enthalpy that control the relative stabilities of the corresponding isotopic hydrides. It is evident from Table 1 that there is no substantial isotopic effect on the enthalpy of dehydrogenation/de-deuteration for $\text{ZrCo}_{1-x}\text{Ni}_x\text{-H}_2/\text{D}_2$ systems. Hence, the difference in equilibrium plateau pressure arises due to the difference in entropy of reaction. Based on this observation, it is expected that the equilibrium pressure of tritium will be higher than that of deuterium and hydrogen for $\text{ZrCo}_{1-x}\text{Ni}_x$ alloys.

Conclusion

Hydrogen isotope effect on the storage behavior of $\text{ZrCo}_{1-x}\text{Ni}_x$ alloys is investigated by generating the deuterium desorption pressure-composition isotherms (PCIs) in the temperature range of 524-603 K and comparing the data with the hydrogen PCIs reported

in an earlier study. A single desorption plateau is observed for all the PCIs. Thermodynamic parameters and desorption temperature for release of 100 kPa of deuterium are calculated and compared with the literature values. The T_{des} found to systematically decrease with increase in Ni content. Normal hydrogen isotope effect is observed for all $\text{ZrCo}_{1-x}\text{Ni}_x$ alloys which shows that equilibrium pressure of deuterium is higher than that of hydrogen at all experimental temperatures.

References

1. R.-D. Penzhorn, M. Devillers and M. Sirch, *J. Nucl. Mater.* 170 (1990) 217.
2. M. Devillers, M. Sirch, S. Brendendiek-Kemper and R.-D. Penzhorn, *Chem. Mater.* 2 (1990) 255.
3. R.A. Jat, S.C. Parida, R. Agarwal, S.G. Kulkarni, *Int. J. Hydrogen Energy* 38 (2013) 1490.
4. T. Gongli, L. Xiaopeng, J. Lijun, W. Shumao, L. Zhinian, L. Hualing, *Trans. Nonferrous Met. Soc. China* 17 (2007) s949.
5. B.M. Andreev, E.P. Magomedbekov, G.H. Sicking, *Interaction of Hydrogen Isotopes with Transition Metals and Intermetallic Compounds*, Springer-Verlag, New York, (1996).

BARC NEWSLETTER

Founder's Day

OCCUPATIONAL SAFETY AND HEALTH ISSUES FOR CONSTRUCTION PROJECTS-SUPPLY CHAIN IN BARC

Praveen Dubey, S.D. Bharambe and S. Soundararajan

Industrial Hygiene & Safety Section, HS&E Group

and

Kaushik Kayal

Civil Engineering Division, Engineering Services Group

This Paper received the Best Paper Presentation Award at the International Conference on Managing Supply Chain for Global Competitiveness, held at the Indian Institute for Industrial Engineering, Nagpur, Oct. 25-27, 2013

Abstract

Most of the construction projects are handled by the principal contractor under umbrella package contract and executed through sub-contracting system. Challenge in terms of effective coordination and communication and accountability among participants, inhibits innovation as firms holding umbrella contract is often evaluated based on their specialized fields, and involves a large number of workforces from sub-contractors who are exposed to various hazards of construction sites.

Approaches such as Total Loss Control (TLC), Total Quality Management (TQM), and Supply Chain Management (SCM), which are typically associated with manufacturing industries, are required to be introduced into the construction industry.

The construction of new facilities and maintenance of existing facilities is being carried out in BARC through public tender. These works are mostly carried out by contractors through the labourers, who are from varied background. BARC recognizes the responsibility of ensuring safety of these workers at site. Dynamic nature of works at construction sites invites attention on the adoption of standard procedures and continual supervision during execution. This paper reflects the principle of management of health and safety issues for construction projects in BARC through various engineering practices and safety management techniques.

Introduction

The construction sector in the country employs approximately 32 million people, accounts for about 1/10th of GDP and is the largest employment sector after agriculture. The construction industry in general has an annual growth rate of about 10%, primarily due to the increased domestic and international manufacturing activities and industrial growth.

In the years ahead, the construction industry in India has a number of challenges with respect to issues

related to protection of environment, transportation, power requirements, natural hazards and occupational safety and health of the work force which are required to be overcome to meet the demands of the industry and public.

Occupational Safety and Health Aspects in Construction Activities

Construction activities include building of new structures, renovation/modification of existing structures, demolition, etc. Normally, large number

BARC NEWSLETTER

Founder's Day

of workforces are engaged at construction projects through contractors and sub-contractors. A major portion of construction workers is unskilled while a few of the workers are skilled in trades. Throughout the world, over 90% of construction workers are men while in India- the proportion of women is higher and they tend to be concentrated in unskilled occupations ^[1].

Construction works are always associated with occupational risks related to excavation work (use of explosives, earthmoving machines, exposure to chemicals, excavated & deep pits, earth sliding/subsidence); working at heights (use of scaffolding, gangways and ladders; work on fragile roofs, openings); handling of materials (use of cranes, hoists, escalators), and so on, which are specific to the sector. The working conditions at the construction site being dynamic in nature, a systematic approach to manage the occupational safety and health at workplaces is essential.

Safety Management at Construction Site

The work activities in the construction industry are of diversified nature in addition to the problems of employment of unskilled labour. This creates a challenging task for the safety professional to foresee the management of variety of hazards.

The occurrences of unsafe incidents have direct impact on time, cost and legal aspects of supply chain management and therefore it is imperative to ensure that work packages are framed in such a manner and awarded to such contractor, who along with their subcontractors & suppliers, are capable of executing the work in efficient and accident-free manner. Principles of Approaches such as Total Loss Control (TLC), Total Quality Management (TQM), and Supply Chain Management (SCM), which are typically associated with manufacturing industries, have been introduced for application into the construction industry.

Total Loss Control

Total Loss Control (TLC) is a systematic approach to the management of loss, integrating reliability and quality with the reduction of risk to people, the environment, assets and to production. Applications of TLC in construction activity are a growing field that has incorporated tools such as production scheduling, Kaizen, "huddle meetings", 5S Principles (Sort, Set, Shine, Standardize and Sustain) and visualization to improve all facets of the construction process including safety. Use of visualization techniques includes mobile signs to attract attention to important information, daily huddle meetings address safety issues among other things, use of 5S ensures materials supply and 7 E Principles (Engineering revision, Evaluation, Enforcement, Education, Example setting, Enthusiasm and Employment Practices) ensures workplace safety.

Total Quality Management (TQM)

TQM is a comprehensive management system which (i) Focuses on meeting owners'/customers' needs by providing quality services at a cost that provides value to the owners/customers (ii) Driven by the quest for continuous improvement in all operations (iii) Views an organization as an internal system with a common aim rather than as individual departments acting to maximize their own performances (iv) Focuses on the way tasks are accomplished rather than simply what tasks are accomplished and (v) Emphasizes teamwork and a high level of participation by all employees. Total Quality Management (TQM) advocates continuous improvement focused on meeting both internal and external customer needs.

Supply Chain management (SCM)

SCM is a network of different organizations, linked upstream and downstream forming a chain, aiming to achieve objectives of delivering quality product in time and value addition in the services and products for the end consumers through integrated processes and

BARC NEWSLETTER

Founder's Day

activities. In the context of construction activity, supply chain refers to the end to end "chain" of stakeholders and partners that come together both on individual projects and particularly during the construction phase.

Most of the projects are handled by the principal contractor under umbrella package contract and executed through sub-contracting system. The problems of multi-layered subcontracting practice have long been an issue and a controversial subject in the industry. Recently researchers have suggested having legislation for restricting the subcontracting practice in the construction industry for better safety performance^[3]. Although such restrictions may help in improving the safety performance, it would be extremely difficult to implement such restriction in the workplace due to the traditional work practices.

Construction Safety Management Programme In BARC

BARC is committed to ensure the highest standard of occupational health, safety and environment in all construction activities undertaken in order to achieve zero-accident working period in all projects and thereby contributing towards enhancement of the safety performance of the centre^[4]. The principles of TLC, TQM and SCM are applied during the execution of construction activities thereby site management gets streamlined.

Construction Safety Management Objectives

Management intends to execute the construction project without any interruptions either related to supply of materials, equipment, workforce or may be due to undesired events/incidents. To meet this objective the projects are evaluated phase wise which begins with the design, planning, procurement, contracting, workplace monitoring, etc. The process of finalization of design after detailed safety review by

experts follows the contract evaluation phase where the records of the bidding contractors with respect to safety management are also reviewed at par with the other executing parameters. The selected contractor needs to meet the requirements of the Construction Safety Manual for Works Contract^[4] which also forms a part of contract agreement.

Work Planning

Construction activities are mainly divided in four stages viz. Substructure works, RCC and Structural works in Superstructures, Masonry and Waterproofing works and Finishing works. These activities with severe potential hazards require a thorough planning for safe execution at site. Keeping in view of probability of occurrence of accidents/injuries contributing to substantial absence of persons from work and even leading to fatalities, the Job Hazard Analysis (JHA) is carried out prior to beginning of project which helps in integrating accepted safety and health principles and practices into a particular operation.

Selection of Execution Team

Departmental as well as Contracting engineers are responsible for the execution of the construction activities as per planned schedule. Ensuring execution of work within the timeframe in a safe manner are the responsibilities of the execution team. This team is supported by Safety Officers/Stewards, Services staff, Stores staff, Paramedical staff, Welfare Officer.

A site level safety organization is formed prior to execution of work at site as per the provisions of BOCW Central Rules, 1996 who regularly meet to discuss the safety issues at site and to improve the safety performance of the project.

Hazard Communication Mechanism

Safety Induction Training: Each new worker attends initial safety induction training before reporting at

BARC NEWSLETTER

Founder's Day

respective place of work. This training is followed by daily training e.g. use of various Personal Protective Equipments (PPEs) and tools, housekeeping, hot job, RCC works, electrical works, etc. The workers are also enlightened with the security requirements to be observed inside BARC premises.

Walk-through survey: Members of the safety team carry out a walk through survey every morning at site in order to monitor any unsafe conditions and unsafe acts. The safety related deficiencies are reported immediately for corrective actions and followed up for preventing recurrences.

Signboards, Posters, Displays: Signboards (written/painted in photo-luminescent paint) are displayed at various workplaces, movement area of mechanical equipment, diesel store, scaffoldings, first aid post, etc.

Structured Plan for Execution and Ensuring Safe workplaces

System Implementation – Work Permit System: Aim of work permit system is to identify the unsafe conditions in advance and to take corrective action prior to commencement of work. Work permit system is generated by the concerned site engineer, in quadruplicate. Later, Work Permit is sent to the site safety officer for obtaining the clearance before the work starts. Site Safety Officer then visits the area of work and if working condition is found to be safe and satisfactory, then he clears the work permit for the said work. Copy of work permit is available with engineer, site supervisor, safety officer and departmental representative. The closure of the proposed work, status of incomplete activities, etc. are registered separately.

System Implementation – Height Pass System: Aim of the height pass system is to reduce the probability

of fall accidents by engaging medically fit people. All new workers, who may work at height, are first sent for a medical check-up, done by a medical practitioner. Those workers who are declared to be medically fit are issued height passes by Safety Officer / Site Medical Attendant after undergoing practical test. The fit workers are instructed to carry their height passes all the time.

System Implementation – Scaffolding System: Erection of safe working scaffolding is an important part in the construction activity. A standard checklist [4] is prepared by the site engineer after erection of the scaffolding and submitted to the Safety Officer. Safety Officer visits the site and gives clearance for the scaffolding / issues the observations for rectification.

Conclusion

In this paper we have discussed how BARC is committed to ensure the highest standard of OHS in all construction activities undertaken in order to achieve zero-accident working period in all projects. In nutshell following points must be incorporated during construction activities.

- Establishment of clear rules and procedures.
- Significant emphasis on safety during the contract bid and award process
- Establishing a clear understanding of the work process and responsibilities from conceptual design to acceptance of completed work
- Assure that job related hazards have been identified and controlled and are communicated to workers in effective manner
- Vigilance through frequent site visits with a focus on safety helps in prevention of interruptions and thereby maintaining supply chain.
- Continuous training and awareness building process.

BARC NEWSLETTER

Founder's Day

Acknowledgement

The authors sincerely acknowledge their deep sense of gratitude to Dr. D.N. Sharma, Director, H S& E Group for his constant encouragement and support throughout this study.

References

1. Occupational safety and health in the construction work, A. López-Valcárcel, *African Newsletter*, Volume 11, number 1
2. Proverbs, D.G and Holt, G.D (2000), Reducing construction costs; European best practice supply chain implications, *European Journal of Purchasing and supply management*, Vol. 6, pp. 149- 158
3. Linehan, A.J, 2000, Subcontracting in the construction industry. A speech presented in Safety and Health Conference, Hong Kong
4. Kaushik Kayal, B. Srinivas, G.L.N. Padmavathi and Praveen Dubey, "Construction Safety Manual for Works Contract", BARC/2011/E/006 (Available on www.barc.gov.in, manual forms part of requirement for tender document)

PRE-TEST ANALYSIS OF MOLTEN SALT NATURAL CIRCULATION LOOP USING FLiNaK SALT

A.K. Srivastava, A. Borgohain, N.K. Maheshwari and P.K. Vijayan
Reactor Engineering Division

This Paper received the Best Poster Presentation Award at the [International Conference on Molten Salts In Nuclear Technology] held at Mumbai, from Jan. 9-11, 2013

Abstract

Molten Salt Natural Circulation Loop (MSNCL) has been setup in BARC. It is a rectangular loop comprising of five components- heater, cooler, melt tank, expansion tank and loop piping. A steady state and transient analysis for the MSNCL has been performed using a one dimensional finite difference code, LBENC. Molten fluoride salt, eutectic mixture of lithium, sodium and potassium fluoride (FLiNaK) has been used as heat transfer medium for the analysis. Various transients such as startup of natural circulation, loss of heat sink, heater trip and step power increase have been analyzed for different orientation of heater and cooler.

Introduction

Present water cooled nuclear reactors have a limitation of temperature not going beyond 325°C. Increasing the system temperature increases the plant efficiency. Going beyond a certain temperature in case of water, need its pressurization which causes safety concern. Keeping in mind the cost and safety issues, researchers have a challenge to develop coolants for nuclear reactors which can be operated at higher temperature and low pressure. Molten fluoride salt mixtures have been considered as heat transfer media for core heat removal in advanced nuclear reactors as they have high boiling points. This allows reactors to be operated at high temperature and nearly atmospheric pressure. The high temperature heat is proposed to be used for generating hydrogen by thermo-chemical splitting of water.

Studies of natural circulation with water are abundant in literature. Both experimental and theoretical studies on the nature of unstable flow were performed by Vijayan et. al. [1]. There are some numerical studies

for stability and other transient analysis of single-phase natural circulation loops [2-5]. Furthermore, the RELAP5, CATHARE2, and ATHLET system codes have been used in transient analysis for single-phase natural circulation loops [6-8].

The study of natural circulation in molten salt is still quite limited. Although a few analytical works exist for the thermal-hydraulics of molten salt cooled reactors [9], little experimental data have been published to demonstrate the thermal-hydraulic performance of molten salt-cooled systems.

The paper deals with the analysis performed for steady state and transient behavior of MSNCL, installed in BARC using FLiNaK salt mixture.

Natural Circulation Loop Detail

Molten salt loop is a 15NB uniform diameter rectangular natural circulation loop as shown in Fig. 1(a) and Fig. 1(b). It comprises basically four components- heater, cooler, melt tank and expansion tank. The height and

BARC NEWSLETTER

Founder's Day

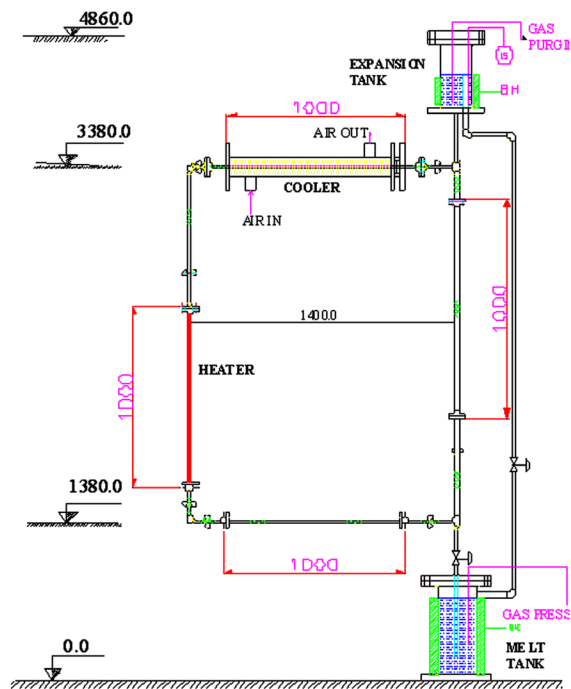


Fig. 1(a): Schematic of Molten Salt Natural Circulation Loop (MSNCL)

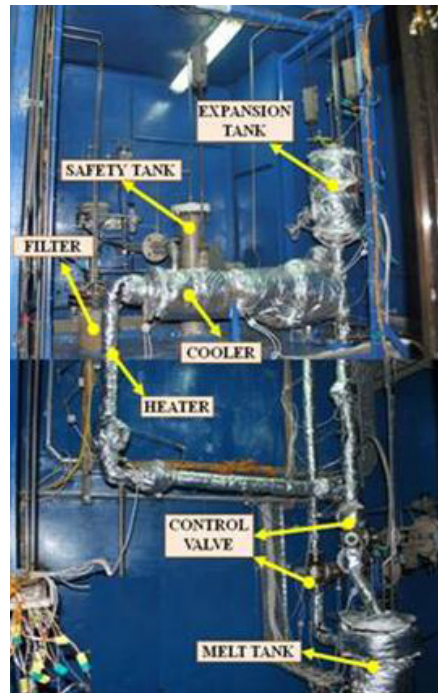


Fig. 1(b). Photograph of Molten Salt Natural Circulation Loop (MSNCL)

total length of the loop are 2000 mm and 6800 mm respectively. The loop is designed in such a way that the orientation of heater and cooler can be changed to study its effect on natural circulation flow rate. Air is used as secondary side coolant.

Analysis for Molten Salt Natural Circulation Loop (MSNCL)

This analysis has been performed using one dimensional finite difference code LBENC [10]. The code is validated with water and liquid metal [11]. This study is performed for FLiNaK salt (eutectic mixture of LiF-NaF-KF), proposed as a candidate coolant for HTRs. For the sake of analysis, the loop geometries are divided into segments. Each segment is then divided into nodes. The number of nodes was taken as 20 for each segment of the loop. Pressure drop due to sudden expansion, contraction, bends etc. associated with each segment was accounted using suitable loss coefficient. Temperature dependent thermo-physical properties [12] are considered for the analysis. The

transients performed with the help of LBENC code include the loss of heat sink, heater trip and start-up of natural circulation. Analysis is performed for all four different orientations of heater and cooler i.e. Horizontal Heater & Horizontal Cooler (HHHC), Horizontal Heater & Vertical Cooler (HHVC), Vertical Heater & Horizontal Cooler (VHHC) and Vertical Heater and Vertical Cooler (VHVC). Prior to each transient analysis, steady-state conditions are usually established in the loop, which are the initial conditions of the subsequent transient analyses.

Steady state mass flow rate

Steady state mass flow rate is calculated for different heater power. Initially the fluid is in stagnant condition, heater power is zero and temperature of salt and the loop is 500°C. Heater power is then increased to 1000W in steps of 200W. Fig. 2 shows the calculated steady state mass flow rate at different power for all the four orientations. On applying the power at every step, the mass flow rate gives a steady

BARC NEWSLETTER

Founder's Day

state value. The power step is allowed to change after every 10000s. It is observed that the predicted steady state flow rate is highest in HHHC orientation and lowest in VHVC orientation at each power step. This is because the effective elevation difference between the hot and the cold leg, which is the driving force for natural circulation, is highest (2000 mm) in HHHC orientation and lowest (500 mm) in VHVC orientation. The effective elevation difference for HHVC and VHHC orientations are 1300 mm and 1200 mm respectively.

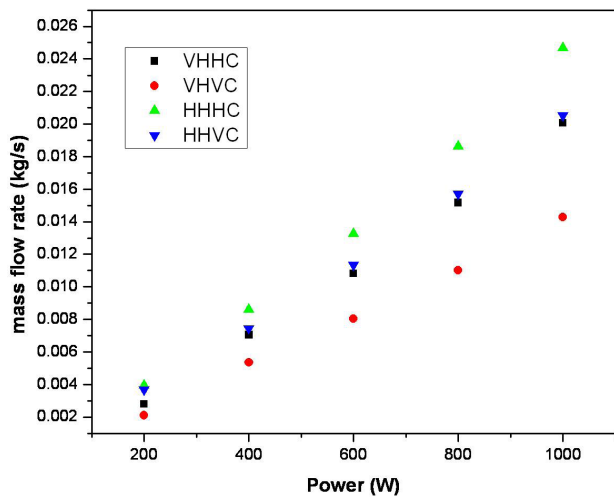


Fig. 2: Steady state mass flow rate vs. power in MSNCL

Start-up of natural circulation

Initially the fluid is in stagnant condition, heater power is zero and temperature of salt and the loop is 500 °C. Full power of 1000W is then applied to the heater in a single step at 0s. Fig. 3(a) shows the mass flow rate transient in start-up condition for all the four orientations. As the salt gets heated up, the mass flow rate starts increasing in the loop. At initial stage, the salt flow rate is low due to its inertia. Sudden application of full power causes a peak in mass flow rate which comes almost to steady state after 10000s. It can also be seen from Fig. 3(b) that after 10000s the temperature at inlet/outlet of heater and cooler reaches a constant value for VHHC orientation.

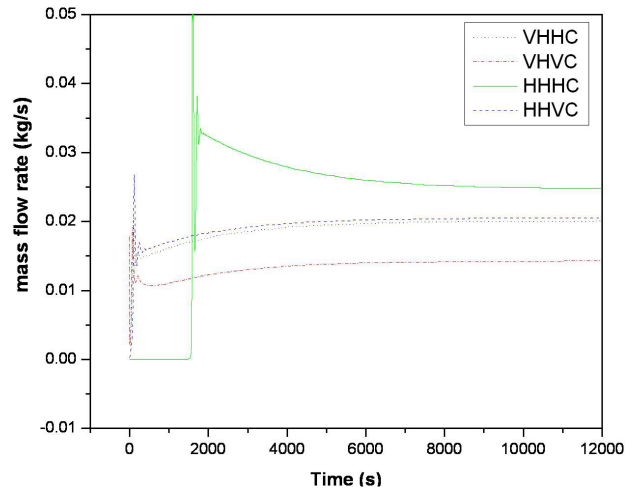


Fig. 3(a): Variation of mass flow rate during start-up of natural circulation from stagnant condition

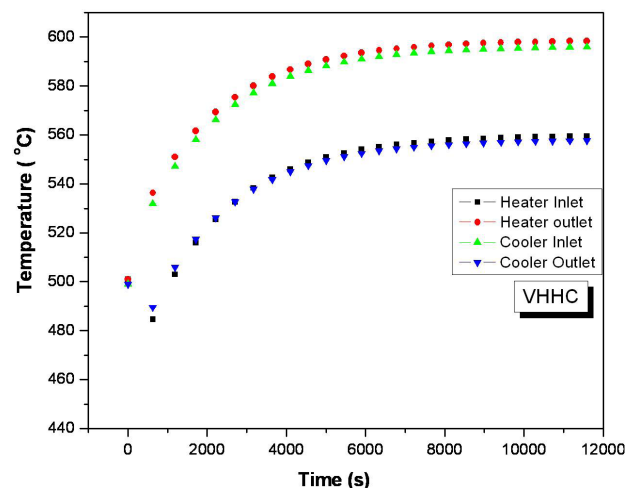


Fig. 3(b): Heater and Cooler Inlet/Outlet Temperature Variation for VHHC orientation

Loss of Heat Sink

This analysis is carried out at 1000W power. Initially the system is allowed to come in steady state at 1000W heater power and then secondary side heat transfer coefficient is set to 5W/(m²-K) at 10000s, a non-zero small value to account heat loss from cooler. Fig. 4(a) shows the transient mass flow rate variation for loss of heat sink case for all the four orientations. Due to unavailability of the cooler, the average temperature of the molten salt starts increasing. It can be seen from Fig. 4(a), after 10000s the mass flow rate suddenly decreases. This decrement in mass flow rate continues

BARC NEWSLETTER

Founder's Day

and goes towards zero as expected. This is because after loss of heat sink the temperature difference between hot leg and cold leg decreases and hence the driving force. Figure 4(b), temperature transient, shows the sudden temperature rise in the molten salt after loss of heat sink for VHHC orientation. After $t=10000s$, the temperature difference between the heater and cooler decreases. The temperature of the loop suddenly increases and reaches to $1000^{\circ}C$ in just 2000s.

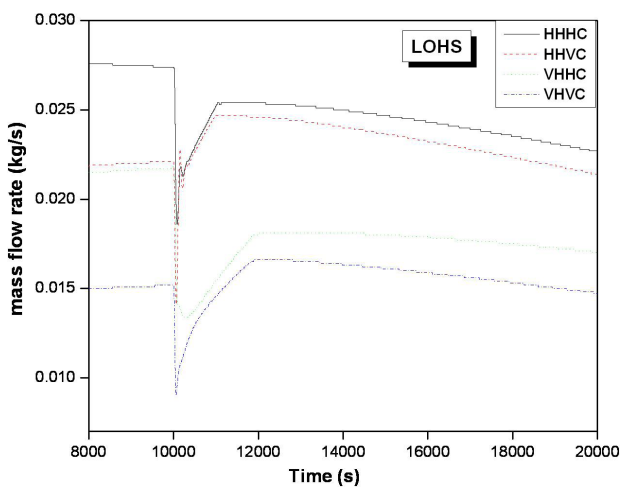


Fig. 4(a): Variation of mass flow rate during simulated loss of heat sink

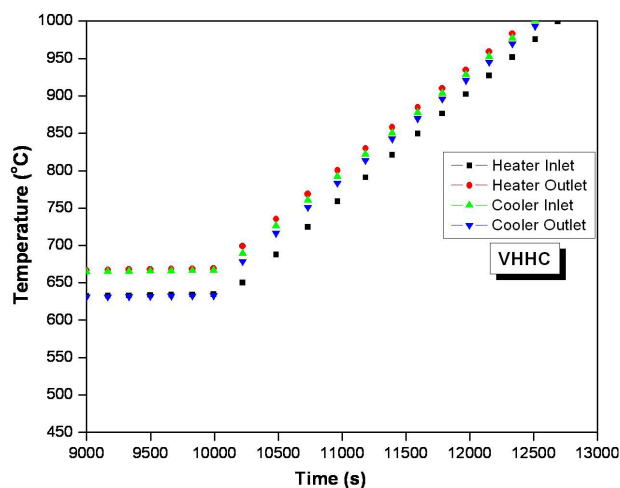


Fig. 4(b): Heater and Cooler Inlet/Outlet Temperature Variation in VHHC orientation for simulated loss of heat sink

Heater Trip

This transient is realized by removing the applied power from the heater. Initially a steady state was

achieved at heater power of 1000W, then for the transient heater power was set to zero in single step at 10000s. Figure 6(a) and Fig. 6(b) show mass flow rate and temperature transients respectively following heater trip. Due to unavailability of the heater, molten salt temperature starts decreasing drastically. Mass flow rate also decreases continuously because of reduction in the available driving head i.e., temperature difference in hot leg and cold leg. The transient is stopped as soon as molten salt temperature reaches $454^{\circ}C$, the freezing point of the FLiNaK salt mixture.

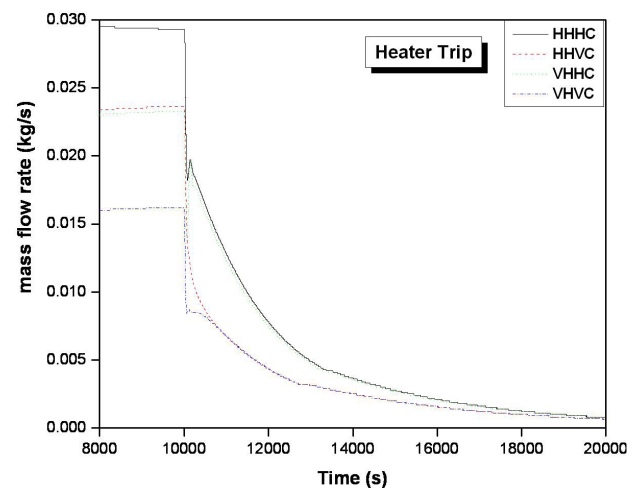


Fig. 5(a): Variation of mass flow rate during the simulated loss of heater trip

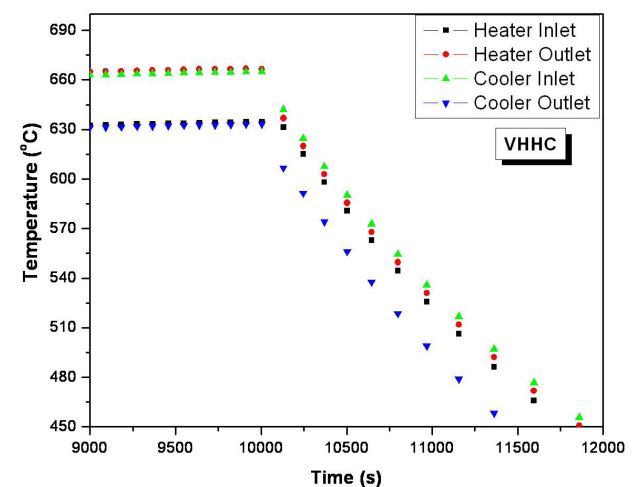


Fig. 5(b): Heater and Cooler Inlet/Outlet Temperature Variation in VHHC orientation for simulated heater trip

BARC NEWSLETTER

Founder's Day

Conclusions

A Pre-test analysis of MSNCL has been performed using LBENC code. Various transients such as: startup of natural circulation, loss of heat sink and heater trip has been analyzed. Steady state mass flow rate has been predicted for different heater power. Effect of orientation of heater and cooler on all the transients has been studied with the above analysis. The experimental results are awaited for the comparison of these results.

References

1. Vijayan, P.K, et al., 2004, 17th National and 6th International ISHMT-ASME HMTC, 600-606.
2. Ambrosini, W., and Ferreri, J.C., 1998, NED, 183, 53-76.
3. Ambrosini, W. and Ferreri, J.C., 2003, *Annals of Nuclear Energy* 30, 1505-1537.
4. Doster, J.M., Kendall, P.K., 1999, *Nuclear Science and Engineering*, 132, 105-117
5. Cammarata, L., et al., 2003, *Applied Thermal Engineering* 23, 965-977.
6. Vijayan, P.K., et al., 1995, NED 155, 623-641
7. Misale M., et al., 1999, Eurotherm Seminar, 6-8 September, Genoa, Italy.
8. Petruzzi, A., et al., 2001, CAMP Meeting, 23-25 April, Prague, Czech Republic.
9. Zhang et al., 2009, NED, 239 2778-2785
10. Jaiswal, B.K., et al., 2008, 19th National and 8th International ISHMT-ASME HMTC, NHT-5/41B.
11. Jaiswal, B.K., Srivastava, A.K., Borgohain, A., Maheshwari, N.K., Vijayan, P.K., ICONE-19, May 16-19, 2011, Makuhari, Chiba, Japan
12. Y.M.Ferng, Kun-Yueh Lin, Chen-Wei Chi, *Applied Thermal Engineering* 37 (2012) 235-240.

TEMPLATE-FREE ELECTROSYNTHESIS OF GOLD NANOPARTICLES OF CONTROLLED SIZE DISPERSION FOR THE DETERMINATION OF LEAD AT ULTRATRACE LEVELS

Saurav K. Guin, Jisha S. Pillai, Arvind S. Ambolikar and Suresh K. Aggarwal
Fuel Chemistry Division

This paper received the Best Poster Presentation Award at the 64th Annual Meeting of International Society of Electrochemistry (ISE) on "Electrochemistry for a new era" held at Santiago de Querétaro, Mexico, Sep. 8-13, 2013

Abstract

A methodology is presented for the template free electrosynthesis of gold nanoparticles (AuNPs) on a glassy carbon (GC) electrode with controlled particle size dispersion. Two strategies viz. multiple potentiostatic pulse (MPP) and multiple galvanostatic pulse (MGP) were adopted for electrochemically synthesizing the AuNPs. In the MPP strategy, the tapered hemispherical gold nanoparticles (AuNPs(P)/GC) of average diameter of 250-300 nm and average height of 10-15 nm were deposited on a GC electrode covering about 61% of the effective surface area of the electrode. In the MGP strategy, the tapered hemispherical gold nanoparticles (AuNPs(G)/GC) of average diameter of 350-400 nm and average height of 25-30 nm were deposited on a GC electrode covering about 18% of the effective surface area of the electrode. Excellent control of the particle size dispersion was achieved in both the routes of synthesis. The synthesized AuNPs showed excellent sensitivity to the determination of Pb(II) by square wave anodic stripping voltammetry (SWASV). The limits of detection (LOD) of Pb(II) obtained with a bare GC, bare Au, AuNPs(G)/GC and AuNPs(P)/GC electrodes were calculated as $1.22 \mu\text{g L}^{-1}$ (5.86 nM), 122 ng L^{-1} (587 pM), 86.4 ng L^{-1} (416 pM) and 57 ng L^{-1} (274 pM), respectively, at $S/N = 3$. The analytical response of the AuNPs(P)/GC electrode was found to be the best among the four electrodes. The stability, repeatability, reproducibility and accuracy of the analytical response were found to be satisfactory for the analytical purposes. Bi(III), Cd(II) and Tl(I) showed major interferences with the analytical signal of Pb(II). The concentrations of Pb(II) in the laboratory tap, lake and river water were found to be $1.7 (\pm 2.3\%) \mu\text{g L}^{-1}$, $3.2 (\pm 1.1\%) \mu\text{g L}^{-1}$ and $8.4 (\pm 3.9\%) \mu\text{g L}^{-1}$, respectively using the AuNPs(P)/GC electrode. The results showed a good agreement with the ICP-MS data for the same samples.

Introduction

Lead (Pb) has been found to be toxic to a wide variety of organs in both humans and animals. The low-level exposure of Pb changes the neurotransmitter levels in the nervous system, harms the vitamin-D metabolism, decreases the sexual hormone levels, and prevents lymphocyte function in living beings. Pb is common in the environment due to its widespread historic use in petrol, paint, lead-acid batteries, and geological

radioactive decay chains. Pb is present in the drinking water primarily because of the corrosion of household plumbing systems containing lead in pipes, solder, fittings or the service connections to homes. Though there is no evidence of threshold or safe exposure of Pb, the World Health Organization (WHO) has set a provisional guideline value of Pb in drinking water as $10 \mu\text{g L}^{-1}$. As per the survey report of the Quality Council of India in 2010, the water samples collected from bore well, well water and municipal water from

BARC NEWSLETTER

Founder's Day

the top cities of India viz. Kolkata, Kochi, Mumbai, Pune, Nagpur, Nasik, Guwahati tested positive for harmful content of Pb.

Nanoparticles supported electrodes generally offer better electroanalytical performance than the corresponding bulk materials because of their high effective surface area, high rate of mass transport through convergent diffusion and electrocatalytic action at the nano-surfaces. However, the size and shape of the metal nanoparticles control the overall analytical response generated by these electrodes. Electrosynthesis is one of the promising techniques for preparing supported metal nanoparticles of controlled size, shape, crystallographic orientation, mass, thickness and morphology. It is challenging in modern electrochemistry to electrosynthesize metal nanoparticles on various substrates without using any template or structure directing agent. Therefore, we have been putting constant effort into the development of template free electrosynthesis of metal nanoparticles with controlled size, shape and of narrow size dispersion without using any protective and stabilizing agent [1]. In the present work, we report the investigation and development of novel multiple potentiostatic pulse (MPP) and multiple galvanostatic pulse (MGP) strategies for the template free electrosynthesis of metal nanoparticles on a glassy carbon (GC) electrode with the objective of achieving better electroanalytical performance compared to that of the bulk metal electrode. The electroanalytical performance of the synthesized AuNPs by MPP and MGP strategies was studied for the determination of lead(II), i.e. Pb(II) by square wave anodic stripping voltammetry in the drinking water collected from three different locations in India.

Experimental

The electrochemical experiments were performed at room temperature ($T = 294\text{ K}$) in a conventional three-electrode cell by using electrochemical workstations. A commercial glassy carbon (GC) or gold (Au) electrode

was used as the working electrode, Ag/AgCl/KCl (saturated) ($E_{\text{Ag/AgCl}} = +0.197\text{ V vs. NHE}$) was used as the reference electrode and a platinum wire acted as the counter electrode. All the potentials quoted are with respect to the Ag/AgCl reference electrode. The morphology of the AuNPs was characterized by atomic force microscope (AFM) and scanning electron microscope (SEM). An inductively coupled plasma orthogonal acceleration mass spectrometer was employed to validate the Pb(II) concentrations obtained by square wave anodic stripping voltammetry (SWASV).

Results and Discussion

Development of MPP strategy

The mechanism of electrocrystallization of gold on glassy carbon electrode was studied in details by cyclic voltammetry and chronoamperometry experiments. Then MPP strategy was designed by a sequence of 1500 potentiostatic pulses in such a way that the seed (or nucleation) pulse was applied only once at -0.13 V for 60 ms followed by a short anodic pulse of 0.92 V for 5 ms to dissolve the subcritical nuclei. Then a pair of growth pulses at 0.55 V for 1 s and an anodic pulse at 0.92 V for 5 ms were applied for 749 times. After the end of 1500 potentiostatic pulses, the tapped hemispherical gold nanoparticles (AuNPs(P)/GC) of average diameter of 250-300 nm and average height of 10-15 nm were deposited on a GC electrode covering about 61% of the effective surface area of the electrode (Fig. 1).

Development of MGP strategy

The mechanism of electrocrystallization of gold on glassy carbon electrode was studied in details by cyclic voltammetry and chronopotentiometry experiments. Then MGP strategy was designed by a sequence of 1500 potentiostatic pulses in such a way that the seed (or nucleation) pulse was applied only once at -0.64 mA cm^2 for 60 ms followed by a short anodic pulse

BARC NEWSLETTER

Founder's Day

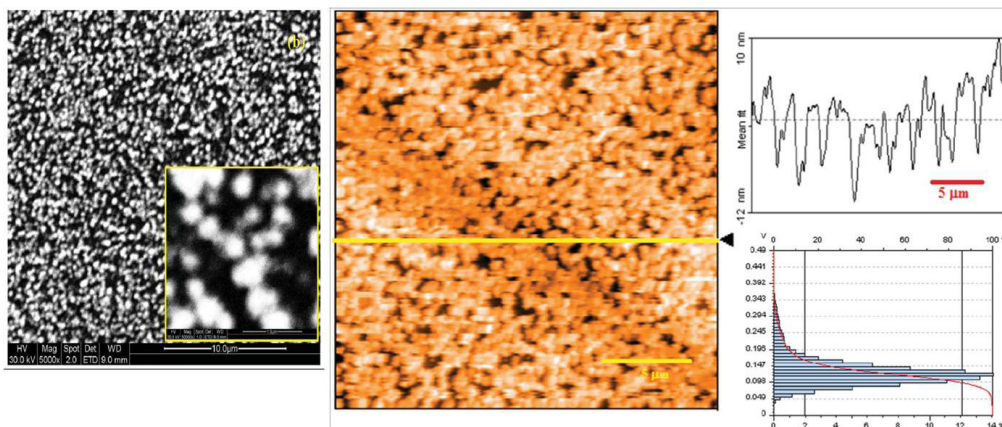


Fig. 1: SEM (Left), AFM-XY view (centre), AFM-YZ view (top right) and AFM-histogram (bottom right) of AuNPs(P)/GC.

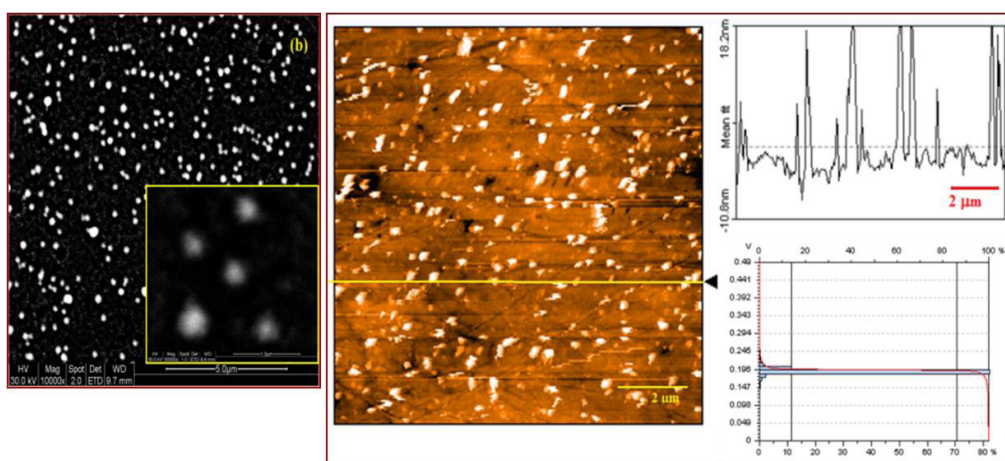


Fig. 2: SEM (Left), AFM-XY view (centre), AFM-YZ view (top right) and AFM-histogram (bottom right) of AuNPs(G)/GC.

of 1.26 mA cm^{-2} for 5 ms to dissolve the subcritical nuclei. Then a pair of growth pulses at -0.46 mA cm^{-2} for 1 s and an anodic pulse at 1.26 mA cm^{-2} for 5 ms were applied for 749 times. After the end of 1500 potentiostatic pulses, the tapped hemispherical gold nanoparticles (AuNPs(G)/GC) of 350-400 nm and average height of 25-30 nm were deposited on a GC electrode covering about 18% of the effective surface area of the electrode. (Fig. 2).

Determination of Pb(II) in 0.1 M KCl by SWASV

The binding energy of Pb on Au is greater than the binding energies of Pb in a Pb metal lattice and Au in a Au metal lattice. Therefore, an atomic monolayer or

submonolayer of Pb electrochemically deposits on Au at electrode potentials which are more positive than the Nernstian potential required for the deposition of the corresponding bulk Pb phase. This phenomenon is known as the UPD of Pb on Au. It was considered interesting to utilize the UPD of Pb on Au for the determination of Pb(II) at the ultra-trace level. The UPD of Pb on Au is a consequent effect of the adsorption of Pb(II) on Au surface. The chloride ions (Cl^-) also adsorb at the Au surface and they induce the adsorption of Pb(II) on Au through a ligand (Cl^-) bridge. Therefore, we chose 0.1 M KCl as the supporting electrolyte for the determination of Pb(II) at ultratrace levels. The optimization of SWASV parameters were carried out. The limits of detection (LOD) of Pb(II) obtained with

BARC NEWSLETTER

Founder's Day

a bare GC, bare Au, AuNPs(G)/GC and AuNPs(P)/GC electrodes were calculated as $1.22 \mu\text{g L}^{-1}$ (5.86 nM), 122 ng L^{-1} (587 pM), 86.4 ng L^{-1} (416 pM) and 57 ng L^{-1} (274 pM), respectively, at $S/N = 3$. The analytical merit of the AuNPs(P)/GC electrode was the best among the four electrodes. This is attributed to the higher surface coverage of AuNPs on the GC in the case of the AuNPs(P)/GC electrode. Therefore, further studies were carried out with only the AuNPs(P)/GC electrode and it exhibited a highly sensitive, precise (5.4% RSD; $n=10$), reproducible (4.8% RSD; $n=5 \times 5$) and stable response for the ultratrace determination of Pb(II). The recovery results obtained were within $\pm 10\%$ of the expected values. Bi(III), Cd(II) and Tl(I) were found to be the most interfering ions during the determination of Pb(II) on the AuNPs(P)/GC electrode.

limit of $10 \mu\text{g L}^{-1}$ as per the provisional guidelines set by WHO in 2011. The results showed that the waters in laboratory tap, lake in RRCAT and Ganges river are safe to drink as far as Pb(II) is concerned.

Conclusion

Simple methodologies for the electrosynthesis of gold nanoparticles on a glassy carbon (GC) electrode with controlled particle size dispersion without using any template or directing agents are reported. Excellent control in the particle size dispersion was achieved for both the strategies and the AuNPs, as synthesized, showed excellent electrocatalytic activity in spite of using no surface stabilizing agents. These methodologies may open up a few possibilities

Table 1: Determination of Pb(II) in Drinking Water Samples.

Determination of Pb(II) in Drinking Water Sample in $\mu\text{g L}^{-1}$		
Samples	Determined by SWASV at Gold NPs Modified Electrode ($n=3$)	Determined by ICP-MS ($n=10$)
Tap Water	$1.7 (\pm 2.3\%)$	$2.3 (\pm 10.7\%)$
Lake water from RRCAT	$3.2 (\pm 1.1\%)$	$3.0 (\pm 2.6\%)$
Ganges river water	$8.4 (\pm 3.9\%)$	$9.4 (\pm 3.5\%)$
Provisional guidelines set by WHO in 2011 is $10.0 \mu\text{g L}^{-1}$		

The developed methodology was utilized for the determination of Pb(II) in the water samples collected from the laboratory tap, lake of Raja Ramanna Centre for Advanced Technology (RRCAT), Indore and near the Aassi ghat of the Ganges River in Varanasi, India. The calculated concentrations of Pb(II) in the water samples obtained by the present methodology are listed in Table 1. It can be seen that the concentrations of Pb(II) obtained from the present methodology are in good agreement with the concentrations of the same samples measured by ICP-MS. The concentrations of Pb(II) in all the samples are below the threshold value

for the electrochemical preparation of pure metal nanoparticles without adding any template, directing or stabilizing agent. The linear dynamic range, sensitivity, stability, repeatability, reproducibility, accuracy and LOD of the AuNPs(P)/GC electrode were found to be quite satisfactory for the electrochemical determination of Pb(II) in drinking water.

Reference

1. S.K. Guin, H.S. Sharma and S.K. Aggarwal, *Electrochim. Acta*, 55 (2010) 1245–1257.

TITANIUM – STAINLESS STEEL BRAZING USING AG-BASED ALLOYS

A. Laik and G.K. Dey

Materials Science Division

and

A.A. Shirzadi

Materials Engineering, The Open University, Milton Keynes MK7 6AA, United Kingdom

This paper received the Best Poster, 2nd Prize (Materials Science) at the International Conference on Electron Microscopy & XXXIV Annual Meeting of EMSI, Kolkata, 3-5 July, 2013

Abstract

A detailed characterization of vacuum brazed joints of titanium and stainless steel type 304L, using three Ag-based brazing alloys, Cusil, Ticusil and Silver-ABA has been carried out. The intermetallic compounds formed at the braze zone due to interaction of the joining components with the brazing alloys were identified. The microstructural evolution at the interfaces and the mechanisms of brazing in the three cases are compared.

Introduction

Both titanium and stainless steel (SS) are widely used as engineering materials in industries due to their excellent mechanical properties as well as corrosion resistance. The extensive use of Ti and its alloys in various sectors, for example, aerospace, transportation, chemical, nuclear and power generation, requires them to be joined to other materials for integration and fabrication of various components [1, 2]. Of particular interest to the nuclear industry, is the application of Ti in fabricating the dissolvers of spent nuclear fuel used in reprocessing plants. This requires it to be joined to the piping of the plant, which is generally made of stainless steel (SS) [3].

Conventional fusion welding has not been a good choice since it needs to be performed in inert atmosphere due to the reactive nature of Ti, and the significant difference in physico-chemical properties of the two materials that lead to chemical, mechanical and structural inhomogeneities [7]. Although the progress of research on diffusion bonding of SS to Ti with

suitable interlayers has led to some success, formation of undesirable intermetallic compounds of various combinations such as Ti-Fe, Ti-Cr, Ti-Ni could not be completely eliminated [2, 9]. The formation of these intermetallics produce residual stresses originating from a mismatch in their thermal expansion [7, 10, 11]. Further, the method is expensive and not an obvious choice for mass production [8]. In comparison to these techniques, vacuum brazing offers two major advantages: (a) low thermal residual stresses in the joints, as a major part of the stresses generated due to differential contraction of the two materials is relieved by plastic deformation of the ductile braze alloys, and (b) a low compressive stress is required for joining [7]. Dececco and Parks [12] suggested the use of silver and its alloys to braze Ti and since then various Ag-based filler alloys have been extensively used for the brazing of Ti and its alloys, primarily due to good flow characteristics of these filler alloys and high strength and adequate ductility of these brazed joints.

The present study compares the brazing characteristics of stainless steel/titanium brazing using different Ag-

BARC NEWSLETTER

Founder's Day

based brazing alloys. The mechanisms of brazing and microstructural evolution at the interfaces are also determined.

Experimental Procedure

The base materials used in the experiments were annealed plates of commercially pure grade-2 titanium (ASTM B265) and austenitic stainless steel (SS 304L). The nominal compositions of these materials are given in Table 1. Specimens of Ti grade 2 and SS 304L, in the form of cylindrical pieces with dimensions of 35 mm length and 14 mm diameter were vacuum brazed using 50 μm thick foils of Ag-based alloys Cusil, Ticusil and Silver-ABA at temperatures 835 $^{\circ}\text{C}$, 920 $^{\circ}\text{C}$ and 930 $^{\circ}\text{C}$, respectively. The nominal compositions of these alloys are given in Table 2. The joining faces of the pieces were ground with successive grades of emery papers up to 1200 grit, followed by 1 μm diamond polish. Prior to brazing, all the components were ultrasonically cleaned with ethyl alcohol followed by acetone. The brazing operation was carried out in a furnace under vacuum of 5×10^{-5} mbar.

scanning electron microscope (SEM), energy dispersive spectrometry (EDS), electron probe microanalyser (EPMA) and transmission electron microscope (TEM).

Results

Brazing with Silver-ABA

A typical backscattered electron (BSE) image showing the microstructure of the cross section of the BZ of the SS-Ti joint, brazed at 930 $^{\circ}\text{C}$ for 15 minutes using Silver-ABA alloy is shown in Fig. 1. It was noted that the interfaces between the braze alloy and the base materials, on either side, were free from pores, cracks, or discontinuities. The entire BZ, may be divided into four zones A-D, as marked in Fig. 1. X-ray maps of elements Fe, Ni, Cr, Ag, Cu, Al, and Ti along with the corresponding backscattered electron (BSE) image of a typical region of the BZ is shown in Fig. 2.

On the SS-side, at the interface between SS and braze alloy, a layer A of solid solution consisting of about 5 at. % of Al and 21 at. % of Cr in Fe along with 5.5 at.

Table 1: Nominal chemical composition of the base materials (in wt. %).

Elements	C	H	O	Mn	Si	Ni	Cr	Fe	Ti
Ti Gr-2	0.009	0.008	0.12	---	---	0.011	---	0.09	Bal.
SS 304L	0.02	---	---	1.47	0.52	10.6	19.1	Bal.	---

Table 2. Nominal chemical composition of the Ag-based brazing alloys used (in wt. %).

Elements	Ag	Cu	Ti	Al
Cusil	72	28	---	---
Ticusil	68.8	26.7	4.5	---
Silver-ABA	92.75	5	1.25	1

The joints was sectioned in the direction perpendicular to the bond interface, using slow speed diamond blade and the cross-sections were prepared for microscopic examination using standard metallographic techniques and were subsequently etched with a solution of 5% HF, 40% HNO₃ and 55% H₂O, by volume. The microstructure of the braze zone (BZ) was characterized using an optical microscope, and a

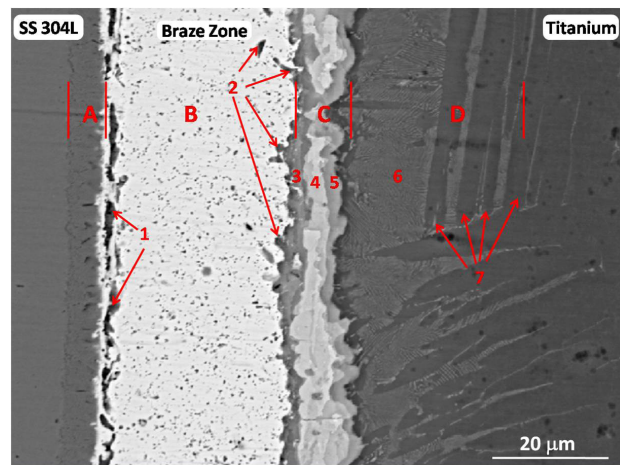


Fig. 1: BSE micrograph of the Ti-SS joint brazed using Silver-ABA alloy at 930 $^{\circ}\text{C}$. A: Fe(Al), B: unreacted layer, 1: $(\text{Ni,Fe})_2\text{TiAl}$, 2: Cu_4Ti , 3: CuTi , 4: AgTi , 5: $(\text{Ag,Cu})\text{Ti}_2$, 6: $\alpha\text{-Ti} + \text{CuTi}_2$ eutectoid layer, 7: $\alpha\text{-Ti}$ Plates.

BARC NEWSLETTER

Founder's Day

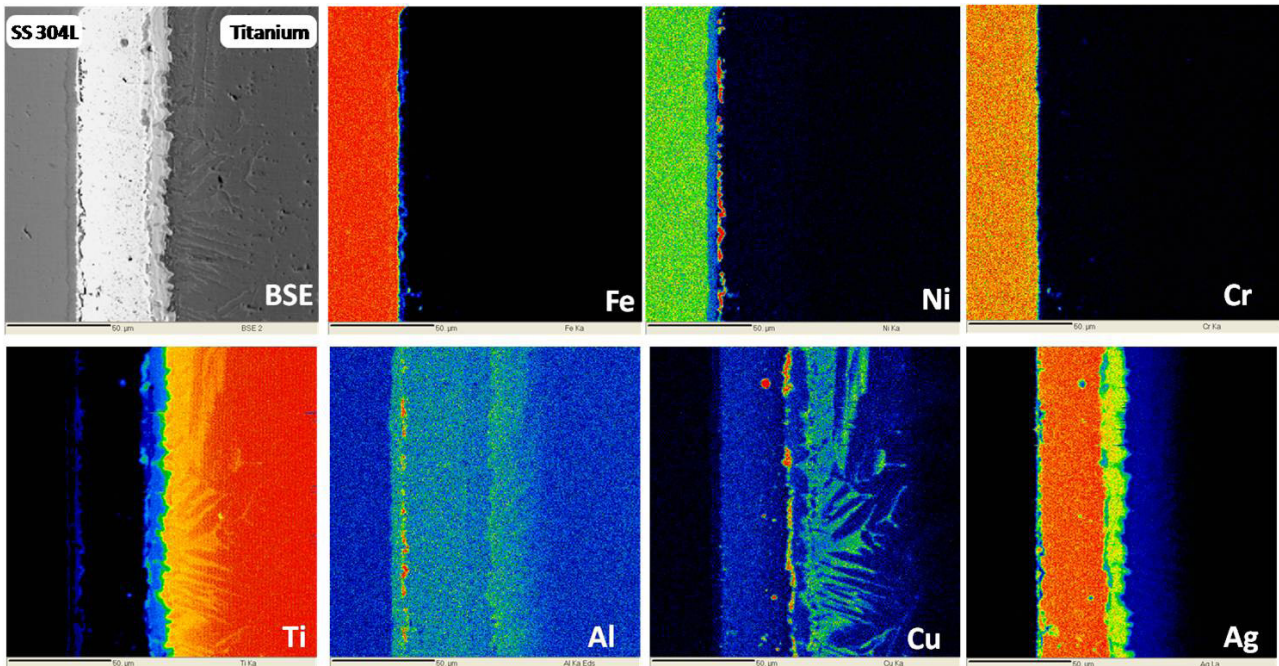


Fig. 2: X-ray maps of elements Fe, Ni, Cr, Ti, Al, Cu and Ag along with the BSE image of a region at the SS-Ti joint interface, showing the distribution and variation in the relative concentrations of these elements in the BZ.

% Ni. Layer B was identified as the unreacted braze alloy, consisting mainly of Ag and Cu. Due to solid-liquid interaction on the Ti-side of the BZ, parallel layers of intermetallic compounds (IMC) with planar morphology, collectively marked as zone C, were formed. These IMCs were identified as Cu_4Ti , CuTi , AgTi , and $(\text{Ag,Cu})\text{Ti}_2$ [13]. On the Ti-side of the BZ, Cu, Ag, and Al were found to diffuse into the Ti-base material up to a depth of about 40 μm , labeled as zone D. In most of the regions of this zone, a fine lamellar two-phase microstructure consisting of $\alpha\text{-Ti}$ and CuTi_2 , marked as 6, formed in colonies. Fig. 3 shows the bright field, dark field micrographs and SADP of the eutectoid structure as acquired in TEM. The lamellae measured almost 5 to 6 μm in length, and the interlamellar spacing was about 600 nm. The orientation relationship between the phases is $(0001)_\alpha \parallel (0-13)_{\text{CuTi}_2}$ and $[2-1-10]_\alpha \parallel$

$[-100]_{\text{CuTi}_2}$ [13]. The CuTi_2 phase was found to be internally twinned as evidenced in Fig. 3.

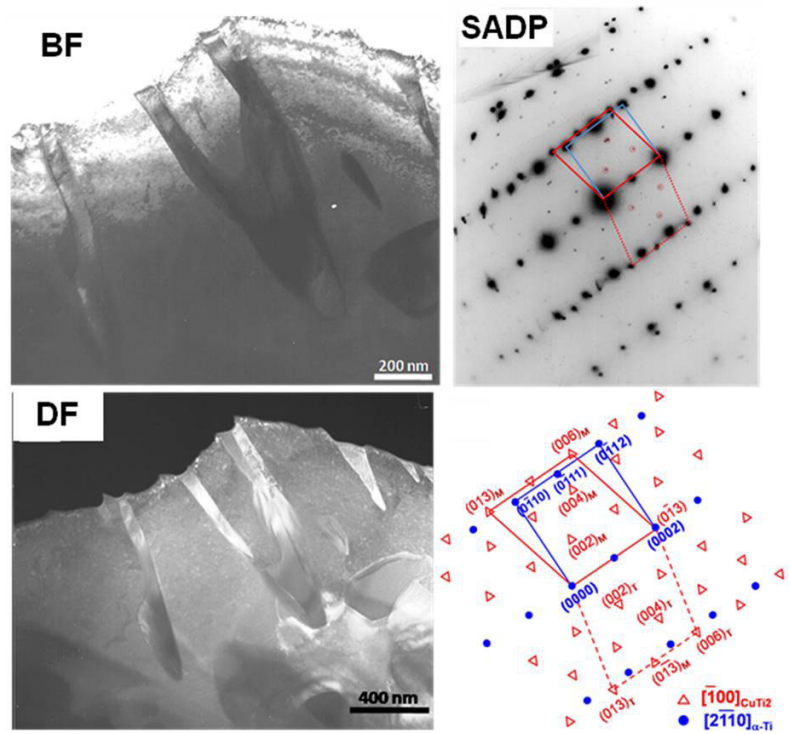


Fig. 3: Bright field and dark field micrographs of the eutectoid structure, labeled 6 in Fig. 1, along with the selected area diffraction pattern and its key.

BARC NEWSLETTER

Founder's Day

Brazing with Cusil

The microstructure of the interface between SS and Ti in case of SS-Ti joints brazed at 835 °C for 10 min, using Cusil alloy. The basic scheme of the microstructure was similar to that of the Silver-ABA brazed joints. Fig. 4 shows a typical BSE image of the interface. The formation of layers of IMCs is evident from the micrograph. On the SS side, a layer marked 1 with composition Cu-37 % Ti-10% Fe was found to form as continuous layer. On the Ti side, three binary Cu-Ti IMCs, viz., Cu₃Ti₂, Cu₄Ti₃ and CuTi, as marked as 3, 4 and 5 in Fig. 4, formed as contiguous layers. Islands of bright phase, labeled 2 in Fig. 4, showed to be almost pure Ag with about 9 % Cu and 1.5 % Ti. This phase was hence identified to be solid solution Ag(Cu), which remained unreacted in the process of brazing [14]. The compositions of these phases were determined using electron microprobe analysis.

Adjacent to the CuTi layer, on the Ti side, a 10 μm thick two-phase layer formed. It was evident from its lamellar morphology that it was a eutectoid layer,

formed due to phase transformation during cooling. Microanalysis results showed that the layer contained substantial amount of Cu. Therefore, during the process of brazing, Cu had diffused into Ti to a depth of about 10 μm. Being a β-stabiliser, it had promoted the formation of a layer of β-Ti even at temperatures lower than the α-β transus. Laik et al. [15] have recently demonstrated the formation of such β-Ti layer below the α-β transus in Cu-Ti diffusion couples. The structure was resolved in FESEM and EDS analysis was used to identify the structure as lamellar aggregate of β-Ti and CuTi₂.

Brazing with Ticusil

Fig. 5 shows a BSE image of the interface between SS and Ti in case of SS-Ti joints brazed at 920 oC for 10 min, using Ticusil alloy. Although the microstructure seems quite identical to that of Cusil brazed joint, the number of IMCs formed in the BZ is not as many. Apart from the layer of Cu-37Ti-10Fe adjacent to SS, marked as 1 in Fig. 5, the only other IMC layer that formed in the BZ is CuTi (layer 3). Islands of unreacted Ag were

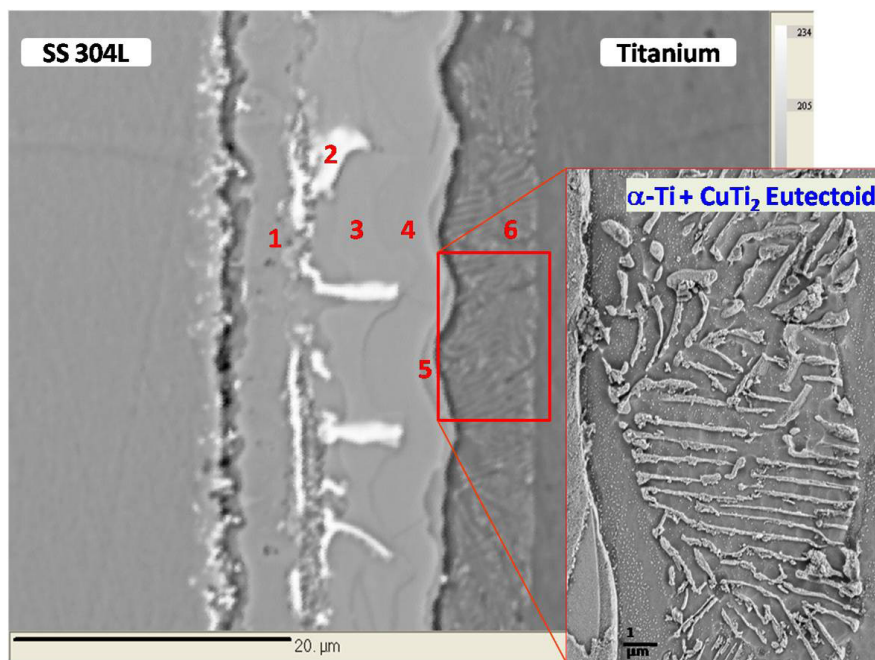


Fig. 4: BSE micrograph of the Ti-SS joint brazed using Cusil alloy at 835 °C. 1: Cu-37Ti-10Fe, 2: Ag(Cu), 3: Cu₃Ti₂, 4: Cu₄Ti₃, 5: CuTi, 6: α-Ti + CuTi₂. The eutectoid layer 6 is shown at higher magnification in the inset.

BARC NEWSLETTER

Founder's Day

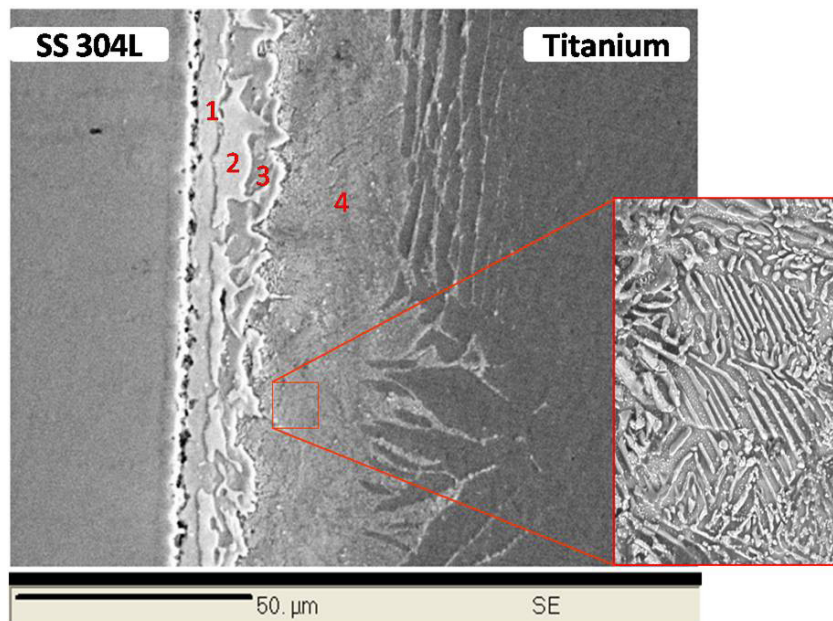


Fig. 5: BSE micrograph of the Ti-SS joint brazed using Ticusil alloy at 920 °C. 1: Cu-37Ti-10Fe, 2: Ag(Cu), 3: CuTi, 4: α -Ti + CuTi₂. The eutectoid layer 4 is shown at higher magnification in the inset.

also found to form in this case, between the Fe rich layer 1 and that of CuTi. The fraction of unreacted alloy is quite substantial as compared to Cusil. Cu was found to have diffused to a depth of about 50 μm inside Ti, because of higher temperature of brazing. A similar α -Ti + CuTi₂ eutectoid layer formed during cooling of the β -Ti(Cu) solid solution phase from the brazing temperature. However, some elongated plates of β -Ti formed on the Ti side of the eutectoid layer, which can be attributed to partitioning of Cu to the β -phase since the solubility of Cu in the β -phase in room temperature is negligible. The interlamellar spacing in the eutectoid aggregate in this case is finer than that in Cusil braze joint [14].

Discussion and Summary

The microstructures of the SS/Ti joint interfaces revealed that the interfaces between the braze alloy and the base materials, on either side, and the braze zones were free from pores, cracks, or discontinuities, in all the three cases. It was also noted that in all the three cases the BZ consisted of layered structure due to the formation of intermetallic compounds by

reaction of the substrate materials and the braze alloy. Although the basic microstructure of the BZ remained identical, the nature of the intermetallic compounds varied with the braze alloy. In the case of Silver-ABA brazing the compounds were identified as (Ni,Fe)2TiAl, Cu4Ti, CuTi, AgTi and (Ag,Cu)Ti2, and those in Cusil brazing were Cu3Ti2, Cu4Ti3 and CuTi formed, while during brazing with Ticusil primarily CuTi formed in the reaction zone.

A part of the brazing alloy remained unreacted in the BZ in all the cases. The fraction of the unreacted alloy was quite substantial in Silver-ABA brazing, and consisted of a major portion of the BZ. However, this fraction in Cusil brazing was small and the BZ consisted primarily of the intermetallic compounds. A significant feature of the microstructure is the formation of eutectoid layer consisting of lamellae of (Cu,Ag)Ti2 in α -Ti matrix. The orientation relationship between the two phases was determined using composite SADP in TEM. The CuTi2 phase was found to be internally twinned. The variation in the width of this eutectoid layer can be attributed to the difference in the brazing conditions in different cases.

BARC NEWSLETTER

Founder's Day

Acknowledgements

The authors are thankful to Shri P. Mishra, Materials Processing Division, for providing the Silver-ABA foils. The authors would also like to thank Dr. R. Tewari for the TEM analysis of the samples. The assistance of Shri P. G. Adiga in conducting the brazing experiments is gratefully acknowledged.

References

1. A. Shapiro and A. Rabinkin: *Weld. J.*, 2003, vol. 83, pp. 36–43.
2. S. Kundu, M. Ghosh, A. Laik, K. Bhanumurthy, G. B. Kale, and S. Chatterjee: *Mater. Sci. Eng. A*, 2005, vol. 407, pp. 36–43.
3. U. K. Mudali, B. M. Ananda Rao, K. Shanmugam, R. Nataraj, and B. Raj: *J. Nucl. Mater.*, 2003, vol. 321, pp. 40–48.
4. P. He, J. Zang, R. Zhou, and X. Li: *Mater. Charact.*, 1999, vol. 43, pp. 287–292.
5. N. Orhan, T. I. Khan, and M. Eroglu: *Scripta Mater.*, 2001, vol. 45, pp. 441–446.
6. J. G. Lee, S. J. Hong, M. Lee, and C. Rhee: *Scripta Mater.*, 2009, vol. 395, pp. 145–149.
7. X. Yue, P. He, J. C. Zhang, and F. Q. Zhu: *Mater. Charact.*, 2008, vol. 59, pp. 1721–1727.
8. A. Elrefaey and W. Tillmann: *Weld. J.*, 2008, vol. 87, pp. 113s–118s.
9. J. G. Lee, S. J. Hong, M. K. Lee, and C. K. Rhee: *J. Nucl. Mater.*, 2009, vol. 395, pp. 145–149.
10. P. He, X. Yue, and J. H. Zhang: *Mater. Sci. Eng. A*, 2008, vol. 486, pp. 171–176.
11. M. Ghosh, S. Chatterjee, and B. Mishra: *Mater. Sci. Eng. A*, 2003, vol. 363, pp. 268–274.
12. N. A. Dececco and J. N. Parks: *Weld. J.*, 1953, vol. 32, pp. 1071–1081.
13. A. Laik, A. A. Shirzadi, R. Tewari, Anish Kumar, T. Jayakumar, G. K. Dey: *Metall. and Mater. Trans. A*, 2013, vol. 44A, pp. 2212–2225.
14. A. Laik, A. A. Shirzadi, G. K. Dey, Intl. Conf. Electron Microscopy and XXXIV Annual Meeting of EMSI, Kolkata, 3-5 July, 2013, p. 219.
15. A. Laik, K. Bhanumurthy, G. B. Kale, B. P. Kashyap: *Int. J. Mater. Res.*, 2012, vol. 103, pp. 661–672.

DEVELOPMENT OF RARE EARTH BASED MAGNETIC ALLOY POWDERS BY REDUCTION-DIFFUSION METHOD

Kinshuk Dasgupta, Deepak Sahoo and Harvinderpal Singh

Rare Earths Development Section, Materials Group

and

Alok Awasthi

Materials Processing Division

This paper received the Best Presentation Award at the International Conference on Magnetic Materials and Applications (MagMA 2013), IIT Guwahati, Dec. 5-7, 2013

Abstract

Samarium-cobalt based magnetic alloy powders have been prepared by calciothermic reduction of samarium oxide in presence of cobalt under argon atmosphere. The resultant alloy powders were subjected to decalcification. The effect of processing parameters in obtaining the desired magnetic phases and on residual calcium has been studied. The products have been characterized by various microscopic and spectroscopic techniques. Higher samarium content and lower calcium content in the powder improve the magnetic properties of the final product.

Introduction

Permanent magnets based on rare earth-transition metal intermetallics are the basis of ever increasing number of commercial and scientific applications, including electric motors, NMR scanners, wind-mills, compact discs, actuators for robotics and flight control, etc [1-3]. The advantage of permanent magnets in these applications is their ability to exhibit high level, constant magnetic fluxes without applying an external magnetic field or electrical current. Samarium-cobalt based magnets with high energy product and excellent coercive force, are ideally compact and suitable to highly efficient machine and components in which higher operation temperature, higher corrosion and oxidation resistance are crucial [4]. Iron-neodymium-boron (Nd-Fe-B) and other rare earth-iron/cobalt-based intermetallics have been investigated due to their superior magnetic properties [5-7]. However, corrosion resistance is a primary concern with Nd-Fe-B type of magnet and it has limitations to be used at higher temperature. In view of growing indigenous

demand of samarium-cobalt based permanent magnets, namely SmCo₅ and Sm₂Co₁₇ for specific applications, attention has been paid to prepare this magnetic material. In this paper the preparation of Sm-Co alloy powders by reduction-diffusion process followed by decalcification has been discussed.

Experimental

Sm₂O₃ powder (supplied by IREL: 95-96% pure) was mixed with calculated amount of Co (purchased from local vendor: 98.5 % pure) and Ca granules in a glove box. The charge was taken in a crucible and heated to high temperatures (1000-1200°C) under inert atmosphere in a resistance-heating furnace. After required duration of heating (3-10 hrs) the furnace was cooled and the charge was subjected to leaching for removal of Ca/CaO. The leaching was performed initially by water wash and followed by organic acid. The product was characterized by XRD (for phase identification), SEM (for morphology and size of the powder), EDX, XRF (for chemical composition) and

BARC NEWSLETTER

Founder's Day

ICP-AES (for residual calcium). The powder was used to make a bar magnet and its magnetic properties were measured. The process has been developed to produce the powder in one kg batch scale with residual Ca ~ 2000 ppm.

Results and Discussion

The desired phases were obtained when the reduction was carried out with more than 50% stoichiometric excess of Ca. 5-15% excess Sm_2O_3 was found to be necessary to get the desired phases. The reduction was incomplete when it was carried out below 1050°C.

Almost 95% CaO was removed by leaching the product with water. For further decrease of residual calcium, leaching with buffer solution containing

ammonia and organic acid was necessary. Fine control of pH was found necessary to bring down the calcium content below 2000 ppm in the final product without disturbing the magnetic phases. Improper leaching results in loss of rare earth values. Fig. 1 (a) and (b) are the XRD patterns of the leached SmCo_5 and $\text{Sm}_2\text{Co}_{17}$ powders, respectively.

Typical SEM image and the corresponding EDX pattern of the decalcified powder is shown in Fig.2 (a) and 2 (b) respectively.

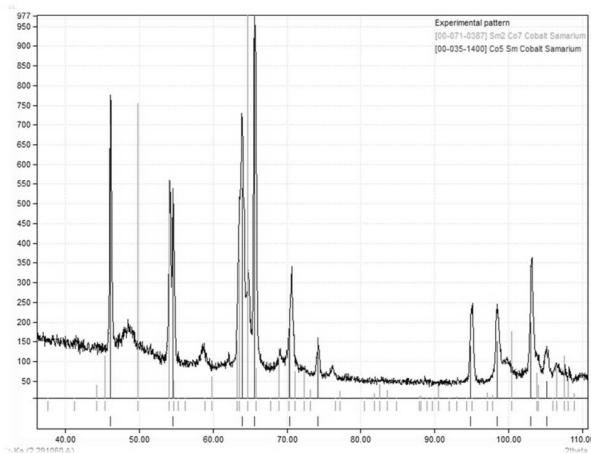


Fig. 1 (a): XRD of SmCo_5 powder

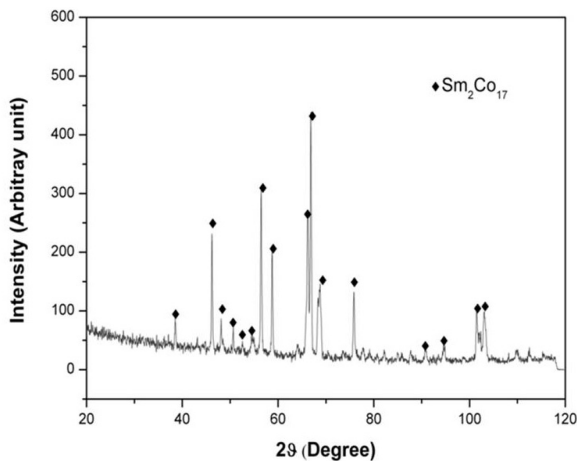


Fig. 1 (b): XRD of $\text{Sm}_2\text{Co}_{17}$ powder

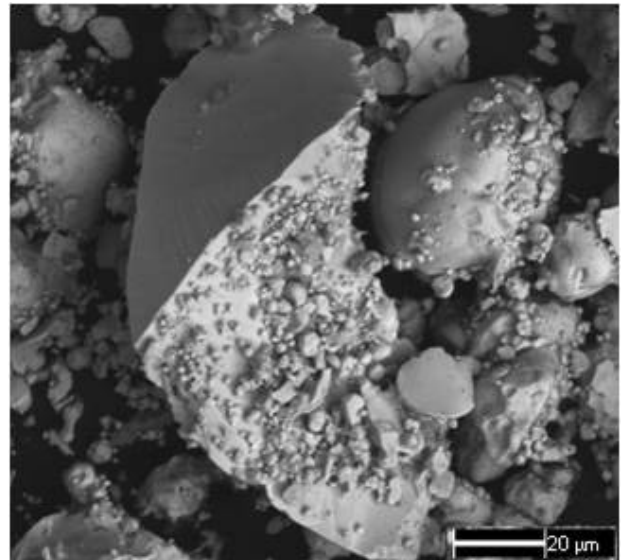


Fig. 2 (a): SEM of decalcified SmCo_5 powder

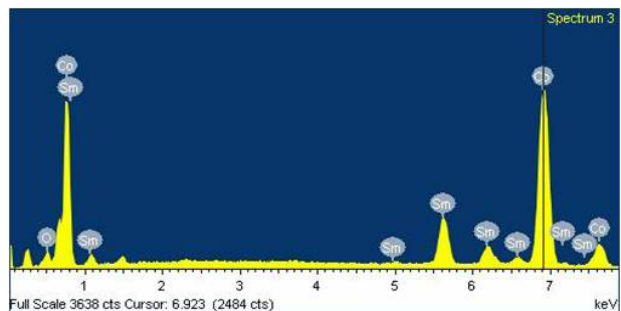


Fig. 2 (b): EDX of the powder

The energy product improves with lower Ca content and higher Sm content. Fig 3 (a) shows a magnetization curve of a product which has 27% Sm and 5000 ppm Ca, whereas Fig. 3 (b) represents the curve of a product containing 37% Sm and 2000 ppm Ca. Definitely the product with higher Sm and lower Ca shows much

BARC NEWSLETTER

Founder's Day

better residual magnetization and energy product, which are required for a good permanent magnet.

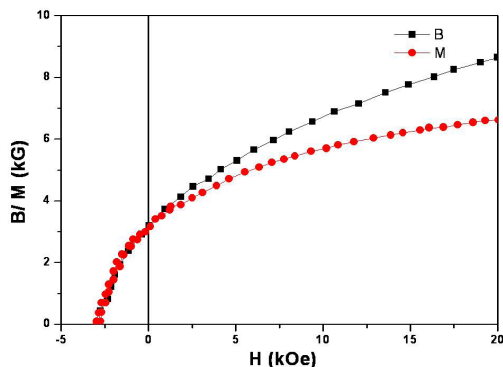


Fig. 3 (a): Magnetization curve of a product containing 27% Sm and 5000 ppm Ca

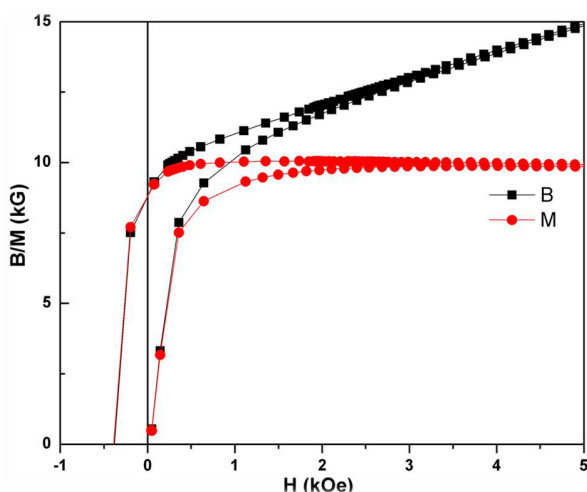


Fig. 3 (b): Magnetization curve of a product containing 37% Sm and 2000 ppm Ca

Conclusion

Preparation of Sm-Co alloy powder by reduction-diffusion process has been optimized. Leaching conditions were also standardized for successful removal of calcium from the products. Improper leaching resulted in loss of Sm. XRD pattern showed the formation of required phases. The oxygen and calcium contents in the final products are 0.5 and 0.2

wt % respectively which are well within the permissible limit for magnet preparation. The magnetic properties improve with increase in Sm content in the final product.

Acknowledgement

The authors are grateful to Dr. D. K. Singh for technical inputs during leaching, Dr. M. Anitha for chemical analysis and Shri Bhaskar Paul for SEM analysis.

References

1. P. Campbell, Permanent Magnet Materials and Their Application, Cambridge University Press, Cambridge, 1994.
2. H.R. Kirchmayr, Permanent magnets and hard magnetic materials, *J. Phys. D: Appl. Phys.* 29 (1996) 2763-2778.
3. S. Sugimoto, Current status and recent topics of rare-earth permanent magnets, *J. Phys. D: Appl. Phys.* 44 (2011) 1-11.
4. S.R. Trout, Permanent magnets based on the lanthanides: Raw materials, processing and properties, Proc. The International Symposium on Magnetism, Seoul, Korea, Nov 8-10, (1990) pp 79-90.
5. S. D. Bham, V. Swaminathan, P. K. Deheri, R. V. Ramanujam, Exchange coupled Nd₂Fe₁₄B/ α -Fe nanocomposite by novel autocombustion-reduction-diffusion synthesis, *Adv. Sci. Lett.* 3 (2010) 1-6.
6. D. Brown, B. M. Ma, Z. Chen, Developments in the processing and properties of NdFeB-type permanent magnets, *J. Magn. Mater.* 248 (2002) 430-440.
7. M. Sagawa, S. Hirosawa, H. Yamamoto, S. Fujimura, Y. Matsuura, Nd-Fe-B Permanent Magnet Materials, *Jap. J. Appl. Phys.* 26 (1987) 785-800.

THERMODYNAMIC STUDY OF URANIUM SORPTION ON TO BIOSYNTHEZIZED MELANIN

Amardeep Singh Saini and Jose Savio Melo
Nuclear Agriculture and Biotechnology Division

This Paper received the Best Oral Presentation Award at the 19th DAE-BRNS Symposium on Thermal Analysis, held at Mumbai from Dec. 19-21, 2013

Abstract

Biosorption has emerged as an alternate technology for the removal of heavy metals, present at low concentrations. Present study describes the thermodynamics of uranium sorption onto melanin pigment, which has been synthesized through green technology. The negative values of ΔG^0 at all studied temperatures indicate the spontaneous nature of the adsorption process. Positive values of ΔH^0 and ΔS^0 suggest that the process is endothermic and shows increased surface randomness. The value of activation energy was calculated to be 16.17 kJ mol⁻¹. Binding of uranium to melanin surface was confirmed by energy dispersive spectroscopy (EDS).

Introduction

Conventional treatment methods are inefficient for treatment of effluents having metal ions less than 100 mg L⁻¹. Metal ions at this level are potentially toxic and hazardous and hence, treatment of such high volume dilute waste is important. Uranium is one such heavy metal having both radiochemical and toxicological effects. Biosorption has gained importance as an alternative for the remediation of such waste. Thermodynamics is an integral part of biosorption study and helps to understand the behavior of adsorption process. Also, it gives an idea about the feasibility of the sorption process and the accompanied changes in parameters such as enthalpy and entropy. Natural resource materials such as *Hydrilla verticillata*¹, *Ocimum basilicum*², *C. repens*³, have been used for metal uptake applications. In the present study, thermodynamic parameters such as free energy, enthalpy, entropy and activation energy of uranium adsorption onto biosynthesized melanin were studied. The presence of uranium on melanin was detected by EDS analysis.

Experimental

Materials

Melanin was synthesized using tyrosinase enzyme and L-Dopa as substrate. It was then acidified and collected by centrifugation, washed thoroughly with distilled water and air dried till further use. A uranium metal stock solution of 2000 mg L⁻¹ was prepared in distilled water and later diluted to the desired concentration as required. All chemicals used were of analytical grade.

Experiment

Uranium solution (200 mg L⁻¹) was contacted with melanin (1 g L⁻¹) and incubated at different temperatures of 288, 298, 308, and 318 K and agitated at 150 rpm on an orbital shaker. Samples were collected at suitable time intervals and subjected to centrifugation to estimate residual uranium concentration in supernatant. The estimation was done using arsenazo III reagent and the uptake of uranium per unit melanin was calculated using following expression:

BARC NEWSLETTER

Founder's Day

$$q_e = (C_0 - C_e) V / W \quad (1)$$

where ' C_0 ' and ' C_e ' = Concentrations of uranium (mg L⁻¹) before and after the sorption, respectively, ' V ' = volume of uranium solution (L) and ' W ' = amount of melanin (gm).

Energy Dispersive Spectroscopy (EDS) of uranium sorption on melanin

EDS analysis was done using SEM-EDS Zeiss-Evo 18 special edition system. Melanin powder with and without uranium was used as test and control respectively.

Results and discussion

Effect of temperature

As seen from Fig. 1, the metal uptake capacity went on increasing as the temperature increased from

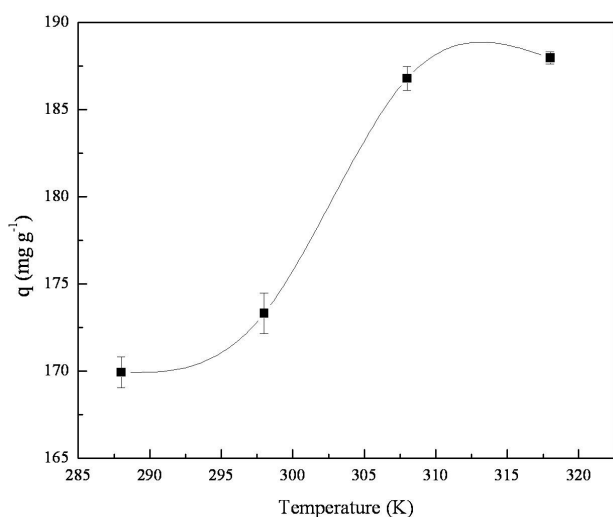


Fig.1. Effect of temperature on uranium loading capacity.

288 K to 318 K; suggesting an endothermic nature of the system. The rise in sorption capacity at higher temperature is due to the increase in collision frequency between the sorbent and the solute which results in increased sorption on the surface of melanin.

Evaluation of thermodynamic parameters

In order to describe the thermodynamic behavior of uranium biosorption by melanin, the change in free energy (ΔG^0) was calculated using the following equation:

$$\Delta G^0 = -RT \ln K_D \quad (2)$$

where R is the universal gas constant (8.314 J mol⁻¹ K⁻¹), T is the temperature (K) and KD (q_e / C_e) is the distribution coefficient. The enthalpy and entropy parameters were estimated from the following equation :

$$\ln KD = \Delta S^0/R - \Delta H^0/RT \quad (3)$$

where ΔS^0 represents the entropy and ΔH^0 denotes enthalpy. The values of ΔG^0 at all studied temperatures were found to be negative which confirms the thermodynamic feasibility and spontaneous nature of the adsorption process (Table 1). The value of change in enthalpy, calculated from slope of $\ln K_D$ versus reciprocal of temperature is positive which further confirms the previous observation that biosorption in the present study is an endothermic process. Positive value of change in entropy calculated from the intercept of the same plot, suggests increased randomness during the process of adsorption.

Table 1. Thermodynamic parameters for uranium uptake by melanin

ΔH^0 (kJ mol ⁻¹)	ΔS^0 (kJ mol ⁻¹ K ⁻¹)	ΔG^0 (kJ mol ⁻¹)			
		288 K	298 K	308 K	318 K
18.75	0.077	-0.0116	-0.0122	-0.0150	-0.0154

BARC NEWSLETTER

Founder's Day

Determination of activation energy

The activation energy E_a was determined using the Arrhenius equation

$$\ln k_2 = \ln A - (E_a / RT) \quad (4)$$

where k_2 is the rate constant value for metal biosorption, determined by the most appropriate kinetic model (pseudo-first-order or the pseudo-second-order kinetic model), E_a is the activation energy in kJ mol^{-1} , T is the temperature in Kelvin and R is the gas constant ($8.314 \text{ J mol}^{-1} \text{ K}^{-1}$). The activation energy E_a calculated from the slope of the plot was found to be $16.17 \text{ kJ mol}^{-1}$. The value of activation energy helps to understand about the type of sorption i.e. physisorption or

chemisorption. In case of physisorption; weak forces are involved in which E_a value less than 4.2 kJ mol^{-1} are observed. Chemisorption on the other hand, involves forces that are specific and stronger than in physical adsorption and is accompanied by E_a of more than 4.2 kJ mol^{-1} . The sorption of uranium onto melanin is therefore chemisorption process.

Energy Dispersive Spectroscopy (EDS)

Conclusive identification of the presence of uranium on melanin surface was made with the help of characteristic EDS peak pattern of uranium in the test sample (Fig. 2).

References

1. Srivastava, S., Bhainsa, K.C., D'Souza, S.F. "Investigation of uranium accumulation potential and biochemical responses of an aquatic weed *Hydrilla verticillata* (L.f.) Royle". *Bioresource Technology*, 101, (2010): 2573–2579.
2. Melo, J.S., D'Souza, S.F. "Removal of chromium by mucilaginous seeds of *Ocimum basilicum*". *Bioresource Technology*, 92, (2004): 151–155.
3. Bhat, S.V., Melo, J.S., Chaugule, B.B., D'Souza, S.F. "Biosorption characteristics of uranium (VI) from aqueous medium onto *Catenella repens*, a red alga". *Journal of Hazardous Materials*, 158, (2008): 628-635.

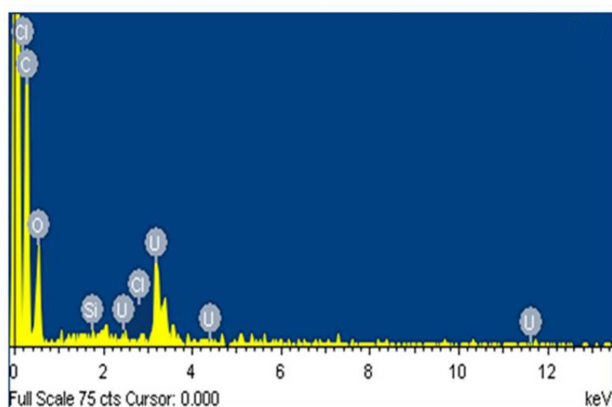


Fig. 2: EDS spectra of melanin after contact with uranium solution

CORROSION OF MODIFIED 9CR-1MO STEEL AND INDIAN RAFMS IN STATIC Pb-17Li AT 773K

P. Chakraborty, R.K. Fotedar and N. Krishnamurthy

Fusion Reactor Materials Section, Materials Group

and

M. J. Naik

Indian Institute of Technology, Roorkee

and

P. K. Pradhan

Materials Processing Division

This paper received the Best poster award at the XXXVIII Annual Conference of Environmental Mutagen Society of India (EMSI) on "Current Perspectives on Environmental Mutagenesis and Human Health", Mumbai, Jan. 28-30, 2013

Abstract

Corrosion of (IN-RAFMS) modified 9Cr-1Mo steel (P91) and Indian Reduced Activation Ferritic Martensitic Steel was studied in static lead-17 atom% lithium eutectic for 355 h at 773 K. Exposure to molten Pb-17Li led to loss of weight in P91 material whereas IN-RAFMS gained weight which was possibly due to longer incubation period and post-exposure surface oxidation. Depletion of Fe and Cr occurred from a thin surface layer in both P91 and IN RAFMS although higher oxygen buildup on the surface of IN-RAFMS justified its weight gain.

Introduction

The Lead-Lithium cooled Ceramic Breeder (LLCB) blanket concept proposed by India for testing at ITER; uses lead-17 atom % lithium (Pb-17Li) eutectic as multiplier, breeder, and coolant for the CB zones. [1] A serious problem arising from the use of Pb-17Li is the corrosion of the containment material and its deleterious effect on the mechanical properties. [2] Thus, the choice of the best suited material becomes critical and includes consideration of its thermo-mechanical properties, capability to withstand radiation and compatibility with the coolant. Considering the mechanical integrity and radiation stability aspects; ferritic - martensitic (FM) steels containing low Ni and 7%-10% Cr and more recently, the reduced activation varieties of FM steels have been considered as potential candidates for fusion

reactor applications. [3] The Indian variety of Reduced Activation Ferritic Martensitic Steel (IN-RAFMS) has been derived from its surrogate material, modified 9Cr-1Mo steel (P91) by replacing the radioactive elements like Mo and Nb by W and Ta respectively. [4] The high temperature corrosion compatibility of such materials with Pb-17Li over a specific time interval will be an important parameter in qualifying such steels within the operating band of fusion reactors like ITER. [5] In this regard, the compatibility of P91 and IN-RAFMS was studied in molten Pb-17Li at 773 K for duration of 355 h and the results have been reported here.

Experimental

Fig. 1 shows the schematic of two static corrosion test capsules specifically developed for high temperature corrosion testing in liquid metals and alloys. Each

BARC NEWSLETTER

Founder's Day

capsule consists of a one end closed SS316L cylinder having 12 mm I.D. for containing the liquid metal/ alloy. Rectangular shaped metallic samples of 2 mm thickness having a hole of 4 mm diameter drilled on one side are initially prepared by wire EDM cutting and later by metallographic grinding, diamond polishing and ultrasonic cleaning. The samples are tied to a molybdenum rod with the help of molybdenum wires and the rod is fixed to the top cover of the capsule which is also made of SS316L. After the sample assembly is inserted into the test capsule, it is filled with solid Pb-17Li chunks of required quantity which will allow complete dipping of the samples in molten condition. Later the top cover is welded to the capsule and a positive pressure of high purity argon gas is maintained inside it. The set up is heated by coil heaters having 3 kW capacity and temperature of the capsule are monitored by K- type thermocouples. In the present experiment, two such capsules viz. Tube A and Tube B; having 4 samples each of IN-RAFMS and P91 respectively, were maintained at 773 K for 355 h continuously.

Afterwards, the samples were separated from molten Pb-17Li under inert gas atmosphere and later cleaned off the adherent Pb-17Li with a mixture of acetic acid, acetone and hydrogen peroxide in the ratio 1:1:1. The weight loss of the samples on exposure was measured to obtain the rate of weight change. Thereafter, the cross section of the samples were analyzed through optical microscopy and Scanning Electron Microscope coupled with Energy Dispersive Spectrometry (SEM – EDS) for analysis of micro-structural and composition changes due to Pb-17Li exposure.

Results and Discussion

The P91 samples showed an average weight loss of 0.9 mg after exposure to Pb-17Li for 355 h as indicated in table I. This could be extrapolated to a corrosion rate of $2.53 \mu\text{g/h}$ for P91 in static Pb-17Li. If the sample dimensions are taken into account, this weight loss would lead to a thickness reduction rate of $0.026 \mu\text{m/yr}$ as shown in table II. It is expected that this corrosion rate will be magnified in an actual fusion reactor system, due to the presence of flowing Pb-

17Li which would enhance its corrosive capability. Moreover, the existence of high intensity magnetic field would create a change in the velocity profile of the flowing Pb-17Li thereby significantly affecting its interaction with the structural material [6]. On the other hand, no weight loss was observed for the IN-RAFMS material. Instead, gain in weight was noted at an average rate of $45.07 \mu\text{g/h}$ (Table 1). Such weight gains may be due to immediate surface oxidation post exposure and longer incubation periods (up to 500 h) as have been previously reported for various other

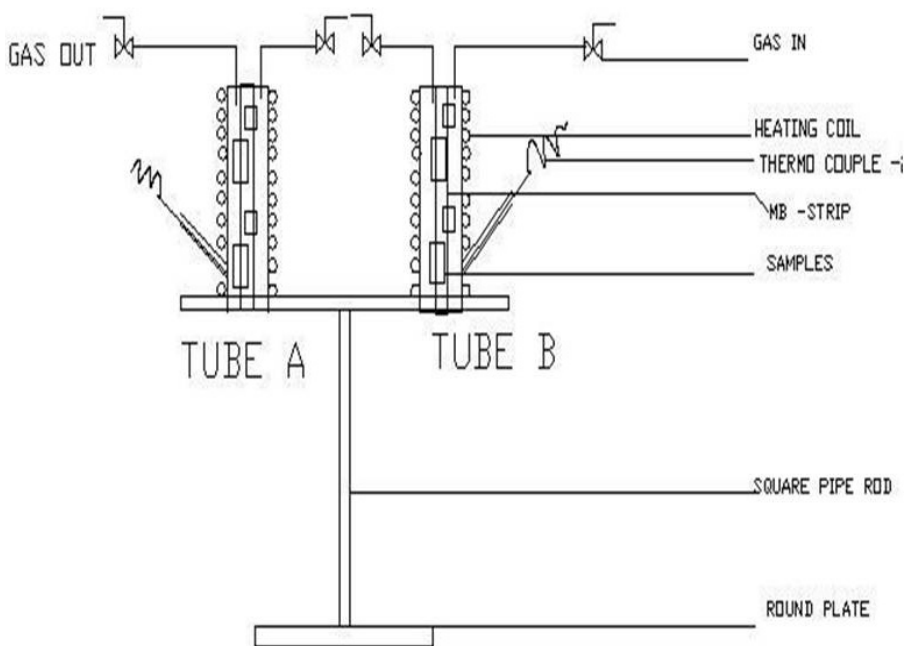


Fig 1: The static corrosion test facility

BARC NEWSLETTER

Founder's Day

Table 1: Weight loss of the P91 and IN RAFMS sample after exposure to Pb-17Li at 773 K for 355 h

Sample	Initial weight (before exposure) = a (gm)	Final weight (after exposure and cleaning) = b (gm)	Weight Change $\Delta m = b - a = c$ (gm)	% Weight Change $(c \div a) * 100$	Rate of weight change $(\Delta m) \div 355$ ($\mu\text{g/h}$)
P91	1.434 \pm 0.002	1.4331 \pm 0.001	0.0009	0.06276	2.53
IN-RAFMS	5.62 \pm 0.001	5.6360 \pm 0.002	0.016	0.28469	45.07

Table 2: - Thickness Reduction of a P91 and IN RAFMS sample after exposure to Pb-17Li at 773 K for 355 h

Sample	Weight Change Δm (mg)	Dimension of the exposed surface (L-length, B- breadth)	Change in thickness $\Delta H = \Delta m / (\text{surface area} \times \text{density})$, (μm) ($d = 7.8$)	Rate of thickness change ($\mu\text{m}/\text{hr}$)
P91	-0.9	L=11.39mm, B=9.56mm	0.528	-0.0026
IN-RAFMS	+16	L=20mm, b=12.4mm	4.13	+0.0116

RAFM steels.[7, 8] In case of surface oxidation, the weight gain of the IN-RAFMS sample will correspond to thickness increase at a rate of 0.0116 $\mu\text{m}/\text{hr}$ as shown in Table 2.

Fig. 2 show the optical micrographs of the cross section of the P91 sample before and after exposure to Pb-17Li at 773 K. As compared to the unexposed surface in Fig. 2(a), the exposed surface in Fig. 2(b)

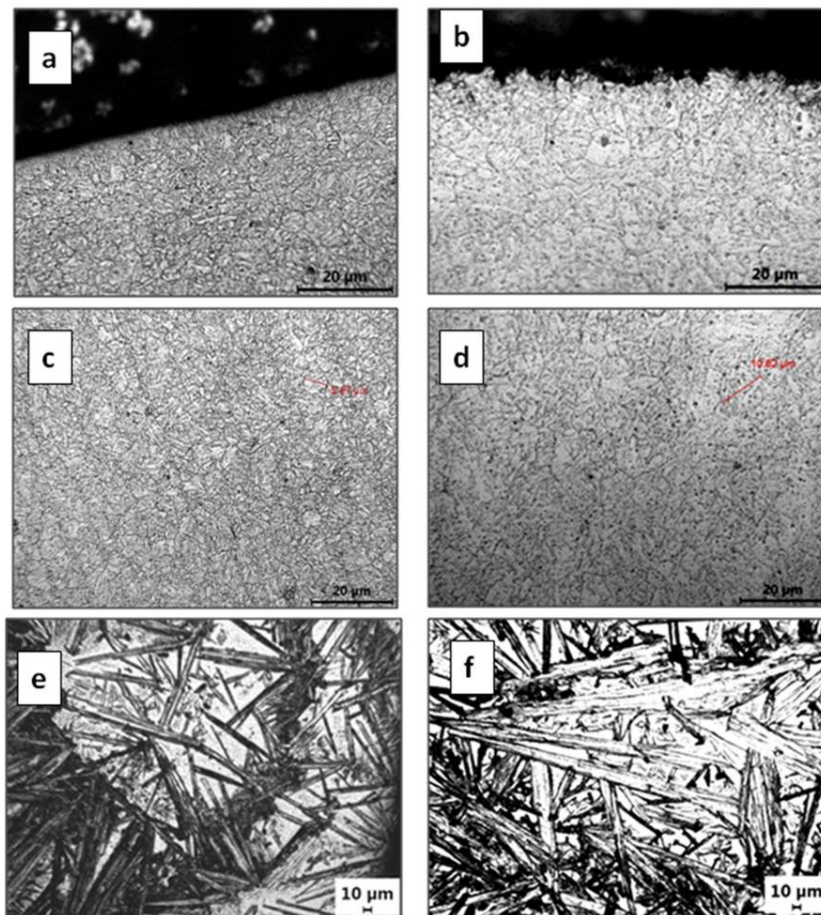


Fig 2 : Optical micrographs of P91 sample before and after exposure to Pb-17Li at 773 K for 355 h: (a) surface before exposure; (b) surface after exposure; (c) matrix before exposure; (d) matrix after exposure; (e) martensite lath before exposure; (f) martensite lath after exposure.

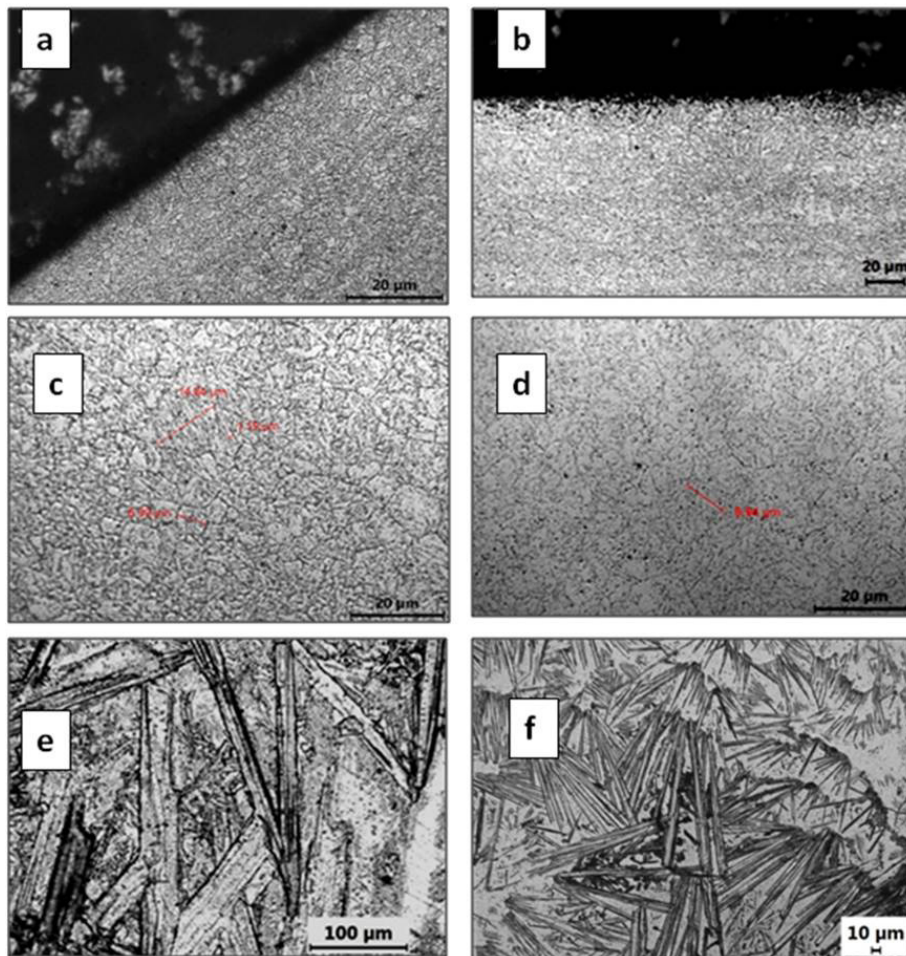


Fig 3 : Optical micrographs of IN RAFMS sample before and after exposure to Pb-17Li at 773 K for 355 h: (a) surface before exposure; (b) surface after exposure; (c) matrix before exposure; (d) matrix after exposure; (e) martensite lath before exposure; (f) martensite lath after exposure.

showed preferential attack along grain boundaries. Moreover, the grain size of P91 material was found to have almost doubled from $5.6 \mu\text{m}$ in the unexposed sample (Fig. 2(c)) to $10.6 \mu\text{m}$ (Fig. 2(d)) in the sample exposed to Pb-17Li. This is possibly because of the long term thermal ageing effect at 773K. Fig. 2(e) and 2(f) shows the martensite laths of the unexposed and exposed P91 material respectively. It could be observed that both the size and density of these laths had significantly increased after exposure to Pb-17Li for 355 h.

Fig. 3 shows the optical micrographs of the cross section of the IN-RAFMS sample before and after exposure to Pb-17Li at 773 K. The unexposed

surface of IN RAFMS is shown in Fig. 3(a). As compared to the P91 material, preferential grain boundary attack was not observed on the surface of the IN-RAFMS material exposed to Pb-17Li as shown in Fig. 3(b). Moreover, the grain size of IN-RAFMS became more uniform after exposure (Fig. 3(d)) as compared to the uneven grain size distribution noted in the unexposed matrix of IN-RAFMS in Fig. 3(c). It could be observed that the martensitic lath size of unexposed IN-RAFMS material (Fig. 3(e)) was larger than that of P91 (Fig. 2(e)). Nevertheless, the lath size of IN-RAFMS decreased after exposure to Pb-17Li at 773 K (Fig. 43(f)) although an increase in lath density as noted in the case of P91, was observed in IN-RAFMS too.

BARC NEWSLETTER

Founder's Day

Fig. 4 (a) and (b) show the SEM images of the cross section of the P91 and IN-RAFMS samples after exposure to Pb-17Li. No affected layer was found on the Pb-17Li facing surface of both the exposed samples. However, when EDS line scans of Fe, Cr and O were taken across the sample boundaries; it was observed that the concentrations of Fe and Cr decreased slightly from their matrix compositions at the exposed surface of both the samples. As shown in Fig. 4(a), the oxygen concentration remained almost constant over the cross section of the P91 sample. The source of this oxygen could be from the metallographic grinding and polishing procedure followed during sample preparation. On the other hand, the oxygen content was found to increase significantly at Pb-17Li exposed surface of the IN-RAFMS sample as shown in Fig. 4(b.) This indicated that IN RAFMS material exposed to Pb-17Li is prone to post exposure surface oxidation which also explains the reason behind its weight gain.

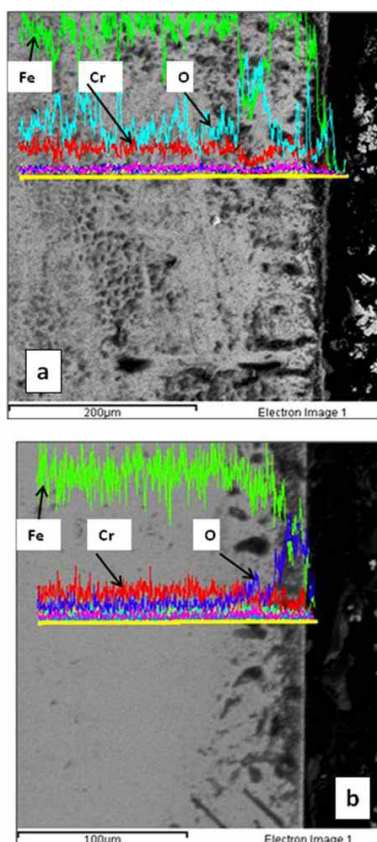


Fig 4: SEM images and EDS profiles of Fe, Cr and O on the (a) P91 and (b) IN-RAFMS sample exposed to Pb-17Li eutectic at 773 K for 355 h

Conclusion

1. The corrosion compatibility of P91 and IN-RAFMS material was tested in molten lead-17 atom% lithium eutectic for 355 h at 773 K in static condition.
2. Weight loss occurred at a rate of 2.53 $\mu\text{g/h}$ for P91 material whereas IN-RAFMS gained weight at a rate of 45 $\mu\text{g/h}$. The weight gain in IN-RAFMS was possibly due to a higher incubation period and post-exposure surface oxidation.
3. Corrosion of both P91 and IN-RAFMS in Pb-17Li at 773K led to depletion of Fe and Cr from the exposed surface. Grain boundary attack and grain size increase was prominent in P91. The size of martensitic laths increased in P91 whereas decreased in the case of IN-RAFMS.

References

1. E. Rajendra Kumar C. Danani, I. Sandeep, Ch. Chakrapani, N. Ravi Pragash, V. Chaudhari, C. Rotti, P. M. Raole, J. Alphonsa, S. P. Deshpande., *Fusion Engineering and Design*, 83 [2008]1169–1172
2. P. Chakraborty, P. K. Pradhan, R. K. Fotedar and N. Krishnamurthy, *Journal of Materials Research and Technology*, doi : 10.1016/j.jmrt.2013.04.001, [2013]
3. N. Baluc, D. S. Gelles, S. Jitsukawa, A. Kimura, R. L. Klueh, G. R. Odette, et al., *Journal of Nuclear Materials* 367–370 (2007) 33–41
4. B. Raj, K. B. S. Rao, A. K. Bhaduri, *Fusion Engineering and Design*, 85 (2010) 1460–1468.
5. H. Glasbrenner, J. Konys, Z. Vob, *Journal of Nuclear Materials*, 281 (2000) 225-230
6. E. Platacis, A. Ziks, A. Poznjak, F. Muktepavela, A. Shisko, S. Sarada, P. Chakraborty, K. Sanjay, M. Vrushank, R. Fotedar, E.K. Rajendra, A.K. Suri, *Magnetohydrodynamics*, 48 (2) [2012] 343-350.
7. Y. Chena,, Q. Huanga, S. Gaoa, Z. Zhua, X. Ling, Y. Songa, Y. Chenb and W. Wanga, *Fusion Engineering and Design* 85 (2010) 1909–1912
8. H. Glasbrenner, J. Konys, H.D. Rohrig, K. Stein-Fechner, Z. Vosset, *Journal of Nuclear Materials*, 283-287 [2000] 1332-1335

STRUCTURE BASED VARIATION IN THE ANTIMUTAGENIC/ ANTIOXIDANT PROPERTIES OF DIFFERENT NAPHTHOQUINONES

Sanjeev Kumar, Satyendra Gautam and Arun Sharma
Food Technology Division

This paper received the Best poster award at the XXXVIII Annual Conference of Environmental Mutagen Society of India (EMSI) on "Current Perspectives on Environmental Mutagenesis and Human Health", Mumbai, Jan. 28-30, 2013

Abstract

The structure-function relationships of the naphthoquinone phytochemicals, plumbagin (5-hydroxyl-2-methyl-1,4-naphthoquinone), juglone (5-hydroxyl-1,4-naphthoquinone), and menadione (2-methyl-1,4-naphthoquinone), have been studied. Plumbagin showed strong antimutagenic and antioxidant activities, whereas juglone displayed only strong antimutagenic, and menadione only strong antioxidant activities. Thus, functional groups (5-OH/2-CH₃) seem to play important roles in the differential bioactivity of naphthoquinones. *Escherichia coli* microarray analysis as well as studies with its single-gene knockouts showed that *ybaK* (tRNA editing) and *speE* (spermidine synthesis), reported to prevent mistranslation, are likely to be involved in the antimutagenicity displayed by juglone, and *sodC* (superoxide dismutase) to be involved in the antioxidant activity of menadione.

Introduction

Mutation is an important cause of the initiation and progression of many diseases, including atherosclerosis, heart diseases, and cancer. Hence, phytochemicals that reduce mutagenesis may be considered to have health protective potential. Naphthoquinones, such as ubiquinone, plastoquinone, and K vitamins, have already been reported for multiple health promoting effects. However, still in many cases their mechanism of action is not clear. Hence, to address this issue, three structural naphthoquinones analogues - plumbagin, menadione, and juglone were examined for antimutagenic and antioxidant potential. Plumbagin (PL), a yellow compound isolated from the genus *Plumbago*, has been reported to have anti-inflammatory, anticarcinogenic, immunosuppressive, and anti-atherosclerotic activities [1]. Juglone (JU), known in the food industry as natural brown, is isolated from the black walnut (*Juglans nigra*) and other plants of the Juglandaceae family. It has been

used as an herbicide, a dye for cloth and inks, and a colouring agent for foods and cosmetics. Menadione (2-methyl-1,4-naphthoquinone) (ME) is a synthetic compound also known as vitamin K₃. On the 1,4-naphthoquinone nucleus, plumbagin possesses 5-hydroxyl and 2-methyl functional groups, whereas juglone has only the 5-hydroxyl and menadione only the 2-methyl group. To further understand the molecular mechanisms contributing to these activities, microarray transcriptome analyses were performed using *E. coli* cells grown in the presence of each of these naphthoquinones, separately. The relevance of certain upregulated genes was tested using *E. coli* knockout mutants.

Material and Methods

Analysis of antimutagenicity

The antimutagenic properties of these naphthoquinones were evaluated by the Ames test and

BARC NEWSLETTER

Founder's Day

rifampicin resistance assay against ultraviolet (UV) and ethyl methanesulfonate (EMS) mutagenesis. The Ames test measures reversion of auxotrophic his- mutants of *Salmonella typhimurium* and the rifampicin resistance assay measures acquisition of rifampicin resistance by *Escherichia coli* cells due to mutations in the *rpoB* gene, which encodes the β subunit of RNA polymerase [2,3].

Analysis of antioxidant activity

***In vitro* antioxidant assays**

It was performed by DPPH (2,2-diphenyl-1-picryl-hydrazyl) radical scavenging assay at 517 nm [4] and also hydroxyl radical scavenging by estimating malondialdehyde at 532 nm [5]. Superoxide scavenging activity was measured by the nitro blue tetrazolium assay [5]. Reducing power was determined using the potassium ferricyanide reduction method [4]. Protection of plasmid DNA from gamma radiation-induced oxidative damage was assayed using agarose gel electrophoresis.

***In vivo* antioxidant assays**

Protection of *E. coli* cells by these naphthoquinones against oxidative damage caused by gamma radiation was assayed by survival analysis using fluorescence activated cell sorting (FACS) using propidium iodide staining and calculating the decimal reduction dose (D_{10}). Similarly, their protective effect on the functionality of radiation exposed pBR322 was measured in terms of its transformation efficiency on selection plates [LB agar plates containing ampicillin (50 μ g/ml)], and the transformants were scored/ 10^6 cells/ μ g of DNA.

Molecular mechanism contributing to antimutagenic/antioxidant activities

Analysis of effect on SOS phenotype upon mutagenic exposure (LexA status and cell filamentation frequency)

Overnight grown cultures of *E. coli* were subcultured in LB, grown to mid-log phase, and exposed to mutagens

(UV 15 s; EMS 133 mM for 45 min), then incubated in dark for 15 min at ambient temperature to monitor the transient degradation of LexA [6]. The status of cell filamentation in *E. coli* was assayed by crystal violet staining followed by light microscopy [6]. The cells were grouped into four categories, based on length of filaments: 3-5 μ m, 6-15 μ m, 15-25 μ m, and >25 μ m.

Microarray analysis

Overnight grown *E. coli* cells were diluted in phosphate buffer saline (PBS) to ~ 500 cfu/ml. An aliquot (100 μ l) was added to 5 ml LB and grown (~ 18 h) until cell density reached to $\sim 10^9$ cfu/ml. Total RNA was isolated from the cell pellet using RNeasy Mini Kit column (Qiagen, CA, USA). RNA was quantified and quality checked using ND 1000 spectrophotometer (Nanodrop, ThermoScientific, USA) and a Bio-analyzer (Agilent, USA). Affymetrix *E. coli* genome 2.0 arrays were used for microarray analysis. *E. coli* samples for hybridization were processed using 3' in vitro transcription (3' IVT Express Kit, Affymetrix, USA). In the GeneChip® 3' IVT Express Protocol, total RNA was reverse transcribed to first-strand cDNA, which was further converted into a dsDNA template. This was later transcribed *in vitro* to amplified RNA (aRNA) having biotin-conjugated nucleotides. The aRNA was then purified to remove unincorporated NTPs, salts, enzymes, and inorganic phosphate. Fragmentation of the biotin-labelled aRNA was performed by array fragmentation reagents and used as sample for hybridization onto GeneChip® 3' expression arrays. The role of genes showing differential upregulation in the presence of test compounds were further ascertained by antimutagenicity or antioxidant analysis using their *E. coli* knockout strains.

Measurement of intracellular reactive oxygen species (ROS)

ROS was measured in the wild type *E. coli* cells and *sodC* knockout by H2DCFDA (2',7'-dichlorofluorescein

BARC NEWSLETTER

Founder's Day

diacetate) staining in the presence and absence of these naphthoquinones. The cells were grown overnight in LB, centrifuged, resuspended in PBS, diluted to ~ 108 cfu/ml, subjected to gamma radiation (0.07 kGy) in presence of H2DCFDA (2',7'-dichlorofluorescein diacetate; 25 μ M), and further incubated for 40 min in the dark at 37°C. Fluorescence intensity was measured using a microplate reader (Bio-Tek, Vermont, USA) at excitation and emission wavelengths of 488 and 525 nm, respectively.

Results and Discussion

PL and JU displayed strong antimutagenicity

Suppression of UV/EMS-induced reversion in S. typhimurium TA102/TA100

Spontaneous reversion (SR) of *S. typhimurium* TA102 and TA100 was found to be 170 and 90 revertants/plate, respectively. UV (10 s) treated *S. typhimurium* TA102 cells showed ~ 1800 revertants/plate, ~ 10 -fold higher than SR. PL was found to inhibit this reversion by 26 and 39% at 50 and 100 μ M, respectively. Significant inhibition was also observed with JU. Only 9% inhibition was noted with ME, even at 100 μ M. A similar trend was observed with the UV dose of 15 s. Similarly, EMS (66.5 mM) treatment of *S. typhimurium* TA102 strain resulted in 600 revertants/plate, more than 3-fold above SR. PL and JU significantly inhibited this reversion. Antimutagenicity of ME was only 5% at 100 μ M. With EMS (66.5 mM), the number of revertants/plate was 1467, ~ 16 -fold higher than SR. PL inhibited reversion by 67 and 87% at 50 and 100 μ M, respectively. JU inhibited the reversion by 72 and 87% at 50 and 100 μ M, respectively. Only slight inhibition of mutagenesis was observed with ME (100 μ M). Similar trend was observed with EMS at 133 mM. Inhibition of UV/EMS-induced Rif^R mutation in *E. coli* Spontaneous mutation leading to rifampicin resistance in *E. coli* was low (< 1 cfu/100 million cells). UV (10 s) treatment resulted in Rif^R mutant frequency close to 450 cfu/100 million cells. PL reduced the Rif^R frequency

by 41 and 75% at 50 and 100 μ M, respectively. JU reduced mutation frequency by 46 and 76% at 50 and 100 μ M, respectively. ME (100 μ M) was found to have little effect. A similar trend was observed with the UV dose of 15 s. EMS (66.5 mM) treatment of cells resulted in Rif^R mutant frequency ~ 1070 cfu/100 million cells. PL reduced the frequency by 58 and 66% at 50 and 100 μ M, while JU by 59 and 69% at 50 and 100 μ M, respectively. ME had little effect, even at 100 μ M. A similar trend was noticed with EMS at 133 mM.

PL and ME displayed strong antioxidant capacity

In vitro antioxidant potential

The percent scavenging of hydroxyl radical was 26, 23 and 9% for PL, ME, and JU, respectively, at ≥ 120 μ M. Scavenging of superoxide radical was 27 and 30% at ≥ 120 μ M of PL and ME, respectively, whereas negligible scavenging was observed with JU. DPPH radical scavenging activity and ferric reducing power of these three compounds were very low (5-9%) even at 160 μ M. PL and ME was found to protect plasmid pBR322 DNA topology against oxidative damage from gamma radiation exposure.

Protection of E. coli cells from gamma radiation-induced oxidative damage

The effect of these compounds on the viability of *E. coli* cells exposed to gamma radiation was assessed by FACS analysis. Killing of 27% of the cells was observed at 250 Gy dose, which was significantly reduced in the presence of PL in a concentration-dependent manner. With 25 μ M of PL, $\sim 13\%$ cell killing was noticed, which further reduced to $\sim 8\%$ at 50 μ M. In the presence of ME (25 μ M) radiation-induced cell killing was $\sim 15\%$. However, in the presence of JU (25 μ M) not much protection was observed and the cell killing was found to be comparatively high ($\sim 21\%$). The decimal reduction dose (D10) for gamma radiation was found to be 142 Gy for *E. coli* cells. In the presence of PL (25 and 50 μ M), the D10 value increased to 196 and 262

BARC NEWSLETTER

Founder's Day

Gy, respectively. For ME (25 μ M), the D10 was very similar to that for PL. However, with JU, the D10 was not quite less (166 Gy). PL and ME were also found to protect plasmid pBR322 DNA functionality against oxidative damage from gamma radiation exposure in terms of transformation efficiency.

Mechanism of antimutagenic/antioxidant activity

Suppression of UV-induced SOS response in *E. coli* by PL and JU

The level of LexA repressor protein in *E. coli* was analyzed by Western blotting (Fig. 1). Upon UV exposure, almost complete degradation of LexA was observed, which was found to be 46% protected in the presence of PL, and 35% in the presence of JU (Fig. 1A). Less protection (14%) was observed in case of ME (Fig. 1A). In EMS-treated cells, LexA level was not affected as EMS works through SOS-independent mechanism (Fig. 1B). Also, status of positive control (RecA) remained unchanged (Fig. 1C and D). The morphology of UV exposed *E. coli* cells changed drastically to long filaments after growing for 2 h (Fig. 2A). These cells failed to septate upon division resulting in the filamentous morphology. The filamentation frequency in control cells was \sim 0.3% which increased to 38% upon UV-exposure (Fig. 2A). PL or JU reduced cell filamentation frequency to \sim 1/4 (\sim 10%); however, ME did not affect the frequency significantly (Fig. 2B-D).

Differential gene expression in *E. coli* cells in presence JU and ME

Transcriptome analysis of *E. coli* indicated that many genes showed differential expression (EMBL-EBI, MIAMExpress, accession number: E-MEXP-3765). Further study was focused on some of the genes. In *E. coli* cells grown in the presence of PL and JU, upregulation of genes such as *rep*, *ybaK*, *speE*, and *yjfc*

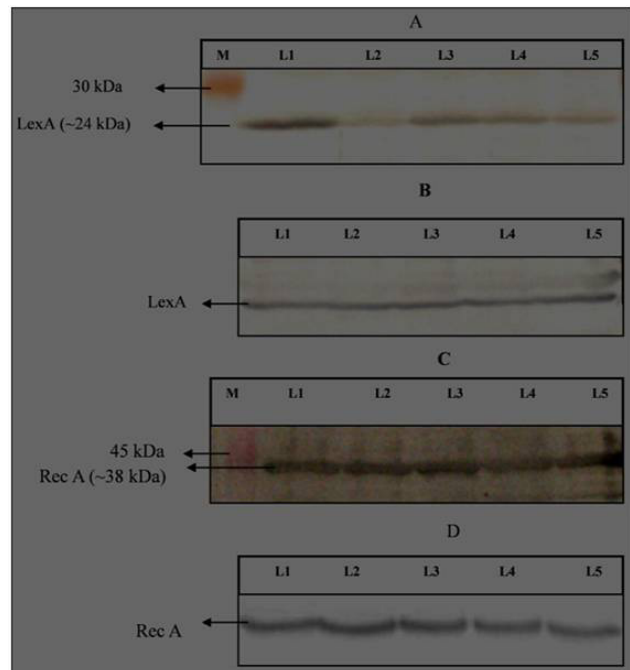


Fig. 1: LexA profile of *E. coli* MG1655 in absence or presence of PL and its structural analogues (50 μ M), (A) UV (15 s) treated, and (B) EMS (133 mM) treated, (C and D) status of RecA (positive control) in UV and EMS treated cells, respectively. M: colour protein molecular weight marker; L1: control; L2-L5: treated in presence of vehicle control DMSO (L2); PL (L3); JU (L4); and ME (L5).

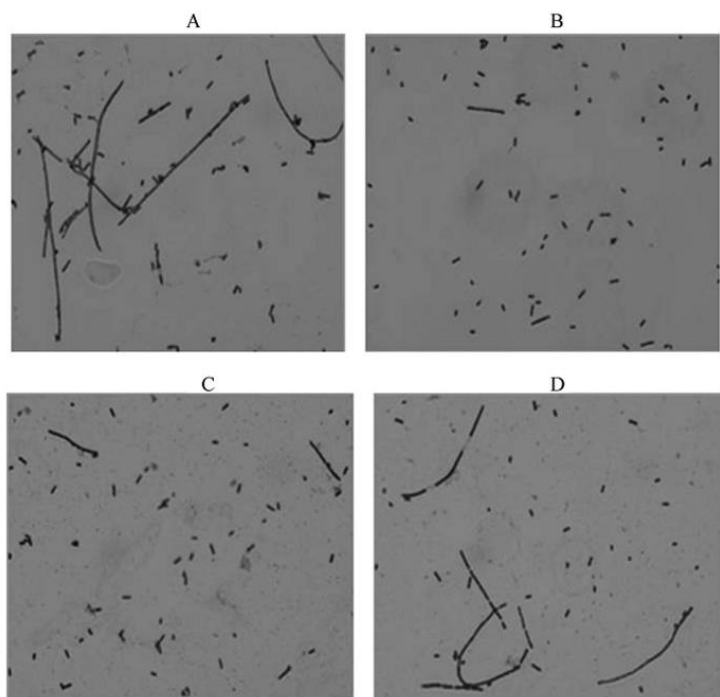


Fig. 2. UV induced cell filamentation in *E. coli* MG1655 cells in absence or presence of PL and its structural analogues (50 μ M). (A-D) UV (15 s) treated in presence of vehicle control DMSO (0.75%) (A); PL (B); JU (C); and ME (D).

BARC NEWSLETTER

Founder's Day

was observed. These genes are reported to be involved in DNA replication and repair, tRNA editing, spermidine synthesis, and glutathionyl spermidine synthesis, respectively. In case of PL and ME-treated cells, upregulation of *sodC* was observed. Gene *xthA*, reported to have a repair function during oxidative stress, was also upregulated. Gene *hycB*, encoding an intermediate electron carrier between hydrogenase 3 and fumarate dehydrogenase, and *ligA*, encoding an enzyme that catalyses the formation of phosphodiester bonds in duplex DNA, were also found to be upregulated in cells grown with PL and ME.

Dependence of antimutagenicity of JU on *ybaK* and *speE* gene functions

JU reduced UV induced mutagenicity by 78% in *E. coli* wild type (WT) (Fig. 3A). However, in *ybaK* and *speE* knockouts, JU reduced the mutagenicity only by 27 and 40%, respectively (Fig. 3A). Reduction in mutation frequency in UV-exposed *yjfC* and *rep* knockouts was ~68% in the presence of JU, indicating less dependence on these gene functions for the observed antimutagenicity of JU (Fig. 3A). With EMS-exposed cells, JU reduced mutagenicity by 58% in WT, which

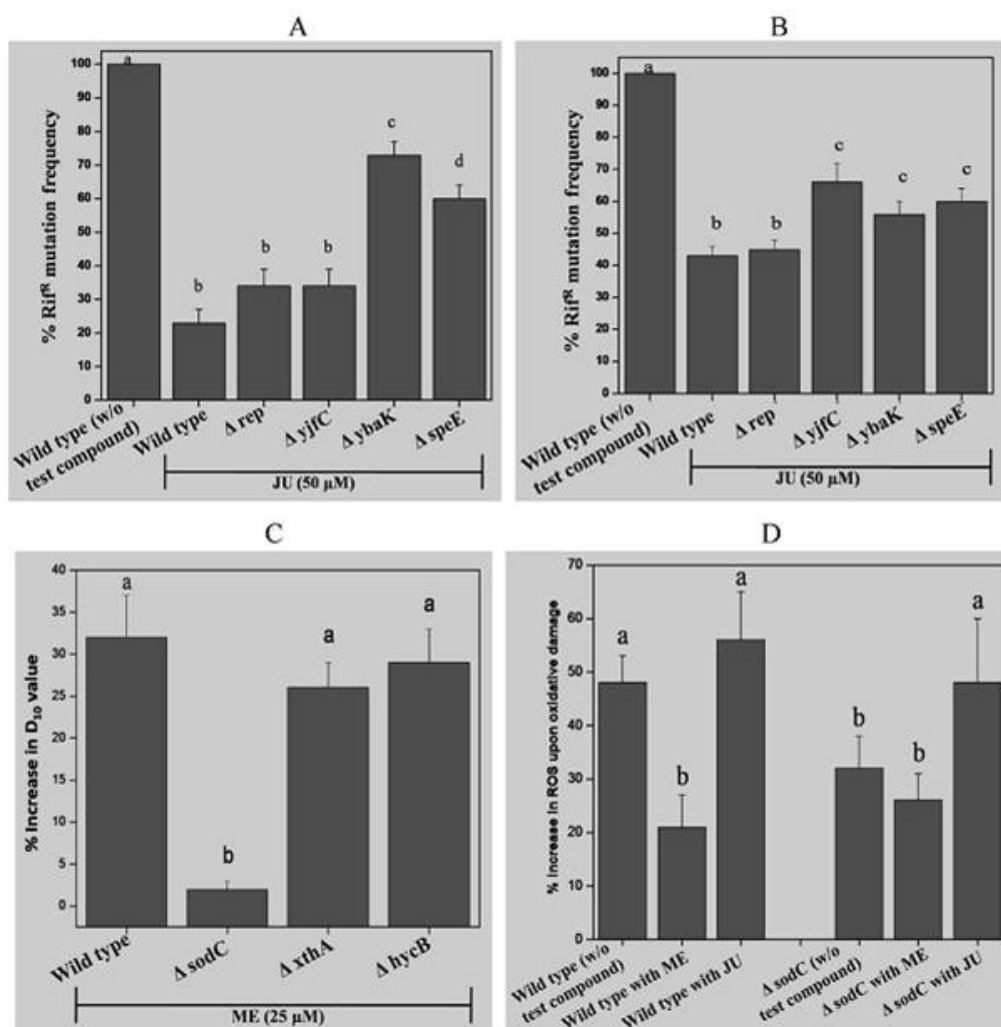


Fig. 3. Antimutagenic activity of JU (50 μM) in (A) UV (15 s) and (B) EMS (133 mM) treated *E. coli* MG1655 cells and its knockout strains; (C) cell viability in terms of decimal dose reduction (D₁₀) indicating protection against gamma radiation induced oxidative damage in presence of ME (25 μM) in *E. coli* MG1655 and its knockout strains; (D) increase in intracellular ROS level upon radiation exposure of *E. coli* MG1655 cells and its *sodC* knockout strain in presence of ME or JU (25 μM). Different letters on the top of the bars indicate significant difference in means at $p \leq 0.05$.

BARC NEWSLETTER

Founder's Day

was further reduced to 44% in *ybaK*, 41% in *speE*, and 34% in *yjfc* knockouts (Fig. 3B). Reduction in mutant frequency observed in EMS mutagenesis was 53% in *rep* knockout, close to WT in the presence of JU (Fig. 3B).

Requirement of *sodC* gene function for ME mediated rescue of *E. coli* cells from radiation induced death

Increase in D_{10} value of radiation exposed *E. coli* (WT) cells in the presence of ME was 32%, whereas it was negligible (2%) in the cells of *sodC* knockout (Fig. 3C). In the other knockouts, *xthA* and *hycB*, the increases in D_{10} were 26 and 29%, respectively (Fig. 3C).

Requirement of *sodC* gene function for ME mediated suppression of ROS generation

In *E. coli* (WT) cells grown in the absence of ME, the increase in ROS upon radiation exposure was found to be 48% which was reduced to 22% in the presence of ME (Fig. 3D). However, no reduction in ROS level was observed in cells grown in the presence of JU (Fig. 3D). In the *sodC* knockout, these observed differences were nullified. In *sodC* knockout grown in the absence and presence of ME, the increase in ROS was 32 and 27%, respectively (Fig. 3D). As observed in case of WT cells, in the *sodC* knockout too, JU did not show any reduction in ROS level (Fig. 3D).

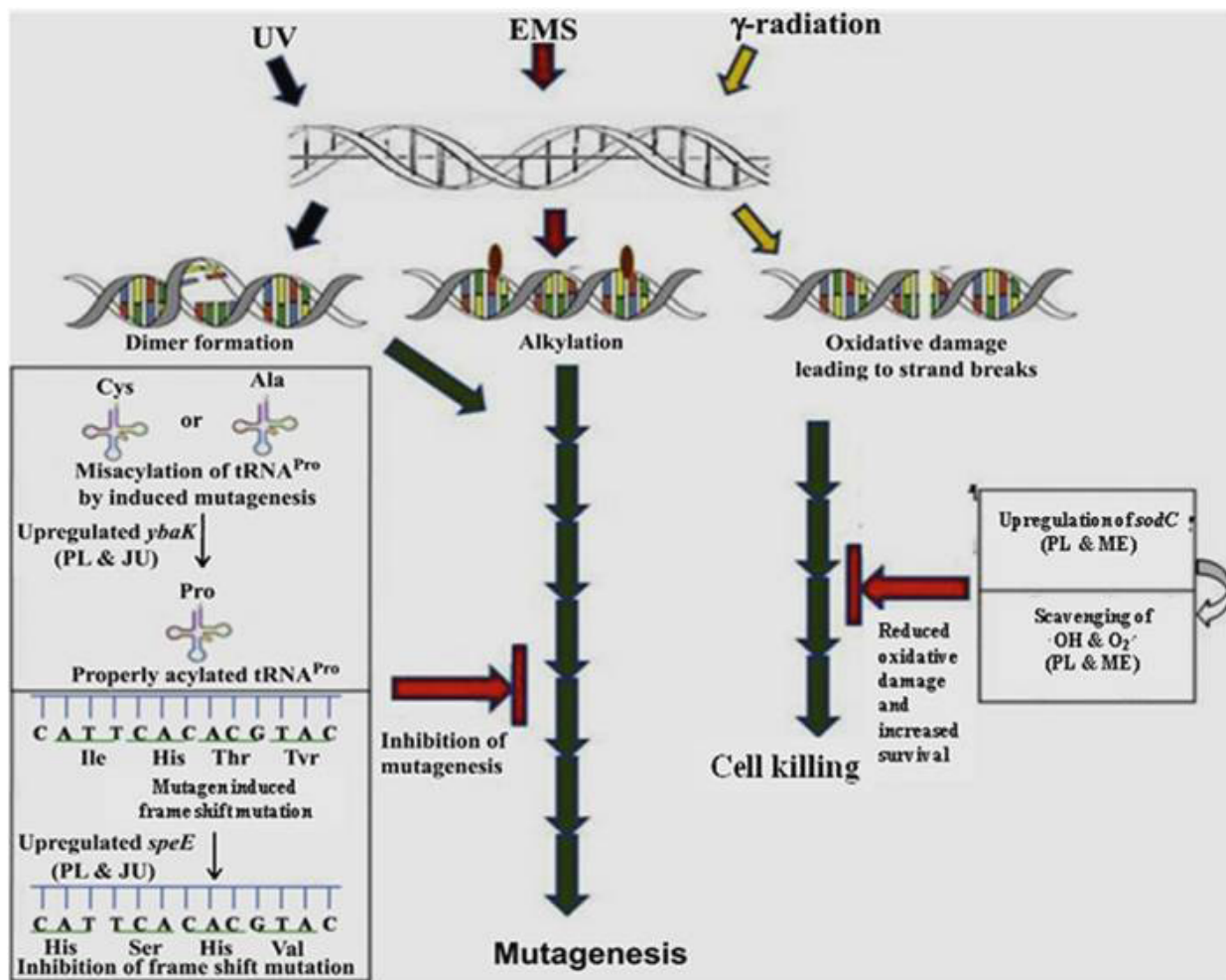


Fig. 4. Model to explain the differential antimutagenic/antioxidant potential of PL and its analogues. PL and JU upregulated *ybaK* and *speE* genes leading to inhibition of mistranslation contributing in reduced mutagenicity upon mutagenic challenges. PL and ME upregulated *sodC* gene resulting in $O_2^{\bullet-}$ scavenging. Additionally, direct free radical ($\cdot OH$ and $O_2^{\bullet-}$) scavenging activity of PL and ME also reduced the extent of oxidant-induced DNA damage, eventually leading to increased survival.

BARC NEWSLETTER

Founder's Day

Based on these observations, a model is proposed to explain the antimutagenic activity displayed by PL and JU against UV and EMS-induced mutagenic damage and antioxidant activity of PL and ME against oxidative damage (Fig. 4). Transcriptome analysis has indicated differential expression of genes by PL, JU and ME. The upregulation of *speE* and *ybaK* genes reduces mistranslation, as the *speE* gene is involved in maintenance of the proper reading frame, whereas the *ybaK* gene is involved in hydrolysis of wrongly aminoacylated tRNA. Thus, inhibition of mistranslation could eventually lead to suppression of SOS-dependent or independent mutagenesis. On the other hand, the upregulation of *sodC* gene by PL and ME may lead to increased scavenging of hydroxyl and superoxide radical, resulting in the observed reduction in cell killing in oxidant-exposed cells. This study demonstrates a strong structure-function relationship among the naphthoquinones and provides a mechanistic view of their differential activity.

References

1. Babula P, Adam V, Havel L, Kizek R (2009) Noteworthy secondary metabolites Naphthoquinones-their occurrence, pharmacological properties and analysis. *Curr Pharm Anal* 5:47–68.
2. Maron DM, Ames BN (1983) Revised methods of the Salmonella mutagenicity test. *Mutat Res* 113:173-215.
3. Kumar S, Gautam S, Sharma A (2013) Antimutagenic and antioxidant properties of plumbagin and other naphthoquinones. *Mutat Res* 755:30-41.
4. Kumar S, Gautam S, Powar S, Sharma A (2010) Microbial decontamination of medicinally important herbals using gamma radiation and their biochemical characterization. *Food Chem* 119:328-335.
5. Kunchandy E, Rao MNA (1990) Oxygen radical scavenging activity of curcumin. *Int J Pharm* 58:237–240.
6. Saxena S, Gautam S, Maru G, Kawle D, Sharma A (2012) Suppression of error prone pathway is responsible for antimutagenic activity of honey. *Food Chem Toxicol* 50:625-633.

PERTURBATION OF CELLULAR REDOX AS A NOVEL STRATEGY TO AMELIORATE RADIATION-INDUCED GASTRO-INTESTINAL SYNDROME

Lokesh Gambhir, Rahul Checker, Deepak Sharma and S. Santosh Kumar
Radiation Biology and Health Sciences Division

This paper received the Best Poster Award at the International Conference on Advances in Free Radicals, Redox Signalling and Translational Antioxidant Research, Lucknow, Jan. 30- Feb. 1, 2013

Abstract

Intestinal epithelial cells and stem cells are highly sensitive to ionizing radiation as they are continuously proliferating. These cells are damaged during radiotherapy of gastro-intestinal (GI) cancers resulting in severe side effects including diarrhoea, loss of appetite and weight loss. Here we describe a novel strategy to mitigate radiation induced GI syndrome using a pro-oxidant molecule 1,4-naphthoquinone (NQ). Administration of NQ to mice rescued them against whole body irradiation (8Gy) induced mortality by perturbing cellular redox leading to activation of pro-survival transcription factor Nrf-2 in intestinal epithelial cells.

Introduction

Enhanced use of radiation in various aspects of human life may lead to situations like planned or unplanned exposure to radiations. Planned exposure is the result of the use of radiation in diagnosis and treatment in radiation therapy. In spite of the fact that radiotherapy is an effective tool for cancer treatment, the normal tissues adjacent to the tumor are exposed to radiation which limits the therapeutic efficacy. High sensitivity of the intestine tract due to high proliferation rate is one of the factors contributing to the adverse side effects of cancer radio therapy. Ionizing radiation induced mortality is largely dependent on the dose of radiation received by organism. Acute effects after Whole body irradiation of 8Gy are known as gastro-intestinal syndrome that causes death within 7 to 10 days. Gastro-intestine (GI) tract is lined by numerous luminal protrusions villi and submucosal invaginations called crypts of Lieberkuhn constituting the absorptive surface of small intestine called as jejunum. GI syndrome is characterized by loss of absorptive surface

of small intestine due to denudation of villi and apoptosis in crypts.

Although different radiation countermeasures are currently under development but none of them have been approved by food and drug administration for human use. Previously reported countermeasures against GI syndrome like fibroblast growth factor, TLR 5 agonist CBLB502, S1P and anti-ceramide antibody offered protection by reducing apoptosis in intestinal crypts (1,2). Radiation exposure is followed by a marked increase in oxidative stress induced cellular damage, thus targeting a molecule which serves as a master regulator of antioxidant and cytoprotective gene expression seems a logical approach. Nuclear factor erythroid 2- related factor 2 (Nrf-2) is a redox sensitive transcription factor which upon activation translocates into the nucleus and binds to antioxidant response element (ARE) and induces the expression of phase II detoxifying enzymes, anti-oxidant enzymes and stress responsive proteins. 1,4-naphthoquinone (NQ), a pro-oxidant, is a strong electrophile with high

BARC NEWSLETTER

Founder's Day

affinity for cellular nucleophiles like thiols of cysteine group present in proteins contributing to its biological activity. Hence we postulated to explore the potential of NQ to protect against radiation induced gastro-intestinal syndrome and also delineate the underlying molecular mechanism.

Results

NQ protected against radiation induced cell death in INT 407 (human intestinal epithelial cells)

NQ treatment prior to radiation dose of 6Gysignificantly protected INT 407 cells against radiation induced loss of clonogenicity. Radiation induced apoptotic death is marked by an increased caspase activity. NQ pre-treatment significantly inhibited radiation induced caspase-3 activity.

NQ modulated cellular redox status by increasing cellular ROS and depleting GSH/GSSG

Perturbation in cellular redox by NQ treatment was marked by a transient increase in basal ROS levels compare to control as measured by redox sensitive fluorescent dye (Fig. 1A) and a transient depletion in GSH/GSSG ratio (Fig. 1B).

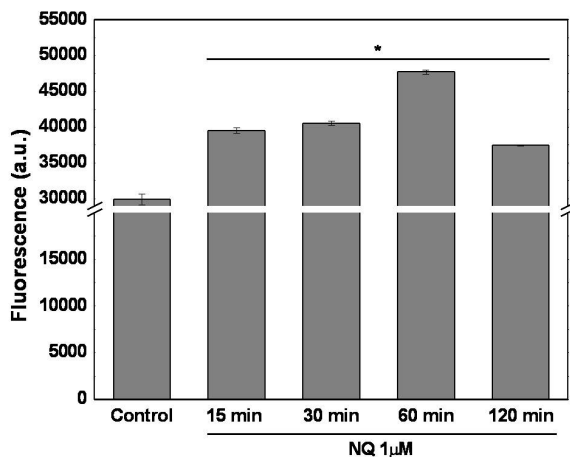


Fig. 1A: A transient increase in basal ROS levels compare to control as measured by redox sensitive fluorescent dye

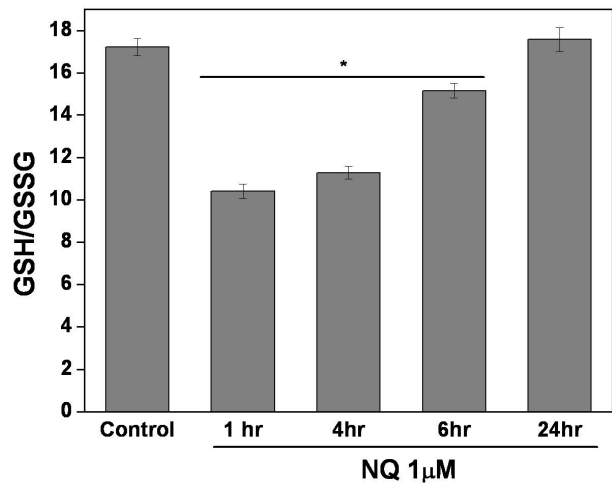


Fig. 1B : A transient depletion in GSH/GSSG ratio

NQ induced activation and upregulation of Nrf2 and its dependent gene in INT 407

NQ treatment showed an increase in nuclear translocation of Nrf2 in a time dependent manner (Fig. 2A). NQ treatment significantly enhanced the mRNA expression of Nrf2 and its dependent gene hemeoxygenase 1(HO1) in a time dependent manner (Fig. 2B).

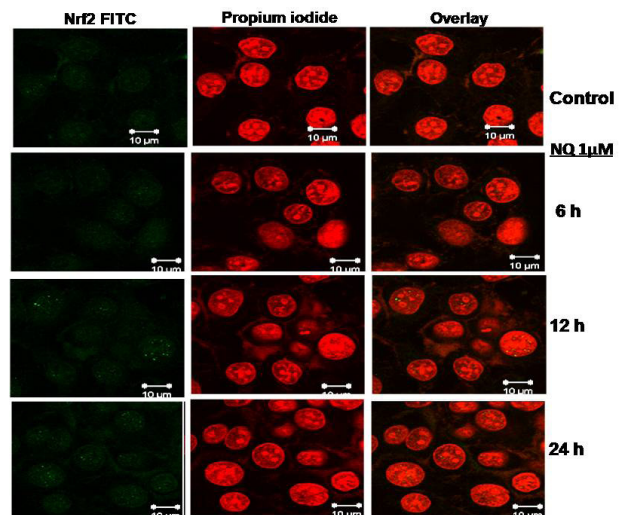


Fig. 2A : An increase in nuclear translocation of Nrf2 in a time dependent manner

BARC NEWSLETTER

Founder's Day

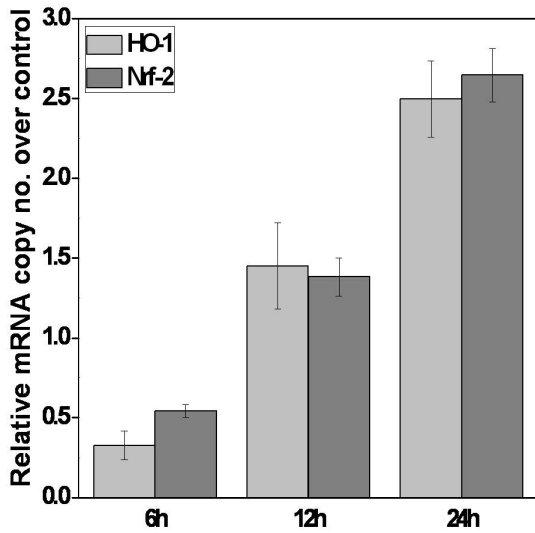


Fig. 2B : NQ treatment significantly enhanced the mRNA expression of Nrf2 and its dependent gene hemoxygenase 1(HO1) in a time dependent manner

Inhibitors of Nrf2 and its upstream kinases Erk abrogated NQ mediated protection

ATRA (Nrf2 inhibitor) and PD98059 (Erk inhibitor) significantly reverted the NQ mediated protection against radiation induced loss of clonogenicity in INT 407 cells (Fig. 3) suggesting the pivotal role of Nrf2 pathway as underlying mechanism.

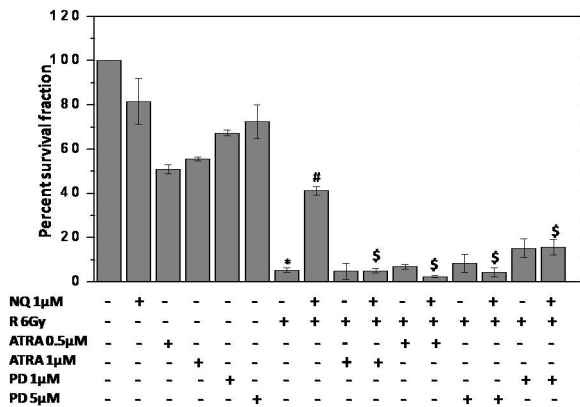


Fig. 3: ATRA (Nrf2 inhibitor) and PD98059 (Erk inhibitor) significantly reverted the NQ mediated protection against radiation induced loss of clonogenicity in INT 407 cells

NQ administration protected mice against WBI induced mortality

Administration of NQ (2mg/kg bw 4 doses) prior to irradiation protected mice against WBI 8Gy induced

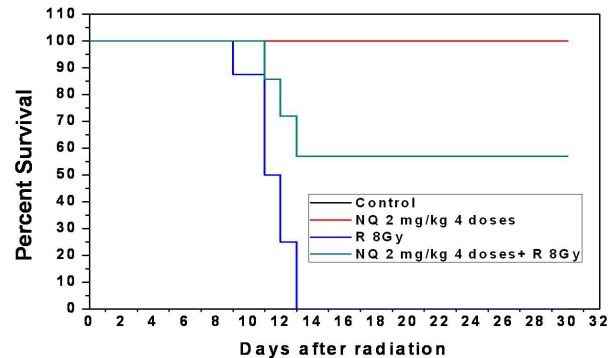


Fig. 4 : NQ treated mice showed significantly higher survival after WBI

mortality. NQ treated mice showed significantly higher survival after WBI (Fig. 4)

NQ protected against WBI induced gastrointestinal injury:

Normal villous architecture, epithelial alignment and crypts were observed in NQ administered group when compared to shortened and oedematous villi with epithelial irregularities in radiation treated group (Fig 5).

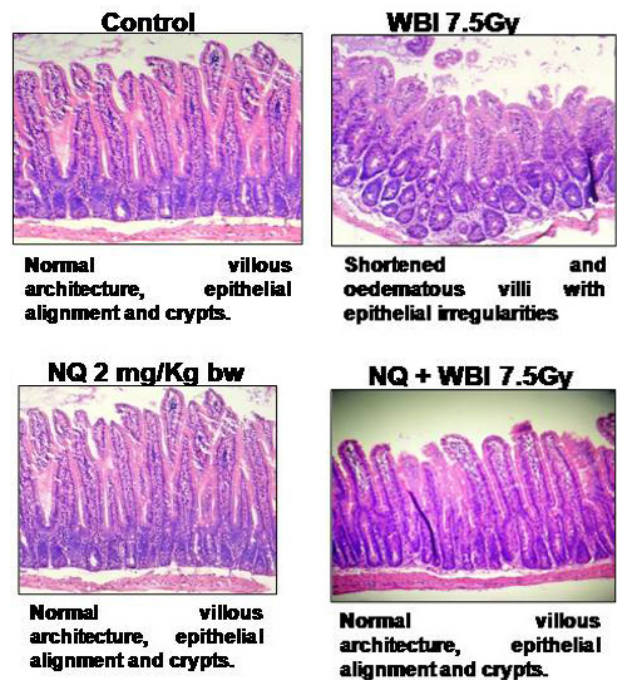


Fig. 5: Normal villous architecture, epithelial alignment and crypts were observed in NQ administered group when compared to shortened and oedematous villi with epithelial irregularities in radiation treated group

BARC NEWSLETTER

Founder's Day

Discussion

Earlier findings from our laboratory showed the potential of NQ to protect against hematopoietic system (3). Our current findings highlight the efficacy of NQ to protect gastro-intestinal tract from radiation induced toxicity. INT 407 cells served as a model for in vitro studies. Clonogenicity is defined as the potential of single cell to form a colony determining its proliferating efficiency. NQ significantly protected against radiation induced loss of clonogenicity. Radiation induced cell death is mainly due to induction of apoptosis which is marked by higher caspases activity. NQ protected against radiation induced increase in caspase activity. Balanced cellular redox status is required for normal functioning of cell. However transient modulation in cellular redox is associated with the induction of redox sensitive cytoprotective transcription factors like Nrf2. NQ being a pro-oxidant modulated cellular redox by transiently enhancing the basal ROS levels and depleting the abundant redox couple GSH/GSSH ratio (Fig. 1A and B). Further NQ showed an increase Nrf2 nuclear translocation and an increase in mRNA expression levels of Nrf2 and its dependent cytoprotective gene (Fig. 2A and B). Inhibitors of Nrf2 and its upstream kinases Erk, which is responsible for Nrf2 phosphorylation thus activation, reverted the effect of NQ on radiation induced cell death (Fig 3) implicating the pivotal role of Nrf2 pathway in NQ functioning as radioprotector. Further in vivo studies suggested the potential of NQ to act as radioprotector.

As discussed previously, doses from 8Gy and above induces mortality due to induction of GI syndrome. NQ significantly rescued mice from WBI 8Gy induced mortality (Fig. 4). NQ treated mice showed normal epithelial lining indicating intact absorptive surface of intestine when compared to denuded and oedematous villi with irregularities in epithelial lining in WBI group (Fig 5). Our findings highlight the efficacy of NQ to ameliorate radiation induced gastro-intestinal syndrome by modulating cellular redox and activating Nrf2 pathway.

References

1. Rotolo J, Stancevic B, Zhang J, Hua G, Fuller J, Yin X, Haimovitz-Friedman A, Kim K, Qian M, Cardó-Vila M, Fuks Z, Pasqualini R, Arap W, Kolesnick R. Anti-ceramide antibody prevents the radiation gastrointestinal syndrome in mice. *J Clin Invest.* 2012 May 1;122(5):1786-90.
2. Burdelya LG, Krivokrysenko VI, Tallant TC, Strom E, Gleiberman AS, Gupta D, Kurnasov OV, Fort FL, Osterman AL, Didonato JA, Feinstein E, Gudkov AV. An agonist of toll-like receptor 5 has radioprotective activity in mouse and primate models. *Science.* 2008 Apr 11;320(5873):226-30.
3. Khan NM, Sandur SK, Checker R, Sharma D, Poduval TB, Sainis KB. Pro-oxidants ameliorate radiation-induced apoptosis through activation of the calcium-ERK1/2-Nrf2 pathway. *Free Radic Biol Med.* 2011 Jul 1;51(1):115-28

INVESTIGATION OF THE EFFECTS OF -OH GROUP SUBSTITUTION ON THE RADIATION STABILITY OF FAP (FLUORO ALKYL PHOSPHATE) BASED IMIDAZOLIUM IONIC LIQUIDS

Apurav Guleria, Ajay. K. Singh, Sisir K. Sarkar and Soumyakanti Adhikari
Radiation & Photochemistry Division

This paper received the Best Poster Award at the National Symposium on Radiation & Photochemistry (NSRP-2013), North Eastern Hill University, Shillong, 20-22 March, 2013

Abstract

The radiation stability and the mechanism for FAP imidazolium ionic liquids (ILs) have been investigated owing to their superior hydrolytic stability and ultra hydrophobic nature. The ILs were subjected to very high radiation doses ranging from 50 kGy to 500 kGy. Various characterization studies involving density, viscosity, refractive index, conductivity, thermal stability and electrochemical window were performed on the irradiated ILs to determine the radiation effects on these properties. Qualitative studies i.e. NMR & Mass spectrometric studies were conducted on the ILs to identify the radiolytic products and the amount of decomposition was found to be <5% at higher radiation doses of 400 kGy. Introduction of -OH group in the alkyl side chain of the imidazolium moiety resulted into significant changes in the physical properties of these ILs with respect to their onset temperatures, conductivity and electrochemical window. Besides these, the H₂ gas yields of the ILs were determined and found to be comparable to that of a radiolytically stable aromatic compound, benzene. Through transient spectroscopic studies, we could delineate the mechanism for the radiation induced changes in the physicochemical properties of the non-hydroxyl and hydroxyl containing FAP ILs.

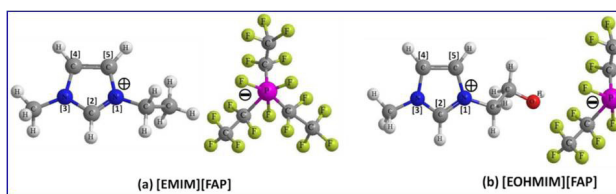
Introduction

Room Temperature Ionic Liquids (RTILs) are a rapidly expanding family of condensed-phase media with important applications in synthesis, extraction, catalysis and electrochemistry [1]. In the present scenario, RTILs are being considered as potential candidates in the reprocessing of spent nuclear fuel. It is therefore imperative to study the radiation chemistry of ILs to determine their radiolytic products and degradation pathways. No surprise that several radiation stability studies on ILs have already been reported. Most of these studies have been carried out on imidazolium ILs having anions such as PF₆⁻, BF₄⁻ or halogens. Essentially, these

ILs have been found to be hydrolytically unstable giving off highly toxic and corrosive HF. Further, the application of hydrophobic ILs in nuclear separations may put the ILs both in high radiation fields and in contact with aqueous raffinate containing 1-6 M HNO₃. Amongst various ILs, imidazolium ILs with bulky FAP (tris(perfluoroalkyl) trifluorophosphate) anion are ultra hydrophobic and possess excellent hydrolytic stability. Therefore, we performed an assortment of characterization and qualitative studies to explore the radiation stabilities of FAP ILs in the radiation doses, ranging from 50 to 500 kGy. Pulse radiolysis experiments were carried out to determine the transient species and their kinetic behavior on radiolysis.

Materials and methods

1-ethyl-3-methylimidazolium tris (pentafluoroethyl) trifluorophosphate, [EMIM][FAP] and 1-(2-Hydroxyethyl)-3-methylimidazolium tris (pentafluoroethyl) trifluorophosphate, [EOHMIM][FAP] were obtained from Merck KGaA, Darmstadt, Germany, with a purity > 99%. All other chemicals were of spectroscopic grade. The ILs were irradiated with a 7 MeV electron beam (FWHM ~ 2 μ s) obtained from a linear accelerator (LINAC, in conjugation with Pulse radiolysis system). The electron pulse used for carrying out the Pulse radiolysis experiments was 500 ns, while the dose per pulse was kept as 12 Gy. The structures of the ILs studied are shown below.



Results and discussion

On irradiation, both the ILs exhibited color evolution which further became intense with the increase in radiation dose. However, the color darkening was more in case of -OH group containing IL i.e. [EOHMIM][FAP]. The color evolution in [EMIM][FAP] at various radiation doses has been shown in the inset of Fig.1. This gives the indication of the radiolytic degradation occurring in the ILs. A typical optical absorption spectra of irradiated and unirradiated [EMIM][FAP] are shown in Fig.1. It was observed that [EMIM][FAP] displayed linear variation in the absorbance values (at 290 nm) with the radiation dose, while such trend was not observed in the case of [EOHMIM][FAP]. This result indicates, the -OH group can influence the radiolytic degradation pathways of [EOHMIM][FAP].

Qualitative studies such as NMR and Mass spectrometry were conducted on the pre- and post-irradiated ILs to identify the radiolytic products and the amount of degradation. Predominantly, the oligomeric species of

imidazole and its derivatives were observed however, their amounts were found to be very less (<0.5%) [2]. Nevertheless, the oligomeric products of imidazole are chromophoric in nature having high molar extinction co-efficient (ϵ) of the orders of $10^4 \text{ dm}^3 \text{ mol}^{-1} \text{ cm}^{-1}$ and exhibit similar optical absorption spectral features as in the present case of irradiated ILs. Therefore, the color evolution and the appearance of absorption peaks in case of irradiated ILs can be ascribed to π - π^* transition that originates from the radiolytic products derived from the imidazolium cation.

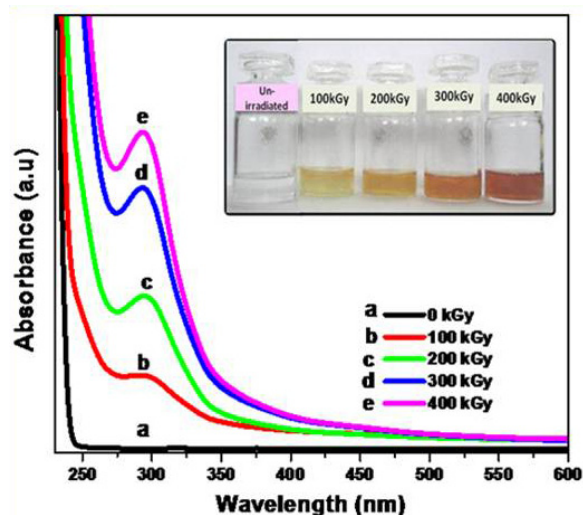


Fig.1: UV-VIS absorption spectra of pre-anti post-irradiated [EMIM][FAP]. Inset: Picture showing the color variation of IL on irradiation.

Various characterization studies were performed on the irradiated ILs to determine the radiation effects on their properties i.e. colour, density, viscosity, refractive index, conductivity, thermal stability and electrochemical window. As can be noticed from Table 1, the variation in the values of aforementioned properties of [EMIM][FAP] was very less even a high radiation doses of 400 kGy. While, significant decrease in the thermal stability and the conductivity values was observed for -OH group containing IL on irradiation. Besides, the gaseous products evolution is a crucial factor to be considered for any industrial or reactor scale application. Therefore, H_2 gas yields (G (H_2)) were measured from the irradiated FAP ILs ($(7.6 \pm 0.2) \times 10^{-9} \text{ mol/J}$ for [EMIM][FAP] and $(8.5 \pm 0.4) \times 10^{-9} \text{ mol/J}$ for [EOHMIM][FAP]) and were found to be

BARC NEWSLETTER

Founder's Day

Table 1: Physico-chemical properties of FAP ILs at various radiation doses. Density, viscosity and refractive index were measured at 25°C. Conductivity values were recorded at 20°C Taken from Ref [2]

FAP IL	Dose (kGy)	Refractive Index	Density, (g/cc)	Viscosity, cP	Conductivity, mS.cm ⁻¹	Electrochemical window (V)	Onset Temp., T _d (K)
[EMIM][FAP]	0	1.36886	1.7065	57	3.20	5.5	361
	100	1.36882	-	52	3.50	5.6	-
	300	1.36919	1.7067	-	-	-	-
	400	1.36925	-	59	3.21	5.5	360
[EOHMIM][FAP]	0	1.37775	1.7618	177	1.0	4.7	301
	100	1.37821	-	174	1.02	5.1	-
	300	1.37847	1.7627	-	-	-	-
	400	1.37841	-	179	0.636	4.8	283

almost equivalent to that of radiolytically stable aromatic compounds, i.e. benzene ($(6.5 \pm 0.4) \times 10^{-9}$ mol/J) [2].

Transient spectroscopic studies were carried out by Pulse radiolysis technique to delineate the mechanism for the radiation induced changes in the physicochemical properties of the non-hydroxyl and hydroxyl containing FAP ILs. Both the ILs give rise to similar transients with absorption peaks at 320 nm and a weak shoulder at 370 nm (Fig. 2A&B). However, the absorbance at 320nm in case of [EOHMIM][FAP] is 1.3 times higher than that in case of [EMIM][FAP]. A faster rate of formation of the transients was observed in case of [EOHMIM][FAP] (5.7×10^6 s⁻¹) cf. [EMIM][FAP] (3.26×10^6 s⁻¹). Furthermore, a marked difference was noted in the transient decay behavior of both the

ILs in the presence of O₂. As can be observed from Fig. 2C, the formation of a new species was evident in case of [EOHMIM][FAP] and was quite prominent while measuring at 370 nm. It was inferred that the formation of alkyl radical at the ethoxy side chain of the cation is quite likely as the addition of O₂ to this radical would form a peroxy radical which shows a strong absorption in the wavelength region 320-370 nm [2]. Thus, it becomes clear that the two ILs behave differently in radiation environment which has also been reflected in the number and yield of products.

Conclusions

All the results discussed here clearly indicate the hidden potential of the FAP imidazolium ILs to be a good solvent for various applications involving high radiation fields. Also, we have clearly demonstrated that a simple functionalization of the molecular structure of these ILs might cause marked differences in the reactivity, reaction center and the nature of the radiolytic products, which eventually lead to the significant changes in their physicochemical properties.

References

- Sun X., Luo H., Dai S., *Chem. Rev.* 112 (2012): 2100–2128.
- Guleria A., Singh A. K., Adhikari S., Sarkar S. K., *Dalton Trans.*, 43 (2014): 609–625.

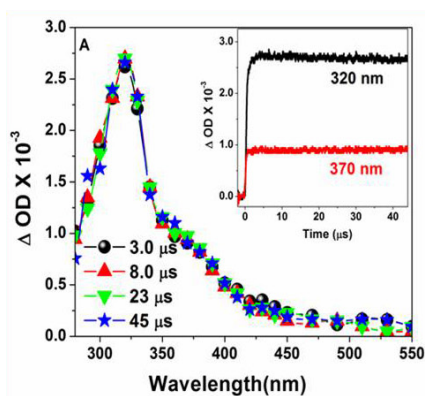


Fig. 2A: Transient absorption spectra for [EMIM][FAP] and traces in the inset

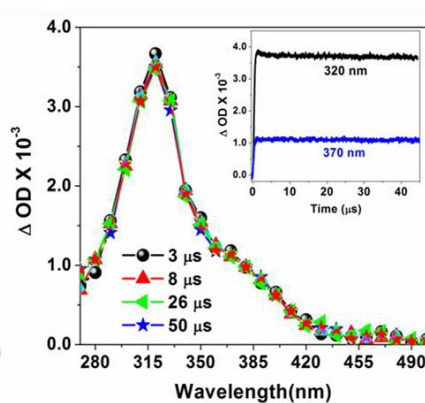


Fig. 2B: Transient absorption spectra for [EOHMIM][FAP] and traces in the inset

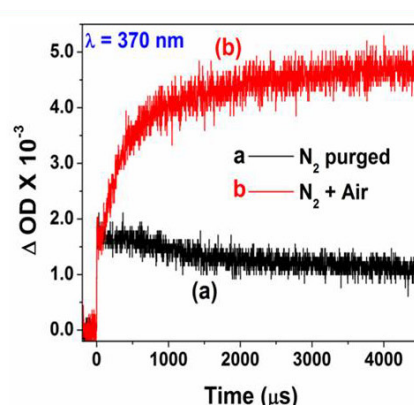


Fig. 2C: O₂ effect on the decay kinetics of [EOHMIM][FAP]

STRUCTURE AND PROPERTIES OF WATER IN THE HYDRATION SHELL OF HALIDE IONS AS REVEALED BY RAMAN SPECTROSCOPY

Mohammed Ahmed, Ajay K. Singh, Jahur A. Mondal and Sisir K. Sarkar
Radiation & Photochemistry Division

This paper received the Best Poster Award at the National Symposium on Radiation & Photochemistry (NSRP-2013), North Eastern Hill University, Shillong, 20-22 March, 2013

Abstract

The structure and properties of water at the vicinity of ions play an important role in chemistry and biology. We have investigated the properties of water in the presence of alkali halides in D_2O and in isotopically diluted water (HOD) using spontaneous Raman spectroscopy. Our results revealed that the water in the hydration shell of the halide ions has weaker hydrogen-bonding, reduced intra-/intermolecular coupling, and enhanced Raman cross-section (OH-stretch) compared to those of the bulk water. Quantitative analysis revealed that the Raman cross-section of hydrating water increases due to pre-resonance enhancement by a higher excited electronic state of water.

Introduction

Interactions between ions and water play important roles in biological, environmental, and industrial processes. Vibrational spectroscopic methods are widely used to understand these interactions because the vibrational transitions in a molecule are highly sensitive to its local environments/ions. In general, a comparison of the spectral width, position, and intensity of the vibrational spectrum of neat water with those of aqueous electrolyte solutions would reveal the effect of electrolyte/ions on the vibrational properties of water [1]. However, the band shape and the intensity of the vibrational spectrum of water are heavily affected by the intermolecular coupling and Fermi Resonance (FR) in the OH stretch regions, which may vary with the environment or the presence of ions. As a result, the analysis of the vibrational spectrum of water in different environments becomes complicated. Several studies have investigated the hydrogen-bonding properties of water in the hydration shell of

halide ions or in other environments. However, less attention has been put in investigating the intra-/intermolecular coupling and Raman cross-section of water in the hydration shell of the halide ions/ or in other environments [2,3]. Here, we have investigated the intermolecular coupling and the FR of water in the hydration shell of the halide ions by recording the Raman spectra of D_2O and isotopically diluted water (HOD) with different alkali halides (NaX) of varying concentrations.

Experimental

The alkali halide salts ($\geq 98.0\%$) and D_2O (atom % D ≥ 99.0) were purchased from Sigma Aldrich. Milli-Q water (H_2O ; $18.2\text{ M}\Omega\text{ cm}$ resistivity) was used for isotopic dilution of D_2O . The spontaneous Raman spectra of the samples were recorded using a STR-300 micro-Raman spectrometer (SEKI Technotron, Japan) with 532 nm excitation (power $\sim 20\text{ mW}$ at the sample). The scattered light was collected through a

BARC NEWSLETTER

Founder's Day

fiber coupled 300 mm spectrograph and detected by a thermo-electric cooled (-75°C) charge-coupled device (CCD). The total acquisition time was 500 sec. or more for a single spectral measurement.

Results and Discussion

Fig. 1 shows that with increasing the concentration of NaBr in D_2O (i) the Raman intensity in the red regions (strongly H-bonded) of the OD stretch band decreases and that in the blue regions (weakly H-bonded) increases, and (ii) the integrated Raman intensity increases too. A similar spectral change is observed on addition of H_2O in D_2O (isotopic dilution), as shown in inset of Fig.1 Presumably, on isotopically dilution, the H-bond strength and the Raman cross-section of $\nu_{\text{OD-str}}$ does not change but the intra-/intermolecular coupling of water is significantly reduced. Thus, the reduced intra-/intermolecular coupling might have a contribution to the spectral changes in Fig. 1. To investigate this issue, we measured the Raman spectra of isotopically diluted water, $\text{D}_2\text{O}/\text{HOD}/\text{H}_2\text{O} = 1/18/81$, which is free from the intermolecular coupling and FR in the OD stretch regions [4], in presence of different concentrations of NaBr as shown in Fig.2. On increasing concentration of NaBr, the intensity in the red regions of the OD stretch band decreases and that in the blue region increases with an isobestic point at $\sim 2490\text{ cm}^{-1}$. These spectral changes suggest that the water in the hydration shell of Br- has weaker H-bonding compared to that in the bulk. Comparing Figs. 1 and 2, it is observed that with increasing concentration of Br- the spectral width (FWHM) of the OD stretch band decreases significantly in D_2O than that in isotopically diluted water (Inset of Fig.2). The band width (OD stretch) decreases with decreasing intermolecular coupling and FR. Assuming that the isotopically diluted water ($\text{D}_2\text{O}/\text{HOD}/\text{H}_2\text{O} = 1/18/81$) does not have significant intermolecular coupling and FR, the large decrease in ΔFWHM in D_2O is assignable to the significant reduction in intermolecular coupling and FR of D_2O in the hydration shell of Br-.

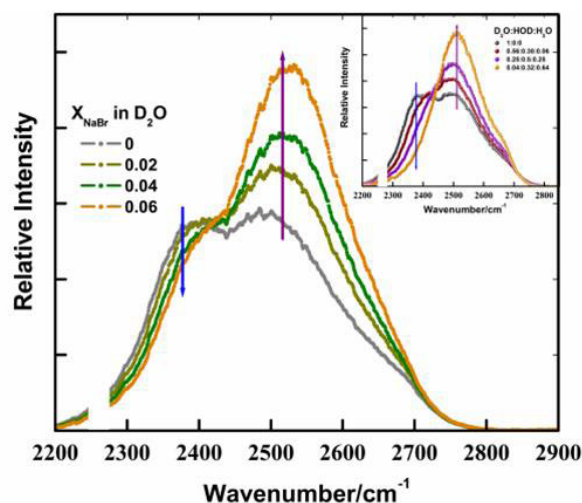


Fig.1. Raman spectra in OD stretch regions (A) NaBr in D_2O . Inset: $\text{D}_2\text{O}/\text{D}_2\text{O}-\text{H}_2\text{O}$ mixtures with different mole ratios.

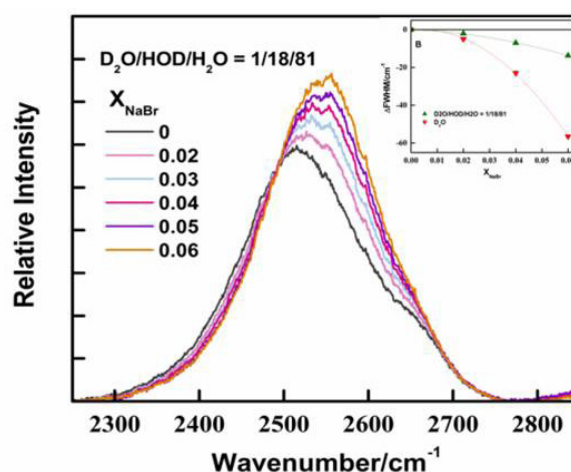


Fig.2. (A) Normalised Raman Spectra of $\text{D}_2\text{O}-\text{H}_2\text{O}$ mixture ($\text{D}_2\text{O}/\text{HOD}/\text{H}_2\text{O} = 1/18/81$) with different mole fractions of NaBr. Inset: Change in FWHM of the OD stretch band with X_{NaBr}

Quantitative analysis in D_2O and isotopically diluted water ($\text{D}_2\text{O}/\text{HOD}/\text{H}_2\text{O} = 1/18/81$) shows that the relative Raman cross-section $(\frac{\sigma_{\text{H}}}{\sigma_{\text{b}}})$ are the Raman cross-sections of hydrating and bulk water) in D_2O is higher than that in HOD (Fig. 3). The higher $\frac{\sigma_{\text{H}}}{\sigma_{\text{b}}}$ in D_2O is due to the reduced intra-/intermolecular coupling of water in the hydration shell of the halide ion compared to that in bulk water [4]. Fig. 4 shows the plot of $\frac{\sigma_{\text{H}}}{\sigma_{\text{b}}}$ vs. the energy of the excited electronic state ($\nu_{e(b)}$) of water. The $\frac{\sigma_{\text{H}}}{\sigma_{\text{b}}}$ increases as the size of the halide ion increases, which is attributed to the

BARC NEWSLETTER

Founder's Day

pre-resonance enhancement of Raman cross-section in the hydration shell of halide ion. The experimental data points (orange circles) are lower than those predicted by the simulated curve (dark yellow)

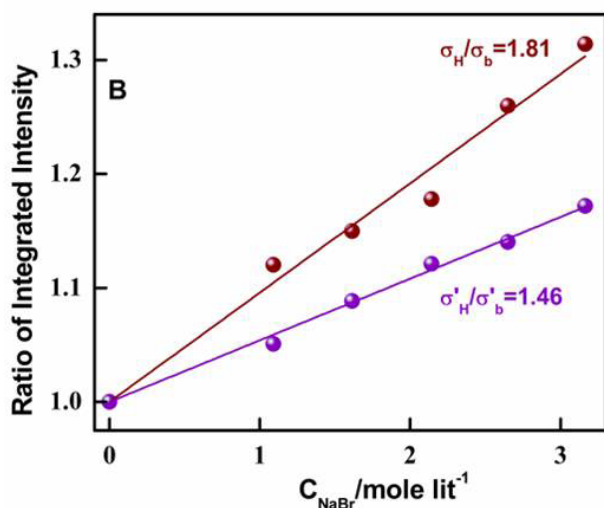


Fig. 3: Normalized integrated intensity vs concentration of NaBr in D₂O (black) and HOD (red).

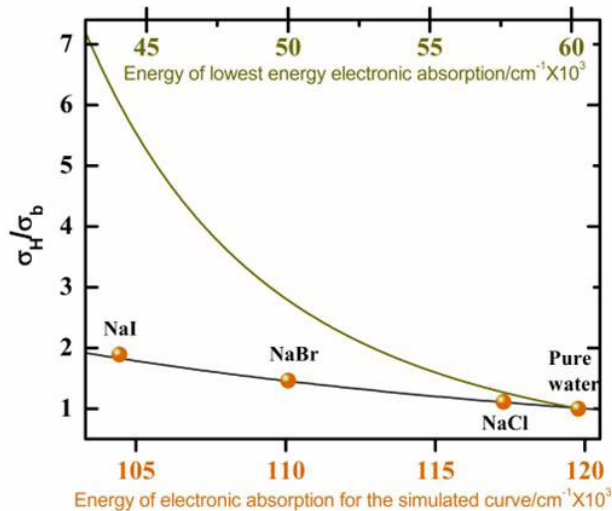


Fig.4: Plot of relative Raman cross-section vs. the energy of electronic absorption of water.

corresponding to the lowest energy ($\nu_{e(b)}$) ~ 60240 cm⁻¹) electronic absorption of water. However, the gray simulated curve corresponding to a higher energy ($\nu_{e(b)}$) ~ 120000 cm⁻¹) excited electronic states of water nicely reproduce the experimental results. We propose that the higher excited electronic state of water governs the pre-resonance enhancement of the Raman cross-section of water and the lowest excited electronic state of water does not contribute efficiently to the σ_H of OD (OH)_{str.}

Conclusions

We have investigated the effect of halide ions on the intermolecular coupling, Fermi-Resonance (FR), hydrogen-bonding properties, and the Raman cross-section of neat D₂O and isotopically diluted water (D₂O/HOD/H₂O = 1/18/81) by measuring the Raman spectra in the OD stretch regions. Our results reveal that water poses for reduced intermolecular coupling and FR in the hydration shell of the halide ions compared to those in the bulk. Quantitative analysis revealed that pre-resonance enhancement of the Raman cross-section of hydrating water is only weakly enhanced by the lowest energy charge transfer electronic excited state of water.

References

1. Omta A.W., Kropman M.F., Woutersen S., and Bakker H.J., *Science* 301(2003):347-349.
2. Perera P.N., Browder B., and Ben-Amotz D., *J. Phys. Chem. B*, 113 (2009):1805-1809.
3. Smith J.D., Saykally R.J., and Geissler P.L., *J. Am. Chem. Soc.*, 129 (2007):13847-13856.
4. Ahmed M., Singh A.K., Mondal J.A., Sarkar S.K., *J. Phys. Chem. B* 117 (2013): 9728-9733.

NOVEL DESIGNING OF THERMO-ELASTIC MACROPOROUS AGAROSE-ALGINATE COMPOSITE BIOMATERIAL

Anuj Tripathi and Jose Savio Melo
Nuclear Agriculture and Biotechnology Division

This Paper received the Best Poster Award at the 19th DAE-BRNS Symposium on Thermal Analysis, held at Mumbai from Dec. 19-21, 2013

Abstract

The present study describes the synthesis of macroporous polymeric composite matrix using natural polymers like alginate and agarose by the process of cryotropic polymerization. The synthesized matrix was examined for their thermal stability and mechanical property at different temperature. The results indicated thermal tolerance of the composite matrix. However with increasing temperature, elastic behavior of matrix shows increase in tensile property but decrease in elastic modulus. The results suggest that there is potential in the use of naturally derived polymers for the synthesis of porous biomaterials with thermo-elastic properties for various biomedical applications.

Introduction

One of the most exciting areas of advanced materials science research is in the applications of biomaterials to healthcare and especially to reconstructive surgery. At a time when technological research should contribute to improvements in the quality of life, it is obvious that the developments of advanced materials for application either inside or outside the body in order to treat disease and injury have a high priority. The variety of natural chemical structures together with the precise control of their molecular architecture and morphology, rationalize the numerous uses of biopolymers (natural polymers) as biomaterials in high technological and biological applications. Because of inherited properties, biopolymers are of interest as a bio-mimetic component for tissue engineering application but there are also some concerns like loss of bioactivity of the biopolymer during its extensive processing prior to application. In addition, they have also been widely used in drug and protein delivery system, cell culture, medical and biological sensors, water absorbent pads, hygiene products, breast implants, wound dressing and for enzyme and cell immobilization¹⁻³. Porous polymeric

matrices are attractive class of substrates for various biotechnological applications. Among other properties, the thermal stability and mechanical properties are important parameters to understand the biomaterial behavior in a biological (*in situ*) environment.

We aimed to synthesize a composite porous polymeric matrix, which could retain 3D porous structure even after drying, show improved thermal stability and elastic behavior for biomedical application. We have used different ratios of polymers and optimized the matrix properties. The thermo-elastic stability was accessed by thermo-gravimetric and mechanical analysis. The use of cryotropic polymerization technology to produce customized porous matrix with controlled internal micro-architecture is also addressed.

Experimental

Synthesis of agarose-alginate (Ag-Al) cryogel monolith

Ag-Al cryogel was synthesized using N-(3-dimethylaminopropyl)-N'-ethylcarbodiimide

BARC NEWSLETTER

Founder's Day

hydrochloride (EDC) with N-hydroxysuccinimide (NHS) for chemical crosslinking. Low viscosity alginate solution (3.75%) was prepared in a plastic tube (50 mL) using deionized water as a solvent. On the other hand, agarose (Low EEO; gelling temperature 38-40 °C) (6%) was dissolved in deionized water by placing the agarose containing tube in the boiling waterbath until the solution became transparent. Further, 4 mL of stock solution of alginate (3.75%) was added to 5 mL of hot agarose solution (6%) and then cooled at room temperature. When the temperature of the heterogeneous solution reached to 45 °C, 500 μ L of 0.35 M freshly prepared EDC solution was added which was followed by adding 500 μ L of 0.2 M NHS solution. The reaction mixture of Ag-Al was transferred into 5 mL plastic syringe and immediately frozen at -12 °C for 16 h in liquid cryobath (Grant, Cambridgeshire, UK). After completion of incubation, gels were thawed in deionized water and dried at room temperature till further use.

Characterization of porous agarose-alginate matrix

The structural morphology of synthesized Ag-Al cryogel was analyzed by scanning electron microscopy (SEM). Thermo-gravimetric (TGA) analysis of Ag-Al cryogel was performed using calorimeter under nitrogen atmosphere over the temperature range of 20 to 500 °C at increment of 10 °C/min. Cylindrical cryogel samples of height 5 mm and diameter 13 mm were saturated with 0.1 M phosphate buffer saline (PBS) and then used for conducting the tensile tests. Uniaxial elongation was performed to the cryogel samples with 10 kN load cell under displacement control at the rate of 1 mm/min. The slope of the graph with stress (kPa) on Y-axis and strain (%) on X-axis was measured at 10% strain to calculate elastic modulus and tensile strength.

Results and discussion

Ag-Al cryogels were synthesized by optimizing the concentration of agarose in co-polymer. The synthesis

is based on cryotropic gelation of agarose and alginate chains at subzero temperature in the presence of crosslinker EDC and NHS. Synthesized Ag-Al cryogel was white in color, soft, spongy and retained 3D porous architecture (Fig. 1a). Upon complete drying, cryogel was shrunk approximately 1 to 2 mm in diameter from its original size (13 mm diameter). Interestingly, Ag-Al gel shows shape memory property i.e. returns to its original shape and size while soaking in aqueous medium.

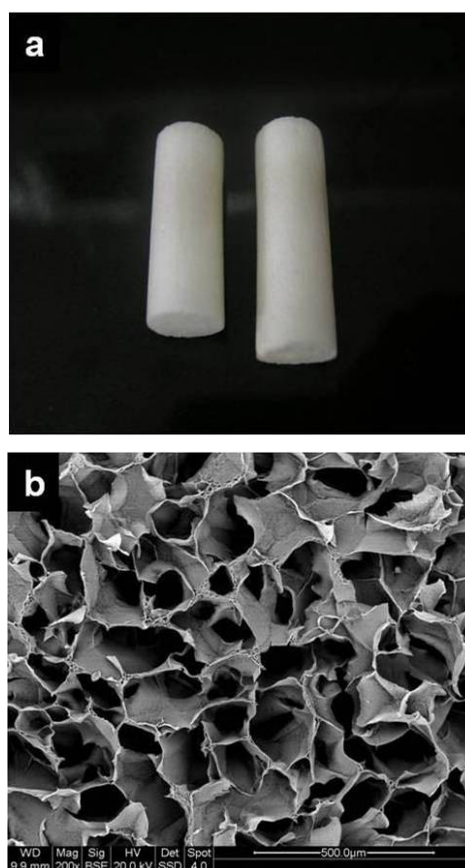


Fig 1. Physical form of AA monolith gels (a) and its scanning electron microscopic image showing homogenous macropores distribution (b). (SEM scale bar: 50 μ m).

Microstructure analysis of Ag-Al cryogel was evaluated by scanning electron microscope (SEM). The pore range of the cryogel sections of a monolith was 30 μ m to 100 μ m with an average pore diameter of \sim 70 μ m. The SEM observation showed uniform pore distribution (Fig. 1b). The size of pores can be controlled by the heat transfer ratio within the system. For example, at defined temperature, the smaller cryogel system

BARC NEWSLETTER

Founder's Day

will have better heat transfer ability and maintain the temperature compared to bigger sample. So, during the cryogelation process, variations in the temperature besides other parameters can change the structural homogeneity of a cryogel.

The thermal stability of alginate gel and Ag-Al gel was accessed by thermo-gravimetric analysis (TGA). The graph of percentage weight loss v/s time showed onset of decomposition approximately at 60 °C, which is due to the dehydration of gel in both the cases. The second decomposition was observed at 200 °C in both the matrices, but the degree of abjection was higher in case of plain alginate with 50% weight loss at 250 °C, which is a typical behaviour of alginate. While in the composite Ag-Al gel, a linear decomposition was observed, which began at 200 °C and 50% decomposition was noticed at 340 °C. This might be due to the higher intermolecular/interfibrillar crosslinking of polymer chains of agarose and alginate resulting in increased thermal stability.

Unconfined compression tests showed significant elasticity of Ag-Al cryogels and maintained their physical integrity even after compressing them up to 80% of their original length. The elastic modulus was observed in the range of 36-39 kPa. The aggregate tensile modulus showed good elasticity of the Ag-Al cryogels. At different temperatures i.e. 27 °C and 37 °C, the tensile modulus was 320 ± 63 kPa and 250 ± 94 kPa, respectively. These results suggest that temperature affects the elastic behavior of the matrix.

Conclusion

Nevertheless, the physico-mechanical studies compliment the macroporosity of these polymeric biomaterials, which is an important parameter in tissue engineering, bioreactors and bio-separation applications. This particular polymer combination has also been synthesized by authors in other type of formats like disks, sheets and beads⁴. Agarose itself has physical crosslinking property and can make a

porous three-dimensional scaffold. However, the presence of alginate in the composite increases the softness of the cryogel as well as the spongy nature. On the other hand, alginate presence is also beneficial to cultivate different cell types for tissue engineering applications and immobilization purposes. Alginate has also been used for capturing of heavy metals and bacteria from the waste water⁵. Our group is using these cryogels with suitable chemistry, porosity as well as thermal and mechanical stability, modulated as per the application. Our purpose is to provide a novel approach to design such materials which can be cost effective and highly efficient for cell and enzyme immobilization, bio-processing, separation technologies as well as in regenerative medicine and tissue engineering applications.

References

1. Park, K. "Superporous hydrogel for pharmaceuticals and other applications". *Drug Delivery Technology*, 2(5), (2002): 38-44.
2. Tripathi, A., Kathuria, N., Kumar. A. "Elastic and macroporous agarose-gelatin cryogels with isotropic and anisotropic porosity for tissue engineering". *Journal of Biomedical Materials Research A* 90A (3), (2009): 680-694.
3. Tripathi, A., Sami, H., Jain, S.R., Vilorio-cols, M., Zhuravleva, N., Nilsson, G., Jungvid, H., and Kumar, A. "Improved bio-catalytic conversion by novel immobilization process using cryogel beads to increase solvent production". *Enzyme and Microbial Technology* 47, (2010), 44-51.
4. Tripathi, A., and Kumar. A. "Multi-featured macroporous agarose-alginate cryogel: synthesis and characterization for bioengineering applications". *Macromolecular Bioscience* 11(1), (2011):22-35.
5. Tripathi, A., Melo, J.S., D'Souza, S. F. "Uranium (VI) recovery from aqueous medium using novel floating macroporous alginate-agarose-magnetite cryobeads". *Journal of Hazardous Materials* 246-247, (2013): 87- 95.

BARC NEWSLETTER

Founder's Day



FrnE: A CADMIUM INDUCIBLE PROTEIN IS CHARACTERIZED AS A DISULFIDE ISOMERASE HAVING ROLE IN OXIDATIVE STRESS TOLERANCE IN *DEINOCOCCUS rADIODURANS*

Nivedita P. Khairnar and H.S. Misra

Molecular Biology Division

and

Min-Ho Joe, Sang-Yong Lim and Dong-Ho Kim

Radiation Research Division for Biotechnology, Korea Atomic Energy Research Institute

This paper received the Best Poster Award during XXXIII Annual Conference of Environmental Mutagen Society of India and National Conference on Current Perspectives on Environmental Mutagenesis and Human Health, Mumbai, Jan. 28-30, 2013

Abstract

Deinococcus radiodurans R1 is characterized for its extraordinary resistance to DNA damaging agents including gamma radiation, UV rays, desiccation and genotoxic chemicals like H₂O₂ and MMC. These stressors produce oxidative stress and cause severe damage of DNA and proteins, which eventually lead to cell death. It can tolerate extensive DNA damage and oxidative stress without a measurable loss of cell viability. The antioxidant enzymes like catalase, superoxide dismutase, antioxidant metabolites like thioredoxins, pyrroloquinoline quinone, deinoxanthin and Mn²⁺ involved processes have been contributing to the extraordinary oxidative stress tolerance in this bacterium. Its genome also encodes homologues of putative Disulfide bond (Dsb) forming proteins. *D. radiodurans* exposed to a lethal dose of cadmium shows differential expression of a large number of genes including *frnE* and others involved in DNA repair and oxidative stress tolerance. Levels of *frnE* expression increased by nearly 7 fold in response to cadmium treatment. *FrnE* mutant of *D. radiodurans* showed ~15 and ~3 fold less tolerance to 10 mM cadmium and diamide respectively, as compared to wild type. Recombinant FrnE showed disulfide isomerase activity on scrambled Rnase A substrate and could maintain insulin in its reduced form in presence of dithiothreitol (DTT). In trans expression of *FrnE* could complement the loss of DTT resistance in *dsbC* and *dscbCD* mutants of *E. coli*. Equimolar amount of purified recombinant *FrnE* protected malate dehydrogenase completely from thermal denaturation at 42°C, indicating the chaperon role of *FrnE in vitro*. The results suggesting *FrnE* role in oxidative stress tolerance of *D. radiodurans* most likely by protecting the proteins from oxidative damage would be presented.

Footnote: This work is published as "Khairnar NP, Joe M-H, Misra, HS, Lim S-Y, Kim D-H. 2013 FrnE: a cadmium inducible protein in *Deinococcus radiodurans* is characterized as a disulfide isomerase chaperon *in vitro* and for its role in oxidative stress tolerance *in vivo*. *J. Bacteriol.* 195:2880-2886.

BARC NEWSLETTER

Founder's Day

Introduction

Deinococcus radiodurans R1 a member of Deinococceae family is characterised for its extraordinary resistance to DNA damaging agents including γ radiation, UV rays, desiccation and genotoxic chemicals like H_2O_2 and MMC (Misra et al., 2013). It can tolerate extensive DNA damage and oxidative stress without a measurable loss of cell viability. The antioxidant enzymes like catalase and superoxide dismutase, thioredoxins, antioxidant metabolites like pyrroloquinoline quinone, deinoxanthin and Mn^{2+} complexes of small molecules involved processes are attributed to extraordinary oxidative stress tolerance in *D. radiodurans*. Its genome also encodes putative Dsb homologues (Heras et al., 2009), which have not been characterized in greater details. Recently, it has been observed that *D. radiodurans* exposed to lethal doses of cadmium and gamma radiation upregulates the transcription of DR_0659 by nearly 7 fold (Joe et al., 2011). DR_0659 encodes a putative FrnE type protein in this bacterium and the levels of expression of proteins belonging to this family are induced in response to oxidative damage in other bacteria. Proteins belonging to thioredoxin family are involved in disulfide bond formation (Dsb) in many organisms including in eukaryotes. In prokaryotes, the Dsb proteins are located in periplasm and six members of this class have been identified, which are named as DsbA-E and G redox proteins (Singh et al., 2008). Roles of Dsb redox proteins have been demonstrated in virulence of many pathogenic bacteria (Peek and Paylor, 1992). These proteins have redox-active dithiol Cys-X-X-Cys motif in the active site. DsbA and DsbB are involved in disulfide bond formation while DsbC and DsbD are in the disulfide bond isomerisation function. Disulfide bond plays an important role in proper folding, stability and secretion of such proteins (Tomb, 1992, Missiakas and Raina, 1997) and therefore, mutations in *dsb* genes lead to incorrect folding of cellular proteins involved in various processes including oxidative stress tolerance (Kamitani et al., 1992). During severe oxidative stress, these systems get inactivated or overburdened, thus

the cytosolic cysteine residues become susceptible to oxidation. Most organisms encode machineries that protect proteins from oxidative damage and thioredoxin superfamily proteins play important roles in this process. Therefore, the characterization of Dsb proteins and their roles in oxidative stress tolerance in bacteria belonging to the Deinococceae family would be worth undertaking. Here, we characterized DR0659 protein (hereafter referred as drFrnE) a member of Dsb family as a disulfide isomerase and demonstrated its roles in bacterial resistance to oxidative stress producing agent *in vivo* and in protection of malate dehydrogenase from thermal inactivation *in vitro*.

Results and conclusion

Genomic copy of *drfrnE* gene was inactivated and its effects of normal growth and oxidative stress response of *D. radiodurans* was evaluated. Inactivation of this gene led to the sensitivity to Cd by ~ 15 fold, ~ 3 fold for diamide, ~ 6 fold to γ rays and ~ 2 fold losses to hydrogen peroxide at 40mM, suggesting the role of drFrnE in oxidative stress tolerance of *D. radiodurans* (Khairnar et al., 2013). Recombinant drFrnE was produced in our laboratory and various activities related to Dsb proteins were checked. The recombinant protein could reduce insulin and reactivate scrambled RNase *in vitro* (Khairnar et al., 2013). These results suggested that drFrnE is a member of protein disulfide isomerase (PDI) family protein having roles in oxidative stress tolerance in *D. radiodurans*. The PDIs function in the reactivation of scrambled RNaseA by correcting the wrong disulfide interaction to correct disulfide bond formation. Such proteins are known to act as molecular chaperon *in vitro*. Since, drFrnE does reactivate scrambled RNaseA *in vitro*, the possibility of drFrnE having chaperon like activity was tested using malate dehydrogenase (MDH) *in vitro*. Both wild type as well as active site mutant as generated through site directed mutagenesis, derivatives were made and drFrnE role in protection of MDH from higher temperature was evaluated. Results showed that wild type drFrnE protected MDH from heat denaturation at

BARC NEWSLETTER

Founder's Day

42°C in a concentration dependent manner (Khairnar et al., 2013). This activity was not observed with active site mutant of *FrnE*. This indicated that the possible mechanisms underlying in vitro protection of MDH from inactivation could be through both holdase as well as stabilization of disulfide bonds by PDI function of drFrnE. Nevertheless, these results suggested that wild type drFrnE could protect MDH from thermal denaturation and seems to have chaperon functions at least *in vitro*.

Acknowledgements

We are grateful to Professor S. K. Apte, for his support and criticisms and Korean Atomic Energy Research Institute (KAERI, South Korea) for postdoctoral fellowship to NPK.

References

1. Misra HS, Rajpurohit YS, Kota S. 2013. Physiological and molecular basis of extreme radioresistance in *Deinococcus radiodurans*. *Curr. Sci.* 104: 194-205.
2. Heras B, Shouldice SR, Totsika M, Scanlon MJ, Schembri MA, Martin JL. 2009. DSB proteins and bacterial pathogenicity. *Nat. Rev. Microbiol.* 7:215–225.
3. Joe MH, Jung SW, Im SH, Lim SY, Song HP, Kwon O, Kim DH. 2011. Genome-wide response of *Deinococcus radiodurans* on cadmium toxicity. *J. Microbiol. Biotechnol.* 21:410–419.
4. Singh AK, Bhattacharyya-Pakrasi M, Pakrasi HB. 2008. Identification of an atypical membrane protein involved in the formation of protein disulfide bonds in oxygenic photosynthetic organisms. *J. Biol. Chem.* 283:15762–15770.
5. Peek JA, Taylor RK. 1992. Characterization of a periplasmic thiol:disulfide interchange protein required for the functional maturation of secreted virulence factors of *Vibrio cholerae*. *Proc. Natl. Acad. Sci. U. S. A.* 89:6210–6214.
6. Tomb JF. 1992. A periplasmic protein disulfide oxidoreductase is required for transformation of *Haemophilus influenzae* Rd. *Proc. Natl. Acad. Sci. U. S. A.* 89:10252–10256.
7. Missiakas D, Raina S. 1997. Protein folding in bacterial periplasm. *J. Bact.* 179:2465–2471.
8. Kamitani S, Akiyama Y, Ito K. 1992. Identification and characterization of an *Escherichia coli* gene required for the formation of correctly folded alkaline phosphatase, a periplasmic enzyme. *EMBO J.* 11:57–62
9. Khairnar NP, Joe M-H, Misra, HS, Lim S-Y, Kim D-H. 2013 FrnE: a cadmium inducible protein in *Deinococcus radiodurans* is characterized as a disulfide isomerase chaperon in vitro and for its role in oxidative stress tolerance in vivo. *J. Bacteriol.* 195:2880-2886.

